Advances in Natural and Technological Hazards Research

Tsunamis

Case Studies and Recent Developments

Kenji Satake (Editor)

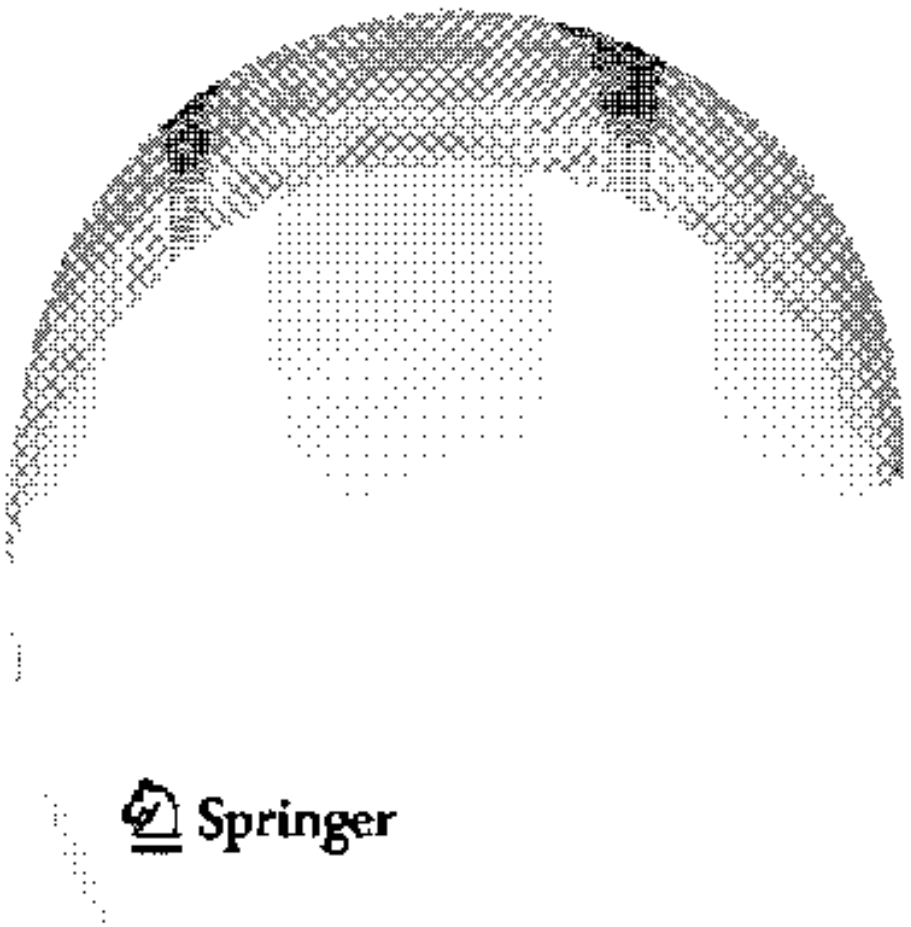

Springer

Tsunamis

Advances in Natural and Technological Hazards Research

VOLUME 23

The titles published in this series are listed at the end of this volume.

Tsunamis

Case Studies and Recent Developments

Edited by

KENJI SATAKE

National Institute of Advanced Industrial Science and Technology,
Tsukuba, Japan

Springer

A C.I.P. Catalogue record for this book is available from the Library of Congress.

ISBN 10 1-4020-3326-5 (HB) Springer Dordrecht, Berlin, Heidelberg, New York
ISBN 10 1-4020-3331-1 (e-book) Springer Dordrecht, Berlin, Heidelberg, New York
ISBN 13 978-1-4020-3326-1 (HB) Springer Dordrecht, Berlin, Heidelberg, New York
ISBN 13 978-1-4020-3331-5 (e-book) Springer Dordrecht, Berlin, Heidelberg, New York

Published by Springer,
P.O. Box 17, 3300 AA Dordrecht, The Netherlands.

Printed on acid-free paper

Printed in the Netherlands.

TABLE OF CONTENTS

PREFACE

This book contains 20 papers reflecting the state-of-the-art tsunami research. Most of them were presented at the two international meetings held in 2003: the 21st International Tsunami Symposium, held on July 9 and 10th as a part of IUGG general assembly in Sapporo, Japan, and an International Workshop on Tsunamis in the South Pacific, held on September 25 and 26th in Wellington, New Zealand. More recent work, including the field survey report of the Tokachi-oki earthquake tsunami of September 26, 2003, is also included.

Synolakis and Okal summarize the survey results of International Tsunami Survey Teams, as well as seismological and numerical modelling studies of 15 tsunami events occurred between 1992 and 2002. In this active decade of tsunami disasters, the tsunami community has learned how to organize ITST, describe, document and share the results of surveys. The authors also propose a method to discriminate the seismic tsunamis from landslide tsunamis based on the observed runup heights, and demonstrate it for the recent tsunamis. *Power et al.* report the tsunamis generated by the 2003 Fiordland, New Zealand, earthquake (M 7.2). This earthquake generated two kinds of tsunamis; a local large (4-5 m) tsunami generated by rockslide in a sound, and a smaller tsunami generated by earthquake faulting and detected on tide gauges in Australia.

Three papers discuss volcanic tsunamis in the western Pacific region. *Nishimura et al.* report the tsunami from the 1994 eruption of Rabaul volcanoes. They use a geological method to this modern tsunami deposits and infer the timing and size of tsunamis generated several times in the eruption series. *Pelinovsky et al.* present 35 tide gauge records from the 1883 Krakatau eruption, one of the largest tsunamis instrumentally-recorded all over the world. While the tsunamis in Indian Ocean and Atlantic appear as predicted from ray tracing computations on modern bathymetry, those in Australia, New Zealand and North America do not, indicating that they are not hydrodynamic tsunamis. *Kawamata et al.* report the hydraulic experiments of landslide to estimate the parameters for numerical simulation of two-layer models. They model the 1741 tsunami from landslide of the Oshima-Oshima volcano in Japan Sea to show that the landslide source yields better fit with the observation than an earthquake fault model.

Five papers examine tsunami sources, propagation and coastal behaviour of tsunamis around Japan and Kuril Islands. *Abe* reports seiche periods at 36 bays on Sanriku coast of Japan and compare them with the tsunami amplification factors of each bay from past tsunamis, the 1896 and 1933 Sanriku, 1968 Tokachi-oki and 1960 Chilean tsunamis. He shows that the amplification factors are the largest near the dominant period of incoming tsunamis. *Namegaya and Tsuji* discuss the delayed phase, which appear about 2.6 hours after the first tsunami arrival, of tide gauge records at Miyako from earthquakes off eastern Hokkaido. By making numerical computations for actual and fictitious bathymetry, they conclude that the delayed peak is caused by combination of reflected and edge waves. *Tanioka et al.* summarize the tsunami survey results of the recent 2003 Tokachi-oki earthquake. More than 200 runup height measurements, photographs of actual tsunamis and the descriptions of deposits are presented, as well as a result of numerical simulation at Ootsu harbor where very dense measurements were made. *Satake et al.* review the earthquakes and tsunamis along the Kuril trench from 17th century through the 2003 tsunami. The coastal runup distribution, inversion of tsunami waveforms and tsunami deposits indicate that the tsunami sources along the Kuril trench are variable. *Iliev et al.* report 17 layers of tsunami deposits in the

Holocene. They study the grain size of deposits and diatoms included in the deposits to identify the tsunami origin, use ^{14}C and volcanic ash for dating the tsunamis, and further correlate the tsunamis with those from other Kuril Island and eastern Hokkaido.

Three papers discuss tsunamis on the North and South American coasts, as well as Iberian coasts. *Hatori* compiles tsunami heights along the Aleutian-Alaska coasts, calculates mean tsunami heights squared in each 200-km long segment, and estimates the cumulative tsunami energy since 1788. *Arreaga-Vargas et al.* report the tsunami inundation map for Esmeraldas, Ecuador, based on the inundation modelling from large earthquakes along the Ecuador-Columbia subduction zone. *Mendes-Victor et al.* summarize the European multi-disciplinary and multi-national projects to study the tsunami source of the 1755 Lisbon earthquake. The projects include multi-channel seismic surveys, numerical modelling and paleotsunami studies to examine the tsunami source.

Two papers discuss the waveform analysis of tide gauge records for tsunami forecast and source estimation. *Lee et al.* propose a method to quickly forecast tsunami heights on the Korean coast, based on pre-computed coastal tsunami heights stored on database. Once the source parameters of an earthquake in Japan Sea are estimated, the tsunami heights can be computed based on the superposition principle. *Pires and Miranda* introduce an adjoint method to the inversion of tsunami waveforms. Unlike conventional Green's function approach, this method allows direct estimation of fault parameters from tide gauge records. They demonstrate the method in an idealized sloping beach using the computed waveforms as the observed data.

Three papers are on physical and numerical experiments on submarine landslide and coastal forests. *Fleming et al.* report the design and preliminary results of their tank experiments to study submarine landslides. They use both solid block and granular materials as landslide analogues and adopt various measurement techniques to measure physical quantities. *Harada and Imamura* discuss the effects of coastal forest on tsunami hazard. In addition to the literature surveys to itemize the control factors, they report the results of numerical simulation for various forest width, density, tsunami heights and period, to quantitatively examine the effect of coastal forests. *Imai and Matsutomi* describe their flume experiment to evaluate the fluid forces of tsunami acting on coastal vegetation. They show the temporal variation of drag force, inertia force and wave-making resistance force, as well as estimation of drag and mass coefficients.

The last two papers propose the use non-traditional methods for future tsunami warning systems. *Sasorova et al.* discuss hydro-acoustic signal possibly generated from "dilatant zone" before an earthquake and propose to use such a signal for location of submarine earthquakes and tsunami warning. *Novik et al.* propose to use electromagnetic signals generated by earthquakes for tsunami monitoring and warning. They recommend magnetic recording on the sea surface and atmosphere as well as ocean bottom measurements of seismic, magnetic and temperature.

All the papers were peer-reviewed by at least two colleagues. The editor acknowledges the authors and reviewers to their time and efforts to make this possible.

Kenji Satake
National Institute of Advanced Industrial Science and Technology
Tsukuba, Japan

November 2004

1992–2002: PERSPECTIVE ON A DECADE OF POST-TSUNAMI SURVEYS

C.E. SYNOLAKIS[1] and E.A. OKAL[2]

[1]*Department of Civil Engineering, University of Southern California, Los Angeles, CA 90089, USA*

[2]*Department of Geological Sciences, Northwestern University, Evanston, IL 60208, USA*

We present a discussion of the field surveys conducted in the wake of fifteen locally devastating tsunamis in the period 1992-2002. The goal of these surveys has been to gather homogeneous databases of run-up and inundation, for the purpose of documenting precisely the penetration of the waves along the affected beaches. In turn, these can be used as datasets to be matched by numerical simulations of the generation of the tsunamis, their propagation and interaction with the beaches. These surveys have provided new insight into some complex phenomena, such as the existence of a leading depression in an N–wave, the importance of beach topography on the local enhancement of run-up, the contribution of underwater landslides to tsunami hazard, and the value of an educated population in terms of the mitigation of human losses. We review a simple and robust algorithm allowing the discrimination between tsunamis generated by dislocations and landslides, based on the aspect ratio of the distribution of run-up on a nearby beach, and the comparison of maximum run-up to the seismic slip involved in the parent earthquake. Some of the techniques developed in these recent post-tsunami surveys can be extended to events dating back a few decades through the interview of elderly witnesses and the surveying of remanent watermarks. When applied to the case of the 1946 Aleutian tsunami, the resulting data require both a large dislocative source to explain the far-field tsunami, and a coeval underwater landslide to account for the near-field run-up values which reached 42 meters at the site of the Scotch Cap lighthouse.

1. Introduction

Over the past twelve years, a number of substantial tsunamis have resulted in significant damage to coastal areas, in the wake of large but not gigantic earthquakes. They have resulted in more than 3000 fatalities, of which 2100 took place during the catastrophic 1998 Aitape tsunami in Papua New Guinea. For the purpose of adequate mitigation of future tsunamis, it is important to understand which factors control most crucially the final characteristics of the flooding, namely run-up and inundation. In turn, their successful modeling requires a reliable database of inundation parameters, against which models can be tested through numerical simulation of the generation of the tsunami, its propagation to the local shores, and its final interaction with the relevant beaches.

K. Satake (ed.), Tsunamis: Case Studies and Recent Developments, 1-29.

In this framework, the past decade has seen the development of systematic post-tsunami field surveys by international teams of scientists, generally within a few weeks of the disaster. Although isolated surveys had occasionally taken place following more ancient events [*e.g., Abe et al.,* 1986], the latter had usually concentrated principally on macroseismic effects. Rather, and starting with the 1992 Nicaragua earthquake, specific tsunami surveys have been carried out systematically for a total of fifteen events (Figure 1).

This paper presents a review of each of those surveys, and highlights the most important results obtained in their course, and in particular their influence on the understanding by the tsunami community of the factors affecting the destructive and occasionally lethal power of the waves as they attack the coastal communities. We also discuss a simple algorithm allowing to quantify the distribution of run-up values, as well as our experience in extending the concept of post-tsunami field surveys to historical events.

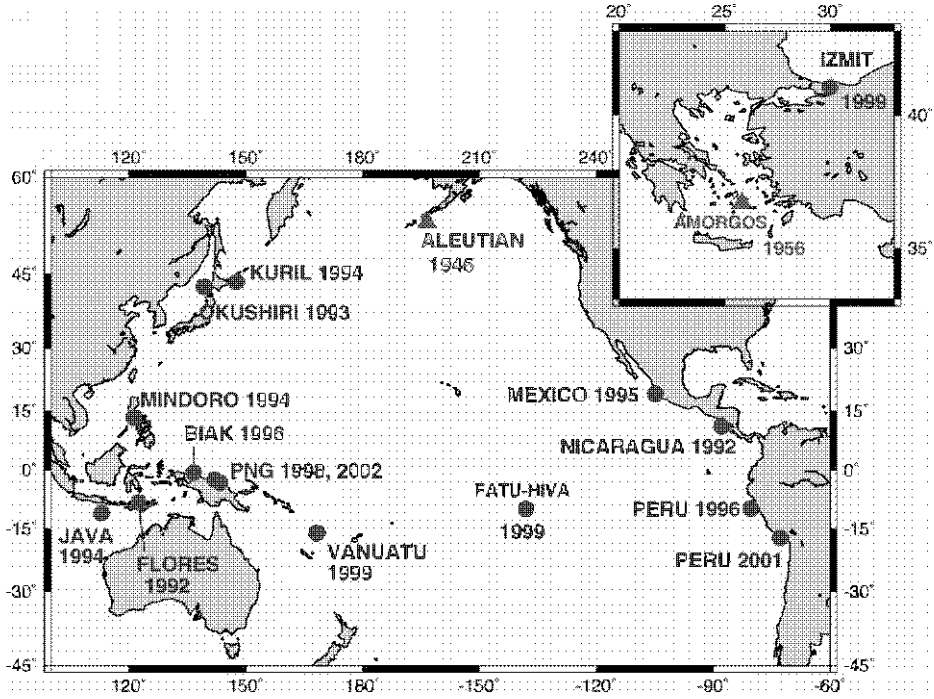

Fig. 1. Map of the Pacific Ocean showing the locations of the tsunami surveys conducted in the past 12 years. The triangles show the source locations for the surveys of historical tsunamis. Note that the 1946 Aleutian survey was taken both in the near and far fields. The inset shows the Aegean Sea, site of the 1999 Izmit and 1956 historical Amorgos surveys.

2. Goals and Methods

The objective of a tsunami field survey is to identify quantitatively the inundation pattern and determine the run-up height distribution along the stricken coastline. Such datasets help better predict what the inundation might be in nearby areas should the same seismic zone rupture at a comparable location in the future, possibly involving an earthquake of a different size. In particular, and through hydrodynamic inversion, the results may help determine if this is the worst-possible event expected in the relevant area and whether the possibility for a transoceanic tsunami exists in a future rupture. Detailed survey results and comparisons with model predictions may also help explain why an event may appear initially anomalous, in the sense that the tsunami damage reported may be incommensurate with the size of the parent earthquake. This type of understanding can lead to the production of inundation maps, similar to those in Hawaii, Japan, and currently in the final stages of completion for parts of California, Oregon, Washington and Alaska. In turn, such maps can help local authorities plan the location of schools, hospitals, fire stations and other critical facilities.

While the scientific rationale behind tsunami surveys is evident, International Tsunami Survey Teams must strike a delicate balance between the necessity to act promptly in order to recover field evidence of an often ephemeral nature, and the obvious priority to be given to search-and-rescue operations in the immediate aftermath of a disaster involving large scale loss of life, shelter, and essential life-sustaining supplies. In this context, we note that most tsunami watermarks are short-lived and may be lost after a single large storm. Similarly, the disposal of debris involving earth-moving equipment may destroy vegetation holding clues to the direction and intensity of tsunami currents. Eyewitnesses usually move to safer areas or are relocated, and sometimes may not welcome being tracked down months later to discuss what may well have been the most painful experience of their lives. In addition, and quite frequently, once an official version of an event circulates, all eyewitnesses report identical information, as it is in human nature for people to trust what they hear or read from the press more than what they see with their own eyes.

In this context, it has been the experience of the international teams that surveys can be successfully conducted within a two- to three-week period from the event, which in general provides a sufficient time window to see the conclusion of search-and-rescue efforts. We wish to emphasize the inobstrusive character of the work of the field survey teams; ITST members have always met the enthusiastic support of the local "lay" people, who have been receptive to the eventual benefits to their communities of the team's work, and usually ask many interesting and difficult questions that further guide in a substantial fashion the team's work.

The essential elements of the database recovered during post-tsunami surveys consist of measurements of *run-up* and *inundation*. We define the former as the maximum vertical elevation of a point located on initially dry land and inundated by the waves, and the latter as the maximum horizontal penetration of the waves in the direction normal to the beach during the flooding (Figure 2). The identification of a data point characterizing water penetration can be made either on the basis of the recognition of a watermark, such as a line of debris deposited by the wave either on land or in vegetation, or through the personal report of an eyewitness to the phenomenon. On occasion, it

may be possible to determine neither run-up nor inundation, but only to infer the local flow depth, usually from watermarks on the sides of walls or from debris left dangling on trees or posts.

Once a data point has been identified and its coordinates recorded with GPS technology, run-up is measured using topographic techniques, either by running a traditional leveling transect to the nearby beach, or through three-dimensional laser surveying. In cases of extreme penetration where running a full transect is impractical (*e.g.,* over more than 1 km), run-up can be measured from differential barometric readings taken

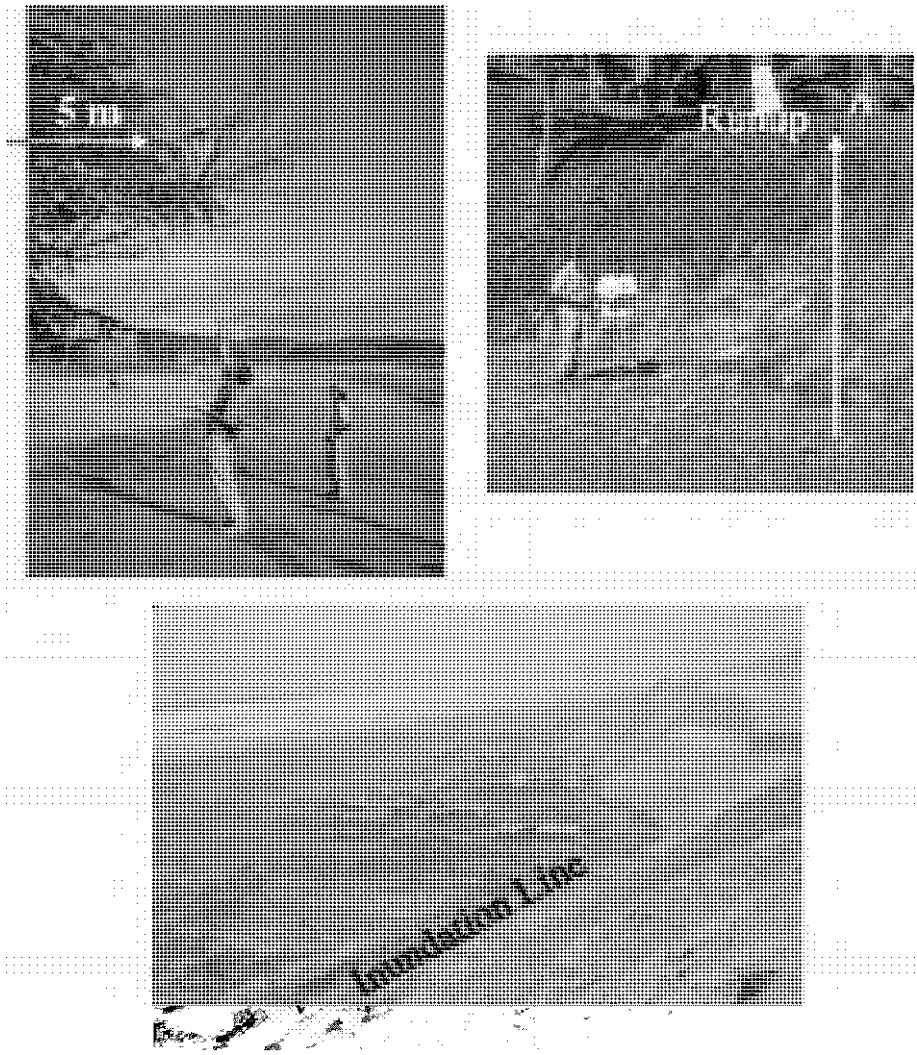

Fig. 2.: Photographs illustrating the definition and measurement of vertical flow depth (top left; 1992 Nicaragua tsunami), run-up (top right; 1995 Mexican tsunami), and inundation (bottom; 2001 Peru tsunami).

at the point of maximum penetration and at the shoreline, within a few minutes of each other to minimize the potential for atmospheric perturbation [*e.g., Okal et al.,* 2003*a*]. In all cases, a record is kept of the precise time of the measurements, in order to later effect the tidal corrections necessary to refer measurements to the same still waterline datum at the time of the event.

Post-tsunami surveys also include the geotechnical documentation of dynamic flow over inundated areas, for example the quantification of the amount and direction of sedimentation or erosion, as well as of the granular nature of deposits. Such data can be used to reconstruct quantitatively the currents involved in the inundation [*e.g., Gelfenbaum and Jaffe,* 2003].

An additional element of post-tsunami surveys is the conduct of interviews of eyewitnesses. We seek to record the experience of survivors, both from the standpoint of documenting the physical properties of the waves making up the tsunami (through parameters such as their number and intervals in time, and the occurrence of down-draws leaving no watermarks), and also regarding the human response to the phenomenon, *e.g.,* the recognition by the population of its nature, and the behavior of the individuals with respect to evacuation before or upon arrival of the waves. Such information can be used to identify the most important factors mitigating tsunami hazard [*e.g., Dengler and Preuss,* 2003].

In addition to photographic documentation of the damage inflicted by the tsunami, and whenever possible, a full video recording of the interview of witnesses is taken and permanently archived, after obtaining informed consent on their part.

Another aspect of the work of International Tsunami Survey Teams is their outreach to local communities. By working closely with community leaders and local teachers, we seek to hold meetings in town and church halls, schools, hospitals, etc., in which we make presentations to the local populations. In a more casual fashion, we never cease to talk to groups of residents, who simply congregate around the scientists during the surveys (Figure 3). Not surprisingly, we have found considerable differences in the level of sensitivity to tsunami hazards among the populations of various regions. In the most earthquake-prone areas, such as the coast of Peru, the local residents feel many earthquakes every year, and most of them have been or will be exposed to a perceptible tsunami in their life times. As a result, the concept of tsunami hazard is passed along by ancestral tradition, and the populations are well educated in this respect; the reflex of self-evacuation upon noticing an anomalous behavior of the sea is well developed, to the extent, for example, that it contributed significantly to the reduction of the death toll, during the 2001 Camaná, Peru tsunami [*Okal et al.,* 2002*a*]. In areas less exposed to tsunamis, there is obviously a lower awareness of tsunami hazard, and a greater education effort is warranted.

In this general framework, the message from the ITST strives to repeat a few fundamental facts regarding tsunamis and their mitigation, namely (i) that tsunamis are a natural phenomenon which is part of the normal geological processes occurring in the Earth, and that they do aud will recur; (ii) that any local earthquake felt strougly enough to disrupt people's activities could produce significant changes in sea level and should dictate evacuation of low-lying areas; and (iii) that any withdrawal of the sea is the harbinger of the destructive return of an inundating wave and should trigger au immediate evacuation of the beaches. Based on local topography, we seek to give

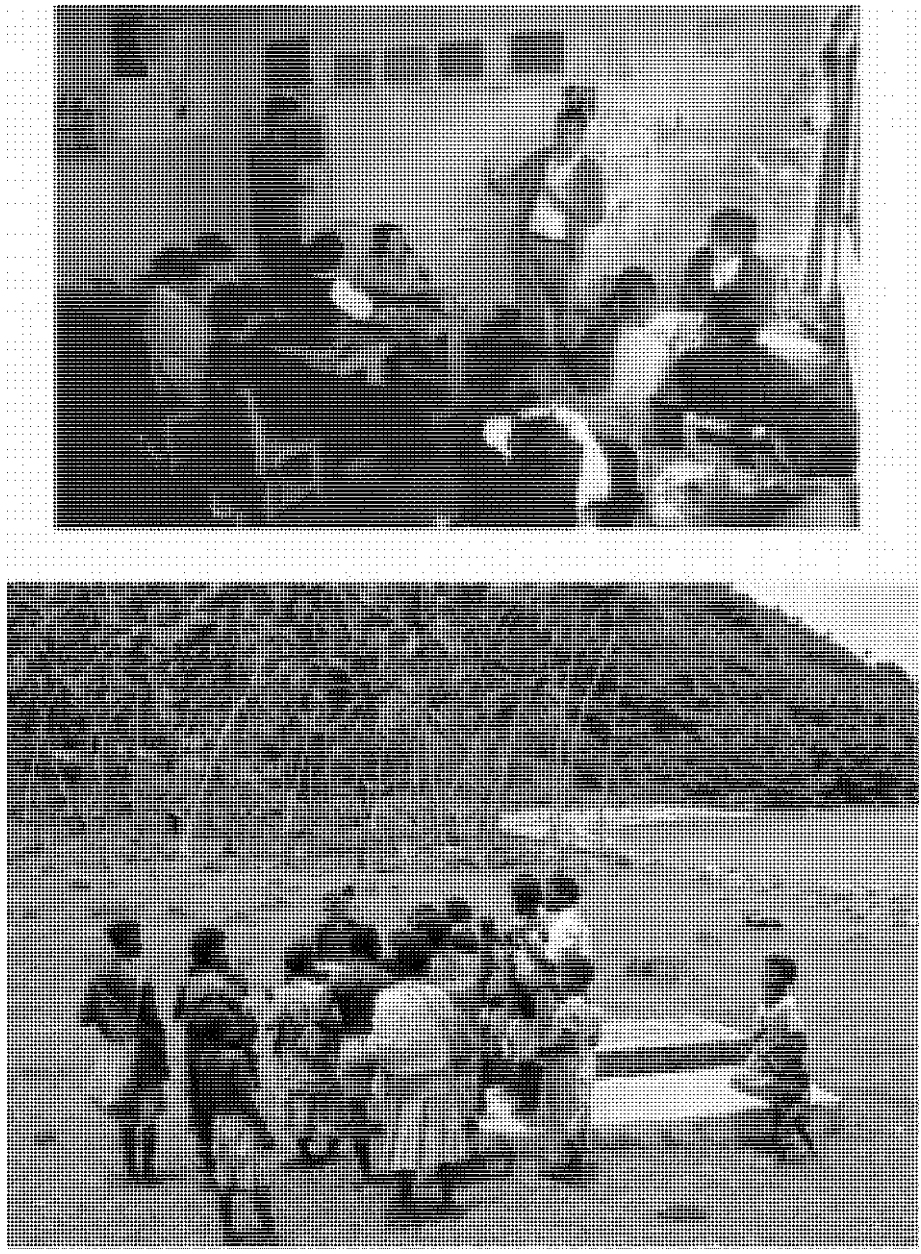

Fig. 3. Outreach to local communities by members of the International Tsunami Survey Teams. *Top:* Drs. J.C. Borrero (left) and E.A. Okal (right) give a presentation at the San Juan Batista public school on Juan Fernández Island, Chile, during the 1946 Aleutian survey in the far field. *Bottom:* Dr. C. Ruscher (with hat) answers questions at a spontaneous gathering with local residents during the 1999 Vanuatu survey.

guidelines as to the spatial extent of an adequate evacuation, and emphasize the need to remain vigilant for several hours, as tsunamis consist of multiple waves whose period cannot be safely evaluated from the first arrivals. We also strive to distribute pamphlets, if possible translated in a local language, which summarize tsunami hazards and simple rules for their mitigation, and we generally attempt to leave a master copy with local officials and school teachers.

To local government officials and civil defense authorities, we also stress the importance of a sensible control on the development of real estate in low-lying areas, and of the value of keeping the population aware of tsunami hazard through various exercises, such as the yearly drills conducted for example in Japan and Peru.

On a more formal level, the teams have enthusiastically sought to include members from the affected countries, in order to provide opportunities for *in situ* training during and after the survey, thus establishing the basis of closer international cooperation in science. Local scientists also contribute regularly to the data analyses and are joint authors of most publications resulting from field surveys. Repeatedly, scholars from the home countries have later pursued graduate studies abroad (*e.g.*, in the United States, Japan or New Zealand) in the wake of their participation in International Tsunami Survey Teams.

3. Individual tsunami surveys

In this section, we detail the fifteen surveys taken by International Tsunami Survey Teams since 1992, and in particular emphasize the fundamental contributions which each of them has brought to the advancement of our understanding of tsunami hazard.

3.1. NICARAGUA, 02 SEPTEMBER 1992; $M_0 = 3.4 \times 10^{27}$ dyn-cm [*Dziewonski et al., 1993a*]; INITIAL FIELD REPORT: *Satake et al.* [1993].

With more than 160 people killed along the coast of Nicaragua, this was the first tsunami in over a decade to result in a substantial number of casualties. This, and its clear nature as a "tsunami earthquake", motivated a number of detailed surveys, which became the model for all subsequent field work by the International Tsunami Survey Teams in the aftermath of later tsunamis. We recall that "tsunami earthquakes" were defined by *Kanamori* [1972] as events whose tsunamis have far greater amplitude than expected from their conventional magnitudes.

The seismic characteristics of the earthquake have been described in a number of publications [*Kanamori and Kikuchi,* 1993; *Satake,* 1994; *Velasco et al.*, 1994; *Kikuchi and Kanamori,* 1995]. Its strong deficiency in high-frequency energy release is best illustrated by its low body-wave magnitude, $m_b = 5.3$, which resulted in the earthquake not being felt along certain segments of coastline, and thus in the absence of natural warning for the impending disaster. *Newman and Okal* [1998] computed their lowest value of the parameter $\Theta = \log_{10} E^E / M_0$ as -6.30 for that event (this parameter expresses the dimensionless ratio of estimated radiated energy to seismic moment; under generally accepted scaling laws, it is expected to be an invariant ($\Theta = -4.90$) related to source strain release). In addition, *Okal et al.* [2003*b*] documented the

deficient hydroacoustic ("T") waves of the 1992 Nicaragua earthquake. *Okal and Newman* [2001] noted the absence of comparable or larger interplate thrust earthquakes along the Nicaragua subduction zone.

Results from the field survey are given by *Abe et al.* [1993]. They confirm substantial values of run-up, reaching 8–10 m and spread over a 290–km long segment of coastline, extending from the Honduran border to the Costa-Rican one. These first datasets based on modern surveys were impossible to model using the then-available simulation codes, which would stop the wave evolution calculations at some threshold depth (*e.g.*, 5 or 10 m), and essentially treat the shoreline as a rigid and fully reflecting vertical wall. In practice, those simulations predicted run-up values too low by close to an order of magnitude, when based on dislocation models acceptable from the seismological standpoint [*Imamura et al.*, 1993]. By contrast, *Titov and Synolakis* [1993] presented a largely successful simulation based on a prototype algorithm handling the full interaction of the wave with an initially dry beach.

3.2. FLORES, INDONESIA, 12 DECEMBER 1992; $M_0 = 5.1 \times 10^{27}$ dyn-cm [*Dziewonski et al.*, 1993*b*]; INITIAL FIELD REPORT: *Yeh et al.* [1993].

The parent earthquake of this tsunami took place in the Flores Sea, north of the Sunda arc, and represented subduction of the proposed Banda block below the Australian plate, under a complex regime of back-arc compression probably associated with the incipient collision between continental Australia and the Sunda trench farther East [*Beckers and Lay*, 1995; *Hidayat et al.*, 1995].

The field survey conducted in the aftermath of the tsunami [*Tsuji et al.*, 1995*a*] documented several intriguing results: while it established a maximum run-up of 4–5 m on most of the Northern coast of Flores Island, it revealed catastrophic values of up to 26 m at some localities (Rangrioko) in Northeastern Flores. Underwater surveys by *Plafker* [1997] showed that the latter resulted from submarine landslides triggered locally by the earthquake.

In addition, a remarkable observation on the nearly circular island of Babi showed that the maximum run-up (7.2 m) was observed in the lee of the tsunami, following a process of convergence of the tsunami waves behind the circular obstruction [*Yeh et al.*, 1993; *Imamura et al.*, 1995*a*], which was successfully reproduced in the laboratory by *Briggs et al.* [1995], and simulated numerically by *Yeh et al.* [1994] and *Tinti and Vannini* [1995].

Finally, it was noticed at the community of Wuring, off Maumere on the northern coast of Flores, that a strong overland flow had over-run a peninsula, illustrating the vulnerability of such features due to bathymetric focusing of tsunami energy by shallow structures.

3.3. HOKKAIDO-NANSEI-OKI, 12 JULY 1993; $M_0 = 4.7 \times 10^{27}$ dyn-cm [*Dziewonski et al.*, 1994]; INITIAL FIELD REPORT: *Shuto et al.* [1993].

This tsunami remains to this date the last catastrophic one to affect Japan, with 198 fatalities confirmed on the small island of Okushiri. The Aonae peninsula at the southern tip of the island was completely over-run by the waves, despite the presence of a

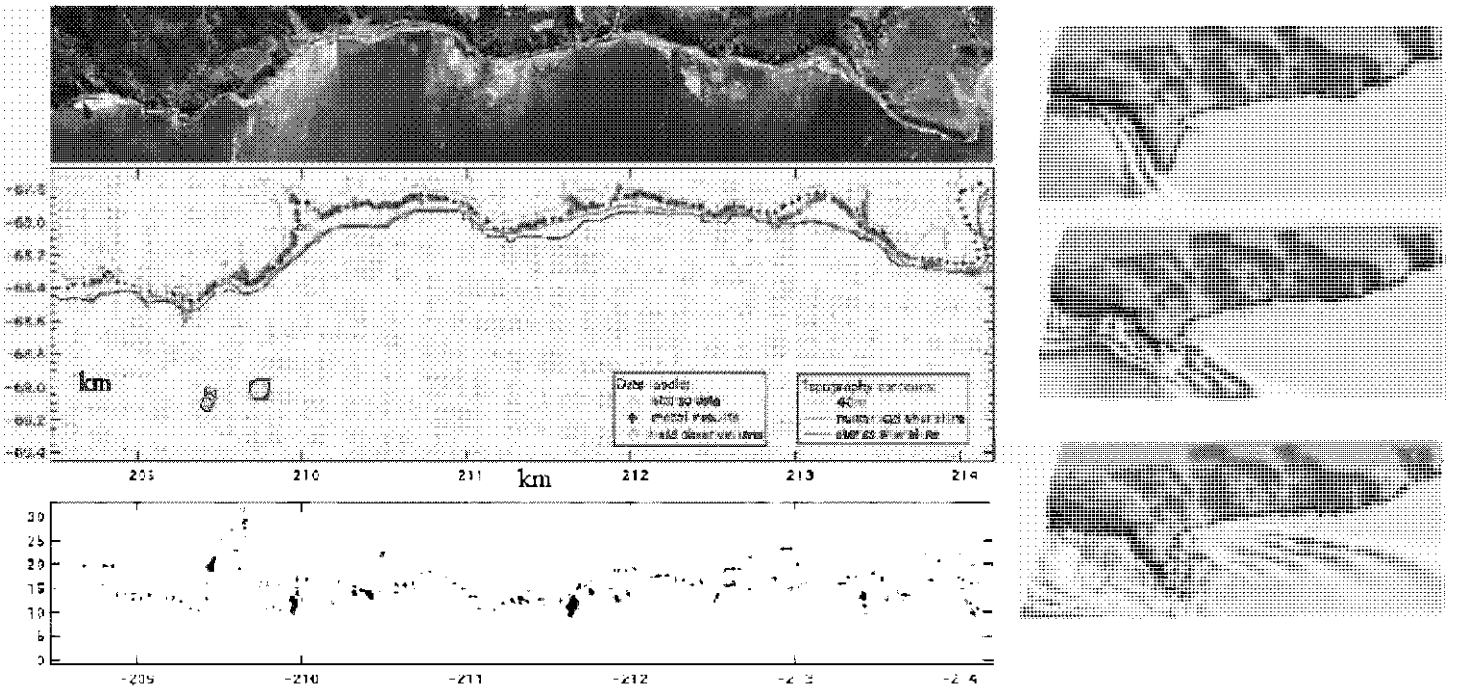

Fig. 4. Modeling of the Hokkaido-Nansei-Oki tsunami on the island of Okushiri. *Left:* Aerial view (top) of damage along the Western coast of Okushiri Island; map (center) showing inundation points measured in the field (open circles) and interpreted from stereographic aerial pictures (triangles), compare to the result of modeling (crosses); cross-section (bottom) showing measured and modeled values of run-up (in meters). *Right:* Video snapshots showing modeling of the inundation and over-run of the Southern-most tip of Okushiri island at Aonae. After *Titov and Synolakis* [1997].

7–m high protection wall. Seismological investigations of the parent earthquake were carried out by *Tanioka et al.* [1995*a*] and *Kuge et al.* [1996]. Post-tsunami field surveys [*Shuto et al.*, 1993; *Shuto and Matsutomi*, 1995] documented run-up reaching 31 m at a river gully near Monai on the Western shore of the island, emphasizing the importance of the topography at the receiving shore on the eventual amplitude of run-up.

Based on the DCRC-17a source model of *Takahashi et al.* [1995], the modeling by *Titov and Synolakis* [1997] of those maximum run-up values and of the inundation flow over the Aonae peninsula using the MOST code [*Titov and Synolakis*, 1998] was the first successful demonstration of the capability, for simulation techniques, to reproduce the highly non-linear interaction of the wave with originally dry land (Figure 4).

The Okushiri tsunami was relatively unique in the extreme proximity of the source region to the island which left practically no time for the residents to escape the onslaught of the waves. This tragedy had a profound effect on the evolution of mitigation strategies, notably concerning sea walls, shoreline development and vertical evacuation.

3.4. JAVA, 02 JUNE 1994; $M_0 = 5.3 \times 10^{27}$ dyn-cm [*Dziewonski et al.*, 1995*a*]; INITIAL FIELD REPORT: *Synolakis et al.* [1995].

This was the second "tsunami earthquake" of the 1990s, characterized once again by an extreme deficiency in energy-to-moment ratios (*Newman and Okal*'s [1998] parameter $\Theta = -6.01$). The absence of ground shaking proved lethal to the population (223 killed by the tsunami, none by the earthquake), put helped evaluate the wave damage. *Tanioka and Satake* [1996] suggested that a sloping ocean bottom in the epicentral area could have enhanced tsunami generation through the contribution of horizontal displacement of the sea bottom. *Abercrombie et al.* [2001] proposed that the earthquake involved slip over a subducting seamount, which had provided a single locking asperity along an otherwise aseismic subduction segment [*Okal and Newman*, 2001], an idea originally expressed in Japan by *Lallemand and Le Pichon* [1987].

The field survey [*Tsuji et al.*, 1995*b*] identified run-up amplitudes reaching 14 m at Rajekwesi, and documented the importance of the local topography, capable of amplifying and funneling tsunami energy, notably over so-called pocket beaches.

3.5. SHIKOTAN, KURIL ISLANDS, 04 OCTOBER 1994; $M_0 = 3.0 \times 10^{28}$ dyn-cm [*Dziewonski et al.*, 1995*b*]; INITIAL FIELD REPORT: *Pelinovsky et al.* [1995].

This earthquake was at the time the second largest in the Harvard CMT catalogue; it was not, however a subduction event, but rather involved tearing of the subducting slab along a nearly vertical fault plane [*Tanioka et al.*, 1995*b*]. It produced very strong shaking resulting in the opening of large fissures in the ground, and led to environmental damage due to leakage from oil storage tanks. The resulting tsunami was surveyed by *Yeh et al.* [1995], with run-up in the range of 5 to 9 m; none of the 12 deaths were directly attributable to the tsunami. However, most of the locations surveyed on Shikotan Island lacked significant accumulation of tsunami deposits, indicating a lack of universal correlation between substantial inundation and sedimentation.

The distribution of run-up was made relatively complex by the intricate geography of the islands and straits in the region, but was nevertheless successfully modeled by *Yeh et al.* [1995] and *Titov* [1996], even though *Piatanesi et al.* [1999] have suggested that the surveyed dataset is insufficient to resolve the two conjugate fault planes of the focal mechanism.

3.6. MINDORO, PHILIPPINES, 14 NOVEMBER 1994; $M_0 = 5.1 \times 10^{26}$ dyn-cm [*Dziewonski et al.*, 1995*b*]; FIELD REPORT: *Imamura et al.* [1995].

This relatively moderate earthquake, characterized by a strike-slip mechanism, generated a significant tsunami, featuring run-up as high as 7.3 m. While some of the large run-up values could be attributable to local landslides (as in the case of Flores (1992), but on a smaller scale), the survey conducted by *Imamura et al.* [1995*b*] revealed local on-land deformations departing from the expected field of static displacements, and highlighted the importance of the horizontal displacement of a coastline traversed by a strike-slip fault as a possible mechanism of generation of a local tsunami, as modeled by *Tanioka and Satake* [1996] and more recently *Legg et al.* [2003]. Finally, it pointed out the existence of complex and powerful flow regimes at the mouths of rivers, due both to the tsunami and the presence of cracks on the river bed, as exemplified at Wawa, on the Baruyan River, where a 4000-ton barge was moved 1.6 km inland.

3.7. MANZANILLO, MEXICO, 09 OCTOBER 1995; $M_0 = 1.15 \times 10^{28}$ dyn-cm [*Dziewonski et al.*, 1997*a*]; INITIAL FIELD REPORT: *Borrero et al.* [1997].

This earthquake was the largest one to affect the Mexican coastline since the devastating 1932 series, but remained significantly smaller than the latter's mainshock [*Pacheco et al.*, 1997; *Zobin*, 1997], a conclusion upheld by *Ortíz et al.*'s [1998] modeling of tidal gauge records.

During the field survey, *Borrero et al.* [1997] documented on a photograph taken by a coastal resident the leading depression (down-draw) expressing the first phase of interaction of the tsunami with a local beach (Figure 5). This is believed to be the first documented observation of this phenomenon, which had been predicted theoretically, for an adequate focal geometry, by *Tadepalli and Synolakis* [1994, 1996], and which is rooted in the dipolar nature, involving both subsidence and depression, of the ground deformation during the earthquake. It confirms the challenge to the paradigm of the soliton model for the leading waveform of an earthquake-generated tsunami.

3.8. BIAK, INDONESIA, 17 FEBRUARY 1996; $M_0 = 2.4 \times 10^{28}$ dyn-cm [*Dziewonski et al.*, 1997*b*]; INITIAL FIELD REPORT: *Imamura et al.* [1997].

This very large earthquake took place along a segment of the New Guinea Trench with no previously documented large scale seismicity, leading *Okal* [1999] to suggest a regime of subduction through large events separated by long recurrence times, the previous one tentatively dated to 1914. The tsunami was damaging throughout Northwestern Irian Jaya, and in particular on Biak Island, where run-up reached 7.7 m. The field work of the ITST [*Matsutomi et al.*, 2001] documented for the first time the feasibility

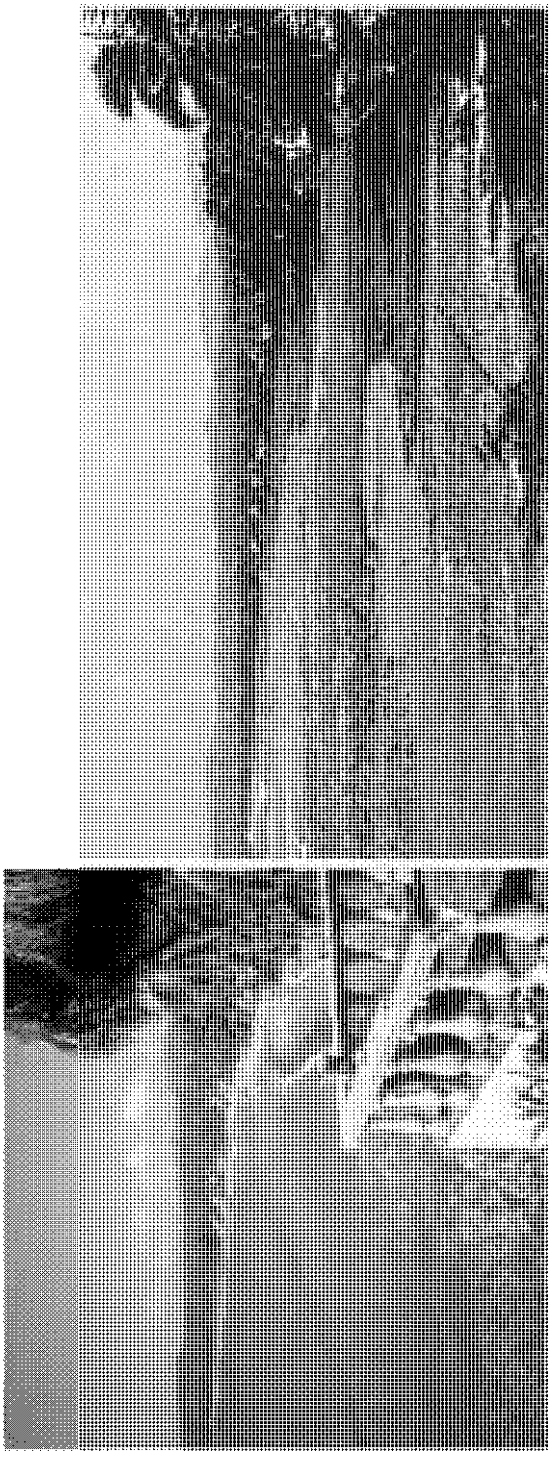

Fig. 5. Right: Initial down-draw during the early phases of the 1995 Mexican tsunami at Tenacatita Bay (photograph courtesy of J. Lehemen). *Left:* Same location photographed later during the survey by the ITST (note the balustrade damaged by the earthquake).

of obtaining a database of current velocities, estimated from differences in inundation depths upstream and downstream of obstacles such as house walls, based on an application of Bernouilli's theorem [*Matsutomi and Iizuka,* 1998].

3.9. CHIMBOTE, PERU, 21 FEBRUARY 1996; $M_0 = 2.2 \times 10^{27}$ dyn-cm [*Dziewonski et al.,* 1997*b*]; INITIAL FIELD REPORT: *Bourgeois et al.* [1996].

This represents the last of the recent "tsunami earthquakes" characterized by a deficient energy-to-moment ratio ($\Theta = -5.94$); as in the case of the Nicaragua and Java events described above, no other large subduction earthquakes are known along that section of the Northern Peru coastline [*Okal and Newman,* 2001]. The earthquake also showed a spectacular deficiency in hydroacoustic T waves at teleseismic distances [*Okal et al.,* 2003*b*]. The field survey [*Bourgeois et al.,* 1999] documented run-up in the 2 to 5 m range over a 250–km stretch of coast, and the total run-over of a flat, 1.5–km wide isthmus separating the local bays at Chimbote and Samanco.

The run-up of the tsunami along the Peruvian coast, as well as in some bays of the Marquesas Islands, was successfully modeled by *Bourgeois et al.* [1999] and *Heinrich et al.* [1998], after allowing for a low value of source rigidity, in order to reflect the anomalous character of the earthquake [*Ihmlé et al.,* 1998]. *Satake and Tanioka* [1999] modeled regional tidal gauge records to constrain the width of the fault.

3.10. AITAPE, PAPUA NEW GUINEA, 17 JULY 1998; $M_0 = 3.7 \times 10^{26}$ dyn-cm [*Dziewonski et al.,* 1999]; INITIAL FIELD REPORT: *Kawata et al.* [1999].

Despite the relatively small size of the parent earthquake, this tsunami resulted in over 2100 fatalities, officially surpassed in the 20th century only by the 1933 Sanriku, Japan tsunami. The field survey was organized within two weeks of the disaster and confirmed exceptional run-up heights, reaching 15 m at Arop, but concentrated on a 25–km stretch of coastline outside which the effects of the tsunami were benign. As documented in detail in *Synolakis et al.* [2002], the combination of excessive amplitude and concentration of the run-up was quickly recognized as incompatible with any simulation model based on the excitation of the tsunami by the seismic dislocation; in addition, the earthquake did not feature a slow source comparable to those of documented "tsunami earthquakes" [*Newman and Okal,* 1998; *Synolakis et al.,* 2002].

Finally, witness reports generally indicated that the tsunami had arrived at least 10 minutes later than predicted by all acceptable models of propagation from the earthquake source [*Davies et al.,* 2003]. Based on the identification of a hydroacoustic signal recorded near Wake Island and featuring an anomalous combination of amplitude and duration, *Okal* [1998; 2003] proposed that the tsunami had been generated by an underwater landslide, itself triggered by the earthquake with a delay of 13 minutes. A number of ship-based surveys, using seismic refraction and remotely operated submersibles [*e.g., Sweet and Silver,* 2003] later identified a 4–km^3 slump contained in a bowl-shaped amphitheater located 25 km from the coast, which was used as the source of the tsunami in several successful numerical simulations of run-up along the Sandaun coast [*Heinrich et al.,* 2000; *Synolakis et al.,* 2002; *Imamura and Hashi,* 2003].

Results from the post-tsunami field survey thus led to the identification of a submarine landslide as the source of the devastating 1998 Papua New Guinea tsunami, and renewed sensitivity was aroused in the tsunami community for the hazards created by underwater landslides [*Bardet et al.*, 2003]. As a result, the level of hazard posed by relatively moderate earthquakes (typically at the magnitude 6 level) must be re-examined upwards, on a case-by-case basis [*Borrero et al.*, 2001].

3.11. IZMIT, TURKEY, 17 AUGUST 1999; $M_0 = 2.9 \times 10^{27}$ dyn-cm [*Dziewonski et al.*, 2000*a*]; INITIAL FIELD REPORT: *Altınok et al.* [1999].

The devastating Izmit earthquake [*e.g.*, *Barka et al.*, 2002], which killed upwards of 18,000 people, was accompanied by a significant tsunami which inflicted additional destruction to coastal areas at the Eastern end of the Sea of Marmara, including environmental damage due to a major oil spill at a refinery in Izmit. A database of results from tsunami surveys is given by *Altınok et al.* [2001], who attribute the origin of the tsunami principally to the activation of underwater normal faults located at pull-apart basins offsetting the main strike-slip fault, and documented by seismic refraction [*Altınok et al.*, 1999], with additional contributions from localized coastal slumps.

The modeling of the 1999 Izmit tsunami, proposed by *Yalçıner et al.* [2000], has led to a better understanding of tsunami risk in the Sea of Marmara [*Yalçıner et al.*, 2002], where a major earthquake with potentially catastrophic effects on the Istanbul metropolis is generally expected in the next decades [*Parsons et al.*, 2000].

3.12. FATU HIVA, MARQUESAS, 13 SEPTEMBER 1999; FIELD SURVEY: *Okal et al.* [2002*b*].

Without any warning (earthquake tremor, acoustic rumbling, etc.), a series of two waves reaching 5 m in amplitude inundated the beach front in the village of Omoa on the island of Fatu Hiva, and inflicted severe damage to the local school. Miraculously, there were no victims among the estimated 85 children attending school that afternoon. The cause of this local tsunami was an aerial landslide resulting from the collapse of a weathered cliff, 3 km from the village (Figure 6). The resulting survey [*Okal et al.*, 2002*b*] provided a volume estimate of (2 to 5) $\times$ 10^6 m^3 for the slide, and successful simulations were carried out by *Hébert et al.* [2002] and *Okal et al.* [2002*b*]. To our knowledge, the landslide was not detected instrumentally anywhere in the Pacific Basin, and this event thus constitutes the first surveyed occurrence of an "aseismic tsunami".

As a result of this disaster, the school was rebuilt more than 1 km inland, in what one would hope represents a reversal of the recent trend towards development of beachfront real estate in the Marquesas.

3.13. VANUATU, 26 NOVEMBER 1999; $M_0 = 1.7 \times 10^{27}$ dyn-cm [*Dziewonski et al.*, 2000*b*]; FIELD SURVEY: *Caminade et al.* [2000].

This event, discussed in detail by *Pelletier et al.* [2000], took place behind the main Vanuatu arc, and featured a thrusting mechanism. The field survey documented run-up

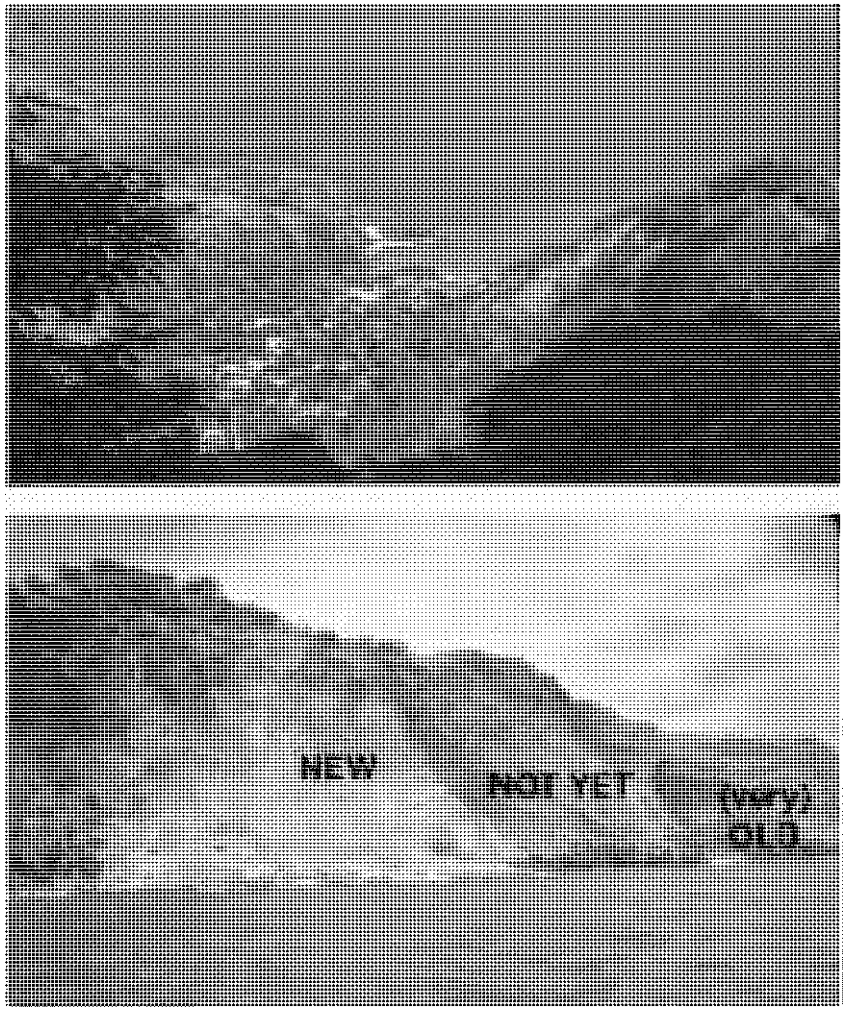

Fig. 6. 1999 Tsunami at Fatu Hiva, Marquesas. *Top:* View of the village of Omoa, inundated by the wave. *Bottom:* Landslide at Vaifaite, 3 km from Omoa, photographed by the ITST 22 days after the event. The landslide (labeled "NEW") is approximately 300 m across and 250–300 m tall. It expresses the ongoing erosion of the island, with older episodes expressed in the morphology of the cliff, while the central part of the picture (labeled "NOT YET") constitutes permanent hazard.

reaching 6–7 m on Pentecost Island and 7–8 m on Ambryn. It is probable that small-scale landslides contributed locally to the larger values. From the standpoint of tsunami mitigation and warning, the 1999 Vanuatu event served as a spectacular illustration of the value of education of the coastal populations. The story of the village of Baie Martelli is a case in point: only a few months before the event, the villagers had been shown on portable, battery-operated television sets, a video based on the 1998 Papua New Guinea disaster, stressing the need to evacuate coastal areas following any strong earthquake, and especially in the event of anomalous variations in sea level. When the earthquake struck, in the middle of the night, and a villager reported a withdrawal of the sea, the entire village was evacuated before the tsunami destroyed it totally; out of a population of 300, the only five victims were elderly invalids who could not evacuate, and a drunken man, who would not.

3.14. CAMANA, PERU, 23 JUNE 2001; $M_0 = 4.7 \times 10^{28}$ dyn-cm [*Ekström et al.*, 2003]; FIELD REPORT: *Okal et al.* [2002*a*].

This earthquake remains, to this day, the largest event in the past 39 years, as documented by the Harvard CMT catalogue, and *Kanamori* [1977]. While exhibiting a trend towards slowness ($\Theta = -5.48$), the event did not qualify as a "tsunami earthquake", and its tsunami was adequately modeled as due to a standard seismic dislocation. The tsunami affected the coastal communities from Ilo in the South to Tanaca in the North and resulted in 86 people killed or reported missing in the coastal area. Most of the inundation and damage took place in the Camaná river delta area.

One of the major results from the initial field survey [*Okal et al.*, 2002*a*] was that this death toll could have been much greater, had the tsunami struck during a Summer night, when the beach would have been packed with vacationers. The survey team was also impressed with the level of education and sensitivity to hazard of the local population, especially in fishing communities with a deeply rooted ancestral tradition. Indeed most of the victims at Camaná were farm workers from the hinterland.

Another highlight of the international surveys following the event [*Dengler et al.*, 2003] was the access to a video of the arrival of the tsunami in the bay of Matarani harbor, documenting a small initial positive wave (not exceeding a few tens of cm, and thus within the range of tidal oscillations), followed by a strong down-draw, emptying the bay and grounding many boats for a period of about 20 minutes, during which the bay developed complex patterns of vortical flow. This video, filmed by a television cameraman before he was ordered to evacuate the harbor (and thus missed filming the subsequent inundation) is one of a handful of existing films of the actual motions of water in a harbor during a tsunami. Finally, a systematic investigation of the tsunami deposits in the Camaná delta revealed a large variation in thickness and layering, even on the small scale of the delta, stretching approximately 10 km along a generally rectilinear shoreline [*Dengler et al.*, 2003].

3.15. WEWAK, PAPUA NEW GUINEA, 08 SEPTEMBER 2002; $M_0 = 2.9 \times 10^{27}$ dyn-cm [*G. Ekström*, pers. comm., 2002]; FIELD REPORT: *Borrero et al.* [2003].

In contrast to the 1998 disaster, which occurred only 135 km to the Northwest, the 2002 earthquake was a larger seismic source, which did more significant damage

onland, killing five persons , but resulted in a much weaker tsunami (maximum run-up on the coast: 3.5m), observed on a longer stretch of coast [Borrero et al., 2003]. This confirmed, if need be, that the 1998 tsunami was generated by an exceptional source — the underwater landslide — absent from the 2002 scenario.

4. The use of regional run-up datasets as identifiers of tsunami sources

In a recent contribution, *Okal and Synolakis* [2004] have shown that datasets of run-up amplitudes in the near field can be used to identify the nature (dislocation or landslide) of the source of a tsunami based on the analysis of the aspect ratio of the distribution of run-up along beach, and of the maximum run-up measured in the near field, scaled by the co-seismic slip Δu on the fault plane. Specifically, given a distribution $\zeta(y)$ of run-up values along a beach oriented in the y direction, these authors fit by trial and error a function of the type

$$\zeta(y) = \frac{b}{\left(\frac{y-c}{a}\right)^2 + 1} \tag{1}$$

and define the two dimensionless quantities $I_1 = b/\Delta u$ and $I_2 = b/a$. They propose that these behave as invariants, characteristic of the class of tsunami source considered (dislocation *vs.* landslide), but largely independent of the exact parameters describing such sources. They are motivated by the intuitive observation that maximum run-up (hence b) should be principally controlled by the amount of deformation of the sea floor, and hence by the slip Δu on the fault, while its distribution (hence a) should reflect the lateral extent of the source. Noting the fundamentally different distribution fields of underwater deformation for dislocations and landslides, and in particular that the strain release in an earthquake is limited inherently by the strength of crustal rocks, *Okal and Synolakis* [2004] showed that I_2 (as well as I_1 when Δu is sufficiently well known) can be used as a *discriminant* of the nature of a tsunami source (Figure 7). This was supported by the systematic processing of more than 70 simulations of regional tsunamis using both kinds of sources, and letting their geometric parameters vary widely. A simple rule of thumb is that dislocations sources cannot feature aspect ratios I_2 greater than 10^{-4}.

Figure 8 presents the application of this approach to seven profiles obtained from the above modern surveys (and the 1946 Unimak field survey; see Section 5. below). We eliminated those surveys taken along contorted shorelines or those featuring islands, where in both cases the definition of the coordinate y is difficult. These results clearly identify the 1998 Papua New Guinea and 1946 Aleutian tsunamis as the only ones requiring a non-dislocative source to model their tsunamis in the near field (Figure 7). In particular, Figures 8*b* and 8*c* illustrate the fundamentally different nature of the run-up distribution for the two Papua New Guinea events: the 1998 Aitape tsunami, generated by a landslide, and the 2002 Wewak one, resulting form a standard dislocation.

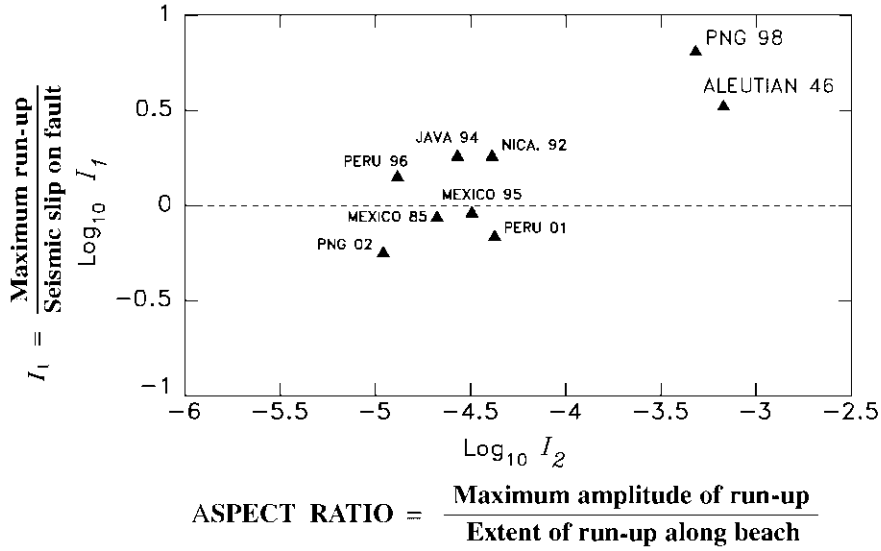

Fig. 7. Plot of the dimensionless parameters I_1 and I_2 obtained by regressing the distribution of run-up along near-field beaches for a number of tsunamis surveyed by the ITSTs. This figure clearly identifies the 1998 Papua New Guinea and 1946 Aleutian tsunamis as the only ones with $I_1 > 2$; $I_2 > 10^{-4}$, thus requiring generation by a landslide rather than by the earthquake dislocation. After *Okal and Synolakis* [2004].

5. Extension to historical events: The case of the 1946 Aleutian tsunami

Some of the techniques used by the International Tsunami Survey Teams can be extended to build quantitative data bases of run-up and inundation for historical events. When available, historical archives can be used successfully, as demonstrated by the reconstruction of the effects of the 1700 Cascadia tsunami in Japan [*Satake et al.*, 1996; *Atwater et al.*, 2004]. In their absence, and for more recent events, we have found that many elderly residents throughout the Pacific had kept vivid memories of the damages wrought by the 1946 Aleutian tsunami, both in the near and far fields, to the extent that quantitative information on run-up and inundation could be recovered more than 50 years after the fact (Figure 9).

However, in dealing with historical events, the surveyor is faced with the additional challenge of assessing the reliability of the recollection provided by a necessarily elderly witness, whose memory may be failing. In particular, it is of paramount importance to establish beyond doubt the association of a recollection with the correct tsunami. As detailed in *Okal et al.* [2002*c*], this may involve techniques of "cross-examination" of the witnesses regarding time of the day (which often is characteristic of a given tsunami on a particular island) and age of the witness (expected to vary significantly between candidate events, due to the general rarity of destructive tsunamis). We discuss here the application of this approach to two historical tsunamis.

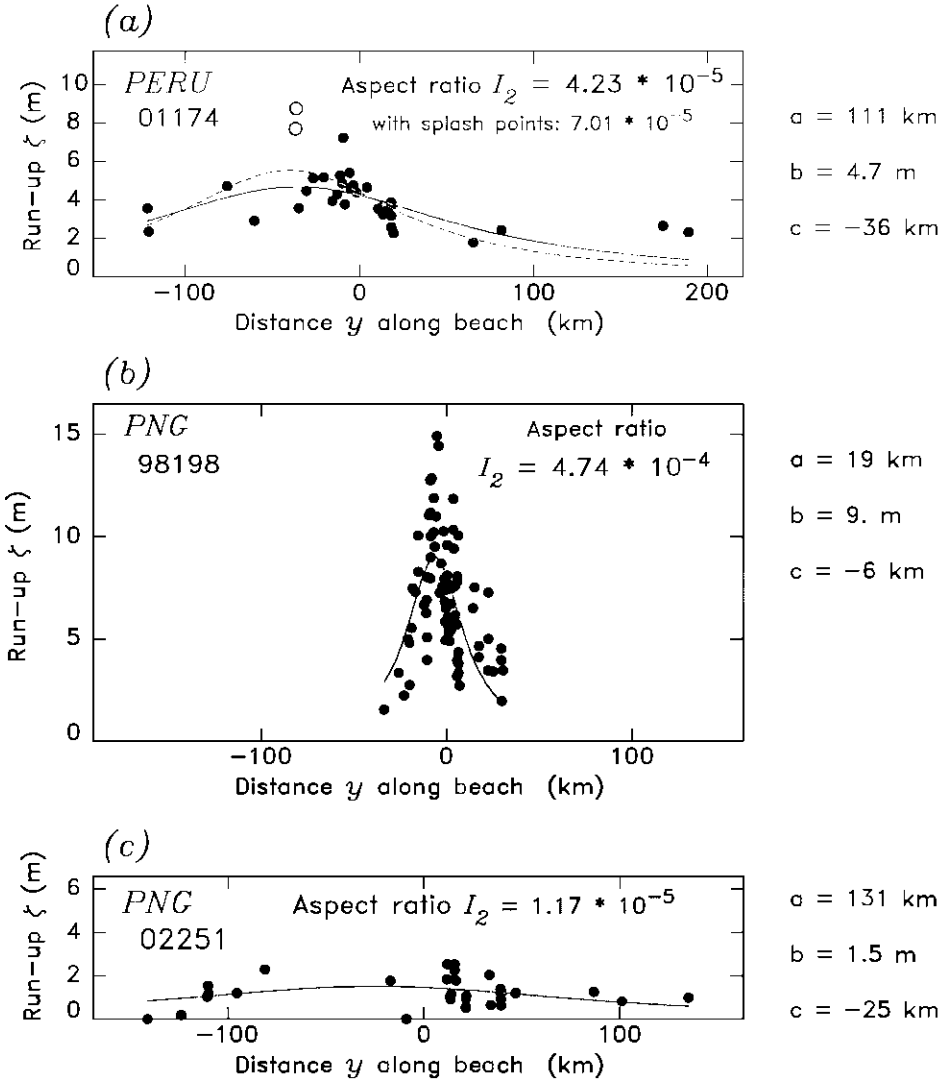

Fig. 8. Field survey profiles of run-up fitted to an equation of the form (1). *(a):* 2001 Peruvian tsunami. The solid dots are the individual measurements; the red line the best-fitting function of the type (1). Open symbols are run-up values affected by splashing against a steep cliff, which should be discarded from the data. *(b):* Same as (a) for the 1998 Papua New Guinea tsunami. *(c):* Same as (a) for the 2002 Papua New Guinea tsunami. All three diagrams are plotted using the same horizontal and vertical scales, to allow direct comparisons between events. The striking contrast between the distributions of the 1998 and 2002 events in Papua New Guinea expresses the anomalous character of the 1998 event, which features $I_2 > 10^{-4}$ and requires a non-dislocative source. After *Okal and Synolakis* [2004].

5.1. UNIMAK, ALEUTIAN IS., 01 APRIL 1946; $M_0 = 9 \times 10^{28}$ dyn-cm [*López and Okal*, 2002].

The case of the 1946 Aleutian tsunami remains a challenge to the seismological and tsunami communities. The earthquake, featuring a conventional magnitude of only 7.4 [*Gutenberg and Richter*, 1954] is deceptively small in regard of the catastrophic tsunami which it generated, in both the near field, where it eradicated the Scotch Cap

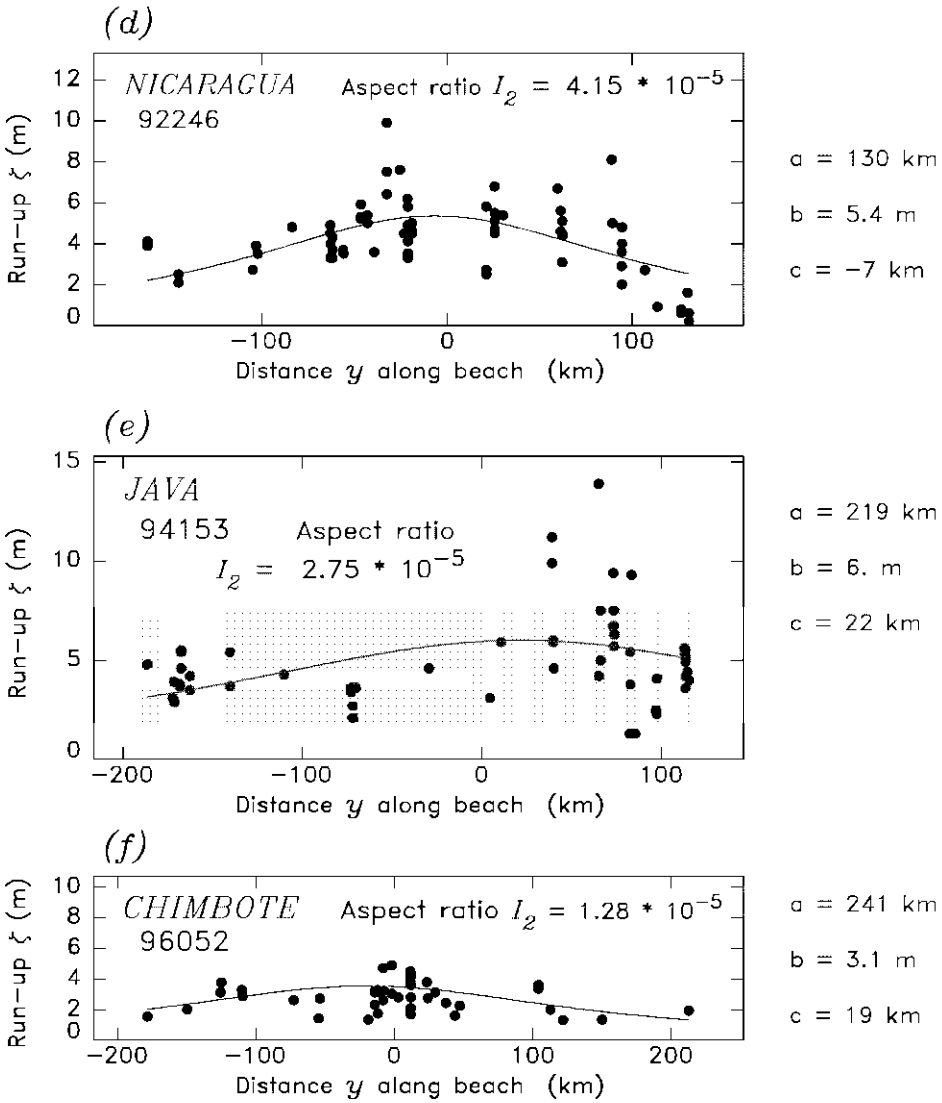

Fig. 8 (ctd.). Same as Figure 8*(a)* for the "tsunami earthquakes" of Nicaragua (1992), Java (1994), and Chimbote, Peru (1996).

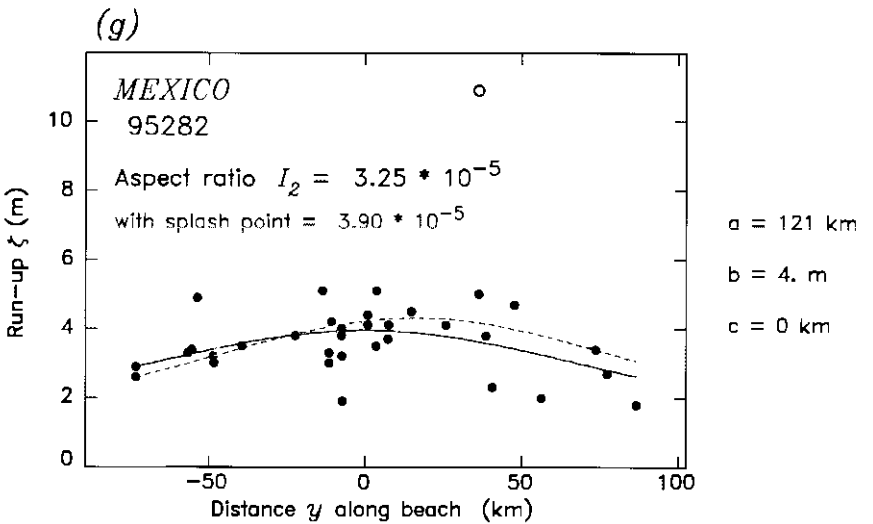

Fig. 8 (ctd.). Same as Figure 8*(a)* for the 1995 Mexico tsunami *(g)* and the 1946 Aleutian tsunami *(h)*. All frames *(a – h)* in Figure 8 share the same ratio of vertical-to-horizontal scales, allowing direct comparison of aspect ratios.

lighthouse, and in the far field, where it killed 159 people in Hawaii, and wrought significant damage in the Marquesas, and probably as far as Antarctica [*Fuchs,* 1982]. It was recognized early on by *Kanamori* [1972] as a "tsunami earthquake" featuring exceptionally slow rupture. During several campaigns of field work in 1999-2002, described in detail in *Okal et al.* [2002*c*; 2003*a*], we were able to successfully compile a database of 57 far-field and 29 near-field run-up measurements through the interview of 69 witnesses aged 59 to 89 at the time of the interview [*Okal et al.,* 2002*c*; 2003*a*]. These field surveys produced two fundamental results: in the near field, we revised to a maximum of 42 m the amplitude of run-up at Scotch Cap, and established that it decays relatively fast along the coast of Unimak Island. These two observations require the involvement of a major underwater landslide as they indicate an aspect ratio $I_2 = 6.7 \times 10^{-4}$ and a ratio of maximum run-up to seismic slip $I_1 = 3.4$ both in excess of those theoretically acceptable for any dislocation [*Okal and Synolakis,* 2004]. The presence of a landslide in the source of the 1946 tsunami is also supported by anecdotal testimony from retired fishermen. In contrast, in the far field, and based principally on our results at Juan Fernández Island, we document a very pronounced directivity, which cannot be reconciled with a landslide source, and requires a substantial dislocation.

A detailed seismological reassessment of the 1946 Aleutian earthquake established that it involved bilateral rupture over a fault extending at least 200 km, and that it featured one of the slowest ruptures ever documented, with *Newman and Okal*'s [1998] parameter Θ reaching -7.0 [*López and Okal,* 2002]. Using simulations based on an estimated seismic moment of $M_0 = 9 \times 10^{28}$ dyn-cm (suggested from the evolution of mantle wave spectral amplitudes with frequency, as recorded on broad-band instruments at Pasadena), *Hébert and Okal* [2003] have successfully reproduced the directivity in run-up amplitudes surveyed in the far field, and *Titov et al.* [2003] have similarly, but with the help of a different code, modeled the inundation at Hilo, Hawaii, as reported by *Shepard et al.* [1946].

The model emerging from these studies is that of a complex process, comprising an extremely slow and very large earthquake (required to explain the far field tsunami, as well as for example, the distribution of aftershocks), and of a coeval landslide responsible for the exceptional amplitude of run-up in the near field.

5.2. AMORGOS, GREECE, 09 JULY 1956; $M_0 \approx 5 \times 10^{27}$ dyn-cm [this study].

This relatively large earthquake was followed by a locally destructive tsunami, with maximum run-up reported to have reached 30 m on the Southern coast of the island of Amorgos. *Ambraseys* [1960] suggested that the source of the tsunami must have involved underwater landslides off the Eastern coast of Amorgos. There is considerable disagreement on the exact focal mechanism of the earthquake [*Shirokova,* 1972; *Ritsema,* 1974], suggesting the possibility of a composite rupture, in the general framework of extensional neotectonics in the the back-arc Aegean Basin. A number of marine surveys [*Ambraseys,* 1960; *Perissoratis and Papadopoulos,* 1999] have suggested the involvement of an underwater slump as a source of the tsunami.

We have initiated a tsunami survey through the interview of a dozen elderly witnesses on the island of Amorgos in the Summer of 2003, and compiled a preliminary dataset of 6 run-up measurements. Its peaked character on the Eastern coast of Amorgos would

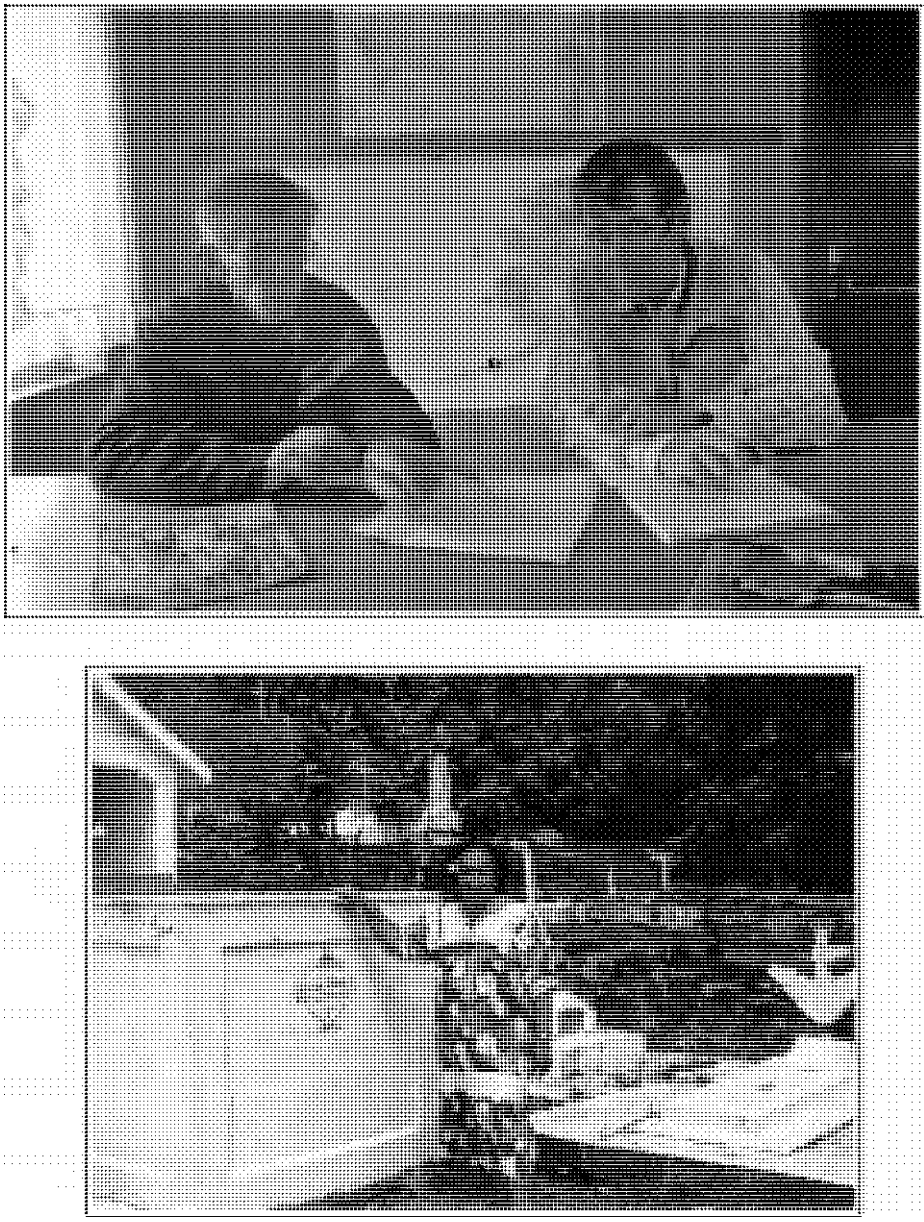

Fig. 9. Interviews of witnesses of the 1946 Aleutian tsunami. *Top:* In the near field, Dr. Okal interviews Mr. Ronald Wilson, aged 10 in 1946, who is seen directing him on a map to driftwood deposited on the island of Sanak, a watermark later surveyed by the team. *Bottom:* In the far field, Ms. Yvonne Katuai, a resident of Hatiheu, Nuku Hiva (Marquesas Islands) aged 8 in 1946, remembers how the tsunami destroyed her father's store and carried a bag a flour into the cemetery, depositing it on this tomb, surveyed to lie 8.2 m above sea level.

support a landslide origin for the tsunami. Further work is also in progress on the Turkish coast of the Aegean Sea, in collaboration with Prof. A.C. Yalçıner.

6. Conclusion

Over the past twelve years, the post-tsunami field surveys conducted by the International Tsunami Survey Teams have provided homogeneous datasets of run-up and inundation measurements which have proven critical to the development of our understanding of the interaction of a tsunami wave with a receiving beach. Some of the milestones in this progress include the need for, and feasibility of, the precise handling of the interaction with the beach by numerical algorithms of hydrodynamic simulation (Nicaragua, 1992; Okushiri, 1993), the observation of the leading depression predicted by theoretical models (Mexico, 1995), the identification and recognition of underwater landslides as posing major hazard to coastal communities (Papua New Guinea, 1998), and the value of education as a mitigating factor of the death toll during near-field tsunamis (Vanuatu, 1999; Peru, 2001).

An important development brought about during the field surveys is the possibility of applying modern techniques designed in the aftermath of recent events to historical tsunamis, through the interview of elderly witnesses and the surveying of preserved watermarks, both in the near and far fields. The application of these techniques to the 1946 Aleutian event clearly requires both a large dislocation to explain the far-field data, and a major underwater landslide to generate the local tsunami. Because no tsunami with catastrophic transoceanic amplitudes has occurred in the past 40 years, the surveying of the 1946 event in the far field also provides some practice towards the challenge of conducting a basin-wide far-field survey when the next such event inevitably occurs in the future.

Acknowledgments

This research is supported by the National Science Foundation, most recently under grants CMS-0301054 to EAO and CMS-0301081 to CES. We acknowledge constructive comments from Dr. Kenji Satake and two anonymous reviewers on an initial version of the manuscript. Raiden Hasegawa of Evanston Township High School is thanked for his help in compiliug and orgauizing the datasets used in Figures 7 and 8. We are grateful to our colleagues all over the world, for their help in the field; they are simply too numerous to list. Finally, we thank the community leaders and the local residents in the various field areas, for making our work possible and enjoyable, despite the frequent hardships of the post-tsunami environments.

References

Abe, Ka., M. Hakuno, M. Takeuchi, and T. Katada, Survey report of the Michoacan, Mexico earthquake of September 19, 1985, *Bull. Earthq. Res. Inst. Tokyo Univ.*, **61,** 475–481, 1986.

Abe, Ku., Ka. Abe, Y. Tsuji, F. Imamura, H. Katao, I. Yohihisa, K. Satake, J. Bourgeois, E. Noguera, and F. Estrada, Field survey of the Nicaragua earthquake and tsunami of September 2, 1992, *Bull. Earthq. Res. Inst. Tokyo Univ.*, **68,** 23–70, 1993.

Abercrombie, R., M. Antolik, K. Felzer, and G. Ekström, The 1994 Java tsunami earthquake: Slip over a subducting seamount, *J. Geophys. Res.*, **106,** 6595–6607, 2001.

Altınok, Y., B. Alpar, Ş Ersoy, and A.C. Yalçıner, Tsunami generation of the Kocaeli earthquake (August 17, 1999) in Izmit Bay: coastal observations, bathymetry and seismic data, *Turkish J. Mar. Sci.*, **5,** 131–148, 1999.

Altınok, Y., S. Tinti, B. Alpar, A.C. Yalçıner, Ş Ersoy, E. Bortolucci, and A. Armigliato, The tsunami of August 17, 1999 in Izmit bay, *Nat. Haz.*, **24,** 133–146, 2001.

Ambraseys, N.N., The seismic sea wave of July 9, 1956 in the Greek archipelago, *J. Geophys. Res.*, **65,** 1257–165, 1960.

Atwater, B.F., S. Musumi, K. Satake, Y. Tsuji, K. Ueda, and D.K. Yamaguchi, The orphan tsunami of 1700, *U.S. Geol. Survey Prof. Paper,* in press, 2004.

Bardet, J.-P., C.E. Synolakis, H.L. Davies, F. Imamura, and E.A. Okal, Landslide tsunamis: Recent findings and research directions, *Pure Appl. Geophys.*, **160,** 1793–1809, 2003.

Barka, A., and 21 co-authors, The surface rupture and slip distribution of the 17 August 1999 Izmit earthquake (M = 7.4), North Anatolian fault, *Bull. Seismol. Soc. Amer.*, **92,** 43–60, 2002.

Beckers, J., and T. Lay, Very broadband seismic analysis of the 1992 Flores, Indonesia, earthquake (M_w = 7.9), *J.Geophys. Res.*, **100,** 18179–18193, 1995.

Borrero, J.C., M. Ortiz, V.V. Titov, and C.E. Synolakis, Field survey of Mexican tsunami produced new data, unusual photos, *Eos, Trans. Amer. Geophys. Un.*, **78,** 85 and 87–88, 1997.

Borrero, J.C., J.F. Dolan, and C.E. Synolakis, Tsunamis within the Eastern Santa Barbara Channel, *Geophys. Res. Letts.*, **28,** 643–646, 2001.

Borrero, J.C., J. Bu, C. Saiang, B. Uslu, J. Freckman, B. Gomer, E.A. Okal, and C.E. Synolakis, Field survey and preliminary modeling of the Wewak, Papua New Guinea earthquake and tsunami of September 9, 2002, *Seismol. Res. Letts.*, **74,** 393–405, 2003.

Bourgeois, J., C. Petroff, H. Yeh, J.F. Lander, J. Kuroiwa, C.E. Synolakis, V.V. Titov, B.E. Benson, Tsunami survey from the Feb. 21, 1996, Peru earthquake, *Eos, Trans. Amer. Geophys. Un.*, **76,** *(46),* 382, 1996 [abstract].

Bourgeois, J., C. Petroff, H. Yeh, V.V. Titov, C.E. Synolakis, B.Benson, J. Kuroiwa, J. Lander, and E. Norabuena, Geologic setting, field survey and modeling of the Chimbote, northern Peru tsunami of 21 February 1996, *Pure Appl. Geophys.*, **154,** 513–540, 1999.

Briggs, M.J., C.E. Synolakis, G.S. Harkins, and D.R. Green, Laboratory experiments of tsunami runup on a circular island, *Pure Appl. Geophys.*, **144,** 569–594, 1995.

Caminade, J.-P., D. Charlie, U. Kánoğlu, S. Koshimura, H. Matsutomi, A. Moore, C. Ruscher, C.E. Synolakis, and T. Takahashi, Vanuatu earthquake and tsunami cause much damage, few casualties, *Eos, Trans. Amer. Un.*, **81,** 641 and 646–647, 2000.

Davies, H.L., J.M. Davies, R.C.B. Perembo, and W.Y. Lus, The Aitape 1998 tsunami: Reconstructing the event from interviews and field mapping, *Pure Appl. Geophys.*, **160,** 1895–1922, 2003.

Dengler, L., and J. Preuss, Mitigation lessons from the July 17, 1998 Papua New Guinea tsunami, *Pure Appl. Geophys.*, **160,** 2001–2031, 2003.

Dengler, L., J. Borrero, G. Gelfenbaum, B. Jaffe, E. Okal, M. Ortiz, and V. Titov, Tsunami, **in:** *Southern Peru earthquake of 23 June 2001, Reconnaissance Report,* Ed. by A. Rodriguez-Marek and C. Edwards, *Earthquake Spectra,* **19,** *Supp. A.*, 115–144, 2003.

Dziewonski, A.M., G. Ekström, and M.P. Salganik, Centroid-moment tensor solutions for July-September 1992. *Phys. Earth Planet. Inter.*, **79,** 287-297, 1993*a*.

Dziewonski, A.M., G. Ekström, and M.P. Salganik, Centroid-moment tensor solutions for October-December 1992, *Phys. Earth Planet. Inter.*, **80,** 89-103, 1993*b*.

Dziewonski, A.M., G. Ekström, and M.P. Salganik, Centroid-moment tensor solutions for July-September 1993, *Phys. Earth Planet. Inter.*, **83,** 165-174, 1994.

Dziewonski, A.M., G. Ekström, and M.P. Salganik, Centroid-moment tensor solutions for April-June 1994, *Phys. Earth Planet. Inter.*, **88,** 69-78, 1995*a*.

Dziewonski, A.M., G. Ekström, and M.P. Salganik, Centroid-moment tensor solutions for October-December 1994, *Phys. Earth Planet. Inter.*, **91,** 187-201, 1995*b*.

Dziewonski, A.M., G. Ekström, and M.P. Salganik, Centroid-moment tensor solutions for October-December 1995, *Phys. Earth Planet. Inter.*, **101,** 1-12, 1997*a*.

Dziewonski, A.M., G. Ekström, and M.P. Salganik, Centroid-moment tensor solutions for January-March 1996, *Phys. Earth Planet. Inter.*, **102,** 1-9, 1997*b*.

Dziewonski, A.M., G. Ekström, and N. Maternovskaya, Centroid-moment tensor solutions for July-September 1998, *Phys. Earth Planet. Inter.*, **114,** 99-107, 1999.

Dziewonski, A.M., G. Ekström, and N. Maternovskaya, Centroid-moment tensor solutions for July-September 1999, *Phys. Earth Planet. Inter.*, **119,** 311-319, 2000*a*.

Dziewonski, A.M., G. Ekström, and N. Maternovskaya, Centroid-moment tensor solutions for October-December 1999, *Phys. Earth Planet. Inter.*, **121,** 205-221, 2000*b*.

Ekström, G., A.M. Dziewoński, N.N. Maternovskaya, and M. Nettles, Global seismicity of 2001: centroid-moment tensor solutions for 961 earthquakes, *Phys. Earth Planet. Inter.*, **136,** 165–185, 2003.

Fuchs, Sir V., *Of ice and men: The story of the British Antarctic Survey, 1943–73,* 383 pp., Anthony Nelson, Oswestry, 1982.

Gelfenbaum, G., and B. Jaffe, Erosion and sedimentation from the July 17, 1998 Papua New Guinea tsunami, *Pure Appl. Geophys.*, **160,** 1969–1999, 2003.

Gutenberg, B., and C.F. Richter, *Seismicity of the Earth and associated phenomena,* Princeton Univ. Press, 310 pp., Princeton, 1954.

Hébert, H., and E.A. Okal, Hydrodynamic modeling of the 1946 Aleutian tsunami in the far field using a dislocation source, *Eos, Trans. Amer. Geophys. Un.*, **84,** *(46),* F810, 2003 [abstract].

Hébert, H., A. Piatanesi, P. Heinrich, F. Schindelé, and E.A. Okal, Numerical modeling of the September 13, 1999 landslide and tsunami on Fatu Hiva island (French Polynesia), *Geophys. Res. Letts.*, **29,** *(10),* 122_1–122_4, 2002.

Heinrich, P., F. Schindelé, S. Guibourg, and P. Ihmlé, Modeling of the 1996 Peruvian tsunami, *Geophys. Res. Letts.*, **25,** 2687–2690, 1998.

Heinrich, P., A. Piatanesi, E.A. Okal, and H. Hébert, Near-field modeling of the July 17, 1998 tsunami in Papua New Guinea, *Geophys. Res. Letts.*, **27,** 3037–3040, 2000.

Hidayat, D., J.S. Barker, and K. Satake, Modeling the seismic source and tsunami generation of the December 12, 1992 Flores Island, Indonesia earthquake, *Pure Appl. Geophys.*, **144,** 537–554, 1995.

Ihmlé, P., J.-M. Gomez, P. Heinrich, and S. Guibourg, The 1996 Peru tsunamigenic earthquake: Broadband source process, *Geophys. Res. Letts.*, **25,** 2691–2694, 1998.

Imamura, F., and K. Hashi, Re-examination of the source mechanism of the 1998 Papua New Guinea earthquake and tsunami, *Pure Appl. Geophys.*, **160,** 2071–2086, 2003.

Imamura, F., N. Shuto, S. Ide, Y. Yoshida, and K. Abe, Estimate of the tsunami source of the 1992 Nicaraguan earthquake from tsunami data, *Geophys. Res. Letts.*, **20,** 1515–1518, 1993.

Imamura, F., E. Gica, T. Takahashi, and N. Shuto, Numerical simulation of the 1992 Flores tsunami: Interpretation of tsunami phenomena in Northeastern Flores Island and damage at Babi Island, *Pure Appl. Geophys.*, **144,** 555–568, 1995*a*.

Imamura, F., Synolakis, C.E., E. Gica, V.V. Titov, E. Listanco, and H.J. Lee, Field survey of the 1994 Mindoro Island, Philippines tsunami, *Pure Appl. Geophys.*, **144,** 875–890, 1995*b*.

Imamura, F., D. Subandono, G. Watson, A. Moore, T. Takahashi, H. Matsutomi, and R. Hidayat, Irian Jaya earthquake and tsunami cause serious damage, *Eos, Trans. Amer. Geophys. Un.*, **78,** 197 and 201, 1997.

Kanamori, H., Mechanisms of tsunami earthquakes, *Phys. Earth Planet. Inter.*, **6,** 346-359, 1972.

Kanamori, H., The energy release in great earthquakes, *J. Geophys. Res.*, **82,** 2981–1987, 1977.

Kanamori, H., and M. Kikuchi, The 1992 Nicaragua earthquake; a slow tsunami earthquake associated with subducted sediments, *Nature,* **361,** 714–716, 1993.

Kawata, Y., B.C. Benson, J.C. Borrero, J.L. Borrero, H. Davies, W. deLange, F. Imamura, and C.E. Synolakis, Tsunami in Papua New Guinea, *Eos, Trans. Amer. Un.*, **80,** *(9),* 101–105, 1999.

Kikuchi, M., and H. Kanamori, Source characteristics of the 1992 Nicaragua tsunami earthquake inferred from teleseismic body waves, *Pure Appl. Geophys.*, **144,** 441–453, 1995.

Kuge, K., J. Zhang, and M. Kikuchi, The 12 July 1993 Hokkaido-Nansei-Oki, Japan earthquake: effects of

source complexity on surface-wave radiation, *Bull. Seismol. Soc. Amer.*, **86,** 505–518, 1996.

Lallemand, S., and X. Le Pichon, Coulomb wedge model applied to the subduction of seamounts in the Japan trench, *Geology,* **15,** 1065–1069, 1987.

Legg, M.R., J.C. Borrero, and C.E. Synolakis, Tsunami hazards from strike-slip earthquakes, *Eos, Trans. Amer. Geophys. Un.*, **84,** *(46),* F810, 2003 [abstract].

López, A.M., and E.A. Okal, Aftershock relocation, rupture area, mantle magnitude and energy estimates of the 1946 Aleutian tsunami earthquake and neighboring events, *Eos, Trans. Amer. Geophys. Un.*, **83,** *(47),* F1045, 2002 [abstract].

Matsutomi, H., and H. Iizuka, Tsunami current velocity on land and its simple estimation method, *Proc. of Coastal Eng., JSCE,* **42,** 346–350, 1998.

Matsutomi, H., N. Shuto, F. Imamura, and T. Takahashi, Field survey of the 1996 Irian Jaya earthquake tsunami in Biak Island, *Nat. Haz.*, **24,** 199–212, 2001.

Newman, A.V., and E.A. Okal, Teleseismic estimates of radiated seismic energy: The E/M_0 discriminant for tsunami earthquakes, *J. Geophys. Res.*, **103,** 26885–26898, 1998.

Okal, E.A., *T* waves from the Sandaun earthquake and its aftershocks, *Eos, Trans. Amer. Geophys. Un.*, **79,** *(45),* F572, 1998 [abstract].

Okal, E.A., Historical seismicity and seismotectonic context of the great 1979 Yapen and 1996 Biak, Irian Jaya earthquakes, *Pure Appl. Geophys.*, **154,** 633-675, 1999.

Okal, E.A., *T* waves from the 1998 Papua New Guinea earthquake and its aftershocks: Timing the tsunamigenic slump, *Pure Appl. Geophys.*, **160,** 1843–1863, 2003.

Okal, E.A., and A.V. Newman, Tsunami earthquakes: The quest for a regional signal, *Phys. Earth Planet. Inter.*, **124,** 45–70, 2001.

Okal, E.A., and C.E. Synolakis, Source discriminants for near–field tsunamis, *Geophys. J. Intl.*, in press, 2004.

Okal, E.A., L. Dengler, S. Araya, J.C. Borrero, B. Gomer, S. Koshimura, G. Laos, D. Oleesc, M. Ortiz, M. Swensson, V.V. Titov, and F. Vegas, A field survey of the Camaná, Peru tsunami of June 23, 2001, *Seismol. Res. Letts.*, **73,** 904–917, 2002*a*.

Okal, E.A., G.J. Fryer, J.C. Borrero, and C. Ruscher, The landslide and local tsunami of 13 September 1999 on Fatu-Hiva (Marquesas Islands; French Polynesia), *Bull. Soc. Géol. France,* **173,** 359–367, 2002*b*.

Okal, E.A., C.E. Synolakis, G.J. Fryer, P. Heinrich, J.C. Borrero, C. Ruscher, D. Arcas, G. Guille, and D. Rousseau, A field survey of the 1946 Aleutian tsunami in the far field, *Seismol. Res. Letts.*, **73,** 490–503, 2002*c*.

Okal, E.A., G. Plafker, C.E. Synolakis, and J.C. Borrero, Near-field survey of the 1946 Aleutian tsunami on Unimak and Sanak Islands, *Bull. Seismol. Soc. Amer.*, **93,** 1226–1234, 2003*a*.

Okal, E.A., P.-J. Alasset, O. Hyvernaud, and F. Schindelé, The deficient *T* waves of tsunami earthquakes, *Geophys. J. Intl.*, **152,** 416–432, 2003*b*.

Ortíz, M., S.K. Singh, J. Pacheco, and V. Kostoglodov, Rupture length of the October 9, 1995 Colima-Jalisco earthquake ($M_w = 8$) estimated from tsunami data, *Geophys. Res. Letts.*, **25,** 2857–2860, 1998.

Pacheco, J., S.K. Singh, J. Domínguez, A. Hurtado, L. Quintanar, Z. Jiménez, J. Yamamoto, C. Gutiérrez, M. Santoyo, W. Bandy, M. Guzmán, and V. Kostoglodov, The October 9, 1995 Colima-Jalisco, Mexico earthquake ($M_w = 8$): An aftershock study and a comparison of this earthquake with those of 1932, *Geophys. Res. Letts.*, **24,** 2223–2226, 1997.

Parsons, T.E., S. Toda, R.S. Stein, A. Barka, and J.H. Dieterich, Heightened odds of large earthquakes near Istanbul; an interaction-based probability calculation, *Science,* **288,** 661–665, 2000.

Pelinovsky, E., B. Levin, E. Kulikov, V. Gusyakov, V. Kaistrenko, A. Ivashenko, A. Poplavsky, V. Khramushin, H. Yeh, and V.V. Titov, Preliminary report of field survey in South Kurile Islands due to the Shikotan tsunami (October 4, 1994), *Eos, Trans. Amer. Geophys. Un.*, **76,** *(17),* 305, 1995 [abstract].

Pelletier, B., M. Régnier, S. Calmant, R. Pillet, G. Cabioch, Y. Lagabrielle, J.-M. Bore, J.-P. Caminade, P. Lebellegard, I. Christopher, and S. Temakon, Le séisme d'Ambrym-Pentecôte (Vanuatu) du 26 novembre 1999 ($M_w = 7,5$); données préliminaires sur la séismicité, le tsunami et les déplacements associés, *C.R. Acad. Sci, Sér. II,* **331,** 21–28, 2000.

Perissoratis, C., and G. Papadopoulos, Sediment instability and slumping in the Southern Aegean Sea and the case history of the 1956 tsunami, *Mar. Geol.*, **161,** 287–305, 1999.

Piatanesi, A., P. Heinrich, and S. Tinti, The October 4, 1994 Shikotan (Kuril Islands) tsunamigenic earthquake: An open problem on the source mechanism, *Pure Appl. Geophys.*, **154,** 555-574, 1999.

Plafker, G., Catastrophic tsunami generated by submarine slides and backarc thrusting during the 1992 earthquake on eastern Flores I., Indonesia, *Geol. Soc. Amer. Abstr. with Prog.*, **29,** *(5)*, 57, 1997 [abstract].

Ritsema, A.R. Earthquake mechanisms of the Balkan region, *R. Neth. Meteorolog. Inst. Sci. Rep.*, **74,** *(4)*, 36 pp., 1974.

Satake, K., Mechanism of the 1992 Nicaragua tsunami earthquake, *Geophys. Res. Letts.*, **21,** 2519–2522, 1994.

Satake, K., and Y. Tanioka, Sources of tsunami and tsunamigenic earthquakes in subduction zones, *Pure Appl. Geophys.*, **154,** 467–483, 1999.

Satake, K., J. Bourgeois, Ka. Abe, Ku. Abe, Y. Tsuji, F. Imamura, Y. Iio, H. Katao, E. Noguera, and F. Estrada, Tsunami field survey of the 1992 Nicaragua earthquake, *Eos, Trans. Amer. Geophys. Un.*, **74,** 145 and 156–157, 1993.

Satake, K., K. Shimazaki, Y. Tsuji, and K. Ueda, Time and size of a giant earthquake in Cascadia inferred from Japanese tsunami records of January 1700, *Nature*, **374,** 246–249, 1996.

Shepard, F.P., G.A. Macdonald, and D.C. Cox, The tsunami of April 1, 1946 [Hawaii], *Bull. Scripps Inst. Oceanog., Univ. Calif.*, **5,** 391–528, 1950.

Shirokova, E.I., Napryazheniya i razryvy v ochagakh zemletryaseniĭ sredizemnomorsko-aziatskovo seĭsmicheskovo poyasa, **in:** *Polye uprugikh naprazheniĭ zemli i mekhanizm ochagov zemletryaseniĭ*, ed. by L.M. Balakina, A.V. Vvedenskaya, N.V. Golubyeva, L.A. Misharina and E.I. Shirokova, pp. 112–148, Nauka, Moskva, 1972.

Shuto, N., and H. Matsutomi, Field survey of the 1993 Hokkaido-Nansei-Oki earthquake tsunami, *Pure Appl. Geophys.*, **144,** 406–449, 1995.

Shuto, N., and 23 co-authors, Tsunami devastates Japanese coastal region, *Eos, Trans. Amer. Geophys. Un.*, **74,** 417 and 432, 1993.

Sweet, S., and E.A. Silver, Tectonics and slumping in the source region of the 1998 Papua New Guinea tsunami from seismic refraction, *Pure Appl. Geophys.*, **160,** 1945–1968, 2003.

Synolakis, C.E., F. Imamura, Y. Tsuji, H. Matsutomi, S. Tinti, B. Cook, Y.P. Chandra, and M. Usman, Damage, conditions of East Java tsunami of 1994 analyzed, *Eos, Trans. Amer. Geophys. Un.*, **76,** 257 and 261–262, 1995.

Synolakis, C.E., J.-P. Bardet, J.C. Borrero, H.L. Davies, E.A. Okal, E.A. Silver, S. Sweet, and D.R. Tappin, The slump origin of the 1998 Papua New Guinea tsunami, *Proc. Roy. Soc. (London), Ser. A*, **458,** 763–789, 2002.

Tadepalli, S., and C.E. Synolakis, The runup of N –waves, *Proc. Roy. Soc. London, Ser. A*, **445,** 99–112, 1994.

Tadepalli, S., and C.E. Synolakis, Model for the leading waves of tsunamis, *Phys. Rev. Letts.*, **77,** 2141–2145, 1996.

Takahashi, To., Ta. Takahashi, N. Shuto, F. Imamura, and M. Ortiz, Source models for the 1993 Hokkaido-Nansei-Oki earthquake tsunami, *Pure Appl. Geophys.*, **144,** 747–767, 1995.

Tanioka, Y., and K. Satake, Tsunami generation by horizontal displacement of ocean bottom, *Geophys. Res. Letts.*, **23,** 861–864, 1996.

Tanioka, Y., K. Satake, and L.J. Ruff, Total analysis of the 1993 Hokkaido-Nansei-Oki earthquake using seismic waves, tsunami, and geodetic data, *Geophys. Res. Letts.*, **22,** 9–12, 1995*a*.

Tanioka, Y., L.J. Ruff, and K. Satake, The great Kurile earthquake of October 4, 1994 tore the slab, *Geophys. Res. Letts.*, **22,** 1661–1664, 1995*b*.

Tinti, S., and C. Vannini, Tsunami trapping near circular islands, *Pure Appl. Geophys.*, **144,** 595–620, 1995.

Titov, V.V., Hydrodynamic modeling of 3-D tsunami runup, *Ph.D. dissertation,* Univ. Southern Calif., Los Angeles, 150 pp., 1996.

Titov, V.V., and C.E. Synolakis, A numerical study of wave runup of the September 2, 1992 Nicaraguan tsunami, *Proc. Intl. Un. Geol. Geophys. Tsunami Symp.*, ed. by Y. Tsuchiya and N. Shuto, Japan Soc. Civil Eng., pp. 627–635, Wakayama, Japan, 1993.

Titov, V.V., and C.E. Synolakis, Extreme inundation flow during the Hokkaido-Nansei-Oki tsunami, *Geophys. Res. Letts.*, **24,** 1315–1318, 1997.

Titov, V.V., F.I. González, H.O. Mofjeld, and J.C. Newman, Short-term tsunami inundation forecasting for tsunamis, **in:** *Submarine landslides and tsunamis,* ed. by A.C. Yalçıner, E.N. Pelinovsky, E. Okal, and C.E. Synolakis, *NATO science Ser.,* **IV: 21,** pp. 277–284, 2003.

Tsuji, Y., H. Matsutomi, F. Imamura, M. Takeo, Y. Kawata, M. Matsuyama, T. Takahashi, Sunarjo, and P.

Harjadi, Damage to coastal villages due to the 1992 Flores Island earthquake tsunami, *Pure Appl. Geophys.*, **144,** 481–524, 1995*a*.

Tsuji, Y., F. Imamura, H. Matsutomi, C.E. Synolakis, P.T. Nanang, Jumadi, S. Harada, S.S. Han, K. Arai, and B. Cook, Field survey of the East Java earthquake and tsunami of June 3, 1994, *Pure Appl. Geophys.*, **144,** 839–854, 1995*b*.

Velasco, A.A., C.J. Ammon, T. Lay, and J. Zhang, Imaging a slow bilateral rupture with broadband seismic waves; the September 2, 1992 Nicaraguan tsunami earthquake, *Geophys. Res. Letts.*, **21,** 2629–2632, 1994.

Yalçıner, A.C., Y. Altınok, and C.E. Synolakis, Tsunami waves in Izmit Bay, *Earthquake Spectra,* **16,** *Suppt. A,* 55–62, 2000.

Yalçıner, A.C., B. Alpar, Y. Altınok, I. Özbay, and F. Imamura, Tsunamis in the Sea of Marmara: Historical documents from the past, models for the future, *Mar. Geol.,* **190,** 445–463, 2002.

Yeh, H., F. Imamura, C. Synolakis, Y. Tsuji, P. Liu, and S. Shi, The Flores Island tsunami, *Eos, Trans. Amer. Geophys. Un.,* **74,** 369 and 371–373, 1993.

Yeh, H., P.-L. Liu, M. Briggs, and C.E. Synolakis, Propagation and amplification of tsunamis at coastal boundaries *Nature,* **372,** 353–355, 1994.

Yeh, H., V.V Titov, V. Gusiakov, E. Pelinovsky, V. Khramushin, and V. Kaistrenko, The 1994 Shikotan earthquake tsunamis, *Pure Appl. Geophys.,* **144,** 855–874, 1995.

Zobin, The rupture history of the $M_w = 8.0$ Jalisco, Mexico, earthquake of 1995 October 9, *Geophys. J. Intl.,* **130,** 220–228, 1997.

THE FIORDLAND EARTHQUAKE AND TSUNAMI, NEW ZEALAND, 21 AUGUST 2003

W. POWER, G. DOWNES, M. MCSAVENEY, J. BEAVAN AND G. HANCOX

Institute of Geological and Nuclear Sciences Limited
PO Box 30368, Lower Hutt
New Zealand

The M_W7.2 earthquake at 12:12 UT August 21 2003 was the largest shallow earthquake in New Zealand for many years. GPS and seismological data are consistent with the earthquake rupturing the plate interface near the coast of Fiordland, a mountainous and largely unpopulated area in the southwest corner of the South Island. Fortunately, because of the remote location, the earthquake resulted in few injuries and relatively minor damage to property. However the earthquake triggered many landslides on the steep slopes that typify Fiordland. The fall of one landslide into Charles Sound caused a small local tsunami that reached a maximum of 4-5 m above high tide mark on the opposite shore. A small tsunami was also generated on the Tasman Sea coast, which was recorded on tide gauges at Jackson Bay (300 mm peak-to-trough) 190 km northeast of the epicentre, and at Port Kembla (170 mm peak-to-trough) on the east coast of Australia. Spectrogram analyses are used to demonstrate that the observed tide-gauge signals are best explained by the excitation of local resonances by the trans-Tasman tsunami. Modelling of the tsunami indicates that the wave amplitudes are compatible with estimates of offshore coseismic deformation of close to 0.5 m vertically as indicated by preliminary modelling of post-earthquake GPS data, and that the tsunami arrival times are compatible with the timing of the mainshock.

1 Introduction

On August 21 2003 at 12:12 UT (12:12 am August 22 NZST) an M_W7.2 earthquake occurred at shallow depth off the coast of Fiordland, New Zealand at 45.19°S, 166.83°E, depth 24.3 km (Figure 1a). Until the end of September, there were 21 aftershocks with $M_L \geq 5.0$. The mainshock was felt widely in the South Island and is reported to have been felt as much as 1800 km away, in Sydney, Australia (Reyners et al., 2003; Leonard, 2004). The maximum intensity, MM9, occurred in rugged, virtually uninhabited mountains, which typify Fiordland, and hence, there was only relatively minor damage to the built environment, mainly in the region of Te Anau and Manapouri, some 70 km east of the epicentre (Figure 2a). The earthquake triggered

K. Satake (ed.), Tsunamis: Case Studies and Recent Developments, 31-42.

over 400 landslides (Figure 2a) in the epicentral area, ranging in size from a few cubic metres to over 600,000 m^3 (Reyners et al., 2003; for details, see Hancox et al., 2003).

During post-earthquake reconnaissance of the epicentral area by helicopter, it was noted that one landslide, in falling 350 m into the waters of Charles Sound, had generated a tsunami, reaching a maximum of 4-5 m above the high-tide level on the opposite shore.

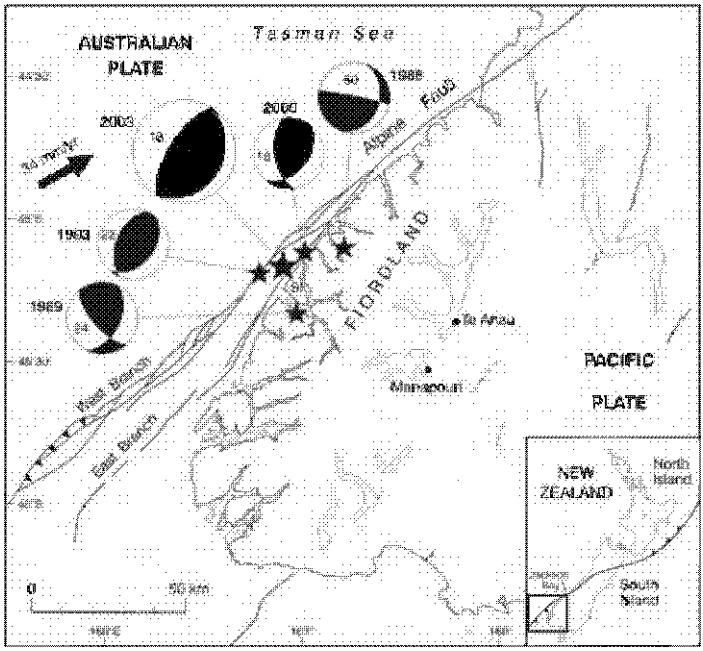

Adapted from Reyners et al. (2003)

Fig. 1a. Tectonic setting of the 2003 Fiordland earthquake, and recent earthquakes of M_W>6 in the same region. Focal mechanisms (lower hemisphere) and depths in kilometres are shown for each event. The mechanism for the 2003 earthquake is the Harvard centroid moment tensor solution, others are from Reyners & Webb (2002) and Robinson et al. (2003). The arrow indicates the velocity of the Australian plate relative to the Pacific plate (De Mets et al., 1994), SI denotes Secretary Island, and CS denotes Charles Sound.

A tsunami was also generated along the Fiordland coast, being recorded on tide gauges at Jackson Bay 190 km northeast of the mainshock (300 mm peak-trough) and at Port Kembla, on the east coast of Australia (170 mm peak-trough). The largest amplitude waves arrived at Jackson Bay shortly after a M_L5.9 aftershock in the epicentral region. This caused some confusion and speculation among emergency response organisations as to whether the source was the mainshock or the aftershock (Walsh, 2003), or a submarine landslide (Cox et al., 2003).

In this paper we report on the effects of the two tsunami, and on the preliminary results of modelling the tsunami generated by the mainshock, using source parameters

based on seismological data, and preliminary modelling of GPS deformation measurements.

2 Tectonic setting

The earthquake occurred in an area of New Zealand where highly oblique convergence of the Australia and Pacific Plates is occurring at a rate of ca. 34 mm/year at 062° (de Mets et al., 1994; Figure 1a). This convergence is accommodated by subduction of the Australian Plate, while the strike-slip component is thought to be principally accommodated by the Alpine Fault, about 10-20 km offshore (Reyners et al., 2003), although no part of the onshore or offshore Alpine Fault is known to have ruptured in the last 160 years. In the vicinity of the 2003 earthquake, the dipping seismic zone associated with subduction of the Australian plate becomes near vertical at ca. 75 km (Reyners et al., 2003).

The 2003 M_W7.2 earthquake is the largest shallow earthquake to occur in New Zealand for 35 years, and is the latest in a series of M_W>6.0 earthquakes within 50 kilometres of each other in the last 16 years, viz. the 1988 (M_W6.7; depth 60 km), 1989 (M_W6.4; depth 24 km), 1993 (M_W7.0; depth 22 km), and 2000 (M_W6.1; depth 18 km) earthquakes (Reyners et al., 2003). Of these, only the 2003 event is known to have initiated a tsunami in the Tasman Sea, or in the Sounds. However, aerial landslide reconnaissance has not occurred previously, and the remoteness of the area precludes the observation of tsunamis in the recent earthquakes, or historically.

3 Earthquake mechanism and deformation

Immediately following the earthquake, portable seismographs, strong motion instruments and GPS recorders were deployed in the epicentral area to record aftershocks and deformation. Analysis of the large volume of seismological data generated (which possibly comprises 5,000-10,000 locatable aftershocks) and subsequent delineation of the fault plane have yet to be completed. However, the locations of mainshock and large aftershocks until the end of September (as relocated by Reyners et al., 2003), and the Harvard CMT solution for the mainshock are compatible with low-angle thrusting on the shallow part of the plate interface (Reyners et al., 2003).

Modelling of the deformation obtained from pre- and post-earthquake GPS measurements (Beavan et al., 2003, Figure 1b), suggest slip of 2.4±0.5 m occurred on a fault plane of length 35±5 km. The local dip of the fault plane is 30±3 degrees, and the rupture surface lies between 13±2 km and 23±2 km deep. The predicted vertical deformation is shown in Figure 1c.

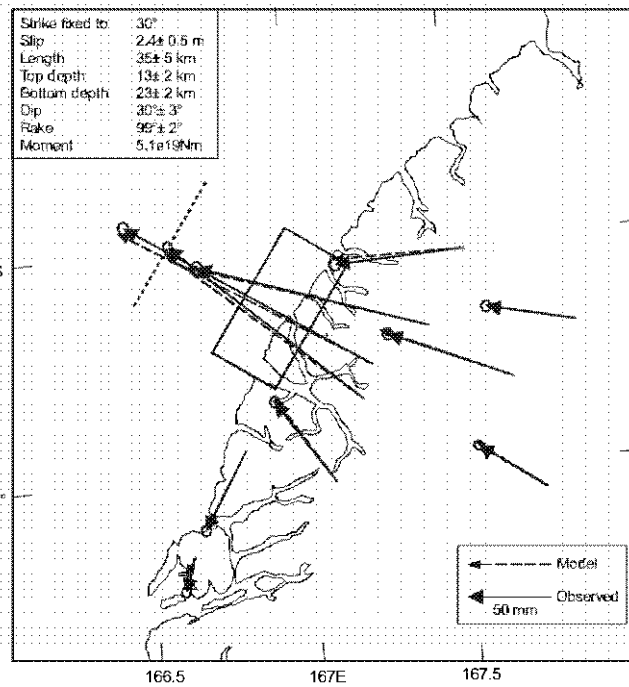

Fig. 1b. Preliminary fault solution based on GPS observations (Beavan et al., 2003).

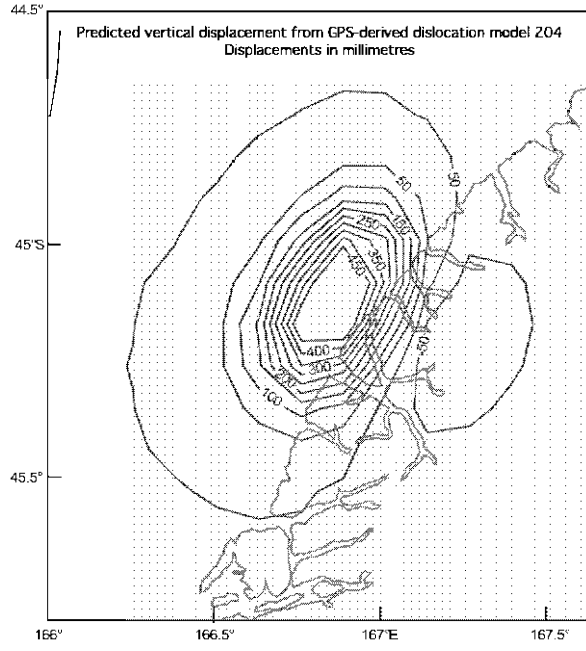

Fig. 1c. Predicted vertical displacement in millimetres derived from the fault solution in Figure 1b. The area of greatest uplift is centred a few kilometres offshore from Secretary Island.

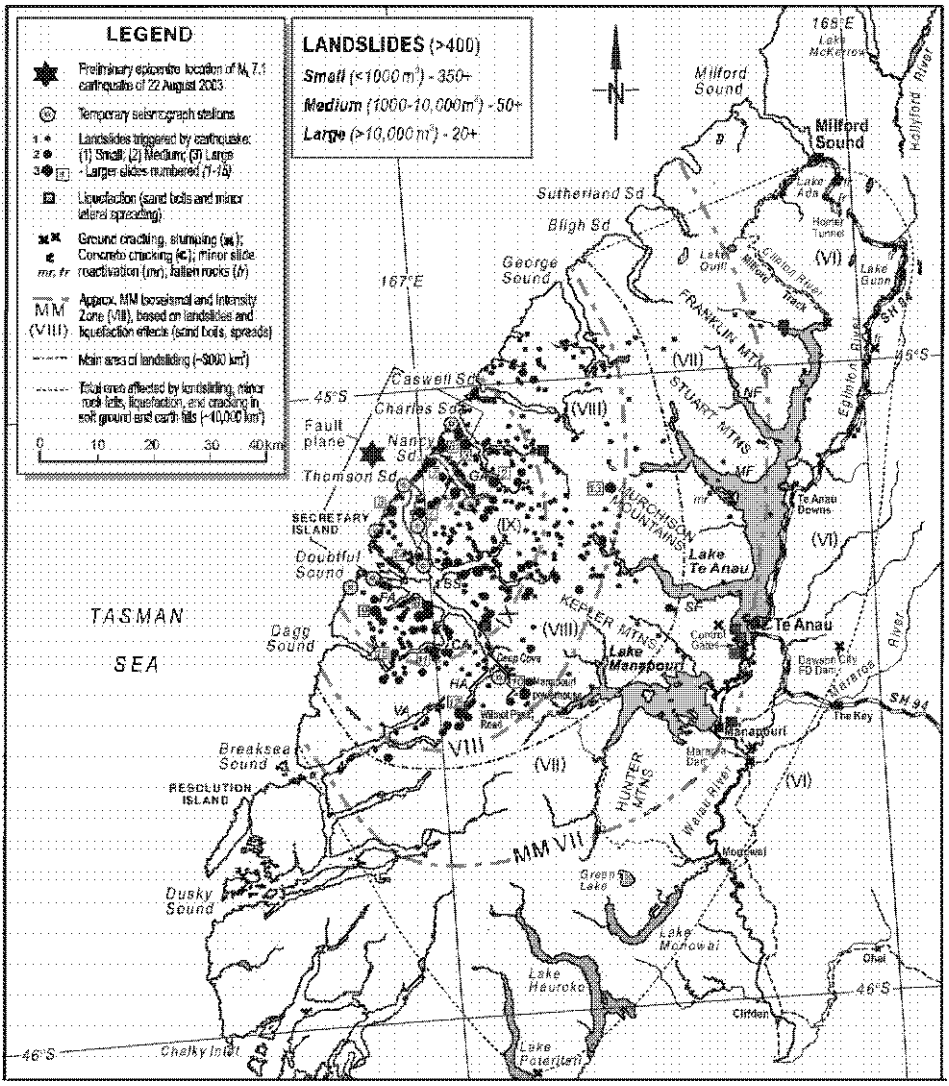

Fig. 2a. Map showing the location of the M 7.1 Fiordland earthquake of 22 August 2003, and the distribution of landslides, liquefaction effects, and other ground damage caused by the earthquake (Reyners et al., 2003; Hancox et al., 2003). Approximate Modified Mercalli (MM) isoseismals and felt intensity zones have been assigned mainly using environmental criteria (landsliding and liquefaction damage). The northern and southern limits of ground damage are approximate as the areas south of Breaksea Sound and Lake Manapouri and north of Sutherland Sound were not surveyed in detail.

4 Tsunami

4.1 GOLD ARM LANDSLIDE GENERATED TSUNAMI

A large rock slide of approximately 200,000 m^3 fell into the upper reaches of Gold Arm in Charles Sound (Hancox et al., 2003), generating a local tsunami within the Sound (Figures 2b,c). The landslide occurred on a 40° slope, not atypically steep for the Fiordland region, and fell about 350 m into water that reaches a maximum of about 18 m depth. The tsunami propagated 800 m across the sound (Figure 2c). On the far side of the sound, vegetation was damaged to a height of 4-5 m above the high-tide level over an area of approximately 0.45 km^2. A small island within the sound was partially stripped of vegetation. The tsunami also damaged a helipad/wharf about 250 m from the landslide along the same shoreline.

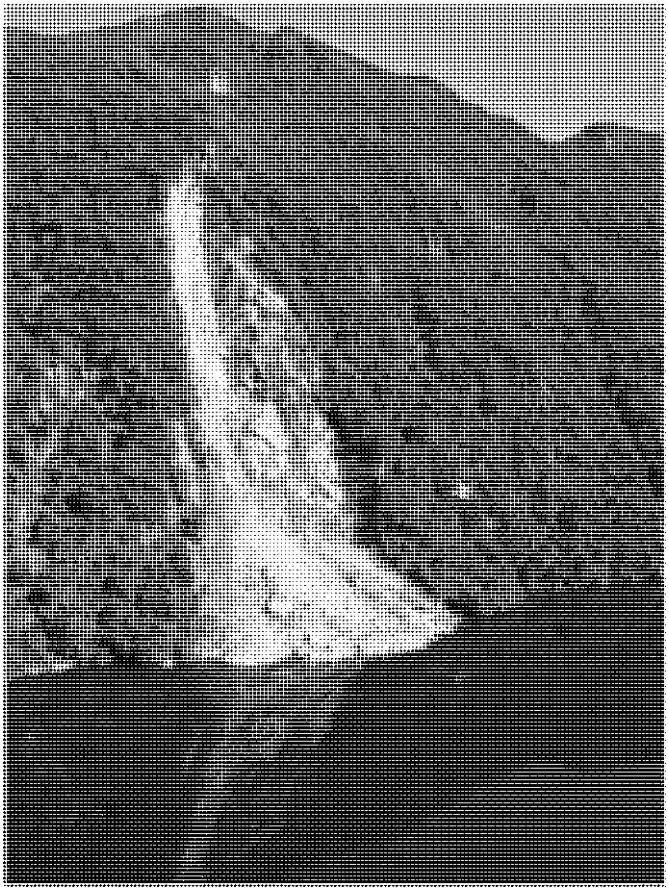

Fig. 2b. The landslide in Gold Arm of Charles Sound which caused a tsunami that affected an area of ~0.45 km^2 on the opposite bank.

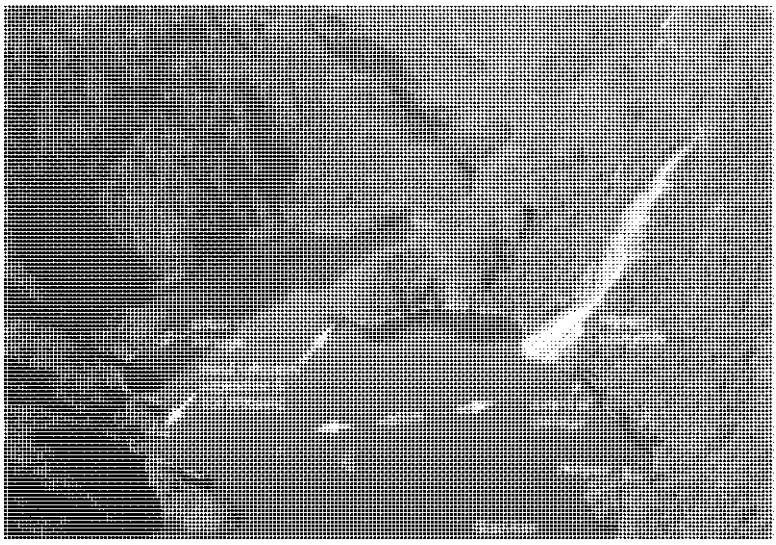

Fig. 2c. Extent of damage caused by landslide-generated tsunami in Gold Arm of Charles Sound.

4.2 TASMAN SEA DEFORMATION-INDUCED TSUNAMI

4.2.1 *Source*

Fault-plane slip of the earthquake caused onshore lateral movement of up to 170 mm. While onshore measurements of vertical movement were smaller, models of seafloor deformation based on slip parameters consistent with the onshore lateral deformation, suggest a raising of the seabed by up to 450 mm over a wide area (Figure 1c). Such a rise, over a short period of time, is sufficient to cause a trans-Tasman tsunami, though additional contributions from events such as undersea landslides cannot be ruled out.

4.2.2 *Observed effects*

The Tasman Sea tsunami was measured at Jackson Bay (Chittleborough, 2003), 180 km northeast of the epicentre, by a tide gauge (jointly operated and maintained by the National Tidal Facility (NTF), Australia, and National Institute of Water and Atmospheric Research (NIWA), New Zealand). It showed a maximum peak-to-trough amplitude of about 300 mm (Figure 3a). The peak tsunami amplitude occurs approximately 135 minutes after the mainshock, and less than 20 minutes after an M_L 5.9 aftershock. The initial onset of the tsunami is difficult to distinguish by eye from background fluctuations in the time series. Frequency analysis using a spectrogram suggests the first arrivals of the tsunami occur approximately 25 minutes after the mainshock (Figure 3b). The tide-gauge record appears to contain a signal of higher than background amplitude which lasted for several hours after the event, probably indicative of the excitation of resonances within Jackson Bay.

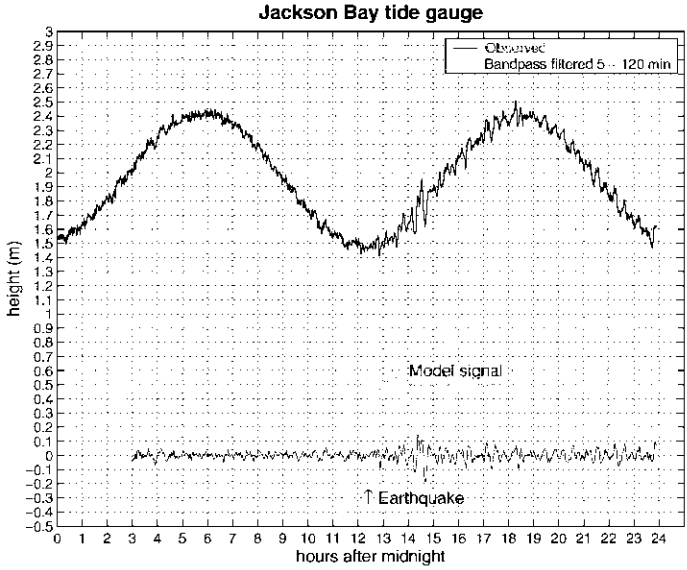

Fig. 3a. Tide gauge record from Jackson Bay (NTF/NIWA), approximately 190 km from the earthquake epicentre. The upper curve shows the original gauge reading, while the lower curve has been filtered to remove the tidal signal. The middle curve segment (offset for visibility) shows the simulated tide gauge reading from the numerical model. Note that as the model does not accurately portray local bathymetry the modelled signal is best considered as an estimate of the forcing of the local bay resonances by the tsunami.

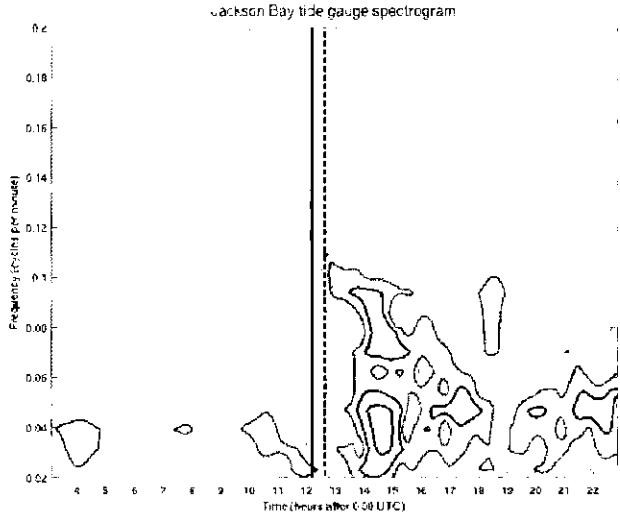

Fig. 3b. Spectrogram of tide gauge signal from Jackson Bay, approximately 190 km from the earthquake epicentre. The solid line indicates the time of the earthquake, and the dashed line indicates the tsunami arrival time as estimated by numerical modelling (time at which model signal first exceeds 1 cm).

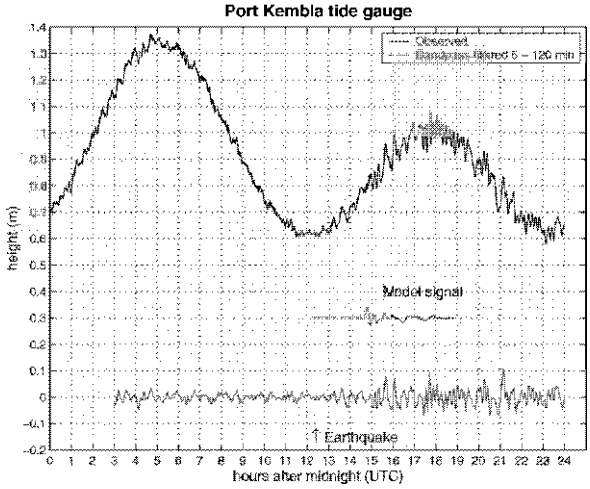

Fig. 3c. Tide gauge record from Port Kembla (NTF), near Wollongong in Australia, approximately 1750 km from the earthquake epicentre. The upper curve shows the original gauge reading, while the lower curve has been filtered to remove the tidal signal. The middle curve segment (offset for visibility) shows the simulated tide gauge reading from the numerical model. Note that as the model does not accurately portray local bathymetry the modelled signal is best considered as an estimate of the forcing of the local bay resonances by the tsunami.

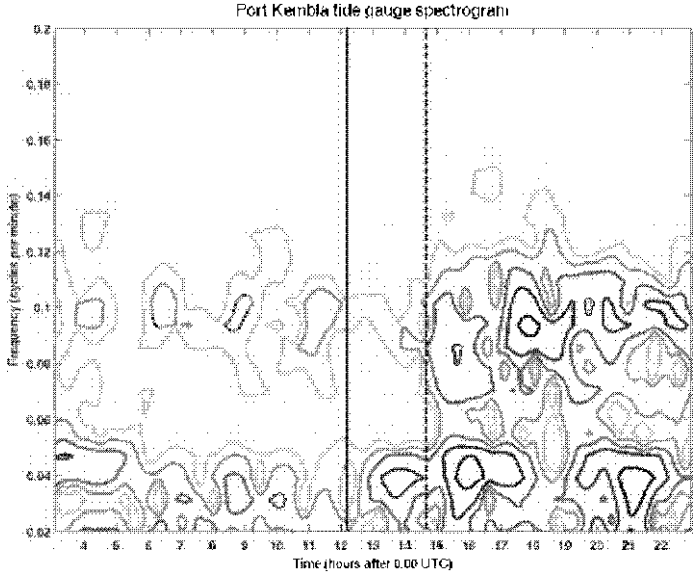

Fig. 3d. Spectrogram of tide gauge signal from Port Kembla, approximately 1750 km from the earthquake epicentre. The solid line indicates the time of the earthquake, and the dashed line indicates the tsunami arrival time as estimated by numerical modelling (time at which model signal first exceeds 1cm).

The tsunami also appears to have excited a resonance within Port Kembla, Australia. The tide gauge (maintained by NTF) shows a signal, with a maximum peak to peak amplitude of 170 mm, which persisted for several hours (Figure 3c). Spectrogram analysis of the tide-gauge record (Figure 3d) clearly demonstrates that the signal contains resonant frequencies of the harbour (indicated by the presence of these frequencies at lower amplitudes, before the tsunami arrival). The timing of the excitation of this resonance is approximately the same as that predicted by computer models of the tsunami (see below), making this the most likely source.

4.2.3 *Model and comparison*

A numerical model of the tsunami propagation was developed using the MOST computer software (Titov and Gonzalez, 1997). The initial conditions for the tsunami were a vertical deformation of the seabed, as deduced from fault parameters deduced from GPS measurements, as shown in Figure 1b. The computer model used bathymetry provided at 2 minute resolution from the ETOPO-2 database, covering the Tasman Sea area.

The tsunami wavefield was numerically propagated for 6 hours and 40 minutes from the time of the earthquake main shock. The model used is appropriate for estimating tsunami propagation over large distances; detailed modelling of run-up was not used, principally because of limitations in the bathymetry resolution close to shore. With this model we would expect to achieve good estimates of tsunami arrival times (Figure 4), but would not expect to capture detailed near-shore dynamics, such as the resonance behaviour within Jackson Bay and Port Kembla.

Comparison of the modelled arrival times with the spectrogram analyses of the Jackson Bay and Port Kembla tide gauges shows a good correspondence between the arrival time and marked changes in the tide-gauge spectrum (Figures 3b, 3d). In both cases this leads to increased confidence in the hypothesis that the seiching behaviour in these bays was initiated by the tsunami.

As the model does not accurately portray local bathymetry, the modelled signal is best considered as an estimate of the forcing of the local bay oscillations by the tsunami. It should be noted that in both cases the observed amplitude generally increases during the period when the modelled signal shows a significant amplitude and decreases thereafter (Figures 3a, 3c). This is further qualitative evidence for the idea of the tsunami acting as a driving source for the resonant oscillations of the bays. It also suggests that the tsunami was primarily generated by the mainshock rather than the M_L5.9 aftershock which occurred two hours later.

The amplitude of the modelled signal for Port Kembla is significantly smaller than the tide-gauge observations, some of this difference may be accounted for in terms of resonant amplification, but it may also be an indication that the model is underestimating the true wave heights.

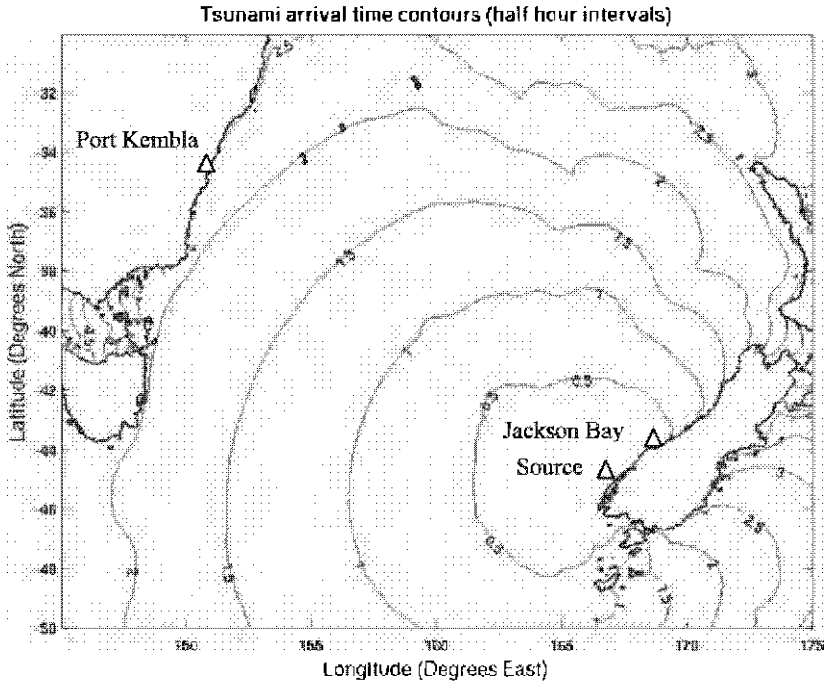

Fig. 4. Estimated tsunami arrival time as determined by numerical model. Contours are at intervals of 30 minutes and record the time between initial uplift and wave height exceeding 1 mm. The locations of Jackson Bay and Port Kembla are also shown.

5 Summary and Conclusions

The M_W7.2 Fiordland earthquake of 21 August 2003 generated shaking of intensity MM9 which caused extensive landsliding over a large area. Since Fiordland is largely uninhabited, there were few injuries and little property damage. Analysis of GPS movements and seismological data suggest that the earthquake rupture occurred on the interface between the Pacific and Australian Plates.

Evidence has been found for two tsunami generated in response to the earthquake. One tsunami was generated by a substantial rock slide into Charles Sound, this tsunami was confined to a small area, yet reached heights of 4-5 m, and caused damage to vegetation and a wharf.

The second tsunami was of relatively small amplitude, but is believed to have propagated widely around the Tasman Sea. Evidence for this tsunami is presented in the form of tide-gauge signals from Jackson Bay (200 km northeast from the source), and Port Kembla on the East coast of Australia (approximately 1650 km distant). Spectrogram analysis of these signals, and comparison with numerical models of tsunami propagation, lends credence to the interpretation that the observed water

height fluctuations were initiated by a tsunami generated by seafloor deformation following the mainshock of the Fiordland earthquake, and that this tsunami excited local resonances in the vicinity of the tide gauges.

Acknowledgements

The authors would like to thank Jose Borrero for his assistance in teaching us about tsunami modelling, and to NOAA for developing the MOST software. Thanks also to James Chittleborough at NTF for the tide gauge data.

References

Beavan, J., Matheson, D., Denys, P., Miller , C. (2003), Fault parameters of Fiordland MW 7.1 earthquake from dislocation modelling of GPS data. Geological Society of New Zealand Miscellaneous Publication 116A, p16.

Chittleborough, J. (2003). South Island, New Zealand, 21 August 2003. Tsunami Newsletter – International Tsunami Information Center, Volume XXXV, Number 5, p3.

Cox, S. C., Hancox, G. T., Turnbull, L. M., McGinity, P., O'Neill, T. (2003), Fiordland shaken and stirred The 22 August 2003 M7.1 Earthquake. Geological Society of New Zealand Miscellaneous Publication 116A, p 37.

DeMets, C., Gordon, R. G., Argus D. F., and Stein, S. (1994). Effect of recent revisions to the geomagnetic reversal time scale on estimates of current plate motions. Geophysical Research Letters, Vol 21, p2191-2194.

Hancox, G. T., Cox, S. C., Turnbull, L. M., and Crozier , M. J.(2003). Reconnaissance studies of landslides and other ground damage caused by the Mw7.2 Fiordland earthquake of 22 August 2003. Institute of Geological and Nuclear Sciences science report 2003/30.

Leonard, M. (2004). T phase perception: The August 2003, Mw 7.1, New Zealand earthquake felt in Sydney 1800 km away. Seismological Research Letters, in press.

Reyners, M., McGinty, P., Cox, S., Turnbull, L., O'Neill, T., Gledhill, K., Hancox, G., Beavan, J., Matheson, D., McVerry, G., Cousins, J., Zhao, J., Cowan, H., Caldwell, G., Bennie S. and the GeoNet team (2003). The Mw 7.2 Fiordland earthquake of August 21, 2003: background and preliminary results. Bulletin of the New Zealand Society for Earthquake Engineering, Vol. 36, No. 4, p233-248, December 2003.

Reyners, M. and Webb, T. (2002). Large earthquakes in Fiordland, New Zealand. New Zealand Journal of Geology and Geophysics, Vol 45, p.109-120.

Robinson, R., Webb, T., McGinty, P., Cousins, J. and Eberhart-Philips, D. (2003). The 2000 Thompson Sound earthquake. New Zealand Journal of Geology and Geophysics, Vol 46, (2003), p.331-341.

Titov, V. V. and Gonzalez, F. L. (1997). Implementation and testing of Method of Splitting Tsunami (MOST) model. NOAA Technical Memorandum ERL PMEL-112.

Walsh, R. (2003). 'Frightening' quake biggest in 35 years. The New Zealand Herald, 23 August 2003.

TIMING AND SCALE OF TSUNAMIS CAUSED BY THE 1994 RABAUL ERUPTION, EAST NEW BRITAIN, PAPUA NEW GUINEA

Y. NISHIMURA[1], M. NAKAGAWA[2], J. KUDUON[3] AND J. WUKAWA[3]

[1] *Institute of Seismology and Volcanology, Hokkaido University, Kita-10, Nishi-8, Kita-ku, Sapporo 060-0810, Japan.*
[2] *Graduate School of Science, Hokkaido University, Kita-10, Nishi-8, Kita-ku, Sapporo 060-0810, Japan.*
[3] *Rabaul Volcanological Observatory, P. O. Box 386, Rabaul, West New Britain, Papua New Guinea*

The timing and scale of the 1994 Rabaul tsunamis accompanying the eruption of Vulcan and Tavurvur volcanoes were estimated from the temporal and spatial distribution of tsunami deposits. The deposits are identified as sand layers or characteristic pumiceous sand layers (mixtures of pumice and sand) sandwiched by tephras from the two volcanoes. The tephras appear to play an important role in preserving the original structures of the tsunami deposits. According to chronological data from both tephra and tsunami deposits, the tsunamis were not generated by the first eruption of Vulcan volcano that occurred close to the coast, but major tsunamis were excited several times by larger pyroclastic flows and base surges during the climactic stage of the eruption. Tsunami run-up heights, estimated from distribution of the tsunami deposits, are about 8 m near Sulphur Creak and more than 3.5 m around western to southern shore of Matupit Island.
Key words: Tsunami, run-up, tsunami deposit, pumiceous sand, Rabaul, eruption.

1 Introduction

Volcanogenic tsunamis are rare events, but they have caused huge damage not only around volcanoes, but also much further away. The 1883 Krakatau eruption (Indonesia) and tsunami was one of the worst events in the world. More than 36,000 people were killed by this huge tsunami in Indonesia and the surrounding countries. As the tsunamigenic process in volcanic eruptions is complex, the source mechanism of the Krakatau tsunami is still in discussion (e.g., Latter, 1981; Nomanbhoy and Satake, 1995; Carey et al., 2001). Latter (1981) compiled historical volcanogenic tsunami events and listed possible volcanic phenomena as the tsunami source, including caldera collapse, entry of pyroclastic surges and flows into the ocean, underwater volcanic explosion, etc. He also pointed out that there are many volcano-related tsunami events whose original volcanic process is not clear.

K. Satake (ed.), Tsunamis: Case Studies and Recent Developments, 43-56.

The 1994 Rabaul eruption series is one of the most recent eruptive events that were accompanied by significant tsunamis. On September 19, 1994, Vulcan and Tavurvur volcanoes, located at the eastern and western side of Simpson Harbor, respectively (Figure 1), erupted almost at the same time. During the main phase of the Vulcan eruption, tsunamis were recorded on tide gage installed at the township of Rabaul. According to the eyewitness accounts and reported damage, the southwest and west coast of Matupit Island were hit numerous times by tsunami and some boathouses were swept away. In the south of Rabaul, the largest tsunami wave invaded 100-200 m inland. However, as most of the people had been evacuated from Rahaul during the eruption, there are few reliable descriptions of the timing and run-up heights of the tsunamis. A tsunami survey, which has been common after major tsunami events in recent years, has not been carried out. Thus, both tsunami heights around Rabaul and volcanic phenomena causing them are unknown.

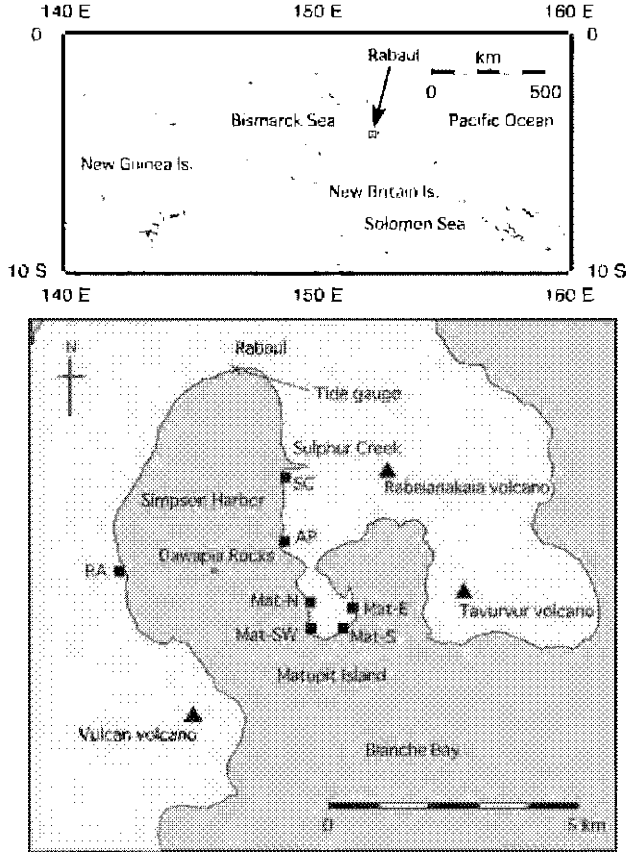

Fig. 1. Map showing Rabaul and Simpson Harbor. Closed triangles indicate active volcanoes. Closed boxes show observation sites for tsunami deposits (RA:Rapolo, SC:Sulphur Creek, AP:Old Rabaul airport).

Geological investigations of coastal sediments give us some important information of past tsunami events (Dawson and Shi, 2000). In some cases, a paleo-tsunami can be represented by a single sand layer. Elsewhere, tsunami deposits can be represented by complex layers containing abundant stratigraphic evidence for sediment reworking and redeposition. These onshore sandy layers used as geological evidence for tsunami are called tsunami deposits. Tsunami deposits have been studied in recent years for reconstruction of prehistoric tsunami recurrence and magnitude (e. g., Nanayama et al., 2003).

In this paper, we examined coastal sediments in Rabaul, and identified tsunami deposits associated with the 1994 Rabaul eruption. Detailed chronological studies of both tephra and tsunami deposits provided a rare opportunity to study the tsunami generating process during the eruption. The size of the tsunamis is also discussed based on spatial distribution of the tsunami deposits.

2 The 1994 Rabaul eruption and tsunamis

At 0615 (LT) on September 19th, 1994, Tavurvur volcano broke into eruption, and about one hour later Vulcan volcano began erupting. The eruptions were immediately preceded by vigorous seismicity; the maximum magnitude of the earthquake was 5.1 (Blong and McKee, 1995). Soon after its onset the eruption at Vulcan increased in strength and included a phase of strong Plinian activity. Pyroclastic flows reached as far as 2 km from the crater, and the eruption column rose up to 20 km.

Continuous sea level changes before and during the eruption period were registered by a tide gauge (Stevens A71) of The Rabaul Volcanological Observatory at Rabaul harbor (Figure 2). The first tsunami was observed associated with one of or both of two earthquakes of M5 occurred at 0251 (LT) on September 18th, 1994, a day before the eruption. Hypocenters of these earthquakes are estimated beneath Tavurvur volcano and Vulcan volcano, respectively (Blong and McKee, 1995). The first tsunami reached the tide gauge about 6 minutes after the earthquakes. The zero-peak amplitude of the tsunami is about 1 foot (30 cm), and the tsunami continued for several hours with a simple decaying amplitude.

The next tsunami phase was observed from 0743 on September 19th. At that time there were no large earthquakes, but Vulcan volcano had started to erupt at 0717. Tide gauge record shows that the zero-peak amplitude of the first wave was ca. 0.8 feet. Compared with the earthquake-generated-tsunami on the previous day, the amplitude did not decay simply, but continued more than 24 hours with a fluctuating amplitude. It suggests that the tsunamis were excited several times or continuously during the eruption.

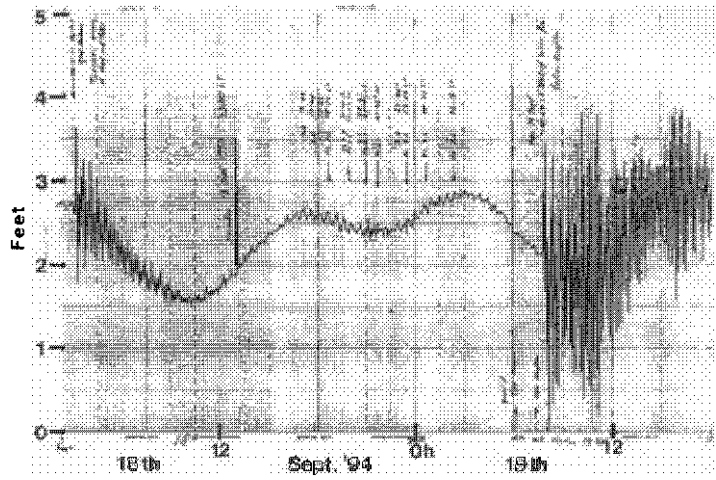

Fig. 2. Tide gauge record at Rabaul, registering two tsunamis. The tsunami that occurred on the morning of September 18th, 1994, was caused by earthquake, and that of September 19th was associated with the eruptive activity of Vulcan volcano. The tide gauge is operated by the Rabaul Volcanological Observatory.

Nishimura (1997) carried out numerical experiments for the 1994 Rabaul tsunami using simple source models and a bathymetric map of Simpson Harbor, and showed that tsunami generated from northern shore of the Vulcan volcano reached Rabaul ca. 5 min. after they were generated. The distribution pattern of tsunami heights along the coast of Simpson Harbor varies significantly with source duration and location. However, in most cases the largest tsunami heights are observed along the western shore of Matupit Island and tsunamis at the eastern side of the island are less than half the amplitude.

3 Tsunami deposits identified from Simpson Harbor

Huge amounts of pumice and ash were deposited from the 1994 eruptions of Vulcan and Tavurvur around Simpson Harbor (e. g. Blong and McKee, 1995). The thickness of the pyroclastic deposits from Vulcan is more than 20 m at sites near to the volcano, and fall deposits both from Vulcan and Tavurvur were piled up near Tavurvur and Matupit Island. This basic information on tephra distribution is helpful for identification of the tsunami deposits, as the tsunami occurred in the middle stage of eruptions.

Characteristic sandy layers, which were distinguished from primary eruptive deposits of 1994 eruption, were found in coastal sediment at six localities (Figure 1). Five of the sites are located on Matupit Island (Mat-S, Mat-SW, Mat-N) and between the eastern end of Rabaul town and the island (AP and CS). The other one is in Rapolo (RA), about 2 km north of Vulcan volcano.

The sandy layers are mainly composed of marine sand and volcanic pumice with flakes of coral, marine shell, wood branches and man-made plastic scraps, and are distinct from primary pumice and ash layers from the eruptions. The thickness of the layers is usually less than 10 cm. In most cases we traced the layers up to 100 m inland, and confirmed that they were sheet-like. Generally, the thickness of the sandy layer tends to decrease with the distance from the sea.

We regard these sandy layers as the 1994 tsunami deposits because the following features are commonly observed: (1) The distribution of the sandy layers is limited in coastal areas. (2) The thickness of the layers tends to decrease with the distance from the beach. (3) The layers contain beach sand and flakes of coral and shell of marine origin. (4) The layers are sandwiched or overlaid directly by tephras from the 1994 Vulcan and Tavurvur eruptions. (5) The weather was good and the sea was not rough during the eruption.

There are three possible origins of the pumice deposited onshore together with beach sand. One is drift pumice, which was ejected from Vulcan and filled Simpson Harbor during the whole eruption period. This can be carried up and deposited inland with beach materials by the tsunamis. As Carey et al. (2001) pointed out, layers composed of drift pumice will be distinguishable from those from primary pumice, by examining roundness of the pumice themselves and existence (or lack) of heavier lithic materials in the layer. The second origin is that tephra fell and was deposited in the surf zone before the tsunami inundation. This tephra could be carried up inland easily by the tsunamis. The other possible origin is primary pumice that was falling on land during the tsunami inundation. The pumice in the tsunami deposits is probably a result of all of these three origins. The possibility that the pumice was from an old eruption of Rabaul is low because there is no evidence for surface erosion by the tsunami and the 1937 tephra (the previous eruption deposit) is still found in the buried soil.

4 Lithofacies of tsunami deposits

The tsunami deposits are continuously distributed along the coasts changing their lithofacies with the distance from the beach and local topography. Representative depositional faces of the tsunami sand sheets at AP, south of the old Rabaul airport are shown in Figures 3, 4 and 5. At AP, we made pits at 10 m intervals along a line perpendicular to the shoreline. Columnar sections around AP are arranged in Figure 6.

Figures 3, 4 and 5 shows parts of the vertical sections of the pits 50 m, 60 m, and 100 m inland from the shore, respectively.

Figure 3 shows a pumiceous sand layer with the thickness of 6 cm. The upper and lower boundaries of the layer are not clear, and a weak laminated structure is seen. At AP 6, landward of a small mound, a single clear sandy layer is sandwiched by volcanic ash. There are few contamination of volcanic material in the layer (Figure 4). From AP7 to AP10, two or three sandy layers are deposited sandwiched volcanic tephra. At AP 10, materials in the uppermost sandy layer changed significantly: from sand-rich layer to a pile of pumice and wood branches (Figure 5).

Thus, the thickness and lithofacies of the tsunami sand sheets changed with distance from the sea and were also affected by local topography. These features might be interpreted as follows. At AP the tsunami inundated at least three times. The deposit here is complicated not only by run-up which may be responsible for the deposition, but also by an episode of sediment erosion. Successive tsunami waves may result in the erosion of pre-existing tsunami deposit. The pattern of tsunami sedimentation is additionally complicated by episode of backwash flow which is more powerful closer to the beach. These processes provide single complicated sandy layer from AP1 to AP5.

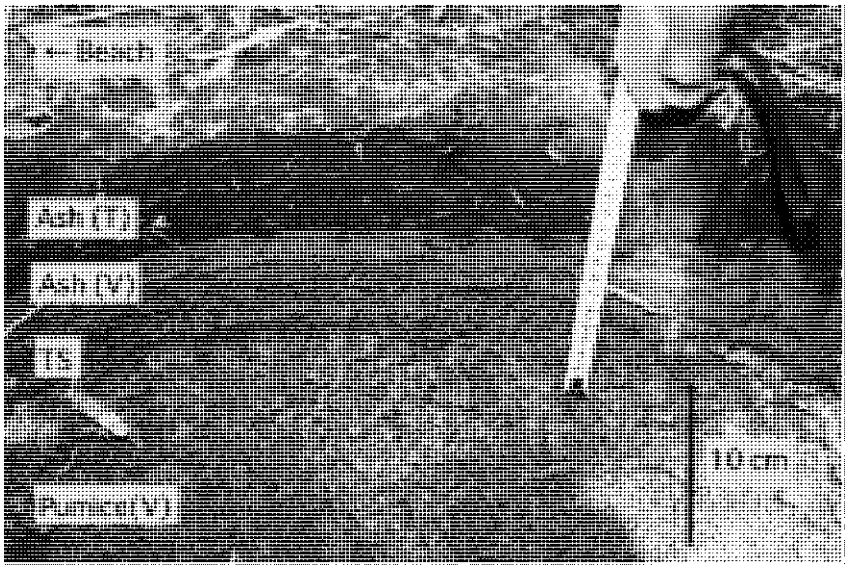

Fig. 3. Tsunami deposit sandwiched by volcanic tephra at AP. Distance from the beach to this pit is about 50 m. TS indicates the tsunami sand sheet. Thin-bedded alternation of sand and pumice layers is probably resulted by successive deposition, reworking and erosion processes by tsunami waves. (V) and (T) represent tephra from Vulcan and Tavurvur volcanoes, respectively.

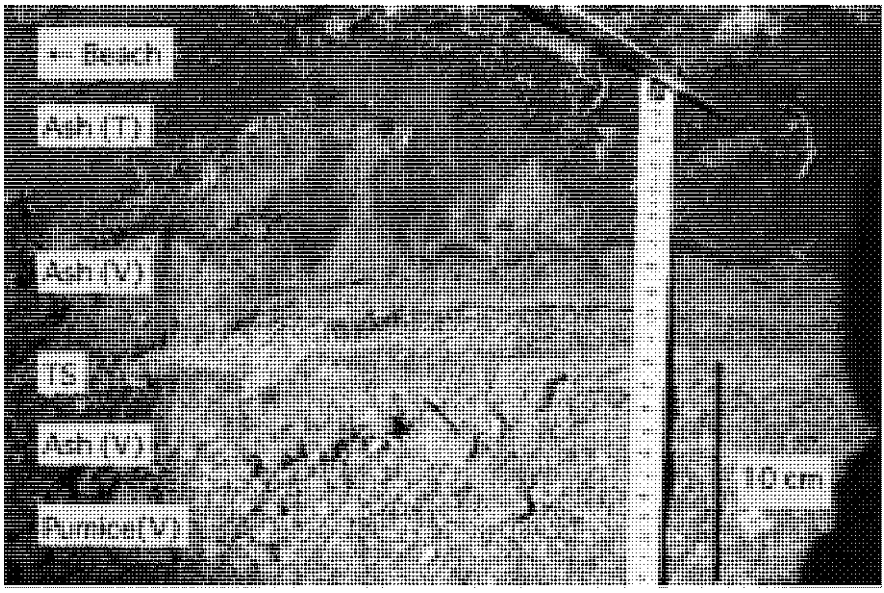

Fig. 4. Tsunami deposit sandwiched by volcanic tephra at AP. Distance from the beach to this pit is about 60 m. The thin sand horizon is tsunami deposit.

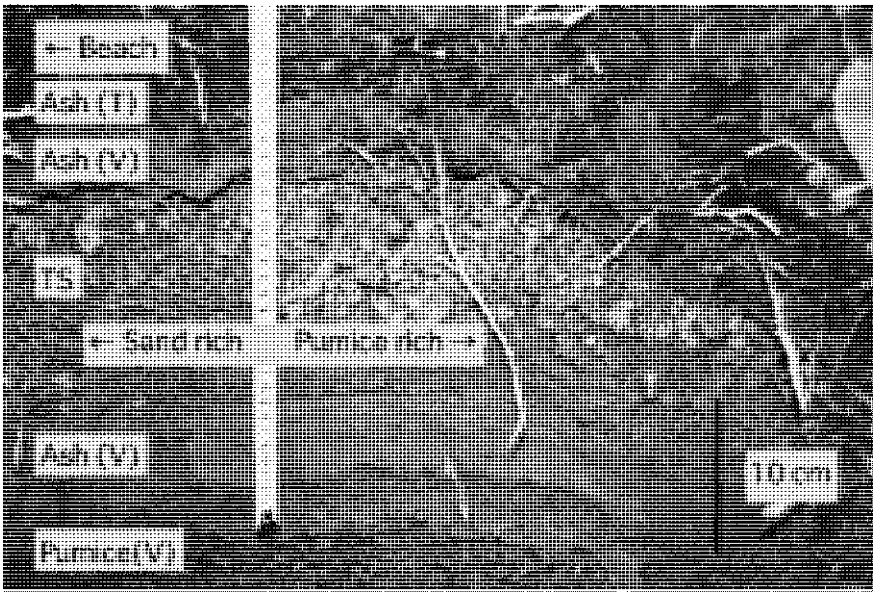

Fig. 5. Tsunami deposit sandwiched by volcanic tephra at AP. Distance from the beach to this pit is about 100 m. A pumice rich layer was deposited at the inland boundary of the tsunami inundation area, with a clear contrast of sand-rich and pumice-rich deposits in a layer.

Separation of light and heavy materials might have occurred as the tsunamis traveled inland over a small mound at AP6. Our interpretation is that pumice in the tsunami deposit was accumulated in the upper part of the layer while it was suspended in the water, and carried inland by advancing sea wave or backwashed. Thus, only relatively heavy sand particles were left and deposited (Figure 4).

It is known that debris composed of light materials such as dried branches or grasses are deposited along the upper boundary of a tsunami inundation area (Sato et al., 1995; Nishimura and Miyaji, 1995; Tanioka et al., 2004). In the case in Rabaul, pumice and wood branches were accumulated at the boundary. It is well displayed in Figure 5 that the components of a tsunami deposits changed from sand-rich to pumice-rich. Usually such weak geological evidence would be quickly disturbed and vanish if it were left on the surface. The covering of tephra might play an important role in preserving the original structures of the tsunami deposits.

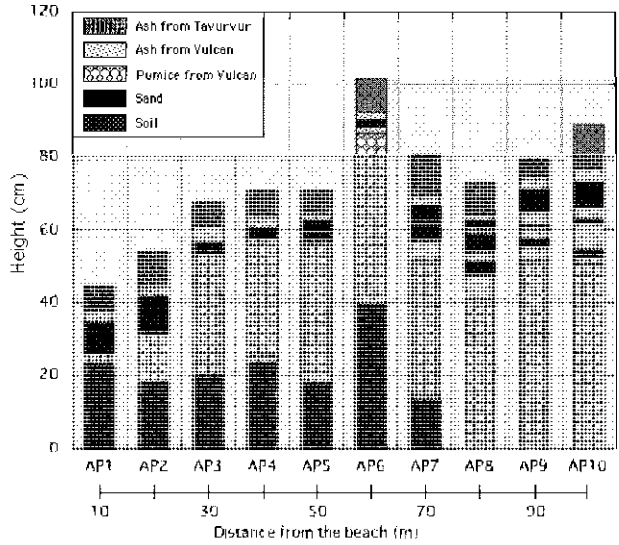

Fig. 6. Columnar sections along a profile perpendicular to the shore at AP. Section intervals are 10 m. At least three tsunami waves invaded inland up to 100 m.

5 Chronology of volcanic eruptions and tsunamis

According to eyewitness accounts and stratigraphic work on tephra, the eruption series is divided roughly into three stages: (1) magma-eruption with small pyroclastic flows at Vulcan on the morning of September 19 th, (2) climactic Plinian stage of Vulcan from morning to midday on September 19 th, (3) strong and continuous ash emission from Tavurvur during the night of September 19 th. (Blong and McKee, 1995; Nakagawa et al., in preparation).

Chronological data from tephra and the tsunami deposits enable us to study the timing of the tsunamis during the eruption series. Figure 7 shows representative columnar sections at seven localities near the beach. In the figure, only sections above the original surface before the 1994 eruption are displayed.

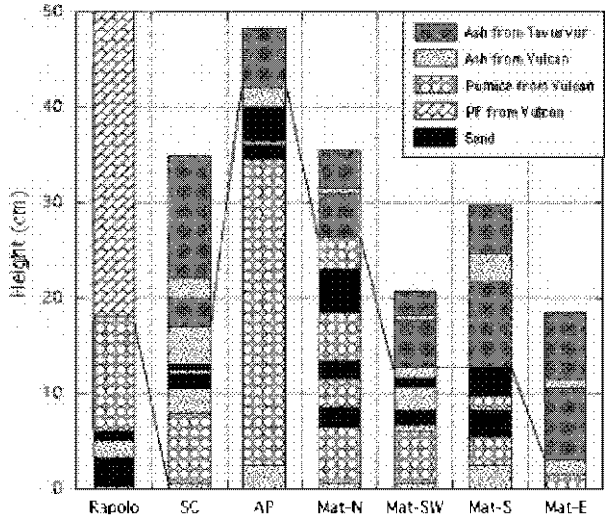

Fig. 7. Representative litho-stratigraphy of coastal sediment in Rabaul area. Localities are shown in Figure 1. At Rapolo (RA), two thin sand layers are recognized in the pyroclastic flow deposits from Vulcan's early stage eruption. On the other hand, sites from Sulphur Creek (SC) to Matupit Island, sandy layers exist in the main pumice and ash layer of the Vulcan eruption which means tsunamis occurred during the climactic stage of the Vulcan eruption.

At Rapolo, about 2 km north from Vulcan, two thin sand layers are recognized in the pyroclastic flow deposits from Vulcan's early stage eruption (stage 1). It suggests that at least two tsunami waves were excited during this stage. As the sand layer does not cover the original surface directly, it is inferred that the first break of the eruption (07:17, September 19th) did not excite tsunami though it started with an eruption close to the sea (McKee, personal communication). The fact that there are no sandy deposits corresponding to these tsunamis in Matupit Island, suggests that they were locally concentrated north of Vulcan volcano.

The eruption of Vulcan volcano was followed by its climactic stage, in which larger pyroclastic flows and base surges occurred continuously. As the ejected ash and pumice fell mainly in northern part of Vulcan, thick (more than 10 m) deposits covered Rapolo district. No sandy layers are recognized in the thick ash and pumice deposits near Vulcan.

Tsunami deposits are also found along the coast from the eastern end of Rabaul town to Matupit Island, where significant tsunami damage was reported. Stratigraphy in this area shows some common features (Figure 7). The original surface is covered by a thin white ash layer from Vulcan, which corresponds to the early eruptive stage of the volcano. The ash layer is overlaid by thicker pumice and ash deposits that correspond to the climactic stage of Vulcan. These are also overlaid by dark-brown ash from Tavurvur eruption in the night of September 19th, with the thickness of the Tavurvur ash increasing closer to Tavurvur volcano.

There are sandy layers in the main pumice and ash layer of the Vulcan eruption, and it means that tsunamis occurred during the climactic stage of the Vulcan eruption. The number of tsunami layers is not same for all localities, and the type of tephra sandwiching the sand layers is also different from site to site. We would like to explain these features as follows. The tsunamis were excited several times or continuously by larger pyroclastic flows and base surges during the climactic stage of the Vulcan eruption. The waves interfered with each other within the sub-closed bay, and some eventually excited higher waves that could far inland and produce a tsunami deposits. The type of tephra (ash or pumice) can easily be affected by local wind direction or eruption column heights, so, it is understandable that the same tsunami deposits can be sandwiched by different tephras at each locality.

6 Scale of the tsunamis

The size of the tsunamis is evaluated from run-up distance and height distribution. Tsunami deposits have been useful in estimating both run-up distances (e.g., Nanayama et al., 2003) and height distribution (e. g., Nishimura and Miyaji, 1995) for ancient tsunami events. Run-up distances and run-up heights at six sites are discussed here. At Rapolo, we traced the deposits at vertical sections along a gully formed by a large mudflow caused by heavy rain. For the other sites, we excavated small pits, less than 1 m deep, and traced the buried tsunami deposits inland with spacing of 10 m or 5 m. The boundary of the tsunami deposits was estimated by the presence of a sandy layer. The height was measured by leveling and horizontal distance was estimated by a tape measure. No tidal correction was made to the data because absolute tidal variation around Rabaul is less than 0.5 m and exact time of the tsunami occurrence could not be estimated.

The results are summarized in Figure 8. The maximum run-up heights in the figure should be interpreted as a minimum estimate as it has been shown in several studies that the highest altitudes reached by individual tsunami deposits cannot be used as indicative of the upper limit of run-up reached by that tsunami (e.g., Dawson and Shi 2000; Nishimura and Miyaji, 1995).

The highest run-up of about 8 m was measured at the site located between Sulphur Creek and the old Rabaul airport. Tsunami deposits were found on the gentle slope of the southern side, which was screened by a steep slope to a landing strip. This local valley-like topography might increase the run-up height significantly. In the case of the 1993 Okushiri tsunami in Hokkaido, Japan, the highest run-up of 31.7 m was observed at the bottom of a small valley at Monai (Hokkaido Tsunami Survey Group, 1993). This was regarded as local topographic effect because almost all run-up heights around this site were less than 20 m.

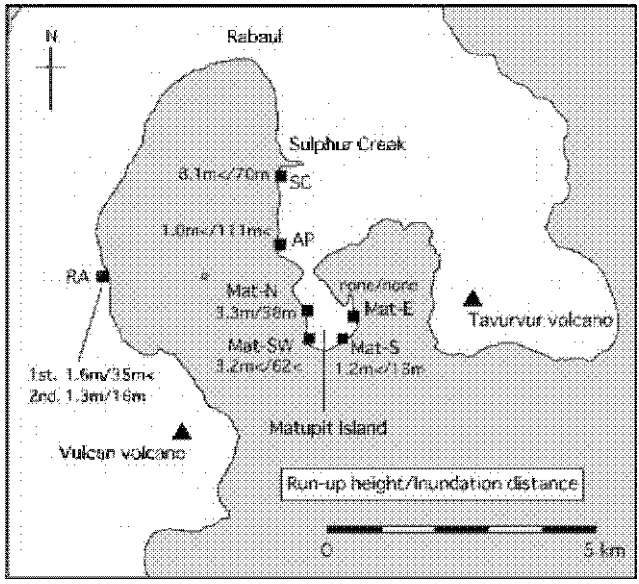

Fig. 8. Maximum run-up heights and inundation distances of the 1994 Rabaul tsunamis as revealed by the tsunami deposit distribution.

Tsunami run-up height of 3.5 m or more was traced at northern part of Matupit Island (Mat-N). The height was well constrained as the low invaded area is surrounded by about 10 m high beach terrace. The maximum run-ups could not be measured where tsunami invaded in the flat area. Based on the run-up distances, tsunami run-up heights along western to southern shore of the Matupit Island are estimated to be the similar size to that of Mat-N. At Rapolo district, run-up heights and inundation distances for two waves are estimated individually, and the first wave was a little larger than the second one.

There is no tsunami evidence along the eastern shore of Matupit Island. As tephra fell immediately after the tsunami and protected the deposit from erosion, we suppose that the tsunami heights along the east shore of Matupit Island was very low. This height distribution pattern is consistent with eyewitness accounts and simple numerical simulation results (Nishimura, 1997).

Wave heights and inundation distances of the tsunamis along the western to southern shore of Matupit Island estimated by the tsunami deposits, are consistent with the other evidences such as eyewitness accounts, reported damage and numerical simulation results. However, for more precise discussion, effect of the vertical deformation of the land should be considered. Just before the eruption began, significant uplift was observed inside the Rabaul caldera. Blong and McKee (1995) reported the ocean bottom was visible both near Vulcan volcano and around Matupit Island before the eruption. The sea level seemed to be back normal after the eruption stopped. Thus, if the uplift was localized at Matupit Island and the amount of uplift was a few meters, then the tsunami heights in Figure 8 are underestimated the same amount and it will make a large difference to the results of this study.

7 Discussion

As the tsunami deposits were overlaid by tephras, the original feature of the deposits has been well preserved. Tsunami deposits investigated here are unique sediment layers containing both drift (reworking) and fall (primary) pumice from the volcano. Detailed study on such pumice is underway.

The following four major volcanogenic tsunami deposits have been reported from the world.

McCoy and Heiken (2000) found a tsunami layer in the tephra stratigraphy on eastern Thera, and suggested that it caused by the 3600-year B. P. (the Late Bronze Age) eruption of Thera (Santorini), Greece.

Waythomas and Neal (1998) found pumiceous sand layers and regard them as volcanogenic-tsunami deposits caused by the 3500-year B.P. Aniakchak eruption. They suggest that these special pumiceous sand layers are formed by tsunamis that carried up floating pumice inland. They also suggested the possibility that the similar deposition process should occur in the 1994 Rabaul eruption.

Carey et al. (2001) found pumiceous sand layers and regard them as volcanogenic-tsunami associated with the 1883 Krakatau eruption, Indonesia. They showed that layers composed by drift pumice are distinguishable from those from primary pumice, by examining roundness of the pumice themselves and existence (or lack) of heavier lithic materials in the layer.

Nishimura and Miyaji (1995) studied tsunami deposit associated with the 1640 Hokkaido Komagatake eruption. They indicate that the tsunami deposit covered the original surface and was overlaid directly by pumice and ash from the volcano. It means that the tsunami was excited by the first summit collapse.

Rabaul has experienced similar volcanic eruptions in the past. At least the previous eruption in 1937 excited tsunamis (e. g., Johnson and Threlfal, 1985), and Arculus and Johnson (1981) translated old document that indicated the 1937 tsunami behavior.

They stated that "the water receded several times over 50 yards from the shoreline" and, "the waters of the harbor at Rabaul rose and fell continuously, taking some four to five minutes between the least and greatest depth". The 1937 tsunami deposits also gave important information on the timing and scale of the volcanic eruption and related tsunami, though it was covered by a thick tephra.

8 Conclusion

In order to investigate the time and size of the 1994 Rabaul tsunamis, we conducted brief surveys of the 1994 tsunami deposits. Tsunami deposits consist mainly of beach sand that was carried up by a tsunami and deposited inland. Around Rabaul, the tsunami deposits are identified as sand layers or characteristic pumiceous sand (mixes pumice and sand) layers sandwiched by tephras from both Vulcan and Tavurvur volcanoes.

According to the chronological studies of both tephra and tsunami deposits, it inferred that the tsunami was not generated by the first small eruption from Vulcan volcano though it occurred close to the sea. The tsunamis were excited several times or continuously by larger pyroclastic flows and base surges during the later climactic stage of the eruption. Tsunami run-up heights estimated from distribution of the tsunami deposits are about 8 m at Sulphur Creek and more than 3.5 m around western to southern shore of the Matupit Island. These are consistent with the other evidences such as eyewitness accounts, reported damages and numerical simulation results.

Acknowledgements

We thank Wally Johnson, Ben Talai, Chris McKee, Patrice de Saint Ours, Ima Itikarai, Steve Saunders and Herman Patia for fruitful discussion on the 1994 Rabaul eruption and tsunamis, two anonymous reviewers for useful comments and suggestions, and Steven Sherburn for revising the manuscript. This research was partially supported by the Ministry of Education, Science, Sports and Culture, Grant-in-Aid for Scientific Research (B), No.13573002, 2001-2003.

References

Arculus, A. and Johnson, R. W., 1981, 1937 Rabaul eruptions, Papua New Guinea: Translations of contemporary accounts by German missionaries. Bur. Mineral. Res. Geol. Geophys., Australia, Rep. 229, BMR Microform MF 158, 78pp.

Blong, R. J. and McKee, C. O., 1995, "The Rabaul eruption 1994: Destruction of a town". Natural Hazards Research Center, Macquarie Univ., 52pp.

Carey, S., Morelli, D., Sigurdsson, H. and Bronto, S., 2001, Tsunami deposits from major explosive eruptions: An example from the 1883 eruption of Krakatau. Geology, 29, 347-350.

Dawson, A., G. and Shi, S., 2000, Tsunami deposits. Pure and Applied Geophysics, 157, 875-897.

Hokkaido Tsunami Survey Group, 1993, Tsunami devastates Japanese coastal regions. EOS Trans. AGU, 74, 417-432.

Johnson, R. W. and Threlfall, N. A., 1985, "Volcano Town - the 1937-43 Rabaul Eruptions". Bathurst, N.S.W., Robert Brown and Assoc., 151pp.

Latter, J. H., 1981, Tsunamis of volcanic origin: summary of causes, with particular reference to Krakatau, 1883. Bulletin of Volcanology, 44, 467-490.

McCoy, F. W. and Heiken, G., 2000, Tsunami generated by the late Bronze age eruption of Thera (Santrini), Greece., Pure and Applied Geophysics., 157, 1227-1256.

Nanayama, F., K. Satake, R. Furukawa, K. Shimokawa, B. F. Atwater, K. Shigeno and S. Yamaki, 2003, Unusually large earthquakes inferred from tsunami deposits along the Kuril trench, Nature, 424, 660-663.

Nishimura, Y. and Miyaji, N., 1995, Tsunami deposits from the 1993 southwest Hokkaido earthquake and the 1640 Hokkaido Komagatake eruption, northern Japan, Pure and Applied geophysics, 144, 719-733.

Nishimura, Y., 1997, Evaluation of phreatomagmatic eruptions by means of tsunamis of volcanic origin. Proceedings of the International Seminar on Vapor Explosions and Explosive Eruptions, 231-236.

Nishimura, Y., Tanioka, Y. and Hirakawa, K., 2004, Beachside trace for moderate tsunami run-up: example from the 2003 Tokachi-oki Tsunami. Submitted to Zishin.(Jour. Seis. Soc. Japan), in Japanese with English abstract.

Nomanbhoy, N. and K. Satake, 1995, Generation mechanism of tsunamis from the 1883 Krakatau eruption. Geophys. Res. Lett., 22, 509-512.

Sato, H., Shimamoto, T., Tsutsumi, A. and Kawamoto, E., 1995, Onshore tsunami deoisits caused by the 1993 southwest Hokkaido and 1983 Japan Sea earthquake. Pure and Applied Geophysics, 144, 693-717.

Tanioka, Y., Nishimura, Y., Hirakawa, K., Imamura, F., Abe, I., Abe, Y., Shindou, K., Matsutomi, H., Takahashi, T., Imai, K., Jin, S., Onuma, Y., Murakami, T., Nagata, Y., Suzuka, A., Harada, K., Namegaya Y., Hasegawa, Y., Hayashi, Y., Nanayama, F., Kamataki, T., Kawata, K., Fukasawa, F., Koshimura, S., Hada, Y., Azumai, Y. and Hirata, K., 2004, Tsunami run-up heights of the 2003 Tokachi-oki earthquake, Earth Planets Space, 56, 359-365.

Waythomas, C. and Neal, C., 1998, Tsunami generation by pyroclastic flow during the 3500-year B. P. caldera-forming eruption of Aniakchak volcano, Alaska. Bulletin of Volcanology., 60, 110-124.

ANALYSIS OF TIDE-GAUGE RECORDS OF THE 1883 KRAKATAU TSUNAMI

E. PELINOVSKY[1], B. H. CHOI[2], A. STROMKOV[1], I. DIDENKULOVA[1] AND H.-S. KIM[2]

[1] *Laboratory of Hydrophysics and Nonlinear Acoustics, Institute of Applied Physics, 46 Uljanov Street, 603950, Nizhny Novgorod, Russia, enpeli@hydro.appl.sci-nnov.ru*
[2] *Department of Civil and Environmental Engineering, Sungkyunkwan University, Suwon, 440-746, Korea, bhchoi@yurim.skku.ac.kr*

The 1883 Krakatau volcanic eruption has generated giant tsunami waves reached heights of 40 m above sea level. Sea level oscillations related with this event have been reported in the Indian, Atlantic and Pacific Oceans. Main goal of this study is to analyze all available tide-gauge records (35) of this event. They are digitized with time step 2 min and processed. First of all, the tidal components are calculated and eliminated from the records. Filtered tide-gauge records are used to re-determine the observed tsunami characteristics (positive and negative amplitudes, wave heights). The results of given analysis are compared with the results of the direct numerical simulation of the tsunami wave propagation in the framework of the linear shallow-water theory using the ETOPO2 bathymetry.
Key words: Tsunami, Krakatau volcanic eruption, tide-gauge records, numerical simulation.

1 Introduction

The eruption of Krakatau volcano, situated in the Sunda Strait (Figure 1) occurred in August 27, 1883 has generated a very devastating tsunami (Murty, 1977; Simkin and Fiske, 1983; Bryant, 2001). The blast, at 9:58 (local time) was largest from the series of the four main explosions during this day (Simkin and Fiske, 1983; Bryant, 2001). Approximately 10 km^3 of solid rock was blown out of the volcano and about 20 km^3 of pyroclastic deposits spread out over 300 km^2 to an average depth of 40 m (Bryant, 2001). A caldera 6 km in diameter and 270 m deep was formed where the central island had once stood (Bryant, 2001). This blast was the largest sound ever heard in recorded history, being heard up to 4,800 km away (Symons, 1888; Simkin and Fiske, 1983; Bryant, 2001). The atmospheric shock wave traveled around the world seven times (Symons, 1888; Simkin and Fiske, 1983; Bryant, 2001). Barometers in Europe and the United States measured significant oscillations in pressure over nine days following the blast (Symons, 1888; Simkin and Fiske, 1983; Bryant, 2001). The total

K. Satake (ed.), Tsunamis: Case Studies and Recent Developments, 57-78.

energy released by this eruption was equivalent to 200 megatons atomic bomb (8.4×10^{17} joules) (Bryant, 2001). It devastated the adjacent coastline of Java and Sumatra with a maximum runup height of 42 m (Merak, see Figure 1), and penetrated 5 km inland over low-lying areas (Bryant, 2001). At least 36,000 people were killed, mostly by the sea waves, and 300 villages were destroyed (Bryant, 2001). Sea surface oscillations have been recorded worldwide in the Indian, Pacific and Atlantic Oceans (Symons, 1888; Simkin and Fiske, 1983). Various descriptions of tsunami wave manifestation can be found in Symons (1888), Murty (1977), Simkin and Fiske (1983), Bryant (2001) and Choi et al. (2003).

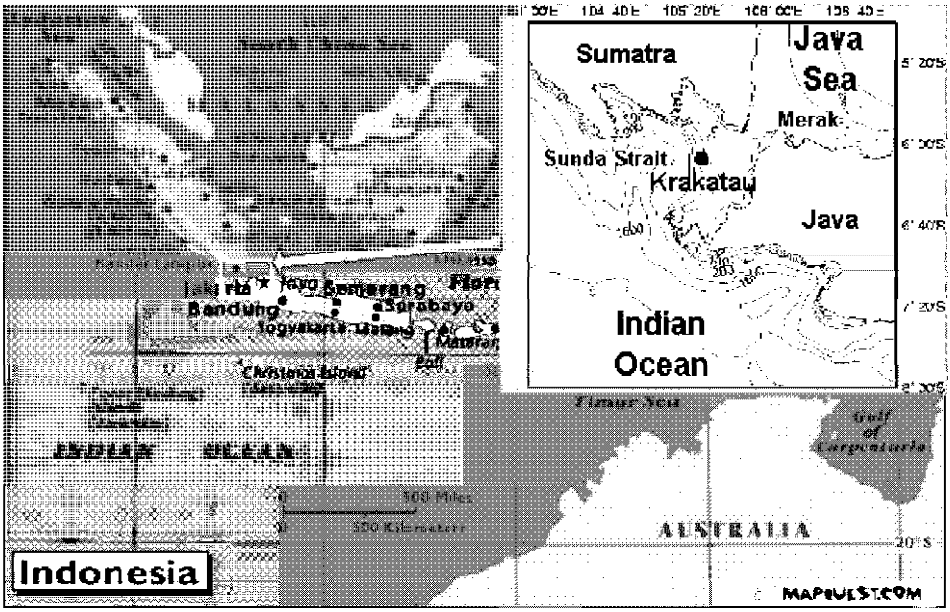

Fig. 1. Location of the Krakatau Island.

Original data of tsunami observations in Indonesia and in the World were collected in Verbeek (1885) and Symons (1888), and then reproduced in part by Murty (1977), Simkin and Fiske (1983) and Bryant (2001). The rough estimates of the tsunami travel time based on the simplified long wave theory (shortest distance from source, constant mean water depth) allow selecting the tide-gauge records of the Krakatau tsunami in the World. In many places the sea level disturbances were weak, and according to Simkin and Fiske (1983) "no precise or close comparison between various tidal diagrams can be made, and this doubt of the identification of any particular wave at different places, causes much uncertainty in the result, as far as it relates to the speed of waves". The main disagreement was obtained with tide-gauge records from American continent. Recently, Choi et al. (2003) recalculated the tsunami travel time using detail bathymetry ETOPO2 dataset in the framework of the ray tracing model on

the rotated Earth and confirmed the disagreement in observed and calculated values of the tsunami travel time for these locations. The disturbances on the tide gauges on the American continent appear earlier than they should be according to the ray theory, sometimes as much as 10 hrs. The time of their appearance coincides roughly with the travel time of the airwaves (barometric perturbations due to volcano eruption in the atmosphere), and such disturbances perhaps were generated by airwaves, see for instance, Ewing and Press (1955), Press and Harkrider (1966) and Garrett (1976). The sea disturbances in New Zealand appeared one day later than expected, and they perhaps have another physical origin (Simkin and Fiske, 1983). Bryant (2001) mentioned the similar disturbances observed at the same time in the Lake Taupo, and, therefore, such waves could not have been caused by tsunami from Krakatau. Data of tide gauges and witness reports in the Indian Ocean correlate with the expected tsunami travel time (Symons, 1888; Murty, 1977; Simkin and Fiske, 1983; Choi et al., 2003). Sea disturbances in the Atlantic Ocean are very weak, and the time of disturbance appearance in Le Havre (France) given by Symons (1888), Murty (1977) and Simkin and Fiske (1983) correlates with an expected time (Choi et al., 2003).

Numerical simulations of the tsunami propagation from the Krakatau volcano eruption have been performed by Yokoyama (1981), Nakamura (1984), Kawamata et al. (1992), Nomanbhoy and Satake (1995) and Choi et al. (2003). In particular, Nakamura (1984) simulated the tsunami wave propagation in the adjacent part of the Indian Ocean using the tsunami source as the deep depression modeled the caldera formation due to volcano eruption. The comparison with the observed data leads to the estimated trough in the equivalent tsunami source in 700 m. Choi et al. (2003) also used this mechanism considering the equivalent source with dimensions 7.2×7.2 km^2 with the negative displacement 222 m providing the observed volume 11.5 km^3. Computed tsunami records are used for comparison of the tsunami travel time and wave amplitude in the World. It was shown that computed data are in reasonable agreement with observations of tsunami in the Indian Ocean, mainly in tsunami travel time. Based on the numerical simulation of the near field, Nomanbhoy and Satake (1995) concluded that the submarine explosion model as the source of the largest tsunami is favored.

The main goal of this paper is to analyze the tide-gauge records of the 1883 Krakatau tsunami given in the report of the Royal Society (Symons, 1888). All tide-gauge records are digitized with a time step of 2 min and filtered from the tidal component. They are used to re-determine observed tsunami characteristics (positive and negative amplitudes, height, travel time). The results of given analysis are compared with the results of the direct numerical simulation of the tsunami wave propagation in the framework of the linear shallow-water theory using the ETOPO2 bathymetry.

2 Processing and Computing

The original tide-gauge records of the Krakatau tsunami (totally, 35) are copied in Symons (1888). Many of them were never reproduced in the tsunami literature. The locations of the tide gauges are shown in Figure 2. We should note that original records contain various difficulties for analysis. The grid of these records is non-uniform. The duration of the records is rather small – it contains only a few tide periods. Visible characteristic tsunami periods on tide-gauge records are about 1-2 hr so this value is close to high tide harmonics. And at last the quality of the records is rather poor. Some of them have been enlarged three times by photography. All records contained in this book are digitized with a time step of 2 min. At the first stage the tidal component in each of the records is selected using the Godin-type filter, which consists of three consecutive running-mean filters with windows 100, 100 and 105 min, as it is recommended by William and Thomson (1998). After that, the selected tide components are subtracted from the initial records. Digitized original and filtered records can be downloaded from our website (Pelinovsky et al, 2004). The residual series as well as original records are analyzed to re-examine the observed tsunami characteristics. Some "disturbances" on the filtered records are due to the high-frequency tide components that cannot be filtered out and should not be interpreted as tsunami related. It concerns also those locations, which record duration contains only a few tide periods. That is the course we use original records for analyses as well as filtered from the tides.

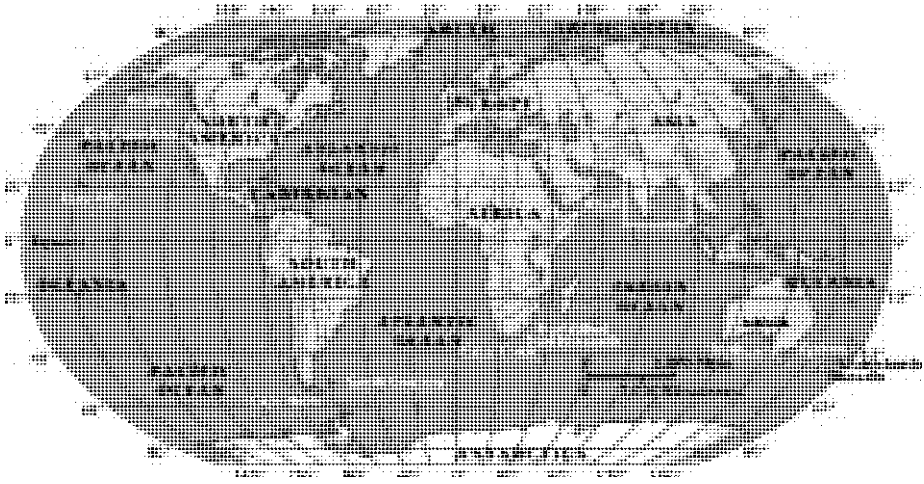

Fig. 2. Locations of the tide-gauge registration of the Krakatau tsunami (segments 1 and 2 are given below).

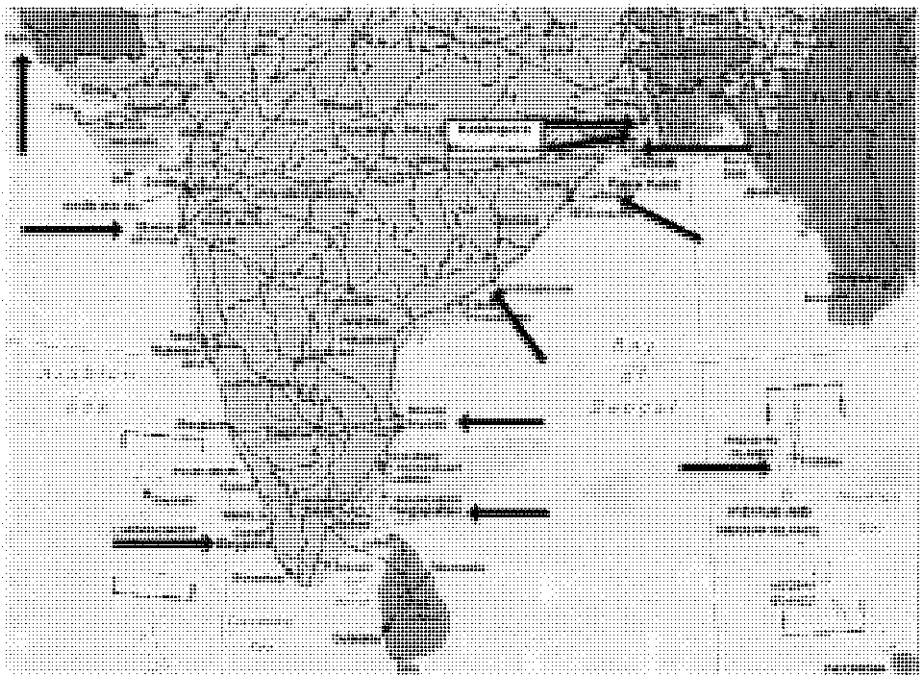

Segment 1

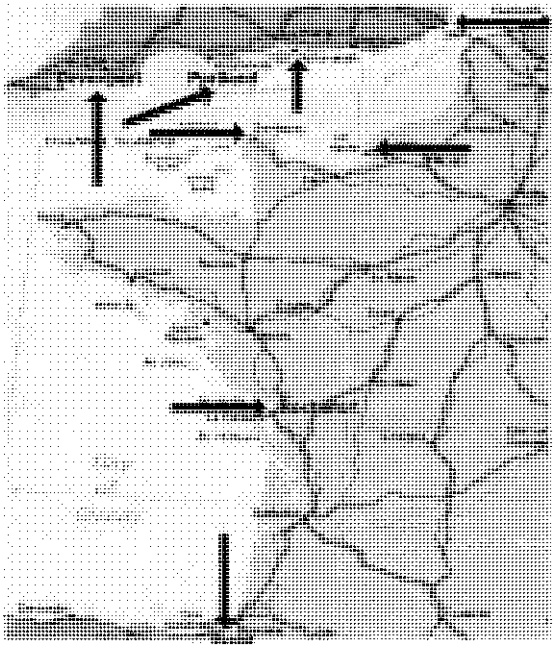

Segment 2

Fig. 2. Locations of the tide-gauge registration of the Krakatau tsunami – continued.

Calculation of the tsunami travel time for the tide-gauge locations is re-performed in the framework of the ray tracing method (Choi et al., 2003). Ray tracing equations are:

$$\frac{d\theta}{dt}=\frac{\cos\zeta}{nR},\quad \frac{d\varphi}{dt}=\frac{\sin\zeta}{R\sin\theta},\quad \frac{d\zeta}{dt}=-\frac{\sin\zeta}{n^2R}\frac{\partial n}{\partial\theta}+\frac{\cos\zeta}{n^2R\sin\theta}\frac{\partial n}{\partial\varphi}-\frac{\sin\zeta\cot\theta}{nR}, \qquad (1)$$

where and are latitude and longitude of the ray, $n = (gh)^{-1/2}$ is the slowness, g is the gravity acceleration, $h(\theta, \varphi)$ is the water depth, R is the radius of the earth, and ζ is the ray direction measured counter-clockwise from the south. Details of the numerical integration are given in Choi et al. (2003). In these simulations we use classical assumptions of ray methods: wave length is larger than the local ocean depth and smaller than large-scale bottom inhomogeneities. The code (Choi et al., 2003) calculates the first wave arrivals only. The limitation of the ray tracing method is discussed in paper by Satake (1988).

The location of the source in those numerical simulations almost coincides with the location of the Krakatau volcano: its coordinates are 6° 10′S, 105° 10′E, and depth in the source is 400 m. The number of rays is 3,600 and they are initially distributed uniformly. For correct calculation of the travel time some additional rays were used. The bathymetry is taken from the 2-min ETOPO2 dataset (Smith and Sandwell, 1997).

This paper presents the simulations for the greater number of locations than in Choi et al. (2003). Geographical positions of 35 locations, mentioned in Symons (1888) are found. The simulations of the arrival times for 30 of them are done.

Results of computing of the tsunami pathways are shown in Figure 3. Tsunami waves affect a whole basin of the Indian Ocean, and also they pass into the Pacific and Atlantic Oceans with reducing energy. The computed travel times for the tide-gauge locations are given in Table 1 (column 2) and they used to estimate the tsunami arrival on the tide-gauge records (column 3 in Table 1).

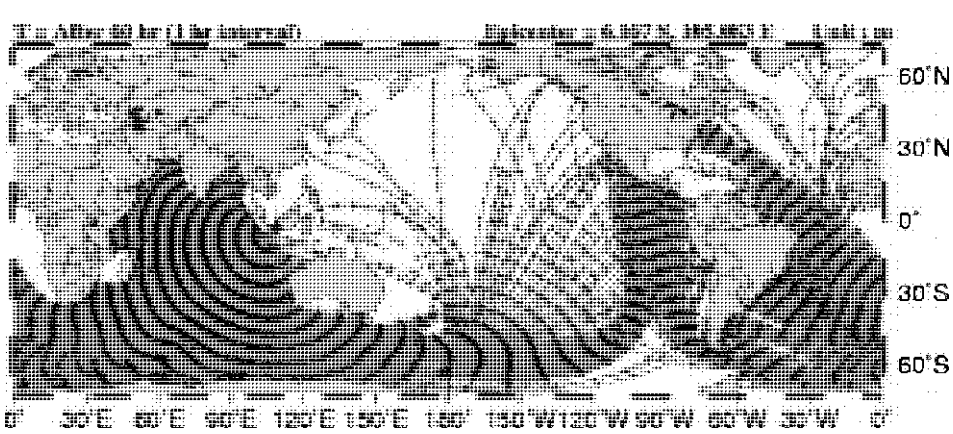

Fig. 3. Computed Krakatau tsunami travel time chart.

Table 1. Estimated travel time and observed maximal tsunami wave heights.

Points	Estimated travel time, hr:min	Estimated local time of tsunami appearance	Positive amplitude (cm)	Negative amplitude (cm)	Height (cm)
Jakarta	0:10	10:10	190 (100)	325 (90)	515 (190)
Ujong Pangka	—	—	17	16	33
Ujong Sourabaya (Surabaya)	—	—	18	14	32
Karang Kleta (Surabaya)	—	—	22	13	35
Port Blair	3:20	11:50	13	16	29
Nagapattinam	3:50	12:20	28	25	53
Chennai	4:00	12:30	9	7	16
Vishakhapatnam	4:40	13:10	15	12	27
False Point	5:10	13:40	27	27	54
Dublat	5:20	13:50	31	23	54
Diamond Harbour	—	—	29	29	58
Kidderpore	—	—	17	30	47
Beypore	4:30	13:00	36	29	65
Mumbai	6:50	15:20	16	20	36
Karachi	8:00	15:00	30	28	58
Aden	9:20	15:20	21	16	37
Port Alfred	11:00	16:00	52	42	94
Port Elizabeth	11:20	16:20	81	77	158
Cape Town	12:10	16:10	32	32	64
Socoa	31:00	11:00 (28/08)	15	14	29
Rochefort	31:00	11:00 (28/08)	27	53	80
Cherbourg	31:00	11:00 (28/08)	13	18	31
Le Havre	31:20	11:20 (28/08)	31	24	55
Plymouth	30:50	9:50 (28/08)	18	30	48
Portland	28:50	7:50 (28/08)	9	14	23
Adelaide	6:50	14:20	12	18	30
Melbourne	8:10	21:10	7	7	14
Sydney	7:40	20:40	14	10	24
Dunedin, Lyttelton Harbour	10:20	1:20 (28/08)	62	68	130
South Georgia	17:00	18:00	22	25	47
Cape Horn	17:40	15:40	21	16	37
Colon Panama	27:20	1:20 (28/08)	20	20	40
Honolulu	22:20	15:20	13	14	27
Kodiak	27:40	21:40	19	22	41
San Francisco	26:10	21:10	15	20	35

3 Analysis of the tide-gauge records

First of all, the near-field records in Indonesia will be discussed. There are four points of tsunami registrations on the north and east coasts of Java: Jakarta (Tanjong Priok at Batavia), Surabaya (Ujong Pangka, Ujong Sourabaya and Karang Kleta localized in the strait of Surabaya); they are shown in Figure 1. The original tide-gauge records and filtered from a tide are presented in Figure 4 (time is a local time in all figures). It is important to mention that tsunami record at Jakarta has "cut-off" of large waves and we use two curves for Jakarta: the original and the smoothed curve as described in Symons (1888). Tsunami at Jakarta is very clearly visible, and at least, three first waves have height exceeded 1 m. Tsunami arrives when water is rising due to tide. The characteristic period of the first wave is 45 min. Nomanbhoy and Satake (1995) simulating the near field tsunami field have shown that observed tsunami record at Jakarta can he explained if the submarine explosion model is applied. Ujong Pangka, Ujong Sourabaya and Karang Kleta (Surabaya) are about 360 miles east of Jakarta. The Ujong Pangka tide-gauge record demonstrates sea disturbances at the 27th August very clearly. But Ujong Sourabaya and Karang Kleta records show sea level disturbances at the beginning of 28th August. The sea disturbances have come to these two locations too late so we suppose that they are related with another origin.

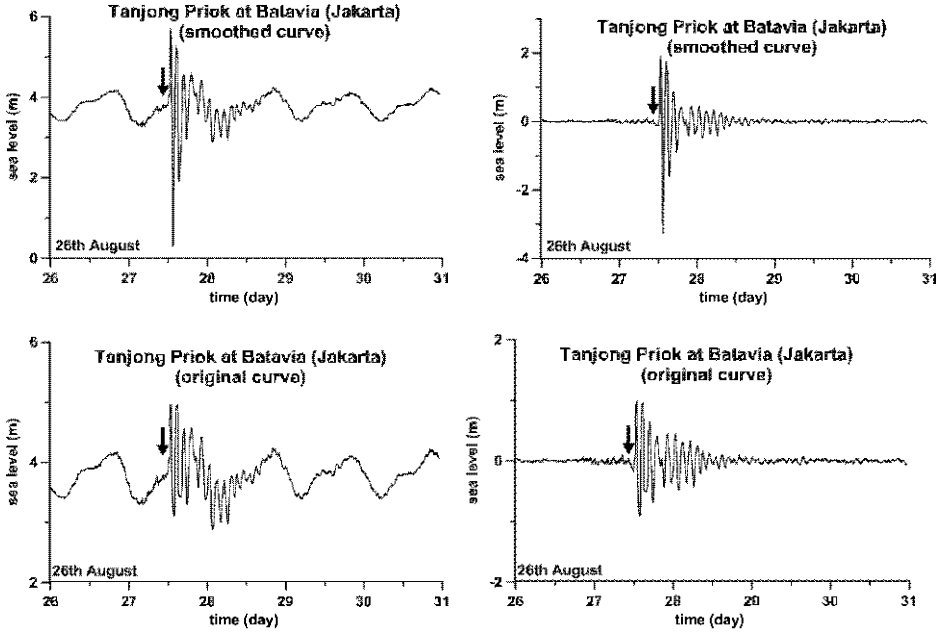

Fig. 4. Tsunami records in Indonesia (left – original data, right – filtered from tide, arrows indicate local time of tsunami arrival estimated by the ray tracing method).

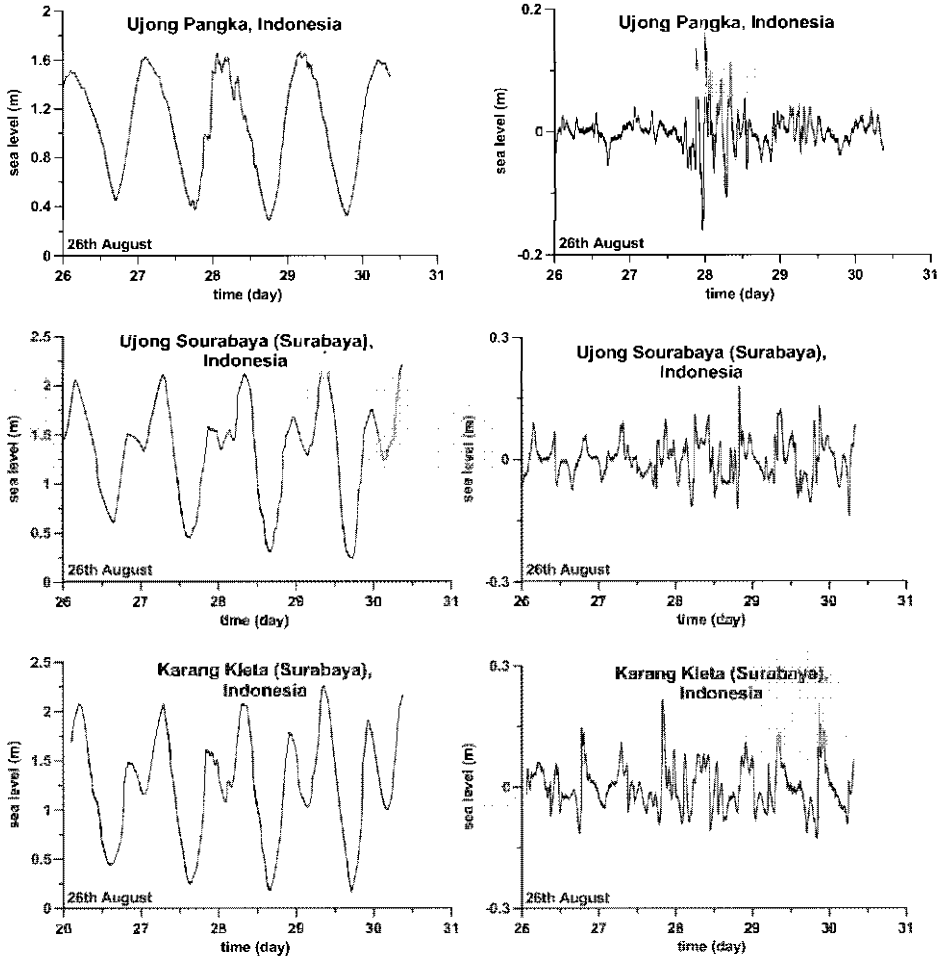

Fig. 4. Tsunami records in Indonesia (left – original data, right – filtered from tide) – continued.

Several tide diagrams in India and Pakistan show the Krakatau tsunami very clearly. The points of registration are India: Port Blair at Andaman Islands; Nagapattinam (former Negapatam), Chennai (Madras), Vishakhapatnam (Vizagapatam) and False Point at east coast of India; Dublat, Diamond Harbour, and Kidderpore (near Calcutta) at the Hugli (Hoogly) River; Beypore and Mumbai (Bombay) at west coast of India; Pakistan: Karachi; these are shown in Figure 2 (map 1). Original tsunami records are presented in Figure 5 (left). Tsunami waves are visible in all points quite well, except Diamond Harbour and Kidderpore situated in the Hugli River (not on the sea coast), and Mumbai (where as it is pointed by Symons (1888), the tidal stream is very strong).

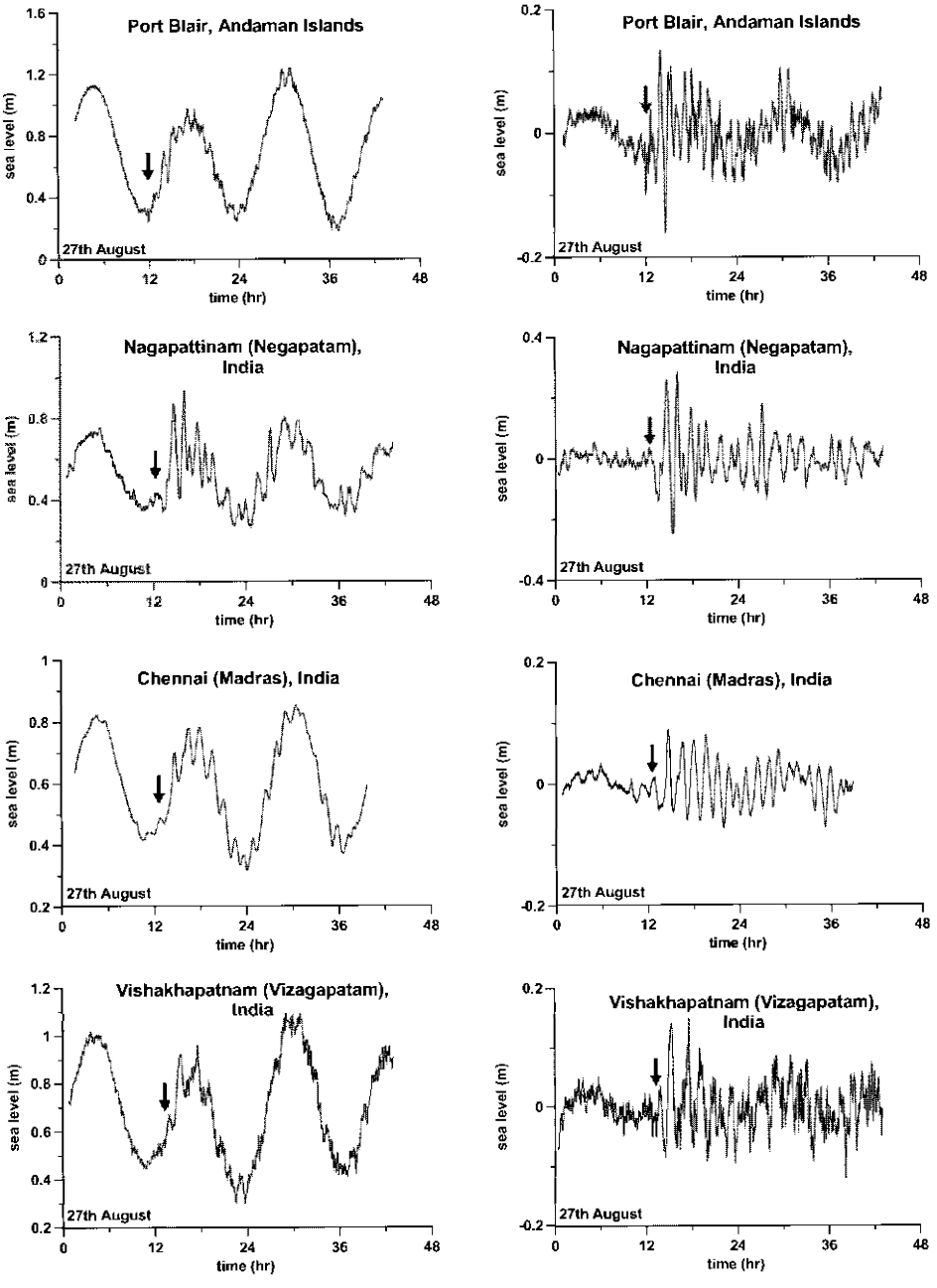

Fig. 5. Tsunami records in India and Pakistan (left – original data, right – filtered from tide, arrows indicate local time of tsunami arrival estimated by the ray tracing method).

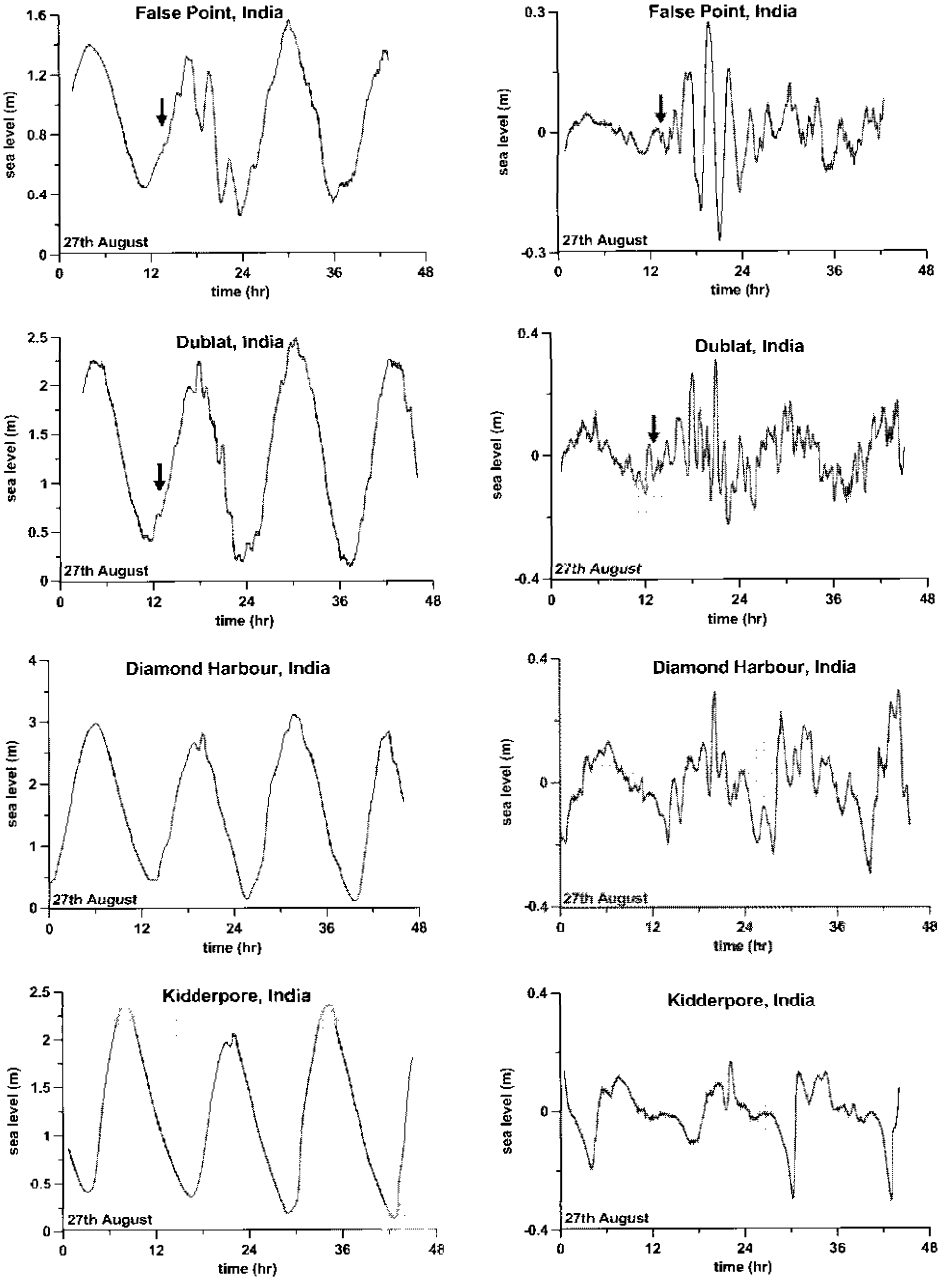

Fig. 5. Tsunami records in India and Pakistan (left – original data, right – filtered from tide, arrows indicate local time of tsunami arrival estimated by he ray tracing method) – continued.

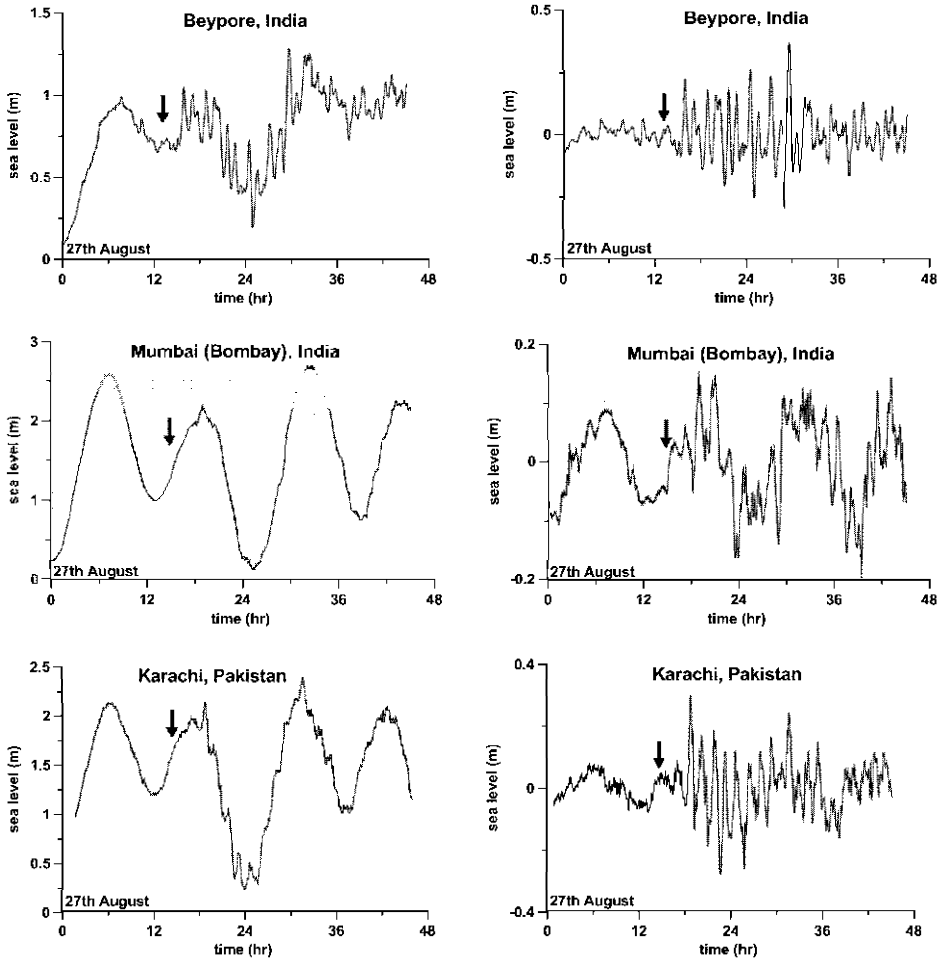

Fig. 5. Tsunami records in India and Pakistan (left – original data, right – filtered from tide, arrows indicate local time of tsunami arrival estimated by the ray tracing method) – continued.

In the "tide filtered" records tsunami waves represent the group waves (except Kidderpore, near Calcutta, 80 miles from sea coast); see Figure 5 (right). The comparison between calculated and observed times of tsunami arrival is very good. Filtered data are used to re-determine the maximal tsunami height as a sum of the maximum values of positive and negative amplitudes, they are given in Table 1 (column 4-6). Maximum wave heights about 65 cm are recorded on south part of India: Beypore (south-west) and about 54 cm at False Point (east), and also at Karachi (58 cm). Characteristic periods of all tsunami records are 1.5 – 2 hr. We would like to point that according to the witness reports (Symons, 1888; Simkin and Fiske, 1983),

characteristics duration of high or low water continued for 15-30 min. According to the simulations by Choi et al. (2003) using the caldera source mechanism, the characteristic period is also about 15-30 min, but numerical simulations do not include tsunami runup on the beach.

Tide-gauge at Aden (Yemen) shows the tsunami manifestation; see Figure 6. Maximum wave height is 37 cm. As it is pointed in Symons (1888), tide-gauge is located in the bay behind the peninsula of Aden protected from the advancing wave. Tsunami travel time, 9 hr 20 min (arrow in Figure 6) corresponds to the second relative large-amplitude disturbance on the tide-gauge record. Visible period is 1-2 hrs.

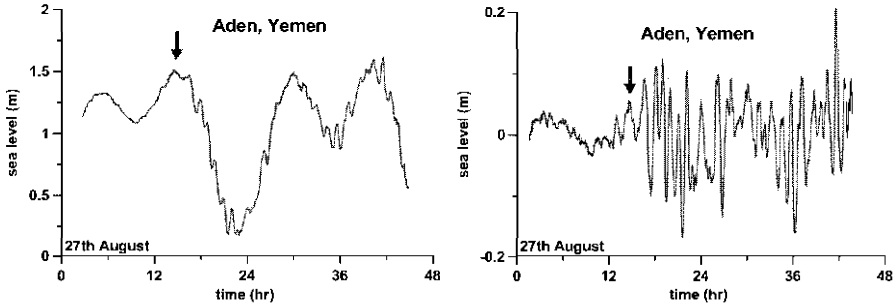

Fig. 6. Tide-gauge record in Aden (left – original data, right – filtered from tide, arrows indicate local time of tsunami arrival estimated by the ray tracing method).

Very distinctive tsunami waves are visible on tide-gauge records in South Africa (Port Alfred, Port Elizabeth and Cape Town; see Figure 2), and they are shown in Figure 7. Estimated tsunami travel time is in good comparison with the "visible" arrival of tsunami waves. Wave height at Port Elizabeth reaches 158 cm, almost one third that in Jakarta (Table 1), meanwhile the wave propagates on large distance in 7,500 km. It is important to mention that measured wave height in Table Bay (Cape Town) is 64 cm, and this confirms that tsunami waves from Krakatau eruption were really propagated in the Atlantic Ocean.

Eight tide diagrams for the Atlantic coast of Europe, in the Bay of Biscay: Socoa (on the border between France and Spain) and Rochefort; in English Channel: Cherbourg and Le Havre in France; Devonport (Plymouth), Portland, Portsmouth and Dover) are given in the book by Symons (1888), the locations are shown in Figure 2 (map 2). The quality of tide-gauge records in the book is not good, because they have been enlarged three times by photography. All digitized tsunami records are presented in Figure 8 (the gauges at Portsmouth and Dover show no sign of any disturbances, and they are not reproduced in the book). Original records at Rochefort, Cherbourg, Le Havre and Devonport have weak sea disturbances, which they are not visible in the filtered records, except Devonport. According to computations (Choi et al., 2003), tsunami travel time from Krakatau to the English Channel is 32 hr, and tsunami should approach at 11 A.M. (Greenwich time) of 28th August (it is shown by arrow). This time

correlates with the appearance of the disturbances on non-filtered records and sometimes with appearance of relative intense waves on filtered records but it is difficult to determine whether observed disturbances are real tsunami waves. The observed wave height (about 20 cm at Devonport) is relative large to compare with computed heights, but this can be explained by the tide-gauge location (as it is pointed by Symons (1888), "the gauge is situated a long way up the harbour, but the form of the land tends to enlarge the wave"). So, our analysis cannot eliminate fully that the observed sea disturbances related with tsunami waves approached from the Krakatau Island directly.

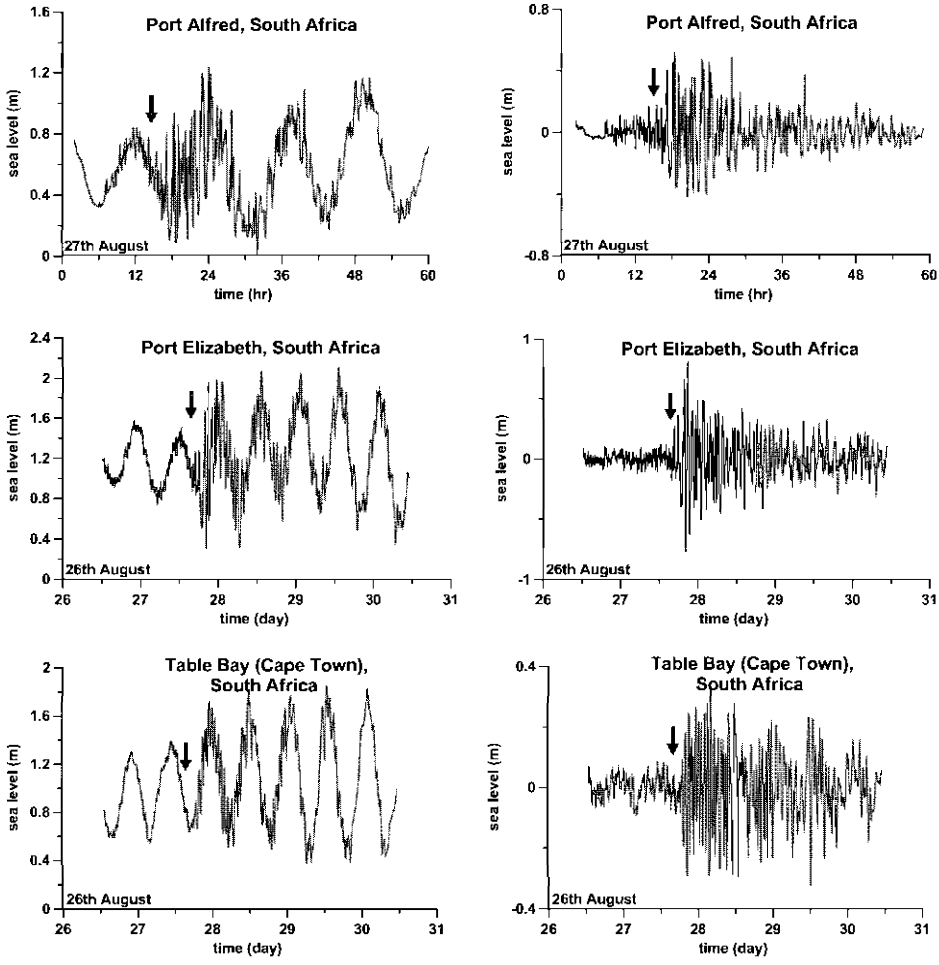

Fig. 7. Tsunami records in South Africa (left – original data, right – filtered from tide, arrows indicate local time of tsunami arrival estimated by the ray tracing method).

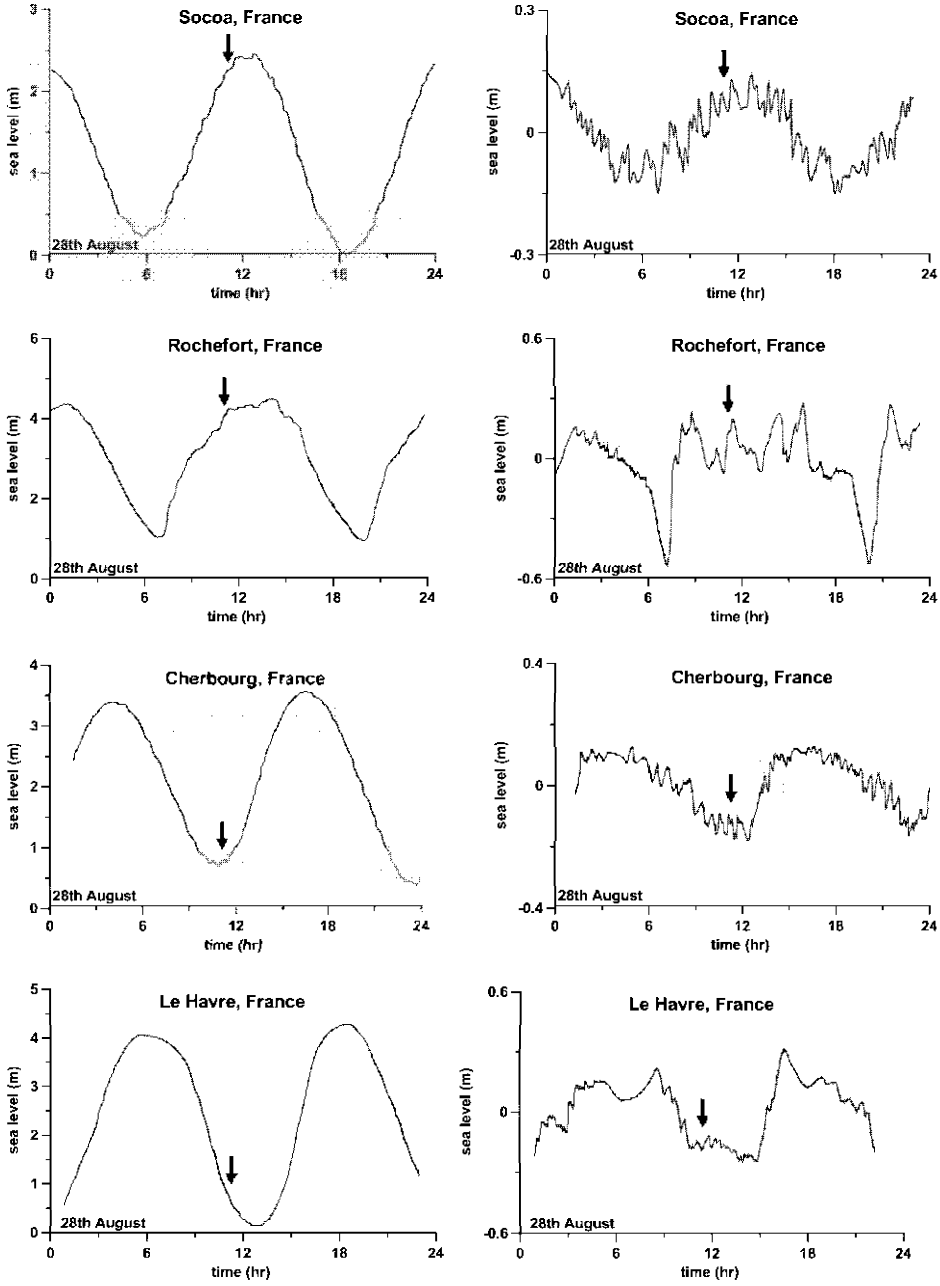

Fig. 8. Tsunami records in Europe (left – original data, right – filtered from tide, arrows indicate local time of tsunami arrival estimated by the ray tracing method).

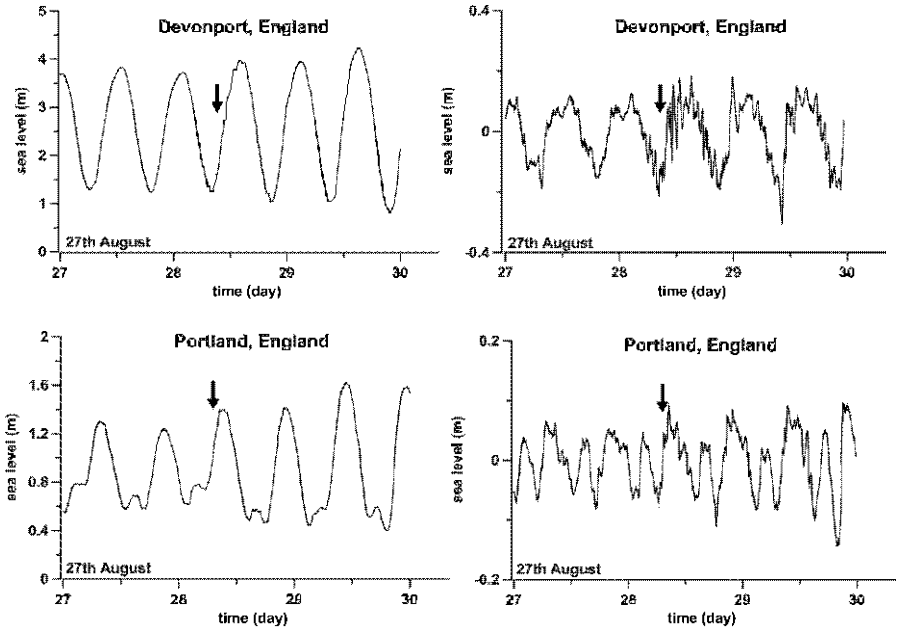

Fig. 8. Tsunami records in Europe (left – original data, right – filtered from tide, arrows indicate local time of tsunami arrival estimated by the ray tracing method) – continued.

Several tide gauges records are collected in Australia and New Zealand. These points are: Port Adelaide, Williamstown (Melbourne, head of Port Phillip), Port Denison (Sydney), Lyttelton Harbour (Christchurch) and Dunedin (both in the South Island, New Zealand); see Figure 2. The tide-gauge record at Dunedin is not given in the book by Symons (1888). Digital tsunami records are shown in Figure 9. All records demonstrate the sea disturbances continued up to 31st August. According to calculations (Choi et al., 2003), tsunami should approach for instance to Melbourne at 21:30 (local time) on 27th August (travel time 8.5 hr), but the observed record is beginning in midday of 28th August. As a result, we cannot distinguish the disturbances from the background, and this is similar for all records in Figure 9. The calculated tsunami travel time for Sydney is less than the appearance of "visible" waves are appeared on the record. On the other hand, according to observations (Bryant, 2001) on 29th August, the wave rose and fell twice for 40 min in the Lake Taupo (center of the North Island of New Zealand), which does not connect with the sea. It means that the origin of sea disturbances occurred on 29 th August in south-east of Australia and New Zealand (and perhaps in Surabaya, Java Sea, mentioned above) are not related to the tsunami generated by the Krakatau eruption. The origin of the observed disturbances is unclear. It also may be related to the air-wave (perhaps not

the first, but a second or third wave). At the same time the digitized and filtered records show disturbances prior to the tsunami from the main blast, which can be attributed to several tsunamis generated prior to the main event. In this case observed disturbances may be related with another blast, but this has not been investigated yet.

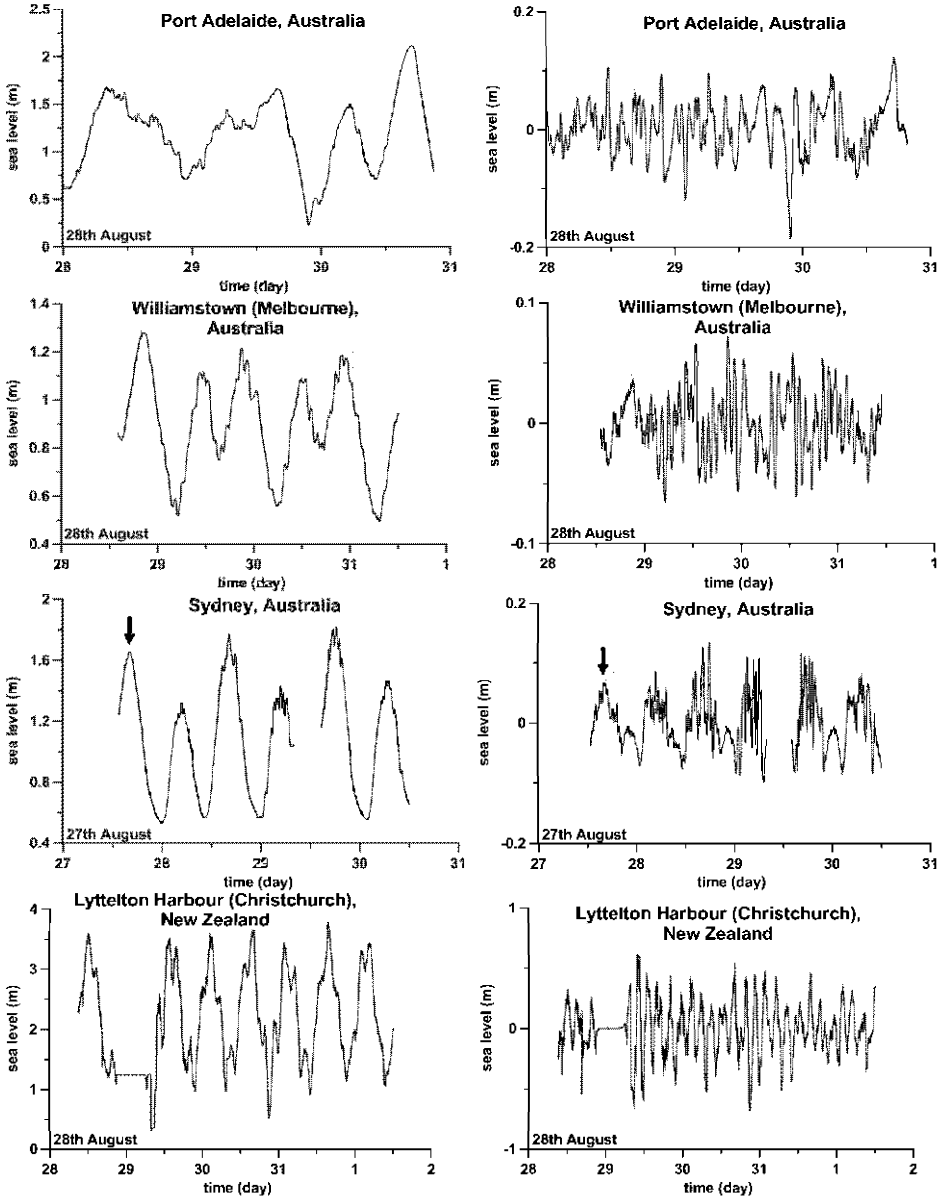

Fig. 9. Tsunami records in Australia and New Zealand (left – original data, right – filtered from tide, arrows indicate local time of tsunami arrival estimated by the ray tracing method).

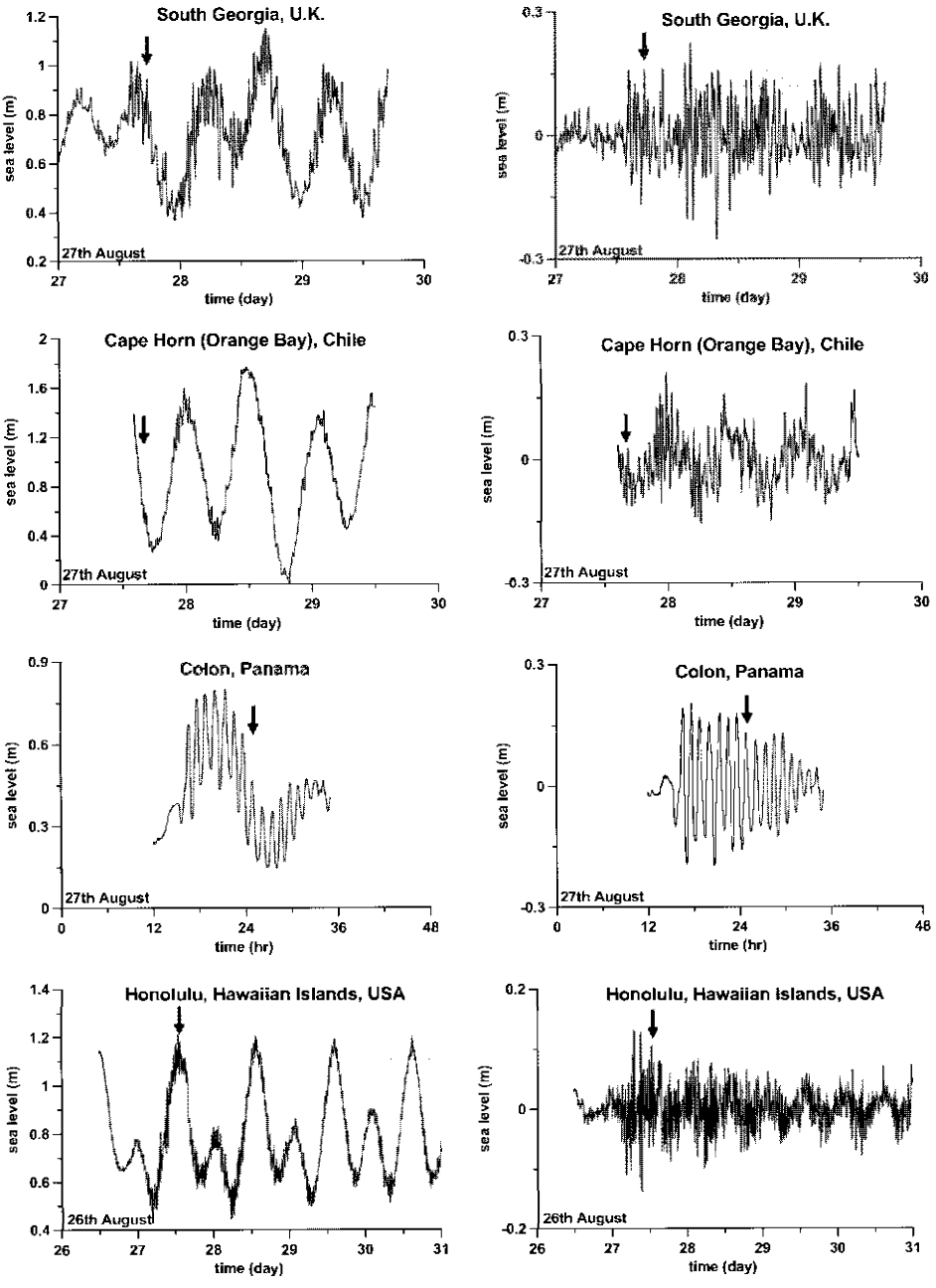

Fig. 10. Tsunami records from American continent (left – original data, right – filtered from tide, arrows indicate local time of tsunami arrival estimated by the ray tracing method).

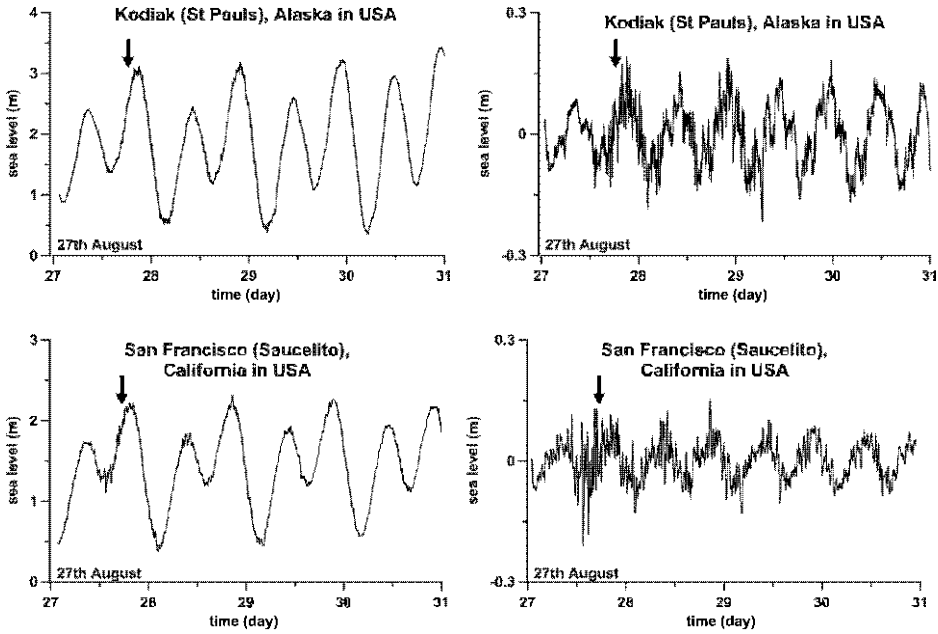

Fig. 10. Tsunami records from American continent (left – original data, right – filtered from tide, arrows indicate local time of tsunami arrival estimated by the ray tracing method) – continued.

Tide gauges for coastal points on the American continent are presented in Figure 10. These points are: Port Moltke at St Georgia, Atlantic Ocean; Cape Horn in Orange Bay, Chile; Colon, Panama, Caribbean Sea; Saucelito (near San Francisco), Honolulu and Kodiak, St Pauls, Alaska in USA; see Figure 2. Estimated tsunami travel time for South Georgia is 17 hr, and tsunami should approach at 18:00 (local time) of 27th August (arrow in Figure 11), but the sea disturbances are apparent 3-4 hrs earlier. The difference in the computed and observed travel times at other American points is: for Honolulu – 11 hrs, for San Francisco – 11 hrs, and for Kodiak - 6 hrs (but for Cape Horn estimated travel time is less than the appearance of intense disturbances in both, non-filtered and filtered records). Early approaching of the tsunami waves cannot be explained by the hydrodynamic theory, because the ray method describes the front (beginning pbase) propagation due to hyperbolicity of the shallow water equations. So, our detailed analysis of the tide-gauge records confirms the previous conclusion given by Symons (1888), that tsunami arrived early to American continent. Early appearance of the tsunami waves have been used by Ewing and Press (1955), Press and Harkrider (1966), and Garrett (1976) to develop the mechanism of sea wave generation by the atmospheric disturbances (air-waves) related with Krakatau eruption. In fact, if tsunami wave propagated "in sea" to these points, they may be hidden in the observed sea disturbances.

4 Conclusion

The original 35 tide-gauge records of the 1883 Krakatau tsunami collected in the Report of Krakatau Committee of the Royal Society (Symons, 1888) are digitized and filtered from tides. All records can be downloaded from site (Pelinovsky et al, 2004). They are used to re-examine the observed tsunami characteristics. The limitations and inadequacies of original and filtered records are discussed. The tide component in not filtered out in some cases, and that some "disturbances" on the filtered records are due to this, and therefore should not be interpreted as tsunami related. Tsunami travel time is computed in the framework of the ray tracing method using detailed 2-min bathymetry. It was used to select the tsunami arrival on the tide-gauge records. In fact, our analysis is in agreement with the conclusions of the tsunami observations summarized by Simkin and Fiske (1983). The Krakatau tsunami was observed on the coasts of the Indian Ocean except Diamond Harbour and Kidderpore situated in the Hugli River far from the seacoast. Tsunami marks are visible for several locations in the Atlantic Ocean (Cape Town, South Georgia, Devonport). A very good record of tsunami in Cape Town confirms the direct tsunami propagation in the Atlantic Ocean. Sea level disturbances in the English Channel (Devonport) arrive at estimated time. So the observed disturbances may be related with the direct propagation of tsunami waves from Krakatau. In South Georgia, tsunami appeared earlier than predicted by 3-4 hrs. It is in agreement with theory of the sea disturbance generation by the atmospheric forcing (Ewing and Press, 1955; Press and Harkrider, 1966; Garrett, 1976). The same is valid for most American data (San Francisco, Honolulu, Kodiak). Sea disturbances on tide gauges in Australia and New Zealand appeared significantly later than estimated time and their origin is not clear. Perhaps, they could be related to the air-wave, but it has not been investigated yet. Digital tsunami records of the 1883 Krakatau event can be used for comparison with the results of the world-wide tsunami propagation models.

Acknowledgement

This study was supported by the Korean Science and Engineering Foundation (KOSEF) through the Korean Earthquake Engineering Research Center (KEERC) at Seoul National University, the Russian Fund for Basic Research (grants 01-0564426, 02-05-65107), and INTAS (grant 01-2156).

References

Bryant, T., Tsunamis, Cambridge University Press, 2001.

Choi, B.H., Pelinovsky, E., Kim, K.O., and Lee, J.S., Simulation of the trans-oceanic tsunami propagation due to the 1983 Krakatau volcanic eruption, Natural Hazards and Earth System Sciences, 2003, vol. 3, No. 5, 321 – 332.

Ewing, M., and Press, F., Tide-gauge disturbances from the Great Eruption of Krakatoa, Trans. AGU, 1955, vol. 36, 53-60.

Garrett, C.J.R., A theory of the Krakatoa tide-gauge disturbances, Tellus, 1976, vol. 22, 43-52.

Kawamata, S., Imamura, F., and Shuto, N., Numerical simulation of the 1883 Krakatau tsunami, Proceedings of 20th IAHR, Tokyo, Japan, 1992.

Murty, T., Seismic Sea Waves Tsunamis, Bull. Dep. Fisheries, Canada, 1977.

Nakamura, S., A numerical tracking of the 1883 Krakatau tsunami, Science of Tsunami Hazards, 1984, vol. 2, 41-54.

Nomanbhoy, N., and Satake, K., Generation mechanism of tsunamis from the 1883 Krakatau eruption, Geophys. Res. Letters, 1995, vol. 22, 509-512.

Pelinovsky, E., Stromkov, A., and Didenkulova, I., Tide-gauge records of the 1883 Krakatau tsunami, 2004. http://www.ipfran.ru/pp/Pelinovsky/krakatau/

Press, F., and Harkrider, D., Air-sea waves from the explosion of Krakatoa, Science, 1966, vol. 154, 1325-1327.

Satake, K., Effects of bathymetry on tsunami propagation: application of ray tracing to tsunamis, PAGEOPH, 1988, vol. 126, 27 36.

Simkin, T., and Fiske, R.S., Krakatau 1883 - the volcanic eruption and its effects, Smithsonian Institution Press, Washington, D.C., 1983.

Smith, W.H.F., and Sandwell, D.T., Global sea floor topography from satellite altimetry and ship depth soundings, Science, 1997, vol. 277, 1956-1962.

Symons, G.J. (ed), The eruption of Krakatoa and subsequent phenomena. Report of the Krakatoa committee of the Royal Society, London: Trubner & Co, 1888.

Verbeek, R.D.M., Krakatau, Batavia, 1885.

William, J.E., and Thomson, R.E., Data analysis methods in physical oceanography, Pergamon GB, London, 1998.

Yokoyama, I., A geophysical interpretation of the 1883 Krakatau eruption, J. Volcanology and Geothermal Research, 1981, vol. 9, 359-378.

MODEL OF TSUNAMI GENERATION BY COLLAPSE OF VOLCANIC ERUPTION: THE 1741 OSHIMA-OSHIMA TSUNAMI

K. KAWAMATA[1], K. TAKAOKA[1], K. BAN[1], F. IMAMURA[2], S. YAMAKI[3] AND E. KOBAYASHI[4]

[1] *Nuclear Power Dept., Electric Power Development Co.,Ltd., 15-1, Ginza 6-Chome, Chuo-ku, Tokyo, 104-8165, Japan*
[2] *Disaster Control Research Center, Tohoku University, Aoba06, Aramaki, Aoba-ku, Sendai, 980-8579, Japan*
[3] *Seamus Ltd., 2235, Kizaki, Toyosaka, Niigata, 950-3304, Japan*
[4] *JP Business Service Corporation, 2-18, Fukagawa, 2-Chome, Koutou-ku, Tokyo, 135-8451, Japan*

Tsunamis generated by landslides are less studied than those caused by fault motion because of the low frequency of such events and the complexity of the generating mechanism. We carried out hydraulic experiments that simulated a debris flow rushing into water. Using parameters obtained from those experiments, we revised a numerical two-layer model to take into account three kinds of shear stress—bottom friction, horizontal viscosity, and interactive force—and the form drag of the debris flow. We then compared our model results with those from the hydraulic experiments. Then, the improved two-layer model was applied to the 1741 Oshima-Oshima tsunami to reproduce the tsunami height along the Hokkaido coast and the Korean Peninsula in the Japan Sea.
Key words: volcanic eruption, two-layer model, 1741 Oshima-Oshima tsunami.

1 Introduction

Tsunamis generated by landslides have been less studied than those by fault motion, because of the rare occurrence of the events and the complexity of generating mechanism. According to a statistical survey of tsunamis during the period 1790-1990 (Imamura, 1998), 3.3% (22 events) and 6.4% (43 events) were generated mainly by landslides and volcanic eruptions respectively. However, it has been reported that the historical landslide-induced tsunamis caused many casualties and serious damage. For example, in 1741 a tsunami caused by the volcanic eruption of Oshima-Oshima killed 1,467 people, and the maximum runup of 14 m was reported (Aida, 1984). And in 1792, a huge tsunami caused by the collapse of Mt. Mayuyama during the volcanic activity attacked the coast around Ariake Sea, Kyushu in Japan and resulted in about 15,000 casualties (Aida, 1975). Therefore, it is very important to study the generating mechanism of such non-seismic tsunamis.

K. Satake (ed.), Tsunamis: Case Studies and Recent Developments, 79-96.

Although simulations of the generation and propagation for tsunamis (Aida, 1974; Imamura and Lee, 1998) have been rapidly developed and applied to historical and recent tsunamis, successful results have been limited to seismic tsunamis. Numerical models of landslide tsunamis have failed to reproduce the observed tsunami heights and damage because less information is available on landslide events owing to their rarity and the complexity of the generation mechanism.

Previous research on landslide-induced tsunamis studied the generation mechanism by hydraulic experiments and numerical simulations but neglected the dynamics of the landslide and its impact on the water surface. A wide variety of physical and numerical models of tsunami generation by landslides, both on land and underwater and based on different assumptions, have been developed. Ming and Wang (1993) proposed two methods to study the process of landslides flowing into water: the inflow-volume method and the unit-width-discharge method. Noda (1970), on the other hand, developed a two-dimensional box-and-wall theory. The box is dropped vertically on the end of a semi-infinite channel to represent the vertical entry of a land mass, and horizontal entry is simulated by a wall moving into the fluid domain. Recently, Imamura et al. (2001), Imamura and Lee (1998), Thomson et al. (2001), and Matsumoto et al. (1998) developed numerical, two-layer models to simulate the tsunami-generating interaction between a landslide and the water, and Matsumoto et al. (1998) used the model to reproduce the historical tsunami of 1741. However, in these models, some parameters still need to be calibrated.

On the other hand, Fritz et al. (2001) carried out hydraulic experiments to simulate the generation of the Lituya Bay tsunami of 1958 by a rockslide, and Togashi and Hirayama (1993) carried out a hydraulic experiment to simulate the tsunami associated with the collapse of Mt. Mayuyama in 1792. However, the results of these studies have not sufficiently clarified the physical mechanism of the interaction that occurs between a debris flow and the water to generate a tsunami when the sediment rushes into the water.

We carried out two kinds of hydraulic experiment to characterize the rush of a debris flow into water, the sequence of landslide motion, and the generation of the tsunami. The water motion was recorded with a high-speed video camera and water gauges in order to investigate the tsunami-generation process. Using parameters obtained from the experiments, we revised the numerical, two-layer model to incorporate three kinds of shear stress —bottom friction, horizontal viscosity, and interactive force—and the form drag of the leading edge of the debris flow. We then compared our model results with those from the hydraulic experiments. Then, we applied the improved two-layer model to the 1741 Oshima-Oshima tsunami and attempted to reproduce actual tsunami heights along the Hokkaido coast and the Korean Peninsula in the Japan Sea.

2 Laboratory Experiments

Hydraulic experimental studies were conducted to investigate the features of a tsunami generated by a volcanic eruption involving a major collapse of the mountain.

Figure 1 shows the experimental setup. A one-dimensional, flat-bottomed, open channel (8.0 m long × 0.4 m wide) was filled with water to a depth of 0.6 m. A board was placed across the channel near one end to create a slope whose angle could be changed. Sand (particle diameter 0.6 mm, specific gravity 2.6, weight 30 kg), released by opening a gate at the top of the slope, flowed down and into the water in the channel. Measurements were made at three slope angles (30°, 37°, and 45°) and for both a rough and smooth slope surface. Four wave gauges were installed at horizontal distances of 0.5, 1.0, 2.0, and 3.0 m from where the slope intersected with the water surface. Moreover, laser distance measurements of the debris flow thickness were made at 0.1, 2.0, and 3.0 m downslope from the gate. A digital video camera and high-speed camera were used to record the tsunami generation sequence induced by the impact of the debris flow entering the water. Moreover, we measured the variation of the debris flow velocity in the channel without water by laser distance measurements, and compared the results with those obtained when the channel contained water.

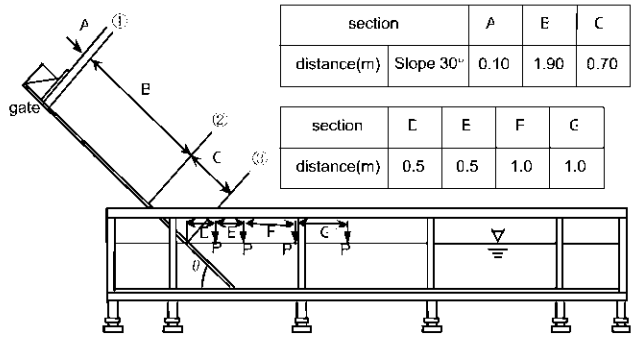

section		A	B	C
distance(m)	Slope 30°	0.10	1.90	0.70

section	D	E	F	G
distance(m)	0.5	0.5	1.0	1.0

Fig. 1. Experimental setup.

A series of photographs show the debris flow rushing into the water and the generated tsunami for the case of a smooth 30° slope (Figure 2). When the debris flow reached the water's surface and displaced the water, it generated a positive wave. After that, the debris became mixed with the water, causing the leading edge of the debris flow to thicken as it descended to the bottom of the slope. Then, the debris flow appeared to pull down the water's surface, generating a negative wave. This negative wave has not been reported before and should be important in controlling the wave period. The continuous flow of debris into the water causes the wave period of the tsunami to be short.

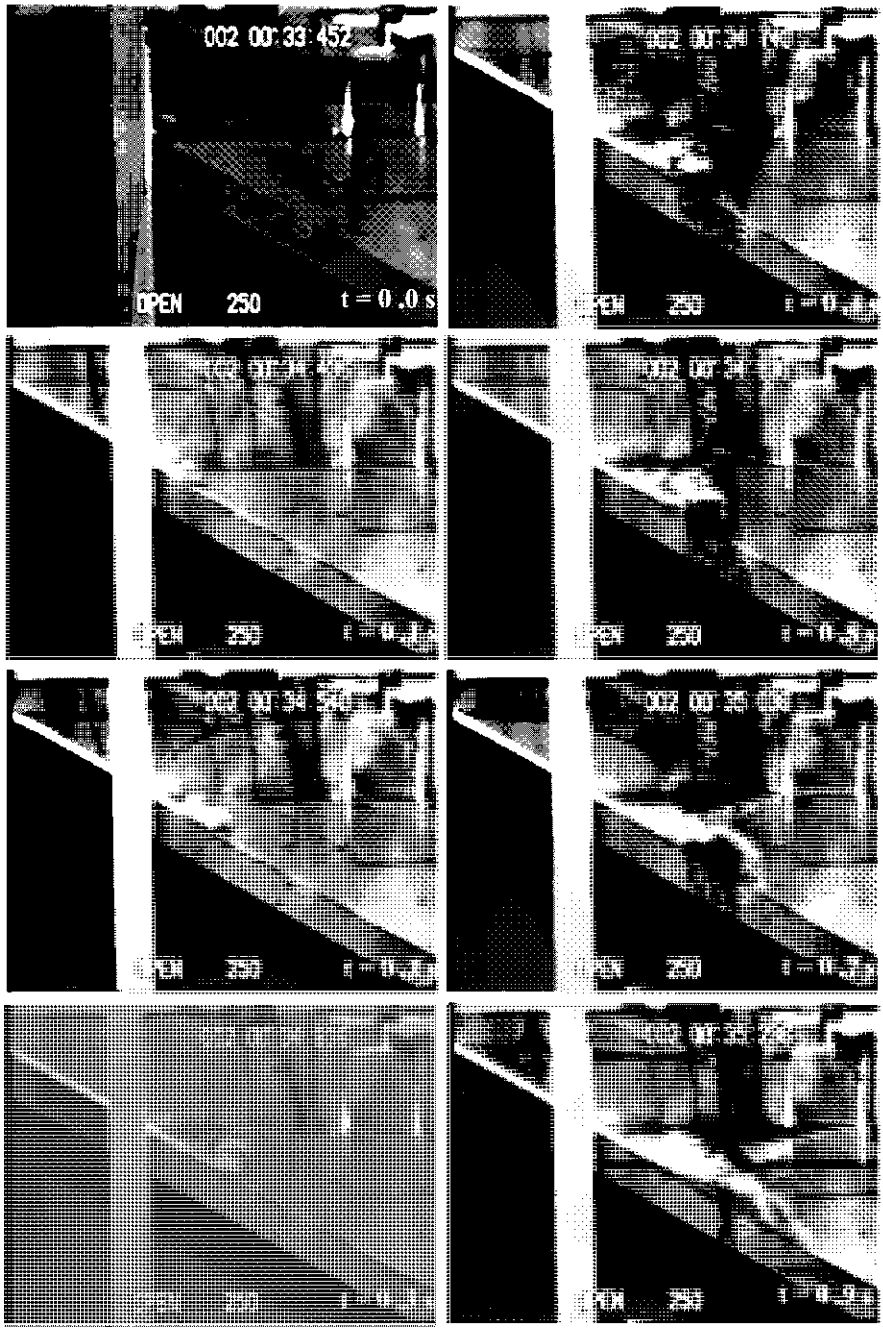

Fig. 2. Series photographs of debris flow.

3 Improvement of two-layer Model

3.1 TWO-LAYER MODEL

A wide variety of numerical methods incorporating many different assumptions have been proposed to model tsunamis caused by the marine mass failure and landslide. We use the model of depth-averaged non-linear shallow water wave equations, in combination with various landslides (Fine et al., 1998; Harbitz, 1992; Imamura and Gica, 1996; Jiang and LeBlond, 1992; 1993;1994). Although it is pointed out that the wave frequency dispersion might be important for far propagation of short waves generated by the landslides, we in the study neglect this because we focus on the early propagation and the leading wave. The shallow water wave equation excluding the dispersion is used for the wave propagation model. The two-layer model was designed to simulate the motion of a landslide as a fluid flow. The equations for a multiphase fluid flow are solved by using the kinetic and dynamic conditions at the surface and interface (Matsumoto et al., 1998). The initial and boundary conditions are illustrated in Figure 3.

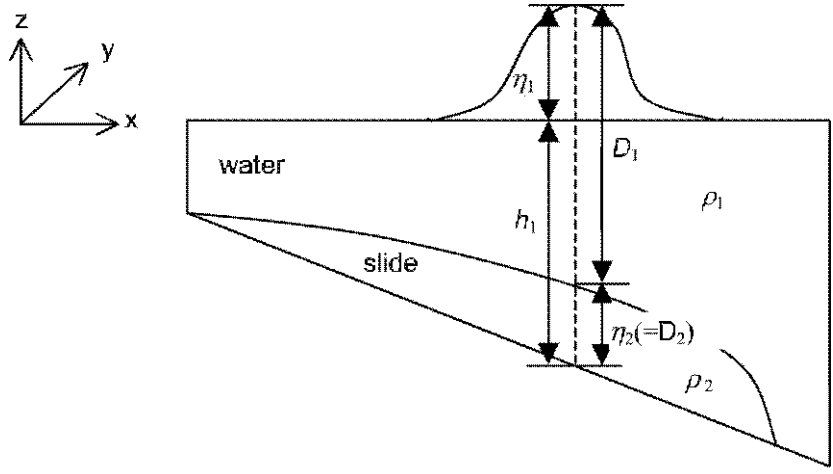

Fig. 3. Initial and boundary conditions of the two-layer model.

The equations of two-layer model are written as follows.

$$\left.\begin{aligned}
&\frac{\partial(\eta_1-\eta_2)}{\partial t}+\frac{\partial M_1}{\partial x}+\frac{\partial N_1}{\partial y}=0\\
&\frac{\partial M_1}{\partial t}+\frac{\partial}{\partial x}\left(\frac{M_1^2}{D_1}\right)+\frac{\partial}{\partial y}\left(\frac{M_1N_1}{D_1}\right)+gD_1\frac{\partial \eta_1}{\partial x}-FD_x-INTF_x=0\\
&\frac{\partial N_1}{\partial t}+\frac{\partial}{\partial x}\left(\frac{M_1N_1}{D_1}\right)+\frac{\partial}{\partial y}\left(\frac{N_1^2}{D_1}\right)+gD_1\frac{\partial \eta_1}{\partial y}-FD_y-INTF_y=0
\end{aligned}\right\} \quad (1)$$

$$
\begin{aligned}
&\frac{\partial \eta_2}{\partial t}+\frac{\partial M_2}{\partial x}+\frac{\partial N_2}{\partial y}=0 \\
&\frac{\partial M_2}{\partial t}+\frac{\partial}{\partial x}\left(\frac{M_2^{\,2}}{D_2}\right)+\frac{\partial}{\partial y}\left(\frac{M_2 N_2}{D_2}\right)+gD_2\left(\alpha\frac{\partial D_1}{\partial x}+\frac{\partial \eta_2}{\partial x}-\frac{\partial h}{\partial x}\right) \\
&+\frac{\tau_x}{\rho_2}+\alpha FD_x+\alpha INTF_x=DIFF_x \\
&\frac{\partial N_2}{\partial t}+\frac{\partial}{\partial x}\left(\frac{M_2 N_2}{D_2}\right)+\frac{\partial}{\partial y}\left(\frac{N_2^{\,2}}{D_2}\right)+gD_2\left(\alpha\frac{\partial D_1}{\partial y}+\frac{\partial \eta_2}{\partial y}-\frac{\partial h}{\partial y}\right) \\
&+\frac{\tau_y}{\rho_2}+\alpha FD_y+\alpha INTF_y=DIFF_y
\end{aligned}
\qquad (2)
$$

where subscripts 1 and 2 indicate the upper and lower layer, respectively, η is the surface elevation, h is the still water depth, D is the total depth, M and N indicate the discharge in the x and y directions, ρ is the fluid density, α is the density ratio (ρ_1/ρ_2), τ_x/ρ and τ_y/ρ indicate the bottom friction in the x and y directions, $INTF_x$ and $INTF_y$ indicate the interfacial resistance in the x and y directions, FD_x and FD_y indicate the form drag in the x and y directions, and $DIFF_x$ and $DIFF_y$ indicate the horizontal viscosity in the x and y directions.

Bottom friction, form drag, horizontal viscosity, interactive force on the interface, and wave frequency dispersion values are essential for the model to simulate the generation of the tsunami induced by the debris flow. Bottom friction, form drag, and horizontal viscosity are properties of the lower debris-flow layer, dispersion is a property of the upper tsunami layer, and the interactive force is a property of both layers. Several studies (Matsumoto et al., 1998; Imamura et al., 2001) have calculated coefficients for the shear and interactive stresses, but the reliability and applicability of models based on those calculations have not yet been tested.

Since we aim to improve the simulation of two-layer flow, we use simple general models for each stress and shear. Both the kinetic viscosity of molecules and the eddy viscosity of the vortex are expressed in a single viscosity parameter of the momentum equation of long-wave theory. By integrating the viscous stress terms vertically over each layer, we can obtain the shear stresses at the bottom, the interface, and the water surface. Generally, shear stresses at the water surface of a tsunami are negligible; only the shear stress at the interface is important. On the other hand, the bottom and interface friction and the form drag of the leading edge of the debris flow are needed to simulate the debris flow. The horizontal viscous stress is also important for the simulation of the debris flow. By reference to previous studies that model each shear stress, we propose eqs. (3), (4), (5), and (6).

The bottom frictions with coefficient n, are

$$\frac{\tau_x}{\rho} = \frac{gn^2}{D^{7/3}} M\sqrt{M^2+N^2}$$

$$\frac{\tau_y}{\rho} = \frac{gn^2}{D^{7/3}} N\sqrt{M^2+N^2} \tag{3}$$

The form drags with coefficient C_D, are

$$FD_x = \frac{1}{2} C_D \rho_1 \bar{u}\sqrt{\overline{u^2}+\overline{v^2}}\,\delta_m$$

$$FD_y = \frac{1}{2} C_D \rho_1 \bar{v}\sqrt{\overline{u^2}+\overline{v^2}}\,\delta_m \tag{4}$$

where δ_m is the maximum thickness of the lower layer at each time instant, $\bar{u}$ and $\bar{v}$ are the relative velocity against the upper layer.

The interactive forces with coefficient f_{inter}, are

$$INTF_x = f_{inter}\bar{u}\sqrt{\overline{u^2}+\overline{v^2}}$$

$$INTF_y = f_{inter}\bar{v}\sqrt{\overline{u^2}+\overline{v^2}} \tag{5}$$

The horizontal viscosities with coefficient ν are

$$DIFF_x = \nu\left(\frac{\partial^2 M_2}{\partial x^2}+\frac{\partial^2 M_2}{\partial y^2}\right)$$

$$DIFF_y = \nu\left(\frac{\partial^2 N_2}{\partial x^2}+\frac{\partial^2 N_2}{\partial y^2}\right) \tag{6}$$

The interactive force pulls down the water's surface when the debris flow rushes into the water. We can explain this effect as follows. The discharge M_1 of the upper layer increases owing to the effect of the force on the interface, and the discharge of the debris flow M_2 has no effect on the upper layer (Figure 4). Therefore, the water surface is pulled down by the increasing value of M_1 in the control-volume, whose area is indicated by diagonal hatching in Figure 4.

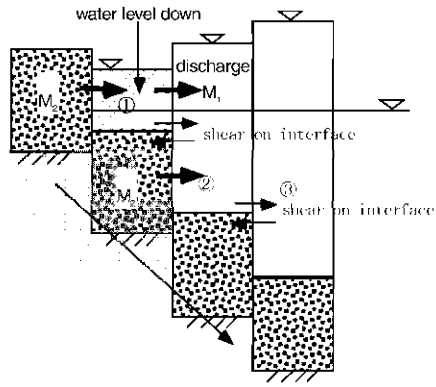

Fig. 4. Model oh the interactive force.

3.2 NUMERICAL CONDITIONS

The governing equations for the two-layer model were discretized using a 2nd-order finite difference method with the staggered leap-frog scheme, and the upwind scheme was used to discretize the nonlinear terms. To stabilize the calculation, the implicit difference scheme was used only for bottom friction. We selected a spatial grid size of 0.02 m, which is small enough to approximate the wavelength of the tsunami, and a time step of 0.001 s to satisfy the calculation stability conditions. The total time of the numerical simulation was 4.0 s. The results from the numerical simulation were compared with the results of the hydraulic experiments to investigate the reliability and applicability of the modified model.

3.3 SIMULATION FOR DEBRIS FLOW

First of all, we determined the reliability of the debris flow model for the time before the debris flow enters the water. We carried out a numerical simulation of the debris flow on the slope using different values for the Manning roughness coefficient n and the horizontal viscous coefficient ν, and compared the results with those from the hydraulic experiments. To evaluate the influence of roughness, three simulations, for a smooth or rough 37° slope and for a smooth 30° slope, were carried out. After several simulations with different values, we concluded that the most appropriate values for the coefficients are those listed in Table 1. Comparisons of calculated and measured values for thickness and water level at point ③ and P1 are shown in Figure 5, suggesting good reliability of the model to simulate the landslide on the slope as well as the generated wave, especially leading wave. The tail of the leading wave is not well reproduced because of the wave dispersion effect which is not included in the model.

Table 1. Coefficients of two-layer model applied to the numerical simulation.

n (s/m$^{1/3}$)	ν (m^2/s)	n_w (s/m$^{1/3}$)	C_D	f_{inter}	t_{inter} (s)
0.01	0.01	0.12	10	0.2	0.37

n : Manning's roughness coefficient (subaerial), n_w : Manning's roughness coefficient (underwater), t_{inter} : continuation time of the interactive force

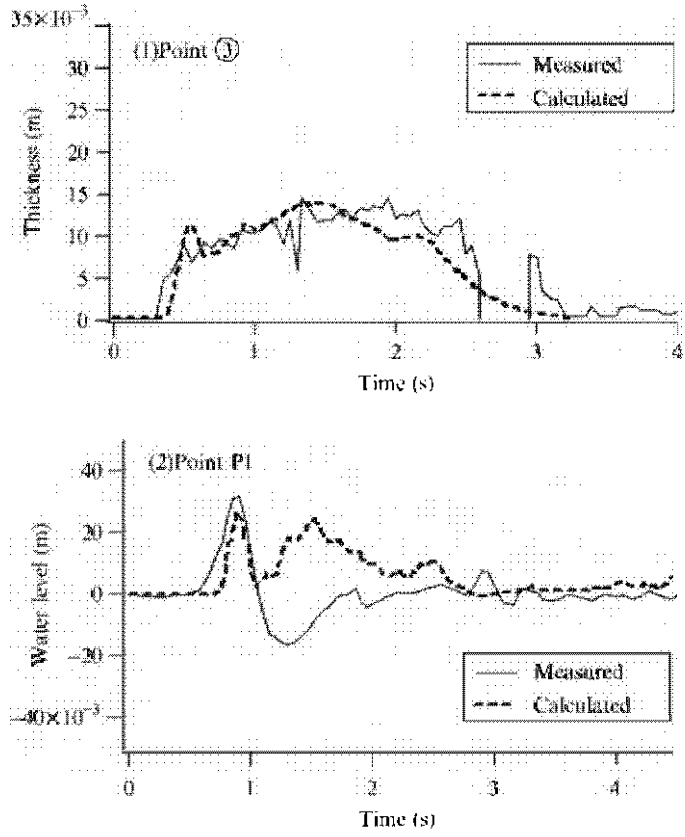

Fig. 5. Comparison between water level and thickness calculated by the revised model and measured values from the hydraulic experiments.

4 Reproducibility of the 1741 OSHIMA-OSHIMA tsunami

4.1 INITIAL CONDITIONS OF TWO-LAYERS MODEL

In order to apply the two-layer model to the 1741 Oshima-Oshima tsunami, it was necessary to reconstruct topographic data before the 1741 collapse to establish the initial conditions of the model.

Satake and Kato (2001) reconstructed the topography before the 1741 collapse and estimated the volume change on the basis of a detailed swath bathymetry survey.

In this study, we use their topographic data (Figure 6). The subaerial slide volume was 0.22 km^3 and the submarine slide volume was 1.86 km^3 for a total slide volume of 2.08 km^3.

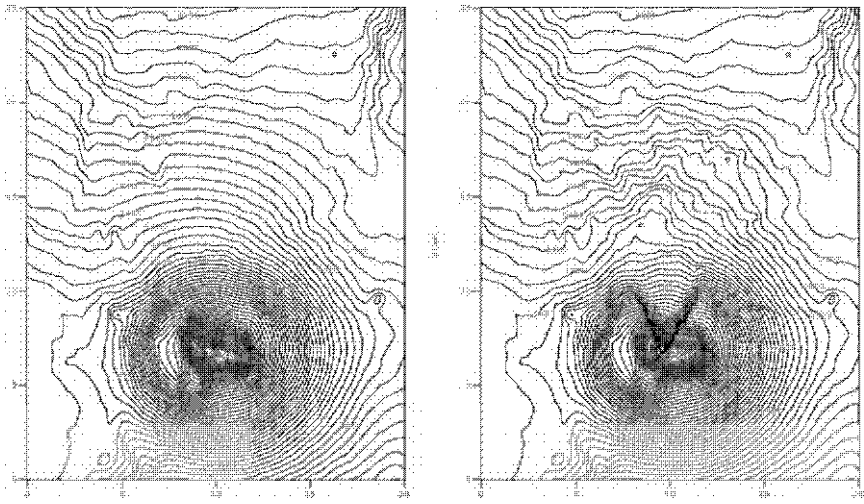

(1) Reconstructed topography (2) Current topography

Fig. 6. Topographic data before and after the sector collapse.

In addition to the two-layer model, we applied a fault model developed by Ban et al. (2001) to the 1741 Oshima-Oshima tsunami in order to compare the calculation results.

This model reproduced the tsunami heights from the Hokkaido to the Aomori coasts. Figure 7 shows the results of the fault model of this tsunami.

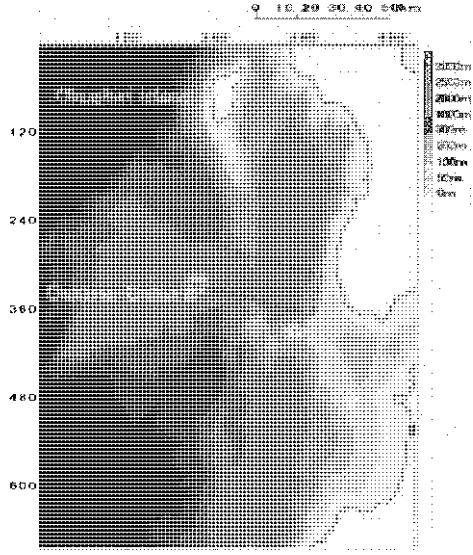

Fault length	50 km
Fault width	19 km
Slip	16 m
Strike	285°
Dip angle	30°
Slip angle	90°
Top depth of fault	2km

Fig. 7. The Oshima-Oshima tsunami modeled with the fault model.

4.3 SIMULATION METHOD

Numerical simulations were made at both local and regional scales.

For the local calculation, the two-layer model was used with a 50 m × 50 m grid.

For the regional calculation, the shallow-water theory with the nonlinear long-wave equation was used (Goto and Sato, 1993). The rectangular coordinate system used for the regional calculation is shown in Figures 8 and 9. The grid sizes used were 2.5 km × 2.5 km (Region B) at the end of calculation area, 833 m × 833 m (= 2.5 km/3; Region C) for most of the Japan Sea, and 278 m × 278 m (= 2.5 km/9; Region D) and 93 m × 93 m (= 2.5 km/27; Region E) for the area along the shoreline, which is the critical calculation area. Furthermore, the area of the tsunami run-up onto the land was also calculated at a grid size of 93 m × 93 m on the basis of the condition of Iwasaki and Mano (1979). The time step of calculation was 0.5 s.

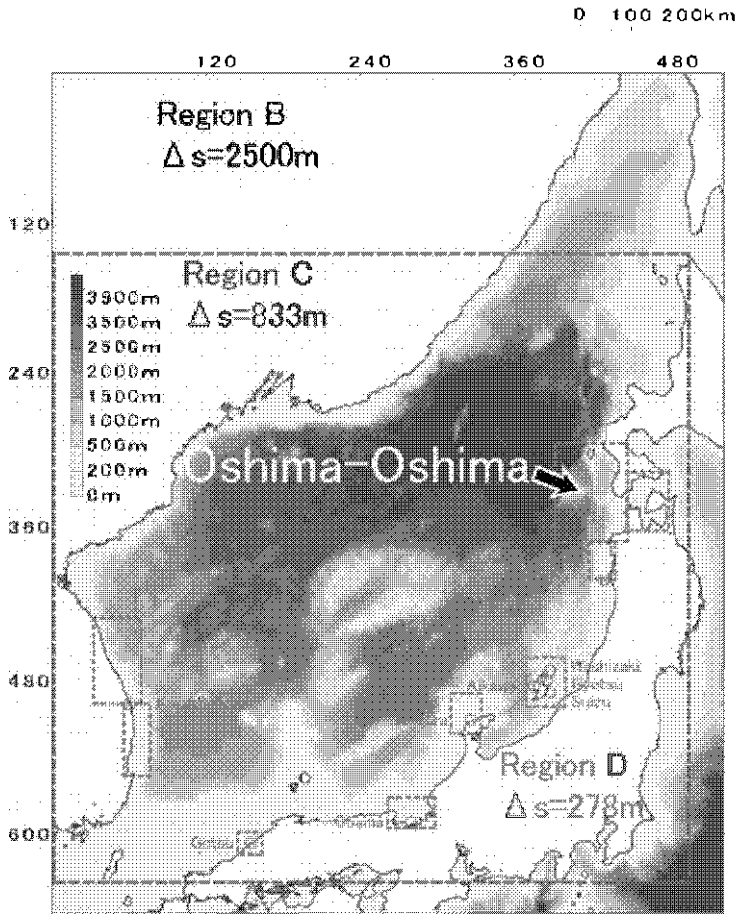

Fig. 8. Area of calculation for entire Japan Sea.

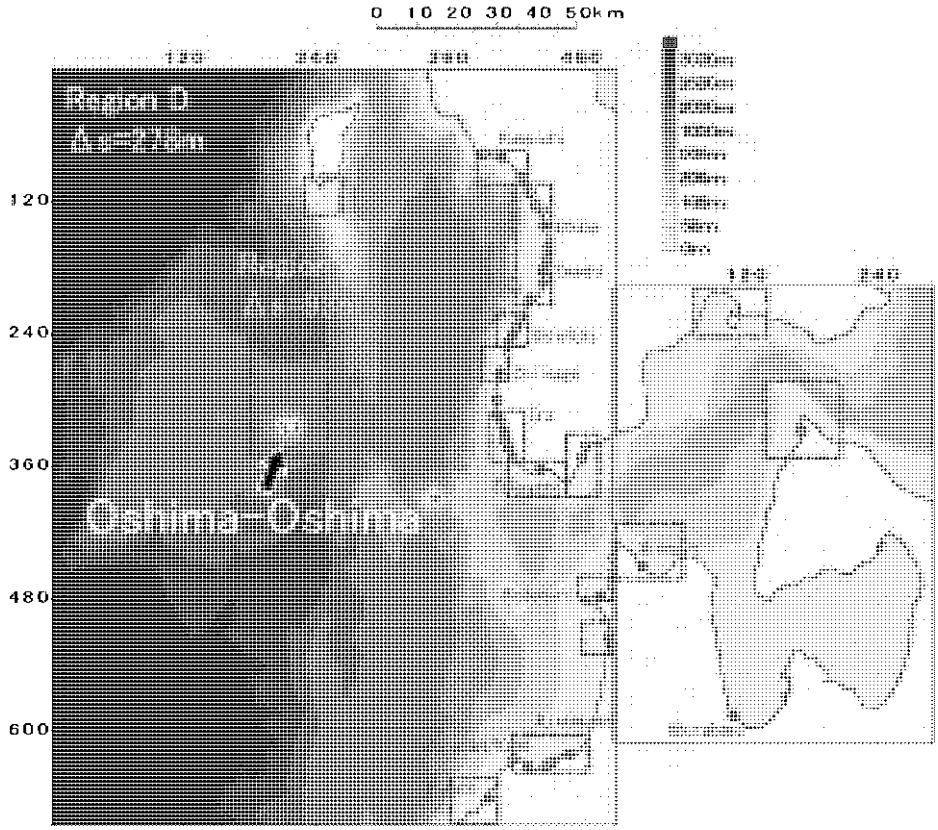

Fig. 9. Area of calculation for near-source region.

4.4 METHOD FOR VERIFYING REPRODUCIBILITY

Two statistical parameters were introduced to compare the observed and computed tsunami heights. The first is the geometric mean K of the observed to computed amplitude ratio (Eq. (7)) at tsunami sites, and indicates the relative size of the observed and computed tsunami waves. The second is an index of scatter κ (Eq. (8)), which can be considered an error factor, if the logarithmic amplitude ratios have a normal distribution N (log K, log κ). Both K and κ were first introduced by Aida (1978) and have been used to measure the goodness of tsunami source models.

$$\log K = \frac{1}{n}\sum_{i=1}^{n} \log K_i \tag{7}$$

$$\log \kappa = \left\{ \frac{1}{n}\sum_{i=1}^{n} (\log K_i)^2 - (\log K)^2 \right\}^{1/2} \tag{8}$$

where n indicates the number of sites and K_i is (observed inundation height)/(computed value) at the i-th site.

4.5 REPRODUCIBILITY OF THE 1741 OSHIMA-OSHIMA TSUNAMI

In the case of the two-layer model, a parametric study was performed by varying several coefficients to estimate appropriate values by taking into account the differences between the hydraulic study and the 1741 Oshima-Oshima tsunami.

As an example, Figure 10 shows the distribution of observed and computed tsunami heights along the Japan Sea coast for different values of Manning's roughness coefficient n. We concluded that the best fit was obtained for n = 0.4, because the K value was 1, and the κ value was small.

Table 2 shows the coefficients of the two-layer model as applied to the 1741 Oshima-Oshima tsunami.

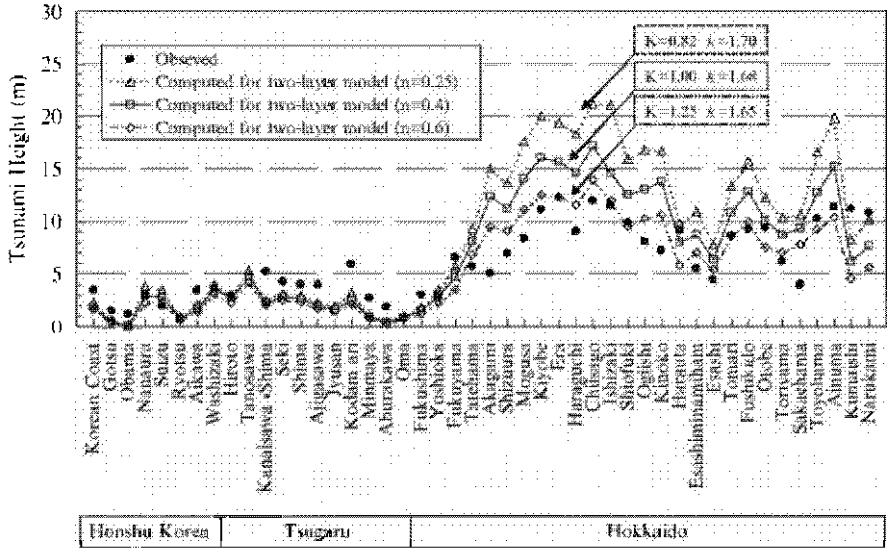

Fig. 10. Distribution of tsunami heights along the Japan Sea for different n values.

Table 2. Coefficients of the two-layer model use to simulate the 1741 Oshima-Oshima tsunami.

n (s/m$^{1/3}$)	ν (m^2/s)	n_w (s/m$^{1/3}$)	C_D	f_{inter}	t_{inter} (s)
0.4	0.1	0.4	2.0		

Figure 11 shows the distribution of observed and computed tsunami heights along the Japan Sea coast. In the case of the two-layer model, K = 0.99 and κ = 1.76 for the near-source region (from Hokkaido to the Tsugaru Peninsula; 35 sites), and K = 1.00 and κ = 1.68 for the entire Japan Sea (from Hokkaido to the Korean Peninsula; 42

sites). The computed tsunami heights reproduce well the observed tsunami heights because the K value is 1 or close to 1 in each case. The κ values show that the reproducibility for the entire Japan Sea is better than that for the near-source region. In the case of the fault model, K = 0.89 and κ = 1.38 for the near-source region (35 sites), and K = 1.01 and κ = 1.58 for the entire Japan Sea (42 sites). The computed tsunami heights are too large by about 10% (K = 0.89) in the near-source region. The computed tsunami heights for the entire Japan Sea area are more scattered than those computed for the near-source region only.

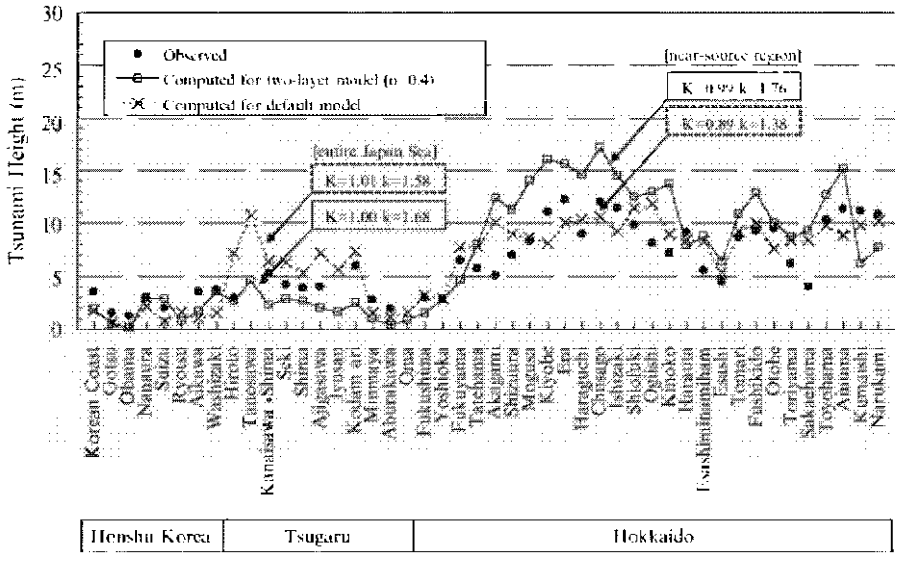

Fig. 11. Distribution of tsunami heights along the Japan Sea, computed by the two-layer model and by the fault model.

Figure 12 shows the maximum tsunami height distribution as computed by the two-layer model, and Figure 13 shows the height distribution computed by the fault model. In the case of the two-layer model, the tsunami heights were larger to the north of Oshima-Oshima, indicating that the tsunami energy had strong directivity. Furthermore, at certain local points, the tsunami height is predicted to have been very large.

Figure 14 shows the waves computed by the two-layer model and fault model at three representative points, Era (Hokkaido), Ajigasawa (Tsugaru), and Nanaura (Honshu). The waves computed by the two-layer model have dominantly short periods in comparison with those computed by the fault model. Therefore, we inferred that waves calculated by the two-layer model were more influenced by local topography than those computed by the fault model.

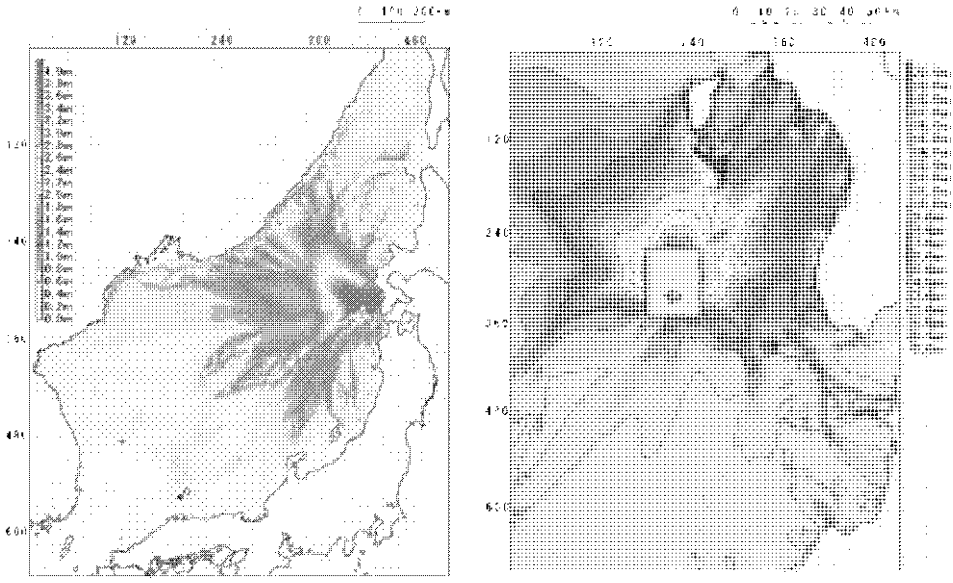

(1)Entire Japan Sea (2)Near-source region

Fig. 12. Maximum tsunami height distribution by two-layer model.

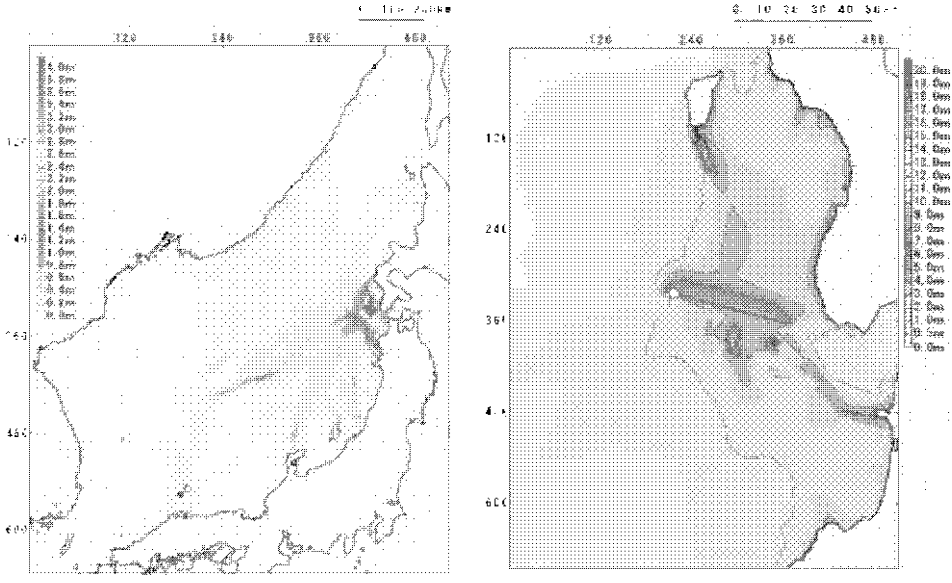

(1)Entire Japan Sea (2)Near-source region

Fig. 13. Maximum tsunami height distribution by fault model.

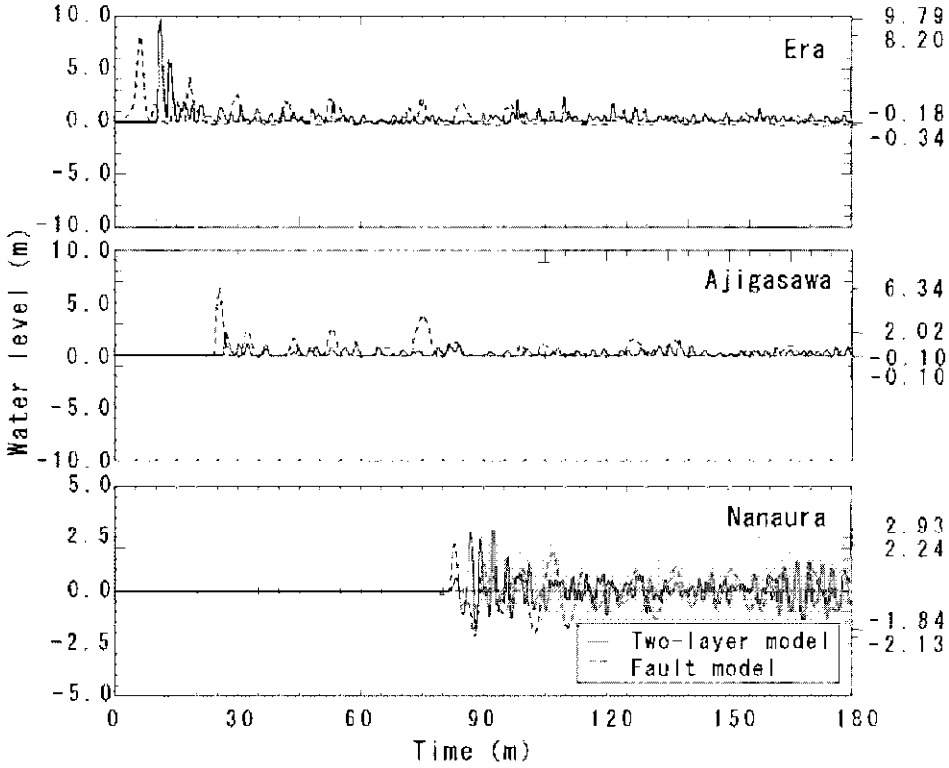

Fig. 14. Computed waves at various locations.

5 Conclusions

(1) The main features of the tsunami caused by a volcanic eruption with major collapse were clarified by hydraulic experiments as follows. First, as the debris flow moves downslope under the water, it pulls down the water's surface, generating a negative wave; such a wave has not been reported before and should play an important role in controlling the wave period. Second, the period of the tsunami wave is short, suggesting the importance of wave frequency dispersion.

(2) On the basis of the hydraulic experiments, we improved the two-layer model by estimating more appropriate values for coefficients and by introducing interface stress to the model. We applied the improved two-layer model to the 1741 Oshima-Oshima tsunami to reproduce the tsunami heights from the Hokkaido coast to the Korean Peninsula in the Japan Sea.

(3) In the case of the two-layer model, the computed tsunami wave did not decay in spite of the short wave period, and the computed tsunami heights reproduced well the observed tsunami heights over the Japan Sea taken as a whole, but the reproducibility

of wave heights related to the directivity of the tsunami energy north of Oshima-Oshima is not as good.

(4) In case of the fault model, with which the two-layer model results were compared, calculation results showed that the computed tsunami heights reproduced well the observed tsunami heights for the near-source region, but the reproduced tsunami heights for the entire Japan Sea contained slightly more scatter.

References

Aida, I.(1974): Numerical computation of a tsunami based on a fault origin model of an earthquake. ZISIN 2nd series, Journal of Seism. Soc. Japan, Vol.27, pp.141-154 (in Japanese).

Aida, I.(1975): Numerical experiments of the tsunami associated with the collapse of Mt. Mayuyama in 1792. ZISIN 2nd series, Journal of Seism. Soc. Japan, Vol.28, pp.449-460 (in Japanese).

Aida, I.(1978): Reliability of a tsunami source model derived from fault parameters. J.Phys. Earth, Vol.26, pp.57-73.

Aida, I.(1984): An estimation of tsunamis generated by volcanic eruptions the 1741 eruption of Oshima-Oshima, Hokkaido -. Bull. Earthq. Res. Inst. Univ. Tokyo, Vol.59, pp.519-531 (in Japanese).

Ban, K., K. Takaoka and S. Yamaki (2001): Study of a tsunami source model of 1741 Kampo Oshima tsunami. Rep. Tsunami Eng. Res. Tohoku Univ.,Vol.15, pp.131-140 (in Japanese).

Fine, I. V., Rabinovich, A. B., Kulikov, E. A., Thomson, R. E. and Bornhold, B. D (1998): Numerical modeling of landslide-generated tsunamis with application to the Skagway Harbor tsunami of November 3, 1994. Proc. Tsunami Symp., Paris.

Fritz, H. M., Hager, W. H. and Minor, H. E. (2001): Lituya bay case: rockslide impact and wave run-up. Sci. Tsunami Hazards, Vol.19, No.1, pp.13-22.

Goto, C. and K. Sato (1993): Development of tsunami numerical simulation system for Sanriku coast in Japan. Report of the Port and Harbour Research Institute, Vol.32, No.2, pp.4-44 (in Japanese).

Harbitz, C. B (1992): Model simulations of tsunamis generated by the Storegga slides. Marine Geology, 105, pp. 1-21.

Imamura, F. and M. M. A. Imteaz (1995): Long waves in two-layers: governing equations and numerical model. Sci. Tsunami Hazards, Vol.13, No.1, pp.3-24.

Imamura, F. and Gica, E. C (1996): Numerical model for tsunami generation due to subaqueous landslide along a coast. Sci. Tsunami Hazards, Vol.14, No.1, pp.13-28.

Imamura, F (1998): Development of numerical simulation of tsunami in 15 years and outlook for future. Journal of Kaiyo, Extra edition, No.15, pp.89-98 (in Japanese).

Imamura, F. and H. J. Lee (1998): State - of arts of numerical simulation for generation and propagation of tsunamis. Bulletin of Coastal Oceanography, Vol.36, No.1, pp.91-101 (in Japanese).

Imamura, F. and T. Matsumoto (1998): Field survey of the 1741 Oshima-Oshima tsunami. Rep. Tsunami Eng. Res. Tohoku Univ.,Vol.15, pp.85-105 (in Japanese).

Imamura, F., D. Goto, Y. Shigihara, Y. Kitamura, T. Matsubara, K. Takaoka and K. Ban (2001): Fundamental study of the generation model of tsunami caused by a debris flow. Proc. 48th Conf. Coastal Eng., JSCE, pp.321-325 (in Japanese).

Imamura, F., S. Okubo, K. Ban, K. Takaoka, A. Sannomiya, S. Yamaki and E. Kobayashi (2003): Field investigation on the 1741 Kampo Oshima tsunami in Tsugaru peninsula, the northern part of Japan-Detailed survey with additional document "Tsugaru-han Okuni Nikki"-. Histrical Earthquakes, Vol.18, pp.166-175 (in Japanese).

Iwasaki, T. and A. Mano (1979): Two-dimensional numerical simulation of tsunami run-ups in the Eulerian description. Proc. 26th Conf. Coastal Eng., JSCE, pp.70-74 (in Japanese).

Jiang, L. and LeBlond, P. H (1992): The coupling of a submarine slide and the surface waves which it generates. J. Geoph.. Res., 97(C8), pp.12731-12744.

Jiang, L. and LeBlond, P. H (1993): Numerical modeling of an underwater Bingham plastic mudslide and the waves which it generates. J. Geoph. Res., 98(C6), pp.10303-10317.

Jiang, L. and LeBlond, P. H (1994): Three-dimensional modeling of tsunami generation due to a submarine mudslide. J. Phys. Ocean., 24, pp.559-573.

Matsumoto, T., K. Hashi, F. Imamura and N. Shuto (1998): Development of tsunami generation and propagation model by a debris flow. Proc. 45th Conf. Coastal Eng., JSCE, pp.346-350 (in Japanese).

Ming,D. and D. Wang (1993): Studies on waves generated by landslide. Proceedings of XXV Congress of IAHR, Technical Session C, pp.1-8.

Noda, E. (1970): Water waves generated by landslide. J. Waterways, Harbours and Coastal Engineering Div., Vol.96, No.WW4, pp.835-855.

Satake,K. and Y. Kato (2001): The 1741 Oshima-Oshima eruption : extent and volume of submarine debris avalanche, Geophys. Res. Lett., 28, pp.427-430.

Satake,K. (2001): Tsunami modeling from submarine landslides. Proceedings of the International Tsunami Symposium., pp.665-674.

Thomson, R. E., A. B. Rabinovich, E. A. Kulikov, I. V. Fine and B. D. Borhold (2001): On numerical simulation of the landslide-generated tsunami of November 3, 1994 in Skagway harbor, Alaska. Tsunami Research at the End of a Critical Decade, edited by G. T. Hebenstreit, Kluwer Acsdemic Pub., pp.243-282.

Togashi, H. and Y. Hirayama (1993): Hydraulic experiment on reapperance of the Ariake-kai tsunami in 1792. Proceedings of the IUGG/IOC International Tsunami Symposium, pp.741-754.

Tsuji, Y., T. Nishihata, T. Sato and K. Sato (1996): Distribution of heights of the tsunami caused by the 1741 Kampo eruption of volcano Oshima-Oshima, Hokkaido. Progr. Abst. Seismol. Soc. Japan, Vol.2, p.81 (in Japanese).

TSUNAMI RESONANCE CURVE FROM DOMINANT PERIODS OBSERVED IN BAYS OF NORTHEASTERN JAPAN

K. ABE

Niigata Junior College, Nippon Dental University,
Hamauracho 1-8, Niigata City, 951-8580, Japan

Seiche oscillations were observed under quiet sea conditions in 36 bays in the Sanriku district of northeast Japan from September 24, 2001 to August 11, 2002. A semiconductor pressure gauge was installed at quays in heads of bays to detect a water level for 6 hours with a sampling interval of 1 minute. Dominant periods were determined from the maximum levels in the amplitude spectra. The resulting dominant periods varied from 7 to 60 minutes, with an average of 25 minutes. Most of them corresponded to those of the fundamental mode. The dominant periods were correlated with amplification factors of tsunamis in the same bays using inundation heights observed in four large tsunamis: the 1896 Meiji Sanriku, the 1933 Showa Sanriku, the 1960 Chilean, and the 1968 Tokachi-oki tsunamis. The amplification factor was defined as the ratio of wave heights between head and mouth. The latters were obtained using a continuous function applied to half of inundation heights observed at the open coast. The amplification factors show a clear dependence on the dominant period, having the maximum levels at 12, 7, 47, and 28 minutes for the 1896, 1933, 1960, and 1968 tsunamis, respectively. These periods nearly coincide with dominant periods of 10, 9.8, 49, and 22 minutes observed at Ayukawa tide station for the 1896, 1933, 1960, and 1968 tsunamis, respectively. This verifies that the response curve from the space distribution is similar to the tsunami spectra from the time history. The amplification factors were plotted versus the tsunami periods normalized by the dominant periods of bays in a tsunami resonance curve. The tsunami resonance curve is a unified expression of tsunamis having the maximums at resonance periods. It was shown that the observed dominant periods are adequate for the resonance curve.
Key words: Resonance of tsunami, dominant period, seiche observations.

1 Introduction

The Sanriku coast of northeast Japan faces a subduction zone of the Pacific Plate and frequently experiences tsunamis. The ria coasts include many bays of various sizes. It is well known that these bays responded to the 1960 Chilean tsunami in a way different from that of the 1933 Sanriku tsunami. Kato et al. (1961) explained the different responses from different resonance periods for the two tsunamis. They plotted the

K. Satake (ed.), Tsunamis: Case Studies and Recent Developments, 97-113.

tsunami's amplification factor between the bay's mouth and head as a function of the seiche period and found a different period dependence. From their results they estimated resonance periods of 16 and 60-70 minutes for the 1933 Sanriku tsunami and the 1960 Chilean tsunami, respectively. Since there was little data regarding the seiche period observed in-situ, except for the data observed by Honda et al. (1908) and Takahashi (1934) at those times, it is reasonable that they must have depended on model calculations with some observed data. Thereafter Nakano and Unoki (1962) investigated seiches observed at tide stations in Japan. Aida et al. (1972) conducted observations at Onagawa and Ogatsu Bays. However, the recent development of a compact pressure gauge now allows to conduct in-situ observations easily. At the heads of bays there exist certain quays that are adequate for the observation of water level oscillation without horizontal movement. The observed dominant period is expected to explain the inundation heights much more completely than that obtained from calculations using a limited model. Moreover, in determining the incident wave height it is more accurate to use the inundation height observed at an open coast instead of inundation heights near the mouth, as observed in the bay by Kato et al. (1961).

2 Methods

2-1 FIELD OBSERVATION OF THE SEICHE

Water levels at a bay were measured under quiet sea conditions by means of a pressure gauge for 6 hours at a time interval of 1 minute. The gauge, having a length of 0.105 m, is made of a semiconductor and is protected from salt water with a titanium cover. It is combined with a recorder powered by a lithium battery with a cable of 30 m in length. The gauge was installed in a quay located at the head of a bay in order to observe the amplified oscillation. Water levels recorded on a memory chip were converted into the difference from mean water level during the recording time. The time series, filtered through a Hanning window, were decomposed into amplitude spectra using the Goertzel method. The spectra, being smoothed by a running average, were obtained in the frequency range of 0.06 to 2.4mHz (6.9 to 278 minutes in period). In this spectral analysis, a Nyquist frequency of 0.00833 Hz $=1/(2\times60)$ s^{-1} demands 2 minutes as the minimum period for the discussion. The recording length of 6 hours gives 360 minutes as a limit of the long period. Resolution of the spectral peak is 4.6×10^{-5} Hz from 1/(record length). This value is so small that we can discuss the difference of 0.1 minutes in the period. The data was processed by a microcomputer. The period at which the spectral amplitude was a maximum was taken to be the dominant period of the bay. This process was repeated for each location of pressure gauge installation.

2-2 AMPLIFICATION FACTOR OF TSUNAMI IN THE BAY

We examine four large tsunamis: the 1896 Meiji Sanriku tsunami, the 1933 Showa Sanriku tsunami, the 1960 Chilean tsunami, and the 1968 Tokachi-oki tsunami. After the events, surveys were conducted by Iki (1897) for the 1896 Sanriku tsunami, the Earthquake Research Institute (1934) for the 1933 Sanriku tsunami, Takahashi (1961) for the 1960 Chilean tsunami, and the Tsunami Research Group (1971) for the 1968 Tokachi-oki tsunami. The tsunami waves are amplified in comparison with those at the mouths of bays. To estimate an amplification factor of a bay being defined as a ratio of an amplified level to an initial level, we need data of the amplified level and the initial level at the mouth. The amplified level is the inundation height observed at the head and the initial level is the inundation height observed at the open coast near the mouth. The inundation heights had been indicated by spots measured on maps in these papers except for the case of the 1896 Sanriku tsunami. The inundation heights observed nearest to our observation point shown in these papers were estimated as the inundation heights as the amplified levels. In the case of the 1896 Sanriku tsunami, they were estimated on the heights observed at the hamlets nearest to our observation points.

Since the inundation height inside the bay is affected by the refraction, it is inadequate to use the data as the incident wave height. As shown in the 1992 Nicaraguan tsunami (Abe et al., 1993) the inundation heights along the flat coast is approximated with a smoothed curve with less deviation. Scattered distributions of the inundation heights observed on the open coast can probably be attributed to a variety of wave refraction effect along the complex coastal structure. Thus, we assume a continuous function to correct the observed inundation heights and apply it to the observed inundation heights at the open coast. As the continuous function we use a normal distribution function of probability and take distance as a parameter. First we determine the coefficients by applying the function to the inundation heights observed on the open coast. Second we assume the initial wave heights as half of the functional values, because of the doubly amplified wave height based on a total reflection. This normal distribution function is assumed along a meridian line instead of the real coastal line. The least square method is applied to determine the coefficients, and two coefficients of this function are estimated. In the application the origin is assumed to be the highest point on the open coast. Thus, incident wave height at a bay is estimated based on a distance of the mouth along the meridian line from the highest point. It is a symmetrical distribution of the distance from the point of the maximum value. The functions are independently determined for four tsunamis. In the case of 1968 tsunami two functions are separately applied to each monotonic decreasing region.

The amplification factor of a bay, defined as the ratio of the height at the head to one at the mouth, is plotted for the bay's dominant period. This is tsunami response

curve. Further, the tsunamis' representative periods are estimated from the dominant periods in the spectra of the tide gage records in this region and are used as the tsunami periods. The abscissa in a tsunami period relative to the bay's dominant period is taken for the amplification factor in the ordinate. This forms a tsunami resonance curve.

3 Observed dominant periods

The context of the observations is illustrated in Figure 1. The pressure gauge is kept 1-3 m below the surface using a weight. Figure 2 shows an example of the obtained records. The observation points are in Miyagi and Iwate prefectures of northeast Japan. The observation points and sources of the tsunamis used are shown in Figure 3. The observations were carried out intermittently for a period from September 24, 2001 to August 11, 2002. The observation points were chosen to cover almost all the bays and include ports at a concave coast with an ultra-short period on the Sanriku Coast. The resulting spectra are given in Figure 4. The dominant period ***Td*** taken from the spectra is the period showing the maximum amplitude except for the case of Noda Bay. In that bay a second maximum level was taken as the dominant period because of the isolated appearance in contrast with the unresolvable highest peak. The dominant period is classified into four groups according to a value of the period. That is, long period type (***Td*** $\geq$30 minutes), intermediate-period type (30 $>$***Td*** $\geq$15 minutes), short-period type (15 $>$***Td*** $\geq$10 minutes), and ultra short-period type (***Td*** $<$10 minutes). These classes are illustrated in Figure 5 and shown in Table 1. Names of observation points, the locations and times of the observations are listed in Table 2. The numbers of sample points are 14, 9, 8, and 5 for long, intermediate, short, and ultra-short period types, respectively. Large bays having cities at their heads such as Sendai, Kesennuma, Hirota, and Miyako are classified into the long period type. On the other hand, ports constructed at the tips of peninsulas such as Nesaki and Aneyoshi are classified as the ultra-short period type. It is evident that the average of 25 minutes is within a typical tsunami period. There are some exceptional cases with two observation points in the same bay. One of them is Samenoura Bay, which has two ports at the head. It is interesting to compare the dominant periods between them. Same dominant periods of 28 minutes were observed at Kamaishi and Heita in Kamaishi Bay. Slightly different dominant periods were observed at Yagawa (25 minutes) and Samenoura (21 minutes) in Samenoura Bay. Another example is Shizukawa Bay showing 47 and 42 minutes at Shizukawa and Oritate, respectively. A difference of 4 minutes is observed at Nonohama and Onagawa at Onagawa Bay. The isolated appearance of the spectral peaks leads us a clearly defined period and gives a stable dominant one, but the wavy one with no isolated peak leads us to an unclearly defined and unstable one. An example of the former is Shizukawa in Shizukawa Bay, and the latter is Niiyamahama.

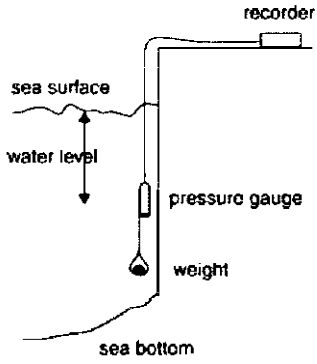

Fig. 1. Block diagram of pressure gauge installation.

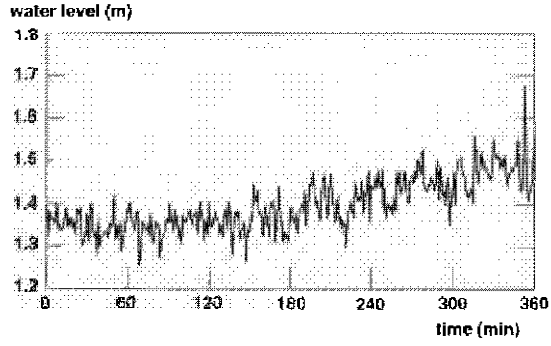

Fig. 2. Sea level observed at Onagawa in Onagawa bay.

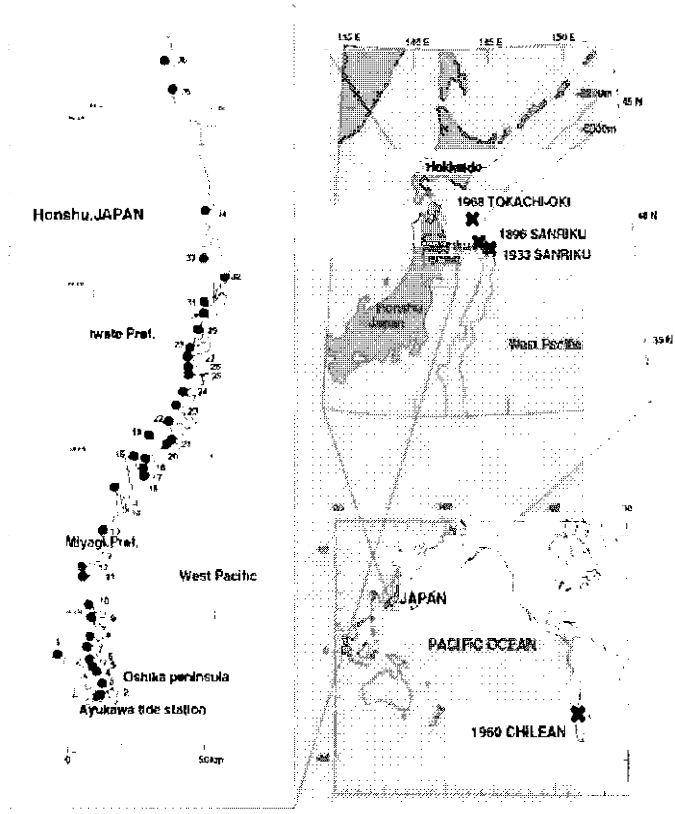

Fig. 3. Observation points shown with solid circle (left) and related tsunamis' sources with (right). Number of the observation points correspond with those of Figure 4 and Table 2.

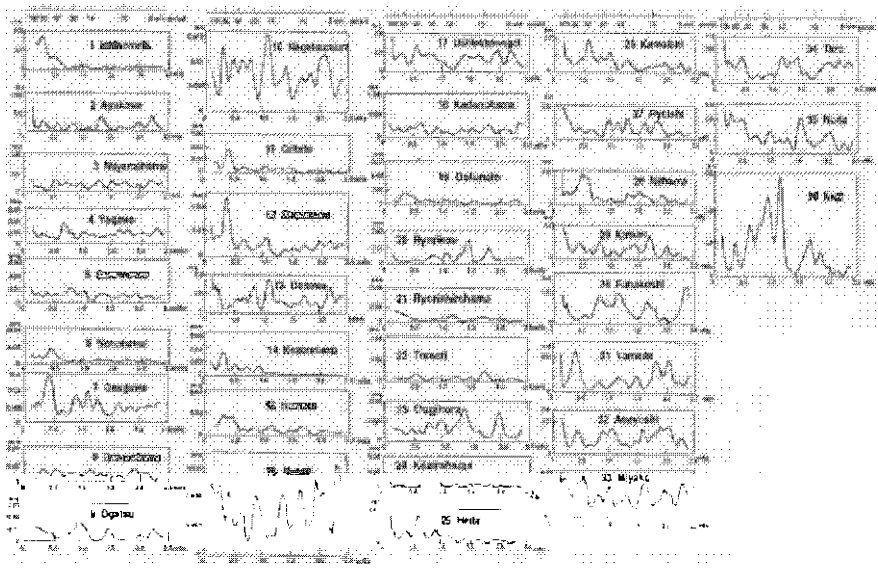

Fig. 4. Spectra of the seiche oscillations observed in bays.

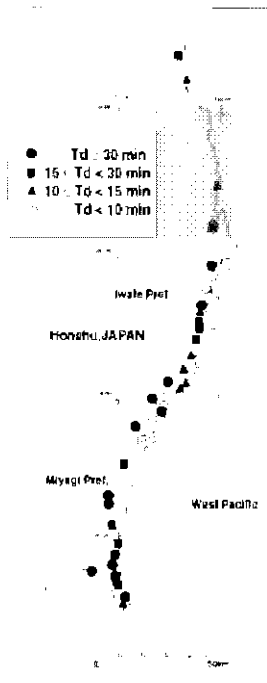

Fig. 5. Classification of bays according to the dominant period.

Table 1. Classification of observation points based on the dominant period ***Td***.

Long-period type	
Observation point	***Td***:min
Ishinomaki	60
Niiyamahama	30
Nonohama	37
Onagawa	41
Onmaehama	31
Oritate	42
Shizukawa	47
Kesennuma	52
Numata	52
Ushirohanagai	31
Oofunato	46
Nehama	35
Yamada	44
Akamae	30

Inter-mediate period type	
Observation point	***Td***:min
Yagawa	25
Samenoura	21
Ogatsu	18
Nagatsuraura	16
Oosawa	15
Kozirahama	19
Heita	28
Kamaishi	28
Kuzi	15

Short-period type	
Observation point	***Td***:min
Ayukawa	13
Ryorikou	12
Ryorishirahama	14
Tomari	10
Ougihora	12
Ryoishi	13
Taro	14
Noda	13

Ultra short-period type	
Observation point	***Td***:min
Nesaki	7
Kadonohama	7
Kirikiri	9.8
Funakoshi	7.1
Aneyoshi	8.8

4 Heights and periods of tsunamis

4-1 INCIDENT WAVE HEIGHT DISTRIBUTION

The inundation heights surveyed at bay heads and defined as h in meter are shown in Figure 6. Original inundation heights observed at open coast and the initial wave height as a in meters calculated on the assumed function are shown in Figure 7. The obtained formula representing incident wave height are as follows:

$a(x)=6.2\exp(-4\times10^{-11}x^2)$ for 1896 Sanriku tsunami

$a(x)=3.4\exp(-2\times10^{-11}x^2)$ for 1933 Sanriku tsunami

$a(x)=1.6\exp(-2\times10^{-12}x^2)$ for 1960 Chilean tsunami

$a(x)=2.7\exp(-8\times10^{-11}x^2)$ $x<120\times10^3$ m for 1968 Tokachi-oki tsunami,

$a(x)=2.2\exp(-1.0\times10^{-10}(x-202\times10^3)^2)$

$x\geq120\times10^3$ m for 1968 Tokachi-oki tsunami,

in which the relative distance x in m is taken from each different origin shown in the figure. At a distance $x=x_0$ in an arbitrary bay, incident wave height is obtained as $a(x_0)$. As for the case of the 1968 Tokachi-oki tsunami first one is for the maximum height around Miyako Bay and second one is for the maximum height around Oshika Peninsula. The critical distance between two is 120 km from the origin, that is a point of the first maximum. At the critical point we have a gap of the estimation of 0.16 m.

The amplitude is an indicator of the tsunami's scale in an open sea. The 1896 Meiji Sanriku tsunami is the largest of these four tsunamis and is about twice the height of the Showa Sanriku tsunami. The decreasing ratio in x direction is the smallest in the 1960 Chilean tsunami and is characteristic of a long period. For each bay the inundation height at the head, ***b***, and initial wave height at the mouth, ***a***, are listed in Table 3. From the pair we calculated the amplification factor as the ratio, ***b/a***.

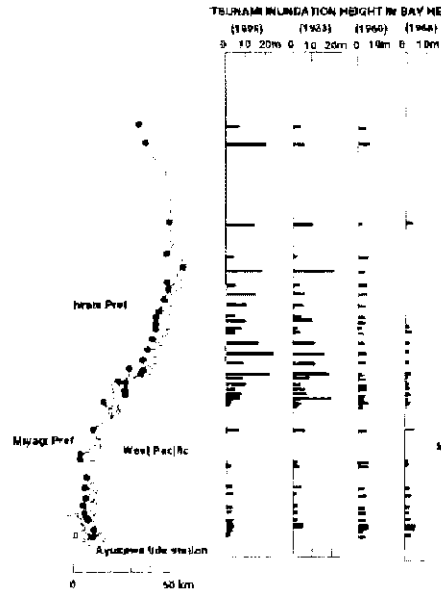

Fig. 6. Left to right inundation heights of tsunamis at the heads of bays after Iki (1897), E.R.I. (1934), Takahashi (1961), and T.R.G. (1971).

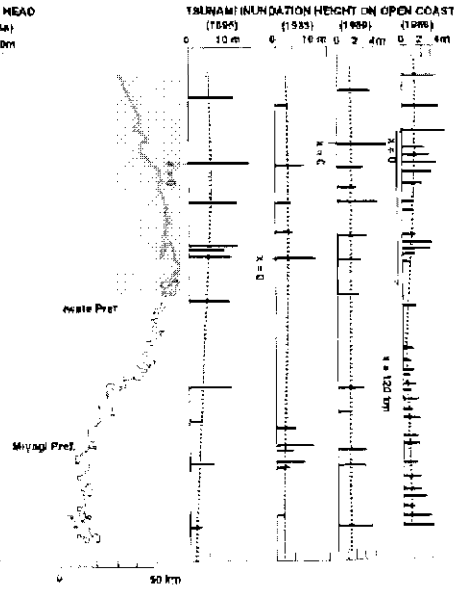

Fig. 7. Left to right inundation heights of tsunamis at the open coast after Iki (1897), E.R.I. (1934), Takahashi (1961), and T.R.G. (1971). Dotted lines are incident wave heights estimated. The origins are shown with 0 on x axes.

4-2 SPECTRA OF TSUNAMIS OBSERVED AT AYUKAWA TIDE STATION

The spectra of four tsunamis observed at the Ayukawa tide station are shown in Figure 8 (Abe, 2002). The periods of tsunamis ***Tt*** were determined based on the maximum levels, except for the 1960 Chilean tsunami. For the 1960 Chilean tsunami, the second maximum level is taken as the period because the maximum level's period of 81 minutes does not show any effect on small bays treated here. They are 10 minutes for the 1896 Sanriku tsunami, 9.4 minutes for the 1933 Sanriku tsunami, 49 minutes for the 1960 Chilean tsunami, and 22 minutes for the 1968 Tokachi-oki tsunami, respectively. The Ayukawa tide station is located at Ayukawa Bay 300m distant from the bay's head as shown in Figure 3.

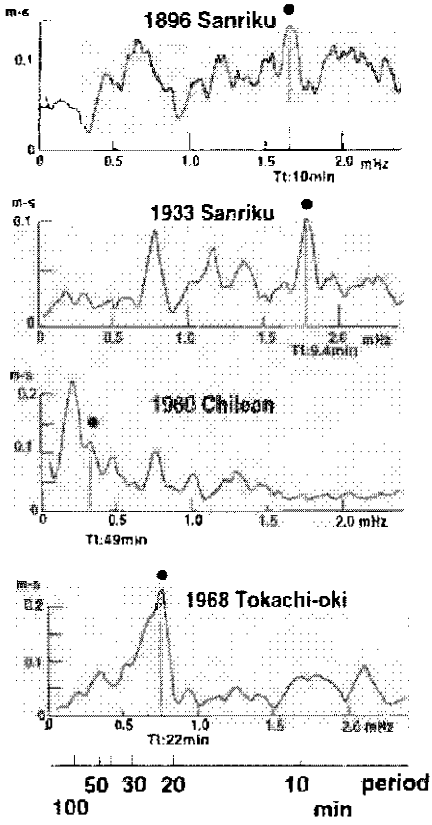

Fig. 8. Amplitude spectra of four large tsunamis observed at the Ayukawa tide station. After Abe (2002). Solid circles indicate periods assumed to be the dominant ones.

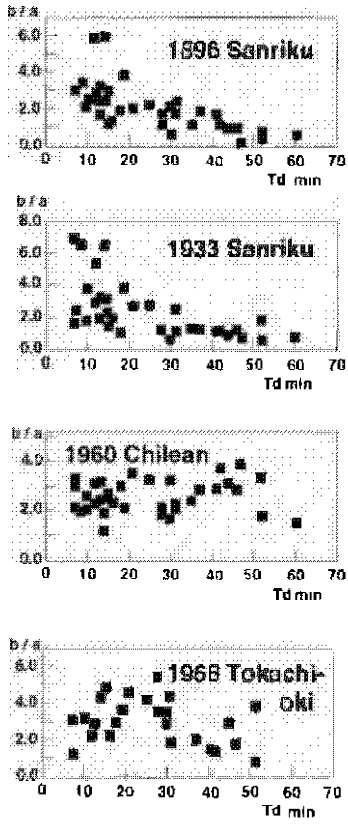

Fig. 9. Amplification factor (wave height ratio) b/a vs dominant period Td of the bay for each tsunami.

5 Tsunami resonance curve

The amplification factor is calculated at each bay for all the tsunamis except for the case of no data. It is plotted in the ordinate versus dominant period of a bay in the abscissa as shown in Figure 9. It is called tsunami response curve. As a result, the maximum ratios converge at 5-7 for three near tsunamis except for the 1960 Chilean tsunami, in which a smaller maximum of 4 is obtained. It is also pointed out that the ratios tend toward 1 at an infinity limit of the period. Maximum values in the ratios were observed at 12, 7, 47, and 28 minutes in the dominant periods for the 1896

Sanriku, 1933 Sanriku, 1960 Chilean, and 1968 Tokachi-oki tsunamis, respectively. These values are nearly equal to the dominant periods of 10, 9.4, 49, and 22 minutes in the tide gage records of Ayukawa shown in Figure 8. This fact suggest that the amplifications were generated with bay resonances of the tsunamis.

Finally, the response curves are summarized in Figure 10 using the normalized tsunami period at the abscissa, which is a ratio of tsunami period to the dominant period of each bay. The figure shows that the maximum amplification factor is obtained around a unit period. In the figure the amplification factors larger than 5 are found concentrated in a range of Tt/Td =1 0.34. These results show that tsunamis are amplified based on the period ratios in bays. This is a representative resonance curve. It is interpreted that the period ratio is an important parameter to control the amplification.

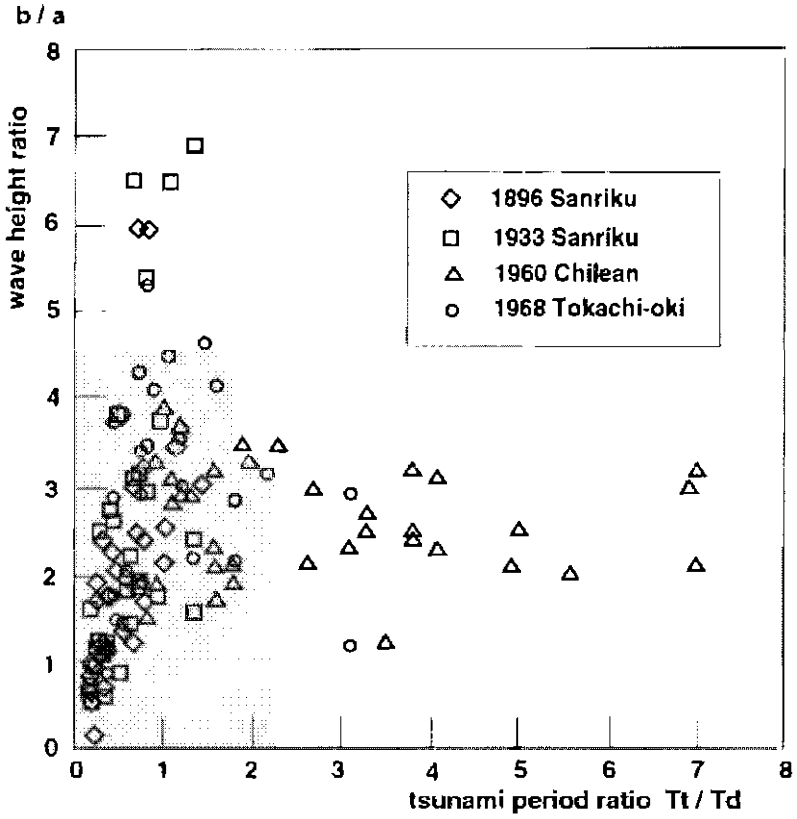

Fig. 10. Amplification factor b/a vs tsunami period normalized by dominant period Tt/Td The tsunami periods Tt are estimated in Figure 8.

6 Discussion

Honda et al. (1908) observed seiches at many bays all around Japan and showed dominant periods of 20.3 and 22.8 minutes at Ryoishi, 20.3 and 24.8-26.0 minutes at Kamaishi, 18.8-20.4 and 24.6 minutes at Toni, 18.5-20.1 minutes at Yoshihama, 27.5-29.9 minutes at Okirai, 18.3 minutes at Ryori, 12.8-16.8 and 36-39.1 minutes at Oofunato, 6.4-7.6 minutes at Niiyamahama, and 6.8-8.9 and 20.9-22.8 minutes at Ayukawa on the Sanriku Coast. Takahashi (1934) observed the seiche on the Sanriku Coast and recorded dominant periods of 2, 12, and 18 minutes at Ryori, 8 and 40 minutes at Oofunato, and 4,12, and 17 minutes at Kadonohama. Aida et al. (1972) also observed seiches and recorded 36 minutes at Onagawa, 17, 28, and 40 minutes at Ogatsu using spectral analysis. We observed seiches and obtained the dominant periods of 13, 28, 19, 12, 10, 14, 46, 7, 18, 41, 30, and 13 minutes for Ryoishi, Kamaishi, Toni, Yoshihama, Okirai, Ryori, Oofunato, Kadonohama, Ogatsu, Onagawa, Niiyamahama, and Ayukawa, respectively. In observing the difference between the former results and ours, we can find a relation between the difference and the spectral structure. Generally speaking the difference is large in the cases of multi-peak structure, for example, Niiyamahama, Tomari and Kadonohama. This fact suggests a difficulty of definitely identifying the dominant period in these bays. On the other hand the small differences are found in cases of single peak structure, for example, Kamaishi, Ryori, Onagawa. Miles and Munk (1961) studied excitations of seiches in harbors and described that the sharpness of resonant oscillation increases with increase of a ratio of the length to the entrance width. In our cases the single peak structure, or isolated peak structure, of the spectrum corresponds to one of spectrum at a bay having a large ratio of the length to the entrance width

Recently Abe (2003) checked a reproducibility of the dominant period at bays in Sado Island by recurrence observations. As the results dominant period of 13-14 minutes was observed two times for four trials at Ryotsu Bay, and one of 44-49 minutes was observed three times for four trials at Mano Bay. The latter one is much isolated in comparison with Ryotsu Bay. The isolated property of a bay is represented by separation of the bay from the outer sea in sea depth and coastal line. This result suggests that the isolation is a measure of the reproducibility. The spectra at Mano Bay is approximated as the single peak structure above described. This result proves a stable spectral structure in the isolated bay. Since many bays in Sariku Coast are much isolated, we can expect a high reproducibility of dominant period. But the appearance is realized not in a deterministic process but in a stochastic process. Accordingly the dominant period should be discussed as a statistical variable. It is a future problem to store dominat periods at the same bay in various conditions.

The seiche is a water wave excited in a limited topographic condition such as lake or bay. In them the longest fundamental mode is expected to be observed most easily because of a small energy loss. Most isolated peaks in the spectra probably correspond with fundamental modes. The period of the fundamental mode in a rectangular bay having a constant depth is approximated in a simple expression as

$$T_0 = 4l \ / \ (gh),$$

in which l is the length of the bay, h is the average sea depth, and g is the acceleration of gravity (e.g., Honda et al. 1908). For example, Shizukawa Bay has a rectangular shape. Approximating the bay by a rectangle with a length of 8.7 km, a width of 5.4 km, and a sea depth of 20 m as the average, we obtain a period T_0 of 41 minutes. Our observation showed values of 42 minutes at Oritate and 47 minutes at Shizukawa port, respectively, which coincide with the results of calculation within an error of 6 minutes. As for a bay having a complex shape, the fundamental mode is estimated based on numerical calculations. Aida et al. (1972) stated that the period of the fundamental mode is 40 minutes in Ogatsu Bay. Accordingly the dominant period observed in this bay, 18 minutes, is that of a higher mode. This fact shows that the observed predominant period includes the higher mode in addition to the fundamental mode. In the observations, bay length l is defined as a linear distance between the mouth and the head in each bay. Dominant period Td versus the length l is shown in Figure 11. A proportional relation shown in the figure suggests that the approximation formula of the fundamental mode is justified under the assumption of constant sea depth. When we apply the formula of fundamental mode to the observed data we obtain the sea depth of about 25m, which is consistent with the average sea depth of 26 meters in all the bays treated here. We also notice that there are some points deviating from the linear trend. It shows that they are not ones of fundamental mode or are obtained from bay with very shallow or very deep sea.

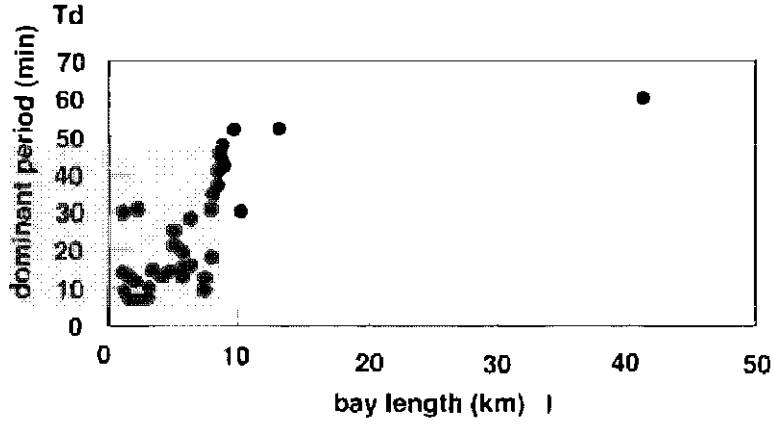

Fig. 11. Dominant period Td of bay vs length l of bay.

Nakamura (1961) theoretically treated the response curve of a bay to tsunamis. Assuming a rectangular bay having a uniform depth and neglecting viscosity, he obtained a dependence of amplitude at the bay's head on the period of an incident wave relative to the period T_0. He showed that the maximum amplitude relative to those of incident waves, depending on the number of crests and troughs contained in the incident wave packet, reaches 6 for 3 incident waves, and 4 for 2 in the resonance period. The maximum amplification factors distributing from 4 to 7 in our cases correspond to 2-3 incident waves. The numbers, not so distant from one, are reasonable ones in considering of an earthquake epicenter as the origin.

Resonance curves of second and third figures in Figure 9 correspond to that by Kato et al. (1961). From these figures we can determine the resonance periods of 9.8 and 49 minutes for the 1933 Sanriku and 1960 Chilean tsunamis, respectively. On the other hand, Kato et al. (1961) estimated the resonance periods as 16 and 60-70 minutes, respectively. These differences result from a different estimation of seiche period period. We obtained the periods at high inundation bays such as Toni, Yoshihama, Okirai, Ryori smaller than those of the same bays obtained by them.

Other data are available regarding the inundation heights of the 1896 Sanriku tsunami that were gathered by Yamana (Unohana and Oota, 1988). But his data is restricted to Iwate Prefecture and does not include that of Miyagi Prefecture, which is southern part of the Sanriku Coast. Accordingly we did not use it. The heights measured by Yamana tend to be larger than those of Iki (1897) in comparison with data obtained at the same hamlet (Hatori, 1995). Miyoshi (1987) indicated an underestimation of 22 m at Ryorishirahama obtained by Iki (1987) and proposed 38.2 m based on his own field survey. The extraordinary high wave resulted from the run-up along a valley. Such an extraordinarily large inundation height was also reported at Okushiri Island in Hokkaido nansei-oki tsunami on July 12, 1993. (e.g. Hokkaido Tsunami Survey Group, 1993; Shuto and Matsutomi, 1995). These extraordinarily high levels are characterized by a local topography such as a valley on land. Accordingly it is difficult to have direct explanation based on a bay oscillation. But the sea level increase occurs as the background of such an extraordinarily high level, arising from the amplification on the resonance of bay. The dominant period of Ryorishirahama, 14 minutes, was close to tsunami period of 10 minutes in the 1896 Sanriku tsunami, and the resonance period ratio was then 0.71. Shuto and Goto (1985) explained Iki's (1897) suggestion regarding the maximum level recorded at the shoreline, not at the maximum running-up point.

Table 2. Data list of the observation points. Left to right, number of observation points, the name, the bay's name, the location (latitude and longitude), starting time of the observation.

no	obs pt	bay	lat	lon	date, time(UT)
	name		d min	d min	y.m.d,h.m
1	Ishinomaki	Sendai	38-25	141-16	2002.8.11,21:20
2	Ayukawa	Ayukawa	38-18	141-31	2002.8.11,06:30
3	Niiyamahama		38-20	141-32	2002.8.10,23:45
4	Yagawa	Samenoura	38-22	141-30	2001.9.24,10:33
5	Samenoura	Samenoura	38-23	141-30	2001.9.24,04:05
6	Nonohama	Onagawa	38-23	141-28	2001.9.24,19:25
7	Onagawa	Onagawa	38-26	141-27	2001.9.25,02:25
8	Onmaehama	Onmae	38-28	141-29	2001.9.25,08:55
9	Ogatsu	Ogatsu	38-31	141-28	2001.9.25,20:08
10	Nagatsuraura	Oppa	38-34	141-29	2001.9.26,02:52
11	Oritate	Shizukawa	38-39	141-27	2001.9.26,19:25
12	Shizukawa	Shizukawa	38-40	141-27	2001.9.26,09:50
13	Oosawa	Koizumi	38-47	141-32	2002.8.10,02:02
14	Kesennuma	Kesennuma	38-54	141-35	2002.3.5,22:45
15	Numata	Hirota	39-00	141-39	2002.3.6,05:43
16	Nesaki		38-56	141-42	2002.8.10,09:40
17	Ushirohanagai	Oono	38-58	141-42	2002.3.6,12:25
18	Kadonohama	Kadonoham	39-00	141-43	2002.3.6,21:03
19	Oofunato	Oofunato	39-04	141-44	2002.3.7,03:35
20	Ryorikou		39-02	141-48	2002.3.7,10:08
21	Ryorishirahama	Ryori	39-03	141-49	2002.3.7,20:32
22	Tomari	Okirai	39-06	141-49	2002.3.8,09:29
23	Ougihora	Yoshihama	39-09	141-51	2002.3.8,20:32
24	Kozirahama	Touni	39-12	141-52	2002.3.9,02:59
25	Heita	Kamaishi	39-15	141-54	2002.7.26,08:30
26	Kamaishi	Kamaishi	39-16	141-53	2002.7.26,02:05
27	Ryoishi	Ryoishi	39-18	141-54	2002.7.25,19:38
28	Nehama	Ootsuchi	39-19	141-54	2002.7.25,08:54
29	Kirikiri	Funakoshi	39-22	141-57	2002.7.25,01:57
30	Funakoshi	Funakoshi	39-25	141-59	2002.7.24,19:26
31	Yamada	Yamada	39-28	141-57	2002.7.24,10:06
32	Aneyoshi		39-32	142-03	2002.7.26,20:03
33	Akamae	Miyako	39-35	141-58	2002.7.24,03:33
34	Taro	Taro	39-44	141-59	2002.7.23,20:36
35	Noda	Noda	40-07	141-50	2002.7.23,01:00
36	Kuzi	Kuzi	40-12	141-48	2002.7.23,05:30

Table 3. Data list of tsunami inundation heights. Left to right, number of observation points, inundation height at the bay head (***b***), incident wave height at the bay mouth (***a***) and the recurrence of ***b*** and ***a***.

no	b(1896)	a(1896)	b(1933)	a(1933)	b(1960)	a(1960)	b(1968)	a(1968)
	m	m	m	m	m	m	m	m
1	0.6	0.95	1.0	1.5	2.1	1.41		1.05
2	2.1	1.24	3.2	1.74	3.4	1.43		1.1
3	3.0	1.36		1.83	2.5	1.44	3.2	1.11
4	3.3	1.47	5.2	1.9	4.7	1.44	4.5	1.1
5	3.0	1.47	5.0	1.9	5.0	1.44	5.0	1.1
6	3.0	1.58	2.4	1.98	4.2	1.45	2.2	1.1
7	2.7	1.58	2.2	1.98	4.2	1.45	1.6	1.1
8	3.0	1.7	2.2	2.06	3.0	1.45	2.0	1.08
9	3.3	1.7	1.8	2.06	4.3	1.45	3.2	1.08
10	2.7	2.01	4.0	2.24	3.4	1.47	2.2	1.03
11	2.7	2.32	2.7	2.4	5.5	1.48	1.3	0.96
12	0.3	2.32	1.7	2.4	5.7	1.48	1.7	0.96
13	8.1	2.68	5.7	2.57	4.0	1.49	4.0	0.86
14	1.5	2.78	1.5	2.61	2.7	1.49	0.7	0.84
15	2.7	3.2	4.5	2.77	5.0	1.5	2.7	0.72
16		3.33	19.5	2.82	3.2	1.5	0.8	0.68
17	7.8	3.26	7.0	2.8	3.4	1.5	3.0	0.7
18		3.33	6.7	2.82	4.8	1.5	2.0	0.68
19	3.3	3.5	3.4	2.87	4.3	1.51	1.8	0.63
20	10.5	3.56	8.5	2.9	3.5	1.51	1.3	0.61
21	21.6	3.63	19.0	2.92	2.9	1.51	2.5	0.59
22	9.6	3.8	11.1	2.97	3.1	1.51	1.7	0.55
23	24.0	4.04	16.3	3.03	4.7	1.52	1.4	0.5
24	16.2	4.24	11.8	3.08	3.2	1.52	2.0	0.56
25	5.1	4.53	3.7	3.14	3.2	1.53	3.4	0.64
26	8.1	4.53	3.5	3.14	2.9	1.53	2.2	0.64
27	11.1	4.6	10.0	3.15	3.8	1.53		0.66
28	5.4	4.85	4.0	3.19	3.7	1.53		0.74
29	10.5	4.94	5.5	3.2	3.9	1.53		0.77
30	15.0	4.94	5.0	3.2	4.6	1.53		0.77
31	5.4	5.28	3.0	3.23	4.8	1.54		0.9
32	18.6	5.36	21.0	3.24	3.1	1.54		0.93
33	3.9	5.69	2.0	3.23	5.0	1.55	3.6	1.06
34	14.4	5.82	10.0	3.21	1.8	1.55		1.12
35	20.0	6.22	5.5	2.91	4.9	1.55		1.34
36	7.5	6.17	4.0	2.78	3.9	1.55		1.34

7 Conclusion

Seiches were observed at the heads of 36 bays on the Sanriku Coast of northeast Japan, and the dominant periods were determined based on the maximums of the spectral amplitudes. The dominant periods were interpreted in relation to the amplification of four large tsunamis in the bays. Obtained conclusions are as follows:

1. Amplification of tsunamis in bays is systematically explained from a tsunami resonance curve.
2. Dominant periods of bays obtained from observations of seiche oscillations are reasonable parameters to the resonance curve.
3. Periods of the resonance correspond with dominant periods in the tide gage records.
4. Incident wave heights interpolated from half inundation heights, which were observed on the open coast, lead to reasonable amplification factors.
5. Most of the observed dominant periods of bays are ones of fundamental modes.

Acknowledgements

Author is grateful to Mr. Fuminori Abe and local persons for helping to observe the seiche oscillations.

References

Abe,Ku., Ka. Abe, Y.Tsuji, F.Imamura, H.Katao, Y.Iio, K.Satake, J.Bourgeiois, E.Noguera and F.Estrada, Field survey of the Nicaraguan earthquake and tsunami of September 2, 1992. Bull. Earthq. Res. Inst, Univ. Tokyo, 68, 23-70, 1993 (in Japanese).

Abe,K., Observations of selective amplification of tsunamis to azimuth of the source, Sci. Tsunami Hazards, 20, 102-117, 2002.

Abe,K., Long wave measurements at bay-shaped coast using a pressure gauge (II) Mano and Ryotsu bay, Bull. Nippon Dental Univ., General Education, 32, 15-26, 2003.

Aida, I., T.Hatori, M.Koyama, H.Nagashima and K.Kajiura. Long-period waves in the vicinity of Onagawa bay ( )-Field measurements in Onagawa and Okachi Bays, J.Oceanogr.Soc.Jpn, 28, 207-219, 1972.

Earthquake Research Institute, Papers and reports on the tsunami of 1933 on the Sanriku coast, Japan, Bull.Earthq.Res.Inst.,Tokyo Imp. Univ.,Suppl. 1,1934.

Hatori,T., Investigation of data of the 1896 Meiji Sanriku tsunami in the coast of Iwate Prefecture, Rep. Tsunami Engineering, Faculty of Engineer., Tohoku Univ., 12,59-65,1995 (in Japanese).

Hokkaido Tsunami Survey Group, Tsunami devastates Japanese coastal region, EOS, Trans. AGU 74, 417-432, 1993.

Honda, K., T.Terada, Y, Yoshida and D.Isitani, An investigation on the secondary undulations of oceanic tides, Jour.Coll.Sci., Imp.Univ.Tokyo, 24,1-113, 1908.

Iki,T., A report of the field investigation of the tsunami of 1896 in the Sanriku District, Shinsai Yobo Chosakai Hokoku,11,5-33,1897 (in Japanese).

Kato, Y., Z.Suzuki, K.Nakamura, A.Takagi, K.Emura, M.Ito and H.Ishida, The Chile tsunami of 1960 observed along the Sanriku coast of Japan, Sci. Rep. Tohoku Univ.,Ser.5,Geophys., 13,107-125,1961.

Miyoshi,H., True run-up heights reached by the huge tsunami of 1896, J.Oceanogr.Soc.Jpn, 43, 159-168, 1987.

Miles,J. and W.Munk, Harbor paradox, J. Waterways and Harbors Div., Proc. ASCE, 87, WW3, 111-130,1961.

Nakamura,K.,Motion of water due to long waves in a rectangular bay of uniform depth, Sci. Rep. Tohoku Univ.,Ser.5, Geophys., 12,191-213,1961.

Nakano,M. and S.Unoki, On the seiches(the secondary undulations of tides) along the coasts of Japan, Records of Oceanographic Works in Japan, (special Number 6), 169-214, 1962.

Shuto, N., and C.Goto, Survey report of trace heights in big Sanriku tsunamis-Okirai bay- , Rep. Tsunami Engineering, Faculty of Engineer., Tohoku Univ.,2,46-54,1985 (in Japanese).

Shuto, N., and H.Matsutomi, Field survey of the 1993 Hokkaido nansei-oki earthquake tsunami, PAGEOPH, 144, 649-663,1995.

Takahashi,R., Seiches and surface waves in Ofunato bay and two other bays, Bull. Earthq. Res. Inst., Suppl.1, 198-217,1934.

Takahashi,R., Report on the Chilean Tsunami of May 24, 1960 as observed along the coast of Japan, edited by Field Investigation Committee for the Chilean Tsunami, 171-191, 1961 (in Japanese).

Tsunami Research Group, Analyses of the tsunami accompanying the Tokachi-oki Earthquake of 1968, General Re. Tokachi-oki Earthquake of 1968,Keigaku Shuppan,153-188,1971.

Unohana,M., and T.Oota, Disaster records of Meiji Sanriku tsunami by Soshin Yamana, Rep. Tsunami Engineering, Faculty of Engineer., Tohoku Univ.,5,57-379,1988 (in Japanese).

DELAYED PEAKS OF TSUNAMI WAVEFORMS AT MIYAKO FROM EARTHQUAKES EAST OFF HOKKAIDO

Y. NAMEGAYA AND Y. TSUJI

Earthquake Research Institute, the University of Tokyo,
Yayoi 1-1-1, Bunkyo-ku, Tokyo, 113-0032, Japan

In the records of tsunami waves observed at Miyako, Sanriku Coast, Japan, there sometimes appears a tendency that after the initial wave arrival, tsunami waves once become attenuated, and the eminent peak suddenly appears in the cases of tsunamis generated in the sea region east off Hokkaido. This eminent peak is called the delayed peak of the tsunami wave. To clarify the causes of this delayed peak, we carried out numerical experiments on tsunami propagation. As a result, we found out that the cause of the delayed peak of the tsunami is the superposition of waves traveled two different routes. One is the route in which the tsunami wave directly reflects at Shimokita Peninsula from the tsunami source, and transfers into an edge wave mode. The other is the route in which the direct wave reflects at south coast of Hokkaido, propagates to Shimokita Peninsula, and transfers to the edge wave mode at Shimokita Peninsula. Because these two components, which run along quite different routes, arrive at Miyako at almost the same time, the heights of the delayed peaks sometimes exceed those of the initial waves.
Key words: Delayed peak of tsunami, edge wave, reflected wave, Shimokita Peninsula, Hokkaido, numerical experiment.

1 Introduction

Delayed peaks are often observed at Miyako tidal station, the Sanriku Coast, north-eastern Japan, when tsunamis are generated by earthquakes that occurred in the sea region east off Hokkaido. For example, we find on recorded paper in the case of the 1973 Nemuro-Hanto-Oki earthquake, that after the initial tsunami wave, it seems to attenuate once, and an eminent peak appeared 2.6 hours after the initial wave arrival. The height of the peak exceeded the initial wave. Hereafter, we call this peak as the delayed peak of the tsunami wave or the delayed peak.

Generally, the causes of the delayed peaks of tsunami waves can be considered that after the initial wave arrival, the arrival of reflected waves at many coasts and/or the edge waves is delayed at the observation. Studies on the reflected waves and edge waves are discussed by Ball (1967), Fuller and Mysak (1977), Abe Ku. and Ishii (1983), Watanabe (1985), González et *al.* (1995) among others. Fuller and Mysak (1977) considered the edge waves along the northeast coast of Japan between Miyako

K. Satake (ed.), Tsunamis: Case Studies and Recent Developments, 115-134.

and Sendai Bay with using the constant sea depth and the Gaussian-random irregularized coastline. Abe Ku. and Ishii (1983) discussed the propagation of the edge wave accompanied by the tsunami generated by the 1952 Kamchatka earthquake. Watanabe (1985) discussed the characteristics of edge waves, and classified them into four types. Moreover, he pointed out that an eminent delayed peak appeared on the record at Kushiro in the case of the 1952 Kamchatka tsunami.

In the present study, we developed the discussion on the causes of the delayed peaks, considering the reflected and edge waves for the cases of the 1973, 1969, and 1994 earthquakes.

In section 2, we introduce three examples of the delayed peaks accompanying the tsunamis of the 1969 Hokkaido-Toho-Oki, the 1973 Nemuro-Hanto-Oki, and the 1994 Hokkaido-Toho-Oki earthquakes. In section 3, we discuss the fault parameters of the earthquake, governing equations of tsunami propagation, method of numerical calculation, and some boundary conditions of the 1973 earthquake. We confirm that the calculated tsunami wave also reproduced the delayed peak in section 4. In section 5, we develop the discussion on the formation of the delayed peak. In section 6, we consider the propagating routes of the reflected wave and mode transfer from direct wave into edge wave, and its role in forming the delayed peak. In section 7, we confirm whether or not the delayed peaks generated by other earthquakes (1969 and 1994) are applicable to the 1973 earthquake.

The conclusion of this paper may contribute to planning for disaster mitigation related to tsunamis on the Sanriku Coast.

2 The delayed peak generated in the sea area east off Hokkaido

As already mentioned, delayed peaks of tsunami waves were sometimes observed at the tidal station on the Sanriku Coast; the Pacific coast of northeastern Honshu. In this section, the following three events are given as examples: the 1969, 1973, and 1994 earthquakes (see Figure 1).

The 1969 Hokkaido-Toho-Oki earthquake occurred on 12th August, 1969, and the JMA (Japan Meteorological Agency) magnitude was 7.8 (see Table 1). Its epicenter was located 50 km east off the Nemuro Peninsula and the focal depth was 30 km. The earthquake was accompanied by a small tsunami, which was observed on the Pacific coast of eastern Hokkaido and Honshu Island, where slight damage occurred. The tsunami magnitude on the Imamura and Iida scale m was estimated to be 1.

A delayed peak was recorded at Miyako tidal station (see the upper figure of Figure 2). The initial wave with a height of 28 cm appeared about one hour after the main shock (A), and after the initial wave train the amplitude of the tsunami gradually attenuated with elapse of time until 2.6 hours after the initial wave arrival (B).

However, an eminent peak (C) suddenly appeared at about 2.6 hours after the arrival of the initial wave. It had a height of 29 cm, which exceeds that of the initial wave.

The tidal records of the tsunamis of the 1973 Nemuro-Hanto-Oki and the 1994 Hokkaido-Toho-Oki earthquakes at Miyako are shown in the center and lower graphs in Figure 2, respectively. The delayed peaks appear in both records. In the case of the 1973 earthquake, the peak (41 cm) of the delayed peak appears at 2.6 hours after the initial wave arrival (31 cm), and the amplitude of the waves is attenuated once. The delayed peak wave is also higher than that of the initial wave in this case. In the case of the 1994 earthquake, the peak (50 cm) of the delayed peak also appears at 2.6 hours after the initial wave (65 cm) arrival.

As can be seen from these three examples, the delayed peak is generally recorded on the Sanriku Coast by tsunamis generated in the sea region eastern off Hokkaido Island. In the present study, we try to clarify why such a delayed peak appears. So, we carry out a numerical experiment on tsunami propagation for the case of the 1973 earthquake.

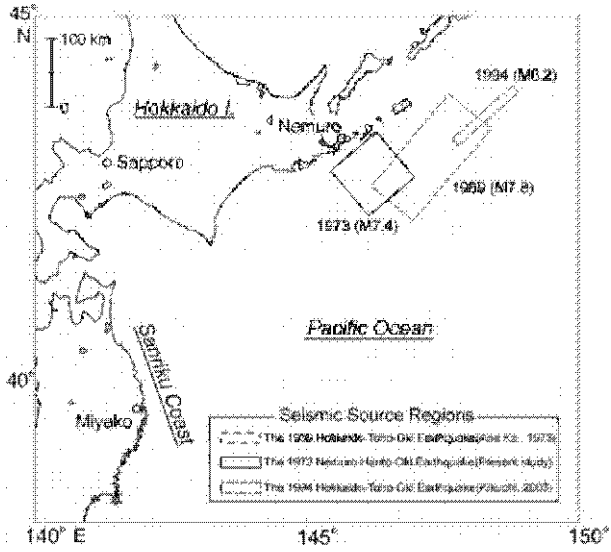

Fig. 1. Locations of the source regions of the earthquakes generated in the sea region east off Hokkaido. The broken and chain rectangles show the faults of the 1969 and 1994 Hokkaido-Toho-Oki earthquake derived from Abe Ka. (1973) and Kikuchi (2003), respectively. The black rectangle shows the faults of the 1973 Nemuro-Hanto-Oki earthquake derived from the present study.

Table 1. Properties of three earthquakes generated in the sea region east off Hokkaido.

Earthquake	Epicenter	Depth	M	m
1969 Hokkaido-Toho-Oki	147.62° E 42.70° N	30 km	7.8	1
1973 Nemuro-Hanto-Oki	145.95° E 42.97° N	40 km	7.4	1
1994 Hokkaido-Toho-Oki	147.68° E 43.37° N	56 km	8.2	2

M – JMA magnitude. *m* – tsunami magnitude in the Imamura and Iida scale.

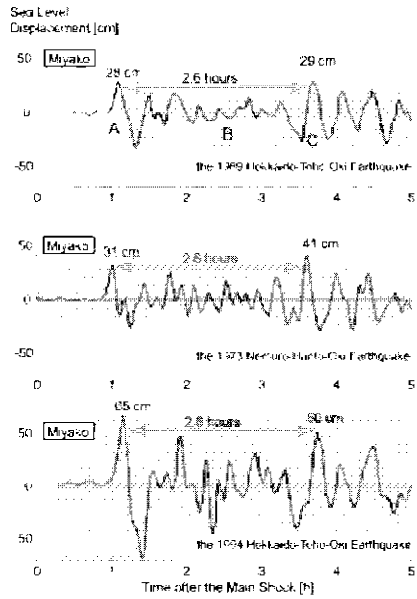

Fig. 2. Tidal records at Miyako station of the tsunamis of the 1969, 1973, and 1994 earthquakes. The component of the astronomical tide is removed. Symbols A-C mean the remarkable points of this tsunami; A: the initial wave at Miyako, B: attenuated tsunami wave, C: the delayed peak.

3 Numerical calculations for The 1973 Nemuro-Hanto-oki earthquake tsunami

To clarify the physical reasons why the delayed peaks appear on the record of tsunamis of eastern Hokkaido earthquakes obtained at tidal stations on the Sanriku Coast, we carried out a numerical experiment on tsunami propagation. In this section, we explain the governing equations for tsunami propagation and the methods of the numerical calculations.

3.1 FAULT PARAMETERS

The fault parameters of the 1973 earthquake were first estimated by Shimazaki (1974), who considered the distribution of aftershocks and crustal deformation of the coastal area of Nemuro Peninsula (see Figure 3). Aida (1978) revised the fault parameters by taking into account the form of the initial and second peaks of the tsunami observed and calculated at several tide stations. We tested the fault parameters given by these two authors. As a result, it was found out that, in the case of Shimazaki's (1974) parameters, the period of the tsunami waves calculated for Kushiro is shorter than the actually recorded ones. We also found out that, using Aida's (1978) parameters, the

calculated initial wave forms at Hachinohe and Miyako do not fit well with actually observed ones.

We therefore revised the fault parameters given in Table 2. Figure 4 shows the distribution of the vertical displacement of the crustal motion given by our fault parameters, which was obtained by using the method of Mansinha and Smylie (1971). We find that the amount of subsidence at Hanasaki is about 5 cm, which coincides with that estimated by Tada (1974), who obtained this value by analyzing the tidal record at Hanasaki.

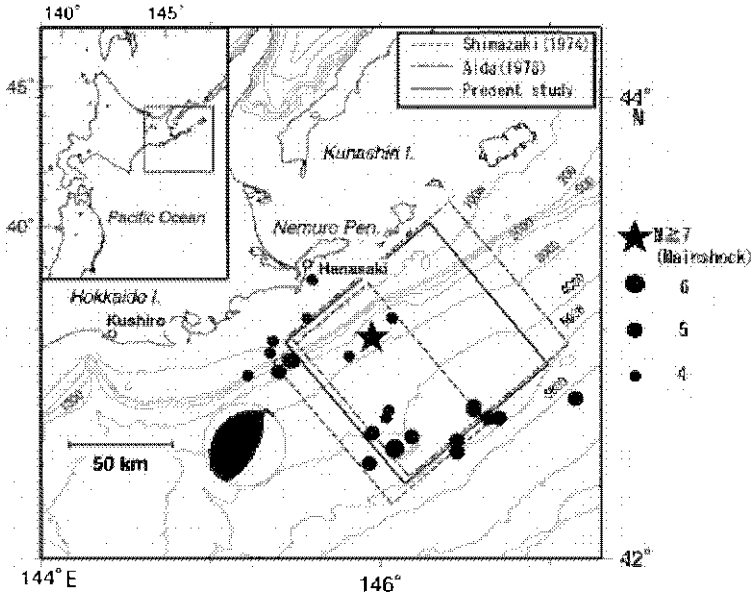

Fig. 3. The source regions of the 1973 Nemuro-Hanto-Oki earthquake. Solid circles show the aftershocks within 24 hours after the main shock (JMA, 1973). Three rectangles show the fault models proposed by Shimazaki (1974) (broken line), by Aida (1978) (chain line), and by the present study (black line). The focal mechanism of the main shock proposed by Shimazaki (1974) is also shown.

Table 2. Fault parameters of the 1973 Nemuro-Hanto-Oki earthquake.

	N	E	d	θ	δ	λ	L	W	U
Shimazaki (1974)	42.59	146.63	2.3	230	27	111	60	100	160
Aida (1978)	42.94	147.11	1	230	27	101	100	100	96
present study	42.85	146.99	1	230	27	111	90	100	120

N = latitude (degree), E = longitude (degree), d = depth (km), θ = strike angle (degree), δ = dip angle (degree), λ = rake angle (degree), L = length (km), W = width (km), U = displacement (cm).

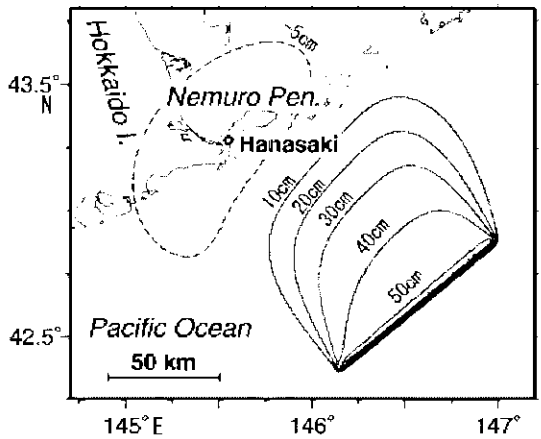

Fig. 4. Distributions of crustal upheaval and subsidence of the sea bed for the case of the fault parameters given by the present study (the third line of Table 1) with using the method of Mansinha and Smylie (1971). Sea surface displacement is assumed to take the same form as that of the sea bed at the main shock.

3.2 GOVERNING EQUATIONS

We neglect viscosity, sea bottom friction, and rotation of the Earth. We assume a linear long wave approximation. We consider the curvature of the Earth's surface, so we introduce a spherical coordinate system.

The conservation of mass is expressed by the following equation as,

$$\frac{\partial \eta}{\partial t} \quad \frac{1}{R\cos\phi}\left\{\frac{\partial Q_\lambda}{\partial \lambda} \quad \frac{\partial\left(Q_\phi \cos\phi\right)}{\partial \phi}\right\} \qquad (1),$$

where t, λ, ϕ, and R denote time, longitude, latitude, and radius of the Earth, respectively. η is the vertical displacement of the sea surface from the mean sea level. Q_λ and Q_ϕ are the flow amounts in λ and ϕ directions, and are defined as,

$$Q_\lambda = \int_{bottom}^{surface} u dz = (D+\eta)u \qquad (2),$$

$$_{\phi} = \int_{bottom}^{surface} v dz = (D+\eta) \qquad (3),$$

where D is the depth of the sea, and u and v are the velocity of the water particle in λ and ϕ directions, respectively.

The equations of motion are

$$\frac{\partial Q_\lambda}{\partial t} = -\frac{g(D+\eta)}{R\cos\phi}\frac{\partial \eta}{\partial \lambda} \qquad (4),$$

$$\frac{\partial Q_\phi}{\partial t} = -\frac{g(D+\eta)}{R}\frac{\partial \eta}{\partial \phi} \qquad (5),$$

where g is the acceleration of gravity.

3.3 CONDITIONS UNDER NUMERICAL CALCULATIONS

We rewrite the governing equations (1), (4), and (5) as difference equations and carry out the numerical calculations by the leap-frog method. The area for the numerical calculations is shown in Figure 5, and covers the region from 140°E to 150°E in longitude and from 35°N to 45°N in latitude. The sizes of the north and the south boundary are 785 km and 910 km, respectively. The sizes of the western and the eastern boundaries are 1111 km. The area is covered by a grid mesh with intervals of 30 seconds in both directions to apply to the difference equations. The sizes of the four sides of one grid mesh square are 926 m in latitude and 655 - 759 m in longitude.

We should consider two kinds of boundary condition. One is the coastal boundary at which the flow amount Q is artificially given as zero. The other is the open boundary of the calculated area. We should give Q a value at which the waves travel outside naturally.

For the initial condition, we calculate the displacement of the sea bed given by Mansinha and Smylie (1971), assuming the fault parameters of length, width, displacement, strike, rake, and dip as shown in Table 2. We can set the initial value of the sea surface displacement as having the same shape as the displacement of the sea bed (Aida, 1974).

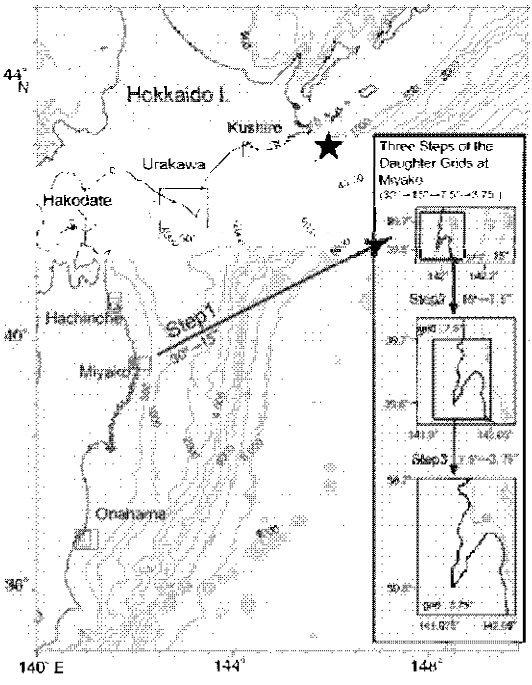

Fig. 5. The area for the numerical calculation.
The rectangles show the areas of the finer grids.

To perform the calculation in a stable and reasonable way, we should consider the CFL (Courant Friedrics Lewy) condition given by the following formula,

$$\frac{\Delta l}{\sqrt{2gD_{\max}}} > \Delta t \qquad (6),$$

where Δl and Δt denote the intervals of grids and time, respectively. $D_{\max}$ is the greatest sea depth in the calculated area. In the present study we select time step Δt to be one second, which satisfies the condition (6).

3.4 SEA REGIONS CLOSE TO TIDE GAUGE STATIONS

Tidal records of the tsunami of the 1973 Nemuro-Hanto-Oki earthquake were obtained at the six stations illustrated in Figure 5. Tide gauge stations are generally situated on coastlines, and the mouths of the intake tube open at points with a depth of several meters. In such a shallow area, the length of the tsunami wave becomes shorter. Shuto (1986) pointed out that if we want to keep calculations of the tsunami propagations accurate, more than 20 grid points are needed for one wave length to express wave shape. So, we need a finer mesh system at six points of the tide gauge stations as shown on Figure 5 to calculate tsunami propagations accurately, because we should compare the time series between the tide gauge records and the calculations. The connections of the flow amounts between the coarse and fine mesh regions are referred to in the method by Aida (1978).

In addition, we replaced the sea depth of less than 50 m with just 50 m in the numerical calculation to maintain numerical stability. The wave heights of the numerically calculated one are considered to be smaller than the actually recorded ones, because the depths of the tide gauge stations are generally about 2 - 5 m. So, amplification in the sea area shallower than 50 m is not reproduced in our calculation. To compensate for the amount of amplification, we apply Green's Law as shown below,

$$\eta_{TG} = K_s \cdot \eta_{50}, \quad K_s \equiv \left(\frac{50}{D_{TG}} \right)^{1/4} \qquad (7),$$

where η_{TG} is the corrected wave height, η_{50} is the calculated wave height, and D_{TG} is the depth at the intake tube of the tide gauge station. The compensation coefficients K_s at the 6 tidal stations are shown in Table 3.

Table 3. Compensation coefficients

	Kushiro	Urakawa	Hakodate	Hachinohe	Miyako	Onahama
D_{TG}[m]	3	2	5	4	5	5
K_s	2.0	2.2	1.8	1.9	1.8	1.8

D_{TG} = the depths at the intake tube of the tide gauge station, which are estimated from the chart. Ks = compensation coefficients as are defined relation (7).

4 The delayed peak of the 1973 Earthquake in the numerically calculated results

The results of the numerical calculation for the tsunami propagation of the 1973 Nemuro-Hanto-Oki earthquake tsunami are shown in Figure 6. The broken lines show the observed sea surface changes and the solid lines are those calculated. We can recognize the good agreement of the calculated arrival times of the initial waves with those of the observed ones. We can also point out that the calculated amplitudes of the initial waves agree well with those of the observations; for example, at Kushiro, the observation is 39 cm and the calculation is 33 cm; at Urakawa, the observation is 15 cm and calculation is 12 cm; at Miyako, the observation is 31 cm and the calculation is 23 cm. In addition, we can note that the fact that the amplitudes at Hakodate and Onahama are relatively small compared to those of the other stations is also reproduced well by our numerical calculation. These facts show that the fault parameters of the present study are reasonable. Moreover, we should note that the delayed peak also appears at Miyako in the calculated result (A in Figure 6).

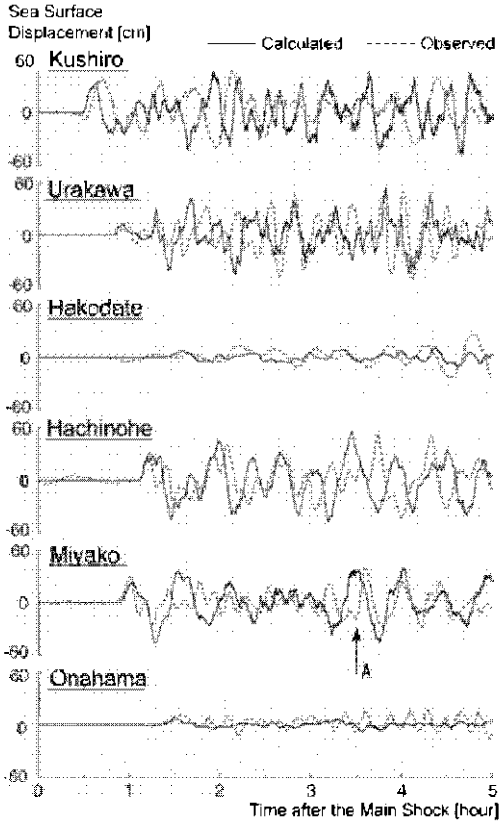

Fig. 6. Numerically calculated water level changes (solid lines) with observed records (broken lines) at 6 stations on the Pacific coasts of Hokkaido and the northern part of Honshu.

The delayed peak of the numerically calculated result at Miyako (A in Fig. 6) appears about 5 minutes earlier than that of the observed result. This discrepancy of appearance times between the calculated and the observed peaks is caused because we replaced the sea depth shallower than 50 meters with just 50 meters in the numerical calculated mesh and so the numerically calculated peak reached apparently faster than that of the observed one.

5 Cause of the delayed peaks

5.1 ANALYTICAL METHOD FOR CLARIFYING FORMATION OF DELAYED PEAK

In the previous section, it was clarified that the delayed peak observed at Miyako is reproduced numerically. The cause of the delayed peak at Miyako is considered that, after the arrival of the initial wave, which traveled along the minimum direct path, another wave component(s) that was (or were) reflected off the coast of another district(s) reached Miyako coast 2 - 3 hours after the initial direct wave. Moreover, we can consider the other possibility that some wave components reached the neighboring coast of Miyako, and were transformed into an edge wave, which slowly propagated toward Miyako. To confirm these possibilities, we made an animation of the propagation of the tsunami. The animation showed that the tsunami wave reflected on the Shimokita Peninsula and the Pacific coast of Hokkaido remarkably, and then the edge wave seemed to appear on the continental shelf regions of Sanriku coast (as for the discussion of forming of the edge wave, see Appendix).

By the way, we assume that we made the numerical calculation of tsunami propagation by fictionally removing coast "A". If we obtained the result that the delayed peak still exists, then we can judge that coast A does not play an important role in the mode transfer. In contrast, if we remove another coast "B" and find the delayed peak has disappeared, then we can judge coast B plays an important role in the mode transfer.

In this section, we therefore make numerical calculations for three cases:

1) Case with Shimokita Peninsula removed,
2) Case with Hokkaido coast removed,
3) Case with both Shimokita Peninsula and Hokkaido coast removed.

Here, the phrase "Removing Coast" means that the real coast and the land behind the coast are replaced with a flat sea of 50 m in depth. The initial incident wave will pass freely through the coastline as if there were no barriers and no mode transfer takes place there (see Figure 7).

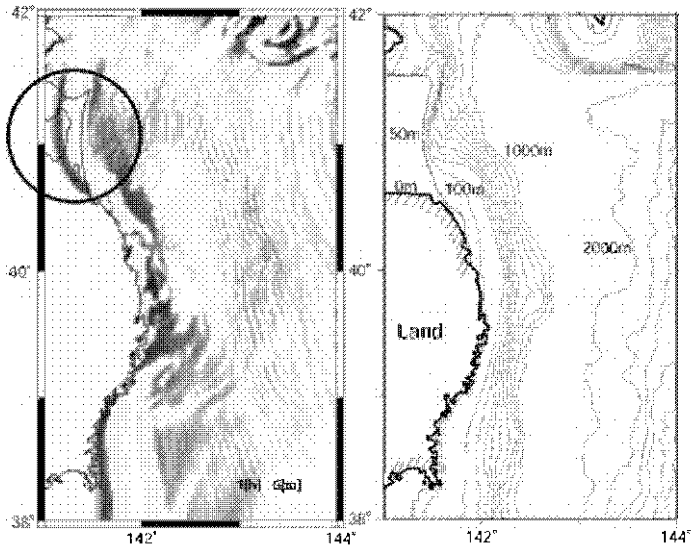

Fig. 7. (a) Snap-shot of tsunami-propagating simulation for the case with Shimokita Peninsula removed at 1 hour and 9 minutes after the main shock. Notice that the tsunami front is passing through the coastline of Shimokita Peninsula. (b) The contour map of the sea depth in the case of Shimokita Peninsula removed. We can see the depth of Shimokita Peninsula is artificially replaced with the flat bed of 50 m depth.

5.2 THE EFFECTS OF SHIMOKITA AND HOKKAIDO COASTS

5.2.1 *The Effect of Shimokita Coast*

Figure 8 shows the result of the numerical calculation for the sea level change at Miyako when the Shimokita coast is removed (solid line). The broken line shows the result for the actual coast. The lower figure shows the observed record. We can see that the height of the delayed peak (arrow A in Figure 8) decreases to 20 cm, while that of the peak is 36 cm for the actual coast; that is, the delayed peak decreases 44% from that of the case without removal. This means that the Shimokita coast contributes remarkably to forming the delayed peak at Miyako.

5.2.2 *The Effect of Hokkaido Coast*

Figure 9 shows the result of the numerical calculation of the sea level change at Miyako for the case of removing the Hokkaido coast. The meaning of each line is the same as in Figure 6. Here, we can see that the height of the delayed peak (arrow B in Figure 9) decreases to 32 cm, while that of the peak is 36 cm for the actual coast; that is, the delayed peak decreases 10% from that of the case without removal. Although the effect of Hokkaido coast for the delayed peak is milder than that of Shimokita coast, the Hokkaido coast makes a smaller contribution than Shimokita Peninsula.

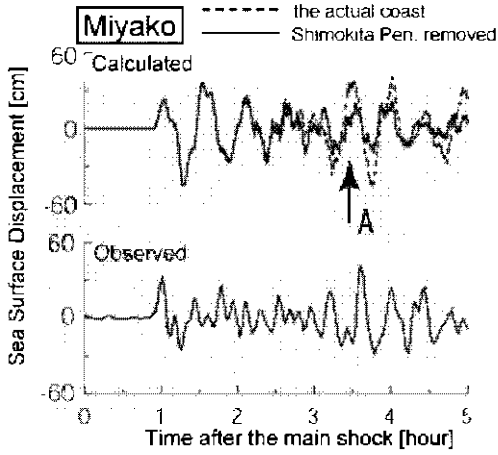

Fig. 8. Numerically calculated water level changes at Miyako in the case with Shimokita Peninsula removed (solid line in the upper figures), and that of the case of the actual coast (no land removed) (broken line). Point A shows the appearance time of the delayed peak.

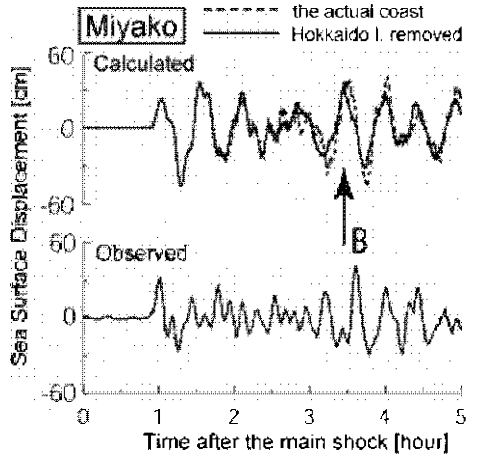

Fig. 9. Numerically calculated water level changes at Miyako in the case with Hokkaido removed (solid line in the upper figures), and that of the case of the actual coast (no land removed) (broken line). Point B shows the appearance time of the delayed peak.

5.2.3 *The Effects of Shimokita and Hokkaido Coasts*

Figure 10 shows the result of the numerical calculation at Miyako when removing both Hokkaido and Shimokita coasts. Here, we can see that the height of the delayed peak (arrow C in Figure 10) decreases to 7 cm, which is 80% of the case without removal; that is, we find that the delayed peak almost completely disappears. This means that both Hokkaido and Shimokita coasts are effective in forming the delayed peaks of the tsunamis at Miyako.

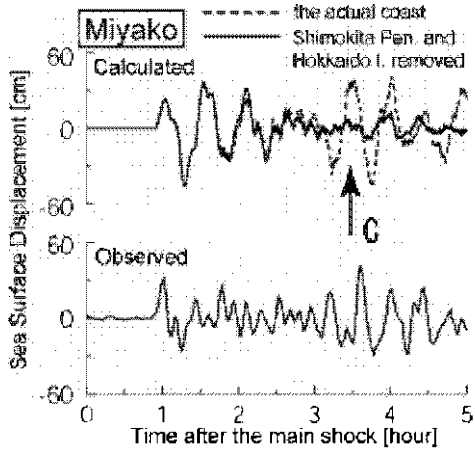

Fig. 10. Numerically calculated water level changes at Miyako in the case with both Shimokita Peninsula and Hokkaido removed (solid line in the upper figures), and that of the case of the actual coast (no land removed) (broken line). Point C shows the appearance time of the delayed peak.

5.3 COASTS THAT INFLUENCE THE FORMING OF THE DELAYED PEAK

As a result of the three numerical calculations with artificially removed coasts, we find out that the coast lines of Shimokita Peninsula and Hokkaido play an important role in forming the delayed peak of the 1973 Nemuro-Hanto-Oki earthquake. The numerical result at Miyako shows that in the case of removing only the Hokkaido coast, the decay of the height of the delayed peak is 10% of that of the actual coast condition. In the case of only the Shimokita Peninsula being removed, the amount of the decay reaches 44%.

If we simply consider, it is likely that in the case of both Shimokita and Hokkaido being removed, the amount of decay becomes 54%. But the result of our numerical calculation for this case shows that the amount of decay reaches 80%, which exceeds the simply superposed value. This shows that the influences of both coasts are not independent.

This fact implies, for example, that there is a process whereby a component of the direct wave reaches the coast of Hokkaido and is reflected, and the reflected wave propagates to the coast of Shimokita Peninsula, and the mode transfer from direct wave to edge wave occurs there.

In the next section we discuss the processes of the propagation of the direct waves and of the mode transfer from incident wave to edge wave at the shelf area of Shimokita Peninsula.

6 The propagating routes of the delayed peaks

6.1 PROCESSES FORMING DELAYED PEAKS

In the previous section, we suggested that the delayed peaks consist of two elements: one was the edge wave formed by the mode transfer of the direct wave from the source at the shelf region of Shimokita Peninsula, and the other was the edge wave formed by the mode transfer of wave reflected on the Hokkaido coast.

Hereafter, we call the former element the element of Process 1 and the latter the element of Process 2 (see Figure 11). Process 1 and 2 elements were suggested to be formed by the following processes:

Process 1: The component of the waves from the source directly reached the Shimokita coast and was reflected. There, the wave mode was transformed into the edge wave, and the edge waves propagated to Miyako.

Process 2: The component of the waves from the source directly reached the Hokkaido coast, was reflected, was propagated to Shimokita Peninsula, and reached Shimokita Peninsula. There, the wave mode was transformed into the edge wave, and the edge waves propagated to Miyako.

To verify whether or not this suggestion is reasonable, we make numerical calculations for two cases: one is the case in which only the Process 1 element exists, the other is for the case of the Process 2 element.

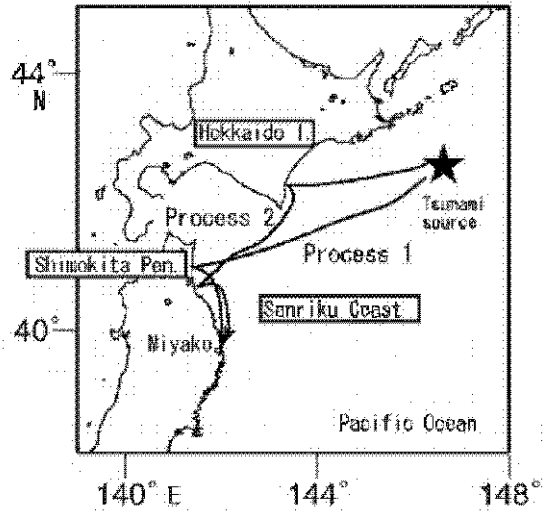

Fig. 11. Two processes of tsunami propagation from the source region to Miyako.

6.2 NUMERICAL EXPERIMENT FOR THE TWO PROCESSES

6.2.1 *Method of verifying the effects of Process 1*

The numerical experiment for verifying the Process 1 should be planned to clarify the mechanism of mode transfer of initial direct wave to edge wave at Shimokita coast. To know the role of Process 1, we artificially remove all coasts except for Shimokita Peninsula, and after passing the initial wave through the removed coasts, we recover only the Sanriku Coast where Miyako tidal station is located. Hokkaido coast was kept removed. Using this procedure, we can clarify the pure effect of Process 1.

6.2.2 *Method of the verifying the effects of Process 2*

We artificially remove all coasts except for Hokkaido Island, and after passing the direct initial wave through the removed coasts, especially Shimokita Peninsula, we recover all of the Sanriku Coast. With Hokkaido coast not removed, only the reflected wave at Hokkaido can reach Sanriku Coast. Using this procedure, we can clarify the pure effect of Process 2.

6.3 RESULTS OF THE NUMERICAL CALCULATIONS VERIFYING THE EFFECTS OF PROCESSES 1 AND 2

Figure 12 (a) and (b) show the results of the numerical calculations verifying the effects of Processes 1 and 2, showing how much Processes 1 and 2 contribute to the formation of the delayed peaks of the tsunamis. The solid lines in the upper and lower figures refer to the calculated sea surface change in the cases of Process 1 and Process 2, respectively. The broken lines in both upper and lower figures refer to the case of the actual coast, which is the same as in section 4.

In the case of Process 1 (upper figure), we find that the peak height forms 80% of that in the case of the actual coast. In the case of Process 2 (lower figure), we also find that the peak height forms 70% of that in the case of the actual coast. We can also point out that the peak of the delayed peak of Process 1 appears 2 minutes before that of the case of the actual coast, and that the peak of Process 2 appears 3 minutes after it. So, we can judge that the delayed peak is formed as the superposition of both peaks of Process 1 and Process 2. Because of the superposition of the two peaks that had passed through quite different routes (Process 1 and Process 2), the delayed peak appeared as a peak with a greater height than that of the initial wave.

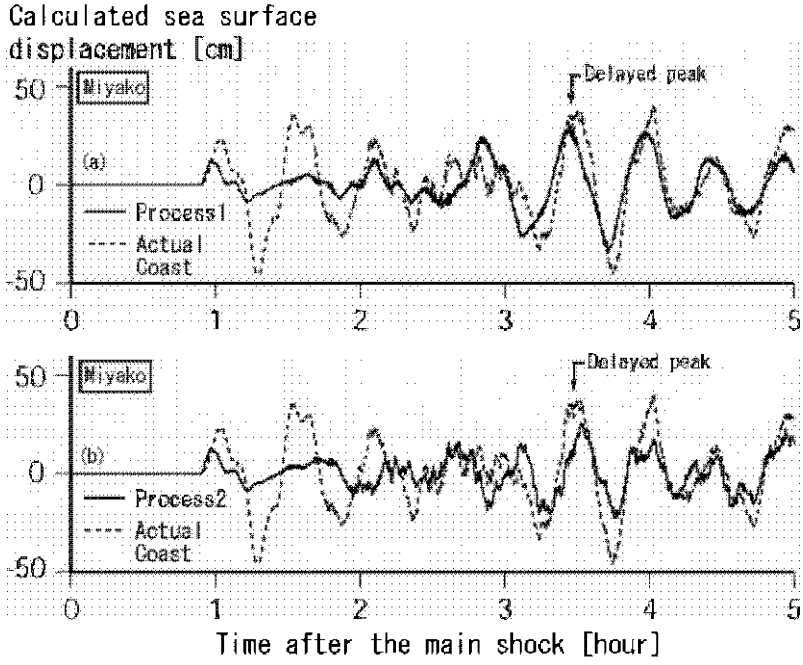

Fig. 12 (a) and (b). Calculated sea surface displacement for Processes 1 and 2 at Miyako. The upper figure (a) shows the case of Process 1, and the lower figure (b) shows the case of Process 2.

7 Generality of the delayed phase

In the previous section, we found that the cause of the delayed peak of the 1973 Nemuro-Hanto-Oki earthquake is the superposition of the delayed peaks by two processes. As we mentioned in section 2, delayed peaks were observed for other tsunamis at Miyako, for example, the 1969 and 1994 Hokkaido-Toho-Oki earthquakes (see Figure 1). The cause of these delayed peaks is suggested to be the same as that of the 1973 earthquake. To verify this, we performed a numerical calculation using the same procedure as in section 5 for those two tsunamis.

The results of the numerical experiments for the 1969 and 1994 earthquakes are shown in Figure 13. The meaning of each line is the same as in Figure 6. We can find that the delayed peaks of both the 1969 and 1994 earthquakes are reproduced also by the numerical calculations (arrows A and B in Figure 13). We can recognize that the delayed peaks do not appear almost completely in the case of removing Shimokita Peninsula and Hokkaido for each earthquake. So, the mechanisms forming the delayed peaks are the same as those of the 1973 earthquake for the tsunamis generated in the sea region east off Hokkaido.

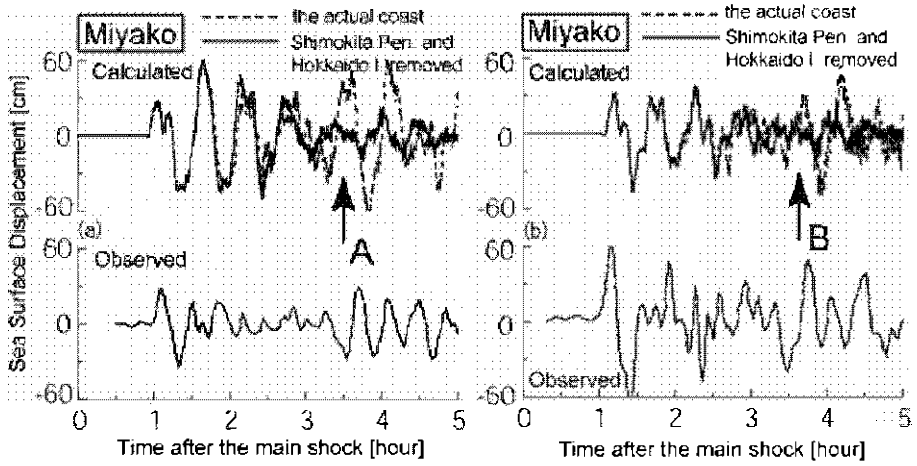

Fig. 13. Numerically calculated water level changes at Miyako of the 1969 and 1994 Hokkaido Toho-Oki earthquakes in the case with both Shimokita Peninsula and Hokkaido removed (solid lines in the upper figures), and those of the case of the actual coast (no land removed) (broken line). The left figures (a) and right figures (b) show the results of the cases of the 1969 and 1994 earthquake, respectively.

8 Conclusions

We investigated the causes of the delayed peaks of the tsunami waves observed at Miyako, which are generated in the sea region east off Hokkaido. The causes consist of two processes. One is the element whereby the initial direct wave from the source region is reflected at Shimokita Peninsula, is transferred to edge wave mode, travels south along the Sanriku Coast, and arrives at Miyako about 2.6 hours after the initial wave arrival. The other process is that the initial direct wave reaches the south coast of Hokkaido, is reflected there, and propagates to Shimokita Peninsula, where it is transferred to edge wave mode, and arrives at Miyako 5 minutes after the arrival of the peak caused by Process 1. Because the delayed peak is formed by these 2 components, which travel along quite different routes and arrive at Miyako at almost the same time, the heights of the delayed peaks sometimes exceed those of the initial waves.

The results in the present study, suggest that future tsunamis, which are generated in the sea region east off Hokkaido, also cause the same phenomenon as the delayed peak in the case of the 1973 Nemuro-Hanto-Oki earthquake. The conclusions of this paper may contribute to planning for disaster mitigation related to tsunamis on the Sanriku Coast.

Acknowledgement

The authors of the present paper wish their thanks to Kushiro Local Meteorological Observatory (JMA), Hakodate Marine Observatory (JMA), Hachinohe Weather Station (JMA), Miyako Weather Station (JMA), Onahama Weather Station (JMA) and Hydrographic and Oceanographic Department, Japan Coast Guard, for the presentation of tidal records.

For this study, we used the computer systems of Earthquake Information Center of Earthquake Research Institute, the University of Tokyo.

Appendix: the transformation of the initial incident wave into the edge wave

In this appendix, we discuss the transformation of the initial incident wave into the edge wave in the sea region off the Shimokita Peninsula. To see the transformation which the only Shimokita Peninsula contributes to, we carried out a numerical experiment as follows; we first artificially replaced the Sanriku coast and land except for the Shimokita Peninsula with the sea of the flat bed of 50 m in the same way as Figure. 7 in section 5. Then, the initial incident wave would pass through the south Sanriku coast and land. We recovered the coast line at 1 hour 20 minutes after the main shock.

Figures 14 (a), (b), (c), and (d) show the distributions of the calculated sea surface displacement of snapshots at 50 minuets, at 1 hour 30 minutes, at 2 hour 22 minutes, and at 3hours and 30 minutes after the main shock, respectively. Figure 14 (d) shows the snapshot at the stage when the delayed peak appears at Miyako. A crest line (X in Figure 14 (b)) which appears on land running parallel to the coast line means that the initial incident wave had passed through the south Sanriku coast and land until 1 hour and 20 minutes after the main shock. Of course in Figure 14 (b), the south Sanriku coast line has already recovered at 1 hour and 30 minutes. So here after, the influence of the direct incident wave towards south Sanriku coast would be excluded. In Figures 14 (c) and (d), this crest line in the land is omitted.

We can see in the rectangular Figure 14 (a) that the initial incident wave approaches the Shimokita Peninsula. We can recognize in Figure 14 (b) that an edge wave has been formed. We can see in Figure 14 (c) that the edge wave moves south to Miyako. Finally, the edge wave appeared at Miyako in Figure 14 (d). These four figures show the processes of the transformation of the initial incident wave into the edge wave in the sea region off Shimokita Peninsula and its approaching Miyako. Thus we can judge that approaching of the edge wave caused the delayed peak observed at Miyako.

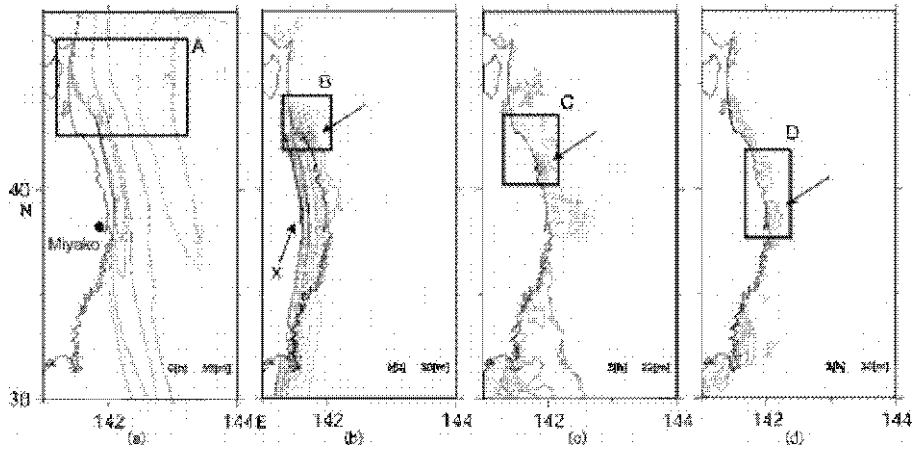

Fig. 14. The distributions of the sea surface displacements at (a) 50 minutes, (b) 1 hour and 30 minutes, (c) 2 hours and 22 minutes, and (d) 3 hours and 30 minuets after the main shock. The solid and broken contours mean the positive and negative sea surface displacements, respectively. A crest line (X in (b)) which appears on land running parallel to the coast line means that the initial incident wave had passed through the south Sanriku coast and land until 1 hour and 20 minutes after the main shock. The south Sanriku coast line has already recovered at 1 hour and 30 minutes in (b). So here after, the influence of the direct incident wave towards south Sanriku coast would be excluded. In Figs. 14 (c) and (d), this crest line in the land is omitted.

We estimate the ratio of the transformed energy forming the edge wave in the sea area off Shimokita Peninsula to the total energy of the direct incident wave at 1 hour and 30 minutes, 2 hours 22 minutes, and 3 hours 30 minutes. The potential energy P and the kinematic energy K of ocean waves are given by the following formulae;

$$P = \frac{\rho g}{2} \iint_S \eta^2 dxdy \qquad (8),$$

$$K = \frac{\rho}{2} \iiint_V \left(u^2 + v^2 + w^2\right) dxdydz \qquad (9),$$

where ρ is density of the sea water, and u, v, w are water particle velocities in x, y, and z components.

In our case, the long wave approximation is assumed, so kinematic energy K turns out to be the following formula.

$$K = \frac{\rho}{2} \iint_S \left(u^2 + v^2\right) D(x,y) dxdy \qquad (10).$$

The calculated areas for the cases of 50 minutes, 1 hour 30 minutes, 2 hours 22minutes, and 3 hours 30 minutes are the rectangular A, B, C, and D in Figures 14

(a)-(d), respectively. Thus, we can calculate the energies of the incident initial wave and the edge wave. We estimate the ratio e of transformation as the following equation,

$$e_R = \frac{\left[P+K\right]_{rectangular\ R}}{\left[P+K\right]_{rectangular\ A}} \left(R:B,C,D\right) \qquad (11).$$

As a result, the e_B, e_C, and e_D are estimated at 52%, 49%, and 27%, respectively. The ratio decreases with the propagation of the edge wave to Miyako. It implies that some energy of edge wave leak to the open ocean.

References

Abe, Ka.: 1973, Tsunami and Mechanism of Great Earthquakes, Phys. Earth Planet. Inter., **7**, 143-153.

Abe, Ku. and H., Ishii: 1983, Study of Shelf Effect for Tsunami Using Spectral Analysis, Tsunamis: Their Science and Engineering, Proceedings of the International Tsunami Symposium 1981 IUGG Tsunami Commission May, 1981, Sendai-Ofunato-Kamaishi, Japan, 161-172.

Aida, I.: 1974, Numerical Computation of a Tsunami Based on a Fault Origin Model of an Earthquake, J. Seismol. Soc. Japan, **27**, 141-154 (in Japanese).

Aida, I.: 1978, Reliability of a Tsunami Source Model Derived From Fault Parameters, J. Phys., Earth, 57-73.

Ball, F., K.: 1967, Edge Waves in an Ocean of Finite Depth, Deep-Sea Res., **14**, 79-88.

Fuller, J., D., and L., A., Mysak: 1977, Edge Waves in the Presence of an Irregular Coastline, J. Phys. Oceanogr., **7**, 846-855.

González, F., I., K., Satake, E., F., Boss, and O., Mofjeld: 1995, Edge Wave and Non-trapped Modes of the 25 April 1992 Cape Mendpeino Tsunami, PAGEOPH, **144**, 409-426.

Japan Meteorological Agency, 1973; The Seismological Bulletin of The Japan Meteorological Agency for June 1973.

Kikuchi, M.: 2003, Realtime Seismology, University of Tokyo Press, pp. 222.

Mansinha, L. and Smylie, D. E.: 1971, The Displacement Fields of Inclined Faults, Bull. Seismol. Soc. Am., **61**, 1433-1440.

Shimazaki, K.: 1994, Nemuro-Oki Earthquake of June 17, 1973: A Lithospheric Rebound at the Upper Half of the Interface, Phys. Earth planet. Inter., **9**, 314-327.

Shuto, N., T., Suzuki, K., Hasegawa, and K., Inagaki: 1986, A Study of Numerical Technique on the Tsunami Propagation and Run-up, Sci. Tsunami Hazards, the Intern. J. Tsunami Soc., **4-1**, 111-124.

Tada, T.: 1974, Fault Model and Crustal Movement of the 1973 Nemuro-Oki Earthquake, J. Seismol. Soc. Japan, **27**, 120-128 (in Japanese).

FIELD SURVEY OF THE 2003 TOKACHI-OKI EARTHQUAKE TSUNAMI AND SIMULATION AT THE OOTSU HARBOR LOCATED AT THE PACIFIC COAST OF HOKKAIDO, JAPAN

Y. TANIOKA[1], Y. NISHIMURA[1], K. HIRAKAWA[2], F. IMAMURA[3], I. ABE[3], Y. ABE[3], K. SHINDOU[3], H. MATSUTOMI[4], T. TAKAHASHI[4], K. IMAI[4], K. FUJIMA[5], K. HARADA[6], F. NAMEGAYA[7], Y. HASEGAWA[8], Y. HAYASHI[8], A. YOSHIKAWA[9], T. SIGA[9], A. KAMIKAWA[9], M. KOBAYASH[9], S. MASAKA[10], T. KAMATAKI[11], F. NANAYAMA[11], K. SATAKE[11], Y. KAWATA[12], Y. FUKASAWA[12], S. KOSHIMURA[12], Y. HADA[12], Y. AZUMAI[12] AND K. HIRATA[13]

[1] *Institute of Seismology and Volcanology, Hokkaido University, Kita-10, Nishi-8, Kita-ku, Sapporo 060-0810, Japan.*
[2] *Graduate School of Science, Hokkaido University, Kita-10, Nishi-8, Kita-ku, Sapporo 060-0810, Japan.*
[3] *Disaster Control Research Center, Graduate School of Engineering, Tohoku University, Aoba 06, Sendai 980-8579, Japan*
[4] *Department of Civil and Environmental Engineering, Faculty of Engineering and Resource Science, Akita University, 1-1 Tegatagakuen, Akita, 010-8502, Japan*
[5] *Graduate School of Science and Engineering, National Defense Academy In Japan, 1-10-20 Hashirimizu, Yokosuka, Kanagawa 239-8689, Japan.*
[6] *Disaster Prevention Research Institute, Kyoto University, Gokasho, Uji, Kyoto 611-0011, Japan*
[7] *Earthquake Research Institute, University of Tokyo, 1-1-1, Yayoi, Bunkyo-ku, Tokyo 113-0032, Japan*
[8] *Seismology and Volcanology Research Department, Meteorological Research Institute, 1-1 Nagamine, Tsukuba, 305-0052, Japan.*
[9] *Sapporo District Meteorological Observatory, N2W18, Cyuo-ku, Sapporo, 060-0002, Japan*
[10] *Japan Meteorological Agency, 1-3-4 Otemachi, Chiyoda-ku, Tokyo, 100-8122, Japan*
[11] *National Institute of Advanced Industrial Science and Technology, Site C7 1-1-1 Higashi, Tsukuba 305-8567, Japan.*
[12] *Disaster Reduction and Human Renovation Institution, 1-5-2 Wakinohama kaigan-dori, Chuo-ku, Kobe, 651-0073, Japan*
[13] *Japan Agency for Marine-Earth Science and Technology, 2-15 Natsuhima-cho, Yokosuka 237-0061, Japan.*

K. Satake (ed.), Tsunamis: Case Studies and Recent Developments, 135-156.

Field survey for the 2003 Tokachi-oki earthquake tsunami was conducted by the scientists from all over Japan [Tanioka et al., 2004a, b]. Large tsunami heights of about 4 m were observed at Hyakuninhama to the east of Cape Erimo and along the beach between Horokayanto and Oikamanai. Those places are close to the source region of the earthquake. In general, tsunami heights gradually decreased to the east and to the west away from those two locations except at Mabiro where a large tsunami height of about 4m was locally observed. The most intensive tsunami survey was conducted at the Ootsu harbor. The survey results indicate that the quay of the harbor was completely submerged by the tsunami, but the road around the harbor was not. Numerical computation of the 2003 Tokachi-oki tsunami was carried out by solving the nonlinear shallow water equations with a moving boundary condition near the Ootsu harbor. The computed tsunami at the Ootsu harbor well explains the above observations.

Key words: The 2003 Tokachi-oki tsunami, tsunami survey, tsunami numerical simulation.

1 Introduction

On 26 September 2003, a great earthquake occurred Tokachi-oki, off the southern coast of Hokkaido, Japan. Hypocentral parameters of the 2003 Tokachi-oki earthquake determined by Japan Meteorological Agency (JMA) are as follows: origin time, 4:50:07.5 sec (JST); latitude, 41°46.7'N; longitude, 144°04.7'E; depth, 42 km; M_J 8.0, where M_J is the JMA magnitude scale. This earthquake occurred in the same region as the 1952 Tokachi-oki earthquake (Mw 8.1). Ichiyanagi et al. [2004] show that the aftershock area of the 2003 event is slightly smaller than that of the 1952 event. Maximum seismic intensity of "6 minus" on the current JMA intensity scale, corresponding to IX on the modified Mercalli scale, was observed in the Tokachi Plain [Hamada and Suzuki, 2004]. The focal mechanism of the earthquake determined by Yamanaka and Kikuchi [2003] using teleseismic body waves indicates thrust faulting with a shallow dip angle (strike=230°, dip=20°, rake=109°) (Figure 1). The seismic moment was also estimated as 1.0×10^{21} Nm by Yamanaka and Kikuchi [2003].

The earthquake generated large tsunami causing damage along the southern coast of Hokkaido. Immediately after the earthquake, the field survey was conducted by tsunami researchers from all over Japan. Several survey teams, from Hokkaido University, Tohoku University, Akita University, Tokyo University, Kyoto University, Japan Meteorological Agency, National Defense Academy, National Institute of Advanced Industrial Science and Technology, Japan Agency for Marine Earth Science and Technology, and Disaster Reduction and Human Renovation Institute, covered the coasts of the eastern Hokkaido and the northern Tohoku regions. Tanioka et al. [2004a]

compiled the tsunami height distribution along the coasts measured by the survey teams. The details of the survey, including information of the survey points, eyewitness accounts, and photographs at the survey points, are presented in Tanioka et al. [2004b].

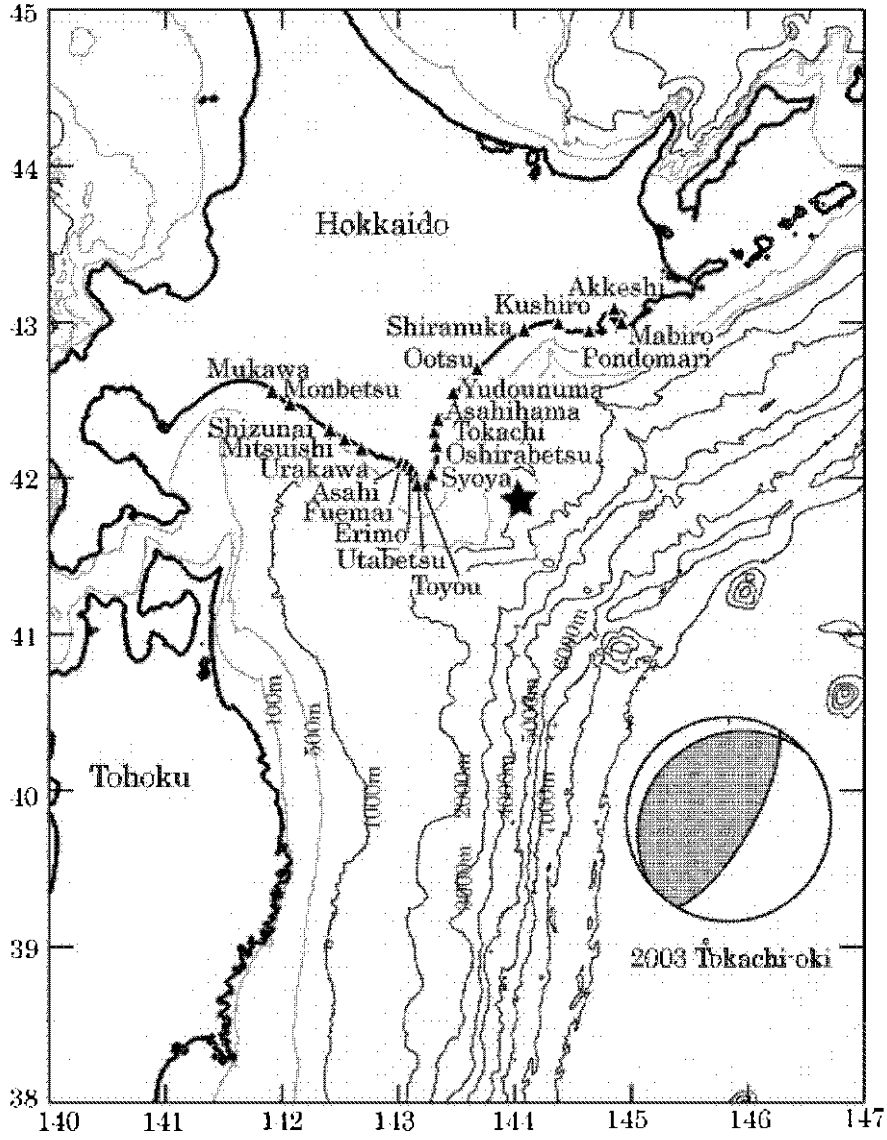

Fig. 1. Map of the source region of the 2003 Tokachi-oki earthquake and the focal mechanism of the earthquake estimated by Yamanaka and Kikuchi [2003]. A star marks the epicenter of the earthquake. Solid triangles show the locations of harbors in the text.

In this paper, we first review the overall pattern of the tsunami height distribution from the 2003 Tokachi-oki event. Then, we focus on Ootsu harbor where many valuable eyewitness accounts, run-up measurements, and photographs of the tsunami were obtained. The tsunami at Ootsu harbor is simulated using numerical computations and the results are compared with the observations.

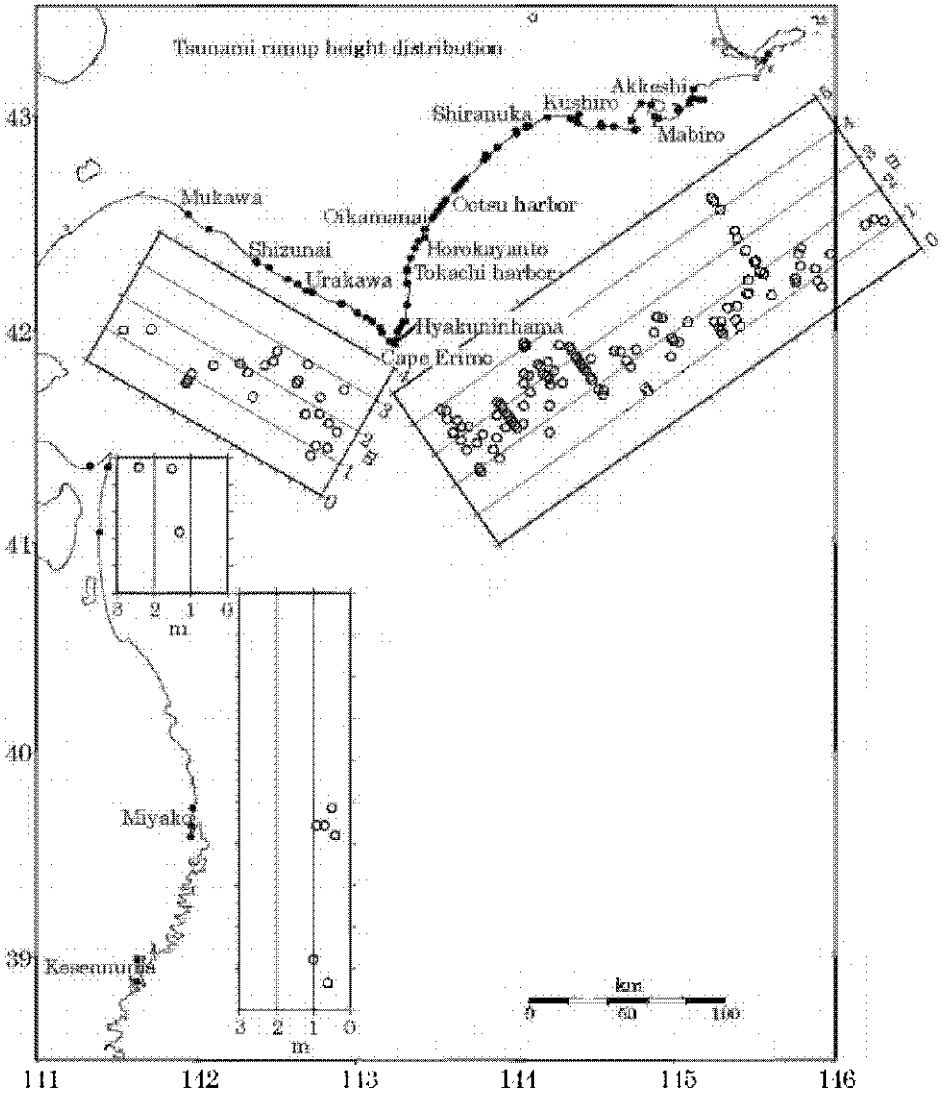

Fig. 2. The measured tsunami heights of the 2003 Tokachi-oki tsunami. Solid circles are the survey points where the tsunami heights are measured.

2. Tsunami run-up distribution

The result of the tsunami height survey [Tanioka et al., 2004a, b] are shown in Figure 2 and Table1. The tsunami heights were measured from various objects that the tsunami left behind, water lines marked along the structures by the tsunami, or eyewitness accounts. Tsunami heights originally referenced to the sea level at the time of measurement are corrected for tide levels using nearby tide gauge records or the calculated tide datum from the tide table provided by the JMA. In Table 1, the reference station name is shown for each survey point. The tsunami heights from the 2003 earthquake shown in Figure 2 are referenced to the mean sea level of Tokyo Bay (T.P.). Detailed results from the survey are discussed below.

2.1 WEST OF CAPE ERIMO

The tsunami heights at Mukawa and Monbetsu harbors measured based on eyewitness accounts were 1.1 and 1.5 m, respectively. The tsunami heights were about the heights of the quays at both ports. Tsunami heights at the survey points located east between Shizunai and Cape Erimo are mostly measured from tsunami deposits that the tsunami left behind as shown in Figure 3. There were also eyewitness accounts at several fishing harbors, Urakawa, Asahi, Fuemai, Erimo, Utabetsu, and Toyou. The tsunami heights between Shizunai and Mitsuishi were 0.7-1.9 m (less than 2 m). The tsunami heights between Mistuishi and the Erimo harbor were 1.4-2.9 m. The tsunami heights between the Utabetsu harbor and the Toyou harbor were 0.8-1.8 m (less than 2 m).

a) Mitsuishi b) Toyou

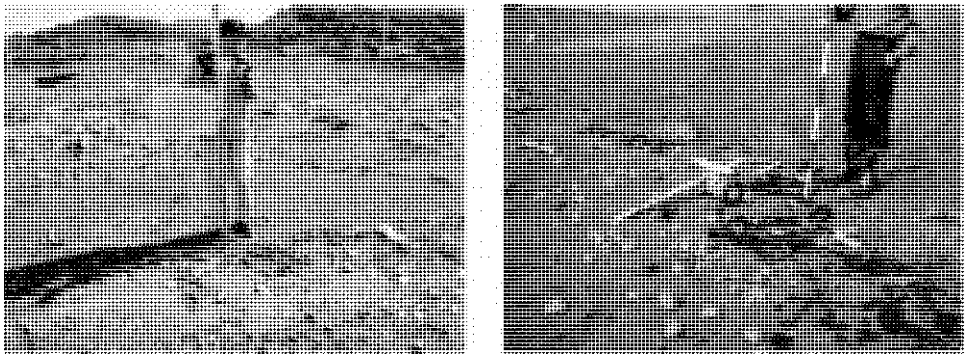

Fig. 3. Photos of the tsunami deposits at a) Mitsuishi and b) Toyou located at the west of Cape Erimo

2.2 EAST OF CAPE ERIMO

The tsunami heights at the survey points located between Cape Erimo and the Tokachi harbor were 2.0-4.0 m, and higher than those in the west of Cape Erimo. The tsunami heights in this region were mostly measured from tsunami deposits that the tsunami left behind as shown in Figure 4. A large tsunami of more than 3.0 m with the maximum of 4.0 m was observed along the beach of Hyakuninhama. There are a few eyewitness accounts at Shoya harbor and Oshirabetsu harbor.

a) Cape Erimo b) South of Tokachi harbor

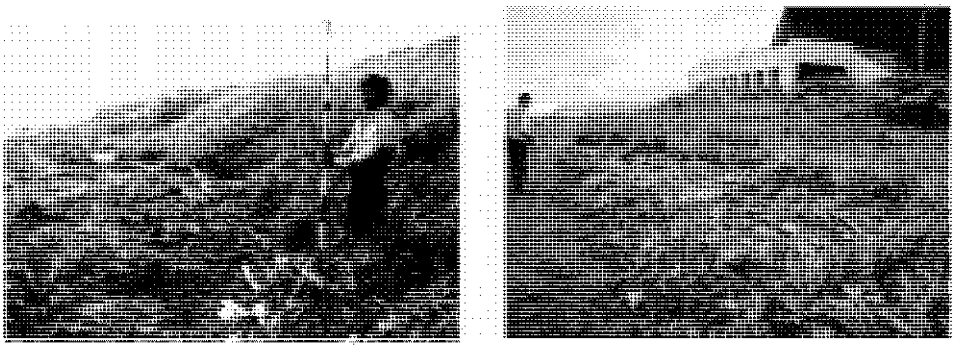

Fig. 4. Photos of the tsunami deposits at a) Cape Erimo and b) South of Tokachi harbor.

At the Tokachi harbor, several cars parked at the quays were washed away by the tsunami. Tokachi harbor was one of the regions most damaged by the tsunami (Figure 5a). At thirty survey points in Tokachi harbor, tsunami heights were 2.4-3.2m; these were mostly measured from water lines marked along the buildings or constructions by the tsunami (Figure 5b).

a) Tokachi harbor b) Tokachi harbor

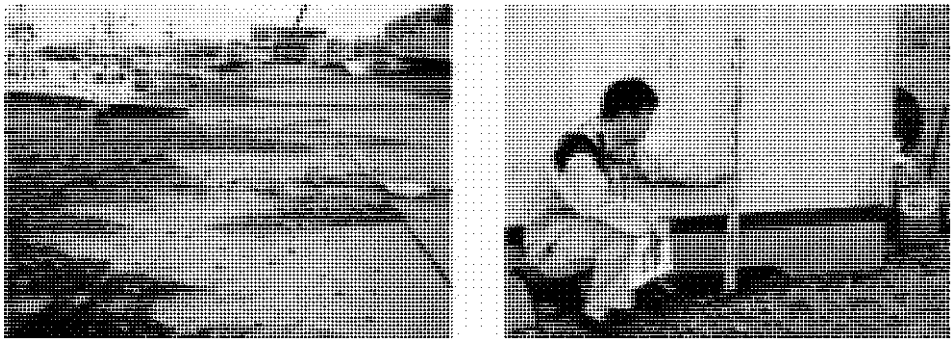

Fig. 5. Photos of a) tsunami deposits on the quay of the Tokachi harbor and b) the water line on the building in the Tokachi harbor.

Between Asahihama and the Ootsu harbor, the tsunami heights were 2.4-4.1m; these were mostly measured from tsunami deposits that the tsunami left behind as shown in Figure 6. The maximum tsunami height of 4.1m was observed along the beach between Horokayanto and Oikamanai.

a) Asahihama b) Yudounuma

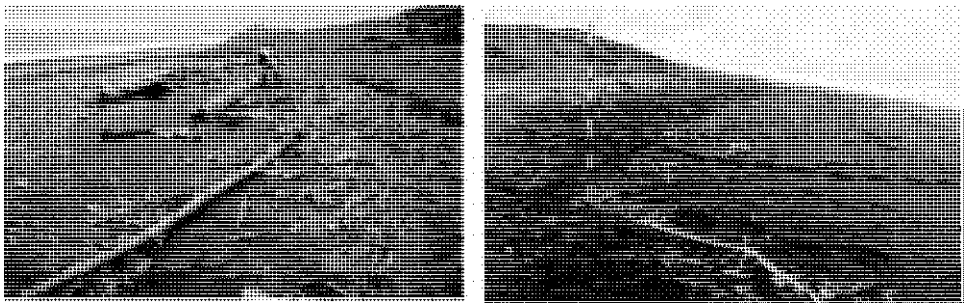

Fig. 6. Photos of the tsunami deposits at a) Asahihama and b) Yudounuma located between the Tokachi harbor and Ootsu harbor.

2.3 OOTSU HARBOR

The Ootsu harbor is one of the regions most damaged by the tsunami. Several ships collided or were washed away by the tsunamis. The most intensive tsunami survey was conducted in this region (Figures 7 and 8). At the northeastern end of the harbor (large circle in Figure 8), the tsunami heights were measured from water level lines left by the tsunami on the buildings and other structures (Figure 7a-c). The tsunami heights in the Ootsu harbor ranged 1.8-3.3m, but mostly 2.4-2.9 m.

Photos of the actual tsunami were also taken by a local official and shown in Figure 9. The photos, Figure 9a and 9b, were taken from the building located at the southeast side of the harbor shown as a star in Figure 8. Figure 9a was taken toward west from the building and shows the receding tsunami wave. After the first wave receded, Figure 9b, taken toward north from the building, shows the ships that were reversed or that collided with nearby ships when the first wave struck. The photos, Figure 9c-e, were taken near the building and show that tsunami run-up water level over the quay and the completely-submerged parking space behind the building. The building shown in the right side of Figure 9e is the same building from which the photos, Figure 9a and 9b, were taken.

In summary, the tsunami ran up over the quay and the dock on the west side of the harbor, and submerged the parking space or the buildings along the quay, but did not submerge a road surrounding the harbor shown as a thick curve in Figure 8. Later in this paper, we compute the tsunami wave in this harbor and compare them with the observed tsunami.

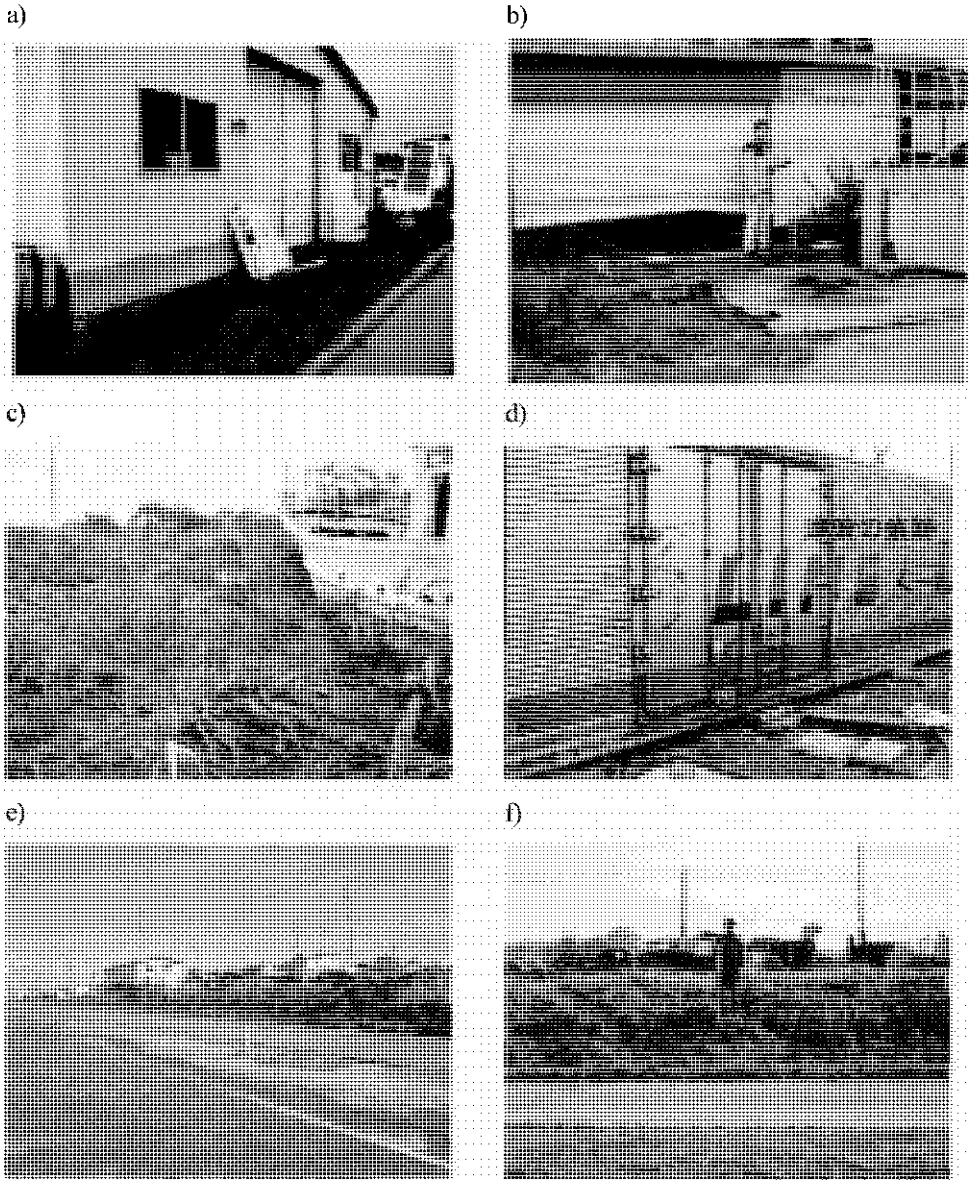

Fig. 7. Photos of the tsunami runup evidences at Ootsu harbor. The places where Photos a)-c) were taken are shown as a large circle in Figure 8. The place where Photo d) was taken is shown as a solid circle in Figure 8. The places where Photos e)-f) were taken are shown as a solid square in Figure 8.

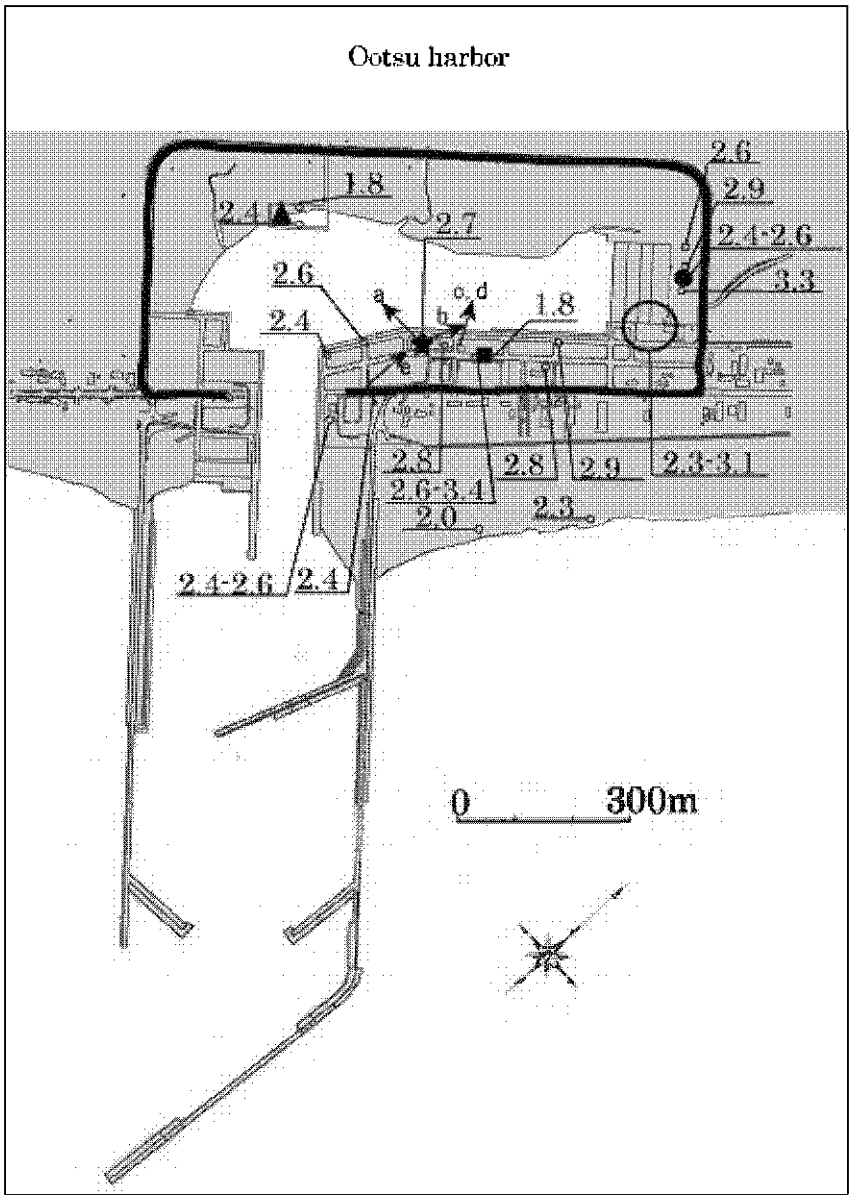

Fig. 8. A map of the Ootsu harbor. Numbers are the measured tsunami heights in meters. A large circle is the location where photos Figures 7 a)-c) were taken. A solid circle is the location where photo Figure 7 d) was taken. A square is the location where photos Figures 7 e)-f) were taken. A star shows the building where photos of the actual tsunamis, Figures 9 a)-b), were taken. Arrows show the directions of the photos Figures 9 a)-e). A triangle is the dock at the west side of the harbor. A thick curve shows the road around the harbor. The height of the road is 3.5-4.0 m.

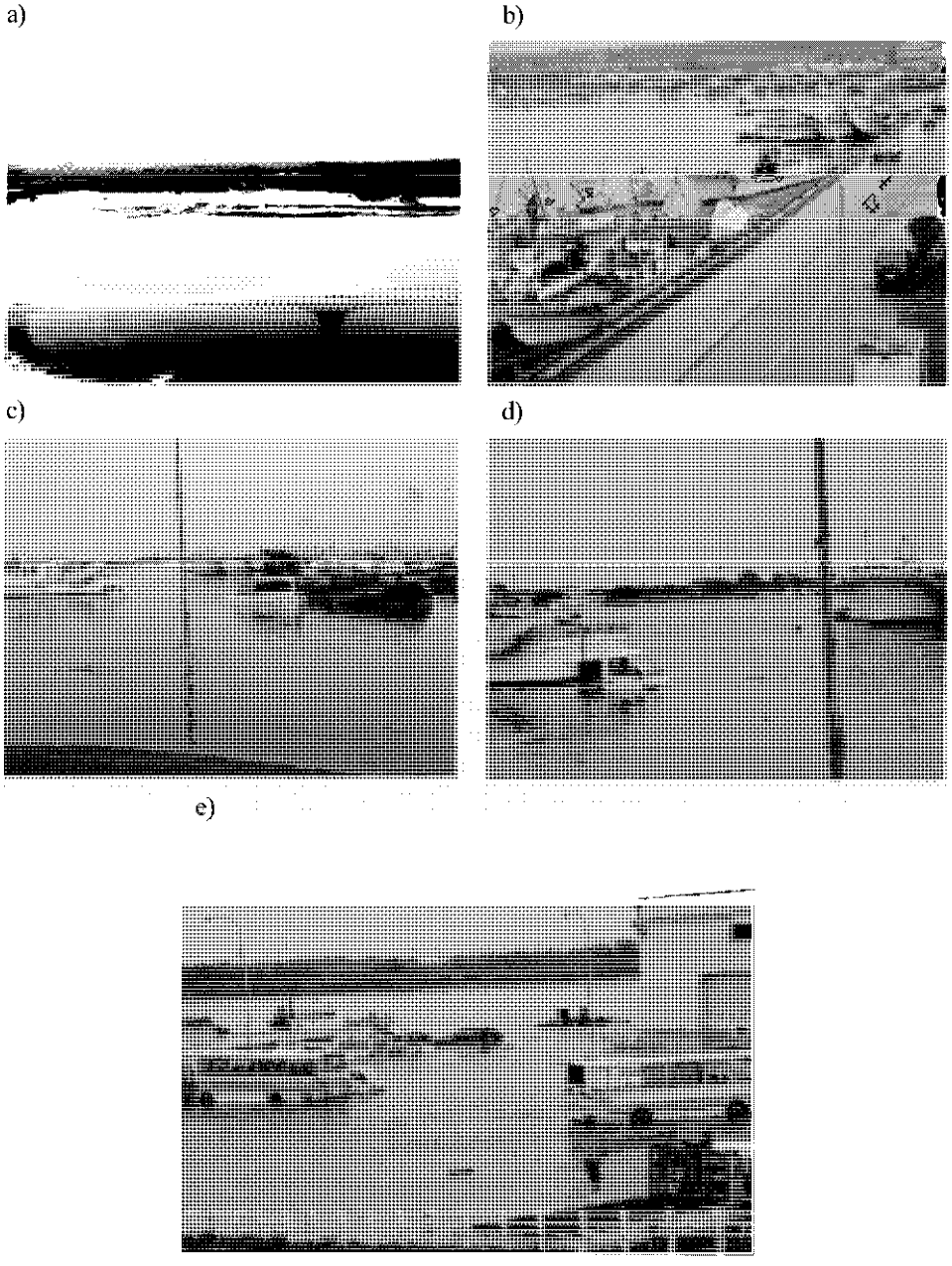

Fig. 9. Photos of the 2003 Tokachi-oki tsunami at the Ootsu-harbor taken by the local official (see Tanioka et al., 2004b). Photos a)-b) were taken from the building shown as a star in Figure 8. Photo a) shows the receding tsunami wave. Photo b) shows the quay after the first tsunami wave. Photos c)-e) show that the later tsunami wave submerged the quay of the harbor.

2.4 EAST OF THE OOTSU HARBOR

Between the Ootsu harbor and Shiranuka harbor, the tsunami heights were 1.3-2.8 m, which were measured based on eyewitness accounts or tsunami deposits that the tsunami left behind as shown in Figure 10a. The tsunami heights in this region were lower than the tsunami heights in the west of the Ootsu harbor. Between Kushiro and the Akkeshi harbor, the tsunami heights were 1.0-1.8 m which were mostly measured based on eyewitness accounts because the tsunami heights were not large as shown in Figure 10b.

At Mahiro (Figure 2), the tsunami heights suddenly became large, 1.7-4.2 m. The tsunami heights distribution near Mabiro shown in Figure 11 indicates that the large observed tsunami (>3 m) was observed in the localized area along the coast of Mabiro. The tsunami heights observed away from Mabiro decease quickly. Therefore, the large tsunami at Mabiro was a localized phenomenon. To the east of Mabiro, the tsunami heights were 0.5-1.7 m, which were mostly measured based on eyewitness accounts.

a) Shiranuka b) Pondomari

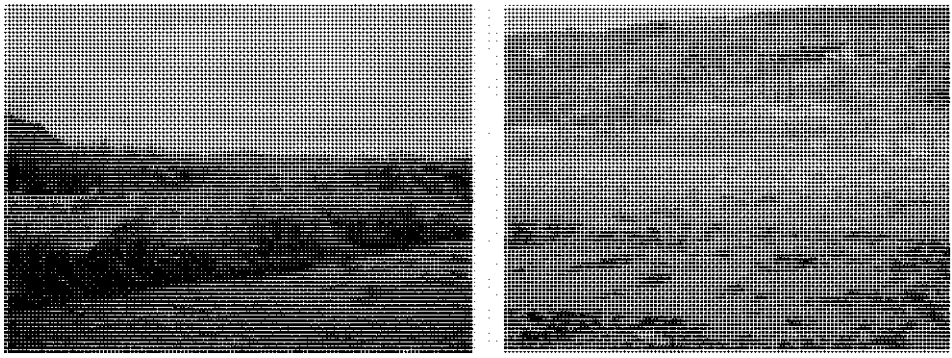

Fig. 10. Photos of the tsunami deposits at a) Shiranuka and b) Pondomari located between the Ootsu harbor and Kushiro.

2.5 SUMMARY OF THE TSUNAMI HEIGHT SURVEY

Large tsunami heights of about 4 m were observed at Hyakuninhama in the east side of Cape Erimo and along the beach between Horakayanto and Oikamanai. Those places are close to the source region of the earthquake. In general, the tsunami heights gradually decreased to the east and to the west away from those two places except at Mabiro where a large tsunami height of about 4 m was locally observed. The tsunami damage was most intensive at the Tokachi harbor and the Ootsu harbor.

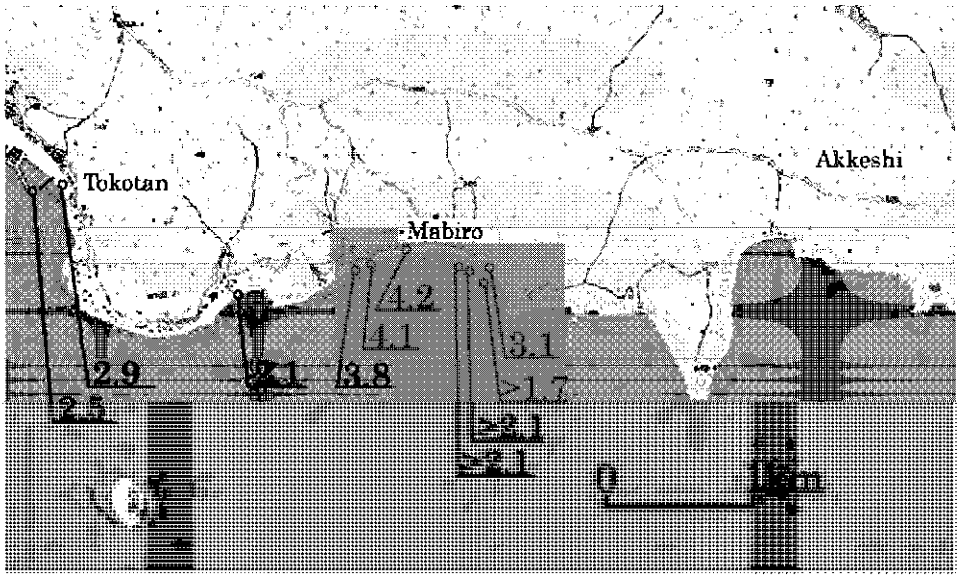

Fig. 11. The tsunami heights distribution near Mabiro. Numbers are the measured tsunami heights in meters.

3 Numerical simulation of tsunami at the Ootsu harbor

In this section, we numerically simulate the tsunami in the Ootsu harbor where the most intensive survey was conducted.

3.1 METHOD OF NUMERICAL TSUNAMI SIMULATION

The governing equation for tsunami propagation is the nonlinear shallow water equations with the bottom friction considered. The equation of motion, or conservation of momentum, can be written as

$$\frac{\partial \boldsymbol{V}}{\partial t} + (\boldsymbol{V} \cdot \nabla)\boldsymbol{V} = -g\nabla h - C_f \frac{\boldsymbol{V}|\boldsymbol{V}|}{d+h} \qquad (1)$$

where $\boldsymbol{V}$ is the depth-averaged horizontal velocity vector, h is the tsunami height, d is the water depth, g is the gravitational acceleration, and C_f is the friction coefficient. The friction coefficient, C_f, is related to the Manning's roughness coefficient n as

$$C_f = \frac{gn^2}{(d+h)^{1/3}} \qquad (2)$$

A typical value of n for coastal water is 0.03 $m^{-1/3}s$ [e.g., Baptista et al., 1989] which we used in our computation. The equation of continuity, or conservation of mass, can be written as

$$\frac{\partial(d+h)}{\partial t} = -\nabla \cdot [(d+h)\boldsymbol{V}] \tag{3}$$

The above equations are solved by a finite-difference method using a staggered leap-frog method. The moving boundary condition described by Tanioka and Satake [1995] is used as the coastal boundary condition.

When the tsunami amplitude h is very small compared to water depth d, we can use "small amplitude" approximation. Then, the equations (1) and (3) can be linearized. The linear long wave equations are

$$\frac{\partial \boldsymbol{V}}{\partial t} = -g\nabla h \tag{4}$$

$$\frac{\partial h}{\partial t} = -\nabla \cdot (d\boldsymbol{V}) \tag{5}$$

The above equations are also solved by a finite-difference method using a staggered leap-frog method. The detailed description of the tsunami computation is shown by Satake [1995].

For the tsunami computation, a grid size of 0.8" (about 25 m) was used for the Ootsu harbor. A large grid size of 20" of arc (about 600m) was used for the computations for the whole region (Figure 1), which included the source region of the 2003 Tokachi-oki earthquake. An intermediate grid size of 4" of arc (about 125m) was used near the Ootsu harbor in order to nest smoothly the area of the smaller grid size within the whole computational region. In the finest grid area for the Ootsu harbor, the nonlinear shallow water equations, (1) and (3), were solved by the finite-deference method with the moving coastal boundary condition. In the other grid size areas, the linear long wave equations, (4) and (5) were solved by the finite-deference method.

3.2 FAULT MODEL FOR THE 2003 TOKACHI-OKI EARTHQUAKE

The slip distribution of the 2003 Tokachi-oki earthquake was already estimated by several researchers using various data. Yamanaka and Kikuchi [1993] estimated the slip distribution using the teleseismic body waves and found a seismic moment of 1.0 x 10^{21} Nm. Yagi [2004] estimated the slip distribution using teleseismic body waves and strong motion data, and estimated a seismic moment as 1.7 x 10^{21} Nm. Honda et al.,[2004] estimated the slip distribution using strong motion data and a seismic moment of 2.9 x 10^{21} Nm. Koketsu et al. [2004] estimated the slip distribution using strong motion and geodetic data and calculated a seismic moment of 2.2 x 10^{21} Nm. Tanioka et al. [2004] estimated the slip distribution using tsunami waveforms and found a seismic moment of 1.0 x 10^{21} Nm. In general, pattern of the slip distribution

from the various studies were all similar. In this study, we multiply the slip distribution estimated by Yamanaka and Kikuchi [1993] by 1.6 and use it as a slip distribution of the 2003 Tokachi-oki earthquake. Therefore, the seismic moment becomes 1.6×10^{21} Nm, closer to the other estimates than the original estimate by Yamanaka and Kikuchi [1993]. The vertical seafloor displacement is computed from the slip distribution using Okada's [1985] equations and used as the initial waveforms of the tsunami computations.

3.3 RESULT

Figure 12 shows seven snapshots of the computed tsunami at the Ootsu harbor. At 25 minutes after the origin time of the earthquake, the tsunami approaches to the harbor. At 30 minutes after the origin time, the tsunami (about 1m) arrives at the beach located outside of the harbor and approaches toward the inside of the harbor. At 35 minutes after the origin time, a large tsunami (>2 m) arrives at the beach located outside of the harbor, and the tsunami (about 1 m) enters in the harbor. The marsh around the harbor begins to be submerged by the tsunami. At 38 minutes after the origin time, the large tsunami outside the harbor retreats, but a large tsunami (> 2 m) also enters in the harbor. The quay of the harbor, which is shown in Figure 9b, begins to be submerged by the tsunami. At 40 minutes after the origin time, the tsunami outside the harbor retreats, and the large tsunami (>2 m) in the harbor submerges the quay in the harbor completely as in the photos in Figure 9. At 44 minutes after the origin time, the tsunami outside of the harbor continues to retreat, and the tsunami in the harbor also retreats. The water on the quay has retreated and the quay appears to be dry. The road around the harbor, shown as a thick curve in Figure 8, was not submerged by the computed tsunami. The height of the road is 3.5-4.0 m. Those results show that the numerically computed tsunami well-simulates the observed tsunami at the Ootsu harbor.

4. Conclusions

The intensive tsunami height survey at the Ootsu harbor and eyewitness accounts including the photos show that the quay of the harbor which is in the photo of Figure 9b was completely submerged by the tsunami. However, the road around the harbor (see in Figure 8) was not submerged by the tsunami. Numerical computation of the 2003 Tokachi-oki tsunami using the fault model of the earthquake well simulated the above observations, confirming that the tsunami at the Ootsu harbor was not an unusual tsunami.

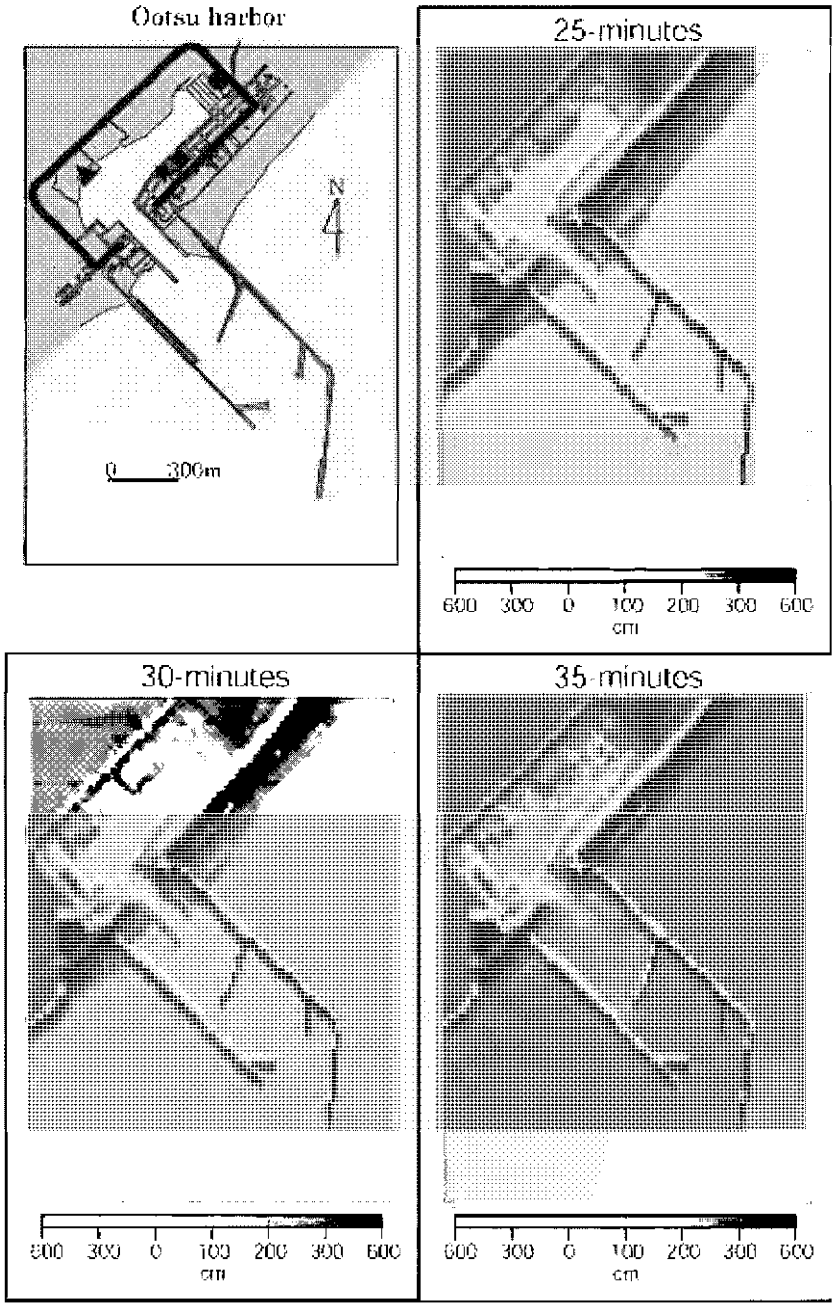

Fig. 12. A map of the Ootsu harbor and seven snapshots of the computed tsunami propagation near the Ootsu harbor at 25, 30, 35, 38, 40, 42, and 44 minutes after the origin time of the earthquake. The symbols in the Map are the same as those in Figure 8.

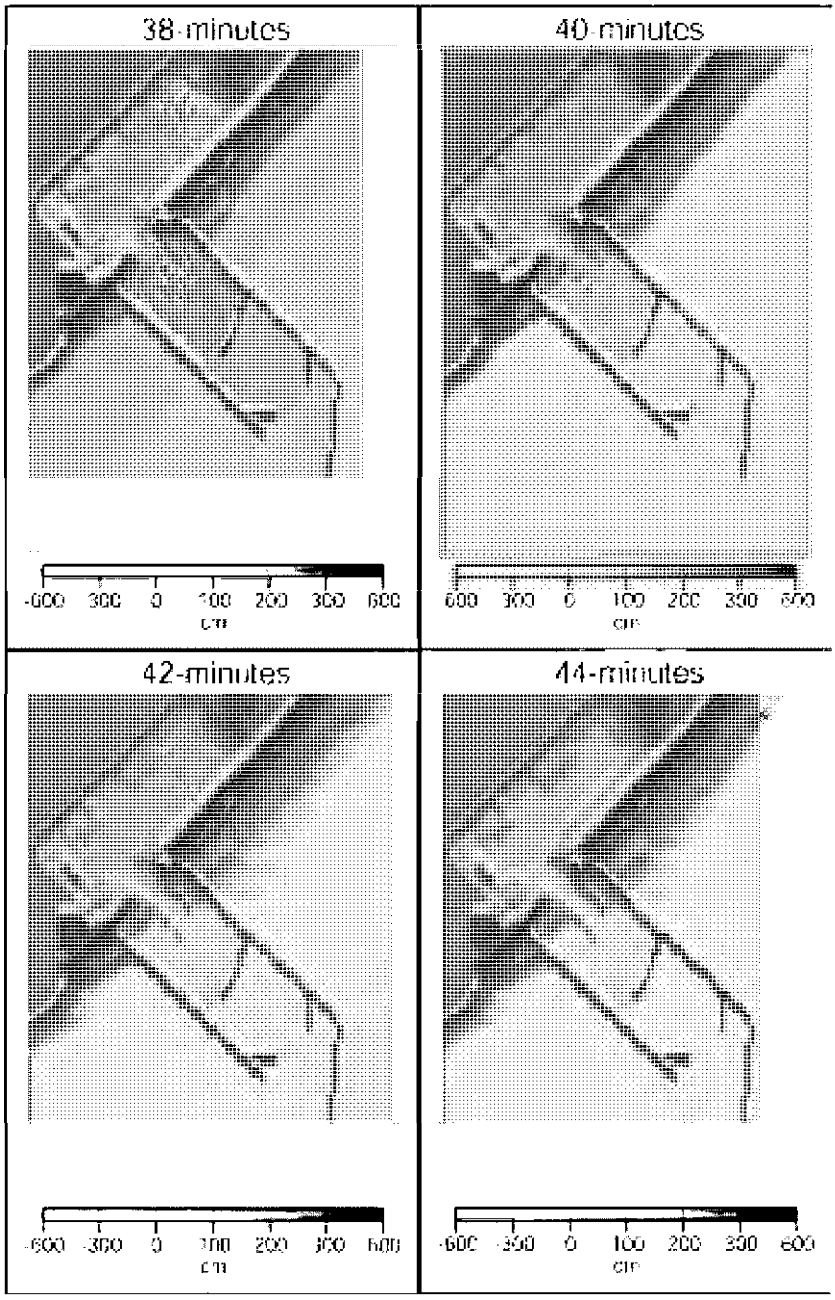
38-minutes
40-minutes
42-minutes
44-minutes
-600 -300 0 100 200 300 600
600 -300 0 100 200 300 600
-600 -300 0 100 200 300 600
-600 -300 0 100 200 300 600

Fig. 12. (cont'd.)

Table 1. Tsunami height survey results

survey point	latitude[1] (N)	longitude[1] (E)	measured height (m)	reference tide gauge[2]	Correctd height[3] (m)
Mukawa	42°32'52"	141°56'27"	0.48	Ura	1.1
Monnbetsu	42°28'24"	142°04'29"	0.60	Ura	1.5
Shizunai	42°19'53"	142°22'04"	1.15	Ura	1.0
Shizunai	42°19'53"	142°22'04"	0.84	Ura	0.7
Irifune	42°19'31"	142°22'14"	1.02	Ura	0.8
Irifune	42°19'31"	142°22'14"	1.27	Ura	1.0
East-shizunai	42°18'04"	142°27'03"	1.79	Ura	1.5
Mitsuishi	42°14'43"	142°34'12"	2.24	Ura	1.9
Mitsuishi	42°13'16"	142°37'46"	2.06	Ura	1.8
Ogifushi	42°11'34"	142°40'38"	2.48	Ura	2.3
Ebuegawa	42°11'06"	142°42'17"	2.98	Ura	2.8
Hidakahorobetsu	42°08'28"	142°50'36"	2.15	Ura	2.5
Urakawa	42°09'53"	142°46'20"	1.40	Ura	1.4
Samani	42°07'58"	142°54'31"	2.57	Ura, Uta	2.9
Samani	42°07'56"	142°54'13"	2.80	Ura, Uta	2.4
Samani	42°07'53"	142°54'40"	1.80	Ura, Uta	2.3
Horoman	42°05'01"	143°00'30"	1.28	Ura, Uta	1.7
Asahi-harbor	42°03'49"	143°03'51"	2.05	Ura, Uta	2.3
Fuemai-harbor	42°02'46"	143°06'06"	1.67	Uta	1.9
Fuemai-harbor	42°02'37"	143°06'10"	1.60	Uta	1.9
Erimo-harbor	42°01'07"	143°08'35"	2.55	Uta	2.8
Utabetsu	41°59'34"	143°09'41"	0.60	Uta	0.8
Utabetsubigashi	41°59'42"	143°09'41"	0.95	Uta	1.1
Utabetsuhigashi	41°58'58"	143°09'49"	1.49	Uta	1.8
Toyou	41°57'20"	143°12'24"	2.19	Uta	1.8
Toyou	41°56'50"	143°13'07"	0.70	Uta	1.3
Cape Erimo	41°55'32"	143°14'57"	2.70	Uta	3.3
Erimo-gyoko	41°56'01"	143°14'37"	3.30	Uta	3.3
Erimo-gyoko	41°56'07"	143°14'39"	2.05	Uta	2.1
Erimo-gyoko	41°56'09"	143°14'39"	1.40	Uta	2.0
Hyakuninhama	41°56'49"	143°14'24"	2.55	Uta	2.7
Hyakuninhama	41°56'47"	143°14'24"	2.40	Uta, Hir	3.0
Hyakuninhama	41°57'33"	143°14'33"	3.10	Uta, Hir	3.7
Hyakuninhama	41°57'34"	143°14'33"	3.90	Uta, Hir	4.0
Hyakuninhama	41°57'30"	143°14'33"	4.01	Uta, Hir	4.0
Hyakuninhama	41°59'39"	143°15'14"	3.04	Uta, Hir	3.5
Hyakuninhama	41°58'06"	143°14'38"	3.45	Uta, Hir	3.9
Hyakuninhama	41°59'45"	143°15'16"	3.20	Uta, Hir	3.3
Hyakuninhama	41°59'52"	143°15'17"	2.55	Uta, Hir	2.7
Hyakuninhama	42°01'23"	143°16'34"	2.95	Uta, Hir	3.2

Shoya	42°02'35"	143°17'45"	1.90	Hir	2.3
Shoya	42°02'39"	143°17'52"	1.50	Hir	2.0
Shoya	42°03'00"	143°18'30"	2.35	Hir	2.8
Meguro	42°07'30"	143°19'00"	1.95	Hir	2.5
Oshirabetsu	42°13'29"	143°19'07"	2.01	Hir	2.5
Oshirabetsu	42°13'37"	143°19'57"	2.59	Hir	2.9
Hiroo-gawa	42°16'48"	143°19'04"	2.70	Hir	3.2
Tokachi-harbor	42°17'26"	143°19'05"	1.90	Hir	2.4
Tokachi-harbor	42°17'22"	143°19'13"	2.27	Hir	2.7
Tokachi-harbor	42°17'12"	143°19'25"	3.43	Hir	3.1
Tokachi-harbor	42°17'12"	143°19'25"	3.50	Hir	3.2
Tokachi-harbor	42°17'12"	143°19'25"	2.84	Hir	2.5
Tokachi-harbor	42°17'12"	143°19'25"	3.10	Hir	2.8
Tokachi-harbor	42°17'12"	143°19'25"	2.99	Hir	2.6
Tokachi-harbor	42°17'12"	143°19'25"	3.07	Hir	2.7
Tokachi-harbor	42°17'10"	143°19'18"	3.12	Hir	2.7
Tokachi-harbor	42°17'10"	143°19'18"	3.20	Hir	2.8
Tokachi-harbor	42°17'10"	143°19'18"	3.07	Hir	2.8
Tokachi-harbor	42°17'10"	143°19'18"	3.10	Hir	2.8
Tokachi-harbor	42°17'10"	143°19'18"	3.48	Hir	3.2
Tokachi-harbor	42°17'14"	143°19'14"	3.00	Hir	2.7
Tokachi-harbor	42°17'14"	143°19'14"	2.99	Hir	2.6
Tokacbi-harbor	42°17'14"	143°19'14"	2.99	Hir	2.6
Tokachi-harbor	42°17'14"	143°19'14"	3.03	Hir	2.7
Tokachi-harbor	42°17'14"	143°19'14"	3.00	Hir	2.7
Tokachi-harbor	42°17'14"	143°19'14"	3.00	Hir	2.7
Tokachi-harbor	42°17'14"	143°19'14"	2.96	Hir	2.6
Tokachi-harbor	42°17'14"	143°19'14"	2.95	Hir	2.6
Tokachi-harbor	42°17'14"	143°19'14"	2.98	Hir	2.6
Tokachi-harbor	42°17'14"	143°19'14"	3.08	Hir	2.7
Tokachi-harbor	42°17'14"	143°19'14"	3.08	Hir	2.7
Tokachi-barbor	42°17'14"	143°19'14"	2.89	Hir	2.5
Tokachi-harbor	42°17'14"	143°19'14"	3.15	Hir	2.8
Tokacbi-barbor	42°17'14"	143°19'14"	3.14	Hir	2.7
Tokachi-harbor	42°17'50"	143°19'22"	2.07	Hir	2.6
Tokachi-harbor	42°17'56"	143°19'24"	2.55	Hir	3.1
Tokachi-harbor	42°17'11"	143°19'22"	2.05	Hir	2.6
Sbinseikaigan	42°20'27"	143°20'29"	2.29	Hir	2.4
Toyoni-gawa	42°23'11"	143°22'08"	3.13	Hir	2.8
Asabihama	42°25'09"	143°23'30"	1.39	Hir	1.7
Asahihama	42°26'12"	143°24'11"	2.94	Hir	3.3
Asahihama	42°26'13"	143°24'13"	3.26	Hir	2.9
Hamataiki	42°28'13"	143°25'44"	3.28	Hir	3.4
Hamataiki	42°28'17"	143°25'48"	3.00	Hir	3.3

Hamataiki	42°28'36"	143°25'54"	2.38	Hir	2.4
Hamataiki	42°28'35"	143°25'53"	2.62	Hir	3.1
Hamataiki	42°28'30"	143°25'56"	3.00	Hir	2.7
Hamataiki	42°28'37"	143°26'00"	3.92	Hir	4.0
Horokayantou	42°31'29"	143°28'40"	4.42	Hir	4.1
Horokayantou	42°31'30"	143°28'41"	3.69	Hir	3.4
Banseionsen	42°31'58"	143°29'09"	4.49	Hir	4.1
Banseionsen	42°32'01"	143°29'11"	3.20	Hir	3.4
Banseionsen	42°32'09"	143°29'20"	2.63	Hir	3.1
Oikamanai	42°33'28"	143°30'31"	4.28	Hir	4.1
Oikamanai	42°33'34"	143°30'39"	2.40	Hir	2.9
Yudonuma	42°34'49"	143°31'50"	2.58	Hir	2.7
Yudonuma	42°35'07"	143°32'09"	3.07	Hir	2.7
Yudonuma	42°35'57"	143°33'00"	3.35	Hir	3.4
Yudonuma	42°36'00"	143°33'05"	3.30	Hir	3.3
Yudonuma	42°36'39"	143°33'46"	2.40	Hir	3.1
Cyobushinuma	42°39'17"	143°36'45"	3.16	Hir	3.5
Cyobushinuma	42°39'37"	143°37'11"	3.52	Hir	3.5
Ootsu-harbor	42°40'14"	143°37'59"	2.62	Hir, Kus	2.9
Ootsu-harbor	42°40'49"	143°38'27"	2.24	Hir, Kus	2.8
Ootsu-harbor	42°40'49"	143°38'27"	2.30	Hir, Kus	2.9
Ootsu-harbor	42°40'49"	143°38'27"	2.21	Hir, Kus	2.8
Ootsu-harbor	42°40'49"	143°38'27"	2.20	Hir, Kus	2.8
Ootsu-harbor	42°40'49"	143°38'27"	2.32	Hir, Kus	2.9
Ootsu-harbor	42°40'49"	143°38'27"	2.30	Hir, Kus	2.9
Ootsu-harbor	42°40'49"	143°38'27"	2.32	Hir, Kus	2.9
Ootsu-harbor	42°40'49"	143°38'27"	2.39	Hir, Kus	2.9
Ootsu-harbor	42°40'35"	143°38'17"	1.97	Hir, Kus	2.4
Ootsu-harbor	42°40'49"	143°38'29"	2.43	Hir, Kus	2.9
Ootsu-harbor	42°40'41"	143°38'21"	2.53	Hir, Kus	2.6
Ootsu-harbor	42°40'41"	143°38'21"	2.50	Hir, Kus	2.6
Ootsu-harbor	42°40'41"	143°38'21"	3.24	Hir, Kus	3.4
Ootsu-harbor	42°40'48"	143°38'27"	2.09	Hir, Kus	2.3
Ootsu-harbor	42°40'48"	143°38'27"	2.05	Hir, Kus	2.3
Ootsu-harbor	42°40'48"	143°38'27"	2.78	Hir, Kus	2.8
Ootsu-harbor	42°40'48"	143°38'27"	2.58	Hir, Kus	2.7
Ootsu-harbor	42°40'33"	143°38'17"	2.60	Hir, Kus	2.7
Ootsu-harbor	42°40'33"	143°38'17"	2.32	Hir, Kus	2.4
Ootsu-harbor	42°40'33"	143°38'17"	2.47	Hir, Kus	2.6
Ootsu-harbor	42°40'42"	143°38'21"	1.65	Hir, Kus	1.8
Ootsu-harbor	42°40'52"	143°38'28"	2.29	Hir, Kus	2.4
Ootsu-harbor	42°40'52"	143°38'28"	2.54	Hir, Kus	2.6
Ootsu-harbor	42°40'49"	143°38'26"	2.21	Hir, Kus	2.6
Ootsu-harbor	42°40'49"	143°38'26"	2.51	Hir, Kus	2.9
Ootsu-harbor	42°40'35"	143°38'13"	2.75	Hir, Kus	2.4

Ootsu-harbor	42°40'50"	143°38'29"	2.90	Hir, Kus	2.6
Ootsu-harbor	42°40'50"	143°38'29"	3.50	Hir, Kus	3.1
Ootsu-harbor	42°40'51"	143°38'30"	3.40	Hir, Kus	3.0
Ootsu-harbor	42°40'52"	143°38'29"	3.65	Hir, Kus	3.3
Ootsu-harbor	42°40'53"	143°38'27"	3.25	Hir, Kus	2.9
Ootsu-harbor	42°40'54"	143°38'26"	2.95	Hir, Kus	2.6
Ootsu-harbor	42°40'45"	143°38'24"	3.10	Hir, Kus	2.9
Ootsu-harbor	42°40'44"	143°38'25"	3.00	Hir, Kus	2.8
Ootsu-harbor	42°40'40"	143°38'16"	2.80	Hir, Kus	2.7
Ootsu-harbor	42°40'37"	143°38'14"	2.70	Hir, Kus	2.6
Ootsu-harbor	42°40'40"	143°38'18"	2.95	Hir, Kus	2.8
Ootsu-harbor	42°40'39"	143°38'05"	2.31	Hir, Kus	2.4
Ootsu-harbor	42°40'39"	143°38'05"	1.77	Hir, Kus	1.8
Ootsu-harbor	42°40'36"	143°38'31"	2.27	Hir, Kus	2.0
Ootsu-harbor	42°40'41"	143°38'37"	2.55	Hir, Kus	2.3
Tokachi-gawa	42°41'26"	143°39'34"	2.03	Hir, Kus	1.9
Tokachibuto	42°42'29"	143°40'58"	2.83	Hir, Kus	2.8
Hamaatsunai	42°47'29"	143°48'05"	2.93	Hir, Kus	2.6
Atsunai	42°48'25"	143°49'11"	1.02	Hir, Kus	1.3
Atsunai	42°48'25"	143°49'11"	2.27	Hir, Kus	2.0
Atsunai	42°48'25"	143°49'11"	1.82	Hir, Kus	2.5
Atsunai	42°48'27"	143°49'16"	0.91	Hir, Kus	1.2
Atsunai	42°48'30"	143°49'21"	2.03	Hir, Kus	2.2
Kinashibetsu	42°51'12"	143°53'03"	2.25	Hir, Kus	2.3
Otobetsuhigashi	42°56'39"	144°03'18"	1.11	Hir, Kus	1.6
Pasyukurunuma	42°55'57"	144°00'03"	2.42	Hir, Kus	2.4
Sarogawa	42°57'07"	144°03'59"	1.54	Hir, Kus	2.0
Sarogawa	42°57'07"	144°03'59"	2.27	Hir, Kus	2.7
Sarogawa	42°56'51"	144°03'59"	1.39	Hir, Kus	1.9
Shiranuka	42°57'11"	144°05'12"	1.50	Kus	1.8
Shiranuka	42°57'10"	144°05'12"	2.11	Kus	2.7
Koitoi	42°59'32"	144°11'55"	1.62	Kus	2.1
Kushiro	43°00'01"	144°19'48"	1.20	Kus	1.8
Kushiro	42°59'46"	144°19'54"	1.25	Kus	1.8
Kushiro	42°59'04"	144°22'08"	1.46	Kus	1.5
Kushiro	42°58'57"	144°22'14"	1.38	Kus	1.4
Kushiro	42°59'38"	144°21'25"	0.85	Kus	1.4
Kushiro	42°59'38"	144°21'25"	0.90	Kus	1.5
Kushiro	42°59'35"	144°21'50"	1.00	Kus	1.6
Chiyonoura	42°58'00"	144°23'35"	1.16	Kus	1.3
Kushiro-gawa	42°58'54"	144°22'41"	1.35	Kus	1.6
Konbumori	42°57'03"	144°31'49"	1.22	Kus	1.3
Konbumori	42°57'05"	144°31'50"	0.42	Kus	1.0
Fushiko	42°56'58"	144°32'25"	1.50	Kus	1.6

Pondomari	42°57'04"	144°37'02"	1.55	Kus	1.6
Chippomanai	42°56'01"	144°44'42"	1.03	Kus, Akk	1.6
Senposhi	42°58'33"	144°43'21"	0.86	Akk	1.5
Monshizu	43°03'15"	144°46'54"	1.18	Akk	1.8
Akkeshi	43°02'33"	144°50'48"	0.46	Akk	1.1
Tsukushikoi	43°00'54"	144°50'47"	2.28	Akk	1.8
Tokotan	42°59'35"	144°52'27"	2.35	Akk	2.9
Tokotan	42°59'44"	144°52'07"	2.20	Akk	2.5
Tokotan	42°59'35"	144°52'18"	1.84	Akk	1.7
Horomanbetsu	42°59'14"	144°53'16"	1.70	Akk	2.1
Mabiro	42°59'20"	144°53'50"	3.74	Akk	3.8
Mabiro	42°59'20"	144°54'24"	2.88	Akk	3.1
Mabiro	42°59'20"	144°53'53"	3.92	Akk	4.1
Mabiro	42°59'22"	144°54'04"	3.76	Akk	4.2
Mabiro	42°59'19"	144°54'19"	>2.28	Akk	>2.1
Mabiro	42°59'17"	144°54'23"	>1.94	Akk	>1.7
Mabiro	42°59'20"	144°54'17"	>2.33	Akk	>2.1
Mochirippu	43°01'17"	145°01'16	1.00	Akk, Och	1.1
Hichirippu	43°01'49"	145°01'39"	1.20	Akk, Och	1.1
Biwase	43°03'33"	145°05'16"	1.49	Akk, Och	1.3
Shinkawa	43°04'48"	145°06'36"	1.80	Akk, Och	1.7
Shinkawa	43°04'48"	145°06'19"	0.59	Akk, Och	0.7
Shinkawa	43°04'48"	145°06'19"	0.38	Akk, Och	0.5
Sakaki-	43°07'21"	145°06'55"	1.14	Akk, Och	1.0
Sakaki-	43°07'27"	145°06'59"	1.82	Akk, Och	1.7
Tofutsu	43°04'29"	145°09'02"	1.20	Och	1.2
Ochiishi	43°10'40"	145°30'29"	0.90	Och	1.5
Cyobushi	43°15'18"	145°33'25"	1.82	Han	1.6
Hanasaki	43°17'08"	145°34'49"	1.41	Han	1.4
Shichikari	41°21'54"	141°26'13"	2.59	Shi	2.6
Furuno	41°21'18"	141°19'47"	1.45	Shi	1.7
Tomarim inani	41°03'07"	141°23'20"	1.50	Shi, Hac	1.5
Taroo	39°43'59"	141°58'41"	0.49	Miy	0.8
Miyako	39°38'35"	141°58'31"	1.11	Miy	1.1
Miyako	39°38'29"	141°58'04"	0.80	Miy	1.0
Akamae	39°35'22"	141°57'40"	0.70	Miy	0.7
Hirotawan	39°59'34"	141°37'23"	1.12	Oof, Kes	1.2
Kesennuma	39°53'01"	141°37'21"	0.70	Kes	0.8

1) The reference datum of latitudes and longitudes is World Geodetic System 1984.

2) Reference tide gauges are Hanasaki(Han), Ochiishi(Och), Akkeshi(Akk), Kushiro(Kus), Hiroo(Hir), Utaro(Uta), Urakawa(Ura), Shimokita(Shi), Hachinohe(Hac), Miyako(Miy), Oofunato(Oof), and Kesennuma(Kes). If two reference tide gauges are listed, an average of two tide data is used.

3) The corrected heights are from the mean sea level of Tokyo Bay (T.P.).

Acknowledgements

We would like to thank Laura Kong and an anonymous reviewer for the helpful comments. This work was partially supported by Special Coordination Funds for Promoting Science and Technology, from Ministry of Education, Sports, Culture, Science and Technology.

References

Baptista, A. M., J.J. Westerink, and P.J. Turner: 1989, Tides in the English channel and southern North Sea. A frequency domain analysis using model TEA-NL., *Adv. Water Resources*, **12**, 166-183.

Hamada, N., and Y. Suzuki: 2004, Re-examination of aftershocks of the 1952 Tokachi-oki earthquake and a comparison with those of the 2003 Tokachi-oki earthquake, *Earth Planets Space*, **56**, 341-345.

Honda, R., S. Aoi , N. Morikawa, H. Sekiguchi, T. Kunugi, H. Fujiwara: 2004, Ground motion and rupture process of the 2003 Tokachi-oki earthquake obtained from strong motion data of K-NET and KIK-net, *Earth Planets Space*, **56**, 317-322.

Ichiyanagi, M., H. Takahashi, and M. Kasahara: 2004, Aftershock activity of the 2003 Tokachi-oki earthquake (M_{JMA}=8.0), *Geophysical Bulletin of Hokkaido University*, **64**, 347-357 (in Japanese).

Koketsu, K., K. Hikima, S. Miyazaki, and S. Ide: 2004, Joint inversion of strong motion and geodetic data for the source process of the 2003 Tokachi-oki, Hokkaido, earthquake, *Earth Planets Space*, **56**, 329-334.

Okada, Y.: 1985, Surface deformation due to shear and tensile faults in a half-space Bull. *Seismol. Soc. Am.*, **75**, 1135-1154.

Satake, K.: 1995, Linear and nonlinear computations for the 1992 Nicaragua earthquake tsunami, *Pure Appl. Geophys.*, **144**, 455-470.

Tanioka, Y., and Satake, K: 1995, Tsunami runup on Okushiri Island, in Yeh, H., P. Liu and C. Synolakis (eds.) Long-Wave Models, World Scientific, 249-257.

Tanioka, Y. et al., 2004a, Tsunami run-up heights of the 2003 Tokachi-oki earthquake, *Earth Planets Space*, **56**, 359-365.

Tanioka, Y. et al., 2004b, The report of the survey of the 2003 Tokachi-oki tsunami, *Tsunami Engineering of Tohoku University*, **21**, part 2, 1-237 (in Japanese).

Tanioka, Y., K. Hirata, R. Hino, and T. Kanazawa: 2004c, Slip distribution of the 2003 Tokachi-oki earthquake estimated from tsunami waveform inversion, *Earth Planets Space*, **56**, 373-376

Yagi, Y.: 2004, Source rupture process of the 2003 Tokachi-oki earthquake determined by joint inversion of teleseismic body wave and strong ground motion data, *Earth Planets Space*, **56**, 311-316.

Yamanaka, K., and M.. Kikuchi: 2003, Source processes of the Toachi-oki earthquake on September 26, 2003, inferred from teleseismic body waves, *Earth Planets Space*, **55**, e21-e24.

VARIABILITY AMONG TSUNAMI SOURCES IN THE 17TH-21ST CENTURIES ALONG THE SOUTEHRN KURIL TRENCH

K. SATAKE[1], F. NANAYAMA[1], S. YAMAKI[2], Y. TANIOKA[3] AND K. HIRATA[4]

[1] *National Institute of Advanced Industrial Science and Technology (AIST)*
[2] *Seamus co. ltd.*
[3] *Institute of Seismology and Volcanology, Hokkaido University*
[4] *Japan Agency for Marine-Earth Science and Technology*

Instrumental, historical, and geological records of tsunamis show that successive plate-boundary ruptures differ in size along the southern Kuril trench off eastern Hokkaido. Tsunami source area of the 2003 Tokachi-oki earthquake (M 8.0), the most recent and the best-measured earthquake, is only about 2/3 of that of the predecessor, the 1952 Tokachi-oki earthquake (M 8.2). This difference is apparent from tsunami waveform inversions of the two events. The inversion of the 1952 event, redone with the clock corrections estimated from comparison of the 1952 and 2003 tsunami waveforms, confirms that the 1952 tsunami source extended about 100 km to the east of the 2003 source. The coastal tsunami runup heights were also different; the maximum height in 1952 was recorded by more than 100 km east of that in 2003. An earthquake in 1843 may have resembled the 1952 event, based on tsunami damage distribution recorded in historic documents. Prehistoric tsunami deposits have shown that larger tsunamis occurred in the eastern Hokkaido in an approximately 500 year interval with the last event in the 17th century. These deposits are best explained by earthquakes that broke not only the area of the 1952 event but also the adjoining Nemuro-oki segment to the east. This evidence for variable rupture mode complicates the task of forecasting future earthquakes and tsunamis in eastern Hokkaido. According to a long-term forecast, issued six months before the 2003 earthquake, probability of an M~8 earthquake, similar to the one in 1952, was 60 % by 2033. The forecast was correct for the timing but overestimated the earthquake size.

Key words: Kuril trench, Tokachi-oki earthquake, earthquake recurrence, paleoseismology.

K. Satake (ed.), Tsunamis: Case Studies and Recent Developments, 157-170.

1 Introduction

Along the southern Kuril trench, where the Pacific plate subducts beneath Hokkaido at a rate of ~8 cm/yr, great (M~8) earthquakes have recurred since 19th century when the region's written history started (Figure 1). In the region offshore Tokachi coast (Tokachi-oki), the southernmost segment of the Kuril trench, earthquakes have been documented in 1843 (M 8.0) and 1952 (M 8.2). Offshore from Nemuro (Nemuro-oki), to the east, large earthquakes occurred in 1894 (M 7.9) and in 1973 (M 7.4). Besides these interplate earthquakes, slab earthquakes have also generated tsunamis. For example, an M 8.1 earthquake occurred in Shikotan-oki in 1994 and generated the tsunami (Tanioka et al., 1995; Satake and Tanioka, 1999).

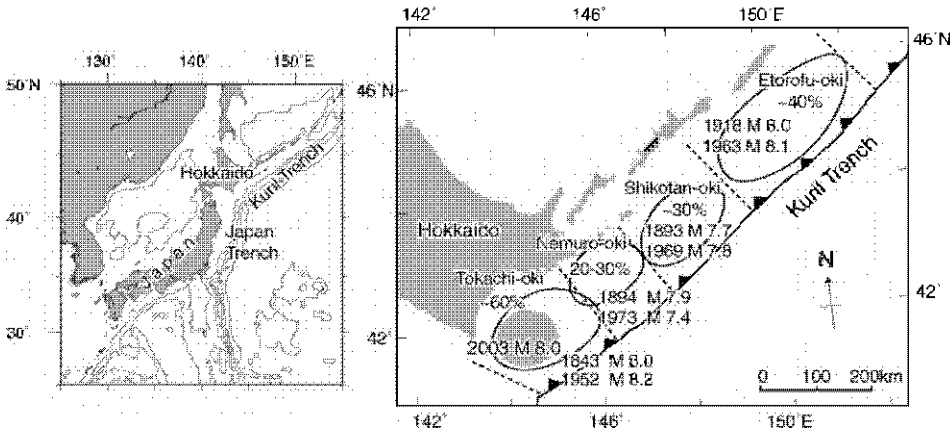

Fig. 1. Location of Kuril trench (left) and the source regions of the great earthquakes along the southern Kuril trench (right). Recurrence of earthquakes in the 19th and 20th centuries in each segment (bordered by dashed lines), as well as the probabilities (in the next 30 years) forecasted before the 2003 Tokachi-oki earthquake are shown (Earthquake Research Committee, 2004). Magnitudes of these events are on the Japanese scale, based on instrumental or historical data (Utsu, 1999).

In March 2003, the Japanese government made long-term forecast for great (M~8) earthquakes along the Kuril trench (Earthquake Research Committee, 2004). The committee estimated that the probability in the next 30 years (starting March 2003) as 60 % in Tokachi-oki and 20-30 % in Nemuro-oki. This forecast was based on the above recurrence of great earthquakes in the 19th and 20th centuries, incorporating key simplifying assumptions: in each of the offshore segments, characteristic earthquakes repeat at regular intervals and the rupture the source area that broke in the 20th century.

Two recent findings cast doubt of these assumptions. First, prehistoric tsunami deposits indicate that unusual large tsunamis have occurred along the Kuril trench (Nanayama et al., 2003). These outsized tsunamis are characterized by large inundation area (kilometers inland from the limits of historical tsunamis) and long (about 500 yrs) recurrence interval. These tsunamis are best explained by earthquakes that rupture multiple segments of the Kuril subduction zone. Soon after this finding was published, an earthquake smaller than forecasted ruptured part of the Tokachi-oki segment in September 2003. Waveform inversion of the 2003 tsunami records (Tanioka et al., 2004a) indicates that the slip distribution on fault is different from that of 1952 earthquake (Hirata et al., 2003).

Improved forecasts will require more attention to variability among successive earthquakes along the southern Kuril trench. To this end, we review earthquakes and tsunamis from 17th through 21st centuries along the Kuril trench. We start with the 2003 Tokachi-oki earthquake, and compare its source region with our reanalysis of the 1952 tsunami. We then make further comparisons with tsunamis of the 19th and 17th centuries. We thereby attempt to define some of the variability among source areas of plate-boundary earthquakes and their tsunamis along the southern Kuril trench.

2 2003 Tokachi-oki tsunami

The source region of the 2003 earthquake has been estimated from seismic waves (e.g., Yamanaka and Kikuchi, 2003), aftershocks (Hamada and Suzuki, 2004) and tsunami first arrivals (Hirata et al., 2004). These studies show that the source was located off the Tokachi coast (Tokachi-oki). The slip and aftershocks extended about as far east as the Kushiro submarine canyon (Figure 2).

Inversion of tsunami waveforms recorded at 9 coastal tide gauges and 2 ocean bottom pressure gauges shows slip distribution on subfaults placed on the subduting plate (Tanioka et al., 2004a). The slip is confined on deep subfaults near the Tokachi coast (Figure 2). The slip distribution is similar to the asperity distribution estimated from seismic waves (e.g., Yamanaka and Kikuchi, 2003). The seafloor deformation calculated from this slip distribution predicts the offshore uplift and coastal subsidence.

The 2003 source area estimated from the seismic and tsunami data is smaller than that of the 1952 Tokachi-oki earthquake estimated by Hirata et al. (2003); the 1952 tsunami source extended to the east of the Kushiro submarine canyon.

The coastal tsunami runup heights, measured within a few days of the tsunami (Tanioka et al., 2004b), were 2-4 m on the Tokachi coast between cape Erimo and Kushiro, and less than 2 m to the east of Kushiro, except for one locality (Mabiro) (Figure 3). While it damaged coastal properties and left two persons missing, the tsunami left no deposits likely to be preserved in coastal geology.

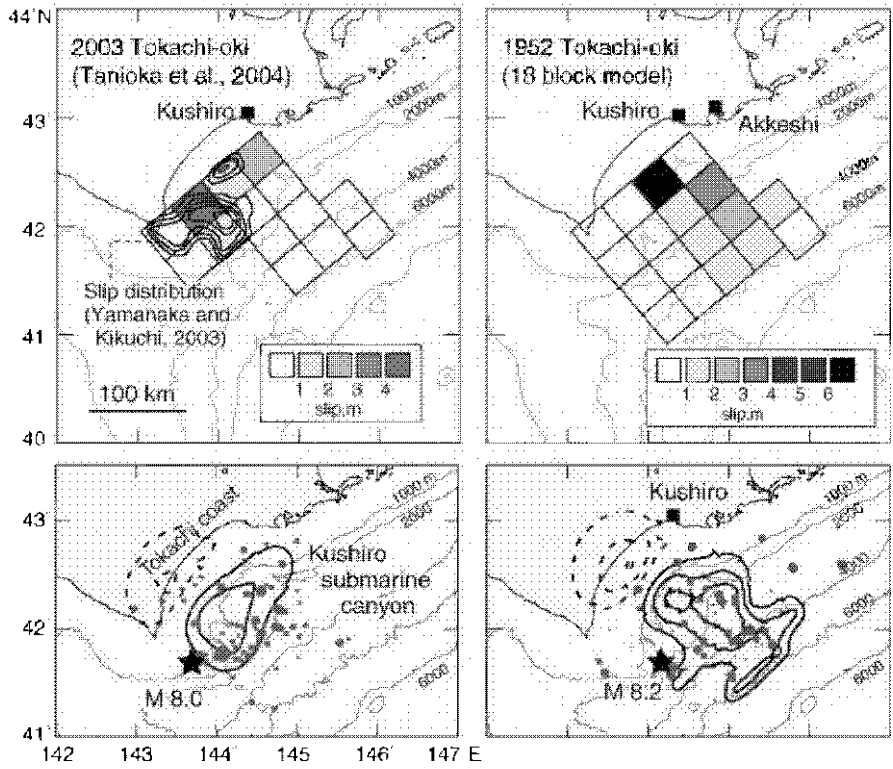

Fig. 2. Slip distribution on subfaults (above) and computed seafloor displacement (below) for the 2003 Tokachi-oki earthquake (left; Tanioka et al., 2004a) and the 1952 Tokachi-oki earthquake (right). The slip distribution estimated from seismic waves (Yamanaka and Kikuchi, 2003) is also shown by contours (interval: 1 m). In the lower map, the mainshock epicenter and the aftershocks within 4 days of the mainshock (Hamada and Suzuki, 2004) are also shown. The contour interval for seafloor displacement is 0.2 m for uplift (solid curves) and 0.1 m for subsidence (dashed curves).

3 Reanalysis of the 1952 tsunami

Distribution of tsunami runup heights from the 1952 Tokachi-oki earthquake is quite different from that of the 2003 event, particularly east of Kushiro (Figure 3). As in 2003, the tsunami heights in 1952 were 2-4 m on the Tokachi coast. To the east of Kushiro, however, the 1952 tsunami heights were 2-7 m, much larger than those in 2003. In fact, the extensive tsunami damage occurred around Akkeshi and Kirittapu, partly because icebergs then floating in the ocean were brought by tsunami to land and caused damage.

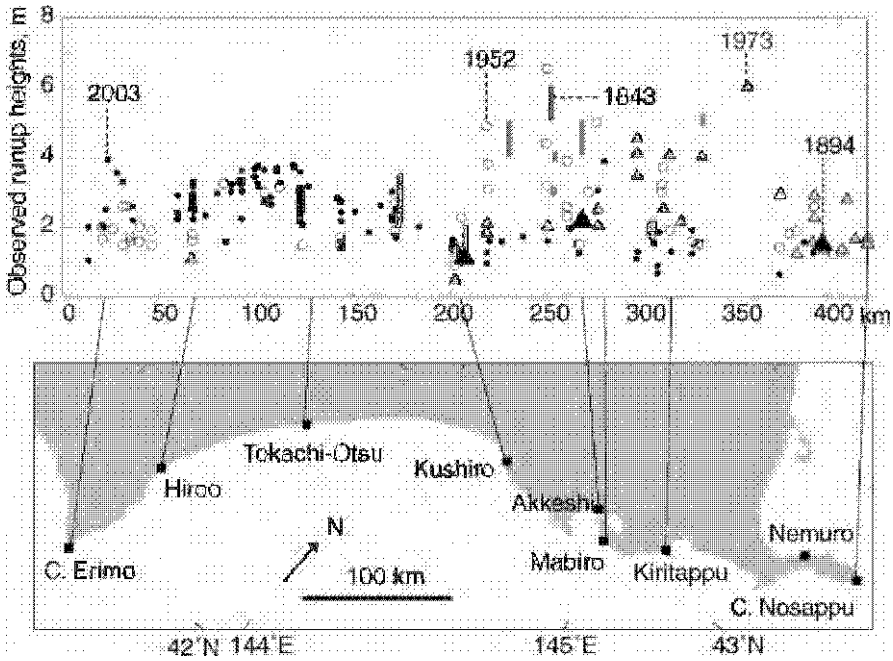

Fig. 3. Measured tsunami heights along the Pacific coast of eastern Hokkaido for the 2003 Tokachi-oki earthquake (Tanioka et al., 2004b), the 1952 Tokachi-oki earthquake (Central Meteorological Agency, 1953; Kusunoki and Asada, 1954), the 1973 Nemuro-oki earthquake (Japan Meteorological Agency, 1974), 1894 Nemuro-oki earthquake (Hatori, 1974), and the 1843 earthquake (ranges estimated from historical documents by Hatori, 1984 and Tsuji, 1994).

We reanalyzed the tsunami waveforms from the 1952 Tokachi-oki earthquake and reestimated the slip distribution by waveform inversion (Satake et al., 2004). We first estimated the clock errors of the 1952 tide gauges, by aligning the 1952 and 2003 waveforms at the first peak. The clock error was as large as 10 min, because the 1952 tide gauges were recorded in paper drums with a typical speed of 2 cm per hour whereas the 2003 tsunami was recorded digitally.

We then computed tsunami waveforms by using the finite-difference method for a linear long-wave equation and the equation of continuity (e.g., Satake, 2002). The grid size is 30" of the arc (about 925 m along the meridian) for deep ocean, and 6" (about 185 m) near the six tide gauge stations. The grid sizes are similar to those used by Tanioka et al. (2004a) for the 2003 Tokachi-oki earthquake tsunami, but much finer than 60" (about 1850 m) used by Hirata et al. (2003) for the 1952 tsunami.

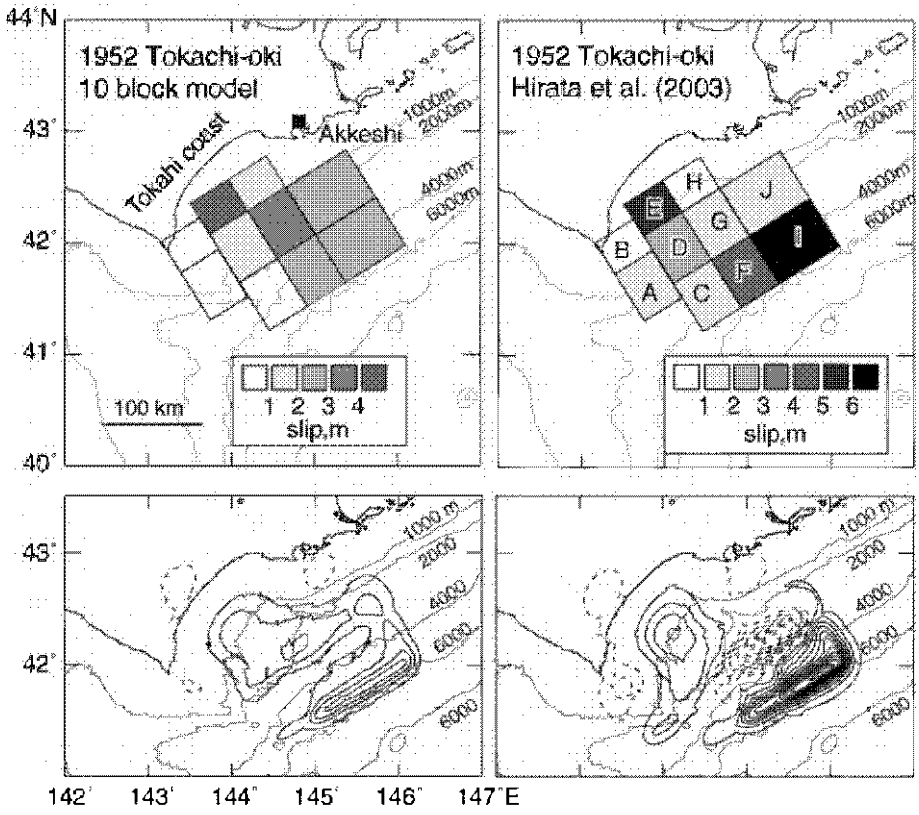

Fig. 4. Slip distribution on faults (above) and computed seafloor displacement (below) for the 1952 Tokachi-oki earthquake. Right panels are those by Hirata et al. (2003) and left panels are those reanalyzed results by Satake et al. (2004). The contour interval for seafloor displacement is 0.2 m for uplift (solid curves) and 0.1 m for subsidence (dashed curves).

To estimate the slip distribution, we divided the source into two kinds of subfaults, 18 blocks and 10 blocks. The 18 block model has the same subfault size (40 km x 40 km) as Tanioka et al. (2004a), except that four additional faults with the same size were added at the southwestern end of the 2003 Tokachi-oki source. The 10 block model has exactly the same configuration as the model of Hirata et al. (2003).

The slip distribution for the 18 block model is quite different from that of 2003 earthquake (Tanioka et al., 2004a) (Figure 2). Seafloor deformation shows two uplift peaks far off Akkeshi and near the Tokachi coast, while there is only one peak near the Tokachi coast in 2003. The slip and seafloor deformation extended to the east of Kushiro submarine canyon in 1952.

The slip distribution for the 10 block model shows that the maximum slip is smaller than that of Hirata et al. (2003) (Figure 4). The largest slip, 4.6 m, is estimated on subfault E, deeper part of Tokachi-oki, where the slip was 5.6 m in Hirata et al. (2003). The slip on subfaults F and I, located off Akkeshi, are less than 3 m, while they were 4.2 m and 7.2 m in Hirata et al. (2003). The seafloor deformation patterns are similar; two peaks near the trench axis off Akkeshi and deeper part of Tokachi-oki, although the amount and the locations are slightly different.

The 10 block and 18 block models have common features that they both have large slip in Tokachi-oki and off Akkeshi. The details of the slip distribution are different, probably reflecting the spatial resolution of the subfaults. Even so, slip distributions for the both models are clearly different from that of the 2003 earthquake.

4 19th century earthquakes and their tsunamis

For the earthquakes in the 19th century, macroseismic data, i.e., distribution of tsunami heights and seismic intensity, are the only available data to estimate the source areas.

The tsunami heights of the 1894 Nemuro-oki earthquake resemble those of the 1973 Nemuro-oki earthquake (Figure 3). The 1894 heights were estimated by Hatori (1974) on the basis of damage report of Omori (1895). The original damage report indicates that the tsunami damage increases from Kushiro towards the east. The eastward increase of tsunami heights seems to be a characteristic feature of Nemuro-oki earthquake.

The 1843 earthquake shows a different pattern more nearly like that of the 1952 tsunami. The tsunami heights were estimated by Hatori (1984) and Tsuji (1994) from damage descriptions. As in 1952, the largest tsunami (4-6 m) was reported from Akkeshi (Figure 2). However, historical documents are limited around Akkeshi, the population center of that time, and no information is available from the Toakchi coast.

Seismic intensity distributions also show different patterns for the Tokachi-oki and Nemuro-oki earthquakes (Figure 5). The isoseismals are elongated along the Pacific coast, because of subducting of Pacific plate, in which seismic waves travel with less attenuation. The largest intensity (6 on JMA scale) was registered around Tokachi coast in 2003 and 1952. The largest intensity was registered at the eastern edge of Hokkaido for the 1973 and 1894 Nemuro-oki earthquakes. The intensity distribution of the 1843 earthquake is limited in eastern Hokkaido and northernmost Honshu, but it seems more similar to Tokachi-oki earthquakes than to the Nemuro-oki events (Hatori, 1984).

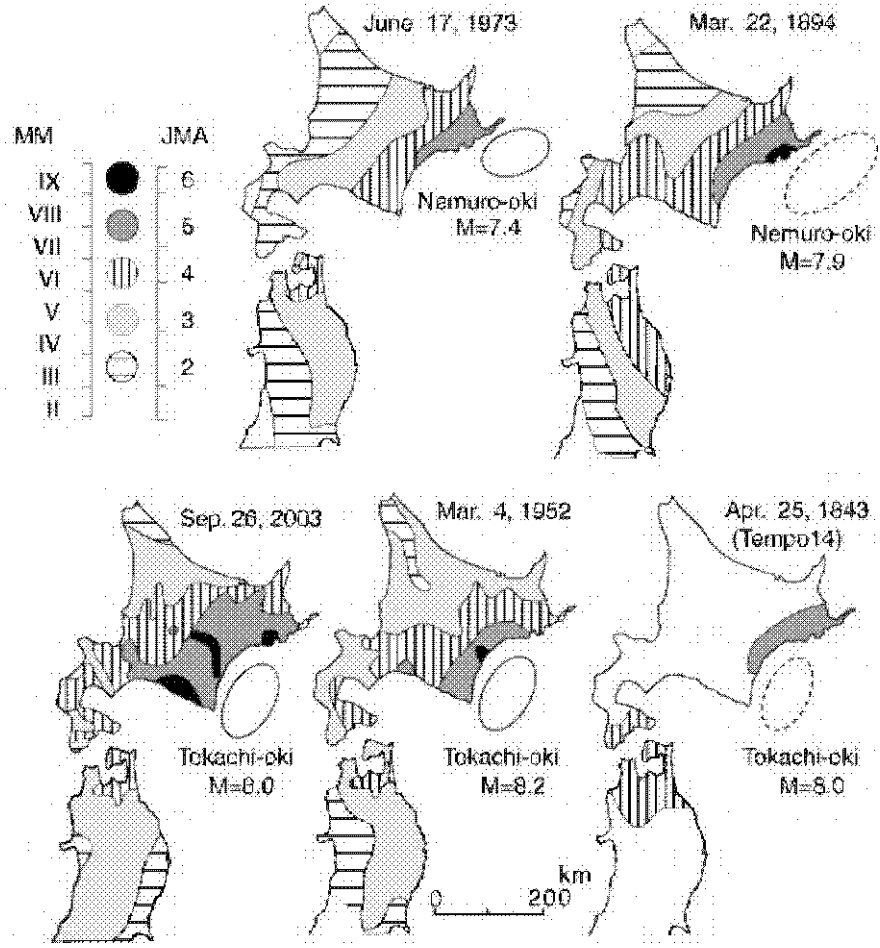

Fig. 5. Seismic intensity distribution of the 1973 and 1894 Nemuro-oki earthquakes (top) and of the 2003, 1952 and 1843 Tokachi-oki earthquakes (bottom). Modified from Hatori (1984); data on the 2003 from Japan Meteorological Agency.

5 17th-century tsunami

Tsunami deposits from the past 7000 years in eastern Hokkaido show that the southern Kuril trench repeatedly produced earthquakes and tsunamis larger than those recorded in the region's 200 years of written history. Deposits of prehistoric tsunamis underlie lowlands and lagoons along 200 km of eastern Hokkaido's Pacific coast (Nanayama et al, 2003).

In Kiritappu, prehistoric sand sheets extend as much as 3 km inland across a beach-ridge plain. The 1952 tsunami, by contrast, penetrated about 1 km from the coast

(Central Meteorological Agency, 1953). Diatom analysis indicates that the prehistoric sand sheets are of marine origin.

At Kiritappu and elsewhere, the time intervals between the extensive sand sheets average about 500 years (Nanayama et al., 2003). Volcanic ash layers aid in this correlation and dating. The youngest of the prehistoric sand sheets shortly predates ash layers from 1663 (Usu volcano) and 1667 (Tarumai). A second, earlier sand sheet postdates a 10th century ash that erupted from Baitoushan on the border of China and North Korea. Three to five sand sheets are commonly found between the 10th century ash and a Tarumai ash about 2500 years old.

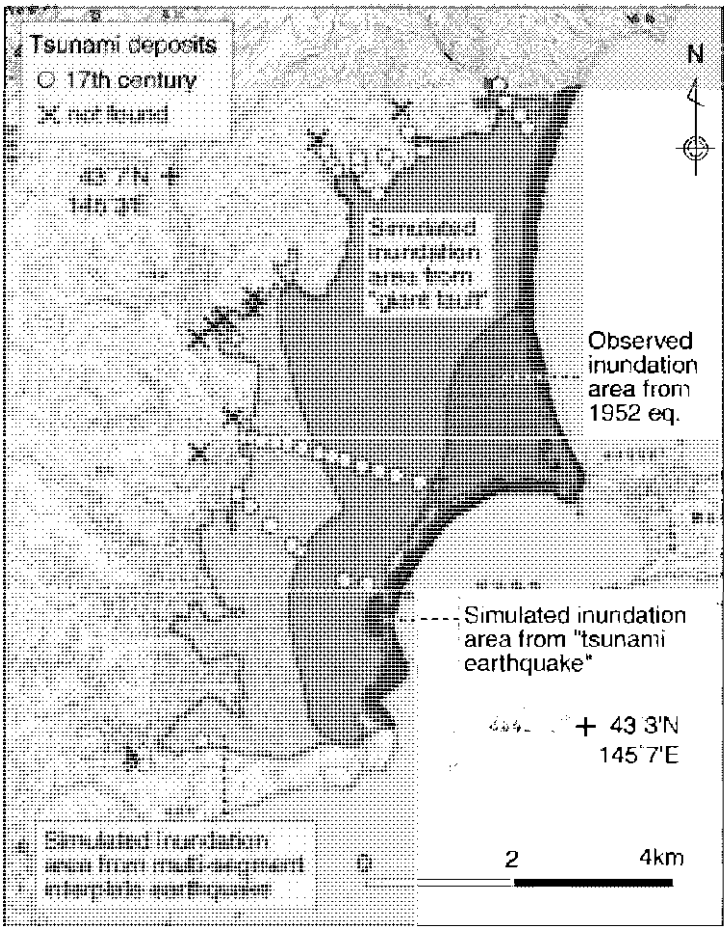

Fig. 6. Distribution of 17th century tsunami deposits in the Kiritappu marsh (Nanayama et al., 2003). Measured inundation area from the 1952 Tokachi-oki tsunami (Central Meteorological Agency, 1953) and computed inundation areas from three different fault models are also shown.

To explain the prehistoric tsunamis we considered three different fault models: giant fault, interplate earthquake, and tsunami earthquake (Figure 7). In all three models, the fault extends 300 km along the trench to include both the Tokachi-oki and Nemuro-oki segments. The giant fault extends 250 km down the plate boundary from the trench to 85 km depth, beneath the Pacific coast. The interplate earthquake fault is 100 km wide, and its depth range is between 17 and 51 km, corresponding to ordinary seismogenic region of subduction zones (Tichelaar and Ruff, 1993). The fault model for the tsunami earthquake is 50 km wide and located near the trench axis, similar to recent tsunami earthquakes (Satake and Tanioka, 1999). The wider the fault, the wider the area of seafloor displacement (Figure 7). For the giant fault, the coast is uplifted at the time of earthquake. For the interplate fault, the coast subsides during the earthquake.

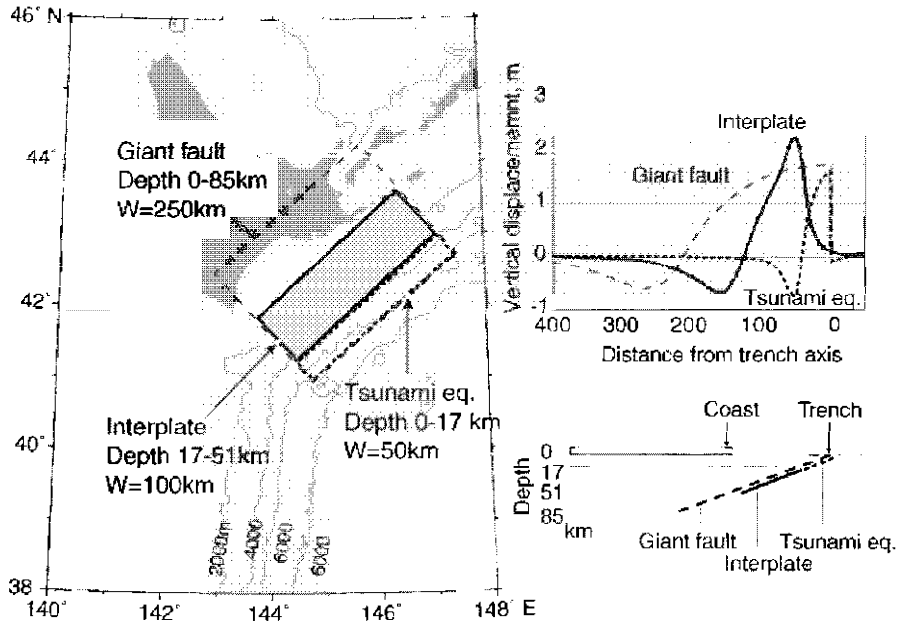

Fig. 7. Three fault models tested for tsunami coastal heights and inundation to Kiritappu marsh. Giant fault is 250 km wide, extending 0-85 km in depth. Interplate fault is 100 km wide and the depth range is 17-51 km. The tsunami earthquake model is 50 km wide, between the depth range of 0-17 km. The average slip is fixed at 5 m.

For inundation modeling, we use the grid size as small as 25 m and include inundation on land, or moving boundary condition, into the computation. For the computations of coastal tsunami heights, we use the finest grid size of 225 m, but without considering inundation or runup on land.

The computed inundation area is largest for the interplate earthquake fault, and the inundation is somewhat less for the giant fault. The tsunami earthquake model yields little inundation. The interplate fault model most nearly matches the mapped distribution of tsunami deposits (Figure 6).

The interplate fault model also yields the largest tsunami heights along the coast, while the giant fault yields the smallest coastal heights (Figure 8). For the giant fault, the coast, as well as the seafloor, is uplifted, hence the vertical displacement effective to tsunami generation is smaller than with the interplate fault, which lowers the coast. The interplate fault model yields larger tsunami heights than the tsunami earthquake on the Tokachi coast, while the heights are similar on the coast east of Kushiro.

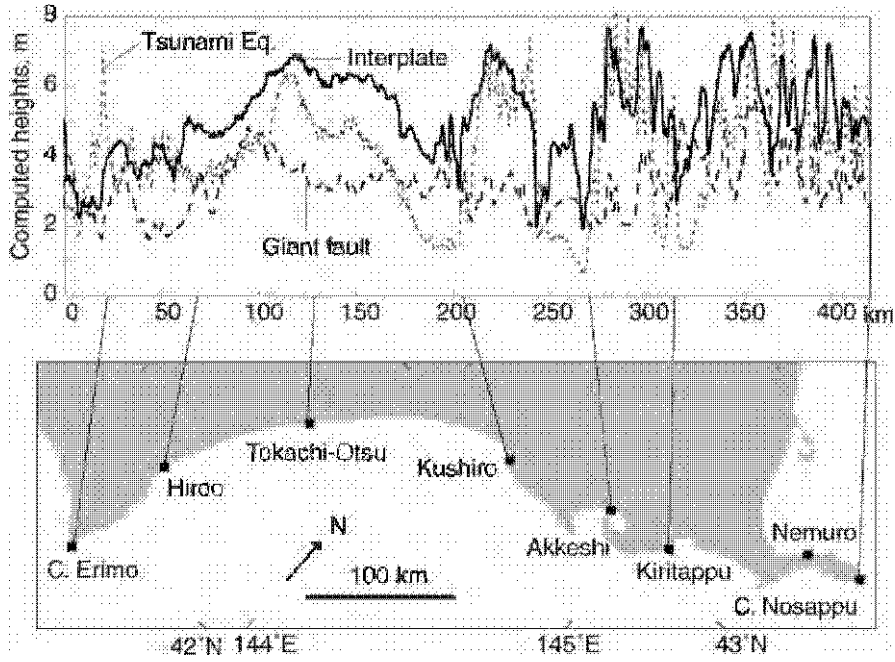

Fig. 8. Coastal tsunami heights computed from the three fault models. For the computation, the smallest grid size along the coast is 225 m.

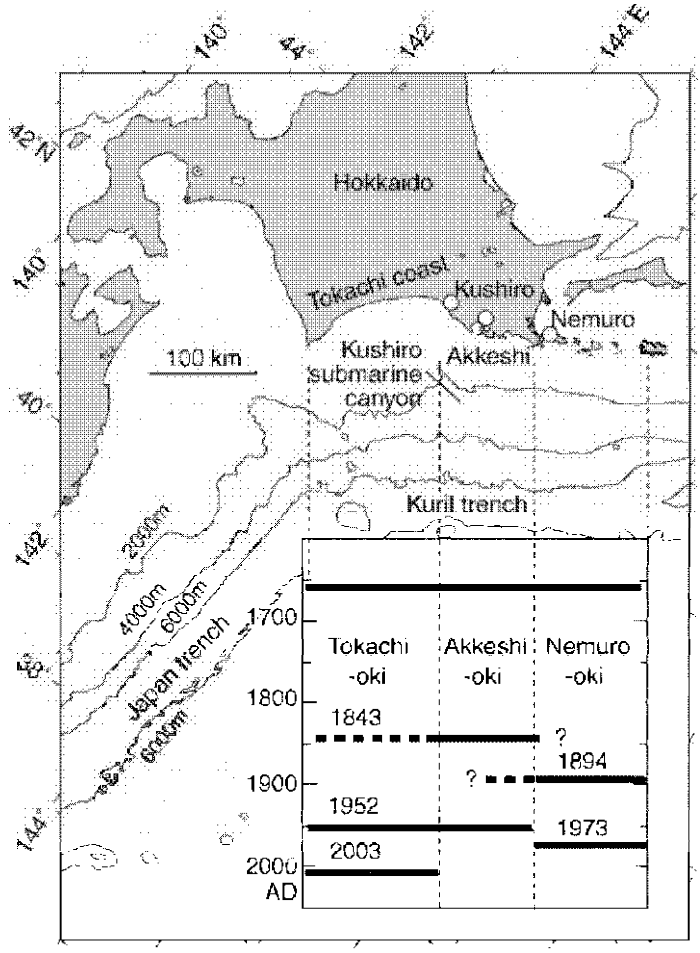

Fig. 9. Space-time diagram of the 17th through 21st century great earthquakes along the Kuril trench. On the basis of Hatori (1984), the 17th century earthquake (Nanayama et al., 2003) and the 2003 earthquake were added.

6 Summary

The source regions probably varied among earthquakes of the 17th through 21st centuries along the southern Kuril trench (Figure 9). Seismic waves and tsunamis indicate that the 2003 Tokachi-oki earthquake (M 8.0) source was limited in Tokachi-oki region, only the western half of Tokachi-oki segment in Figure 1. The tsunami waveforms and coastal runup height distribution of the 1952 Tokachi-oki earthquake (M 8.2) indicate that at least the tsunami source includes both Tokachi-oki and Akkeshi-oki regions, extending to the east of Kushiro submarine canyon (the Tokachi-

oki segment in Figure 1). The 1973 Nemuro-oki earthquake (M 7.4) occurred in the Nemuro-oki segment, as shown by the aftershock distributions and tsunami heights. The 1894 Nemuro-oki earthquake (M 7.9) showed similar tsunami height distribution, but the source may be larger than that of 1973 event (Hatori, 1974). The tsunami height from the 1843 earthquake was largest around Akkeshi, suggesting that the source was located at least in Akkeshi-oki, but lack of historical data cannot constrain the eastern and western ends. A 17th-century earthquake generated unusually large tsunamis along the Pacific coast, and tsunami modeling shows that multi-segment (the Tokachi-oki and Nemuro-oki segments) interplate earthquake best explains such unusual tsunamis.

References

Central Meteorological Agency, Reports of the Tokachi-oki earthquake of March 4, 1952, *Quarterly J. Seismology*, 17 (1-2), 1-135, 1953.

Earthquake Research Committee, Long-term evaluation of seismicity along the Kuril Trench, *Publications of Earthquake Research Committee*, II, 1-74, 2004.

Hamada, N. and Y. Suzuki, Re-examination of aftershocks of the 1952 Tokachi-oki earthquake and a comparison with those of the 2003 Tokachi-oki earthquake, *Earth Planets Space*, 56, 341-345, 2004.

Hatori, T., Source area of the tsunami off the Nemuro Peninsula in 1973 and its comparison with the tsunami in 1894, Special Bull. Earthq. Res. Inst. Univ. Tokyo, 13, 67-76, 1974 (in Japanese with English abst.).

Hatori, T., Source area of the east Hokkaido tsunami generated in April, 1843, *Bull. Earthq. Res. Inst. Univ. Tokyo*, 59, 423-431, 1984 (in Japanese with English abstract)

Hirata, K. E. Geist, K. Satake, Y. Tanioka and S. Yamaki, Slip distribution of the 1952 Tokachi-oki earthquake (M 8.1) along the Kuril trench deduced from tsunami waveform inversion, *J. Geophys. Res.*, 108, 2196 doi: 10.1029/2002JB001976, 2003.

Hirata, K., Y. Tanioka, K. Satake, S. Yamaki and E. L. Geist, The tsunami source area of the 2003 Tokachi-oki earthquake estimated from tsunami travel times and its relationship to the 1952 Tokachi-oki earthquake, *Earth Planets Space*, 56, 367-372, 2004.

Japan Meteorological Agency, Report on the Nemuro-Hanto-Oki earthquake of June 17, 1973, *Tech. Rep. JMA*, 87, 192 pp., 1974.

Kusunoki, K. and H. Asada, Report on the survey of the "tsunami" in Hokkaido caused by the Tokachi earthquake, in *Report in the Tokachi Oki earthquake*, Special Committee for the Investigation of the Tokachi-oki earthquake, Sapporo, 1018 pp., 273-285,1954 (in Japanese).

Nanayama, F., K. Satake, R. Furukawa, K. Shimokawa, B.F. Atwater, K. Shigeno and S. Yamaki, Unusually large earthquakes inferred from tsunami deposits along the Kuril trench. *Nature*, 424, 660-663, 2003.

Omori, F., Preliminary report of Hokkaido earthquake of March 22, 1894 (Meiji 27th), *Rep. Imp. Earthq. Inv. Comm.*, 3, 27-35, 1895 (in Japanese).

Satake, K., Tsunamis, in W. H. K. Lee, H. Kanamori, P. C. Jennings, and C. Kisslinger (eds.) *International Handbook of Earthquake and Engineering Seismology*, 81A, 437-451, 2002.

Satake, K., K. Hirata, S. Yamaki and Y. Tanioka, Reanalysis of tsunami data from the 1952 Tokachi-oki earthquake, to be submitted to Earth Planets Space, 2004.

Satake, K. and Y. Tanioka, Sources of tsunami and tsunamigenic earthquakes in subduction zones, *Pure Appl. Geophys.*, 154, 467-483, 1999.

Tanioka, Y., L. Ruff, and K. Satake, The great Kuril earthquake of October 4, 1994 tore the slab, *Geophys. Res. Lett., 22*, 1661-1664, 1995.

Tanioka, Y., K. Hirata, R. Hino and T. Kanazawa, Slip distribution of the 2003 Tokachi-oki earthquake estimated from tsunami waveform inversion, *Earth Planets Space*, 56, 373-376, 2004a.

Tanioka, Y. and 26 coauthors, Tsunami run-up heights of the 2003 Tokachi-oki earthquake, *Earth Planets Space*, 56, 359-365, 2004b.

Tichelaar, B. and L. Ruff, Depth of seismic coupling along subduction zones, *J. Geophys. Res., 98*, 2609-2623, 1993.

Tsuji, Y., On Tempo Kushiro-oki earthquake, *Seism. Soc. Japan Newsletter*, 5(6), 20, 1994 (in Japanese).

Utsu, T., *Seismicity Studies: A Comprehensive Review*, University of Tokyo Press, 876 pp., 1999.

Yamanaka, K. and M. Kikuchi, Source processes of the Tokachi-oki earthquake on September 26, 2003 inferred from teleseismic body waves, *Earth Planets Space*,55, e21-e24, 2003.

HOLOCENE TSUNAMI TRACES ON KUNASHIR ISLAND, KURILE SUBDUCTION ZONE

A.YA. ILIEV[1], V.M. KAISTRENKO[1], E.V. GRETSKAYA[1], E.A. TIKHONCHUK[1], N.G. RAZJIGAEVA[2], T.A. GREBENNIKOVA[2], L.A. GANZEY[2] AND A.A. KHARLAMOV[3]

[1] *Institute of Marine Geology and Geophysics FEB RAS, Yuzhno-Sakhalinsk, Russia*
[2] *Pacific Institute of Geography FEB RAS, Vladivostok, Russia*
[3] *P.P. Shirshov Institute of Oceanology RAS, Moscow, Russia*

The paper presents the detailed study of sediments deposited by middle-late Holocene tsunami in the Pacific Ocean at the Okhotsk Sea area and Izmena Bay coast of Kunashir Island. Seventeen thin sand-layers were found to be intercalated within peat of lacustrine deposits. Field data, grain-size composition, and biostratigraphical data allow interpretation of them as paleotsunami traces. Age of the sand-sheet was based on radiocarbon dating and tephrostratigraphy. Diatoms helped identify the tsunami deposits' origins and confirm that the sands had a marine source, and establish the landward extent of tsunami inundation. Tsunami deposits contain more contents of neritic and oceanic diatoms than marine units deposited during Holocene transgressions. The sand layers were deposited by tsunami with a maximal run-up more than 7 m, and penetration inland more the 2.5 km. The time period relating to the found tsunami deposits is 6,000–7,000 years. Correlation of tsunami events of Kunashir, Iturup Island, and Eastern Hokkaido have been done.
Key words: tsunami deposits, diatoms, inundation limit, Holocene, Southern Kuriles.

1 Introduction

Located in one of the most active seismic regions of North-Western Pacific, Kunashir Island is known to have several great earthquakes during historical times, some of which were accompanied by tsunami. Tsunami waves produced by the 4 October 1994 earthquake, the epicenter of which was located near Shikotan Island, had the heights up to 8.7 m above mean sea level on the eastern coast of the Kunashir Island (Korolyov et al., 1997). Catastrophic tsunami are rare events, and historical data does not include reliable estimates of their frequency, impact on natural environments, and their effect on coastal development and tsunami hazard prognoses. The modern approach to such problems supposes a search and analysis of geological traces of paleotsumani that allows a reconstruction of the chronology of catastrophic tsunami at the Holocene, estimate their frequency and intensity, and spatial distribution on the

K. Satake (ed.), Tsunamis: Case Studies and Recent Developments, 171-192.

basis of the correlation of tsunami deposits of contiguous areas. Evidence of strong tsunamis and pre-historic earthquakes in this region has been found in Iturup Island (Bulgakov et al., 1995) and Eastern Hokkaido (Nanayama et al., 2000, 2003; Sawai, 2002; Hirakawa et al., 2003).

Existing tsunami catalogues contain the tsunami data for the Kunashir Island coast only since 1958. Such a short tsunami history of this region doesn't allow the creation of a good model for the description of the tsunami activity. However the needed tsunami data can be found in Holocene coastal sequences. Holocene peatlands, widespread along the Pacific coast of Kunashir and within low isthmuses are informative objects for paleotsunami study. Other useful objects for examination are numerous modern, and ancient, coastal lakes in the region.

The paleotsunami study includes searches of their traces in Holocene sequences and, afterwards, the identification of their origins by diatom analysis and sedimentological methods.

Diatoms are particularly useful in studies of paleotsunami deposits because different species are found in freshwater than in brackish-marine environments, and, therefore, can be used to identify past marine incursion, including those associated with tsunami (Minoura and Nakata, 1994; Hemphill-Haley, 1996; Nanayama et al., 2000, 2003; Nishimura et al., 2000; Sawai, 2002). Frequent volcanic activity on Kunashir Island are main factors for favorable diatoms development in different freshwater and marine environments (Grebennikova, 2000). The presence of marine and brackish diatoms among freshwater assemblages in thin sand layers indicates short-time marine influence, which can be connected to storm-surge or tsunami. Marine diatoms from these deposits are rare and most valves are fragmented (Sawai, 2001; 2002). Diatom assemblages from marine deposits that formed during transgressions are characterized by high abundance and high diversity of marine species and well-preserved valves. Ecological parameters of such diatom assemblages are typical for climatic warming. Thickness of transgressive sequences is, as a rule, significant.

This paper presents the result of reconnaissance work, some stratigraphical data, and other evidence, for a several tsunami that occurred about 6,000-7,000 years BP on the South Kurile region.

2 Material and methods

The region studied includes the Pacific Ocean and Okhotsk Sea sides of Kunashir and the Izmena Bay coasts (Figure 1). The areas are different distances from the coastline (up to 2.5 km).

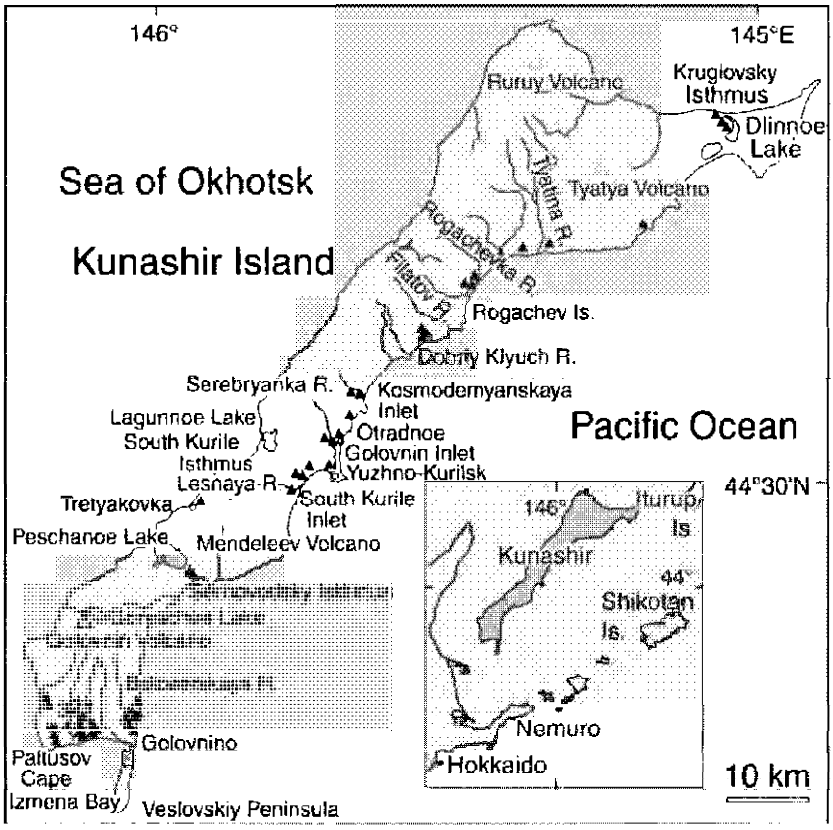

▲active volcano▲ site 1 – Golovnin R.; 2 – Khlebnikov R.; 3 – Sonnaya R.

Fig. 1. Location of study area.

The tsunami traces are moderately or well-sorted massive sharply bounded sand sheets from peat bogs, lacustrine silt-pelitic deposits, and lacustrine diatomites. The thickness of these sand layers ranges from 1 mm to 1–2 cm. Thicker sheets of sediment are visible in coastal stratigraphical sequences. Only fingers usually may find sand sheets of some millimetres in thickness. In some cases, the sand includes fragments of wood and other plant material. Large wood fragments may mark upper inundation limit. Within area development of pumice tuffs (Golovnin Formation on South Kunashir) pumice layers located far inland are also tsunami traces. For definition of the tsunami deposits, we used the criteria for their recognition from the works of last ten years (Minoura and and Nakata, 1994; Alwater et al., 1995; Dawson and Shi, 2000; Goff et al., 2001; Nanayama et al., 2000; 2003; Pinegina and Bourgeois, 2001; Hirakawa et al., 2003; Schedders and Kelltat, 2003).

Our results are based on summer field season from 2001-2002. More than 100 sections (excavated trenches, cores or outcrops) in the peat areas and paleo-lakes along the Kunashir Island coast were investigated. All studied sections are located far from

storm influence zone and it is supposed that tsunami was the only mechanism of sand transportation. Sand layers and volcanic ash layers were sampled in each site. Some outcrops were selected for detailed observations and sampling of underlyed and overlyed deposits of different origin. Paleotsunami height determination was based on level measurement of geomorphologic profiles and inundation by tracing of sand layers from coastline to landward.

Age of the deposits was determined by radiocarbon dating (Table 1). The samples were treated with standard acid and alkali solution. ^{14}C-dates were produced by liquid scintillation counting in the Geological Institute, Russian Academy of Sciences, Moscow. The age calibrations were made using the calibration program Calib 4.3 (Stuiver and Reimer, 1993; Stuiver et al., 1998). The time period related to the tsunami deposits examined is about 7,000 years.

Many tephra layers were used to estimate the tsunami deposits' ages, and the sites' correlation to each other. Tephra layers were identified in the field and later studied in the laboratory under cross-polarised light. The study of the tephra includes chemical analysis of all sample fractions and mineralogy (measurement of refractive indexes of volcanic glass; volcanic glass morphology; heavy fraction study). For mineral analysis, the 0.05-0.1 mm and 0.1-0.25 mm fractions were separated from the sediment samples by wet sieving. Heavy minerals were extracted with tribromomethane (density 2.89 g/cm^3). Refraction indexes of volcanic glass from some ash samples were measured after dehydration (Nakamura et al., 2002). The chemical (wet chemistry) composition of ash layers was also investigated. The correlation of ash layers is based on ^{14}C dates from under- and overlying deposits, on refractive indices and morphology of volcanic glass shards, and on chemical and mineral composition. The sources of ash layers from Kunashir deposits were as Hokkaido as local volcanoes, as Kunashir Volcanoes (Furukawa et al., 1997; Nakagawa et al., 2002; Abdurakhmanov et al., 2003).

The reconstructions of some tsunami parameters (heights and minimal inundation) were based on the presence and elevation of interpreted tsunami deposits and distance from the present shoreline. Grain-size by sieving and mineralogical analysis of some tsunami sands was also made.

In addition, diatom assemblages contained within the sand sheets provide additional argument of their tsunami origin. Diatom samples were analyzed at these sand-layers and the overlying and underlying deposits. The diatom processing method follows those of Gleiser et al. (1974: 55–79). The samples were treated with a solution of hydrogen peroxide and washed with distilled water. For certain diatom preparation, heavy-liquid (mixture of H_2O:CdJ_2:KI=1:1.5:2.25, density 2.4 g/cm^3) was used. Permanent preparations were made with 18 mm x18 mm cover-glasses and Elyashev aniline-formaldehyde resin with refraction indices n=1.66-1.68. Diatoms were identified at magnification x1,000. When possible, 200–300 valves were counted per sample.

The ecological significance of diatoms species was taken from de Wolf (1982), and from Krammer and Lange-Bertalot (1986, 1988, 1991a, 1991b). The ecological Data provided by the above-mentioned authors has enabled most taxa to be grouped into the three categories: marine, brackish, and freshwater. Then marine species were divided into oceanic, neritic, and sublittoral species. Freshwater species into planktonic and benthic forms. Paleotsunami traces are identified by appearance of marine diatoms among fresh-water assemblages, typical for lacustrine-swamp environments.

Table 1. ^{14}C ages of the Holocene deposits of Kunashir Island.

Location	Sample No	Depth (m)	Material	^{14}C-date	cal. ^{14}C-date (2σ) BP	GIN-No.
Rogachevka R.	1/4201	0.42-0.47	peat	1450±60	1510-1270	11906
	2/4201	0.79-0.84	peat	1970±40	2000-1820	11907
	3/4201	1.08-1.15	peat	2360±40	2470-2330	11908
Dobriy Klyuch	1/4901	0.12-0.16	wood	50±30	1899-1952 AD	11881
	2/4901	0.90-1.00	peaty silt	2870±50	2840-2740	12009
Kosmodemian-skaya Inlet	1/1501	2.10-2.15	peat	5290±40	6190-5930	11885
	2/1501	1.65-1.75	wood	4240±40	4862-4649	11892
South-Kurile Ithmus	1/701	0.5-0.55	wood	320±90	1425-1948 AD	11882
	2/701	0.93-0.96	peat	2190±40	2330-2070	11920
Otradnoe	1/1101	0.38-0.42	peat	2650±40	2840-2740	12008
	2/1101	0.84-0.9	peat	3500±70	3975-3590	12221
Lesnaya R.	3/1401	2.05-2.10	wood	5270±80	6280-5900	11891
	4/1400	1.45-1.50	wood	4470±70	5320-4870	11893
	5/1400	1.06-1.10	wood	4080±70	4830-4410	11894
Belozerskaya R.	1/6101	0.20-0.25	peaty silt	870±40	910-690	12010
	1/8201	0.13-0.20	wood	320±40	1490-1640 AD	11882
	2/8201	0.58-0.65	peat	3070±90	3470-3000	12006
	3/8201	0.9-1.0	peat	3820±60	4420-3990	12007
Paltusov Cape	2/7001	0.65-0.70	wood	2310±40	2360-2180	11889
	1/7201	0.57-0.62	peat	2490±100	2780-2340	11917
	2/7201	1.13-1.20	peat	3520±100	4090-3560	11919
Khlebnikov St.	1/7401	1.07-1.43	peat	3760±40	4240-3980	12011
Golovnin R.	1/8801	1.39-1.45	peat	3890±40	4420- 4150	12219
	2/8801	1.2-1.3	peat	5270±70	6270-5910	12220
	1/9001	0.30-0.35	peat	4820±40	5610-5470	11918
	2/9001	0.45-0.50	peat	3610±110	4240-3640	11922
	3/9001	0.57-0.65	peat	3800±40	4350-4020	11921
	4/9001	1.10-1.15	peat	4530±110	5580-4860	11924
	5/9001	1.75-1.85	peat	6360±110	7460-7010	11924
Tyatina R.	1/3101	0.25-0.30	soil	510±90	660-320	11947
Kruglovsky Ithmus	1/1202	0.45-0.54	peat	800±50	790-655	12222
	2/1202	0.85-0.90	peat	1240±40	1260-1060	12223

3 Results

Coastal lowlands of Kunashir can be divided into three groups: low swamp isthmuses with coastal lakes (Sernovodsky and Kruglovsky Ithmusis), mares located within open inlets coasts, and narrow, swampy river valleys that stretch far inland, developed on the southern coast of the island. In all cases, the base of Holocene sequences is composed of marine deposits formed during different middle-late Holocene transgressions. The terrestrial and coastal records are usually discontinuous, and there is a need to study the stratigraphy of numerous sections, composed of different facies, for reliable paleogeographical reconstruction. The sections studied are located on coastal plain and low marine terrace sequences, 3-5 m and more above present sea level. Tsunami deposits are represented by very thin sand-sheets (thickness: 1–5 mm; rarely up to 3 cm), that are found beyond storm-wave influence. Sand sheets over relatively wide areas and considerable distance inland. The base and top boundary of the sheets are sharp, but contacts are not erosion. The observation of modern tsunami in this region (Korolyov et al., 1997) indicate absence of active erosion that directly connected with the nature and scale of tsunami wave in the first instance of backwash flows (Dawson, 1999). Good age-correlation of such sand layers, from the sites located in difference places of the coasts and with surrounding area data (Bulgakov et al., 1995; Nanayama et al., 2000, 2003; Sawai, 2002), is one of criteria for tsunami origin of the deposits. The majority of the peatlands of Kunashir were formed in the late Holocene, and record traces of paleotsunami that took place during the last 2,500–3,000 years. At that time, the configuration of coastline was similar to the present day (Korotky et al., 2000).

3.1. PACIFIC COAST

In north part of the island, accumulative landforms are usually non-extensive. The coast is represented by late Holocene low, marine terraces set up ancient vegetated cliffs. Soils or peat from the upper part of the sections usually include some sand-layers, but it is difficult to define their origin and differ tsunami sediments from sands deposited by storms. Sand layers were not found in soil profiles of flat surfaces with elevations higher than 10 m.

Deposits, which we identified as tsunami traces, were found in peat bog located within coastal plain (up to 1 km wide) near the Rogachevka River mouth (Figure 2). The peat bog is located behind storm ridges with dunes (elevation up to 7 m a. m. s. l.). The peat is formed in river flood lakes. The peat includes up to five thin (3-5 mm) layers of well-sorted medium-to-fine sand with modal fractions 0.25–0.315 mm and 0.16–0.25 mm. The source of material was possibly beach- and dune-sands. Marine origin of the deposits was confirmed by diatom data.

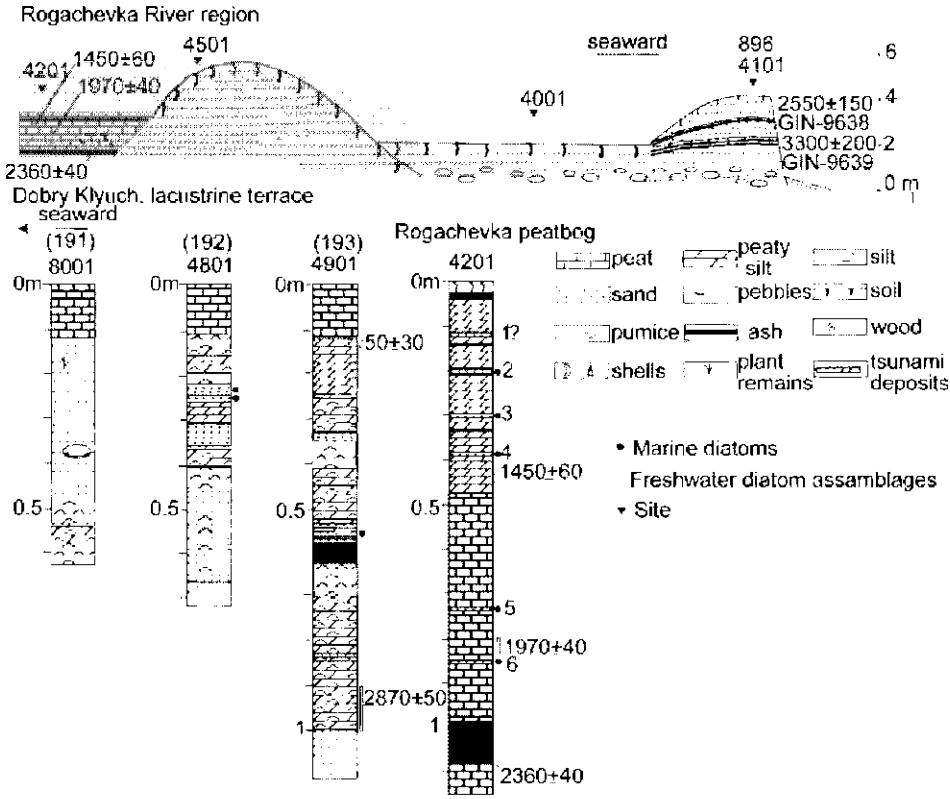

Fig. 2. Geological construction of coastal plain near the Rogachevka River mouth and tsunami deposits of northern Kunashir.

Among rich freshwater diatom assemblages, we found rare marine diatoms: sublittoral *Paralia sulcata* and *Actinocyclus octonarius*. The presence of marine species indicates that tsunami inundated an area more that 300 m inland. Upper sand-layer does not contain marine diatoms, but, in our opinion, this layer is also paleotsunami trace, because the sand-layer of similar age widely distributed in other sites includes marine diatoms. Here the sand does not include marine species because the main source of sand could be the dunes and broad beach. This sand-layer was deposited during the cooling and minor regression of the Little Ice Age. At that time, the sea level fell, leading to the development of extensive dune fields (Korotky et al., 2000), that was crossed by tsunami only at this place.

The base of the section exposes a dacite ash-layer dated about 2,350 BP (^{14}C-date from underlying peat 2,360±40 BP), which can be correlated to Ta-c2 ash widespread in this region (Nanayama et al., 2003; Hirakawa et al., 2003). The upper part includes three andesite-basalt ash layers of Tyatya Volcano that erupted at last 1,000 BP, and in 1973. One of large eruptions of Tyatya was dated about 500 year BP (^{14}C-date obtained from the paleosol, with scoria, is 510±90 year BP, GIN-11947 from soil

profile within 10 m abrasion terrace near the Tyatin River mouth). The peat bog was formed during the past 2.5 ka.

The sea level was similar to modern, or lower than at its present position for two lower sands. The run-up of paleotsunami must exceed the storm-ridge height, and possibly reached to 5-7 m. Two lower tsumani layers were deposited during the beginning of cooling, and was accompanied by a fall in the sea level (Sakaguchi, 1983; Korotky et al., 2000). These estimates are considered minimal.

The coastal plane, at low current of the Dobriy Klyuch Stream, is represented by lacustrine terrace, separated by a series of ancient storm-ridges from the modern beach. The terrace is composed of diatomites with some sand layers (Figure 2).

Diatom analysis indicates that the deposits were formed in small, short-time flood paleolake with mineral spring. The deposits include some sandy layers and ash, correlated to the ash of the Rogachevka site formed about 2.4 ka. Sand sheets are well observed inland. The deposits include rare marine diatoms, and are interpreted as tsumani deposits. Thickness of the sand-sheets reaches 2 cm, penetration inland extends more than 0.5 km. The sand is characterized by unimodal fine-tailed distribution. The sandy layers are composed by medium and coarser sands in the peripheral part of the paleolake. Mean grain size of the deposits decreased further inland (0.5 km) one proceeds, where fine sands with modal fraction 0.1–0.16 mm dominate. Dacite ash layer exposed to the base of the sections allows to correlate some tsunami layers with ones from the peat bog section of Rogachevka River. While the diatomite contains typically diverse freshwater assemblages, the sands include rare marine species such as sublittoral *Odontella aurita, Cocconeis scutellum, Paralia sulcata, Arachnoidiscus ehrenbergii,* neritic *Actinoptychus senarius,* and oceanic *Thalassiosira eccentrica.*

On central Kunashir, the traces of the late Holocene tsunami were found within extensive peatland located on the Pacific side of South Kurile Isthmus near the settlement called South Kurilsk (Figure 3).

Peatbog overlies mid-late Holocene marine deposits and storm-ridges. Peat was formed at the end of Subboreal-Subatlantic and has a thickness of more than 3 m. Active progradation of the coast, with formation of storm-ridges, took place 4,000–3,000 year ago during a relative period of stabilization of the sea level, which was higher than the present (Korotky et al., 2000).

Swamping of the coastal plane began during the late Holocene and the majority of the peatbog accumulated at last 2,000-2,500 years ago. The peat unit includes up to eight sand layers which is observed up to 2.5 km inland. Amount of sand layers is different in the sites. Thickness of the layers changes from 6–10 cm to 1–3 mm, decreasing as the distance from the shoreline increases. One sedimentary feature of the deposits are deformation structures found at the sand/ash interfaces (Figure 4).

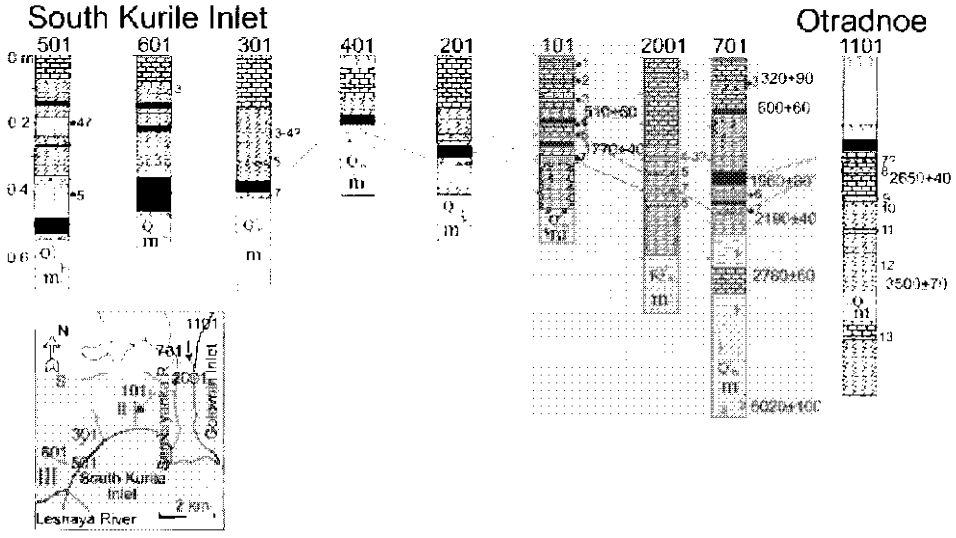

Fig. 3. Tsunami deposits from costal plane of Pacific side of South-Kurile Isthmus.

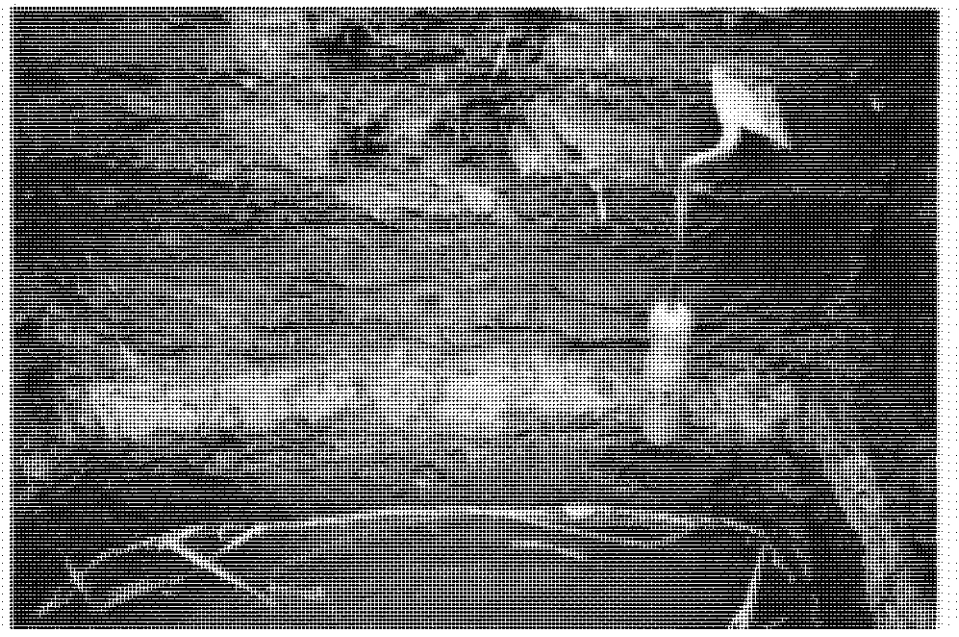

Fig. 4. Flame structure from the base of tsunami sands, peatbog of South Kurile Isthmus (site 501).

One interpretation of the structures is that they resulted from the sinking of sand into underlying soft and wet material (Minoura and Nakata, 1994). The distribution pattern of sediment facies implies that the sand-layer was deposited in a swamp pond located near the former coastline. Such "flame structure" is observed at a site located 250 m

from the present coastline. The deposits are composed of medium-to-fine sand, and includes some amount of silt (up to 22%). The sorting of the tsunami sand is lower than underlying marine sands deposited during transgression and modern dune, beach and tidal flat sediments of South Kurile Inlet (Figure 5).

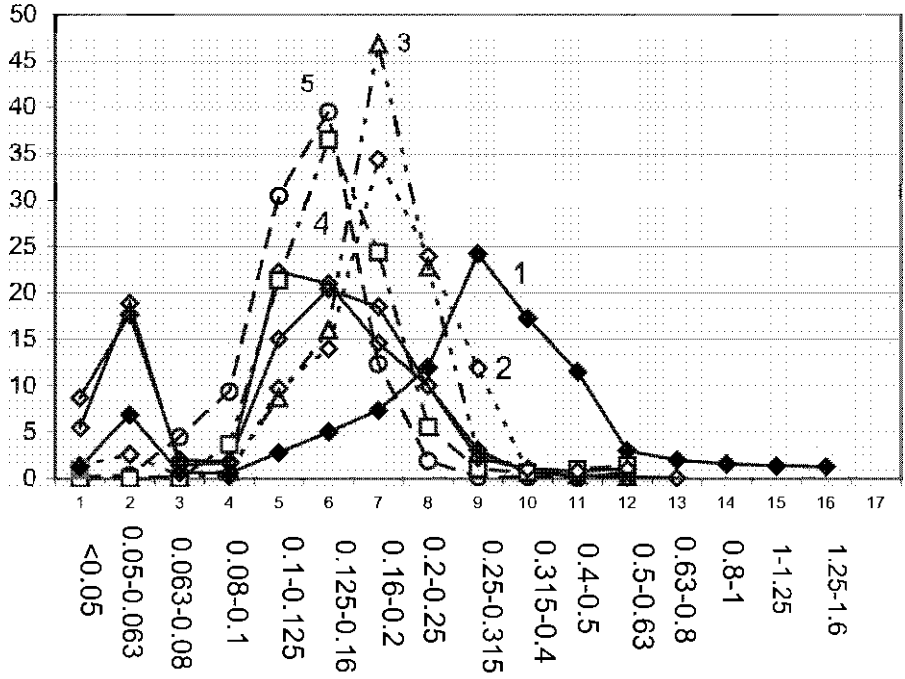

Fig. 5. Grain size curves of tsunami and coastal deposits of South Kurile Inlet, Kunashir Island.
1 – tsunami sand (site 501); 2 – inshore deposits; 3 – eolian deposits;
4 – heach deposits; 5 – tidal flat deposits.

Fossil diatom assemblages were divided into two diatom zones. Zone 1, from sand unit and lower part of peaty silt, contains abundant marine species, and indicates a marine environment. The units were deposited during the last Subboreal transgressive phase, correlated with the Late Jomon transgression of the Japanese Islands (Korotky et al., 2000; Sakaguchi, 1983). Zone 2, from the upper peat, includes mainly freshwater diatoms. Relative abundances of well-preserved marine species increase in the sand as compared to the underlying and overlying peat. Along with freshwater species, the assemblage contains rare marine species. Contents of marine diatoms increase in six intervals. Occurrences of some marine species in the upper part of the peat bog, where a sandy interval is not recognizable, suggest that the tsunami extended farther in to the lowland than was previously inferred from the field stratigraphy.

Diatom assemblages in sand consist of different dominant taxa, but both indicate that the sand units originate from the South Kurile Inlet. Among the marine diatoms in tsunami deposits, sublittoral species (*Paralia sulcata, Cocconeis scutellum, Diploneis smithii, Odontella aurita, Hyalodiscus obsoletus,* etc) dominate. Rare valves of the large specimens of *Arachnoidiscus ehrenbergii,* which lives attached to seaweed, were also recovered from the sand. Also, a high content of neritic (*Actinocychus octonarius, A. divisus, Actinoptychus senarius, Thalassiosira gravida, T. leptopus, Thalassionema nitzschioides* etc.) and oceanic (*Coscinodiscus perforatus, C. radiatus, C. marginatus, Rhizosolenia hebetata*) species were found. The content of these species is higher in the tsunami layers compared to underlying marine deposits (Figure 6). The appearance, and high percentage content of deep-sea species is connected to strong marine water flow, penetrated far inland, and brought large amounts of these forms as compared with storm-induced surge. Possibly, this fact can serve as an informative sign of paleotsunami. It should be noted that some of the marine taxa found under the sand layers may be due to infiltration of marine water into the peat layer.

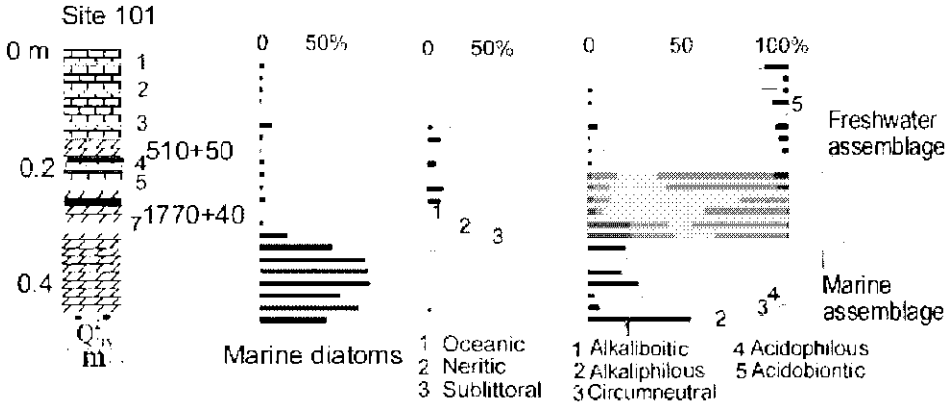

Fig. 6. Diatom assemblages from tsunami deposits of South Kurile Isthmus.

Freshwater diatom assemblage from tsunami layers and overlying deposits indicate that paleotsunami had an influence on the environment's pH (Figure 4). After a tsunami, diatom assemblage common for acidic swamp environments (acidophilous and acidobiontic) changed by diatom flora of neutral and alkaline environments. Circumneutral, alkaliphilous and alkalibiontic forms dominate in diatom assemblage, these species continued their development after a tsunami event during some period. Thus, paleotsunami influence on the environment resulted in changes of development tendency of swamp system, that also could have affected landscape development.

Along the Serebryanka River, the inland limit of sand layers within the peat bog is 2.5 km from the mouth of the river. Three sand-layers, with marine diatoms, are found in a section peat bog located landward at 2.5 km from the Serebryanka River mouth. Lower sand layer contain coarser nonrounded volcanic material. The content of marine

diatoms in sand-layers is higher than in the section near the shoreline. Diatoms add to stratigraphic evidence that tsunamis flooded this part of the lowland three times during the past 2,000 year. Marine assemblages include mainly sublittoral species. Tsunamis, at this site, were probably generated by great earthquakes. We suppose that these sand-layers were deposited by the largest tsunamis.

The sections include three dacite ash-layers, erupted about 1,700 years BP and within the last 500 year. They consist of light gray silt dominated by very fine silt (up to 67%) that indicates a distant source, probably located in Hokkaido. It is possible that younger ash layer correlate to distal ash layers of Ko-c2 (AD1694), which were found in the Tyatya Volcano region (Nakagawa et al., 2002). Identification of volcanic ash is based on refraction indexes of volcanic glass that corresponds to radiocarbon dating (Table 1). Two sand-layers with coarser volcanic material were used for correlation of the sites, too. The age of these layers is about 1,500 and 2,100 year BP (^{14}C-date from underlying soil is 2,130±50 year BP, GIN-7887). The source of coarser volcanic material was the Mendeleev Volcano, which erupted at this time (Abdurakhmanov et al., 2003). Tsunami could transport volcanic material inland. Presence of tsunami sand and volcanic material in the same layers could indicate synchronous events of tsunami and volcanic eruptions. The configuration of the shoreline at this time was similar to the present (Korotky et al., 2000).

More ancient tsunami traces may be reconstructed from the Otradnoe peat bog (Figure 3). The peat includes seven sandy layers which are composed of well-sorted, fine sands. The sorting of this sand is higher than the tsunami deposits of the coastal plane of South Kurile Inlet. The sources of this sand were the sand beach and the inshore zone of the open Golovnin Inlet and the extensive dunes, that developed in this place. Among marine diatoms in the sand-layers, we found rare sublittoral *Paralia sulcata,* and fragments of oceanic *Coscinodiscus* sp. *Thalassiosira* sp. We cannot exactly affirm that these sand-layers were deposited by tsunami, because they are located behind storm-ridge, and the former shoreline was farther inland during transgression, which took place at the time of deposit formation. But good correlation of these sand layers with Eastern Hokkaido paleotsunami data (Nanayama et al., 2000, 2003; Hirakawa et al., 2003) may be the basis for suggestions about their tsunami origin. The base of the section exposes the lagoon's silty sand with rich diatom assemblage. The unit deposited during first phase of Subboreal transgression (^{14}C-date 3,500±70 year BP) correlated to the Late Jomon transgression of Japan.

Extensive peatland is located on south Kunashir southward from the mouth of the Belozerskaya River. The major part of this swamp is very young. The thickness of the peat, underlying the storm ridges and inter-ridge depression, reaches only 15-20 cm, and increases towards the river mouth (up to 2.60 m), where there is an ancient peat bog. Three dacite marker ash-layers are spread in the late Holocene deposits on South Kunashir. Younger ash-layers correlate to distal ash-layers of Ko-c2 (or Ko-c1) and

Ta-a, which are widespread in the Tyatya Volcano region (Nakagawa et al., 2002) and Eastern Hokkaido (Nanayama et al., 2003). The ash-layer, formed about 2,060 year BP, is correlated to the regional tephra Ta-c2 of Eastern Hokkaido (Nanayama et al., 2000, 2003; Sawai, 2001). The main part of the peatbog includes four sand-layers (up to 1 cm), which are located up to 600 m inland from the beach (Figure 7).

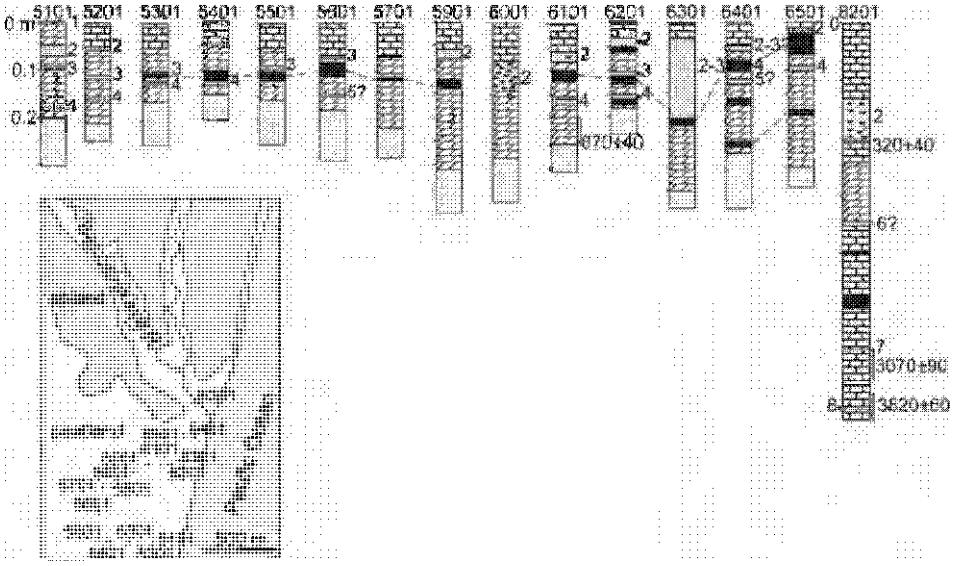

Fig. 7. Tsunami deposits from peatland near Belozerskaya River mouth.

Pumice gravel was found on the peat surface 200 m inland and possibly is evidence of the tsunami of 1994. The site is located far from river (more than 1 km) and the material may have only marine origin.

Other layers of medium-to-fine sand were deposited at last 1,000 year BP. Tsunami deposits have a single-mode distribution, but the sorting of the material is poorer than underlying peat marine deposits. The study of grain size composition of the deposits has revealed the sands are of marine origin and transported from the littoral environment by a great flooding of seawater.

More ancient sand-layers from peat bog near the Belozerskaya River mouth are preliminary considered tsunami deposits on the basis that they are well-correlated (age and composition) with other sites located on Eastern and Southern Kunashir and Eastern Hokkaido (Nanayama et al., 2003). These layers were found in the site located about 50 m from the modern coastline. Their origin must be confirmed by future investigations.

Diatoms from the sand-layers consist of marine and brackish species that indicate their tsunami origin. Diatom assemblages well reflect the configuration of the ancient coastline during a palaeo-tsunami event. Presence of species that usually live in lagoons and closed inlets such as *Nitzschia acuminata, N. levidensis, N. littoralis, N.*

plana, Rhabdonema arcuatum, Thalassiosira bramaputrae, Navicula glacialis, Lyrella forcipata, etc, reflect that the coast was more irregular at Subboreal. Diatom analysis shows the tsunami deposits most likely originated from the lagoon water, and good preservation supposed that the diatoms were deposited and buried rapidly. Diatom flora from the upper Subatlantic layers with the species commonly live in inlets and bays indicate an open coast environment.

Middle Holocene tsunami deposits were also found in lacustrine sequences. During this Holocene stage, a rise in the sea level led to active abrasion, causing a large volume of detrital material to enter the coastal zone. The active formation of barrier forms led to the separation of numerous coastal lakes. The deposits of such paleolakes is composed of a 5-6 m terrace in low current of Lesnaya River. Lacustrine deposits consisting mostly of clay or peaty silt contain intercalated eight thin beds (up to 5 cm) of well-sorted medium-to-fine sands. Deposition of thin, laterally persistent sand-layers in the barrier lakes can be attributed to catastrophic seawater invasion upon low-lying coastal land. The sands are characterized by unimodal distribution with fine-tails. Two lower layers are characterized by low, heavy fraction content and the domination of pyroxenes amongst heavy minerals. The sand was deposited during tsunami penetration into relatively extensive coastal lakes.

The upper four sand-layers were formed at final stage of paleolake development. The deposits are distinguished by high heavy-mineral content, with magnetite in predominance. Six thin layers of well-sorted medium-to-fine sand were found in the Kosmodemianskaya Inlet middle Holocene lacustrine terrace. A lower sand-layer is correlated to one of the sand-layer of the Lesnaya River lacustrine sequences. Evidence of tsunami origin of the upper sand-layers may be well correlated with Eastern Hokkaido paleotsunami data (Nanayama et al., 2000, 2003) on the base of radiocarbon dating.

3.2. IZMENA BAY COAST

Evidence of tsunami penetration into the Izmena Bay coast may be received from the sections of peatbogs stretching upward along the valleys of numerous rivers. In the middle Holocene, and during the first transgression of the late Holocene, correlated to middle/late Jomon transgressions of Japanese Islands (Sakaguchi, 1983), semiopen inlets and estuaries developed at the places of modern swamps. Marine deposits of this age underlay the peat. Late Holocene peat unit includes up to nine thin (up to 2 cm) medium-to-fine sand-layers (Figure 8), located up to 1 km inland. The number of sand layers decrease in peatlands as their distance increased from the Pacific coast. Tsunami deposits contain substantial silt fractions (up to 32 %), and transported inland from the littoral environment of semi-open bays. The presence of pumice and large pieces of wood mark the maximum penetration of the tsunami. Observations of modern tsunami

indicate that large wood fragments are deposited at the point of zero water velocity prior to backwash flow (Korolyov et al., 1997). Mechanism of pumice sedimentation is the same: it marks upper limit of run-up.

Most ancient peatbogs were found near the Golovnin River mouth. The lower part of the section deposited about 5–6 ka ago. Peat includes rich freshwater diatom flora that commonly live in small flood-lakes. Two lower sand-layers contain fragments of marine diatoms, identifying a bayward source of the sand. Lower sand was deposited during the cooling about 4.5 ka ago (Sakaguchi, 1983; Korotky et al., 2000). The sea-level was lower than at present, and we deduce that the sand was formed by tsunami. A second sand-layer possibly has the same origin.

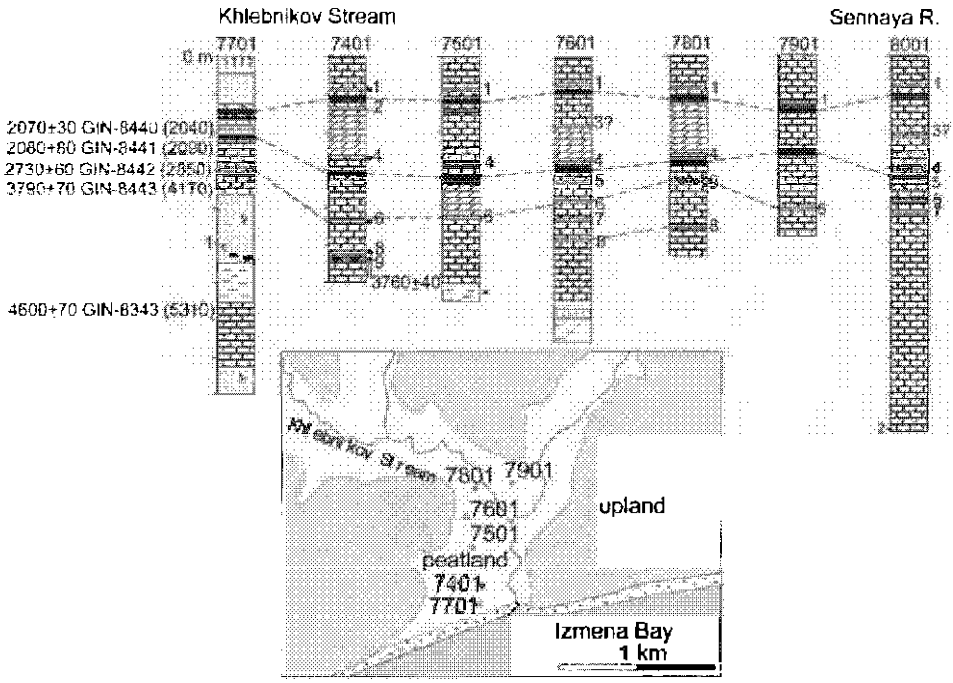

Fig. 8. Tsunami deposits from peatlands of Izmena Bay coast.

The next upper sand-layer has a relatively large thickness (up to 7 cm). This layer includes a high content and diversity of marine and brackish diatoms (17%). Marine assemblage indicates a semi-open inlet environment. Presence of warm-water neritic species such as *Planktoniella sol* and *Thalassionema nitzschioides* indicates the influence of the Kuroshio current. Fresh-water species are common for river input. Radiocarbon dates indicate that the sand was deposited during the first half of the Sibboreal. Diatom analysis suggests that the sand originated from sandy, shallow subtidal deposits of Izmena Bay. The sand may be formed by extensive tsunami, traces of which were recorded on the Eastern Hokkaido coast near Nemuro (Nanayama et al.,

2000, 2003). However, we can not exclude the possibility that the unit was formed during short-time transgression at the first phase of Subboreal that correlated to the peak of Late Jomon transgression of the Japanese Islands.

Late Holocene peaty silt from upper part of the site includes freshwater species which usually live on soil. Rare marine diatoms from sandy intervals consist of species observed on modern tidal flats of the open bay, identifying a bayward source of the sand. The same results were received for site from the other side of the river.

The peatbog from Khlebnikov Stream low current has a late Holocene age. Rich and diverse marine assemblage from the lower sand-layer, with well rounded pumice, possibly record storm surges on the ancient coastline of the second phase of Subboreal transgression. Similar marine diatom assemblage was found in deposits of this transgressive phase exposed near the modern coast (Korotky et al., 2000).

While the peat from upper part of the section typically contains diverse assemblages of freshwater diatoms, the sand-layers have few marine species. In addition, the tsunami sand contains rare specimens of extinct marine diatoms such as *Pyxidicula zabelinae,* which were redeposited from the Pliocene Golovnin Formation, exposed on the coast cliffs. The diatom evidence suggests that the Subatlantic tsunami sand most likely originated from shallow subtidal marine deposits.

The most remote peatbog from the Pacific side is located near Paltusov Cape, in the valley without a stream. The peat contains freshwater species that live on moss and on soil. Marine taxa are observed in sand layers as fragments. Rare marine species were found in the upper sand. Poor preservation of specimens may indicate input transport by the largest tsunami during the past 4 ka. The traces of these tsunami are widely distributed, even along the Izmena Bay coast, separated from direct Pacific influence. It should be noted that Veslovsky Spit was formed only during the last 1,000-2,000 year, and earlier Pacific influence to the Izmena bay coast was more intensive.

3.3. OKHOTSK SEA COAST

Okhotsk Sea coast is a perspective area to search for traces of tsunami generated by underwater volcanic eruptions. Numerous submarine volcanoes are located along the western side of Great Kurile Arc (Avdeiko et al., 1992), the eruption of which may be potential sources of tsunami. The tsunami traces were found in Kruglovsky Isthmus, and near Tretiakovka.

On Kruglovsky Isthmus, extensive swamp is located around Dlinnoe Lake which was lagoon in origin. The swamp is very young, thickness of peat reaches upwards to 0.9 m. The peat is underlied by Subatlantic marine sands (^{14}C–date 1,240±40 year BP) with marine diatoms. The peatbog includes three layers of Tyatya Volcano scoria, the lower of which is dated about 800 year BP (^{14}C–date 800±50 BP). Age lower dacite-rhyolite ash-layer is about 1,000 year BP and correlated to Ma-b (refraction indexes of

volcanic glass and low K_2O content), upper one is correlated to Ta-a (AD 1739). Upper part of the section includes dark-grey ash of Tyatya Volcano eruption of AD 1812, overlied thin sand layer (less than 1 cm) (Figure 9). The appearance of marine diatoms (sublitoralic *Cocconeis scutellum, Paralia sulcata, Odontella aurita,* fragment of oceanic *Rhizosolenia hebetata, Thalassiosira eccentrica, Coscinodiscus* sp., *Thalassiothrix longissima,* and Neogenic species among fresh-water assemblage indicate the tsunami origin of the sand. The sand-layer with marine diatoms was found in soil profile on elevation up to 10 m. Such high tsunami wave may be explained by the penetration of the wave up the narrow mouth of stream from Dlinnoe Lake. The tsunami may be the result of a catastrophic earthquake in AD 1780, the epicentre of which was near Urup (Soloviev, 1978; Iida, 1984) and penetrated across the Ekaterina Strait.

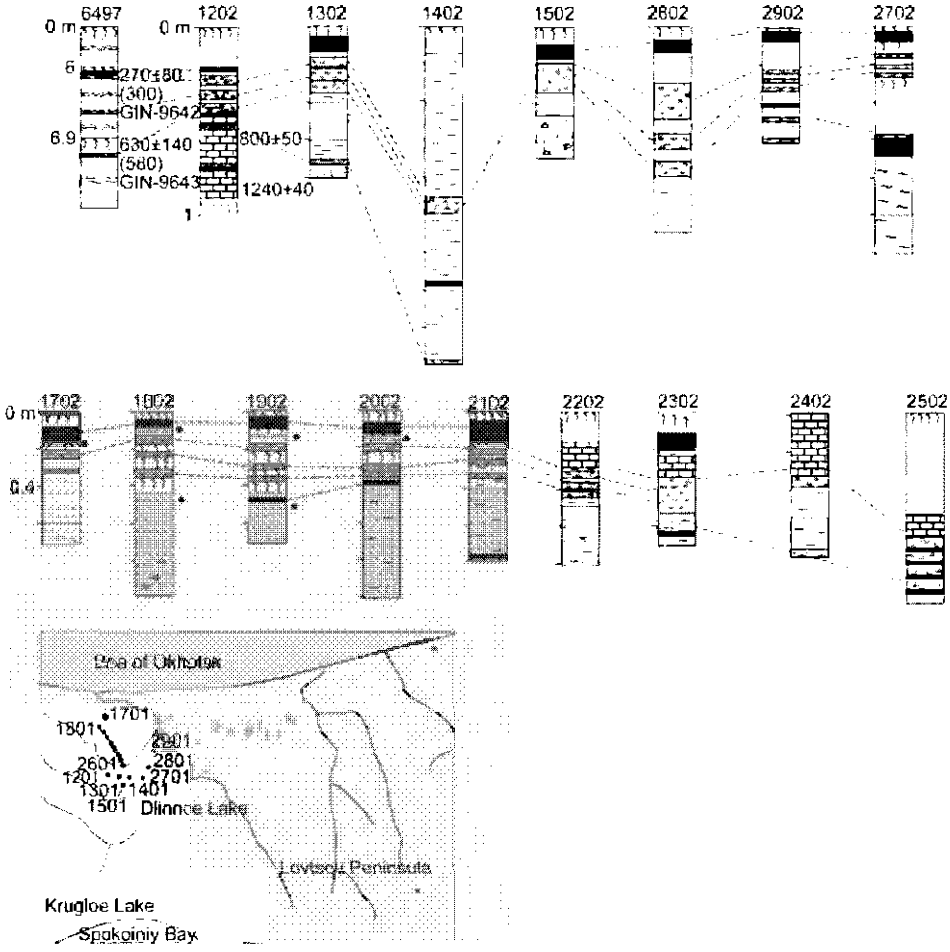

Fig. 9. Geological construction of Kruglovsky Isthmus peatland, Northern Kunashir.

Near Tretiakovka, pumice sand, with rare marine diatoms, was found in a peatbog, located on an elevation of 10 m above modern sea level. Marine species include *Cocconeis scutellum*, *Paralia sulcata*, *Cyclotella striata*, *Nitzschia littoralis*, and numerous fragments of oceanic species (*Coscinodiscus marginatus*). ^{14}C-date from peat underlied sand is 3,120±40 year BP GIN-12218; from wood in the sand is 3,820±110 year BP GIN-12217. The wood may have been redeposited during a tsunami.

4 Discussion

Inferred correlation of tsunami deposits from different places of the Pacific side of the Kunashir coasts is shown in Figure 10. Seventeen isochronal layers can be traced among the several coasts. Some of them are well correlated to Eastern Hokkaido (Nanayama et al., 2000, 2003) and Iturup paleotsunami reconstructions (Bulgakov et al., 1995). Sand on the surface of peatland may correspond to the AD 1994 Tsunami (M 8.0). Traces of a tsunami during the 19th century were found only in South Kurile Inlet, 1 km inland from the modern shoreline. It may be correlated to Ts 1 of eastern Hokkaido, corresponding to AD 1843 Tempo Tokachi-oki Tsunami (M 8.4).

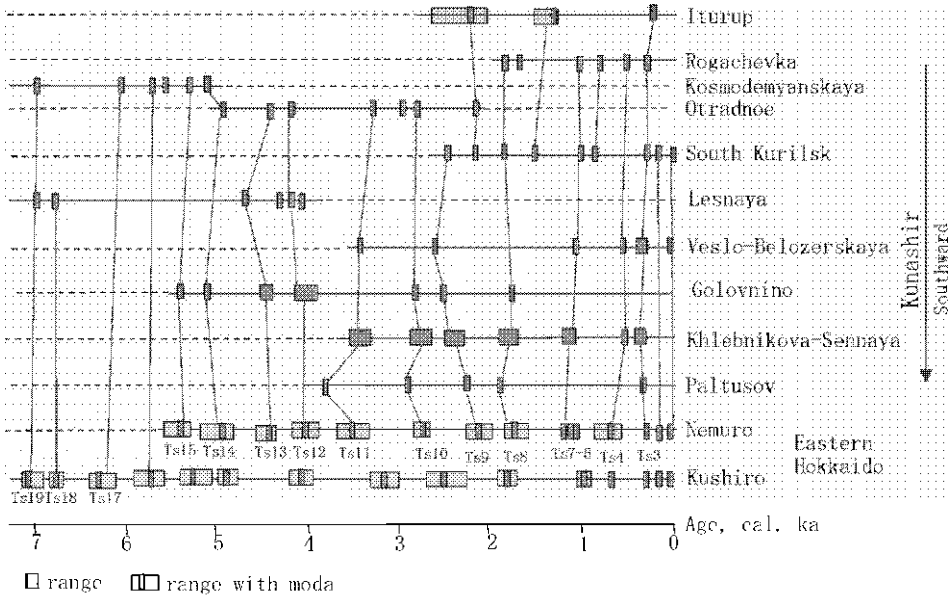

Fig. 10. Correlation of tsunami events on Pacific coast of Kunashir with Iturup Island (Bulgakov et al., 1995) and Eastern Hokkaido (Nanayama et al., 2000).

Amongst historical events, 17th century tsunami (Edo era) were very intensive. Traces of them were found in many places on Eastern Hokkaido (Nanayama et al., 2000; 2003; Sawai, 2002).

Kunashir Island coastal sequences possibly record the trace of a tsunami event named Ts 3 on Eastern Hokkaido than corresponding to the AD 1611 Keicho Sanriku-oki Tsunami event (M 8.1) (Nanayama et al., 2000). Possibly, the trace of this event was found in a Kasatka Bay peatbog on Iturup Island (Bulgakov et al., 1995).

Tsunami of 13th century that correlated to Ts4 of Eastern Hokkaido was mainly distributed on South Kunashir.

A tsunami dated to the 9th century was recorded in central and northern Kunashir, and may correspond to the AD 869 Jogan Sanriku-oki Tsunami event (M 8.3) (Nanayama et al., 2000).

The most of prehistoric tsunami events observed on Kunashir are well correlatd with Eastern Hokkaido data.

Two late Holocene paleosunami traces of which were found on central and northern Kunashir are possibly observed on central Iturup and had their sources located northward.

5 Conclusion

Seventeen thin sand-layers were found to be intercalated within peat of lacustrine deposits of the Pacific coast of Kunashir Island. Field data, grain-size composition, and biostratigraphical data allow interpretation of them as paleotsunami traces. Tsunami that inundated extensive areas along the Pacific coast of Kunashir Island were generated by large earthquakes (M>8) on the Kurile subduction zone. The sand layers were deposited by tsunami with a maximal run-up more than 7 m, and penetration inland more the 2.5 km. The tsunami generated by earthquakes, the epicentres of which were located to the north of Kunashir, may have penetrated to the Okhotsk Sea coast. The time period relating to the found tsunami deposits is 6,000–7,000 years. These events can be correlated with historical, and prehistorical, tsunami of Eastern Hokkaido and Iturup Island.

The presence of the sand with marine diatoms on elevation upward to 10 m in the Okhotsk Sea coast of the island indicates the possibility of the appearance of tsunami as result of eruption of submarine volcanoes.

Diatoms analysis can provide valuable evidence for the arguments that the deposits were made by tsunamis. Presence of marine and brackish species in sandy layers suggest a seaward source for the sand, as opposed to downriver flood deposits, and reflect the configuration of the ancient coastline. Content of marine species, and their diversity, depend as by distance from the seacoast as sand-layer thickness that,

possibly, is connected with tsunami intensity. Content of neritic and oceanic species is higher in tsunami layers compared to marine deposits of Holocene transgressive phases. Appearance, and high percent content, of deep-sea species is connected to strong marine water flow, penetrating far inland and brought large amounts of these forms, as compared with storm-induced surge. Possibly, this fact can serve as an informative sign of paleotsunami. It should be noted that some of the marine taxa found under the sand-layers may be due to infiltration of marine water in to the peat-beds. The rarity, and poor preservation of diatom valves, indicate long-distance transport during a high-energy event.

Acknowledgements

We would like to thank all the participants of our expeditions for their help in the field works. We are grateful to M. Pevzner and L.D. Sulerzhitskiy for providing radiocarbon dating. The work was supported by the Russian Foundation for Basic Research, grants 02-05-65409, and a grant from the Far East Branch of the Russian Academy of Science "Earthquakes and tsunami in Russian Far East: physic of the phenomenon, Holocene appearance, impact to coastal geosystems, estimation and prognoses of tsunami-hazard"

References

Abdurakhmanov, A. I.; Razjigaeva, N. G., and Ribin, A V. 2003. Modern seismic and volcanic activity of Mendeleev Volcano. Reports of Sakhalin State Museum. 10. 277-283 (in Russian).

Atwater B.F., Nelson A.R., Clague J.J., Carver G.A., Yamaguchi D.K., Bobrowsky P.T., Bourgeois J., Darienzo M.E., Grant W.C., Hemphill-Haley E., Kelsey H.M., Jacoby G.C., Nishenko S.P., Palmer S.P., Peterson C.D., Reinhart M.A. 1995. Summary of coastal geologic evidence for past great earthquakes at the cascadia Subduction Zone. Earthquakes Spectra. 11, 1-17.

Avdeiko, G. A.; Antonov, A. N., and Volinets, O. N. 1992. Submarine volcanism and zones of Kurile Island Arc. Moscow: Nauka. (in Russian).

Bulgakov, R. F., Ivanov, V. V., Khramushin, V. N., Pevzner, M. M.; and Sulerzhitsky, L. D. 1995. Investigation of paleotsunami traces for tsunami region study. Physics of the Earth. 2, 18-27. (in Russian).

Dawson A.J. 1999. Linking tsunami deposits submarine slides and offshore earthquakes. Quaternary International. 60, 119-126.

Dawson A.G.; and Shi S.2000. Tsunami deposits. Pure Appl. Geophys., 157, 875-897.

Furukawa, R., Yoshimoto, M., Yamagata, K, Wada K; and Ui T. 1997. Did Hokkaido Komagatake Volcano Erupt in 1694? Kazan. 42, 269-279 (in Japanese with English abstract).

Gleiser, S.L.; Jouse, A.P.; and Makarova, I.V.; Proschkina-Lavrenko, A.I.; Sheshukova-Poretskaya, V.S.; editors, 1974. Diatoms of USSR. Leningrad: Nauka (in Russian).

Goff J., Chague-Goff C., and Nichol S. 2001.Palaeotsunami deposits: a New Zealand perspective Sedimentary Geol. 143, 1-6.

Grebennikova, T.A. 2000. Specific of diatom flora development and formation of Late Pleistocene-Holocene diatomites of Iturup Island (Kurile Islands). In: I.I. Zhirkov, L.A. Pestriakova, G.N. Maksimov; (Eds). Lakes of cold regions. Proc. Of International Conferences. V. IV. 49-65 (in Russian with English abstract).

Hemphill-Haley E; 1996. Diatoms as an aid in identifying late-Holocene tsunami deposits. The Holocene, 6, (4), 439–448.

Hirakawa K., Nakamura Y., and Nishimura Y., 2003. Huge tsunami based on tsunami deposits along the Pacific coast of east Hokkaido, Northern Japan. In: IUGG 2003 Abstracts. Week B. P. B 149-150.

Iida K., 1984. Catalog of tsunamis in Japan and its neighboring countries. Special report, Aichi Institute of Technology, 11.

Korolyov Yu. P.; Zhukova, L. D.; Zolotukhina, N. D. et al; 1997. The aftereffects of 4 October 1994 tsunami on the shore of Kuril Island In: K F Sergeev; (Ed). Geodynamics of tectonosphere of the Pacific-Eurasia conjunction zone. V. VIII. 74 92 (in Russian, with English abstract).

Korotky, A.M., Razjigaeva, N.G., Grebennikova, T.A., Ganzey, L.A., Mokhova, L.M., Bazarova, V.B; Sulerzhitsky, LD; and Lutaenko, K. A. 2000. Middle and late Holocene environments and vegetation history of Kunashir Island, Kurile Islands, Northwestern Pacific. The Holocene, 11. (3), 311–331.

Krammer,K, Lange-Bertalot,H., (1986) Süßwasserflora von Mitteleuropa. Bacillariophyceae 1. Teil:Naviculaceae. Gustav Fischer Verlag, Stuttgart.

Krammer,K, Lange-Bertalot,H., (1988) Süßwasserflora von Mitteleuropa. Bacillariophyceae 2. Teil:Bacillariaceae, Epithemiaceae, Surirellaceae. Gustav Fischer Verlag, Stuttgart.

Krammer,K, Lange-Bertalot,H., (1991a) Süßwasserflora von Mitteleuropa. Bacillariophyceae 3. Teil:Centrales, Fragilariaceae, Eunotiaceae. Gustav Fischer Verlag, Stuttgart.

Krammer,K, Lange-Bertalot,H., (1991b) Süßwasserflora von Mitteleuropa. Bacillariophyceae 4. Teil:Achnanthaceae Kritische Ergänzungen zu Navicula (Lineolatae) und Gomphonema. Gustav Fischer Verlag, Stuttgart.

Minoura, K., and Nakata, T. 1994. Discovery of an ancient tsunami deposit in coastal sequences of southwest Japan: verification of a large historical tsunami. The Island Arc, 3, 66 72.

Nakagawa, M., Yoshizuka, Y., Kudo, T., Yoshimoto, M., Hirose; Ishizaki, Y., Gouchi, N. Katsui, Y; Solovyow, A.W., Steinberg, G.S., Abdukakhmanov, A.I. 2002. Tyatya Volcano, southerstern Kurile Arc; recent eruptive activity inferred from widespread tephra. The Island Arc, 11, 236-254.

Nakamura, Y., Katayama, Y., and Hirakawa, K. 2002 Hydration and refractive indices of Holocene tephra glass in Hokkaido, Northern Japan. Journal of Volcanology and Geothermal Research. 114, 499-510.

Nanayama, F., Satake, K., Shimokawa, K., Furukawa, R., Shigeno, K. 2000. Evaluation of frequency and invasion area of large earthquake tsunamis along the Kurile subduction zone by postulated tsunami deposits. In: Sugiyama, Y. (Ed) Interim Report on Active Fault and Paleoearthequake Research in the

1999 Fiscal Year. Geological Survey of Japan Interim Report # EQ/00/2Geological Survey of Japan. Tsukuba. 1–17 (in Japanese with English abstract).

Nanayama F., Satake K., Furukawa R., Shimokawa K., Atwater B.F., Shigeno K., and Yamaki S. 2003. Unusually large earthquakes inferred from tsunami deposits along the Kurile trench. Nature. 424, 660-663.

Pinegina, T.K., Bourgeous, J., 2001. Historical and paleo-tsunami deposits on Kamchatka, Russian: long-term chronologies and long-distance correlations. Natural Hazards and Earth System Sciences. 1, 177–185.

Sakaguchi, Y; 1983. Warm and cold stages in the past 7,600 years in Japan and their global correlation. Bull. of the Department of Geography University of Tokyo. 15: 1–31.

Sawai, Y. 2001. Episodic Emergence in the past 3,000 years at the Akkeshi Estuary Hokkaido, Northern Japan. Quaternary Research, 56. 231–241.

Sawai, Y. 2002. Evidence for 17th-century tsunami generated on the Kurile-Kamchatka subduction zone, Lake Tokotan, Hokkaido, Japan. Journal of Asian Earth Sciences. 20, 903 911.

Scheffers A., Kelltat D. 2003. Sedimentologic and geomorphologic tsunami imprints worldwide 0 a review. Earth-Science Rev. 63, 83-92.

Soloviev S.L., 1978. Main data about tsunami on Pacific coast of USSR. 1737-1976 yrs. Study of tsunami in open ocean. Moscow. 62. (in Russian)

Stuiver M., Reimer P.L. 1993. Extended 14C data base and revised CALIB 3.0 14C age calibration program. Radiocarbon. 35, 215-230.

Stuiver M., Reimer P.J., Bard E., Beck J.W. et al. 1998. INTCAL 98 Radiocarbon Age Calibration, 24000-0 cal BP. Radiocarbon, 40, 1041-1083.

Stuiver, M., Reimer, P.J. 1993. Extended 14C data base and revised Calib 3.0 age calibration programme. Radiocarbon, 35, 215-230.

Wolf, H. 1982. Methods of coding of ecological data from distoms for computer utilization. Meded. Rijks. Geol. Dienst, 36, 95–110.

DISTRIBUTION OF CUMULATIVE TSUNAMI ENERGY FROM ALASKA-ALEUTIANS TO WESTERN CANADA

T. HATORI

Suehiro 2-3-13, Kawaguchi, Saitama 332-0006 Japan
Member of the Seismological Society of Japan

Large tsunamis generated by earthquakes in the Aleutian Islands to Western Canada region have been recorded since 1788. The 1946 Aleutian tsunami, associated with a moderate earthquake (Ms 7.4), hit the Hawaiian Islands. The 1964 Gulf of Alaska tsunami was the largest (Imamura-Iida scale: m=4). The source areas of large tsunamis in 1957, 1964 and 1965 extend 600-900 km along the trench. These tsunamis were observed throughout the entire Pacific region. In this paper, the distribution of cumulative energy (square value of tsunami height, H^2, where H is the mean height per segment unit) for each 200-km segment along the Aleutian-Alaska trench is investigated for the recent (1900-2002) and historical (1788-1899) periods. For the total tsunamigenic energy, H^2, during the entire 215-year period, percentages of the energy received were 39% in Central Alaska, 32% in the Alaska Peninsula and 11% in the Central Aleutian Islands. During the recent period, the total energy in Central Alaska is nearly comparable with that of the Kamchatka and South Chilean regions. If the tsunami energy is accumulated with a mean rate since 1788, the expect alue in Central Alaska is small in comparison with the observed value for the recent period, because of the 1964 event. Conversely, the expected values for the Central Alaska Peninsula (400-km length) and Yakutat (400-km length) regions are about twice as large as the observed values, suggesting high tsunami risks for those regions.
Key words: Aleutian-Alaska tsunamis, tsunami height distribution, cumulative tsunami energy.

1 Introduction

Tsunamis generated by earthquakes in the Aleutian Islands to Western Canada region have been recorded since the late 18th century. Summaries of these tsunamis are listed in several tsunami catalogs (Cox and Pararas-Carayannis, 1976; Soloviev and Go, 1985; Lander et al., 1993). Recent tsunamis are reported in the International Tsunami Information Center (ITIC, Hawaii) Newsletter.

The behaviors of these tsunamis vary greatly. It is well known that the 1946 Aleutian tsunami hit the Hawaiian Islands, and is "tsunami earthquake" by an unusually long process time. The 1957, 1965 and 1996 Aleutian tsunamis and the 1964

K. Satake (ed.), Tsunamis: Case Studies and Recent Developments, 193-201.

Alaska tsunami were observed at Japanese tidal stations (Hatori, 1965a,b, 1998; Watanabe, 1998). On the other hand, it has been pointed out that seismic gaps exist off of the Alaska Peninsula and Southeast Alaska (Sykes, 1971; McCann et al., 1980; Hatori, 1981; Nishenko, 1991; Johnson and Satake, 1997).

In this paper, the distribution of cumulative energy, the sum of tsunami mean heights squared, for each 200-km segment along the Aleutian-Alaska trench to Western Canada is investigated for the recent (1900-2002) and historical (1788-1899) periods. The runup heights squared is nearly proportional to tsunami energy and corresponds to the tsunami risk. A tsunami forecast is discussed from the comparison of tsunami energy in recent period with the cumulative energy.

2 Tsunami source areas

In Figure 1, the location of the source areas for recent (1900-2002) and historical (1788-1899) tsunamis are shown with dates, earthquakes magnitudes (Ms) and tsunami magnitudes (*m*: Imamura-Iida scale). The source areas of the 1946, 1957, 1965 and 1996 Aleutian tsunamis and the 1938 and 1964 Alaska tsunamis were estimated by means of inverse refraction diagrams (Hatori, 1981,1998; Johnson and Satake, 1997).

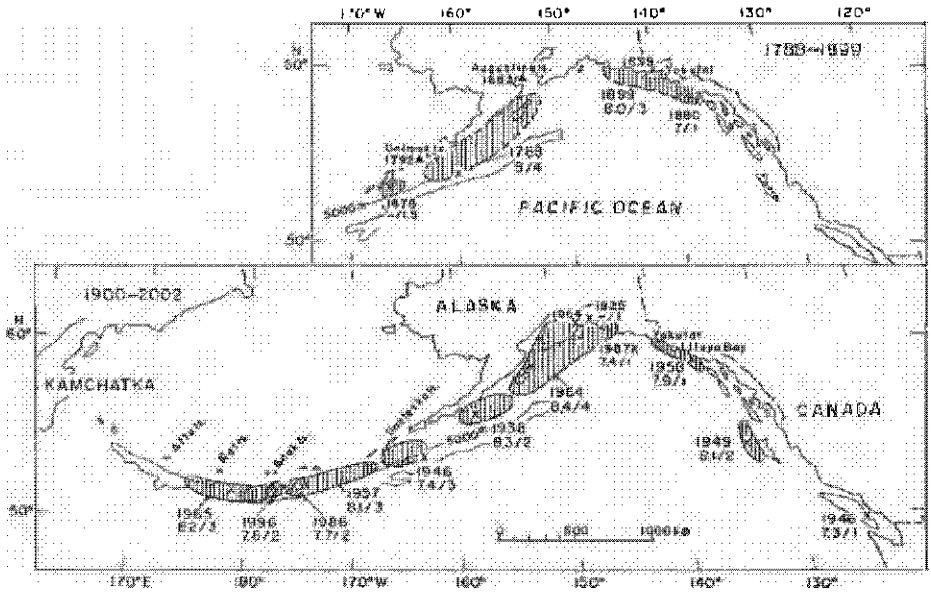

Fig. 1. Location of source areas of the Aleutian-Alaska tsunamis for the periods during 1788-1899 and 1900-2002. Generating years, earthquake and tsunami magnitudes, Ms/*m* are also indicated. Triangles: Tsunami caused by volcanic eruptions.

The 1957, 1964 and 1965 tsunami source areas were 600-900 km long and the tsunami magnitudes were m=3-4. The source areas of the Southeastern Alaska tsunamis were estimated from the aftershock areas (McCann et al., 1980).

The source areas of the historical tsunamis (1788-1899) were estimated from the earthquake magnitudes and tsunami height distributions. The 1788 and 1899 Alaska tsunamis were associated with great earthquakes, M~8, and the tsunami magnitudes were m=3-4 (Soloviev and Go, 1985).

Data are used for tsunamis with magnitudes m>1 (runup height on land >1 m). The giant wave in Lituya Bay caused by landslide and volcanic tsunamis are excluded from the analysis.

3 Distributions of square value of tsunami height

Based on runup heights of the Aleutian-Alaska tsunamis, the mean heights squared for 200-km segments of the Aleutian-Alaska Arc are shown with the bar graphs (Figures 2-4). Taking local amplification of runup heights into account, the mean height at each segment was estimated in less than 50-60% and 20-40% for the runup heights of 8-10 m and 20-30 m, respectively. For tsunamis with sparse data, the sum of mean heights squared at each 200-km segment (runup height >1 m) is estimated to agree with the line defined by the tsunami magnitudes plotted against the sum of mean heights squared (Figure 5).

Figure 2 shows the distribution of tsunami heights and mean heights squared, H^2 (bar graph) for each 200-km segment for the 1938, 1946 and 1964 Aleutian-Alaska tsunamis. The 1964 Alaska tsunami, associated with a great earthquake (Ms 8.4, Mw 9.2), is the largest (m=4). Runup heights reached 27 m near Anchorage (Plafker, 1969). The sum of mean heights squared, $\sum H^2$, for all 200-km segments from the 1964 tsunami is 345 m^2. The 1946 Aleutian tsunami reached 30 m at Unimak Island and hit the Hawaiian Islands. According to the tsunami height-distance diagram, using tide-gauge records from the circum-Pacific region, the tsunami magnitude is m=3 (Hatori, 1981); and the summation of H^2 is 91 m^2. The summation of H^2 for the 1938 Alaska Peninsula tsunami (m=2) is 19 m^2.

The distribution of tsunami heights and mean heights squared (bar graph) for the four Aleutian tsunamis and the four Southeastern Alaska to Western Canada tsunamis are shown in Figure 3. The 1957 and 1965 Aleutian tsunamis (m=3) were both associated with great earthquakes (Ms 8.1-8.2) and the runup heights reached 8-10 m at Adak Island and Shemya Island. The summations, $\sum H^2$, are 53 m^2 and 71 m^2, respectively. Magnitudes of the 1986 and 1996 tsunamis are both m=2 (Hatori, 1988, 1998a) and the summation of H^2 is 15 m^2 for the two tsunamis. The observed heights at the Aleutian Islands were a little small, because the tidal stations are located on the

north side of islands far away from the outer sea. For the tsunamis generated from Southeastern Alaska to Western Canada, the magnitude of the 1949 tsunami is m=2 and the magnitudes of the 1946 and 1987 tsunamis are both m=1. The 1958 landslide-generated tsunami ran up 516 m at the head of Lituya bay (Miller, 1960), but only 0.2-2 m outside of the bay. The magnitude is estimated to be m=1.

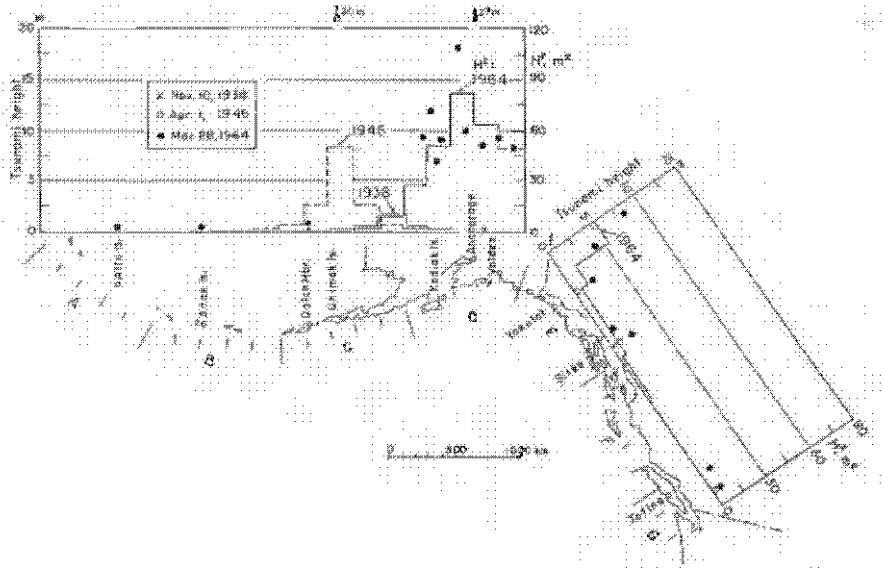

Fig. 2. Distributions of tsunami heights and square of the mean height, H^2 (bars), for the Aleutian-Alaska tsunamis in 1938, 1946 and 1964.

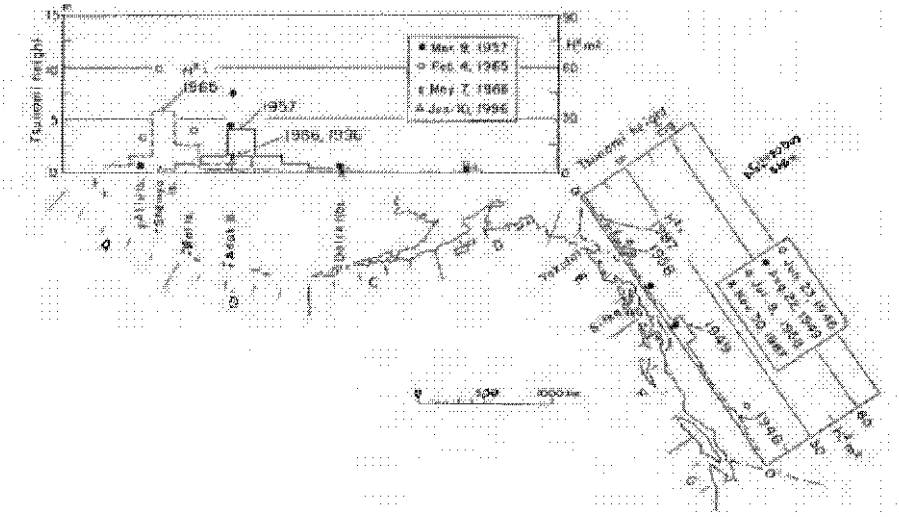

Fig. 3. Distributions of tsunami heights and square of the mean height, H^2 (bars), for the four Aleutian and the four Southeastern Alaska tsunamis.

4 Historical tsunamis (1788-1899)

There are several records of historical tsunamis in the Aleutian region. The distribution of tsunami heights and the mean heights squared at each 200-km segment (bar graph) are shown in Figure 4. The 1788 Alaska tsunami, associated with a great earthquake (M~8), was the largest with m=4, which is similar to the 1964 Alaska tsunami. According to the old documents, runup heights were 20 m at Unga Island, 8 m at Kodiak Island and 5 m at Sanak Island. The sum of the mean heights squared, $\sum H^2$, is 308 m^2. Runup heights of the 1899 Southeastern Alaska tsunami reached 60 m in Lituya Bay, 10 m in Yakutat Bay, and 2 m at Valdez. The summation of H^2 is 53 m^2, based on the tsunami magnitude of m=3 (Soloviev and Go, 1985). Runup heights of the 1878 Aleutian and 1880 Southeastern Alaska tsunamis were recorded as 2-3 m near the source areas and the tsunami magnitudes were m=1-1.5.

Using the runup height data (m>1), the mean heights squared at each 200-km segment are shown with the bar graphs. For the analyzed tsunamis (m>1), the relationship between the total value of the mean heights squared at each 200-km segment and the tsunami magnitudes is shown in Figure 5. The broken line is the relationship obtained from the Kamchatka-Kurile and South American tsunami data (Hatori, 1999, 2002). For tsunamis with sparse data, the summation of H^2 was estimated on the basis of each tsunami magnitude.

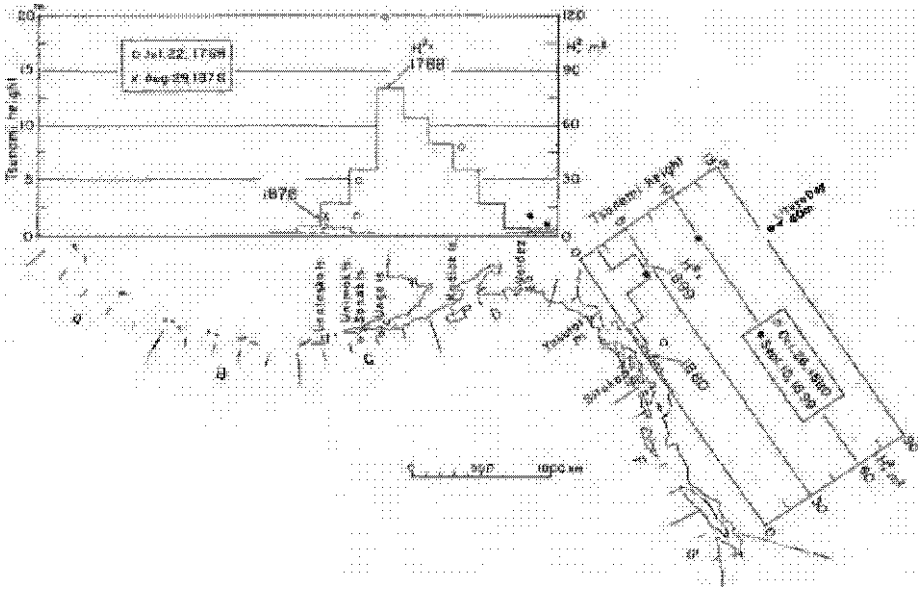

Fig. 4. Distributions of tsunami heights and square of the mean height, H^2 (bars), for the historical Aleutian-Alaska tsunamis.

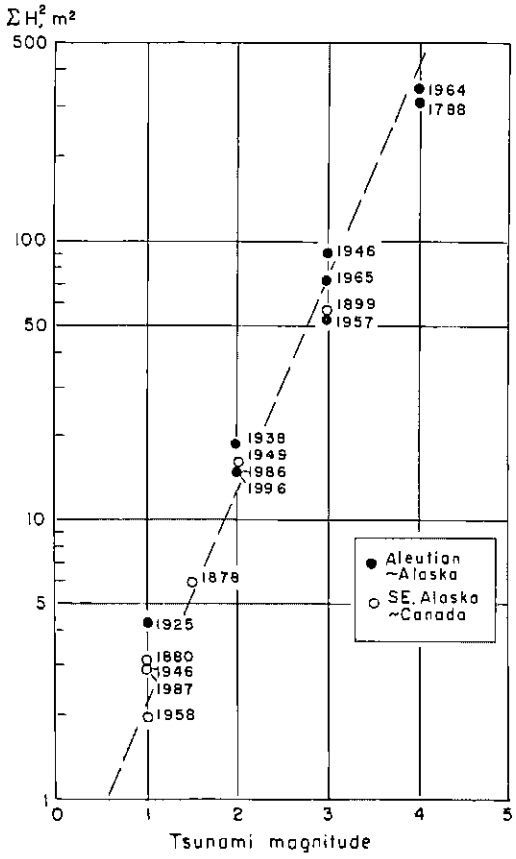

Fig. 5. Relation between tsunami magnitude and summation value of the square heights at each 200-km segment. The broken line is the relationship obtained from the data of Kamchatka-Kurile and South American tsunamis (Hatori, 1999, 2002).

5 Distributions of cumulative tsunami energy

The distribution of cumulative mean heights squared at each 200-km segment for the recent period (1900-2002) and the entire 215-year period (1788-2002) is shown in Figure 6, with hatched and non-hatched bars, respectively. For the entire 1,000 km-segment (A-G regions along the Aleutian-Alaska trench to Western Canada), the arrival energy during the recent 103-year period is the largest (cumulative value: 280 m^2) in the D region (Gulf of Alaska). The total energy is nearly comparable to that of the Kamchatka and South American regions (Hatori, 1999, 2002). The percentages of the total tsunami arrival energy for both periods (1788-2002) for the entire 1,000-km segment are 39% for the D region, 32% for the C region (Eastern Aleutians-Alaska Peninsula), 12% for the E region (Southeastern Alaska), and 11% for the B region

(Central Aleutians). There is no documentation for the historical tsunamis in the A and B (Western Aleutians) or F and G (Western Canada) regions.

If the tsunami arrival energy for each segment is accumulated with a mean rate, the expected cumulative energy for the recent 103-year period is indicated by open circles in Figure 6 (the value is 48% of the entire period). The results show that the arrival energy for the recent 103-year period for the Gulf of Alaska region is remarkably larger than the expected value. Conversely, the expected value in the 400-km segment in the Alaska Peninsula region is twice as large as the observed arrival energy. The expected value in the Yakutat region is also a little larger than the observed value. These areas correspond to seismic gaps, determined from the recent seismic activity.

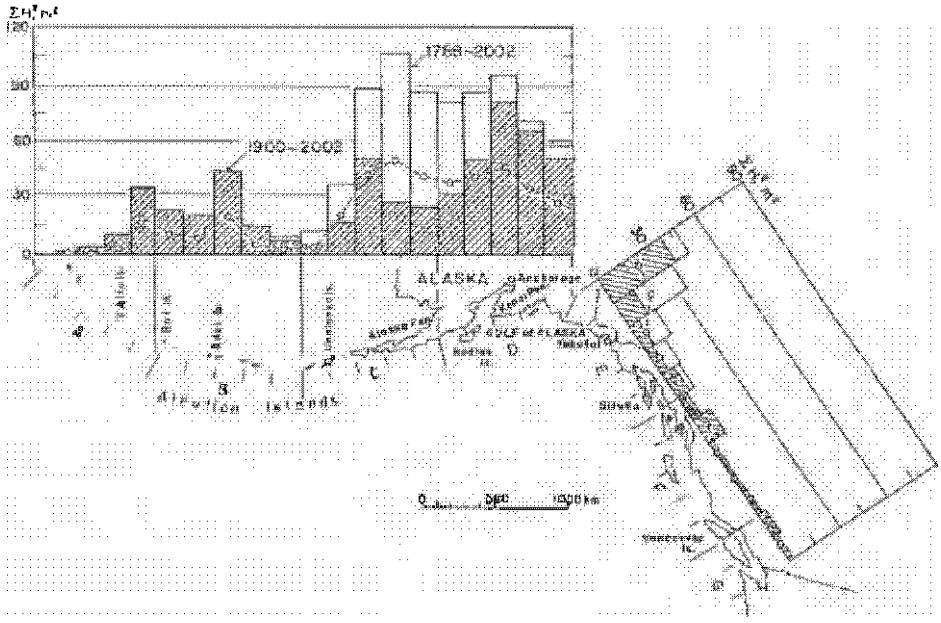

Fig. 6. Distribution of cumulative tsunami energy, $\sum H^2$, for each segment. The white and hatched bars show the values for the periods for 1788-2002 and 1900-2002, respectively. Open circles and dotted lines show the estimated values for the period for 1900-2002 assuming constant accumulation of the tsunami energy.

6 Conclusion

Based on the runup height distributions of the Aleutian-Alaska tsunamis generated during the period of 1788-2002, the cumulative tsunami energy in each 200-km segment along the Aleutian-Alaska trench to Western Canada is investigated. The percentages of the energy received in the entire 1,000-km region were 39% for the Gulf of Alaska and 32% for the Alaska Peninsula.

For the recent period (1900-2002), the observed tsunami energy in the Gulf of Alaska region is larger than the expected value, because of the recent high seismic activity. Conversely, the observed energies in the Alaska Peninsula and Yakutat regions are remarkably small when compared with the expected values. These results indicate that the long-term tsunami hazard necessitates taking precautions against large tsunamigenic earthquakes.

References

Cox, D.C. and G. Pararas-Carayannis, 1976, Catalog of tsunamis in Alaska revised 1976, World Data Center A for Solid Earth Geophysics, NOAA, Report SE-1.

Hatori, T. 1965, On the Aleutian tsunami of February 4, 1965, as observed along the coast of Japan, Bull. Earthq. Res. Inst., 43, 773-782.

Hatori, T., 1981, Tsunami magnitude and source area of the Aleutian-Alaska tsunamis, Bull. Earthq. Res. Ins., 56, 97-110.

Hatori, T., 1988, On Aleutian tsunami of May 7, 1986, as observed along the coast of Japan, Proc. Intern. Tsunami Symp., Vancouver, 1987, 20-34.

Hatori, T. 1998a, Characteristic of the Aleutian tsunami of June 10, 1996 observed along the coast of Japan, Zisin, 51, 75-82.

Hatori, T., 1998b, Magnitude scale of tsunamis generated from the South-East Alaska to Western North America, Zisin, 51, 203-210.

Hatori, T., 1999, Distribution of cumulative tsunami energy from Kamchatka to East Hokkaido, Zisin, 52, 361-368.

Hatori, T., 2002, Distribution of cumulative tsunami energy along the Pacific coast of South America, Zisin, 54, 441-448.

Johnson, J.M. and K. Satake, 1997, Asperity distribution of Alaska-Aleutian earthquakes: Implications for seismic and tsunami hazards, Kluwer Academic Publishers, 67-81.

Lander, J.F., P.A. Lockrige and M.J. Kozuch, 1993, Tsunamis affecting the west of the United States, 1806-1992, Natl. Geophys. Data Cent., Natl. Oceanic and Atmos. Admin., Boulder, Colo., 242p.

McCann, W.R., O.J. Perez and L.R. Sykes, 1980, Yakataga gap, Alaska: Seismic history and earthquake potential, Science, 207, 1309-1314.

Miller, D.J., 1960, Giant waves in Lituya Bay, Alaska, Bull. Seism. Soc. Am., 50, 253-266.

Nishenko, S.P., 1991, Circum-Pacific seismic potential: 1989-1999, PAGEOPH, 135, 169- 259.

Plafker G., 1969, Tectonics of the March 27, 1964 Alaska earthquake, Geological Survey Professional Paper, 543-1.

Soloviev, S.L. and Ch. H. Go, 1985, Catalog of tsunamis on the western shore of the Pacific Ocean (in Russian). Translated by Canada Institute for Scientific and Technical Information National Research Council, Ottawa, Canada KIA OS2.

Sykes, L.R., 1971, Aftershock zones of great earthquakes, seismicity gaps, and earth- quake prediction for Alaska and Aleutians, J. Geophy. Res. 76, 8021-8041.

Utsu, T., 1990, Catalog of disastrous earthquakes in the world during ancient era-1989," Memorial Press of Prof. Utsu, 243p. (in Japanese).

Watanabe, H., 1998, Comprehensive list of tsunamis to hit the Japanese Islands (2nd Edition), Univ. Tokyo Press, 238p (in Japanese).

MAPPING THE POSSIBLE TSUNAMI HAZARD AS THE FIRST STEP TOWARDS A TSUNAMI RESISTANT COMMUNITY IN ESMERALDAS, ECUADOR

P. ARREAGA-VARGAS[1], M. ORTIZ AND S. F. FARRERAS[2]

[1] *Instituto Oceanográfico de la Armada de Ecuador*
Av. 25 de Julio-Km 3 ½ vía Pto. Marítimo Base Naval Sur Guayaquil, Ecuador
[2] *Departamento de Oceanografía Física, CICESE*
Km 107 Carretera Tijuana-Ensenada Ensenada, Baja California, México

Inundation maps for Esmeraldas, Ecuador were produced to identify areas susceptible to tsunami flooding as a first step to develop a reliable early tsunami warning system and to indicate evacuation routes and emergency shelter locations. The identification of possible tsunami source areas was based on the historic record of regional tsunamigenic earthquakes. As expected, results of the simulated tsunamis showed the most destructive tsunamis to Esmeraldas to be those that are generated directly off the coast of Esmeraldas. Among the most vulnerable places in Esmeraldas are Las Palmas and Capitanía de Puerto; this is in spite of the protection offered by structures built up to protect the harbor. Both banks of the Esmeraldas River were also found to be highly vulnerable to tsunami flooding.

1 Introduction

The history of large shallow earthquakes during the XX century along the coasts of Ecuador and Colombia, where Nazca oceanic plate is subducting beneath South American continental plate, is by itself positive evidence of the potential tsunami hazard for the city of Esmeraldas, Ecuador, as well as for the entire region. For example, the tsunami generated by the 31 January 1906 Ecuador-Colombia earthquake (M_w 8.8; Kanamori and McNally, 1982) washed away all the houses on the low-lying coast above the rupture area; by various estimates 500 to 1500 persons were killed by the tsunami (Soloviev and Go, 1975). The rupture length of this earthquake was estimated to be 400-500 km, from Manta to Buanaventura (Kelleher, 1972; see Figure 1). Both the southern and central parts of the 1906 rupture were ruptured again by the 14 May 1942 earthquake ($M_w > 7$; Kelleher, 1972), and by the 19 January 1958 earthquake (M_w 7.7; Kanamori and McNally, 1982). Four customs officers were killed by the 19 January tsunami in Esmeraldas; the waves damaged Tumaco and Guayaquil. No tsunami was observed on 14 May 1942 (Soloviev and Go, 1975). Kelleher (1972)

K. Satake (ed.), Tsunamis: Case Studies and Recent Developments, 203-215.

noted that the 1942 and 1958 earthquakes did not rupture the northeast part of the 1906 rupture area. He pointed out that the region NE of the 1958 earthquake might also be a region of relatively high earthquake risk. His forecast was correct. The 12 December 1979 Tumaco earthquake (M_w 8.2; Kanamori and McNally, 1982) apparently ruptured the gap between the 1906 and 1958 earthquakes. Part of the Pacific Coast of Colombia was swept by a tsunami immediately after the 12 December earthquake. The tsunami almost destroyed San Juan, 60 km north of Tumaco. At least 200 people were killed by the tsunami along the coast of Colombia (Herd et al., 1981). In contrast, no tsunami damage was reported in Esmeraldas, Ecuador, where the recorded tsunami, which arrived at the time of low tide, exhibited a maximum height (peak to peak) of 1 meter (Figure 2).

Encouraged by the experience of the recent well documented 12 December 1979 earthquake in Colombia, and with the purpose of emphasizing the need for tsunami awareness and educational programs in Esmeraldas, Ecuador, we estimate a tsunami inundation map for the city of Esmeraldas by modeling tsunamis generated by synthetic earthquakes occurring at the approximate location of the sequence 1906, 1942, 1958 and 1979 earthquakes.

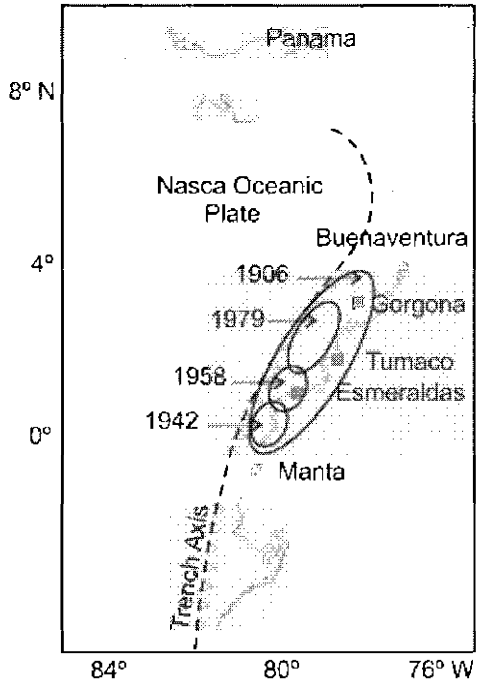

Fig. 1. Rupture areas of large sallow earthquakes in the Ecuador-Colombia region (Kelleher, 1972; Herd et al., 1981; Beck and Ruff, 1984).

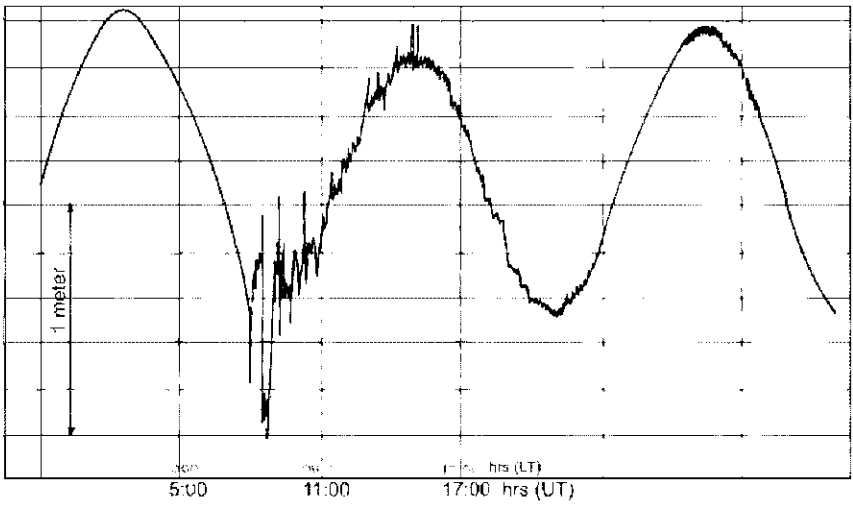

Fig. 2. The 12 December 1979 tsunami as recorded in Esmeraldas, Ecuador. The recession of sea level starts immediately after the origin time of the earthquake (07:59:03 UT; 02:59:03 LT).

2 Numerical modeling of the tsunami

The code used to compute the tsunami inundation map in this study is available through the Tsunami Inundation Modeling for Exchange (TIME) program of the Tohoku University. A description of the model and its use is given by Goto et al. (1997). The theory of shallow-water waves is used to model tsunamis when the ratio of water depth to wavelength is small. The theory assumes that vertical acceleration of water particles is negligible compared to the gravitational acceleration, and that pressure distributions can be approximated by hydrostatic profiles. Consequently, the vertical motion of water particles has no effect on the pressure distribution. In addition, the horizontal velocity of water particles is considered vertically uniform.

On the basis of these approximations, the motion of tsunami waves is expressed by the depth-averaged shallow-water equations:

$$\frac{\partial \eta}{\partial t}+\frac{\partial U}{\partial x}+\frac{\partial V}{\partial y}=0, \tag{1}$$

$$\frac{\partial U}{\partial t}+\frac{\partial}{\partial x}\left(\frac{U^2}{D}\right)+\frac{\partial}{\partial y}\left(\frac{UV}{D}\right)+gD\frac{\partial \eta}{\partial x}+\frac{gm^2}{D^{7/3}}U\sqrt{U^2+V^2}=0, \tag{2}$$

$$\frac{\partial V}{\partial t}+\frac{\partial}{\partial x}\left(\frac{UV}{D}\right)+\frac{\partial}{\partial y}\left(\frac{V^2}{D}\right)+gD\frac{\partial \eta}{\partial y}+\frac{gm^2}{D^{7/3}}V\sqrt{U^2+V^2}=0.$$

Mass conservation is represented by equation (1) and momentum conservation is represented by the set of equations (2). In this set of equations (1) and (2), t is time, η is the vertical displacement of the water surface above the still water level (the equipotential surface), $D = (\eta + h)$ is the instantaneous depth of the water column, where h is the average depth of the water column (land topography is represented by negative values of h). $U = u(\eta + h)$ and $V = v(\eta + h)$ are the horizontal depth-averaged volume flux vectors in the longitudinal (x) and latitudinal (y) directions respectively, u and v are the corresponding velocity of water particles, g is the gravitational acceleration and $m=0.025$ is Manning's roughness parameter, considered constant in this study.

The above set of equations, (1) and (2), are solved by finite differences in an explicit rectangular staggered leap-frog scheme in a set of interconnected grids that allows the use of the linearized set of equations (2) in deep water, and the conservation of the nonlinear and friction terms in the inner higher resolution grid for the selected coastal region of Esmeraldas. One of the most important capabilities of this model is the inclusion of wave run-up estimates in the inner higher resolution grid, where the nonlinear field acceleration terms and bottom friction are kept. Whether a computation cell is dry or submerged is judged in terms of the total water depth, as follows:

$D = \eta + h > 0$, then the cell is submerged, and

(3)

$D = \eta + h < 0$, the cell is dry.

For a wave front located between the dry and submerged cells, the discharge across the boundary between the two cells is computed if the ground height in the dry cell is lower than the water level in the submerged cell. In other cases, discharge is considered zero. The boundary conditions at the seaside of the inner grid are taken from the intermediate resolution grid, whereas the radiation condition at the offshore boundary in the low-resolution grid is taken from the characteristic solution of the wave equation:

$$(U, V) = \pm \eta\sqrt{gh}, \tag{4}$$

where the sign is taken in such manner that the wave will propagate outward from the computational domain.

The initial condition for the tsunami model consists of a description of sea-surface deformation; it assumes that the instantaneous topography of the sea surface approximates the vertical deformation of the sea floor produced by the earthquake. The time evolution of sea-floor displacement is not included in equation (1). The assumption that this time is negligible is valid as long as the tsunami-propagation velocity is small compared to the rupture velocity. Kowalik and Whitmore (1991) have shown that the inclusion of a finite rupture velocity in the model has little effect on the energy-flux distribution of the tsunami.

The vertical deformation of the sea floor, as produced by an earthquake, is determined from analytical expressions for the internal deformation of a continuous media due to shear and tensile faulting (e.g., Mansinha and Smylie, 1971). This model considers a simple rupture geometry and a uniform slip distribution on the fault plane. For the fault planes used to estimate the vertical deformation of the sea floor at the approximate locations of the 1942, 1958 and 1979 earthquakes, we assumed a uniform slip distribution of 4 meters on a fault plane 160 km x 70 km. This fault geometry approximately fit the magnitude and seismic moment of the 12 December 1979 Colombia earthquake. For the 1906 earthquake we assumed a reverse-slip distribution of 7 meters on a fault plane 480 km x 130 km. Dislocation model parameters used to estimate the vertical deformation of the sea floor are described in Table 1. The location of the corresponding fault planes is illustrated in Figure 3.

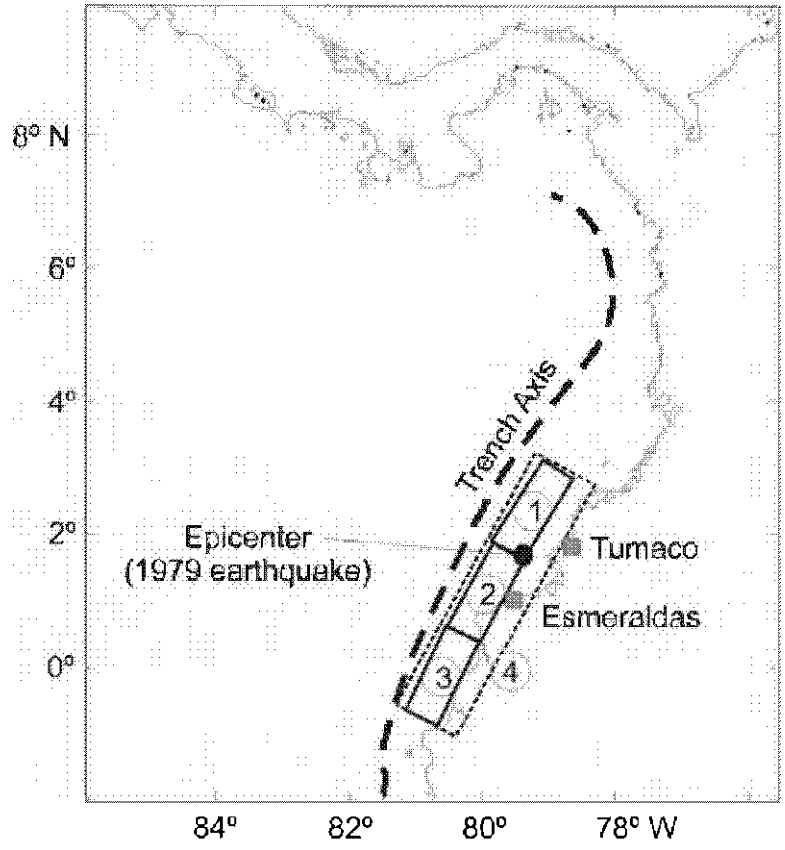

Fig. 3. Surface projection of the fault planes (1, 2, 3 and 4) described in Table 1, used to estimate tsunami hazard for the City of Esmeraldas.

Table 1. Dislocation model parameters used to estimate the vertical deformation of the sea floor. Seismic moment (Mo) estimates assume a rigidity modulus of $4x10^{11}$ dyne cm. M_w estimates uses the relationship: $M_w = 2/3 \log_{10} Mo - 10.7$ (Hanks and Kanamori, 1997). Rupture area (A) estimates use the relationship: $M_w = \log_{10} A + 4.0$ (Utsu and Seki, 1954; Wyss, 1979; Singh *et al.*, 1980) where A is in km^2. Rake of 90° (reverse faulting) is assumed for all of the fault planes.

	Dislocation model (1)	Dislocation model (2)	Dislocation model (3)	Dislocation model (4)
Length (km)	160	160	160	480
Width (km)	70	70	70	130
Depth (km) (shallow edge)	15	15	15	15
Strike (°)	35	30	25	30
Dip (°)	30	30	30	30
Rake (°)	90	90	90	90
Slip (m)	4	4	4	7
Mo (dyne cm)	$2.24 x10^{28}$	$2.24 x10^{28}$	$2.24 x10^{28}$	$1.78 x10^{29}$
M_w	8.2	8.2	8.2	8.8
SW corner coordinates	1.9014° N 79.8436° W	0.7314° N 80.6536° W	0.5961° S 81.2611° W	0.5961° S 81.2611° W

The synthetic tsunamis, at the tide gauge location in the harbor of Esmeraldas resulting from the 4 dislocation models described in Table 1, are illustrated in Figure 4 (tide gauge location is indicated in Figure 7). As expected, results of the simulated tsunamis showed the most destructive tsunamis to the harbor in Esmeraldas to be those that are generated directly off the coast of Esmeraldas, i.e., those generated by dislocation models 2 and 4. In both cases, the water starts rising immediately after the origin time of the dislocation, reaching its maximum (1.3 m and 2.7 m, respectively) ~19 minutes after. Subsequent oscillations (period of 10-15 minutes) having approximately the amplitude of the first maximum are still present during the 2 hours of tsunami simulation. In both cases, the maximum water level (2.3 m and 4.3 m) occurs 88 minutes and 116 minutes, respectively, after the origin time of the dislocation. Tsunamis generated by dislocation models 1 and 3 have small amplitude in comparison with those generated by dislocation models 2 and 4. Table 2 summarizes the arrival time and height of the first maximum and of the highest maximum water level at the tide gauge location, resulting from the synthetic tsunamis illustrated in Figure 4.

The upstream propagation of the tsunami is described by considering the tsunami generated by dislocation model 4. Propagation of the tsunami is summarized in Table 3 and illustrated in Figure 5. The first maximum of the tsunami propagates upstream with no significant attenuation. However, the upstream tsunami wave is triangular in shape, indicating that nonlinear terms in equations (2) are important because of the

shallow depth (~3 m) along the river bed. It causes that most of the high frequency oscillations (period of ~15 minutes) observed offshore are being attenuated upstream by the ebb produced by the recession of the water after the first tsunami arrival (ebb in this case is due only to tsunami flow, no river flow or tide was considered in the numerical simulation). The composed waveform observed in the harbor is produced by reflection of these high frequency oscillations in the river mouth. The fact that only in the harbor the maximum water level does not correspond to the first maximum is due to the superposition of the incoming and reflected wave.

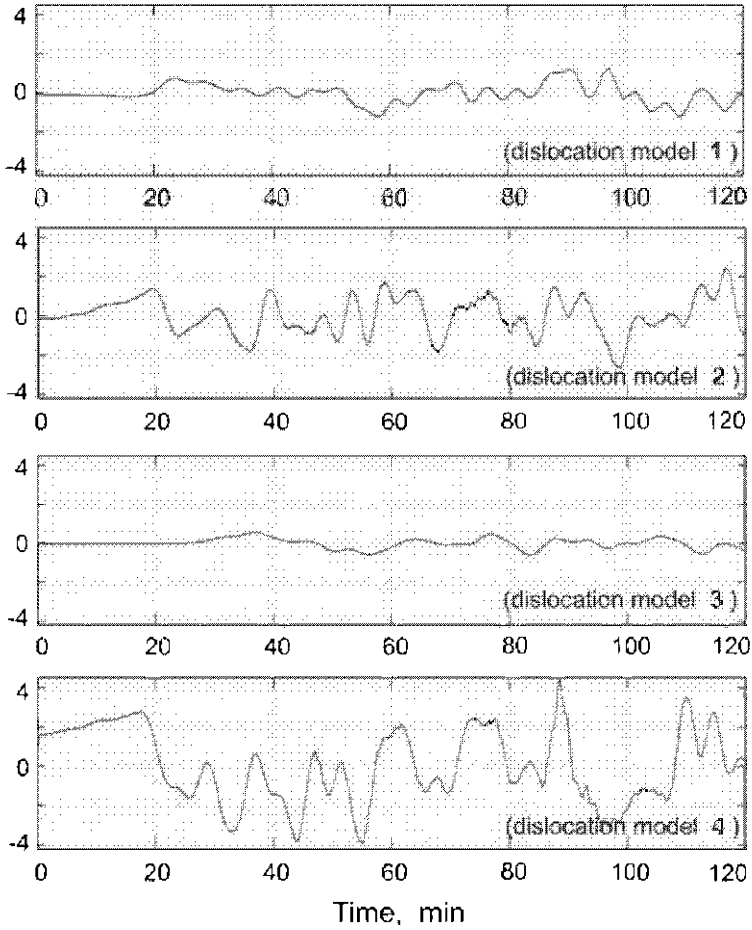

Fig. 4. Synthetic tsunamis at the tide gauge location in the harbor of Esmeraldas. The synthetic tsunamis are simulated assuming the 4 dislocation models described in Table 1. The origin of the time axis is defined as the origin time of the dislocation. Vertical axis indicates water level in meters relative to mean sea level. In each case the start of the tsunami indicates the uplift of the shore.

Table 2. Arrival time and height of the first maximum and of the highest maximum water level at the tide gauge location resulting from the synthetic tsunamis illustrated in Figure 4.

dislocation model	first maximum	highest maximum
1	0.7 m @ 23 min	1.2 m @ 90 min
2	1.3 m @ 19 min	2.3 m @ 116 min
3	0.5 m @ 36 min	0.5 m @ 36 min
4	2.7 m @ 17 min	4.3 m @ 88 min

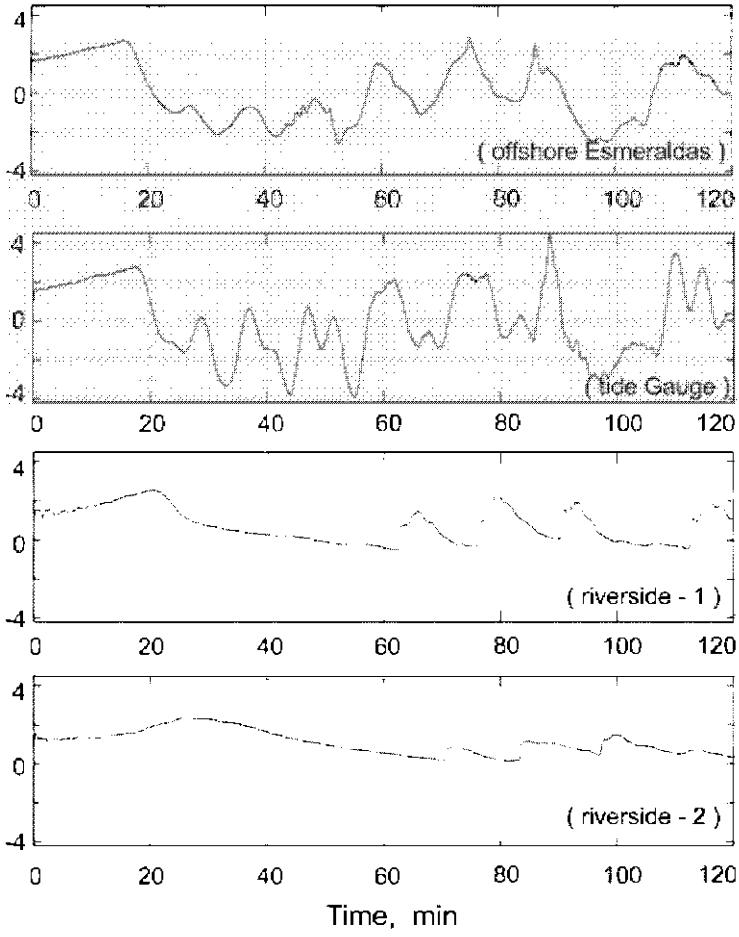

Fig. 5. Synthetic tsunami generated by dislocation model 4 at the locations: offshore Esmeraldas; tide gauge; riverside-1, and riverside-2 (locations are indicated in Figure 7). The origin of the time axis is defined as the origin time of the dislocation. Vertical axis indicates water level in meters relative to mean sea level. In each case the start of the tsunami indicates the uplift of the shore.

Table 3. Arrival time and height of the first maximum, and of the highest maximum water level, resulting from the upstream propagation of the synthetic tsunami generated by dislocation model 4 at the locations: 1 km offshore Esmeraldas; tide gauge; riverside-1, and riverside-2 (locations are indicated in Figure 7).

location	first maximum	highest maximum
1 km offshore Esmeraldas	2.5 m @ 15 min	2.5 m @ 15 min
tide gauge	2.7 m @ 17 min	4.3 m @ 88 min
riverside (1)	2.5 m @ 21 min	2.5 m @ 21 min
riverside (2)	2.3 m @ 26 min	2.3 m @ 26 min

3 Tsunami inundation map for Esmeraldas

The City of Esmeraldas (~140,000 inhabitants) is located mostly on the west side of Esmeraldas River, 3 to 10 meters above mean sea level, and extends from the hill base up to 50 meters high. Since tide range in Esmeraldas, defined here as the difference between the highest and lowest tide levels, is 3.8 meters (Figure 6), a tsunami inundation map for Esmeraldas should take into consideration the tide level at the origin time of the dislocation. For example, computed tsunami run-up height in Esmeraldas by dislocation models 2 and 4, considering the tide at mean sea level, is 1-2 meters along the riverside. This run-up height barely overtops the highest tide level (1.9 m). It may be expected for a large tsunami arriving at the lowest tide to cause no inundation damage. Therefore, to avoid underestimating the flooding risk, the tsunami inundation map for Esmeraldas (Figure 7) is computed considering dislocation model 4 and a high tide level scenario. In the computation, the grid spacing for the inner high resolution grid was set to 1 second (~30 m) interpolated from high-resolution recent soundings. The resulting tsunami run-up height along both sides of the river is nearly constant; the tsunami penetrates inland up to the contour level of 4 meters above mean sea level. Isla del Prado, which is 2-3 meters above mean se level, is completely inundated in this tsunami scenario. In contrast, run-up height along the open coast at both sides of the river mouth is 8 meters. This large run-up amplification is due to the gentle sloping beaches that are continuously fed by river sand. In fact, tsunami flooding in "Capitanía de Puerto" (C. Puerto) is due to the run-up amplification in Las Palmas beach.

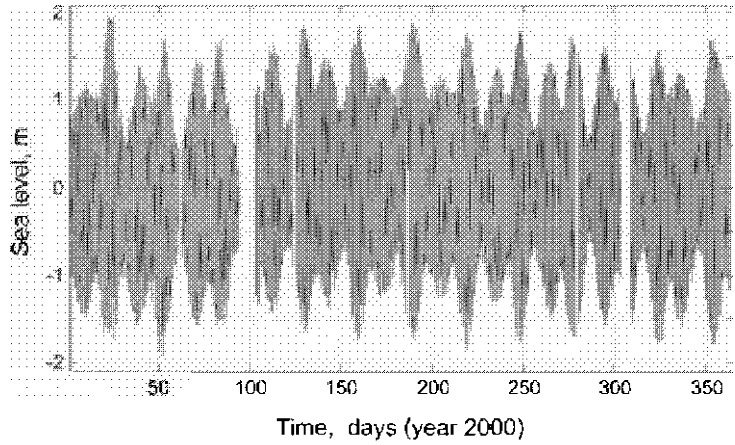

Fig. 6. Recorded sea level in the harbor of Esmeraldas, Ecuador. Sea level data are relative to mean sea level.

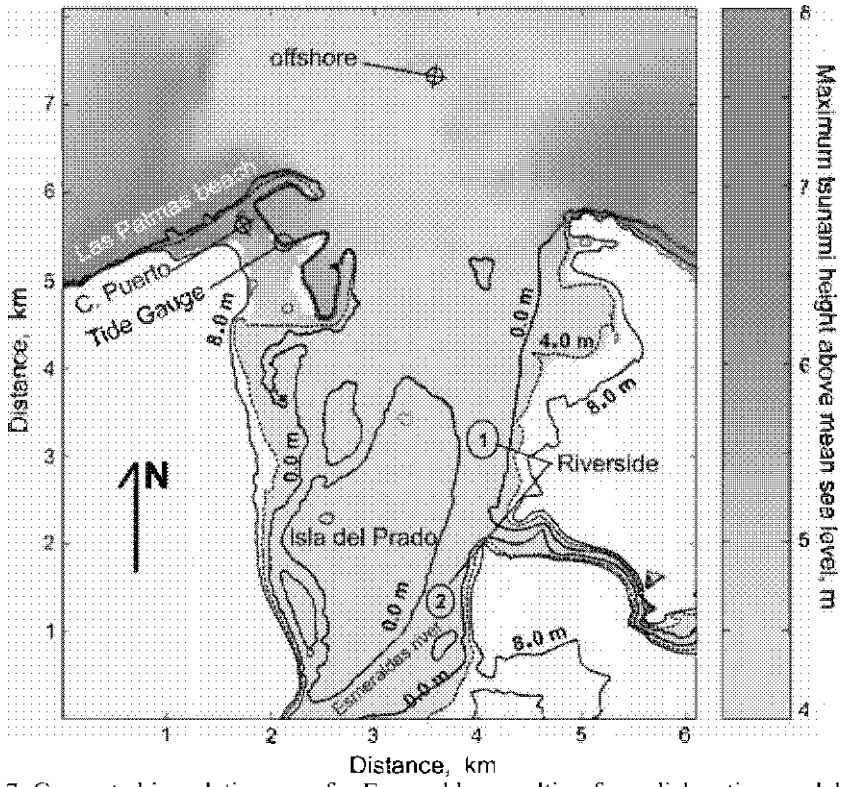

Fig. 7. Computed inundation map for Esmeraldas resulting from dislocation model 4, considering a high tide level scenario. Contours of 0, 4, and 8 meters above mean sea level are indicated on the figure. Locations for synthetic tsunamis (tide gauge, offshore Esmeraldas, riverside-1 and riverside-2), are also indicated.

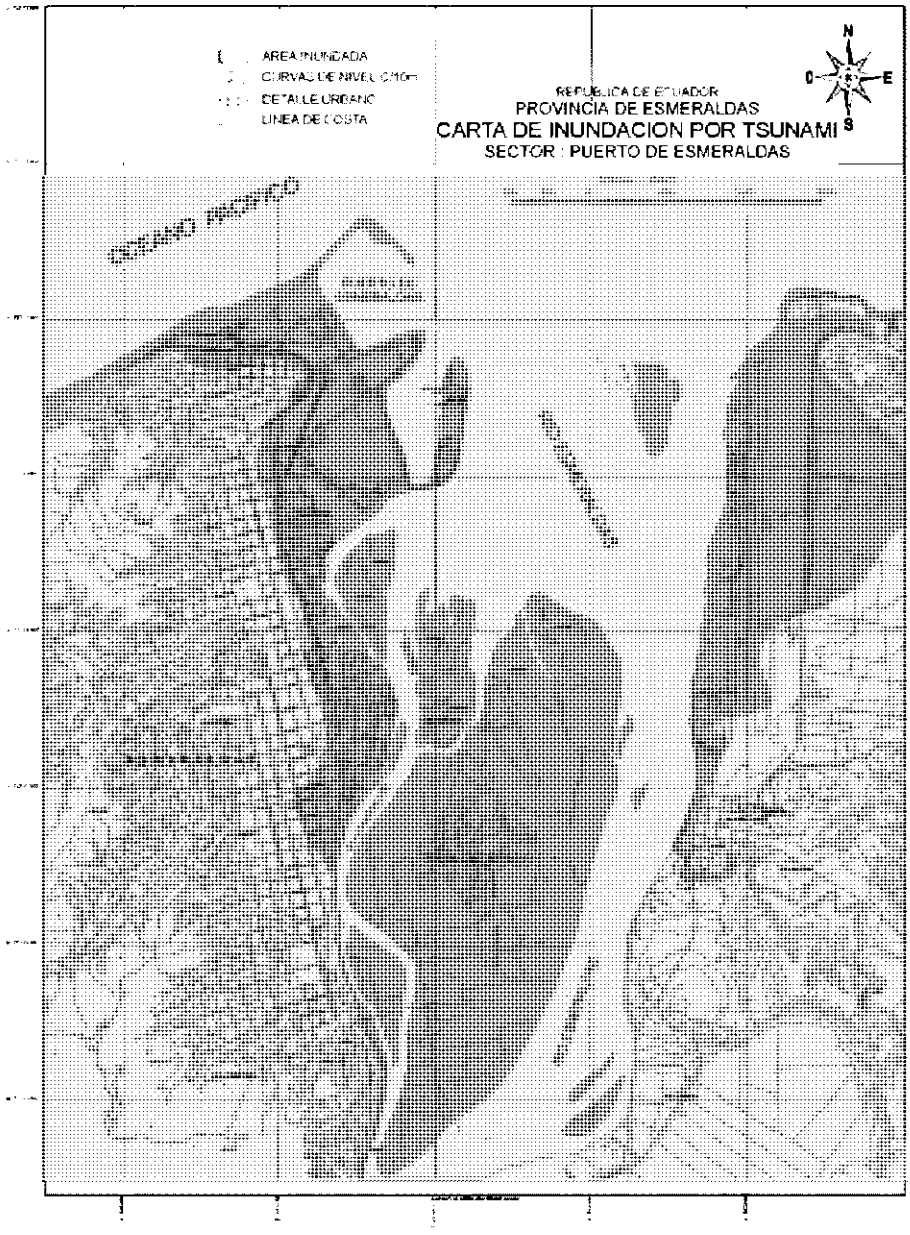

Fig. 8. Abridged copy of Esmeraldas, Ecuador tsunami inundation map.

4 Discussion and conclusions

Since the first peak of the synthetic tsunami in Esmeraldas arrives at the open coast and at the harbor 15-17 minutes after the origin time of the dislocation, and 20-26 minutes at the riverside, there is little time for a regional warning system to alert coastal residents that danger is imminent. However, adjacent hills behind the beach and the city may offer secure evacuation routes if upon feeling the earthquake shaking, people evacuate to higher ground.

In case of local generated tsunamis, like the one simulated here, the best mitigation strategy is to create a tsunami-aware community. Three steps to create a tsunami-resistant community are to (Bernard, 1999):

1. Produce tsunami hazard maps to identify areas susceptible to tsunami flooding,
2. Implement and maintain an awareness/educational program on tsunami dangers,
3. Develop early local warning systems to alert coastal residents that danger is imminent.

The first step has been successfully accomplished for Esmeraldas. The tsunami inundation map for Esmeraldas (Figure 8) is partially based on the results illustrated in Figure 7, and extended in some areas to 8 meters above mean sea level, preventing a worst case scenario. Evacuation routes and emergency shelter locations should be indicated in the inundation map to help the population and local authorities in the event of a future tsunami occurrence. It remains for Ecuador to develop a reliable early tsunami warning system, and implement an educational program for tsunami prevention.

Acknowledgements

We thank the International Tsunami Information Center (ITIC) and IOC/UNESCO funding assistance for P. Arreaga to attend a training course on tsunami modeling at the Center of Scientific Research and Graduate School of Ensenada, Mexico (CICESE). E. Navarrete from Escuela Superior Politécnica del Litoral for providing access to the valuable high-resolution bathymetric data. Modesto Ortiz acknowledges funding support from the National Research Institute for Earth Science and Disaster Prevention-Japan (NIED), for Tsunami Disaster Mitigation Research in Southern Mexico and Central America.

References

Bernard E., 1999. Tsunami. Natural Disaster Management, pp 58-60. United Nations. Tudor Rose Holdings, J. Ingleton editor. 320 pp.

Dronkers, J.J., 1964. Tidal Computations in Rivers and Coastal Waters, North-Holland Publishing Company, Amsterdam. 518 p.

Goto C., Y. Ogawa, N. Shuto, and F. IMAMURA, 1997. IUGG/IOC TIME Project: Numerical Method of Tsunami Simulation with the Leap-Frog Scheme, Intergovernmental Oceanographic Commission of UNESCO, Manuals and Guides # 35, Paris, 4 Parts.

Hanks, T. C., and H. Kanamori, A moment magnitude scale, *J. Geophys. Res.*, 84, 2348-2350, 1997.

Herd, D. G., T. Leslie, H. Meyer, J. L. Arango, W. J. Person, And C. Mendoza, 1981. The Great Tumaco, Colombia Earthquake of 12 December 1979, *Science*, 211, 4481, 441-445.

Kowalik, Z., Whitmore, P., 1991. An investigation of two tsunamis recorded at Adak, Alaska: *Science of Tsunami Hazard*, 9, 2, 67-83.

Kanamori, H., And K. Menally, 1982. Variable rupture mode of the subduction zone along the Ecuador-Colombia coast, *Bull. Seismol. Soc. Am.*, 72, 1241-1253.

Kelleher, J.,1972. Rupture zones of large South American earthquakes and some predictions, *J. Geophys. Res.*, 77, 2087-2103.

Mansinha, L. And E. Smylie, 1971. The Displacement Field of Inclined Faults, *Bull. Seismol. Soc. Am. 61*, 1433-1440.

Singh, S.K., E. Bazan, and L. Esteva., 1980. Expected earthquake magnitude from a fault. *Bull. Seism. Soc. Am.*, 70, 903-914.

Soloviev, L. And N. Go, 1975. A catalogue of tsunamis on the eastern shore of the Pacific Ocean (1513-1968). Nauka Publishing House, Moscow, USSR, 204p. Can. Transl. Fish. Aquat. Sci. 5078, 1984.

Utsu, T. and A. Seki., 1954. A relation between the area of aftershok region and the energy of main shock (in Japanese), *J. Seism. Soc. Jap.*, 7, 233-240.

Wyss, M., 1979. Estimating maximum expectable magnitude of earthquakes from fault dimensions. *Geology.*, 7, 366-340.

PROGRESSES IN THE ASSESSMENT OF TSUNAMI GENESIS AND IMPACTS AROUND THE PORTUGUESE COASTS

L. MENDES-VICTOR[1], A RIBEIRO[2], L. MATIAS[3], M. ANA BAPTISTA[3], J. MIGUEL MIRANDA[3], P. MIRANDA[3], N. ZITELLINI[4], E. GARCIA[5], C. CORELA[1], P. TERRINHA[2], M. ROVERE[4] AND F. TEIXEIRA[6]

[1] *Instituto Geofisico do Infante D. Luis da Universidade de Lisboa (IGIDL), R.Escola Politécnica, 58, 1250 -102 Lisboa, Portugal E-mail: lmvictor@fc.ul.pt*
[2] *Laboratório de Tectonofísica e Tectónica Experimental (LATTEX), Faculdade de Ciências da Universidade de Lisboa Edifío C2 – 5º Piso, Campo Grande, 1749-016 Lisboa, Portugal*
[3] *Centro de Geofísica da Universidade de Lisboa (CGUL), Faculdade de Ciências Edificio C8, 1749-016 Lisboa, Portugal*
[4] *Istituto per la Geologia Marina,CNR, Via Gobetti 101, 40129 Bologna, Italy*
[5] *Institut de Ciències de la Terra "Jaume Almera" (ICTJA-CSIC), c/ Luis Sole i Sabaris s/n, 08028 Barcelona, Spain*
[6] *Rua da Escola Politécnica, 58, 1250 -102 Lisboa, Portugal*

The tsunami generated by the 1755.11.01 earthquake, as reported by coeval sources, was the major event of its kind in the North Atlantic, until nowadays. The coasts of the Iberian Peninsula and Northwest Morocco were deeply affected by that phenomenon, with tremendous impacts on the city of Lisbon. For the last 20 years, significant support was received from EU (Projects DETWS, IAM, GITEC, GITEC-TWO and BIGSETS), national projects (MATESPRO, RIFANO and RIMAR) and bi-lateral cooperation (HITS, TTR-10, SISMAR and VOLTAIRE). This allowed significant improvements on the knowledge of parameters sources and tsunami propagation. Tsunami propagation models were developed, being the simulations controlled by real data, deducted from historical reports or instrumental networks. In order to assess the considerable impacts along the Portuguese coasts, different run-up models have been used and tested. To evaluate the tsunami hazard, comprehensive studies were developed, recognizing the importance of the inter-disciplinary approach, including the study of induced continental sedimentary deposits. The location of the 1755.11.01 source has been a key question, motivating intensive marine research in the southern area of Portugal, looking for unquestionable morphological or geological evidence of fault rupture and the present-day seismic activity.

K. Satake (ed.), Tsunamis: Case Studies and Recent Developments, 217-230.

1 Introduction

The tsunami generated by the 1755.01.11 earthquake affected mainly the coast of the Iberian Peninsula and Northwest Morocco although it was observed all over the North Atlantic coasts. The catastrophic dimension of that phenomenon had a tremendous impact on the city of Lisbon and on several villages along the south coast of Portugal (Pereira de Sousa, 1919). The earthquake was felt all over Europe and the seismic intensity was estimated within X-XI (Mercalli Intensity Scale) at Lisbon and Southwest Portugal (S.Vincent cape) (Martins and Mendes Victor, 1990). Also, the most destructive tsunami waves were observed along the coast of Portugal especially in Lisbon, in the area of the S.Vincent Cape, along the Gulf of Cadiz and Northwest Morocco.

The historical compilation includes most of the available data from Portugal, Spain and several other European countries. The estimated number of casualties due to the earthquake, tsunami and fire points to 10,000 people in Lisbon, but several coeval documents refer to a larger number of victims; the casualties due exclusively to the tsunami is estimated to be 1,000 victims (Baptista et al., 1997).

The methodology followed by the group of researchers seems to be adequate to find out and provide detailed information about the parameters necessary to attempt the modelling of big sources of earthquakes and tsunamis. This information mainly consists of several MCS profiles acquired on board the Italian RV *Urania* during the RIFANO-92 project, BIGSETS-98 projects and also from interpretation data from TTR-10 and HITS cruise.

The overall objectives were established in order to assure significant improvement of tsunami hazard and risk assessments, as well as the methodology to setup early warning systems, taking into account the environment constrains and the location of the related earthquake source.

The mobilization of the different teams to produce new certified documents, that allowed the final geodynamical interpretation, was well grounded and innovative in this specific research domain. Nowadays, it is assumed that the development of a suitable system should be proposed in order to satisfy not only the scientific community but also the policy-makers of risk warning and management, incorporating the effective risk sources monitoring of very large events like this one under study.

2 Earthquake and tsunami source

During the RIFANO-92 survey an MCS line (AR92-10), Figure 1, was acquired across the epicentre location of the 1755 Lisbon earthquake. This seismic profile, Figure 2, reveals a landward dipping listric thrust fault, the *Marquês de Pombal fault* (see

Zittelini et al., 2001), with an offset of the sea-floor of about 1000 m along the base of a NNE-SSW trending morphological scarp. The *Marquês de Pombal fault* is located offshore the southwestern part of the Portuguese coast, between the Gorringe Bank and the S. Vincent Cape.

As a result of the BIGSETS project (Big Sources of Earthquakes and Tsunamis in Southwestern Iberia, contract n° ENV-4CT97-0547), an integrated marine geophysical data set was acquired in the area bounded by lat 36°-38°N and long 9°-10°30'W (Figure 3). The shallow structure of the *Marquês de Pombal* was modelled and the features linked to the identified fault rupture were well visualized and dated with MCS, chirp sonar data, core sampling and land stations.

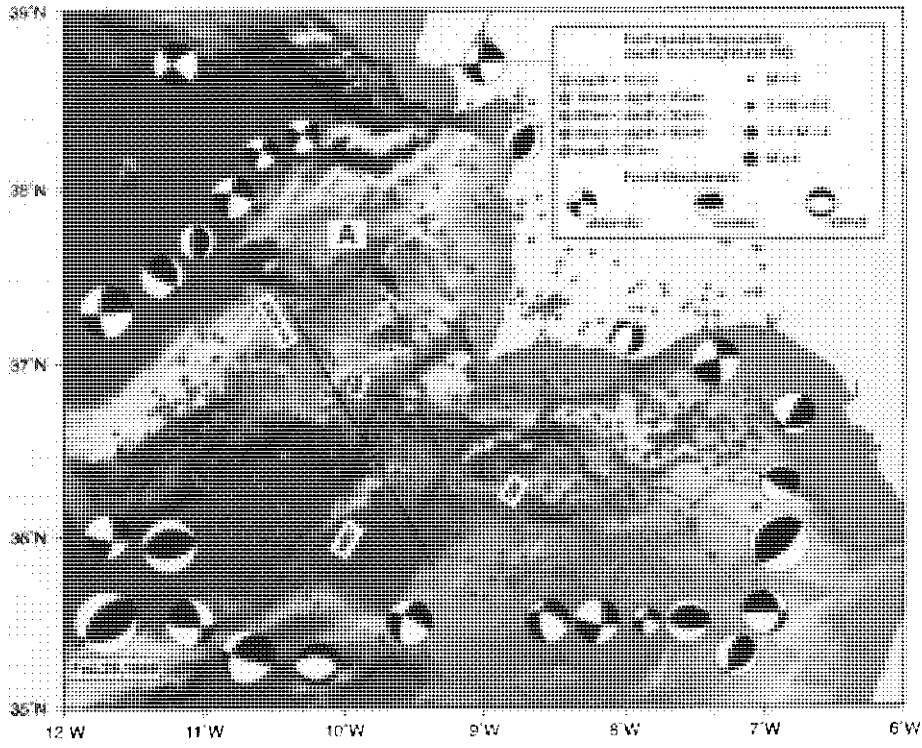

Fig. 1. Bathymetric map of southwestern Iberia with location of earthquake epicentres recorded by the new seismic network from January 1995 to March 2000. The focal mechanisms of main earthquake before March 1995 are from Hayward et al. [1999]. MP: *Marquês de Pombal*; HSF: Horseshoe fault; GB: Guadalquivir Bank; AR92-10: Multi-channel seismic (MCS) line from RIFANO-92.

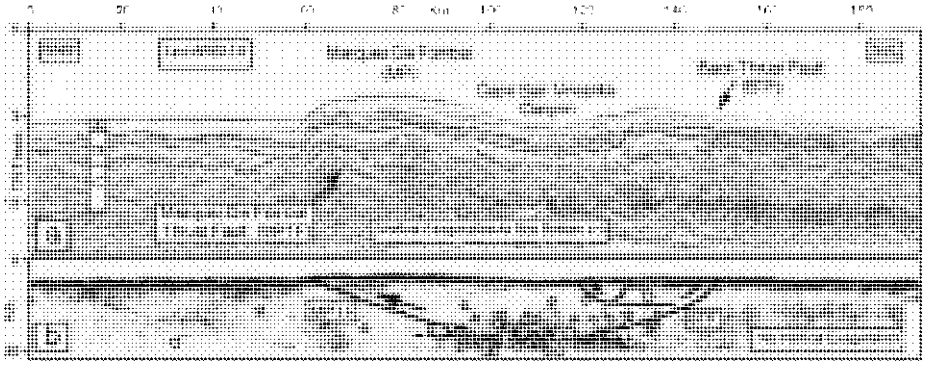

Fig. 2. AR92-10 seismic line. a) After post-stack time migration and b) tectonic sketch of the same line, depth-converted, with projected earthquake hypocenters whose coordinates are within 30 km from AR92-10 line. For location of line AR92-10 and epicenter locations, see Figure 1. The dimension of the circles is proportional to the magnitude. In the upper diagram, A: syn-compressional sedimentary sequence; B: a pre-compressional sedimentary sequence; and C: acoustic basement made up of continental crust thinned during the Eurasia-North America Mesozoic rifting.

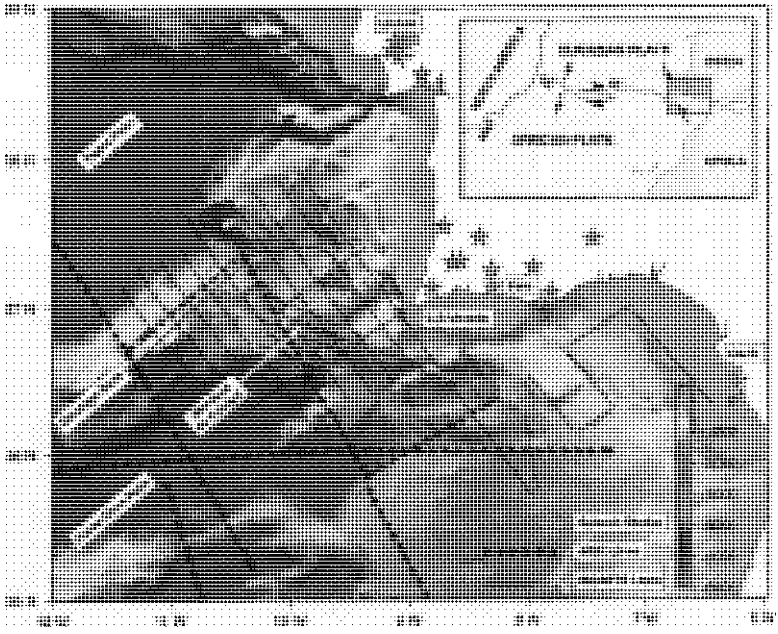

Fig. 3. Location of land seismic stations and MCS lines acquired on board the Italian RV *Urania* during RIFANO-92 and BIGSETS-98 projects. Inset map sketches the main elements of plate boundaries; the stippled patch indicates absence of well-defined plate boundary. MAR: Mid-Atlantic Ridge; TR: Terceira Ridge; GF: Gloria fault. Solid arrows show relative plate kinematics.

Swath-bathymetric data reveal the existence of several seafloor slope ruptures in the area to the west of Portugal. One of the most striking features is the 50 km-long, 1km-high, N20ºE-trending escarpment, (see Eulàlia Gràcia et al., 2003), Figure 4.

The *Marquês de Pombal fault* was more clearly imaged on MCS profiles acquired during the BIGSETS project, Figure 5.

Fig. 4. Three-dimensional image of *Marquês de pombal* thrust front and landslide area; view is from west. The white dot line is the seafloor rupture with 50 km long (HITS cruise).

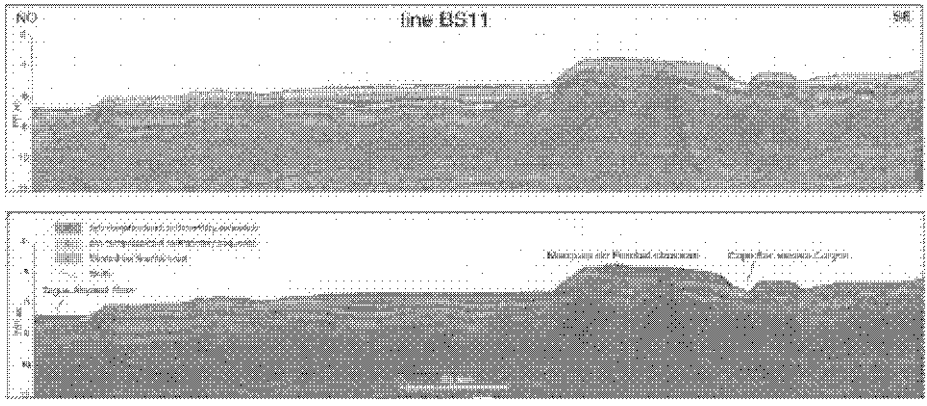

Fig. 5. MCS BS11 acquired during BIGSETS project. A crustal seismo-stratigraphic model was developed using the land recording data, the reflection deep-shooting data in the area of the *Marquês de Pombal* structure.

Although the location, orientation and structural type of the *Marquês de Pombal fault* fits with the proposing seismogenic models, the size of the fault – 50 km long, parallel to the strike direction – is far too small. This length can be enlarged to almost 100 km if the northern termination (a flexure) is assumed to be associated with a blind thrust, Figure 6.

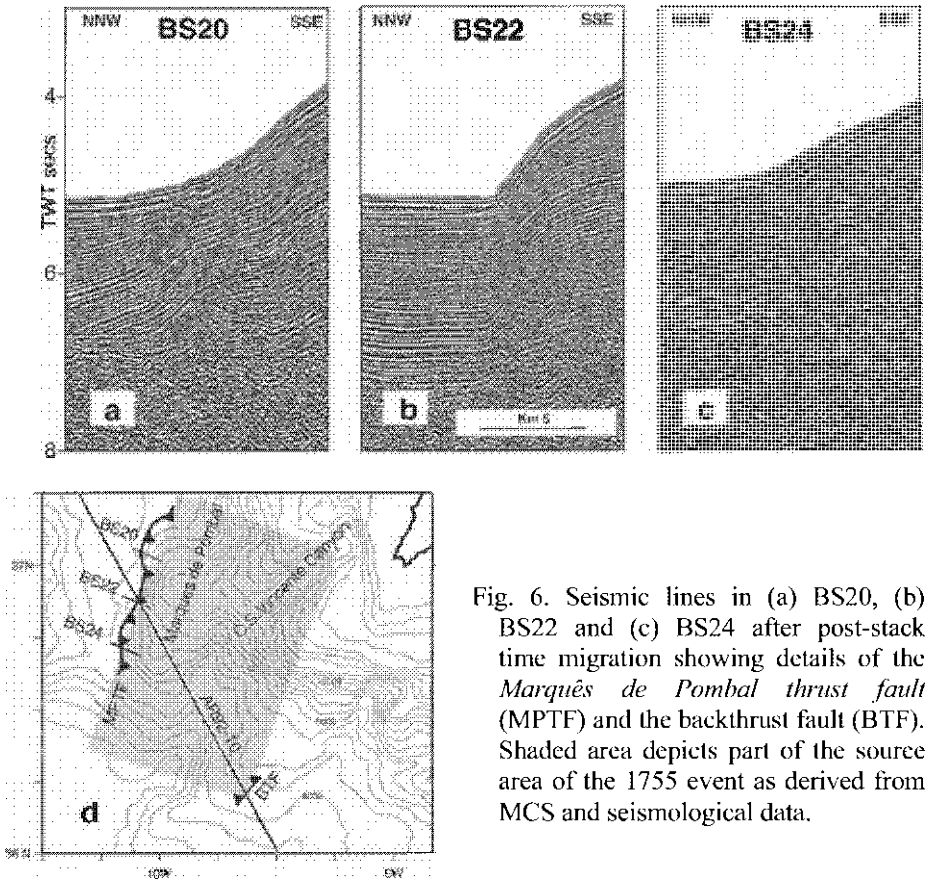

Fig. 6. Seismic lines in (a) BS20, (b) BS22 and (c) BS24 after post-stack time migration showing details of the *Marquês de Pombal thrust fault* (MPTF) and the backthrust fault (BTF). Shaded area depicts part of the source area of the 1755 event as derived from MCS and seismological data.

Tectonically active structures prone to cause devastating earthquakes and tsunamis such as the Lisbon, 1755 earthquake, were investigated during the TTR10 cruise (Training Through Research, UNESCO/IOC) on the southwest Portuguese Continental Margin using single channel seismic profiles, 3.5 kHz hull mounted sea-bottom profiler, 10 kHz OKEAN long range side scan sonar, 30 kHz ORETECH deep towed side scan sonar and high resolution deep towed sea-bottom profiler.

Interpretation of the data acquired during the TTR10 cruise lead to conclude that the *Pereira de Sousa fault* and the *TTR10 fault* are active faults, i.e., they have been active during Pliocene-Quaternary times. The present data and interpretation confirm that the *Marquês de Pombal fault* is an active fault and it is also proposed that the *Pereira de Sousa fault* and *TTR-10 fault* are also active or are experiencing passive uplift and control the mass transport sedimentation in the study area (see Terrinha et al., 2002), Figure 7.

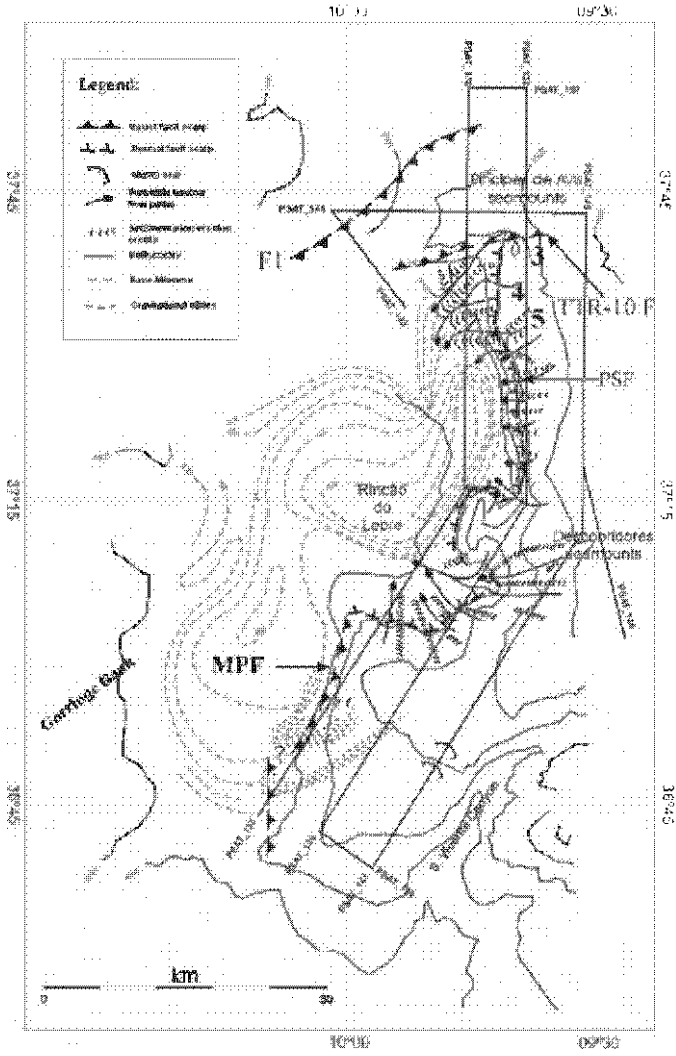

Fig. 7. Interpretation of the sedimentary and morphological system in the study area. Position of seismic and sonar TTR-10 cruise lines are marked as PSAT.

Finding of gravitational slides on the *Marquês de Pombal* slope lead us to conclude that the *Marquês de Pombal fault* is prone to cause important gravitational slides, probably triggered by earthquakes. The remaining of the sediment transport in the study area is accomplished by turbidite or laminar flows into the *Rincão do Lebre* basin that acts as an endorheic sub-marine basin, into which converge the flows from the *Pereira de Sousa fault* and *TTR10 fault* scarps heights. It was also observed that slumps, sediment failure and gravitational slides tend to develop in moderate to high slopes, whereas on steep scarps most of the sediment transport appears to be more continuous by means of formation of several gulleys on the crest of the scarps and

levee type deposits, displaying well developed ridge and trough topography at the base of the scarps.

The structural map and the OKEAN side scan mosaic of the study area, with the main sedimentary and morphological features pointed out, are shown in Figures 8a and b.

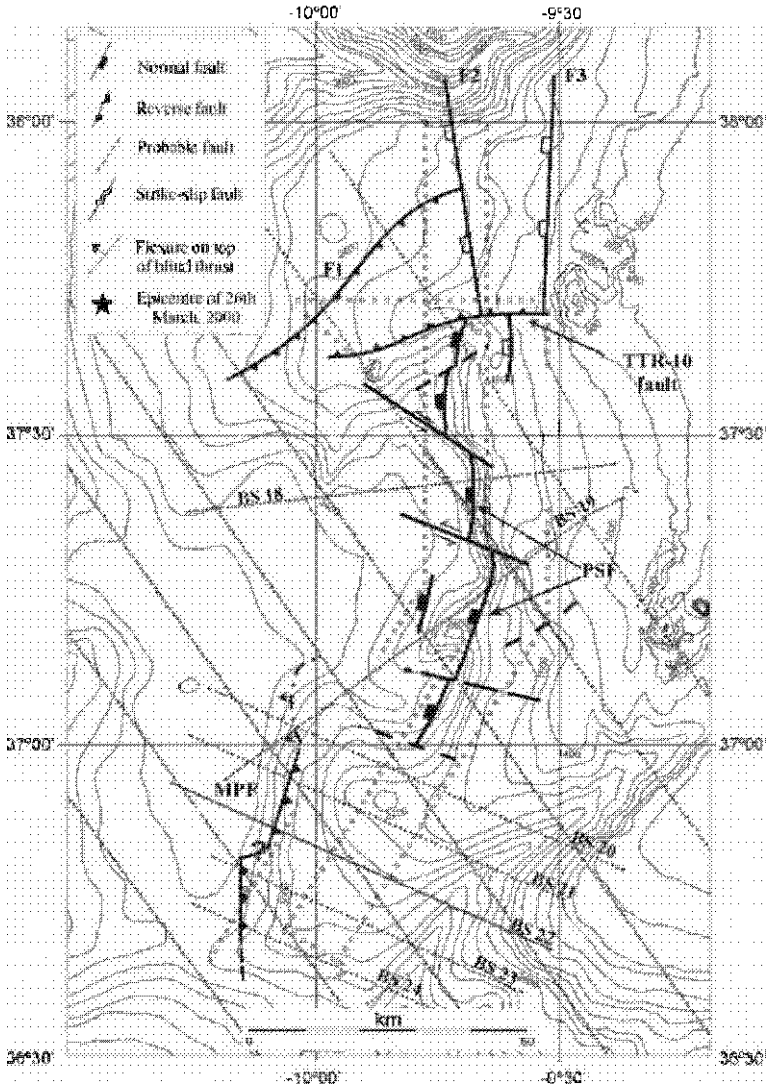

Fig. 8a. Structural map of the study area. Active faults are shown as continuous lines with black ticks. Inactive faults are shown with white ticks (F2 and F3). The MPF is shown as made up of two fault segments possibly connected through a restraining bend. Position of TTR-10 seismic lines is shown as open circles. The position of BIGSETS MCS lines (BS) are shown as dotted lines. MPF: *Marquês de Pombal fault*; PSF: *Pereira de Sousa fault*

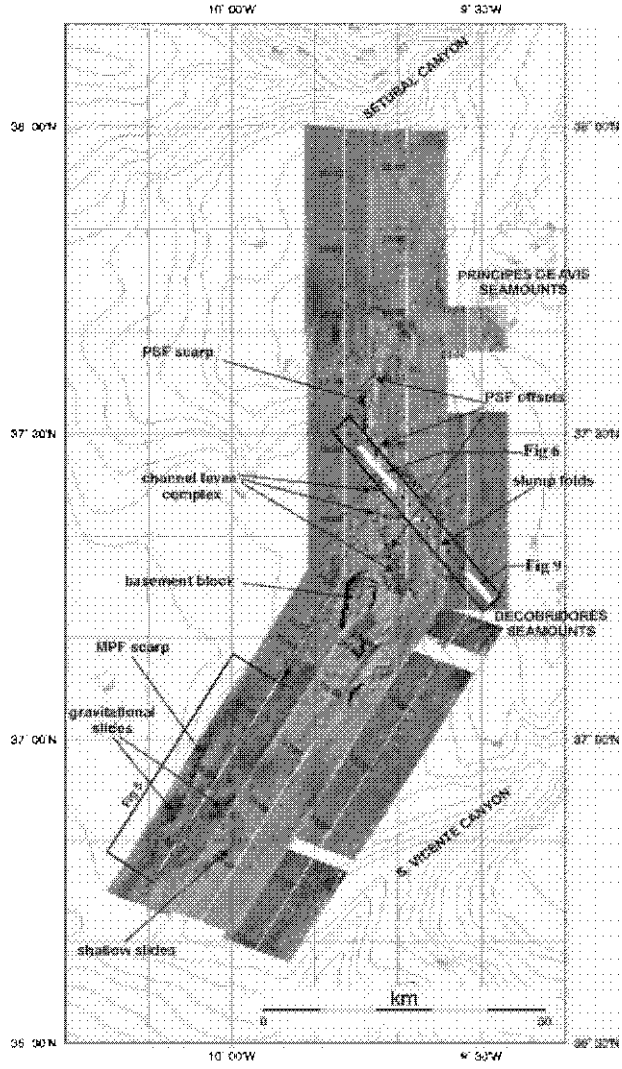

Fig. 8b. Shallow towed 10 KHz OKEAN side scan sonar mosaic.

The new structural interpretation widely accepted, was the final result from the studying of the TTR-10 seismic lines, side scan sonar images, from MCS BIGSETS, AR92-10 and also by the multibeam data acquired by the HITS cruise (High resolution Imaging of Tsunamigenic structures in the Southwest Iberian Margins) in September 2001. The use of seismic profiles and sonar images give a three dimensional view of the *Marquês de pombal fault* and *Pereira de Sousa fault* areas, casting new light on their geometry and also producing new evidences of the active sedimentary processes, and slope instability processes associated with these two faults.

3 Tsunami modeling

Considering that the 1755 event was an intra-plate earthquake with high stress-drop, an average 20 m slip could be attained for an Mw=8.7 event; based on this, the minimum length for the fault that originated the 1755 Lisbon earthquake should be of 150 km. This value suggests that additional rupture areas have to be associated with the MPF to generate such a destructive earthquake.

Although the precise location of the source of the 1755 Lisbon earthquake has been debated, backward ray-tracing tsunami modeling has suggested an L-shaped double rupture, centered ~100 km to the west of S. Vicente cape, Figure 9.

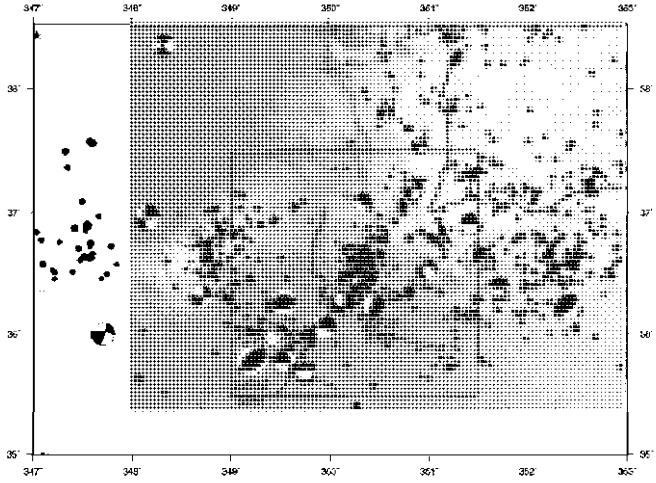

Fig. 9. L-shaped double rupture. (in Baptista et al., 1998)

The hydrodynamical modelling of the tsunami generated by the 1755.11.01 earthquake suggested a source area located along the southwest Iberian margin (see Baptista et al, 1998), Figure 10.

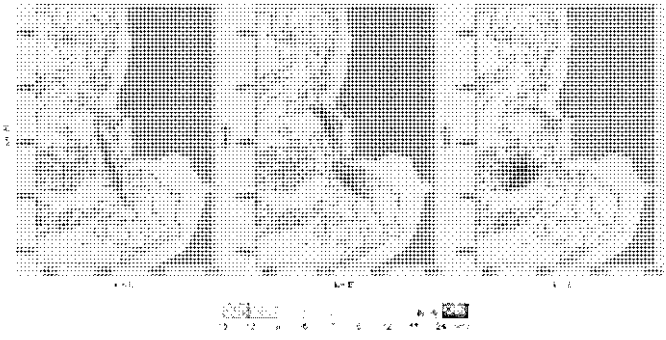

Fig. 10. Hydrodynamical modelling. The two figures on the left shows two possibilities for the new tsunami source. The figure on the right show the previous configuration rejected by the hydrodynamical simulation. (Baptista et al., 1998a)

4 Tsunami hazards

Tsunami deposits have been considered very important paleoseismic indicators such as those from the Spanish coasts. The study of the sedimentary deposits of the Valdelagrana spit barriers (Cadiz, Spain), (see Luque et al., 2001), suggests that an event similar to the 1755 Lisbon earthquake (Ms 8.5-9) might have occurred at 216-218 BC (For the first time, significant data were obtained related to such high magnitude events, that allowed to estimate the return period with some accuracy).

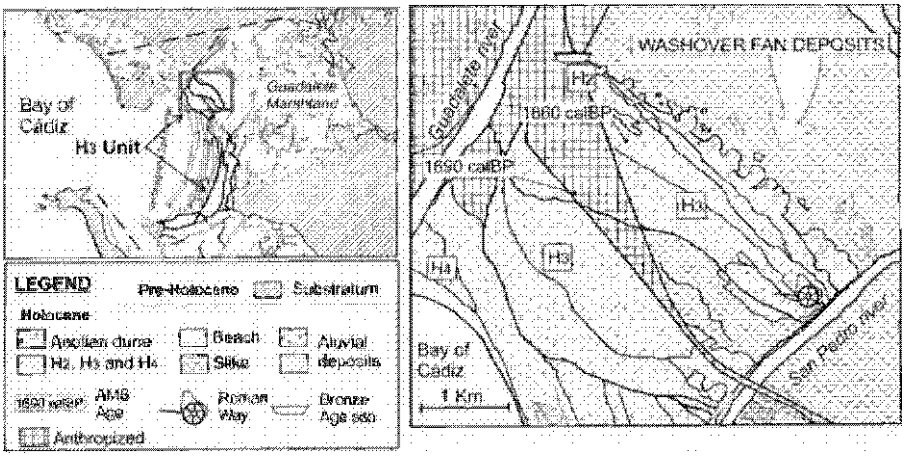

Fig. 11. Sedimentary deposits of the Valdelagrana spit barriers (Cádiz, Spain). (Luque et al., 2001)

The most recent deposits in unit H4 of the Valdelagrana spit bar, Figure 11, are correlated with the 1755 tsunami. The oldest deposits could be contemporaneous and were recorded in H3 unit of the Valdelagrana spit bar and in drill holes in the Donana National Park. According to the historical, archeological and radiometric record, these high energy deposits were probably generated by a tsunami ca 216-218 BC. Accordingly, an interval of about 2000 years between these two events was deduced. The absence of a sedimentary record of tsunamis during this time span can be attributed to the lower magnitude of the seismic events or to paleogeographical changes.

Another example of sedimentary recording is the deep-seated land slide of Praia do Telheiro, Figure 12, SW coast of Portugal, (see Marques, 2001). About 2 km NNE of S.Vincent Cape, SW coast of Algarve, the 60 m high sea cliffs, cut in a very strong lower Jurassic dolomites overlaying Hettangian marls, present fresh evidences of the occurrence of a 0.85 km long land-slide. The information obtained suggests that the land-slide was probably triggered by a strong seismic action. The Praia do Telheiro land-slide is a deep-seated rotational slope mass movement of unusually large size of the Portuguese coast context. The preliminary limit equilibrium analysis of one section

of the movement strongly suggests that the landslide could not start under static loading conditions. Its triggering seems only possible with a strong seismic action, evaluated with a pseudo-static limit equilibrium analysis. It is clear that a large amount of work is needed for detailed study of the land-slide, namely the accurate control of the geometry of the displaced rock mass, of the geotechnical properties of the Hettangian marls that caused the failure, and of the date of the event. This further work will be difficult, because of the extremely adverse terrain conditions. However, the present knowledge of this land-slide strongly suggests that it is a very promising site for paleoseismological studies in Portugal, and deserving thus further reconsideration.

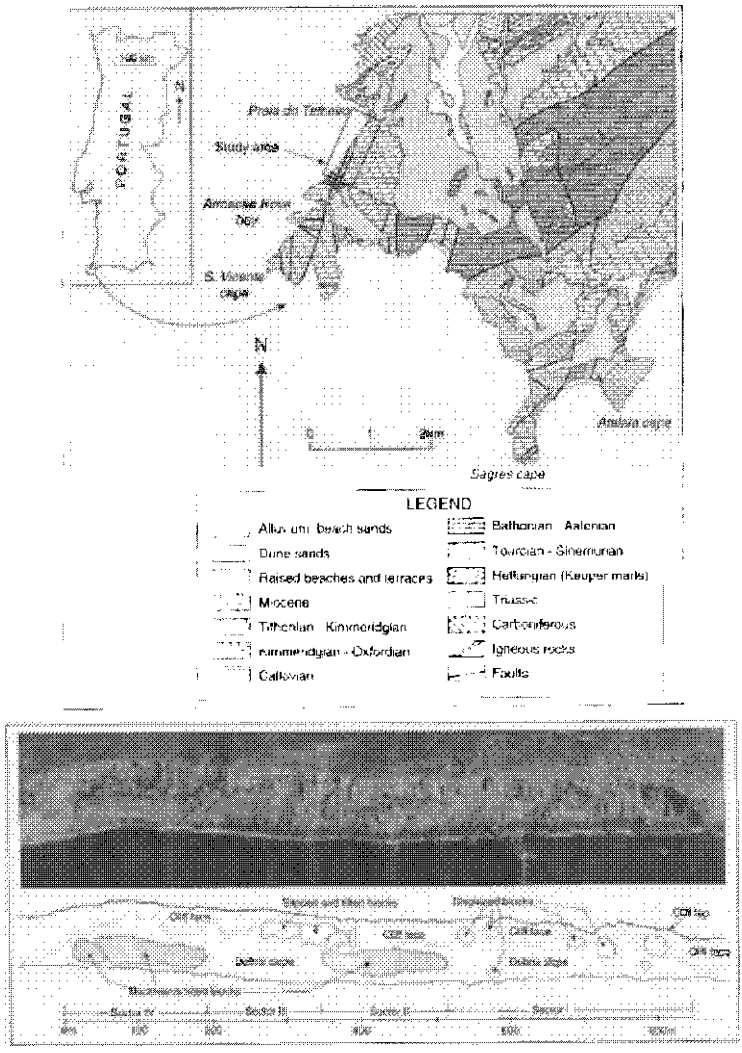

Fig. 12. Deep-seated landslide of Praia do Telheiro. Oblique aerial view of the landslide area and corresponding morphological sketch (Marquês, 2001).

5 Conclusions

The historical research was the fundamental hint provided to launch the projects referred above in order to obtain clarification about the source behavior of 1755 seismic source and induced effects as well as the correlation with sedimentary continental deposits along the southwestern coastal areas of Iberia. Tsunami modeling and hazard assessment were improved thanks to this last interpretation.

Thanks to the results obtained adequate proposal to setup an early warning system is under preparation taking into account the run-up impact along the southern Portuguese coasts.

It is interesting to note that the international cooperation developed since 1992 providing technical resources and participation of experienced scientists was the key factor to produce better understanding of the dynamics of the area under study. We acknowledge the facilities provided by all, the scientific staff and institutions (University of Lisbon, Portugal – CGUL, IGIDL and ICTE, CNR, Italy and CSIC, Spain) as well as the people involved in the operational work.

References

Baptista, M. A., Miranda, P. M. A., Miranda, J. M. and L. Mendes Victor. Constrains on the source of the 1755 Lisbon tsunami inferred from numerical modelling of historical data on the source of the 1755 Libon tsunami. J. Geodynamics, Vol. 25, No.2, 1998, pp. 159-174.

Baptista, M.A., Heitor, S., Miranda, J.M., Miranda, P. and L. Mendes Victor. The 1755 Lisbon tsunami; Evaluation of the tsunami parameters. J. Geodynamics, Vol. 25, 1998, pp. 143-157.

Gràcia, E., Dañobeitia, J., Vergés, J. and Parsifal Team. Mapping active faults offshore Portugal (36°N-38°N): Implications for seismic hazard assessment along the southwest Iberian margin. Geology, Vol. 31, January 2003, pp. 83-86.

Hayward, N., Watts, B., Westbrook, G. K. and Collier, J. S.. A seismic reflection and GLORIA study of compressional deformation in the Gorringe Bank region, eastern North Atlantic. Geophys. J. Int., 138, 1999, pp.831-850.

Luque, L., Lario, J., Zazo, C., Goy, J.L., Dabrio, C.J., Silva, P.G.. Tsunami deposits as paleoseismic indicators: examples from Spanish coast. Acta Geologica Hispanica, Vol. 36, 2001, pp. 197-211.

Marques, F., The deep-seated landslide of "Praia do telheiro" (SW coast of Portugal). Comun Inst. Geol. e Mineiro, 88, 2001, pp. 185-202.

Martins, I., Mendes Victor, L.A. Contribuição para o estudo da sismicidade de Portugal continental. Universidade de Lisboa, Instituto Geofisico do Infante D. Luís, publicatuion nº18, 1990, pp.1-70.

Pereira de Sousa F. L. O terramoto do 1º de Novembro de 1755 em Portugal, Um estudo demográfico. Serviços Geológicos de Portugal, Vol. I e II, 1919.

Terrinha, P., Pinheiro, L. M., Henriet, J-P, Matias, L., Ivanov, M. K., Monteiro, J. H., Akhmetzhanov, A., Volkonskaya, A., Cunha, T., Shaskin, P., Rovere, M. and TTR10 shipboard scientific party. Tsunamigenic-seismogenic structure, neotectonics, sedimentary processes and the slope instability on the Southwest Portuguese margin. Marine Geology, Vol. 195, 2002, pp. 55-73.

Zitellini, N., Mendes, L.A., Cordoba, D., Dañobeitia, J., Nicolich, R., Pellis, G., Ribeiro, A., Sartori, R., Torelli, L., Bartolome, R., Bortoluzzi, G., Calafato, A., Carrição, F., Casoni, L., Corela, C., Correggiari, A., Della Vedova, B., Gràcia, E., Jornet, P., Landuzzi, M., Ligi, M., Magagnoli, A., Marrozi, G., Matias, L., Penitenti, D., Rodriguez, P., Rovere, M., Terrinha, P., Viglioti, L. and Zahinos Ruiz, A.. Source of 1755 Lisbon earthquake and tsunami investigated. EOS Transactions, 82, June 26, 2001, pp. 285-291.

QUICK TSUNAMI FORECASTING BASED ON DATABASE

H.-J. LEE[1], Y.-S. CHO[2] AND S.-B. WOO[3]

[1] *National Institute for Disaster Prevention,*
253-42, Gongdeok-2dong, Mapo-gu, Seoul 121-719, KOREA
[2] *Department of Civil Engineering, Hanyang University,*
17 Haengdang-dong, Seongdong-gu, Seoul 133-791, KOREA
[3] *Department of Ocean Science, Inha University,*
253 Younghyun-dong, Nam-gu, Incheon 402-751, KOREA

This research presents a reliable method to predict tsunami very quickly on a personal computer basis. To solve the linear long wave equations describing tsunami propagation, a superposition of its sub-solution (solution in a sub-region) could be used. Using this principle, we compute unit tsunamis having 5.5 km × 5.5 km area and 1 m height located along the active fault zones in the East Sea (Japan Sea) to obtain sub-solution in advance. Through the computation of unit tsunamis, time series of water levels at certain locations along the Korean eastern coast are collected. To compute a realistic tsunami, the results are multiplied by real initial sea surface displacement at every location of unit tsunami for a real tsunami event. Then, summations of each value on time axis give real tsunami water levels. Consequently, only simple computation of the initial tsunami waves and manipulation of pre-computed data set or data base, makes it possible to deduce tsunami heights and arrival time along the coast in a few minutes on PC. Using this method, the 1983 tsunami event is simulated and the result shows a good agreement with ordinary tsunami computation results.

1 Introduction

The Korean eastern coast has been attacked
severe damage during the last century. Among them, the 1983 Akita and the 1993 Hokkaido tsunami events were recorded as the most devastating events in Korea. The central part of this coast is especially prone to tsunami damage due to tsunami amplification in this zone (Cho et al., 1999). Recently, a number of coastal facilities have been built and are operated along this region. Especially, nuclear power plants are already operated and several more units are to be constructed. It is critical issue for people who live along this coast that the safety is guaranteed from an unexpected danger. For this reason, tsunami research for proper hazard mitigation has become an important coastal issue in Korea recently.

K. Satake (ed.), Tsunamis: Case Studies and Recent Developments, 231-240.

Theoretical/numerical research and field survey of past tsunamis have been actively performed in Korea. The research includes tsunami generation, propagation and run-up in the East Sea. The results show complicated characteristics of tsunamis in the East Sea. Especially, in the case of Korean eastern coast, it is convinced that energy divergence from the Yamato Rise, located at the middle part of the East Sea, causes unusual tsunami heights in specific regions. For this reason, fine spatial grids should be used to accurately model tsunamis (Lee and Kim, 2000). To operate a numerical model covering the entire region of the Korean eastern coast with finer grid meshes, a high performance computer and huge computational time is required to deduce quantitative results of tsunami. However, most of tsunamis take at most two hours to arrive at Korean coast. Development of an effective and quick forecasting system is important for tsunami disasters countermeasures. This research presents a way to compute tsunami within a few minutes with high accuracy on a PC to protect life and property along the concerned coast in Korea from a possible tsunami attack.

2 Data base driven quick tsunami forecasting

In case of homogeneous linear equation, solutions can be obtained by summation and its multiplication of constants. This is known as a superposition principle in linear system and will enable us to generate more complicated solutions from known solutions. Using this principle we can solve linear long wave equation for tsunami propagation. Similar methodology is adopted for further tsunami studies to forecast tsunami heights quantitatively.

For the rapid estimation of actual tsunami, number of hypothetical eartbquake tsunamis were pre-computed and multiplied by scale factor which is determined by observation at the tide gauges by Whitmore and Sokolovski (1996). Titov et al. (1999) also tried to construct database consisting of "unit source" tsunami and computed results for the real time report of tsunami wave heights.

The methodology which suggested in this study can be explained in a following way. The equation for the superposition is

$$F(x,y,t)=\sum_{i=1}^{n} a_i f_i(x,y,t) \qquad (1)$$

in which F is a solution of linear long wave equation, a_i is any constant, f_i is the sub-solution of linear long wave equation when we divide initial sea surface profile of tsunami into number of elements, and n is the number of partitions.

Generally, in tsunami computation, we simplify the fault plane as a single or number of rectangles as its initial shape. For example, we compute initial sea surface profile using earthquake parameters suggested by Aida (1984; model 10) for the case of 1983

Akita event. This is composed of two planes (let n equal to 2) and we can compute these separately. If we superpose independently-computed two water levels at a certain location in a computational domain on time axis, it should be equal to the water level which is computed using two fault planes in the linear system. Then the function f_1 and f_2 are equivalent to a solution of independent tsunami events I_1 and I_2 in Figure 1, and F is to the real solution of tsunami.

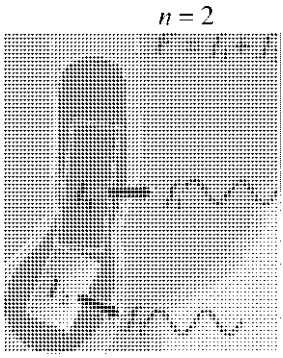

Fig. 1. Superposition principle in tsunami numerical model.

In advance, with the same manner, we can compute f using unit tsunamis (I) having a certain spatial area and unit height. If we suppose that real fault plane is composed of number of unit events, the superposition of pre-computed unit tsunamis will be the same as the real one. After supposing the unit tsunamis along the entire active fault zones in the East Sea, we can compute real tsunamis with manipulation of pre-computed unit events as follows.

During the computation of every unit tsunami, time series of sea water level at certain locations along the Korean eastern coast are collected independently. Finally, these are multiplied by the constant of the real initial sea surface displacement at every location of unit tsunamis in real tsunami event. Then, summations of each value on the time axis will give predicted tsunamis.

In practical case, we set every unit tsunami as covering entire region of active fault zones in the East Sea. Then the time series of sea water levels at every point where we would like to get its height are recorded as data sets. When we deduce the real tsunami elevations, computation of the initial sea surface deformation and manipulation of the

pre-computed data set makes it possible to deduce tsunami heights and arrival time along the coast within a few minutes on a PC. All of the computed results are recorded as a database which has variables of locations of events, location of prediction points and time. This could be used for quick estimation of the East Sea tsunamis. The flow of deducing tsunamis from pre-computed data sets is shown in Figure 2.

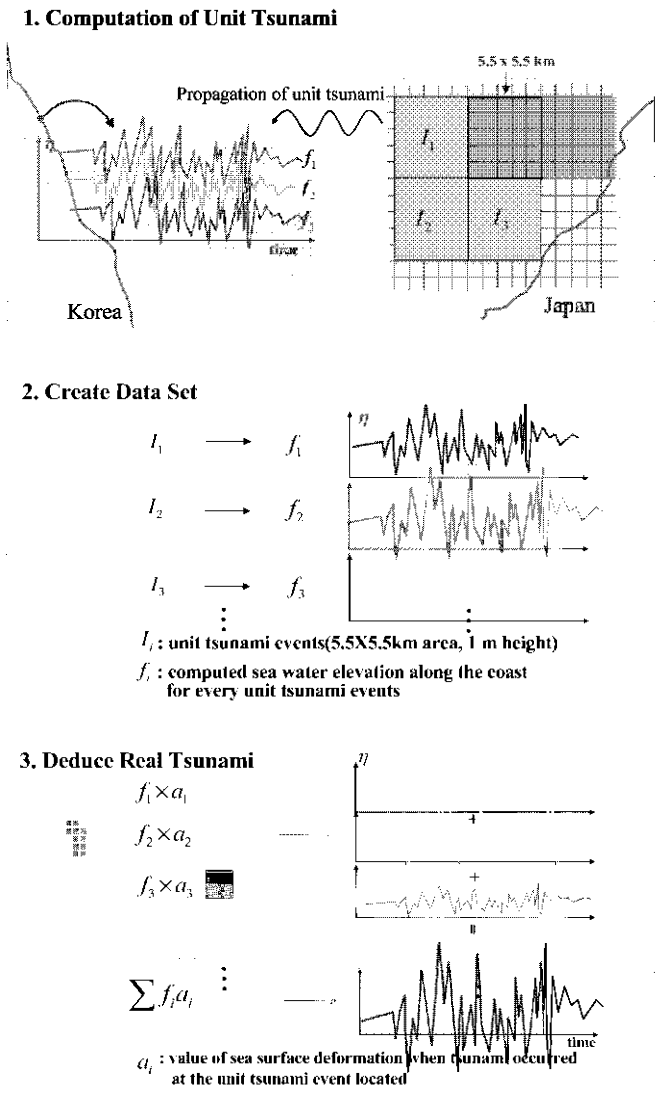

Fig. 2. Flow of deducing tsunamis from pre-computed data sets.

3. Numerical Model

Numerical model is set up using a linear long wave equation for the estimation of tsunami propagation process and its terminal effects. The following equation is the linearized long wave equation without bottom friction in two-dimensional propagation which is widely used as governing equations for computing tsunami propagation (Imamura, 1995).

$$\begin{aligned} &\frac{\partial \eta}{\partial t}+\frac{\partial M}{\partial x}+\frac{\partial N}{\partial y}=0 \\ &\frac{\partial M}{\partial t}+gh\frac{\partial \eta}{\partial x}=0 \\ &\frac{\partial N}{\partial t}+gh\frac{\partial \eta}{\partial y}=0 \end{aligned} \qquad (2)$$

where x and y are the horizontal coordinates, η is the vertical displacement of water surface above the still water surface, g is gravitational acceleration, h is the still water depth. M and N are the discharge fluxes in the x, y directions defined by

$$\begin{aligned} M &= \int_{-h}^{0} u dz \\ N &= \int_{-h}^{0} v dz \end{aligned} \qquad (3)$$

where z is the vertical coordinate, u and v are the depth-averaged velocities in x and y directions. Along the offshore and seashore boundaries, radiation condition and vertical wall condition are respectively used in the numerical model. The minimum water depth in computing domain is set as 10 m. Using the finite difference method, equation (2) turns to be discrete form of a partial differential equation to obtain a numerical solution for tsunami height and discharge.

Generally, we need relatively smaller grid meshes to compute tsunami along the coast as water depth become shallow, because variation of local topography is important in tsunami behavior. However, it is impossible to use a small grid mesh in the total region of large area such as the East Sea. Hence, a dynamic linking method is used to accommodate the various grid intervals.

Figure 3 shows a computing domain covering the East Sea. The total region is covered by a 1.1 km base grid. In Figure 3, dynamic linking is accomplished in the boxed area. According to this method, larger grids in the deep sea are overlapped and dynamically linked with grids having 1/3 of its width in the shallower region. During the computation, water level and discharge are exchanged with each other satisfying a dynamic equilibrium along the boundary of these two regions. This process is repeated until required grid resolution is obtained.

We can reproduce the variation in local topography and shoreline on a discrete grid mesh using this method. Through three 1:3 grid refinements and dynamic linking of 1.1 km to 370 m, 370 m to 123.3 m and 123.3 m to 41.1 m grids, propagation of tsunami is simulated in the domains (Figure 3). Using the final grid mesh of 41.1 m we could represent the shallow water area in the middle part of Korean eastern coast in detail.

For the model test, the 1983 tsunami was computed and the maximum water heights are compared with observed values. Observations are surveyed in 1999 after 16 years of tsunami events on the hasis of interview to residents in each location (Lee et al., 1999).

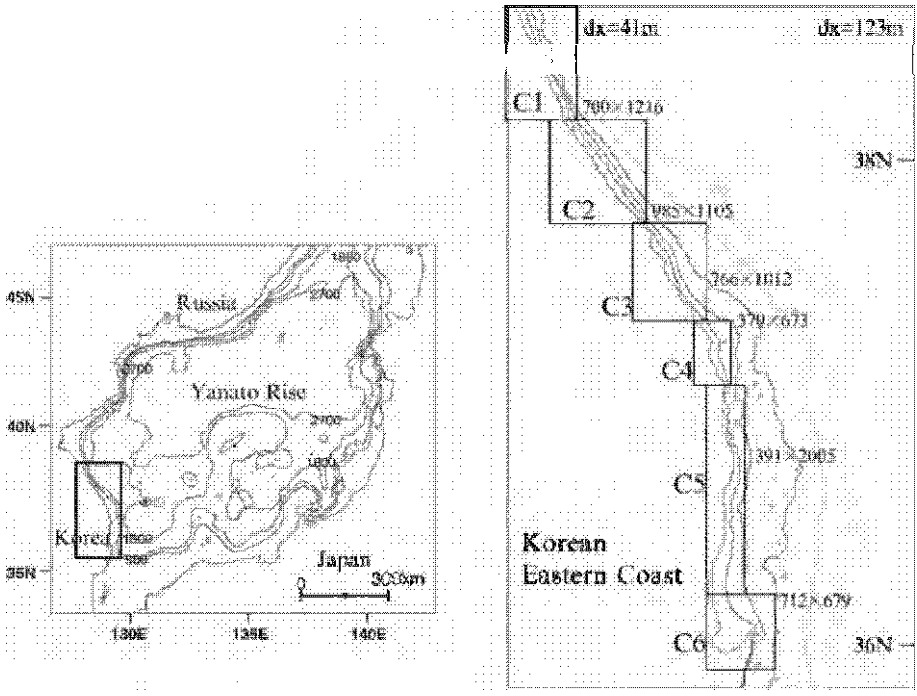

Fig. 3. Computing domain (East Sea, Korean eastern coast)

Figure 4 shows comparisons of computed maximum tsunami heights from 123.3 m and 41.1 m grid meshes with the observed values. Except for a few locations, results show a good agreement in the 123.3 m grid mesh. However, there are differences between the results near the Imwon area where shallow water depth is locally developed. From this fact, it is recognized that these results cannot be used for actual tsunami forecasting because they include too much error due to tsunami amplification near the coast by variation of local topography. To compute tsunami propagation in this region considering local variation of topography, much smaller grid mesh is

needed in the numerical model. Then we tried to compute it on 41.1 m grid mesh again through dynamic linking procedure and compare the results with the observed value. The right panel of Figure 4 shows the comparison result near the Imwon area. It shows a very good agreement between the computed and observed results. Compared with the results computed in 123.3 m grid mesh, it is considered to be more reliable. For this reason, we decided the final grid size in tsunami forecasting model as 41.1 m. Total area of Korean eastern coast is divided into 6 sub-regions which have 41.1 m grid resolution as shown in Figure 3 and Table 1.

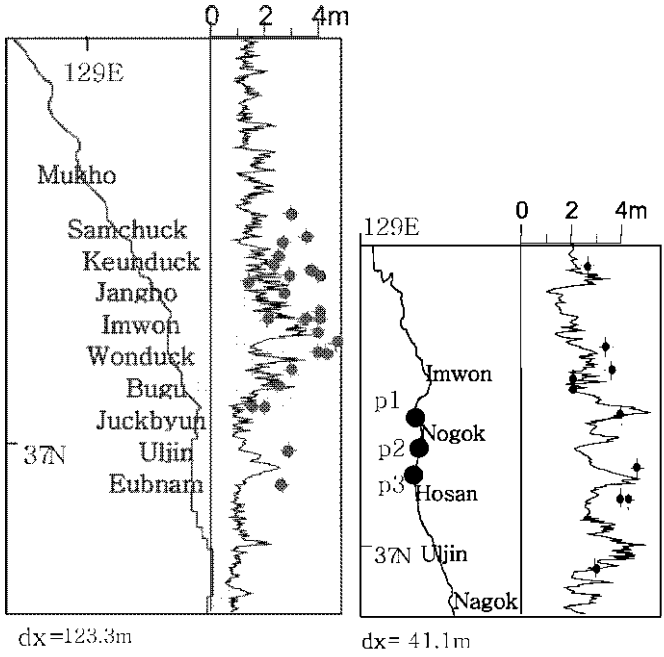

Fig. 4. Comparison of computed and observed results of 1983 tsunami event (dot: observed inundation heights, line: computed maximum amplitude)

Table 1. Computing condition

	O	A	B	C1	C2	C3	C4	C5	C6
Dx	1110.	370.0	123.3	41.1	41.1	41.1	41.1	41.1	41.1
Dt	3.6	1.2	0.6	0.6	0.6	0.6	0.6	0.6	0.6
Nx	1170	916	580	700	985	766	379	391	712
Ny	1170	970	955	1216	1105	1012	673	2005	679

Dx : grid size in x direction (same size in x, y direction) in meter
Dt : computing time step in second
Nx : total number of grid meshes in x direction
Ny : total number of grid meshes in y direction

4. Quick tsunami forecasting of the 1983 tsunami event

A total area of Korean eastern coast is divided into 40.1 m grid mesh through 3 times dynamic linking in our numerical model. It requires a large computer memory and computing time to manipulate the numerical model. For the estimation of tsunami heights, we can manipulate this numerical model directly after tsunami occurred or when we need to estimate it. Even if high performance computing power is utilized, however, computation work load is too heavy to accomplish this whole computation.

This practical yet important problem can be overcome by using database. Before building the database, we verified the reliability in superposition of linear solution in tsunami simulation. We selected the 1983 tsunami event as an example. We needed hundreds of computations to build database of unit tsunamis for this event. Then we used supercomputer of KMA (Korea Meteorological Agency).

First of all, the initial sea surface deformation of the 1983 tsunami event with the initial condition which is based on Aida's model 10, is divided by 5.5 km×5.5 km unit area as discrete form. This is composed of 5 by 5 grid meshes in base computing domain in Figure 3. Using this initial condition, ordinary tsunami computation is performed and time series of sea surface elevation along the Korean eastern coast are recorded.

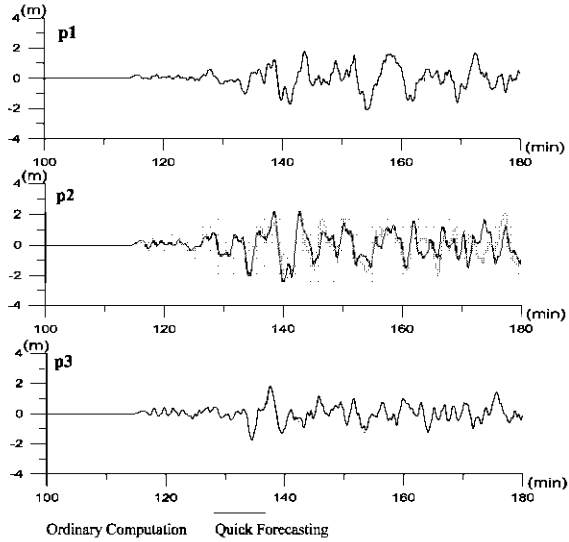

Fig. 5. Comparison of ordinary computation and DB driven quick estimation of tsunami

Secondly, the same event was computed again using 307 unit tsunamis which covers total disturbed area of sea surface by the 1983 earthquake. The unit tsunami has 5.5 km×5.5 km area and 1 m height. The unit tsunamis are computed individually and sea surface elevations are gathered along the Korean eastern coastline. Through this

process, time series of water level along the coast are recorded at 2500 locations on the Korean eastern coast. As a result, 2500 datasets of water elevation are recorded for 307 cases of unit tsunamis as data base which will be extracted during quick tsunami estimation. These are multiplied by their own height independently which are computed as the initial sea surface elevation by the 1983 tsunami event based on Aida's model 10. Finally summation of 307 datasets on the time axis gives real tsunami profile at a certain location where we would like to estimate the tsunami.

To verify whether the database driven quick tsunami estimations agree with those from ordinary tsunami computation, the two results are compared with each other. Figure 5 shows the comparison at three locations of p1, p2 and p3 in Figure 4 along the coast.

The results show a good agreement each other except some differences after 140 minutes from the earthquake. Because we consider only linear part in governing equation, its superposition should coincide with the solution. The difference in the compared results might be from numerical error during summation.

According to this procedure, if the database is established, we can apply any kind of tsunami initial conditions and deduce tsunami height and arrival time from the time series of tsunami height at any location in a few minute. Figure 6 shows a chart of database driven quick tsunami forecasting procedure. This is an early stage of the study and we are now setting up the database for unit tsunami events covering the total active fault zone along the Japanese western coast in the East Sea.

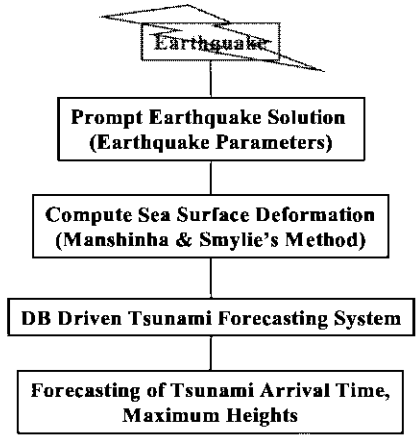

Fig. 6. Flow of Database Driven Quick Tsunami Forecasting

5. Concluding remarks

The tsunami computation model using a fine grid mesh of 40.1 m for forecasting along the Korean eastern coast is established in this study. Based on the superposition of

linear solution of tsunami wave, a reliable quick tsunami forecasting method based on database is suggested, and its possible application is examined.

Tsunamis generated along the active fault zone in the East Sea arrive at Korean coast within two hours generally, so that it is required to forecast a tsunami in detail within two hours. This suggested forecasting method makes it possible for the forecasting office to estimate tsunami along Korean coast in two hours.

It should be emphasized that the accuracy of this database method relies much on the fault parameters. Without accurate initial tsunami condition, it is almost impossible to obtain reliable results on the tsunami inundation. Therefore, for the present methods to be practically applicable, a research on the quick and accurate fault parameter estimation is the most important.

Additionally, thousands of unit tsunamis have to be computed to forecast tsunamis generated in the entire active fault zone in the East Sea. At this stage, only 307 unit tsunamis for the 1983 tsunami events have been computed. To set up the entire database, rest of unit tsunamis in the East Sea should be computed. After it is completed, number of hypothetical tsunami events also can be estimated promptly.

Acknowledgements

The second author appreciates the financial support of the Meteorological Research Institute of the Korea Meteorological Administration.

References

Aida, I., A source models of the 1983 Nihonkai-earthquake tsunami, *Proc. Symposium on Nihonkai-Chubu Earthquake Tsunami, JSCE*, 9-21, 1984.

Cho, Y.S., Lee, H.J. and Jin S.B, Tsunami inundation along the Eastern Coast of Korea, *Proc. Asian and Pacific Coastal Eng. (Dalian, China)*, 1005-1013, 2001.

Imamura F., Tsunami numerical simulation (Numerical code Tunami-N1, N2), *Technical Report of School of Civil Eng., DCRC, Tohoku Univ.*, 1995.

Lee, H. J. and Kim. K. H., Numerical simulation of tsunami inundation at the Imwon Port, *Korea-China Conference on Port and Coastal Eng. (Seoul, Korea)*, 277-286, 2000

Lee H. J., Kim K. H. and Jin S. B., New field survey of 1983 East Sea tsunami, *Tsunami Warning Beyond 2000 Theory, Practice and Plans, IOC-ICG/ITSU*, 20, 1999.

Titov, V.V, H.O. Mofjeld, F.I. Gonzalez and J. C. Newman, Offshore forecasting of Hawaiian tsunamis generated in Alaskan-Aleutian Subduction Zone, *NOAA Technical Memorandum* ERL PMEL-114, 22 pp., 1999.

Whitmore, P.M. and T.J. Sokolowski, Predicting tsunami amplitudes along the north American coast from tsunamis generated in the Northwest Pacific Ocean during tsunami warnings, *Science of Tsunami Hazards*, 14, 147-166, 1996.

ADJOINT INVERSION OF THE SOURCE PARAMETERS OF NEAR-SHORE TSUNAMIGENIC EARTHQUAKES

C. PIRES AND P. M. A. MIRANDA

Department of Physics and Centro de Geofisica, University of Lisbon
Faculdade de Ciências, Edificio C8, Campo Grande, 1749-016 Lisboa, Portugal
capires@fc.ul.pt, pmmiranda@fc.ul.pt

The adjoint method may be designed to perform the direct optimization of tsunami fault parameters, from tide-gauge data, leading to a substantial enhancement of the signal-to-noise ratio, when compared with the classical technique based on Green's functions of the linear long-wave model. A 4-step inversion procedure, which can be fully automated, consists (i) in the source area delimitation, (ii) adjoint optimization of the initial sea state in the grid space, (iii) non-linear adjustment of the fault model and (iv) final adjoint optimization in the fault parameter space. Results with an idealized bathymetry show that the method works well in the presence of reasonable amounts of error and provides, as a by-product, a resolution matrix that contains information on the inversion error, identifying the combinations of source parameters that are best and worst resolved by the inversion. A detailed analysis of inversion sensitivity and of the fine structure of the inversion error is used to identify problems and limitations of the inversion procedure.

1 Introduction

Pires and Miranda (2001) proposed a method for tsunami inversion based on the adjoint technique, which can be used to infer earthquake source parameters from tide gauge data. Pires and Miranda (2003) explored the sensitivity of the method in some idealized setups, and further developed its implementation. In the present paper, a more detailed analysis is performed for one rather simple experimental setup, namely the inversion of tsunamis on a sloping bathymetry, that allows for the elucidation of some properties and limitations of the adjoint inversion procedure.

The inversion of tsunami data is an important aspect of the evaluation of tsunami and earthquake risk in coastal areas. The backward ray tracing approach initially proposed by Miyabe (1934) allows for gross delimitation of the tsunami source area from arrival times at different tide gauges. Because that approach doesn't take advantage of the information of wave amplitude and shape, it gives little information about the tsunami source. A more powerful inversion method, proposed by Satake

K. Satake (ed.), Tsunamis: Case Studies and Recent Developments, 241-258.

(1987, 1989) and developed by different authors (e.g. Johnson *et al.* 1996, Johnson, 1999, Tinti *et al.* 1996, Piatanesi *et al.* 2001), consisted in the use of Green's functions technique to invert for the coseismic slip, in a set of prescribed rectangular sub-faults. This latter method uses the full information on wave shapes, but has serious limitations: (i) it requires the use of linear propagation models, (ii) if the number of sub-faults is large, as needed to fit analytical source models, the number of degrees of freedom is too large, leading to poorly conditioned inversions.

The adjoint technique (Talagrand and Courtier, 1987) allows for a more general inversion procedure (reviews are given by Bennet, 1992, and Wunsch, 1996). Not only it is not limited to linear propagation models, but it can explicitly incorporate source models that may be non-linear functions of sets of parameters, the inversion consisting in the optimization of the values of those parameters (Pires and Miranda, 2001). In this way, the inversion may deal, directly, with earthquake source parameters and may incorporate strong geophysical constraints, independent of the hydrodynamic data.

Okada (1992) proposed an analytical formula describing the sea bed deformation in a homogeneous media, as a function of 9 independent fault parameters: the fault location of the source middle point (x_0, y_0), source length and width (L, W), depth (d), azimuthal angle (α), dip angle (δ), slip angle (γ), and slip dislocation (U_{sl}) (Table 1). When a tsunami source is well approximated by that solution, or by the superposition of a small number of Okada functions, the proposed inversion method deals with a small number of independent parameters and can improve the signal to noise ratio of the inversion, when compared with Green's functions inversions. Otherwise, the adjoint method will be less constrained and will lead to error levels comparable with the other techniques but, will still have, at least, the advantage of being able to deal with general propagation models.

2 Inversion method

As described in Pires and Miranda (2001, 2003) the adjoint inversion procedure is performed in 4 automated steps: (i) source area delimitation by adjoint backward ray-tracing, (ii) adjoint optimization of the initial sea state in the grid space, from a vanishing first-guess, (iii) non-linear adjustment of the fault model, and (iv) final adjoint optimization in the fault parameter space. Step one is equivalent to a backward ray-tracing with some allowance for observation errors, as considered by Gjevic *et al.* (1997). The latter authors incorporated observation errors as arrival time errors, while in the adjoint backward ray tracing they are considered as more general amplitude errors. Steps (iii) and (iv) will only be performed if the source is close enough to one (or the superposition of a small number) of Okada solutions.

The inversion problem consists in the minimization of a cost function given by the square misfit between observed surface displacements ($\varsigma_i^{obs}(t_j)$) and simulated ones ($\varsigma_i^{sim}(t_j)$) at tide gauge station, summed over the totality of observations $N_{ob} = N_{tg} \times N_t$, where N_{tg} is the number of tide gauges and N_t is the number of observations at each gauge:

$$J_{tg} = \sum_{j=1}^{N_t} \sum_{i=1}^{N_{tg}} \left(\varsigma_i^{obs}(t_j) - \varsigma_i^{sim}(t_j)\right)^2 \tag{1}$$

The inversion procedure requires a forward propagation model, which is in this study the shallow water model, and the corresponding linear adjoint model. In order to reach a minimum of the cost function, one uses an iterative quasi-Newton gradient descent method (Gilbert and LeMaréchal, 1989). The method may be applied either in the grid space, where the initial sea height field is given by a combination of simple box functions or as a non-linear function of fault parameters, as given by Okada (1992). The required gradients are then computed by the adjoint model. Details of the theory and implementation may be found in Pires and Miranda (2001, 2003). The performance of the inversion method can be measured by the relative inversion error, given by:

$$\varepsilon = \left[\frac{\sum_i \left(\varsigma_i^{true}(t=0) - \varsigma_i^{inv}(t=0)\right)^2}{\sum_i (\varsigma_i^{true}(t=0))^2} \right]^{1/2} \tag{2}$$

where the sum spans over all the spatial domain, and the superscripts identify the true source field (*true*) and the inverted initial surface displacement field (*inv*).

3 Experimental setup

As shown by Pires and Miranda (2001, 2003), Tinti *et al.* (1996), and Piatanesi *et al.* (2001), the behavior of tsunami inversion is highly sensitive to source geometry, bathymetry and tide gauge spatial distribution. Uncertainties increase when the signal arriving at tide gauges is too short or appears convoluted due to wave interference near regions of significant slope or coastlines. In the present study we will concentrate on a single bathymetric setup (Figure 1), consisting of a 100 km flat bottom followed by 50 km of smooth slope, up to a straight coastline. The entire domain consists of a 150 km × 150 km square, with a bathymetry that has a constant depth of 200 m in its west side.

The bathymetry shown in Figure 1 will be used for a number of inversion tests, using synthetic tsunami data, produced by Okada formulas corresponding to a pure dip-slip fault. The parameters of that idealized fault are shown in Table 1, which also lists the scales used for each parameter in the inversion process. These scales are needed to guarantee that the method responds to reasonable changes in each of the

different parameters, improving the convergence and good behavior of the minimization method. The initial sea surface displacement corresponding to that model is shown in Figure 2.

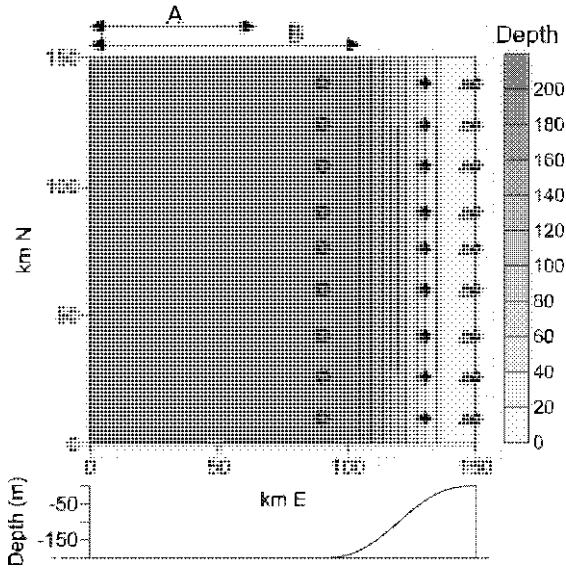

Fig. 1. Bathymetry in all experiments. Top: total domain of 150 km × 150 km with 2 km horizontal resolution. Bottom: cross-section of the bathymetry, showing the smooth continental slope. A and B indicate, respectively, the x extension of the short and long area delimitation domains for tsunami inversion. The symbols indicate the location of the 4 sets of 9 tide gauges each.

The behavior of the inversion method will be tested in 7 experiments (Table 2). In experiment Exp.1 the inversion is limited to Step 2, leading to a grid of sea surface elevations not constrained by the Okada formula, while in all other experiments it is continued up to the computation of optimized fault parameters (Step 4 in the inversion). Exp.1 is also the only experiment using a less constrained spatial domain (B in Figure 1). Exp.2 and Exp.2a (depth at tide gauge locations =0.53 m), Exp.4 (1.7 m), Exp.5 (52.3 m), and Exp.6 (200 m) use different tide gauge locations (symbols in Figure 1), away from the coastline. Exp.3 is exactly equal to Exp.4, except by the fact that it starts from a different first guess for the fault parameters. In all experiments assimilation is done every minute. For experiment 2a assimilation is extended to 200 minutes, in all other experiments it is limited to 100 minutes. All other conditions are common to all experiments, and follow options explained in Pires and Miranda (2003): noise/signal ratio corresponds to 10 % (in terms of standard deviations), there is no bathymetric error, and the errors are assumed to be Gaussian. The time step of the propagation model is 10 s, and the grid spacing is 2 km in both directions.

Table 1. Fault parameters of the seismic source

Parameter	Symbol	Units	Scale	Value
dip angle	δ	°	180°/π	30
depth of the middle point of the fault	d	km	1 km	5
slip dislocation	U_{sl}	m	1 m	5
slip angle counted from horizontal	γ	°	180°/π	90
x-component of the middle point	x_0	km	150 km	30
y-component of the middle point	y_0	km	150 km	75
azimuthal angle (from North)	α	°	180°/π	0
length of fault	L	km	15 km	15
width of fault	W	km	15 km	15

Table 2. List of experiments

Experiment	*Observations at*	*Inversion domain*	*Spatial delimitation*	*First Guess*	*Assimilation period (min.)*
Exp.1	x=148 km	Grid	B	n.a.	100
Exp.2	x=148 km	Grid+Okada	A	FG1	100
Exp.2a	x=148 km	Grid+Okada	A	FG1	200
Exp.3	x=146 km	Grid+Okada	A	FG2	100
Exp.4	x=146 km	Grid+Okada	A	FG1	100
Exp.5	x=130 km	Grid+Okada	A	FG1	100
Exp.6	x=90 km	Grid+Okada	A	FG1	100

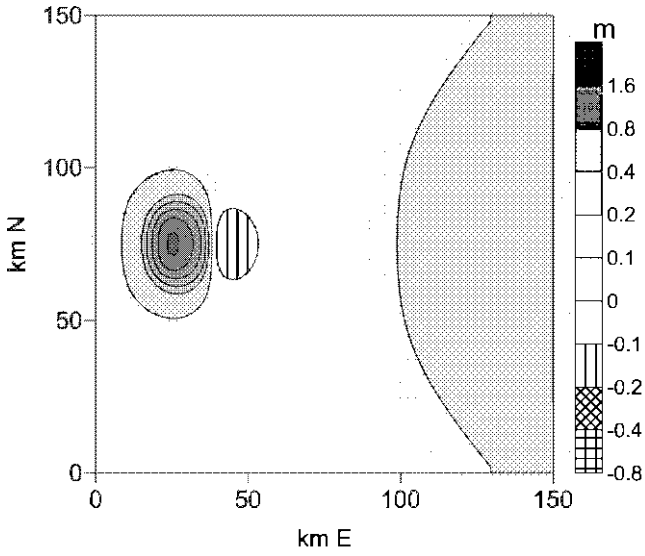

Fig. 2. Dip-slip fault, parameters given in Table 1.

4 Slope effects

The seismic source described in Table 1 and Figure 2 was taken as the initial state of the forward propagation model, which solves the shallow water equations to predict time series of water displacement at the different tide gauge locations. Figure 3a shows the tide gauge data for the central gauge (at y =75 km) in the different tide gauge sets shown in Figure 1. As expected, the arrival times vary significantly between the different sets, with the first arrival before 20 min at the most off shore set, and close to 80 min at the gauge nearest to the coast. Because assimilation is, in all cases, limited to the first 100 min (except for Exp.2a), that means that there will be less information to use in the coastal stations. Another result is the fact that there is a remarkable change in the frequency spectrum of the tsunami waves between stations, with a lower frequency spectrum being observed at shallower locations. This is due to the dispersion of the waves as they approach the coast, and its effects have already been discussed in Miranda *et al.* (1996) and Rabinovich *et al.* (1998). The resulting wave filtering leads to a reduction of information being assimilated near the coast.

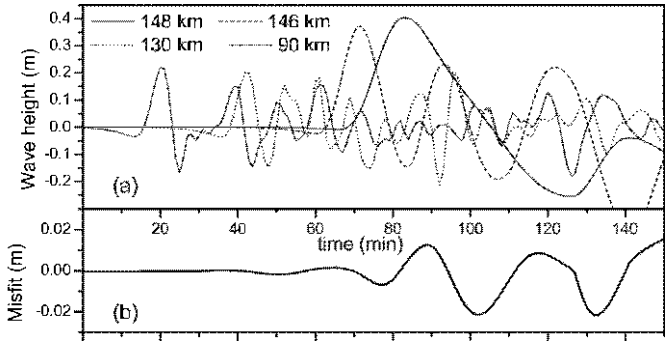

Fig. 3. (a) Tide gauge observations (synthetic tsunami) at the central tide gauge (y =75 km) for the different tide gauge sets. (b) Evolution of the prediction error at the tide gauge (x =148 km, y =75 km) in Exp.1.

A more complete view of the wave propagation field is given in Figure 4, showing the time evolution of water displacement at the central west-east line of the domain (y =75 km) for all values of the x coordinate. The slope of the contour lines may be interpreted as proportional to the inverse of the x-component of the wave velocity, indicating a reduction of that component as the wave train approaches the coast and is affected by dispersion. Wave rippling shown at later stages (after about 50 min) is an indication of wave interference between wave trains propagating shoreward and off shoreward, as a result of refraction and reflection at the coast.

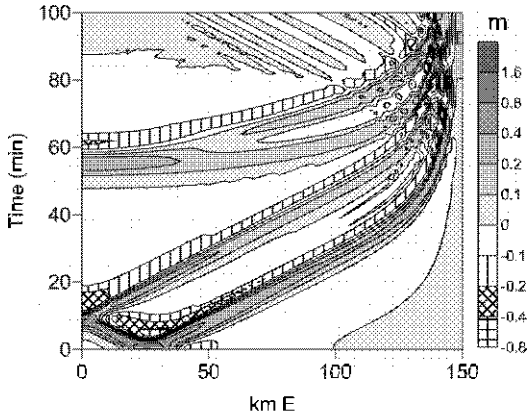

Fig. 4. Time evolution of the water displacement at the y =75 km.

5 Source delimitation and spatially delimited inversion

As shown in Piatanesi *et al.* (2001), the unconstrained inversion of tsunami data is, in general, hopeless, as there are many initial conditions compatible with any finite tide gauge data set, down to a reasonable error level. A simple, and yet powerful method of reducing the number of permitted solutions is given by area elimination, which may be obtained by backward ray tracing. In the context of the adjoint method, the area elimination procedure may be performed by a single integration of the adjoint model, leading to maps as those shown in Figure 5a-d. In that figure, the crossed areas ($N > 8$) correspond to the distributions of source locations that are compatible with each set of tide gauge data. All sets of observations in the slope (Figures 5a-c) give similar area delimitation results. Exp.6 leads to a slightly different area elimination, as it allows for sources near the coast line. However, the coastal area will not be considered as a possible source location.

While most area delimitation results put the source in the area at $x < 65$ km, well away from the slope, it is instructive to look at the results of a less constrained inversion where the source is allowed in the wider domain $x < 105$ km (domain B, Figure 1a). The inverted solution at step 2 (no Okada function fitting) is shown in Figure 6, and the evolution of its error at the central tide gauge (y =75 km) is presented in Figure 3b. The relative error of this solution is bellow observation error (10 %) by one order of magnitude. However, the initial water displacement field is rather different from the true solution (Figure 2), with a much weaker uplift, stronger downward area and spurious features close to the North and South boundaries.

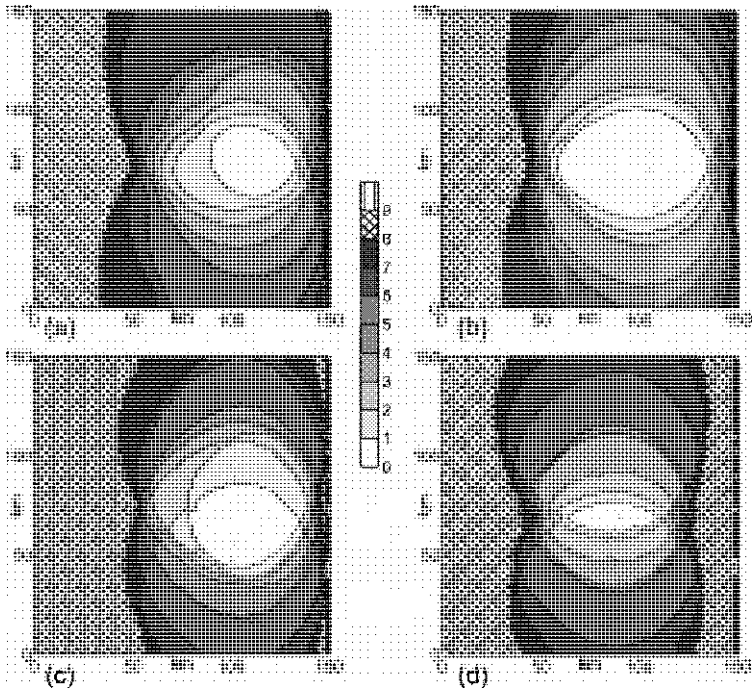

Fig. 5. Area delimitation. Number of arrivals compatible with the location of a source at the given location. Solutions for the 4 sets of tide gauges located at (a) x =148 km, (b) x =146 km, (c) x =130 km, and (d) x =90 km.

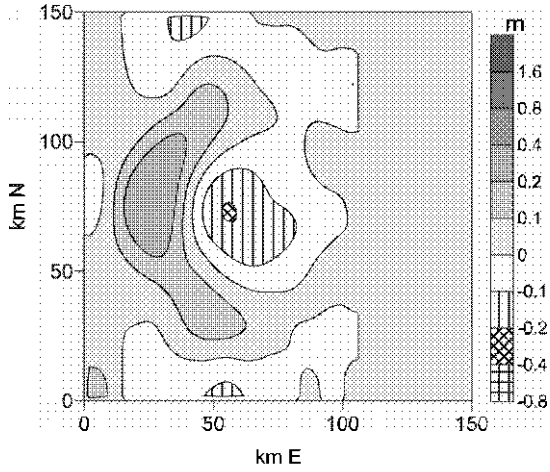

Fig. 6. Inversion with distributed box functions (Exp.1, delimitation B). The inversion error at (y =75 km, x =148 km) is shown in Figure 3b.

Four alternative inversions are shown in Figure 7, where the source area is limited to x < 65 km (domain A in Figure 1a), for the 4 different tide gauge sets. All these inversions are taken at step 2, prior to the Okada function fitting and, so, they can be compared with Figure 6. There is, in general, some improvement, although noisy features near the boundaries appear in all solutions. Those features propagate away from the gauges and will have little impact in the tide gauge observations, and that is the reason why they tend to exist at this stage. The relative error ε of each experiment at this stage is shown in Table 3. In all experiments, the relative drop in the cost function associated with steps 1 and 2 (delimitation + grid inversion) is of two orders of magnitude. The best fit, at this stage, is given by Exp.6 (ε =23 %), which is not much influenced by the coastal effects and has the best azimuthal coverage of the source. At this stage Exp.3 and Exp.4 are identical, and their relative error (73 %) is slightly worst, but better than Exp.2 (80 %). Exp.2a, as expected, has a lower inversion error than Exp.2, due to the increase in the assimilation interval. The table also shows the normalized tide gauge misfit $J_{tg}/(N_{ob}\sigma_{ob}^2)$, where σ_{ob} is the standard deviation of the tide gauge error. Values of the normalized misfit near 1 mean that the level of observation error has been reached in the inversion. The last column in Table 3 includes a parameter (λ_{lead}) that will be discussed later.

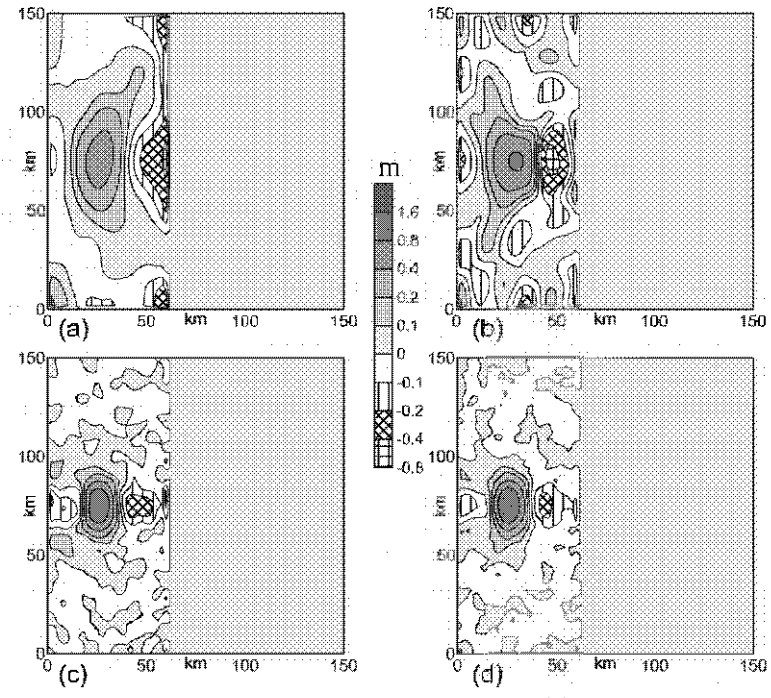

Fig. 7. Grid inversions for delimitation A (a) Exp.2, (b) Exp.3, 4, (c) Exp.5, and (d) Exp.6.

6 Inversion in the Okada space

After the computation of the inversions shown in Figure 7, we may estimate seismic source parameters given by Okada. For that purpose one needs, first, to find the best set of fault parameters that fit the gridded inverted data using one of the raw fist guesses listed in Table 4. Then we proceed using that best fit as the first guess for the final step of the inversion in the Okada parameter domain. An analysis of the results presented in Table 3 allows us to conclude that there is, in all experiments, a significant reduction in the relative error (ε) in the latest steps of the inversion, supporting the advantages of the proposed method. For example, in Exp.4 the relative error decreases from 73 % to 9 %, while in Exp.5 it does from 31 % to about 1 %.

Table 3. Variation of the fitting error in the different steps of the inversion

	Adjoint inversion in the grid domain		*Fit of Okada*	*Adjoint inversion in the Okada parameter domain*		
	ε(%)	$J_{fg}/(N_{ob}\sigma_{ob}^2)$	ε(%)	ε(%)	$J_{fg}/(N_{ob}\sigma_{ob}^2)$	λ_{tcod}
Exp.1	86.8	1.204	n.a.	n.a.	n.a.	n.a.
Exp.2	79.6	1.042	70.6	14.5	0.9679	735
Exp.2a	69.2	1.330	57.5	67.0	1.0116	1290
Exp.3	73.3	1.057	59.2	22.1	1.0041	4712
Exp.4	73.3	1.057	58.3	9.1	0.9754	4208
Exp.5	30.8	0.998	15.6	0.8	0.9620	13716
Exp.6	22.8	0.955	11.7	0.8	0.9525	11870

The final values of all fault parameters for experiments Exp.2-6 are shown in Table 4, together with the values of the fault parameters of the true source, and of the two first guesses used in step 3 (fitting of Okada parameters). The table also shows estimates of the errors in each inverted solution, computed from the Hessian matrix of the tide gauge cost function (see Pires and Miranda, 2001, 2003 for details). Solution in Exp.3 (with a bad first guess in step 3) is wrong, as the true solution is clearly outside the 99 % significance error limits, for reasons that will be later discussed. Solutions Exp.2 (very close to the coastline) and Exp.4 have some discrepancies, but are generally good. Exp.2a shows an improvement over Exp.2, obtained by an increase of the assimilation time, leading to a solution that is within the estimated error intervals. The best solutions were obtained in Exp.5 and Exp.6, where the estimated 99 % significance error limits are small and the fit is overall very good.

The fitting requires a first guess of the fault parameters, and one may find that, due to the nature of the Okada parameters, namely some redundancy between parameters, it is possible to converge to a wrong set of parameters that produces an initial state of the water displacement field that is similar to the true source. This effect is explored in Exp.3, which uses a first guess for the fault parameters that was found, by trial and error, to lead to a spurious solution that exists near a local minimum of the cost-function in parameter space. Figures 8a-b show the two alternative first guesses, while

Figures 8c-d show the corresponding inversion errors, both under the 10 % error limit required by the observation error. The final solutions for the initial water displacement (not shown) are visually almost identical to the true source (Figure 1).

Table 4. Fault parameters for the different inversions[1]

	δ(°)	d(km)	U_M(m)	γ(°)	x_0(km)	y_0(km)	α(°)	L(km)	W(km)
Source	30.	5.	5.	90	30	75	0	15	15
FG1	10.	20.	0.1	90	45	75	0	75	75
FG2	10.	20.	0.1	90	45	75	0	45	45
Exp.2	29.9	**7.35**	**7.7**	89.9	30.4	75.1	1.8	10.8	13.2
	±3.6	**±1.4**	**±2.5**	±6.2	±1.7	±2.8	±4.6	±3.0	±3.3
Exp.2a	29.3	4.32	4.45	91.2	30.2	75.3	1.8	16.1	16.1
	±2.9	±1.2	±1.5	±3.0	±1.2	±1.0	±4.1	±4.6	±2.8
Exp.3	32.1	**10.3**	80.9	89.7	29.1	75.0	-0.7	**6.7**	**1.8**
	±1.4	**±0.3**	±114	±7.2	±0.49	±1.4	±11.6	**±5.4**	**±1.9**
Exp.4	30.0	**6.2**	6.8	90.3	30.0	75.2	-0.5	12.1	15.0
	±1.9	**±1.0**	±4.9	±2.5	±0.7	±0.7	±1.8	±6.0	±4.1
Exp.5	30.0	5.0	5.0	89.5	30.0	75.0	-0.1	15.1	15.0
	±0.7	±0.1	±0.1	±0.9	±0.1	±0.1	±1.0	±0.4	±0.3
Exp.6	29.8	5.0	5.0	90.3	30.0	75.0	0.4	15.0	14.9
	±0.6	±0.1	±0.1	±0.7	±0.1	±0.1	±0.8	±0.2	±0.3

(1) Errors at the 99 % confidence level. Bold values: solutions that are outside the estimated error limits.

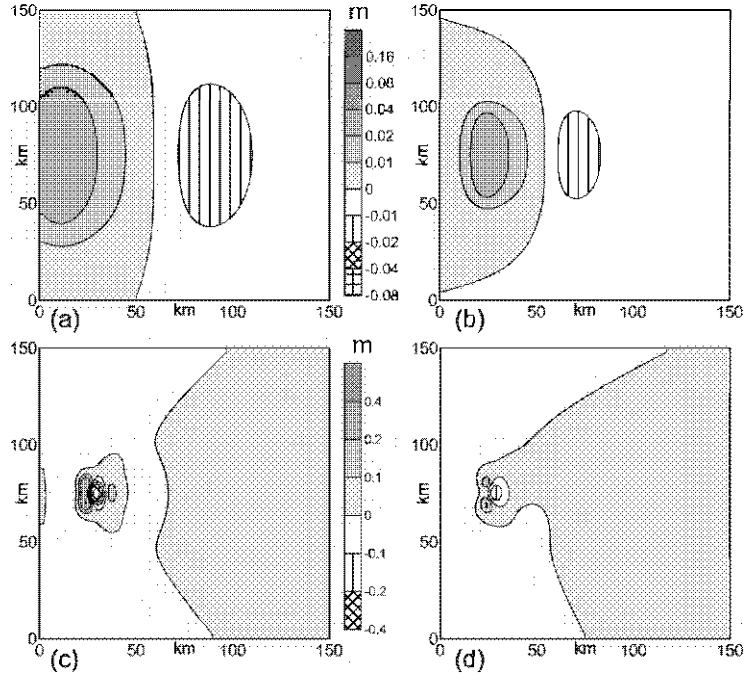

Fig. 8. (a) First guess FG1, (b) FG2, (c) Inversion error Exp.3, (d) Inversion error Exp.4.

Results of Exp.3 and Exp.4 will be further explored to understand the performance of the method in rather difficult conditions. Figure 9 shows the evolution of the relative error and of the normalized cost function in Exp.4, during steps 3 and 4 in the inversion process. The cost function decreases monotonically during the inversion, while the relative error may experience occasional oscillations. On average, both functions decrease by one order of magnitude. At the same time, the normalized error in each fault parameter ((inverted-true)/scale) also decreases (Figure 10), although not indefinitely, due to observation error and bad conditioning in some fault parameters.

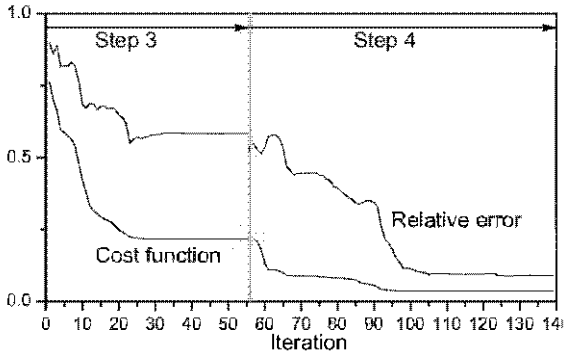

Fig. 9. Evolution of the normalized cost function and relative error in Exp.4. Step 3 corresponds to the fit of Okada parameters to the inverted source in the grid domain, Step 4 to the adjoint inversion.

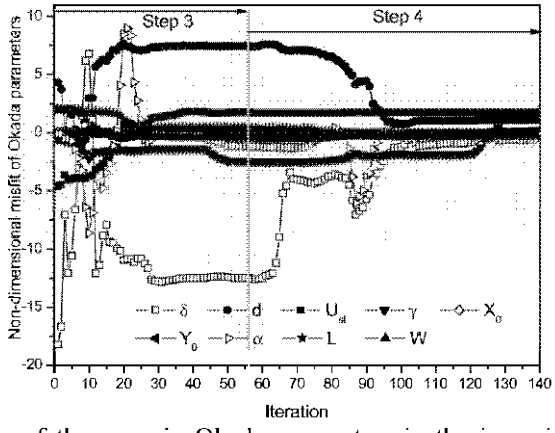

Fig. 10. Evolution of the error in Okada parameters in the inversion process, as in Figure 9.

It is interesting to look in more detail at the solutions obtained in Exp.3 and Exp.4. It is well known, in any inversion problem, that there may be multiple solutions and all methods are bound to converge to a spurious solution, given a bad first guess or insufficient data. However, the real structure of the error in the neighborhood of those solutions may be rather complicated. Figure 11a shows the normalized tide gauge

misfit $J_{tg}/(N_{ob}\sigma_{ob}^2)$ in the neighborhood of the true source and inverted solutions for Exp.4 and Exp.3. For that purpose a plane of the 9-dimensional parameter space was chosen, defined by the true solution (X) and the two alternative inversions (Exp.3, point A, and Exp.4, point B). It is clear that point B is close to the true solution, at a distance compatible with the observation error. Point A, though, is far away, in a local minimum, which is, in this particular case, connected with the true solution by an elongated and curved canyon. In the neighborhood of the true solution there is a lot of structure in the error surface (see zoom) with multiple minima (C1, C2, etc.), which are not directly connected. With all this structure of the cost function it is easy to stop the iteration process at a wrong site.

The splitting of the attraction basin near *XB* is not present in the relative error surface (Figure 11b), which was computed using data at all grid points (and not just the 9 tide gauges as for the computation of the cost function). The splitting is then due to insufficient information going into the inversion process.

The situation depicted in Figure 11a exemplifies two kinds of problems that may arise in the inversion process: (i) convergence to a true secondary local minimum (e.g. C1, C2 in zoom); (ii) reaching of a stopping criterion in a very elongated attraction basin (point A). The Okada space has more difficulties in stock, because some of the fault parameter sets are mathematically acceptable but unphysical. These problems will not be addressed here.

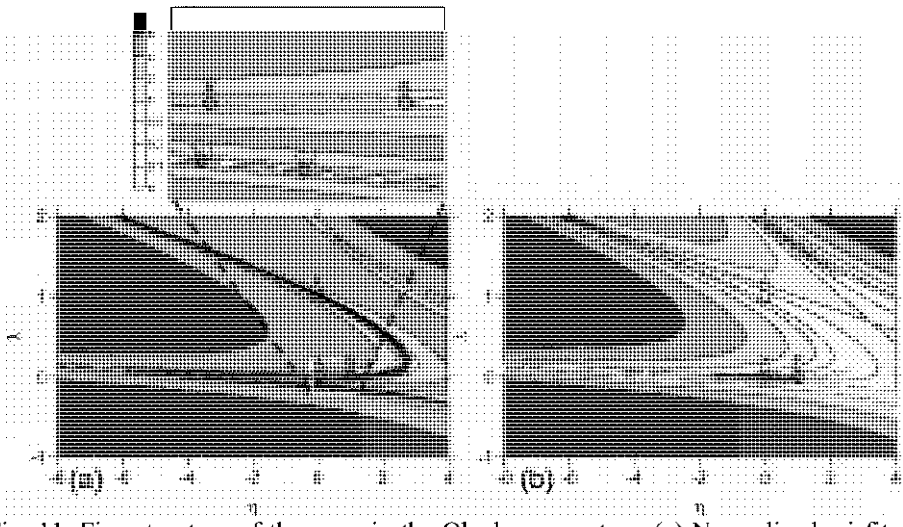

Fig. 11. Fine structure of the error in the Okada parameters: (a) Normalized misfit of tide gauge data ($J_{tg}/(N_{ob}\sigma_{ob}^2)$); (b) relative error (ε). (λ,η) are two directions in the plane that is defined by the true solution (X), a good inverted solution (B, Exp.4) and a spurious solution (A in Exp.3). A zoom of the error surface is also shown above. See text for details.

Once the solution obtained in Exp.4 was found to be a good solution, one will now look to its error structure in the fault parameter space. In Pires and Miranda (2003) the conditioning of the different fault parameters in the inversion process was analyzed in terms of the Hessian matrix of the tide gauge cost function with Okada parameters. Similar conclusions can be drawn here. In general, the inversion problem is badly conditioned in directions corresponding to eigenvectors associated with small eigenvalues (Wunsch, 1996; Fletcher, 1987) of the Hessian matrix. It is important to note that the Hessian matrix is computed locally, in the neighborhood of the inverted solution, and so it can not deal with spurious minima in the parameter space that are far away from the true solution. Close to the true solution, the cost function is well approximated by a quadratic function of the deviations from the true fault parameters, and those deviations are considered to be Gaussian.

The error-covariance matrix of the scaled fault parameters, C, or resolution matrix, can be computed through the Hessian matrix H of the cost-function J_{fg}:

$$C = \mathrm{cov}(\varepsilon_{inv}, \varepsilon_{inv}) = 2\sigma_{ob}^2 H^{-1} \tag{3}$$

where ε_{inv} is a vector containing the errors in the scaled fault parameters. The eigenvectors of H, for Exp.4, are shown in Table 5, together with the errors in the eigendirections (Δ_k) and the 99 % confidence level of those errors ($\sigma_{99,k}$) estimated as:

$$\sigma_{99,k} = P_{99}\sqrt{\frac{2\sigma_{ob}^2}{\lambda_k}} \tag{4}$$

where P_{99} is the 99 percentile of the standard Gaussian distribution and λ_k is the k^{th} eigenvalue of the Hessian matrix. The leading eigenvalues (λ_{lead}) for the different experiments were shown in Table 3. Large eigenvalues lead to faster convergence and good conditioning of the inversion process. The leading eigenvalues of Exp.5 and Exp.6 are larger, by one order of magnitude, than in Exp.2.

An inspection of Tahle 5 shows that 5 eigenvectors almost coincide with 5 of the original fault parameters: v_1 projects along x_0, v_2 along y_0, v_4 along δ, v_5 along α, and v_9 along U_{sl}. The other eigenvectors project on a pair of fault parameters: v_3 and v_6 project on the (L,W) plane, but v_3 represents the source area variation while v_6 represents the variation in the fault aspect ratio. Since v_3 has components of equal sign along L and W, variations of the source area project strongly on v_3. On the other hand, as the components of v_6 along the same parameters have opposite signs, changes in the source aspect ratio associated with opposite changes in L and W, project on v_6. The vectors v_7 and v_8 project on the (d,γ) plane, but while v_7 is mainly along γ, v_8 follows d. Because eigenvectors are sorted in decreasing eigenvalue order, one may conclude that the best fit is obtained for x_0, followed hy y_0, the source area, dip angle (δ), the azimuth (α), the fault aspect ratio, the slip angle (γ), the depth (d), and the slip dislocation (U_{sl}). The fitting errors (computed and estimated) increase with decreasing eigenvalue, as expected.

Table 5. Components of the 9 eigenvectors of Hessian matrix, over the 9 scaled fault parameters (significant values in bold)

	v_1	v_2	v_3	v_4	v_5	v_6	v_7	v_8	v_9
δ	0.14	~0	~0	**0.97**	~0	-0.17	~0	~0	~0
d	~0	~0	~0	~0	~0	0.21	**0.4**	**0.87**	0.18
U_{sl}	~0	~0	0.1	~0	~0	~0	~0	-0.16	**0.98**
γ	~0	~0	~0	~0	~0	~0	**0.91**	**-0.41**	~0
x_0	**0.99**	~0	~0	-0.14	~0	~0	~0	~0	~0
y_0	~0	**1**	~0	~0	~0	~0	~0	~0	~0
α	~0	~0	~0	~0	**1**	~0	~0	~0	~0
L	~0	~0	**0.78**	-0.19	~0	**-0.57**	~0	0.14	~0
W	~0	~0	**0.61**	~0	~0	**0.77**	~0	-0.15	~0
Δ_k	-3.1E-3	1.1E-4	-0.06	0.01	0.01	0.09	0.13	0.33	1.92
$\sigma_{99,k}$	5.5E-4	1.5E-3	0.01	0.02	0.03	0.09	0.27	0.4	4.97

The covariance matrix C for experiment Exp.4 is shown in Table 6, where the largest cross-covariances are shown in bold, indicating some degree of redundancy in the fault parameters. Largest redundancies are found in the pairs (U_{sl}, d), (U_{sl}, L) and (U_{sl}, W). As previously shown, U_{sl} is the most inaccurate parameter in the inversion. This is consistent with the fact that vector XB in Figure 11b, along which the error decreases very slowly, is mostly projected in those 4 parameters.

The large values in cross-covariances are associated with similarities in the spatial distributions of the gradients of the water displacement with respect to the corresponding parameters. From a first order Taylor expansion of the cost-function, one may write:

$$\delta J_{tg} = \nabla_{\zeta} J_{tg} \bullet \left(\sum_{i=1}^{9} \delta f_i \frac{\partial \vec{\zeta}}{\partial f_i} \right) \tag{5}$$

where $\vec{\zeta}$ is the water displacement field and f_i is a generic scaled fault parameter. The dot in (5) means a spatial inner product. The field derivatives $\partial\vec{\zeta}/\partial f_i$ are shown in Figure 12, in the vicinity of the inverted solution of Exp.4. Indeed, Figure 12b, c, h, and i are highly correlated, indicating that there may be error compensation between the involved variables, implying an intrinsic difficulty in the inversion. It is easy to show that positive correlations between derivatives correspond to negative correlations between errors, and vice versa.

We have made some extra experiments to test the sensitivity of the inverted solution to the fault parameter scales (Table 1). These experiments showed that the scales attributed to the fault position (x_0, y_0) and size (L, W) must be smaller enough than the domain size to keep the solution within the spatial domain during the minimization process. The scale attributed to the fault depth d must also be sufficiently small to avoid negative depths, during minimization. On the other hand, if any of the scales is too small the convergence will proceed very slowly in the corresponding direction, and the process may reach the stopping criterion without significant improvement. An

objective way of defining the parameter scales, using only information on the first guess, is by imposing that the squared norm of derivative of the surface displacement field with respect to each parameter ($\|\partial\xi/\partial f_i\|$, see (5)) in the first guess solution is the same for all parameters. With that set of scales, we have obtained the same solution. However, the problem deserves future investigation.

Table 6. Covariance error matrix (×10⁴) for Exp.4 (significant values in bold)

	δ	d	U_{sl}	γ	x_0	y_0	α	L	W
δ	1.2	21.9	105.6	-1.5	-0.2	0.0	-0.3	-7.4	-7.2
d	21.9	1057.3	**4846.5**	-76.7	-3.2	0.6	-13.0	-370.6	-283.6
U_{sl}	105.6	**4846.5**	26244.2	-223.2	-15.1	0.9	-57.6	**-2121.0**	**-1393.4**
γ	-1.5	-76.7	-223.2	101.6	0.2	-1.4	2.0	11.9	19.5
x_0	-0.2	-3.2	-15.1	0.2	0.0	0.0	0.0	1.0	1.0
y_0	0.0	0.6	0.9	-1.4	0.0	0.0	0.0	0.0	-0.1
α	-0.3	-13.0	-57.6	2.0	0.0	0.0	1.2	4.1	3.7
L	-7.4	-370.6	**-2121.0**	11.9	1.0	0.0	4.1	177.5	104.9
W	-7.2	-283.6	**-1393.4**	19.5	1.0	-0.1	3.7	104.9	84.0

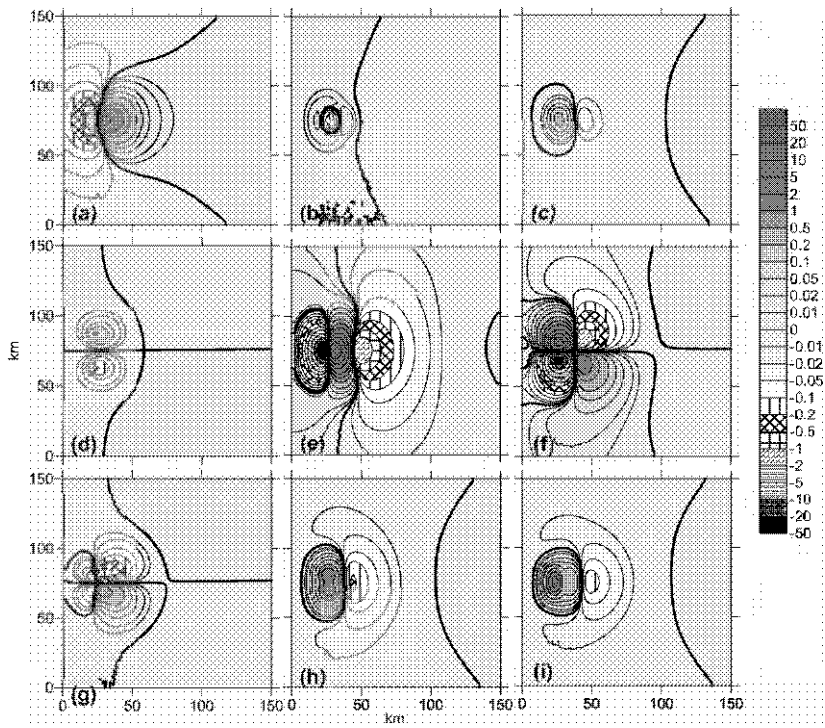

Fig. 12. Derivatives of the water displacement with respect to the scaled fault parameters, corresponding to the final inversion in Exp.4: (a) dip angle δ, (b) depth d, (c) slip dislocation U_{sl}, (d) slip angle γ, (e) x_0, (f) y_0, (g) azimuth α, (h) fault length L, and (i) fault width W.

7 Conclusions

Tsunamis produced by large submarine earthquakes contain information on the location and geometry of the earthquake source that may, in some cases, be successfully inverted providing an independent contribution to the general problem of earthquake inversion. Tide gauge series from near-shore tsunamis are potentially richer in information on the source location and shape, as their signals are less distorted by propagation. Even in those cases, it is not easy to deal with a number of difficulties, arising from observational errors at the tide gauges, from insufficient knowledge of the small scale bathymetry and from many model uncertainties.

In this study problems associated with coastal effects were highlighted in a set of sensitivity experiments, which also addressed some intrinsic problems of tsunami inversion related to the fine structure of the cost-function surface in the fault parameter space. Results from the simulations showed that the inversion skill decreases as waves approach the coastline, due to refraction and reflection effects, which impact on the frequency spectrum of the tide gauge data. However, if tide gauges are too close to the source the azimuthal coverage is reduced, implying a degradation of inversion.

It was also found that, due to insufficient information in the tide gauge data, the cost function has fine structures, with elongated canyons and multiple nearby minima, which are within the observational error level, and which can not be objectively distinguished, in real situations. The orientation of those canyons lies along directions of the parameter space which are poorly inverted. In the case considered, the position of the fault center and its area, azimuth and slip angle were best resolved, while the slip dislocation, the fault aspect ratio and its depth are more uncertain. However, all parameters may be correctly inverted if enough information is available.

These results show the capabilities of the adjoint method proposed by Pires and Miranda (2001) in the inversion of tsunamigenic earthquakes, providing a general framework for the estimation of the parameter values and their uncertainties.

Acknowledgements

This work was carried out at CGUL with funds from the Portuguese Science Foundation (FCT) under Grant POCTI/CTA/11050/98/2001, co-financed by the European Union under program FEDER. Suggestions made by two anonymous referees contributed to improve the text.

References

Bennett, A. F., Inverse Methods in Physical Oceanography, Cambridge Univ. Press, New York, 346 pp., 1992.

Fletcher, R., Practical methods of optimization, 2nd ed., 436 pp., John Wiley and Sons, 1987.

Gilbert, J. C., and Lemaréchal, C., Some numerical experiments with variable-storage quasi-Newton algorithms, Math. Programming, 45, 407-435, 1989.

Gjevik, B., Pedersen, G., Dybesland, E., Harbitz, C. B., Miranda, P. M. A., Baptista, M. A., Mendes-Victor, L., Heinrich, P., Roche, R., and Guesmia, M., Modeling tsunamis from earthquake sources near Gorringe Bank southwest of Portugal, J. Geophys. Res., 102, 27, 931-27, 949, 1997.

Johnson, J. M., Satake, K., Holdahl, S. R., and Sauber, J., The 1964 Prince William Sound earthquake: Joint inversion of tsunami and geodetic data, *J. Geophys. Res.*, 101, 523-532, 1996.

Johnson, J. M., Heterogeneous coupling along Alaska-Aleutians as inferred from tsunami, seismic, and geodetic inversions, in *Tsunamigenic Earthquakes and their Consequences*, edited by R. Dmowska and B. Saltzman, *Adv. Geophys.*, 1-116, 39, 1999.

Miranda, J.M., P.M.A. Miranda, M.A. Baptista and L.Mendes Victor, A comparison of the spectral characteristics of observed and simulated tsunamis, *Physics and Chemistry of the Earth*, 21, 71-74, 1996.

Miyabe, N., An investigation of the Sanriku Tsunami based on marcogram data, *Bull. Earthquake Res. Ins. Tokyo*, Sup. Vol. 1, 112-136, 1934.

Okada, Y., Internal deformation due to shear and tensile faults in a half-space, *Bull. Seismol. Soc. Am.*, 82, 1018-1040, 1992.

Piatanesi, A., Tinti, S., and Pagnoni, G., Tsunami waveform inversion by numerical finite-elements Green's functions, *Natural Hazards and Earth System Science*, 1, 187-194, 2001.

Pires, C., and Miranda, P.M.A., Tsunami waveform inversion by adjoint methods, *J. Geophys. Res.*, 106, C9, 19773-19796, 2001.

Pires, C. and P.M.A. Miranda, Sensitivity of the adjoint method in the inversion of tsunami source parameters, *Natural Hazards and Earth System Science*, 3, 341-351, 2003.

Pires, C., Vautard, R., and Talagrand, O., On extending the limits of variational assimilation in nonlinear chaotic systems, *Tellus*, 48A, 96-121, 1996.

Rabinovich, A.B., P.M.A. Miranda and M. A. Baptista, Analysis of the 1969 and 1975 Tsunamis at the Atlantic Coast of Portugal and Spain, *Oceanology*, 38, No. 4, 463-469, 1998.

Satake, K., Inversion of tsunami waveforms for the estimation of a fault heterogeneity: Method and numerical experiments, *J. Phys. Earth*, 35, 241-254, 1987.

Satake, K., Inversion of tsunami waveforms for the estimation of heterogeneous fault motion of large submarine earthquakes: The 1968 Tokachi-oki and 1983 Japan Sea earthquakes, *J. Geophys. Res.*, 94, 5627-5636, 1989.

Talagrand, O., and Courtier, P., Variational assimilation of meteorological observations with the adjoint vorticity equation, I, Theory, *Q. J. R. Meteorol. Soc.*, 113, 1311-1328, 1987.

Tinti, S., Piatanesi, A., and Bortolucci, E., The finite-element wave propagator approach and the tsunami inversion problem, *Phys. Chem. Earth*, 21, 27-32, 1996.

Wunsch, C., *The Ocean Circulation Inverse Problem*, 456 pp., Cambridge Univ. Press, New York, 1996.

EXPERIMENTAL DESIGN FOR SOLID BLOCK AND GRANULAR SUBMARINE LANDSLIDES: A UNIFIED APPROACH

J. G. FLEMING[1], R. A. WALTERS[1], L. P. SUE[2] AND R. I. NOKES[2]

[1]*National Institute for Water and Atmospheric Research*
PO Box 8602, Christchurch, New Zealand
[2]*Department of Civil Engineering, University of Canterbury,*
Private Bag 4800, Christchurch, New Zealand

Dynamics of submarine landslides and the subsequent generation of surface waves are important topics in current tsunami research. As a part of our studies, we are developing numerical models for landslides as well as conducting laboratory experiments of solid block and granular landslides. This paper is a presentation of the methodologies of the experiments, which were conducted in two phases. The first phase followed the convention of previous investigators and used a semi-elliptical solid block on a 15° slope as a simplified test case. The second phase was an exploration of a wider range of phenomena in a larger parameter space than that undertaken by previous investigators within a single experimental framework. Phenomena under consideration included wave dynamics in the near field and far field regions, wave run up onto the shore, landslide center-of-mass motion, dilation, shape evolution, and internal particle motion as well as velocity distribution in the water column. The parameter space included variation of landslide density, volume, initial submergence, initial shape and deformability (i.e., solid blocks as well as granular material slides); this large parameter space was made tractable through the selection of a statistically balanced experimental design. The second phase also employed three unique measurement techniques: wave height measurement by laser induced fluorescence (LIF), landslide particle tracking using ultraviolet light, and particle tracking velocimetry (PTV) in the water column using visible light. The significance of the study lies in the variety of phenomena under consideration, the size of the parameter space, and in the unique methodology contained in a single experimental framework. Representative examples of each type of data that were produced during the study are also provided to round out this methodological description.

K. Satake (ed.), Tsunamis: Case Studies and Recent Developments, 259-277.

1 Introduction

Landslides are a common feature in the underwater landscape of the Earth. They are part of the mass-wasting process that moves terrigenous material into the deep ocean and have been active for most of geologic history. In New Zealand, terrestrial erosion in the South Island is occurring rapidly due to rapid uplift of the southern ranges; it has been estimated that 1% of all sediment input into the worlds oceans originate from New Zealand (Carter and Saunders, 2003). This sediment supply to the continental shelf, combined with steep shelf bathymetry and significant seismic activity provides an environment conducive to tsunamigenic submarine landslides. In addition, the plate convergence zone on the east coast of the North Island creates a steep continental slope that is prone to failure (de Lange and Fraser, 1999; Lewis and Collet, 2001). Underwater landslides have received increased attention recently because they can generate large localized tsunami in coastal areas (e.g., the 1998 Papua New Guinea tsunami) (Tappin and Shipboard Scientists, 1999). This type of tsunami is characterized by short wavelength and high amplitude and can be very destructive (Murty, 1979; de Lange and Fraser, 1999).

Despite their importance as a hazard to coastal communities, scientific understanding of submarine landslides is currently very limited. Underwater landslides are a special case of the more general class of granular material phenomena, with all the complexities therein. Here the granular material moves downslope under the influence of gravity, while pressurized by water at nearly hydrostatic pressure. The dynamics are characterized by grain-grain and grain-fluid interactions while moving over three-dimensional topography. Until recently, there has been no satisfactory theory to quantify these dynamics. Research has been based on the assumption of a viscous or viscoplastic fluid where the focus was on the development of empirical formulas for the landslide rheology (Jiang and LeBlond, 1993; Jiang and LeBlond, 1994; Rzadkiewicz et al., 1997). However, there are sufficient free parameters in such an approach that one must question whether observations are being reproduced with the correct physics and what the predictive skill of these methods is. At any rate, it is difficult to advance a basic understanding of the dynamics with this approach.

In order to address these problems, we are developing numerical models and have conducted two sets of laboratory experiments using solid block and granular landslides. The first phase followed the convention of previous investigators and used a semi-elliptical solid block on a 15° slope as a simplified test case. The first phase of the experiments was used to build a data set for comparison with international benchmark experiments as described in Watts et al., (2000), Grilli and Watts (1999), and Grilli et al. (2002).

The second phase was designed to capture a wider range of physical phenomena in a larger parameter space than that undertaken by previous investigators. The physical

phenomena—selected for their suitability for comparison with our prototypical modeling efforts—included waves runup, wave dynamics in the wave generation region, wave propagation in the far field and unsteady velocity distribution. In terms of landslide dynamics data, the center-of-mass motion, morphological evolution, volumetric dilation, and internal particle motion within the slide were considered important. A new technique was applied to capture wave run up as well as wave dynamics in the near field region using laser-induced fluorescence (LIF). In addition, particle tracking velocimetry (PTV) was applied to capture the velocity distribution in the water column; although PTV is not novel, it has not been applied to submarine landslide experiments in prior investigations. Finally, a completely new technique was developed and used to capture internal particle motion within the landslide granular material using ultraviolet light.

These phenomena were captured for each designated combination of independent variables. The parameter space included variation in landslide density, volume, initial submergence, initial shape and deformability (i.e., solid blocks as well as granular material slides were used). Exploration of such a large parameter space was made feasible through the selection of a statistically balanced orthogonal array experimental design (Doebelin, 1995; Ross, 1996).

Each of the physical phenomena and each of the parameters under consideration as well as the methodology are described in the following sections. The contribution of this paper lies in its description of the methodology for capturing these dynamics in the given parameter space and of the new techniques that were developed and applied. Examples of each type of data produced during the experiments are also provided.

1.1 PHENOMENA OF INTEREST

Wave run up has a direct effect on the economic and human consequences of submarine landslides; the return wave that propagates in the opposite direction from the landslide motion is responsible for coastal inundation (Tappin and Shipboard Scientists, 1999). Wave run up theory and experiments generally center on the effects of tsunami that propagate from the open ocean to the continental shelf and finally onto a plane beach (Synolakis, 1987). Tsunamis from submarine landslides are quite different in that both run down and run up occur simultaneously with the wave generation process itself. Thus the run up dynamics are intertwined with wave generation dynamics in very shallow water.

Near field wave dynamics are of interest because the spatial origin of all observable tsunami phenomena is the near field (i.e., the wave generation) region. The near field contains inherent complexities because the near field wave dynamics change dramatically as the instantaneous landslide speed approaches the local instantaneous shallow water wave speed (Watts, 1998). Furthermore, the tsunami wave propagates as

it is generated, modifying the wavelengths of waves running up onto the shore as well as those propagating into the far field. Measurement of near field dynamics is required to connect the physics of shoreline and far field back to landslide dynamics.

Far field wave dynamics are necessary to determine the dispersion and nonlinearity present in the waves beyond the wave generation region propagating in water of constant depth. Physical dynamics which were not detectible at the short time and length scales of the near-field region may reveal themselves in the far field (Watts et al., 2000).

Velocity distribution data for the water column in the near-field region was deemed valuable for model validation. The appropriate governing equations are the continuity equation and the Reynolds averaged Navier-Stokes (RANS) equation (Grilli et al., 2002). The first study to examine the coupled fluid/landslide problem applied the hydrostatic (or long wave) assumption to both fluid and landslide (Jiang and LeBlond, 1993). This is a common practice for simplifying the governing equations; however, neither the flow near the moving landslide nor the surface wave is hydrostatic [see examples in Casulli and Stelling (1998) and Casulli (1999)]. More recent studies of submarine landslides have used the full non-hydrostatic RANS equation for the fluid but have used an empirical approximation for the landslide rheology (Rzadkiewicz et al., 1997). All of these studies have made significant contributions, but none of these approaches leads to a rigorous description of the problem.

Landslide center of mass motion data were collected in order to determine the bulk landslide propagation speed for comparison with the local instantaneous shallow water wave speed. Morphology data for quantifying the shape of a submarine granular slide as it evolves in time and the effect of landslide shape on bulk density evolution were necessary to comprehensively determine the time variation of physical properties of the slide. Landslide dilation is important because the bulk density of the slide decreases with respect to time and distance of propagation although the particle density of the debris itself is not changing (Watts, 1997; Watts and Grilli, 2003).

Particle motion within the slide is important for model validation because models must take into account the movement of energy from potential (the initial condition of the slide mass on the slope), to the kinetic motion of the slide itself, to the friction at the interfaces between the slope and the slide as well as the interface between the slide and the surrounding water. Friction causes a shear layer to form at the bottom of the slide, and viscous drag causes the slide-water interface to evolve in time. The time rate of kinetic energy passing into the surrounding fluid causes eddies to develop which depend on the density, volume, and material properties of the slide. For certain combinations of parameters, the wave generation process may be uncoupled from the interaction of the landslide and the surrounding medium. The velocity of the slide and the velocity in the water near the slide-water interface as well as dynamic pressure form the basis of dynamic coupling when it exists.

1.2 EXPERIMENTAL PARAMETERS

A variety of parameters influence tsunami generation from submarine landslides; the most important of these were selected for study in these experiments. The density, the volume, and the initial submergence of submarine landslides affect wave generation. All other things being equal, waves are most intense when they are associated with landslides having high density, large volume, and shallow initial submergence. Therefore these three parameters were varied in these experiments, as they have been in others (Watts, 1998). Two new experimental parameters were also introduced that had not been studied in a systematic way in the past: landslide initial shape and landslide deformability. The experimental design differed from others (Watts, 1997) in that a single unified and statistically balanced design was used to test the main effects of the parameters simultaneously. The details of each of these parameters are described in turn.

Many studies have shown the effect of slide density on all measurable parameters resulting from landslide tsunami (Wiegel, 1955; Watts, 1998). Because the slide density determines the mass present in a given slide volume, it also determines the outcome of the force balance and total potential energy available. The volume of the slide is also a well-known factor that influences tsunami generation and propagation (Murty, 2003). Finally, the nondimensional initial submergence (defined as the depth of the surface of the landslide measured along a vertical through the center of gravity) d, divided by the landslide length (measured on a horizontal line from the shallowest to the deepest points on the slide) b has been recognized in past studies as a significant parameter influencing wave generation (Watts, 1998).

Submarine landslide experiments have generally been performed with a right-triangle initial shape or a streamlined semi-ellipse solid block. However, while reef platforms have a horizontal top face, many sediments rest on the continental shelf at the angle of repose. In addition, granular landslides in the laboratory form a teardrop shape as they evolve, rather than maintaining a streamlined semi-elliptical shape with a sharp front. As a result, an initial shape using a triangle with a top face near the angle of repose was selected as a compromise between the right triangle and the semi-ellipse. This allowed an investigation into the effect the initial shape of the slide has, whether it begins as a dam break problem due to the initial horizontal top face or as a debris flow due to the angle of repose.

Landslide deformability has been examined in previous work using granular material (Rzadkiewicz et al., 1997; Watts, 1997; Watts and Grilli, 2003). In particular, it has been postulated in the literature that landslide center of mass motion does not change significantly whether the landslide propagates as a solid block or as a debris flow (all other things being equal) (Watts and Grilli, 2003). Quantifying the shape of a submarine granular slide as it evolves in time and the effect of landslide shape on bulk

density evolution were necessary to investigate this issue. In addition, a comparison of the wave generation in both the time and frequency domains (using wavelet techniques) for granular and solid blocks will shed new light on the issue of granular and solid block landslide wave generation.

2 Methods

The experiments were conducted in two phases; the first phase used a semi-elliptical block as the landslide and was similar to a set of international benchmark experiments (Watts et al., 2000). The second phase was entirely new, and used both solid blocks and granular materials.

2.1 PHASE ONE: SEMI-ELLIPTICAL SOLID BLOCK

The purpose of phase one of the experimental program was to develop a data set for comparison with a set of international benchmarks from the literature (Watts et al., 2000). These experiments used a semi-elliptical sliding block sliding on a 15° slope (see Figure 1).

The block was 500mm long, 250mm wide, 50mm thick, and constructed using plywood with an aluminum sheet along the water/slide interface. The block was hollow inside to allow mass to be added to achieve the desired density. Teflon buttons were attached to the bottom and sides of the block to minimize the effects of basal friction against the ramp and flume walls. Blue circles were affixed to the outside of the block for later use in particle tracking software for determining the position, velocity, and acceleration of the landslide with time. The ramp and flume were constructed from acrylic; the flume was 15m long, 550mm deep, and 250mm wide. A grid was drawn onto the wall of the flume to provide a scale for the block motion.

The experimental variables for the elliptical solid block experiments were set according to specifications provided by an international submarine landslide benchmark effort. Lead ballast was placed inside the block to provide the correct bulk density of 1900 kg/m^3. The initial submergence of the surface of the block above the center of mass was 130 mm, which provided nondimensional initial submergence of d/b=0.259 to match benchmark case c_2. In order to measure water elevation in the near-field region, three wave gauges were installed with the first above the landslide initial center of mass position and the second and third 150 mm and 300 mm down range (see Figure 2).

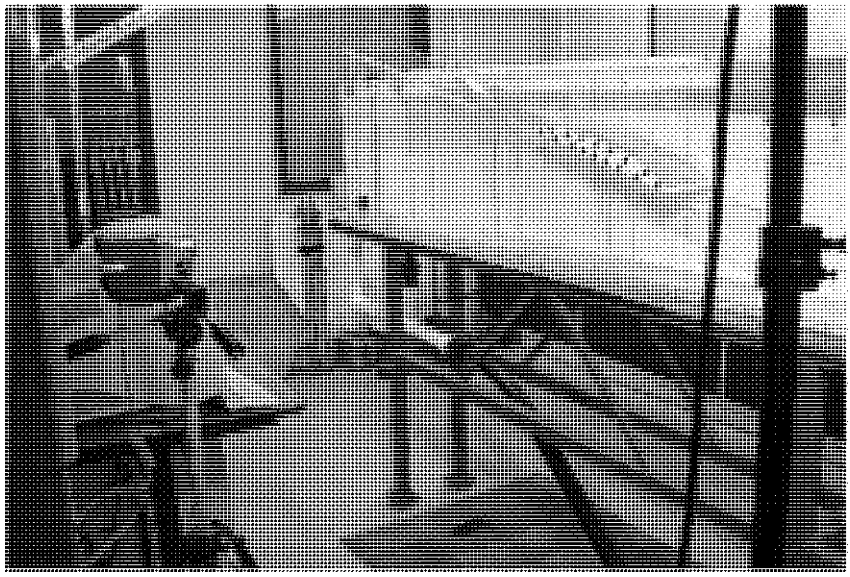

Fig. 1. Photograph of experimental apparatus for Phase 1 of the experiments using a semi-elliptical solid block as the landslide.

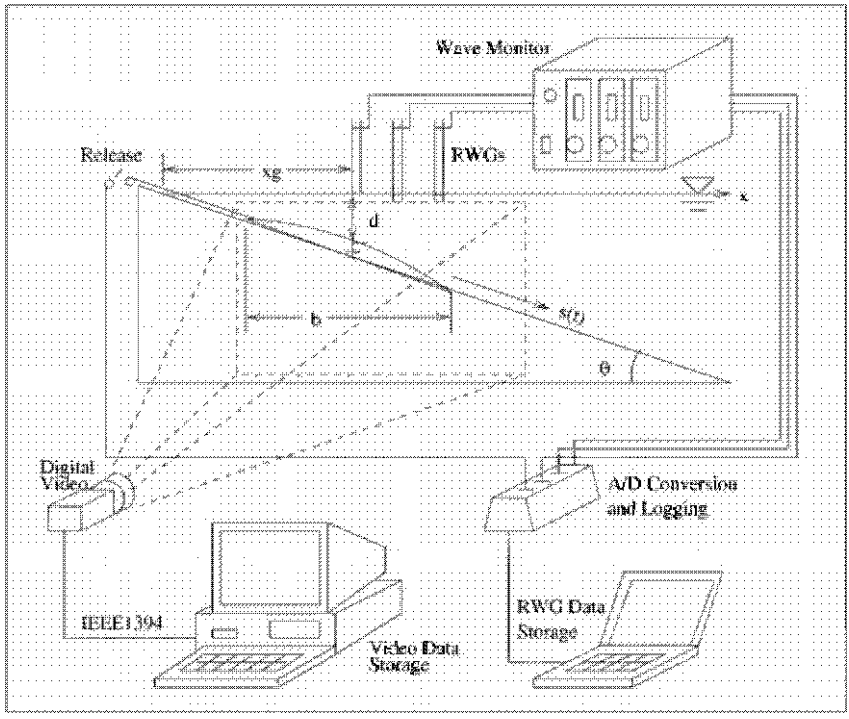

Fig. 2. Schematic diagram of experimental set up for elliptical solid block experiments showing wave gauges, wave monitor module, digital video camera, and data logger.

Wave motion was measured using three wave gauges from Churchill Controls, Ltd. The voltage output from the wave monitors was connected to a Campbell data logger for analog-to-digital conversion at 32 Hz. Logging was initiated when the landslide block was released and the trigger circuit was broken. At the end of the experiment, the voltage data were downloaded from the logger to a laptop for conversion of digital voltage to water level using calibration data. Landslide motion was captured using a Canon MV4i digital video camera and written to disk through an IEEE1394 interface using Adobe Premiere.

The video was exported as a series of image frames; the color tables of these frames were inverted and the resulting particles (the circles affixed to the side of the block) were tracked using StreamLine particle tracking software (Nokes et al., 2003). When using PTV, particle identification uses brightness threshold for each digital video frame. Particle identification is then followed by a classical optimization problem of matching the particles from frame to frame. After the optimal match of particles throughout the video, the particle trajectories are available at any point where particles were visible and good matches were possible. In general, the particle trajectories are useful for calculating many different quantities (including strain rate), but in the case of solid block landslide motion, the particle trajectories were simply averaged together to determine the position, velocity, and acceleration of the solid block landslide.

2.2 PHASE TWO: SOLID BLOCKS AND GRANULAR MATERIAL

The purpose of the second set of experiments was to make a detailed comparison of solid body and granular material submarine landslides by measuring each of the previously described phenomena while varying each of the relevant parameters.

2.2.1 *Experimental apparatus*

A second flume was used, of glass construction, 695 mm high, 5885 mm long and 153 mm wide when dry. With water, the depth was 635 mm and the distance from the shoreline to the opposite end of the flume was 5458 mm for all experiments (see Figure 3).

The ramps representing the continental shelf were constructed of acrylic with a 45° slope. A slot was cut into the acrylic ramps to accommodate the landslide gate release mechanism, which was drawn down through the bottom of the ramp, rather than up through the water surface. The gate was less than one millimeter thick and produced no measurable disturbance when it was retracted.

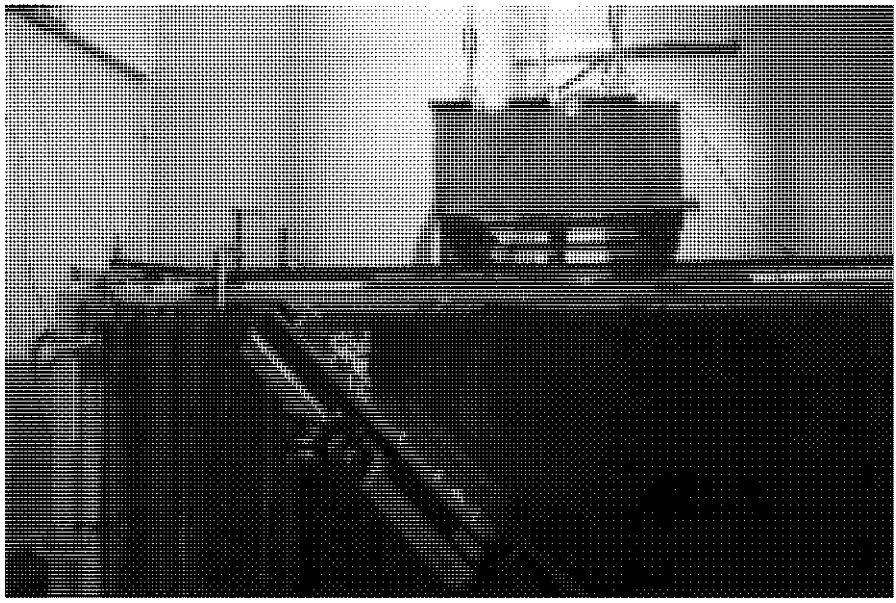

Fig. 3. Photograph of experimental set up for the second phase of experiments using triangular solid block slides as well as granular material slides.

In order to capture the many different phenomena of interest, several different data collection mechanisms were employed beyond the wave gauges used in the first set of experiments (see Figure 4). A second wave monitor module was deployed to measure the output from three additional wave gauges. Wave gauge calibration was performed using a linear variable differential transformer (LVDT) with the output logged by the Campbell data logger for later use in data reduction. The wave gauges were installed in two configurations for each trial: a cluster configuration and a spread configuration. The cluster configuration was designed to capture wave generation in the near field and deployed three wave gauges in this region with the remaining three gauges evenly spaced down range. The spread configuration was designed to capture far field wave propagation and deployed the first wave gauge at the toe of the slope with the remaining five evenly spaced over the far field region.

A new optical wave measurement technique using Laser Induced Fluorescence (LIF) was used to measure wave shape in the near-field region as well as wave run up. Rhodamine dye was added to the water and a 2W laser sheet was applied in a vertical plane parallel to the flume axis. The fluorescence provided a continuous picture of the evolution of the water surface in the wave generation region. This technique was particularly advantageous for shallow water because the initial submergence of the landslides in this set of experiments was insufficient for wave gauges.

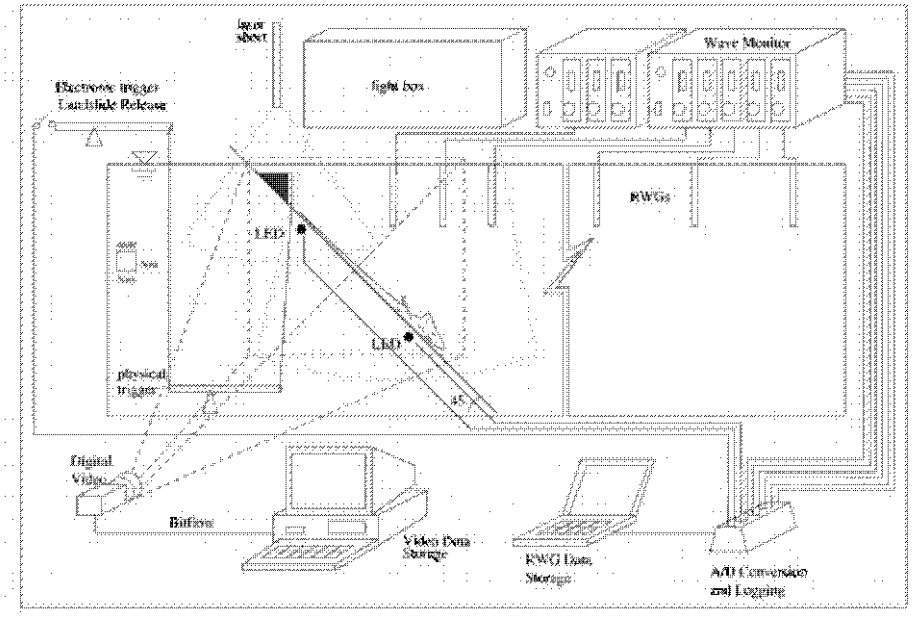

Fig. 4. Schematic diagram of the second phase of experiments using triangular solid block slides as well as granular material slides.

The velocity distribution in the water column was quantified using Particle Tracking Velocimetry (PTV) by adding 250μm pliolite particles and illuminating them with a 6mm thick 1.6kW visible light sheet. The scene was captured using an 8-bit Pulnix 1010 video camera operating at 15 Hz with a 1/250 shutter speed and resolution of 1008x1008 pixels. The camera interface to the computer was controlled by a Bitflow video capture board and LabView software. The flume was too large to capture the entire scene with adequate resolution, so two camera positions were used, with one at the upper end of the ramp and another at the bottom. Data streams were synchronized by software logic in the logging hardware that was programmed to light two LEDs arranged within the video frame when the sediment gate was released.

A new technique was developed to measure the internal strain rates and velocity distribution inside a failing granular mass. In this technique, the granular material was painted with a fluorescent paint and exposed to ultraviolet (UV) light shining on the flume wall during the experiment using a 40W fluorescent light. Combination of simultaneous PTV in the water column and in the granular landslide will allow momentum transport to be measured from the base of the slide through the granular material and overlying water to the air-water interface for the first time.

The granular material itself is plastic infused with lead to provide a range of particle densities (see Figure 5). The particles sizes are uniform across densities and the particle shapes are roughly cylindrical. The differences in dynamics resulting from the motion of a failing granular material as opposed to solid block was quantified by

constructing two different solid block shapes in the initial shapes of the granular slides (angle of repose, triangle) at two different volumes (0.5l, 1.0l) and filling them with the granular materials to achieve each of the granular densities (see Figure 6). The corresponding granular material was also glued to the outside of the blocks to ensure that the drag and external friction between the block and the slope was the same as the deforming granular slides. It is possible that a significant flow of pore water through the granular material may affect the results; diagnostic experiments will be conducted to test for this phenomenon.

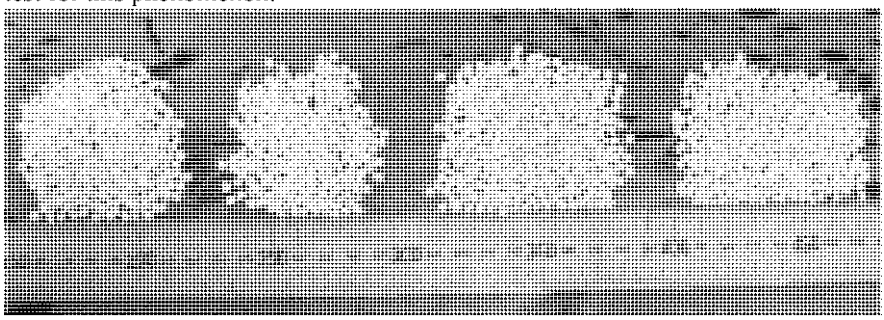

Fig. 5. Photograph of close up of granular materials with scale.

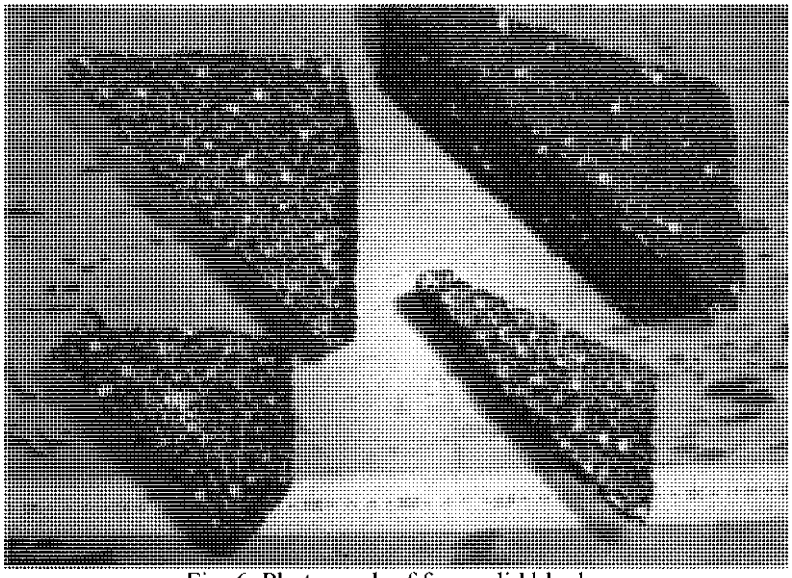

Fig. 6. Photograph of four solid blocks.

2.2.2 *Experimental design*

Overall, the experiments contained five factors: density, volume, initial submergence, initial shape, and deformability. The density levels were constrained hy the granular material, which was available at four specific gravities ranging from 1.41 to 2.46 (corresponding to a bulk density range of 1200 to 1900 kg/m^3).

It was decided that it was necessary to examine two volume levels using a small (0.5L) volume and a large (1.0L) volume landslide. Two initial submergence levels were also used, with a shallow (d/b=0.25) and a deep (d/b=0.5) landslide initial submergence. Landslide initial shape was varied according to two qualitative, rather than quantitative levels, i.e., initially shaped as a right triangle and initially shaped at the angle of repose. Finally, the deformability was also varied at two qualitative levels, using solid blocks with zero deformability and granular material with nonzero deformability (see Figure 6). Creating an experimental design to examine four factors at two levels and one factor at four levels is challenging. For example, a full factorial design exercising each of the combinations of factors at each of the levels would require $2^4 4^1$=64 trials. Although this would yield all of the main effects and all the interactions, it is both inefficient and time prohibitive.

In order to provide coverage of the main effects of all variables, an orthogonal array (see Table 1) was selected to represent $2^4 4^1$ (Doebelin, 1995). This consisted of eight trials where the main effects of the factors were concisely measured (see Table 2). This set of trials is statistically balanced (Ross, 1996) and efficiently provided a tremendous amount of insight from a tractable amount of experimental effort.

Table 1. Orthogonal Array Experimental Design

Trial	Ramp Angle	Initial Shape	Granular Or Solid	Initial d/b	Volume (L)	Particle Sp.Dens.	Bulk Sp.Dens.
1	45	Dam	Solid	0.25	0.5	1.41	1.24
2	45	Repose	Granular	0.5	1.0	1.41	1.24
3	45	Dam	Solid	0.5	1.0	1.61	1.38
4	45	Repose	Granular	0.25	0.5	1.61	1.38
5	45	Dam	Granular	0.25	1.0	2.14	1.67
6	45	Repose	Solid	0.5	0.5	2.14	1.67
7	45	Dam	Granular	0.5	0.5	2.46	, 191
8	45	Repose	Solid	0.25	1.0	2.46	, 191

For each trial, three sets of measurements were made. In the first set, the LIF wave measurement was used for near-field waves as well as run-up. In the second set of measurements, PTV was used near the top of the incline to capture the shallow water velocity distribution as well as the morphological evolution of the slide at early times or the initial acceleration of the solid block. In the third set of measurements, PTV was used near the bottom of the incline to capture the deep water velocity distribution as well as peak dilation of the granular material, peak speed of the solid sliding block, and deposition dynamics. The wave gauges were used during all measurements, split evenly between the two configurations.

Table 2. Detailed Dimensions of Landslide Initial Shape

Tr.	Init. Angle	Length b (m)	Xbar (m)	Depth d (m)	Shore Gate (m)	Length Slope (m)	Length Top (m)	Length Gate (m)
1	0	0.081	0.054	0.020	0.101	0.114	0.081	0.081
2	20	0.143	0.096	0.072	0.180	0.203	0.153	0.091
3	0	0.114	0.076	0.057	0.171	0.162	0.114	0.114
4	20	0.101	0.068	0.025	0.101	0.143	0.108	0.064
5	0	0.114	0.076	0.029	0.143	0.162	0.114	0.114
6	20	0.101	0.068	0.051	0.127	0.143	0.108	0.064
7	0	0.081	0.054	0.040	0.121	0.114	0.081	0.081
8	20	0.143	0.096	0.035	0.143	0.203	0.153	0.091

3 Results

Because the experiments were conducted very recently, only a few examples of the raw data are provided here.

3.1 REPRESENTATIVE DATA FROM PHASE ONE EXPERIMENTS

The wave gauge data for four runs in the phase one experiments is shown in Figure 7. Gauge 1 was directly over the initial center-of-mass position of the slide, and gauges 2 and 3 were 150 mm and 300 mm down range respectively. The consistency of the data indicated good repeatability. Figure 8 shows the position, velocity, and acceleration of the elliptical block with respect to time for the same four runs as shown in the previous figure.

Strictly speaking, the raw data consisted of only the position of the block with respect to time, because this was measured by the digital video. The error at the end of the position time series is the result of mismatches in the PTV algorithm as the block left the frame. The velocity and acceleration curves were obtained by differentiating the data with respect to time, hence the increased noise. However, even with the noise, the repeatability of the results was very good. The motion of the block was adequately described by the length scale s_0=0.7 m and the time scale t_0=0.5 s, resulting in an initial acceleration of a_0=2.8 m/s^2 and terminal velocity u_t=1.4 m/s (Watts, 1998).

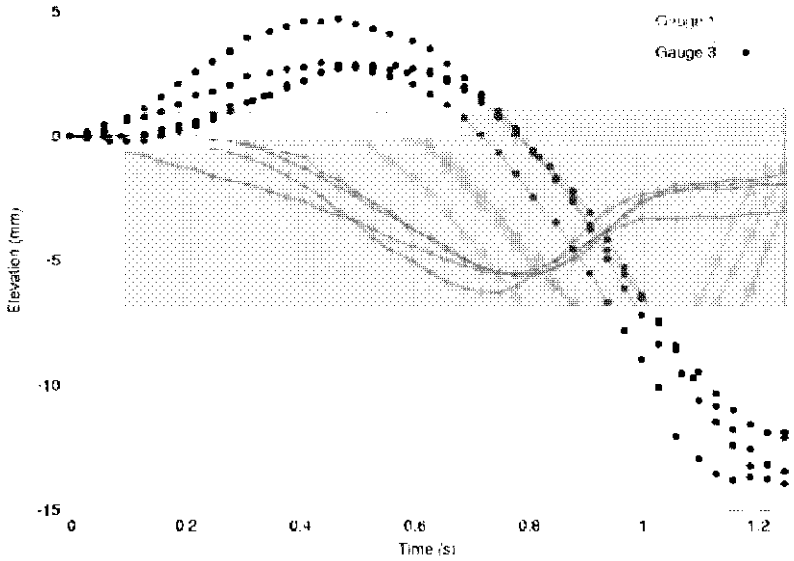

Fig. 7. Graph of solid block wave gauge record.

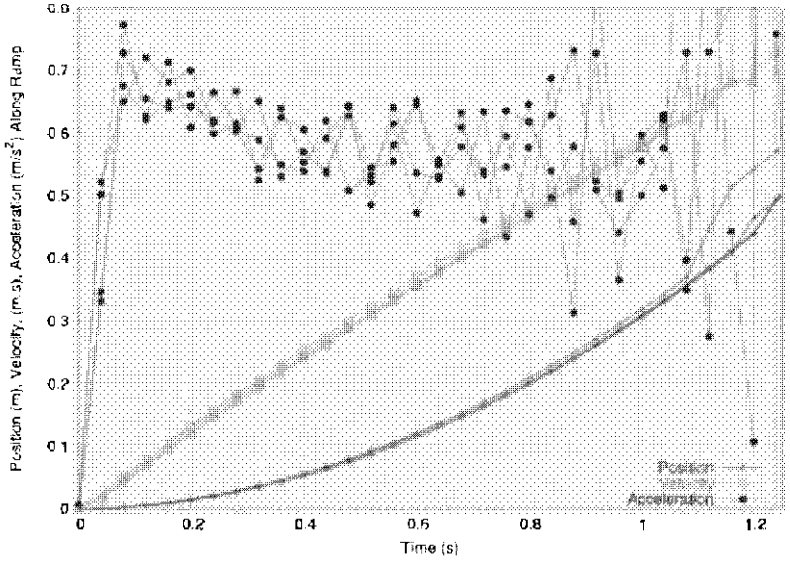

Fig. 8. Graph of solid block position, velocity, and acceleration with respect to time for elliptical solid block trials.

3.2 REPRESENTATIVE DATA FROM PHASE TWO EXPERIMENTS

Raw data from trial 8 is shown in Figure 9. These data show the outline of the solid block as well as the particles in the water column that were illuminated by the light sheet. The data also clearly show the particles on the solid block that were illuminated by the UV light; these will be used to characterize the motion of the landslide. PTV analysis will be applied to the particles in the water column to map the momentum transport throughout the slide event. Incidentally, the water surface is also clearly visible in this image, although it was not collected to quantify the wave shape in the near field region with respect to time. The block has the highest density in the design, and the wave seen here was near breaking by the time the landslide ran out to deposition.

The raw data from trial 8 contrast starkly with the raw data from trial 2, as shown in Figure 10. Trial 2 used the lightest density material in the experimental design and thus had the slowest landslide. The resulting wave was so gentle that it was near the bottom of the detection limit of the wave gauges; in contrast, the voltage output of the wave monitors had to be reduced during trial 8 to prevent the wave from producing voltages that were outside the range of the Campbell data logger. The particles inside the landslide are also visible in the video because of the 40W UV light; many more particles painted with fluorescent dye were present in the granular landslide cases than were glued to the solid blocks. The resulting PTV analysis will provide fascinating results with respect to the internal strain rates of granular landslides.

An example of the data resulting from application of LIF to optical wave elevation measurement is shown in Figure 11. These data are also from trial 8; dye was added to the water surface to capture the entire near field region during wave generation. The images proceed from top left to top right to bottom left then bottom right. The second image clearly shows the depression in the sea surface resulting from bathymetric collapse, as well as the resulting shoreward rush of water. The last image depicts the run up on to the shore as well as the counter-rush of water away from shore and into the void left by the propagating slide mass. Figure 12 provides a close-up of the run down and run up as well as the scale.

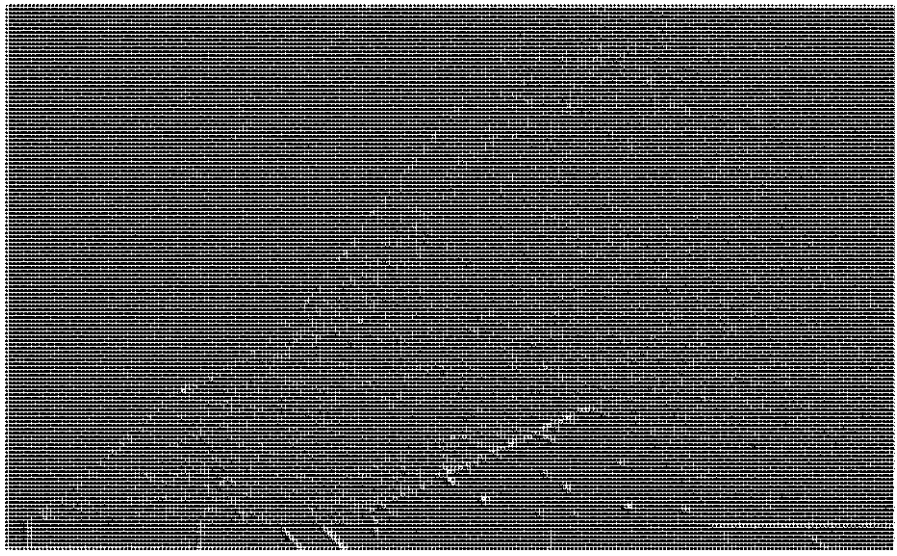

Fig. 9. Illustration of simultaneous landslide and water column PTV data showing the solid block of trial 08. The block represents sediments initially at the angle of repose.

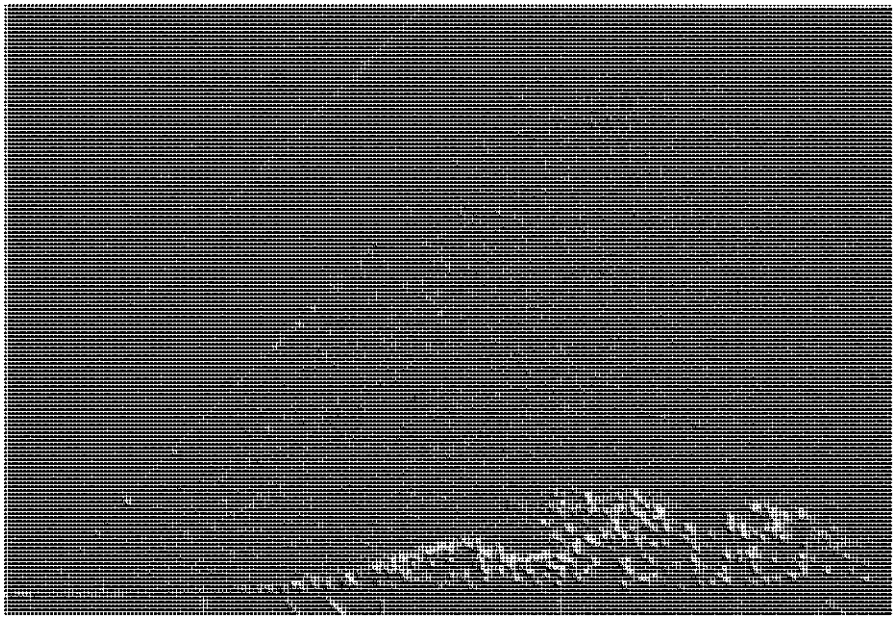

Fig. 10. Illustration of simultaneous landslide and water column PTV showing the granular slide from trial 02. This slide also represents sediments initially at the angle of repose.

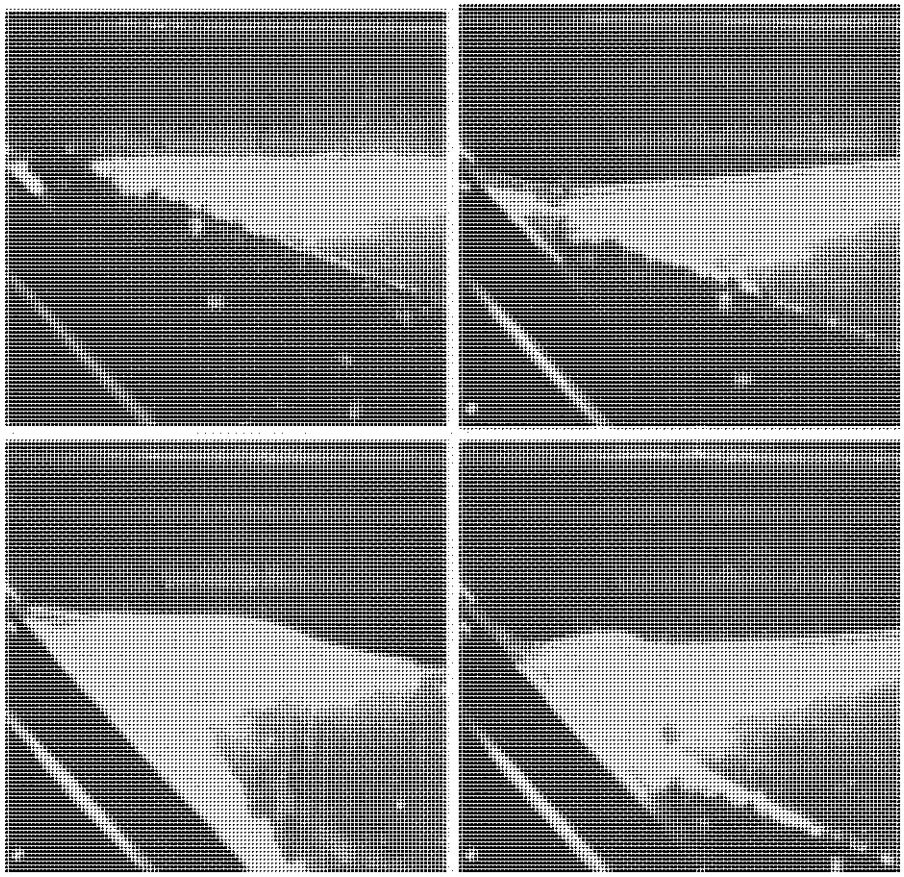

Fig. 11. Digital video series depicting new LIF technique for measuring wave generation in the near-shore region.

4 Concluding remarks

A comprehensive set of experimental data was collected in two phases to characterize the dynamic interaction of a submarine landslide and the surface wave that it generates. The experimental designs included influences from the international tsunami community as well as entirely new elements. When the analysis is complete, the results will provide new insights into landslide motion, deformation, dilation, and entrainment as well as a detailed picture of momentum transfer in the water column, near-field and far-field wave characteristics and wave run down and run up onto the shore.

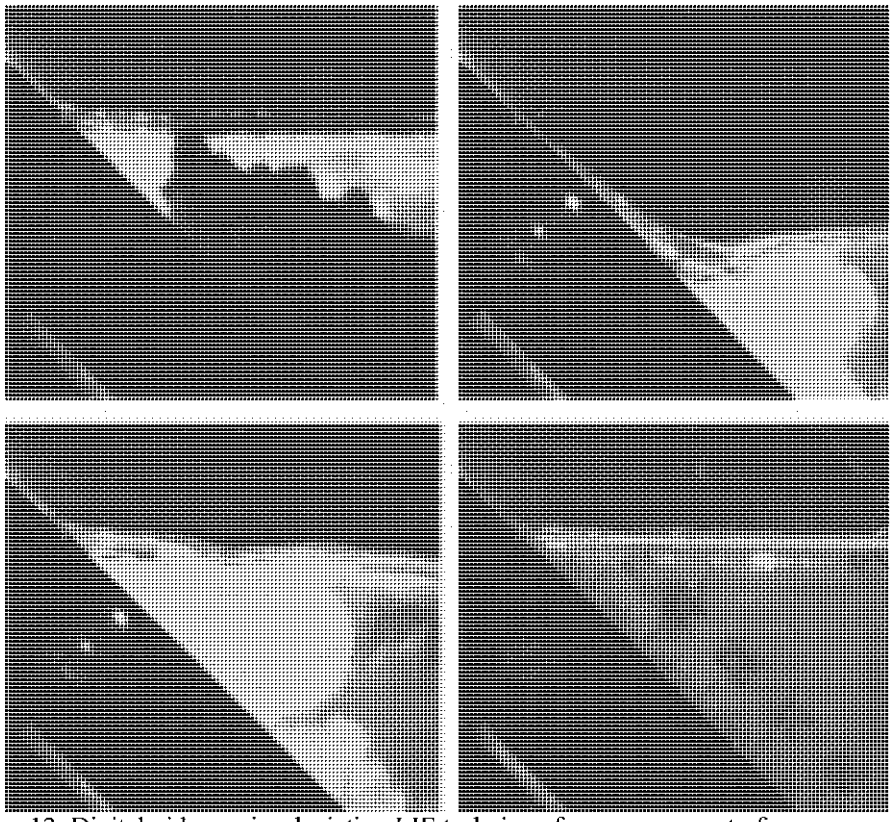

Fig. 12. Digital video series depicting LIF technique for measurement of wave run up. This series is from trial 08 at the initial condition, the point of maximum run-down, and the point of maximum run up. The final image provides scale.

5 Acknowledgements

The development of the LIF wave gauge technique by Mr. Langford Sue is greatly appreciated and acknowledged. This work is supported by a Marsden Grant from the Royal Society of New Zealand.

References

Carter, L. and H. Saunders (2003). Rocky Reefs. *The Living Reef.* M. Francis. Nelson, New Zealand, Craig Potton Publishing: 18-31.

Casulli, V. (1999). "A semi-implicit finite-difference method for non-hydrostatic, free surface flows." *International Journal for Numerical Methods in Fluids* **30**: 425-440.

Casulli, V. and G. S. Stelling (1998). "Numerical simulation of 3D quasi-hydrostatic, free-surface flows." *Journal of Hydraulic Engineering* **124**(7): 678-686.

de Lange, W. and R. J. Fraser (1999). "Overview of tsunami hazard in New Zealand." *Tephra* **17**: 3-9.

Doebelin, E. O. (1995). *Engineering experimentation: planning, execution, reporting*. New York, McGraw-Hill.

Grilli, S. T., S. Vogelmann and P. Watts (2002). "Development of a 3D numerical wave tank for modeling tsunami generation by underwater landslides." *Engineering Analysis with Boundary Elements* **26**(4): 301-313.

Grilli, S. T. and P. Watts (1999). "Modeling of waves generated by a moving submerged body: applications to underwater landslides." *Engineering Analysis with Boundary Elements* **23**(8): 645-656.

Jiang, L. and P. H. LeBlond (1993). "Numerical modeling of an underwater Bingham plastic mudslide and the waves which it generates." *Journal of Geophysical Research* **98**(C6): 10303-10317.

Jiang, L. and P. H. LeBlond (1994). "Three dimensional modeling of tsunami generation due to a submarine mudslide." *Journal of Physical Oceanography* **24**(3): 559-572.

Lewis, K. and J.-Y. Collet (2001). Giant submarine avalanche: Was this "Deep Impact" New Zealand style? *Water and Atmosphere*. **9:** 26-27.

Murty, T. S. (1979). "Submarine slide-generated water waves in Kitimat Inlet, British Columbia." *Journal of Geophysical Research* **84**(C12): 7777-7779.

Murty, T. S. (2003). "Tsunami wave height dependence on landslide volume." *Pure and applied geophysics* **160**(10-11): 2147-2153.

Nokes, R. I., S. A. Blackett and M. J. Davidson (2003). "Design, performance, and application of a generalized optimization-based particle tracking velocimetry system." *Experiments in Fluids* (submitted).

Ross, P. J. (1996). *Taguchi techniques for quality engineering: loss function, orthogonal experiments, parameter and tolerance design*. New York, McGraw-Hill.

Rzadkiewicz, S. A., C. Mariotti and P. Heinrich (1997). "Numerical simulation of submarine landslides and their hydraulic effects." *Journal of Waterway, Port, Coastal, and Ocean Engineering* **123**: 149-157.

Synolakis, C. E. (1987). "The runup of solitary waves." *Journal of Fluid Mechanics* **185**: 523-545.

Tappin, D. R. and Shipboard Scientists (1999). Offshore surveys identify sediment slump as likely cause of devastating Papua New Guinea Tsunami , 1998. *Eos*. **80:** 329.

Watts, P. (1997). Water waves generated by underwater landslides. Thesis. California Institute of Technology, Pasadena, California.

Watts, P. (1998). "Wavemaker curves for tsunamis generated by underwater landslides." *Journal of Waterway, Port, Coastal, and Ocean Engineering* **124**: 127-137.

Watts, P. and S. T. Grilli (2003). *Underwater Landslide Shape, Motion, Deformation, and Tsunami Generation*. The Thirteenth (2003) International Offshore and Polar Engineering Conference, Honolulu, Hawaii, USA, The International Society of Offshore and Polar Engineers.

Watts, P., F. Imamura and S. T. Grilli (2000). "Comparing model simulations of three benchmark tsunami generation cases." *Science of Tsunami Hazards* **18**(2): 107-123.

Wiegel, R. L. (1955). "Laboratory studies of gravity waves generated by the movement of a submerged body." *Transactions of the American Geophysical Union* **36**(5): 759-774.

EFFECTS OF COASTAL FOREST ON TSUNAMI HAZARD MITIGATION – A PRELIMINARY INVESTIGATION

K. HARADA[1] AND F. IMAMURA[2]

[1] *Research Center for Disaster Reduction Systems, Disaster Prevention Research Institute, Kyoto University, Gokashou, Uji, 611-0011, Japan.*
E-mail: harada@drs.dpri.kyoto-u.ac.jp
[2] *Disaster Control Research Center, Graduate School of Engineering, Tohoku University, 06 Aoba, Aramaki, Aoba-ku, Sendai 981-8579, Japan.*
E-mail: imamura@tsunami2.civil.tohoku.ac.jp

In order to utilize coastal forest as tsunami countermeasures, quantitative evaluation for hydrodynamic effect of coastal forest and the clarification of prevention functions against tsunamis were examined in this paper. Field survey and review and summary on the control forest conditions were carried out to evaluate the effect of coastal forest and to find the condition of coastal forest. A relation between the forest density and the diameter of trunk is obtained through the field survey of control forest and some previous researches, which is useful information for the evaluation of the tsunami reduction effects. Numerical simulation including the control forest effect is performed for evaluating the quantitative effect for tsunami reduction and damage. It is found that an increase of forest width can reduce not only inundation depth but also current and hydraulic force behind the coastal forest. By using these results, effects of reducing tsunamis can be quantitatively evaluated in a relation to the tsunami and forest conditions. Finally, review and summary is done to recognize the mitigation effect of tsunami disaster by the coastal forest in the past. Four main functions to reduce tsunami disaster are found; 1) to stop drifts or ships carried by a tsunami, 2) to reduce tsunami energy, 3) to form sand dune protecting tsunamis as well as high waves, and 4) to catch persons carried back by a tsunami to the sea. However, it should be reminded that the coastal forests would be destroyed by a huge tsunami and floating material would cause secondary damage.

1 Introduction

In recent years, demand to coast management is expanded not
prevention but also for environment and utilization by a rise of the environmental consciousness and the citizen participation in Japan. On the other hand, artificial coastal barriers such as seawalls and breakwaters have been constructed along the Japanese coast and have played an important role in protecting the coastal area from

K. Satake (ed.), Tsunamis: Case Studies and Recent Developments, 279-292

natural hazards such as tsunamis, tidal waves and high waves. The artificial coastal barriers have some problems, such as high cost of construction and maintenance, modification of the present environment and inconvenience in utilizing the coastal area. Therefore, the countermeasures against tsunamis by only using the artificial coastal barriers are not recommended for all coastal areas and in future coastal management. For more appropriate management for natural disaster reduction and for keeping good environment, it is required that a new countermeasure method corresponding to each coastal area includes the combination of artificial and natural functions. One of new ways is to utilize a control forest along coast, which is traditional countermeasure for long time. However, quantitative and concrete functions of coastal forest to reduce a tsunami are not established and formulated, so that no guidance to use control forest is available. In order to use a coastal control forests more effectively as countermeasures against tsunamis, it is important to evaluate the hydrodynamic effect of tsunami control forest, and to further discuss a disaster prevention function. The present paper aims to provide the concrete functions of tsunami disaster prevention by control forest from study of old tsunami reports and other sources, and examine the quantitative evaluation of tsunami reduction effect from numerical simulation including the resistance effect of tsunami control forest.

2. Several reduction effects to tsunami disasters by coastal forest

2.1 FUNCTIONS TO REDUCE TSUNAMI DISASTER BY COASTAL FOREST

From old tsunami reports and other sources about reduction effect of coastal control forest against tsunamis (e.g. Shuto, 1987; Ishikawa, 1988), the functions of tsunami disaster prevention by control forest can be summarized as follows.

2.1.1 *Function to stop drifts*

The coastal control forest can stop the attack of drifting boats and ships, woods that would be the secondary disaster to damage houses, causing more severe destruction. This function to stop drifts can be expected as a function of forest until it would be destroyed by huge tsunamis of more than 4 m height.

2.1.2 *Function to reduce tsunami energy*

Hydraulic resistance and reflection of trees could reduce tsunami energy, inundation depth, inundation area, current and hydraulic force behind the forest. As results of forest resistance, tsunamis passing through forest become weaker and the damage would be decreased behind the forest. However, the effect to reduce tsunami has not been understood clearly, hence understanding the hydraulic resistance of complex coastal forest and its model is required (Harada and Imamura, 2002).

2.1.3 *Function to provide life saving*

The report of southwest Hokkaido earthquake in 1993 suggests that 138 persons were carried away and drowned by the tsunami (Mochizuki, 1994). Unless people can resist from the tractive force of a tsunami carrying away from the coast, they would be drowned and cannot be survived. Coastal forests have the function to provide a life saving by catching people who would be carried away by tsunamis. This is an important function to reduce human damage by tsunamis.

2.1.4 *Function to make a natural barrier*

Coastal forest prevents not only tsunami but also sea wind and wind blown sand. And blown sands stopped by forest are accumulated to make dunes higher along seaside of forest. The dunes act as a natural barrier to reduce inflow of a tsunami. In the case of the Nihonkai-Chubu earthquake tsunami in 1983, the tsunami was prevented by the sand dunes with ground level over 10 m on coast of Aomori and Akita Prefectures (Ishikawa, 1988; Murai, 1983). Therefore it can be expected that the coastal forests have the function to form dunes and to prevent inflow of tsunami.

2.2 FUNCTION TO INCREASE DAMAGE BY COASTAL FOREST

The function to increase tsunami damage by coastal forest is also pointed out by Shuto (1987). When huge tsunamis attack the coastal forest, the trees formed forest would be destroyed and washed away by the tsunamis, causing a secondary damage by attacking houses as floating material. In order to use the control forest to prevent tsunami disaster, the limitation of trees against tsunami attacks should be clarified and be evaluated. However, the destruction and the pulling out of trees by tsunamis are not understood yet.

2.3 REDUCTION EFFECTS TO TSUNAMI DISASTERS BY COASTAL FOREST

Figure 1 shows schematic summaries of the functions stated in Sections 2.1 and 2.2. This figure shows that coastal forests have many functions of the effects to reduce tsunami disaster as well as to reduce tsunami energy, and the effect to reduce tsunamis behind the forest. Table 1 shows the relation between the functions and the effect of coastal control forest. The countermeasures that fully utilized the useful disaster prevention functions by these coastal natures should be taken into account. In order to extend or maintain the coastal forest as tsunami prevention countermeasure, it is required to know the system of these functions in the coastal forest and to evaluate its effect by the simulation or field study on target area.

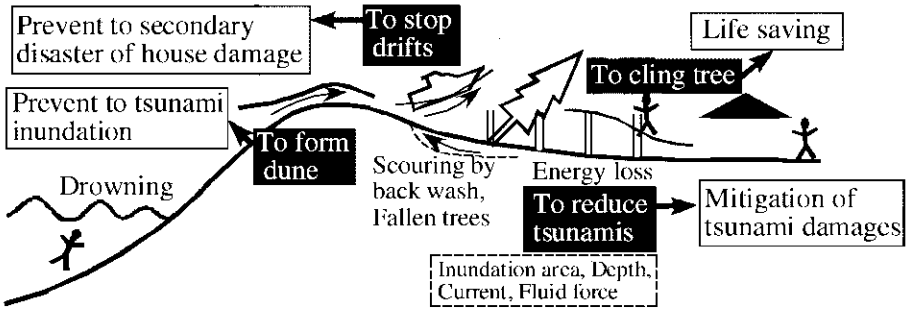

Fig.1 Functions and effects of coastal control forest to prevent tsunami disaster

Table 1. Functions and effects of coastal control forest on tsunami prevention

Functions of forest	Contents of functions	Effects of tsunami prevention
Stop drifts	1.Stop drifts by forests 2.Prevent to crush drifts with house 3.Mitigate to house damage by drifts	Reduction of house damage
Resist to tsunamis	1.Trees resist tsunami 2.Reduce tsunami energy 3.Reduce inundation area and flow current	Reduction of inundation depth and current
Form dune	1.Collect wind blown sand and form dune 2.Act as natural barrier 3.Reduce tsunami inflow	Reduction of inundation tsunamis
Cling tree	1.Parson cling tree 2.Prevent to wash away by tsunami 3.Prevent the drowning death	Life saving

3 Evaluation of the effect on tsunami reduction by using of numerical simulation

3.1 CONDITIONS OF COASTAL CONTROL FOREST IN JAPAN

In order to evaluate the tsunami reduction effect by using numerical simulation, actual forest conditions should be selected. Harada and Imamura (2003) summarized the relation between forest density and trunk diameter from the field survey data of pine tree forest in Japan. In general, the diameter of trunk is related to the amount of leaves, because the trunk takes the role of pipe between the leaf and root. Therefore, they control themselves and so the forest density becomes small when the diameter of trunk becomes large (Tanaka, 1998). By using this relation, the diameter of trunk can be estimated from the forest density. Forest density is an important parameter as well as

for tsunami reduction effects and forest management. From Figure 2, the trunk diameter corresponding to the forest density is selected to 0.3 m and 10 trees /100 m^2, 0.15 m and 30 trees /100 m^2, and 0.1 m and 50 trees /100 m^2 for numerical simulation. Forest width is also an important parameter for tsunami reduction and it varies from place to place. To examine the forest width effect, forest width is selected to be 50, 100, 200 and 400 m, and the forest is put at a distance of 100 m from shoreline. The tree height and the brunch height are selected 10, 2 m and the projected area rate of leaves is given to be 0.65 from the field survey data (Harada and Imamura, 2003). These conditions are used to evaluate tsunami reduction effect by using tsunami numerical simulation. The conditions of forest are shown in Table 2.

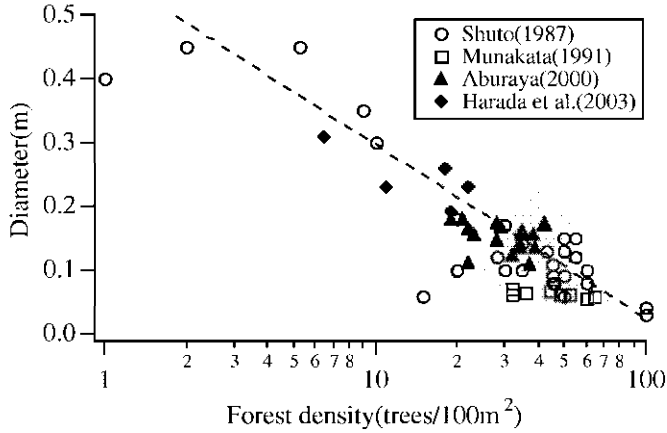

Fig. 2 Relation of forest density and diameter of trunk (Harada et al, 2003)

Table 2. Conditions of coastal forest for numerical simulation

Forest density	10, 30, 50 trees/100 m^2
Trunk diameter	0.3, 0.15, 0.1 m
Forest width	50, 100, 200, 400 m
Tree height	10 m
Branch height	2 m
Projected area rate of leaves	0.65

3.2 RESISTANCE OF COASTAL FOREST IN NUMERICAL SIMULATION

In the numerical simulation, the effect of coastal forest is included as the resistance force in momentum equation. Harada and Imamura (2000) modelled the resistance force as drag and inertia forces based on Morison's equation and obtained the resistance coefficients of coastal forest against tsunamis by using the results of hydraulic experiment. Equations (1) are the resistance coefficients used by them,

where C_D is the drag coefficient; V_o is the volume of tree under water surface in a constant volume; V is the volume of water in a constant volume; C_M is the inertia coefficient. The relation between the inundation depth and the vertical structure of trunk and leaf is varied this drag coefficient. These resistance coefficients include the effect of tree structure. In the numerical simulation, these resistance coefficients are used to calculate the forest effect quantitatively.

$$C_D = 8.4\frac{V_o}{V} + 0.66 \qquad \left(0.01 \le \frac{V_o}{V} \le 0.07\right) \tag{1}$$

$$C_M = 1.7$$

3.3 NUMERICAL SIMULATION CONSIDERING COASTAL FORESTS

In order to evaluate the effect of tsunami reduction quantitatively, numerical simulation of tsunami run up considering the resistance of the control forest is carried out and the change of hydraulic values on the land is examined. The coastal landform for Sendai Bay is selected as an example to discuss the effect of the control forest (Figure 3). In order to examine tsunami reduction effect by coastal forest, the condition of landform is selected to the simplified and small gradient one. To evaluate the tsunami reduction effects by coastal forest, the tsunami height is selected to 1, 2 and 3 m and wave period is 10, 20, 30, 40, 50 and 60 min. When tsunami heights exceed 4 m, trees would start to be broken (Shuto, 1987). In this simulation, trees breaking cannot be properly modelled. Therefore, tsunami height is selected smaller than 4 m.

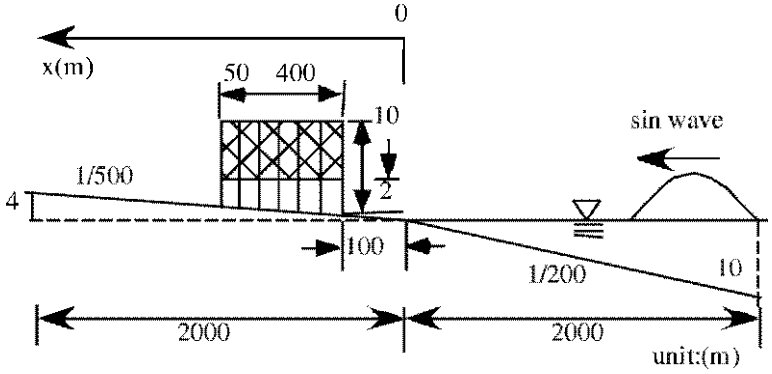

Fig. 3. Conditions for tsunami numerical simulation

Table 3. Conditions of tsunami and landform for numerical simulation

Tsunami height	1, 2, 3 m
Tsunami period	10, 20, 30, 40, 50, 60 min
Gradient of sea floor	1/200
Gradient of land surface	1/500

The governing equation used for the numerical simulation is the momentum equation (2) with the hydraulic resistance force by coastal forest, which is modelled by Morison's Equation.

$$\frac{\partial M}{\partial t}+\frac{\partial}{\partial x}\left(\frac{M^2}{D}\right)+gD\frac{\partial \eta}{\partial x}+\frac{gn^2}{D^{7/3}}M|M| +\frac{C_D}{2}\frac{A_O}{\Delta x\cdot\Delta y}\frac{M|M|}{D^2}+C_M\frac{V_O}{V}\frac{\partial M}{\partial t}=0 \qquad (2)$$

where: M is the flux discharge; D is the total depth; η is the water level; n is the Manning roughness coefficient and is used 0.025 on the slope; A_O is the projected area of trees under the water; Δx and Δy is the grid spatial size and g is the gravitational acceleration. The drag coefficient of forest; C_D and the inertia coefficient; C_M is used the equation (1). The grid spatial size for the numerical simulation are selected as $\Delta x=\Delta y=50$ m, and the time step is $\Delta t=1$ sec.

3.4 RESULTS OF NUMERICAL SIMULATION

Figure 4 shows the calculated waveforms without and with the coastal forest. From this figure, tsunami is reflected at the coastal forest and reduced the inundation depth and the run-up distance behind the coastal forest. In particular, when the inundation depth is over the leaf and branch height, the reflection effect on seaside and the reduction effect on inland side become large. The large resistance force of the leaf and branch calculated from numerical simulation causes these tsunami reduction effects.

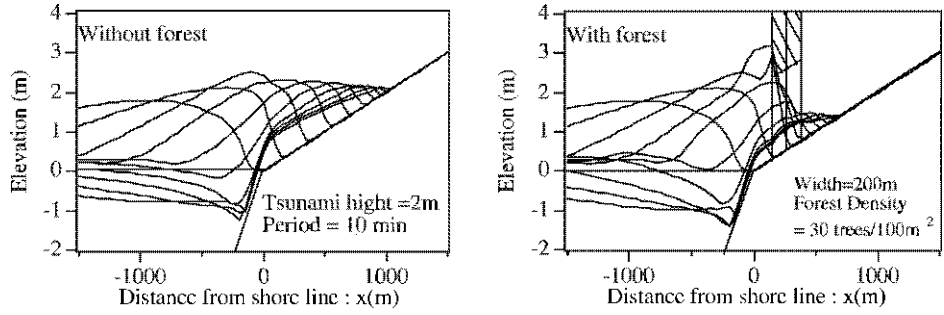

Fig.4 Calculated waveforms without and with forest

3.5 EFFECT OF FOREST WIDTH TO TSUNAMI REDUCTION

The spatial distribution of the maximum inundation depth, current and hydraulic forces are shown quantitatively from the calculated results. Hydraulic force is expressed as a product of fluid density, the inundation depth and the square of current velocity, and used for the estimation of house damage (Hatori, 1984). Figure 5 shows the spatial

distribution of the reduction rate of maximum inundation depth, current and hydraulic force for the cases of forest width of 0, 50, 100, 200, and 400 m, with wave height fixed at 3 m, wave period 10 min and forest density 30 trees/100 m^2. The reduction rate of maximum values is defined by equation (3).

$$r(\textit{Reduction rate of max. values}) = \frac{(\textit{max. value with forest})}{(\textit{max. value without forest})} \qquad (3)$$

The front of the coastal forest is set to be at a distance of 100 m from shoreline and the back is varied with its width. Figure 6 shows the relation between forest width and reduction rate just behind the forest. From Figures 5 and 6, the reduction rates of inundation depth just behind the forest are decreased from r =0.86 with forest width 50 m to 0.18 with forest width 400 m. These inundation depths decrease with a function of the forest width (see Figure 6). This means that the increase in forest width can reduce the inundation damage at the back of coastal forest, which is related to inundation depth. The reduction rates of current just behind the forest decreased from r =0.54 with forest width 50 m to 0.24 with forest width 400 m. The current at the front is decreased due to the reflection at forest front, and the current at the back is reduced by the reflection and the energy loss passing through the forest. As the products of the square of current velocity and the inundation depth define the hydraulic force, the current velocity rather than the inundation depth controls hydraulic force more. Increase in forest width can reduce the house damage, which is related to current velocity and hydraulic force. From these results of numerical simulation, it can be shown that the effects of increasing forest width are large to reduce tsunami inundation depth, current and hydraulic force. By using these numerical simulation results, the effect of coastal forest to tsunami reduction can be evaluated quantitatively. The quantitative evaluation of tsunami reduction would be done in the later section.

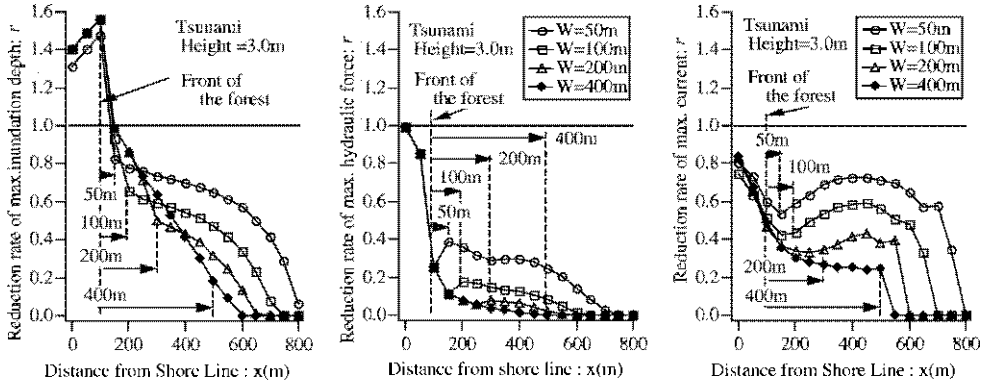

Fig. 5 Spatial distribution on reduction rate of inundation depth, current and hydraulic force (Forest density: 30 trees/100m^2, Trunk diameter: 0.15 m, Tsunami height: 3.0 m, Tsunami period: 10 min)

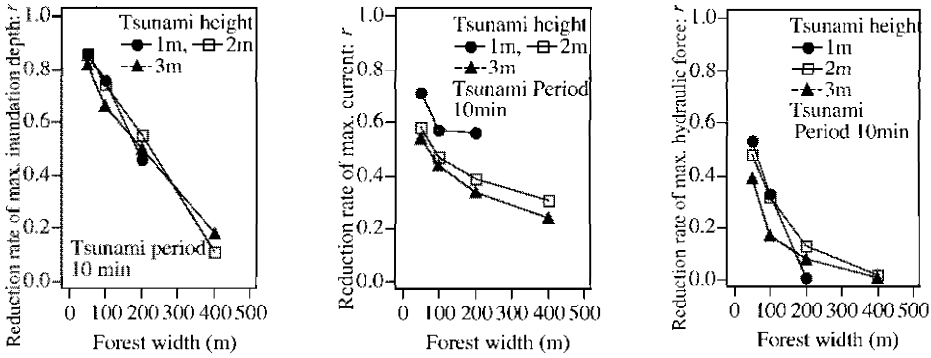

Fig. 6 Effect of forest width to tsunami reduction (Forest density: 30 trees/100m^2, Trunk diameter: 0.15 m, Tsunami period 10 min)

3.6 EFFECT OF FOREST DENSITY TO TSUNAMI REDUCTION

Figure 7 shows the spatial distribution of maximum inundation depth, current and hydraulic force with forest density 10, 30, and 50 trees/100 m^2, with tsunami height fixed at 3 m, and the forest width at 50 m. The reduction rates of inundation depth just behind the forest (x = 150 m) are about r =0.8 in each forest density case. Therefore it can be said that the effect of forest density to reduce inundation depth is small in these calculated conditions. The reduction rate of current decrease with an increase of forest density; the rates are r = 0.6, 0.54, 0.51 in the cases of 10, 30, 50 trees/100 m^2. However the effect of forest density to reduce current is not large. Similar to the inundation depth and current, the hydraulic force just behind the forest decrease with an increase of forest density. Figure 8 shows the relation between forest density and reduction rate. The variation of reduction rate due to the forest density in the same forest width is smaller than the effect of forest width. From these results of numerical simulation, it can be concluded that the effects of forest density based on actual forest condition are not large to reduce tsunami.

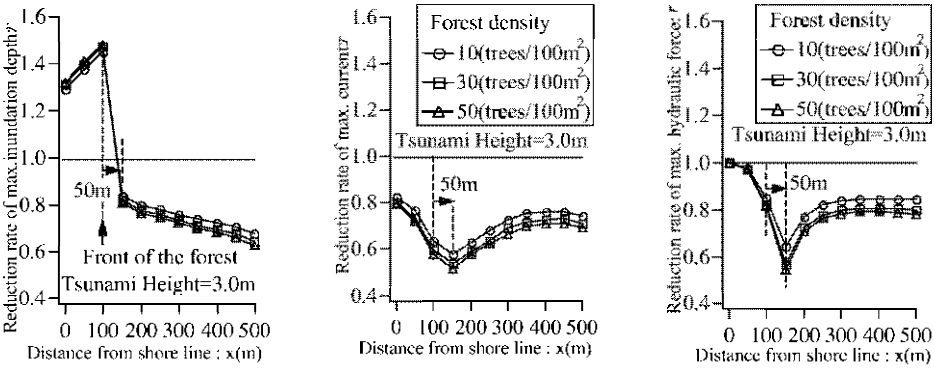

Fig. 7 Spatial distribution on reduction rate of inundation depth, current and hydraulic force (Forest width: 50 m, Tsunami height: 3.0 m, Tsunami period: 10 min)

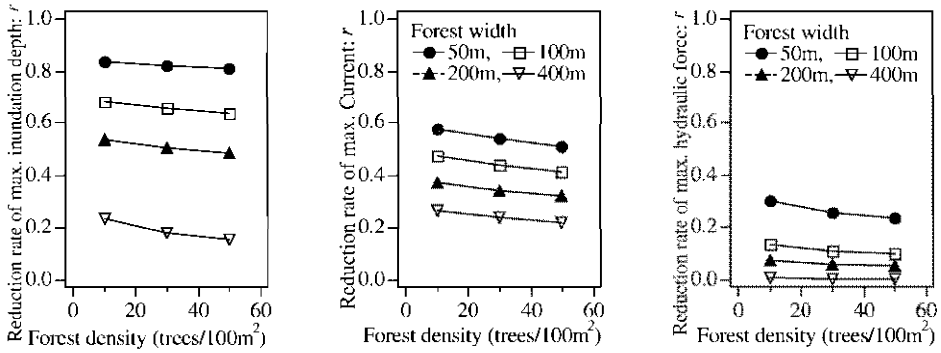

Fig. 8 Effect of forest density to tsunami reduction (Tsunami height: 3 m, Tsunami period 10 min)

3.7 EFFECT OF TSUNAMI PERIOD TO TSUNAMI REDUCTION

In order to examine the effect of tsunami period to tsunami reduction, the relation between tsunami period and reduction rate is shown in Figure 9. When the tsunami period becomes long, the tsunami reduction effect of inundation depth becomes small. As tsunami pass through the same density forest, the variation of reduction rate of current on wave period is small. From these results, when the tsunami period becomes large, inundation depth becomes large but current velocity not so varied.

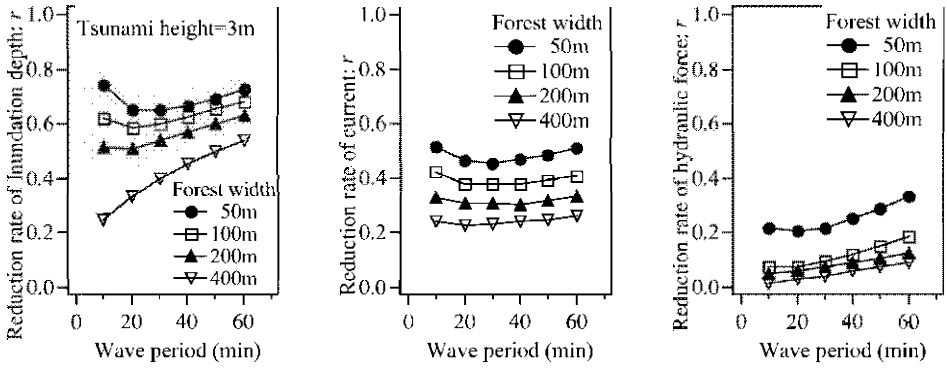

Fig. 9 Effect of tsunami period to tsunami reduction (Forest density: 30 trees/100m^2, Trunk diameter: 0.15 m, Tsunami height =3 m)

3.8 QUANTITATIVE EVALUATION OF FOREST TO TSUNAMI REDUCTION

The relationship of the coastal forest damage and the tsunami intensity or the tsunami height are summarized in Table 4 from the old tsunami disaster reports by Shuto (1992). This table shows that the coastal forest can stop drifts in the case of the inundation depth smaller than 4 m, or tsunami intensity is smaller than 2. However,

Table 4 does not include the quantitative information for the design of the control forest and the effect of forest condition to tsunami reduction. In this section, the quantitative effects to tsunami reduction by coastal forest are discussed by using the results of tsunami numerical simulation. Table 5 shows the reduction rates of maximum run up distance, inundation depth, current and hydraulic force just behind the forest. In order to evaluate the effect against tsunami damage, these hydraulic values are evaluated for 10 min tsunami period. As stated in Section 3.5, the effect to tsunami reduction is strongly influenced by the forest width. So the effects are evaluated for the forest width and the tsunami height. As the mature forest conditions, forest density and diameter of trunk are selected 30 trees/100m^2 and 0.15 m.

Table 4. Relation of tsunami intensity and tsunami damage (Shuto, 1992)

Tsunami intensity	0	1	2	3	4	5
Tsunami height (m)	1	2	4	8	16	32
Effect by coastal control forest	Mitigate damage, Stop drifts, Mitigate tsunami		Partial damage, Stop drifts	Complete damage No reduction effect		

Table 5. Tsunami reduction rate by coastal control forest

			Tsunami height (m)		
			1	2	3
Effect by coastal control forest (Shuto, 1987)			Mitigate damage, Stop drifts, Mitigate tsunami		
Run up distance	Forest width	50 m	0.98	0.86	0.81
		100 m	0.83	0.80	0.71
		200 m	0.79	0.71	0.64
		400 m	0.78	0.65	0.57
Inundation depth	Forest width	50 m	0.86	0.86	0.82
		100 m	0.76	0.74	0.66
		200 m	0.46	0.55	0.50
		400 m	---	0.11	0.18
Current	Forest width	50 m	0.71	0.58	0.54
		100 m	0.57	0.47	0.44
		200 m	0.56	0.39	0.34
		400 m	---	0.31	0.24
Hydraulic force	Forest width	50 m	0.53	0.48	0.39
		100 m	0.33	0.32	0.17
		200 m	0.01	0.13	0.08
		400	---	0.02	0.01

From Table 5, the run up distance is decreased from 0.98 to 0.57 by the increase of forest width and tsunami height. And the inundation depth is also decreased from 0.86 to 0.18 by the increase of forest width and tsunami height. These results are the same results of Aburaya (2000). For further understanding of the effect of damage reduction by tsunami flow, current and hydraulic force would be evaluated from calculated results. The current is decreased from 0.71 to 0.24 and the hydraulic force is decreased from 0.53 to 0.01 by the increase of forest width and tsunami height. However the reduction rates of currents and hydraulic force are larger than run up distance and inundation depth. Additionally, the reduction effects of hydraulic force are larger than the inundation depth and the current, which indicate the most effective mitigation to the tsunami. This means that the reduction effect of coastal forest is larger on house damage than on inundation damage. Table 5 could compensate quantitatively the effect of coastal forest to tsunami reduction of Table 4 (Shuto, 1992). Additionally, Table 5 could evaluate the effect of coastal forest to reduction of tsunami damage by the current. Moreover, Table 5 can be used for a quantitative standard of the tsunami reduction effects by coastal forest for the coastal forest planning. From Table 5, it can be said that the forest width is required to be 200 m or more in order to reduce tsunami, the run-up distance and the inundation depth, to less than 70%. And the forest width is required to be 100 m or more in order to mitigate tsunami damage and current to less than 40%. Table 6 shows an evaluation table of forest effect, which is converted from Table 5. The reduction rates are categorized in three stages, 0.99-0.7 as "a little effective", 0.69-0.4 as "effective" and 0.39- as "much effective". The run-up distance and the inundation depth are considered as the tsunami reduction, and the current and the hydraulic force are considered as the damage mitigation. By using these calculated results of tsunami reduction, the effects can be evaluated quantitatively related to the tsunami and forest conditions. However, the numerical simulation results in this section are calculated in the limited conditions of the tsunami period and the landform. In order to plan the costal forest for tsunami countermeasure, it is needed to further understand the costal forest effect related to the tsunami period and the landform.

Table 6. An evaluation table of forest effect to tsunami reduction

		Tsunami height (m)		
		1	2	3
Tsunami reduction	Forest width < 200 m	A little effective (run-up, inundation depth: 90 -70%)		
	Forest width > 200 m	Effective (run-up, inundation depth: 70 – 40%)		
Tsunami damage mitigation	Forest width < 100 m	Effective (current: 70 - 40%) Much effective (hydraulic force: 50 - 30%)		
	Forest width > 100 m	Much effective (current, hydraulic force: 40 - 0%)		

4 Conclusion

In order to clarify the mitigation effects of tsunami disaster, the literatures on them in Japan are reviewed. Four main functions to reduce tsunami disaster are shown; 1) to stop drifts, 2) to reduce tsunami energy, 3) to form sand dune, 4) to provide life saving. These functions play an important role to use the forest function to prevent tsunami disaster positively and effectively. However, the coastal forests have the limitation against tsunami attacks and the there are possibilities that driftwoods cause secondary damage.

The coastal forest conditions in the actual field are complied to obtain the relation between the forest density and diameter of trunk. Its diameter can be estimated from the forest density by using this relation, which is useful for the plan to coastal forest condition. The numerical simulation considered forest model is carried out to evaluate the quantitative effect of tsunami reduction, and the results are summarized in some tables.

Acknowledgements

The research presented herein is, in part, supported by JSPS Research Fellowships for Young Scientists and MEXT 21st Century COE Program for Disaster Prevention Research Institute, Kyoto University (Program Leader Yoshiaki Kawata). And this study was partly supported by grant-in-aid for Science Research of the Japan Society for the promotion of Science (No.14080203 and No.15310110).

References

Aburaya, T (2000). Tsunami reduction effect of the coastal control forest along Sendai Coast, Graduation thesis of Tohoku University, 60p. (In Japanese)

Harada, K. and Imamura, F. (2000). Experimental study on the resistance by mangrove under the unsteady flow, Proceeding of the 1st Congress of the Asian and Pacific Coastal Engineering, pp.975-984.

Harada, K. and Imamura, F. (2002). Study on the effect in reducing tsunami by the coastal permeable structures, Proceeding of the 13th Congress of the Asia and Pacific Division of the International Association for Hydraulic Engineering and Research, pp.910-915.

Harada, K. and Imamura, F. (2003). Evaluation of tsunami reduction by control forest and possibility of its use for mitigation, Proceedings of coastal engineering, Japan Society of Civil Engineers, pp.341-345. (In Japanease)

Hatori, T. (1984). On the damage to houses due to Tsunamis, Bull. Earthquake Research Inst. Univ. Tokyo, Vol. 59, pp.433-439. (In Japanese)

Ishikawa, M. (1988). The functions of prevent to fog, tide and wind blown sand, Aggregate corporation of Japan Association for Forestry Protection and River Improvement, 83p. (In Japanese)

Izumi, T., Abe, R., Yamauchi, T. and Doi, T. (1961). Consideration on the effect of coastal control forest in Chilean tsunami, Extraordinary report of Miyagi prefectural agriculture experimental station, Vol. 5, 41p. (In Japanese)

Mochizuki, T. (1994). Research report on southwest Hokkaido earthquake in 1993, Center of Urban Science, Tokyo Metropolitan University, 156p. (In Japanease)

Munakata, H., Ohtsuki, K., Arai, S. and Yanagida, N. (1991). Study on the disaster prevention coastal forest, Research report of Fukushima prefectual forest experimental station, Vol. 29, pp.1-12. (In Japanese)

Murai, H. (1983). Earthquakes, Tsunamis and Coastal forest prevent disaster, disasters in Nihonkai-Chubu earthquake tsunami, Ringyo-gijyutu (Forest technology), No. 501, pp.15-18. (In Japanese)

Shuto, N. (1987). The effectiveness and limit of tsunami control forests, Coastal Engineering in Japan, Vol. 30, pp.143-153.

Shuto, N. (1992). Tsunami intensity and damage, Tsunami engineering research report, Vol. 9, pp.101-136. (In Japanese)

Tanaka, K. (1998). Survey the forests density, 50 methods for survey forest, Japan forest Technical Association, pp.74-77. (In Japanese)

FLUID FORCE ON VEGETATION DUE TO TSUNAMI FLOW ON A SAND SPIT

KENTARO IMAI[1] AND HIDEO MATSUTOMI[2]

[1] *Department of Production and Civil Engineering*
Graduate school of Engineering and Resource Science, Akita University
[2] *Department of Civil and Environmental Engineering, Akita University*

One of the features of the 1998 Papua New Guinea tsunami is that a maximum tsunami height of 14.8 m was observed on the vegetated sand spit of Sissano lagoon that faced the tsunami source. This tsunami caused a large number of human casualties. The coastal vegetation in the western Pacific Ocean countries attracts attention from an economical and environmental point of view as a tool of tsunami countermeasures. Fluid force on vegetation mainly consists of drag force F_D, inertia force F_M, and linear wave making resistance force F_W. In this paper, the ratios of these forces and corresponding coefficients are examined. It is clarified that F_M reaches 50 % of the maximum drag force F_{Dmax} at the early stage of inundated flow, and that F_D and F_W are dominant at the quasi-steady state after the early stage. The drag coefficient C_D is found to be 0.9-1.5, the mass coefficient C_M is 1.5-2.5, and the linear wave making resistance coefficient θ is 0.02-0.07. C_D and C_M change with the same tendency as those of group of piles in open channel flows, and they decrease as vegetation density κ increases.

1 Introduction

One of the features of the 1998 Papua New Guinea tsunami is that a maximum tsunami height of 14.8 m was observed on the vegetated sand spit of Sissano lagoon faced the tsunami source (Matsutomi et al., 2001). The tsunami caused a high rate of human casualties and had the following specific characteristics: 1) The maximum tsunami height occurred on the sand spit, and 2) The sand spit was rich in vegetation.

Recently, in the western Pacific Ocean countries, the coastal vegetation attracts attention as a means of tsunami countermeasures from the economical and environmental points of view. Fluid force on vegetation consists of drag force, inertia force, linear wave making resistance force and so on. This study aims to examine these fluid forces on vegetation by an experimental method in order to evaluate the resistance characteristics of the coastal vegetation and to estimate the reducing efficiency of tsunami energy caused by the coastal vegetation.

K. Satake (ed.), Tsunamis: Case Studies and Recent Developments, 293-304.

2 Experiments

Tsunami was experimentally modeled by flows generated by rapidly pulling up a gate. The experimental setup is shown in Figure 1. A rectangular, glass-walled flume of 0.3 m wide, 0.5 m high and 11.0 m long with a horizontal steel bed was used. A slope of 1/26 was installed at a distance of 2.0 m from the gate. Sand spit with a cross section of an arc shape was set to a tangent to the slope and a lagoon that has a constant water depth was located behind the sand spit. The still-water levels on both sides of the sand spit were set equal. A weir was installed at the downstream end of the flume in order to adjust the constant water depth in the lagoon so that the flows can overflow. The model tree consisted of a trunk with a diameter of 0.24 cm and foliage with a void ratio of 0.7. The model trees were arranged in both staggered and grid patterns on the sand spit. The vegetation density κ is defined as the ratio of the total cross section area of the trunks to the vegetation area. Figure 2 shows an example of sand spit model with vegetation at κ=1.0 % and a grid set pattern. An example of tree model (κ= 1.0 %) arranged in the grid pattern is shown in Figure 3. Capacitance-type wave gauges and propeller-type current meters were used to measure the inundation depth and the current velocity on the sand spit, respectively.

The arrangement of the instruments and the definition sketch of the symbols are shown in Figure 4. In this Figure, h_G is the ground height, h_0 is the constant water depth offshore, h_1 and h_2 are inundation depth on the sea and lagoon side respectively, h_4 is the constant water depth in the lagoon, u_1 and u_2 are the current velocities at the same place and time as h_1 and h_2 respectively. Experimental conditions are summarized in Table 1, where h_U is the initial water depth in the upstream region of the gate. When h_U is deeper than 16 cm, a strong bore occurs offshore (ΔH is the theoretical bore height), where the dimensionless bore height $\Delta H/h_0$>0.62 (Stoker, 1948). Furthermore, when h_U is over 18 cm, inundation depth becomes longer than vegetation height. About vegetation density conditions correspond to the vegetation thickness dn = 0 to 400 (d is diameter of trunk, n is number of tree per alongshore distance of 1 m), where dn=400 represents an actual situation (Shuto, 1987).

A scale of 1/200 is assumed in the experiments. These conditions correspond to tsunamis with the wave period of 7.5-9.1 minutes in the real scale. This wave period is almost the same as that of the Papua New Guinea tsunami (Matsutomi et al., 2001). Figure 5 shows a time history of experimental data. The experimental wave period T in Figure 5 was determined by Eq. (1).

$$T \quad 8L_U / \sqrt{gh_0} \qquad (1)$$

where L_U is horizontal distance from the upstream end of the flume to gate, and g is the acceleration due to gravity.

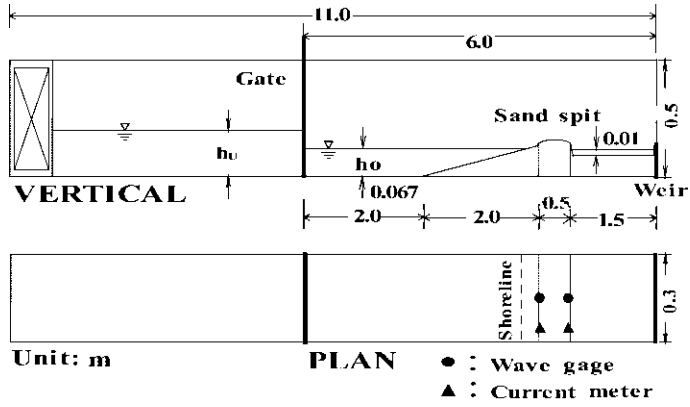

Fig. 1. Experimental flume.

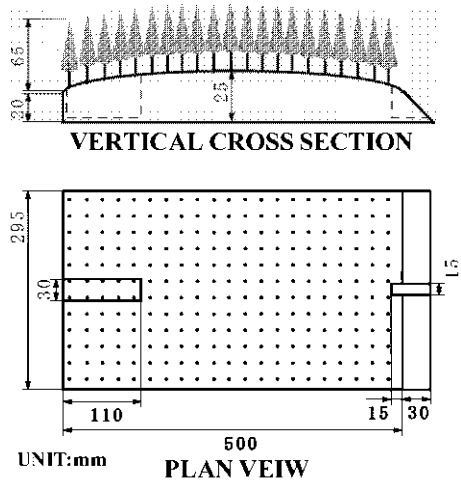

Fig. 2. An example of sand spit model (κ=1.0%).

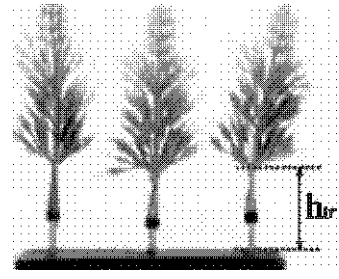

Fig. 3. An example of tree model.

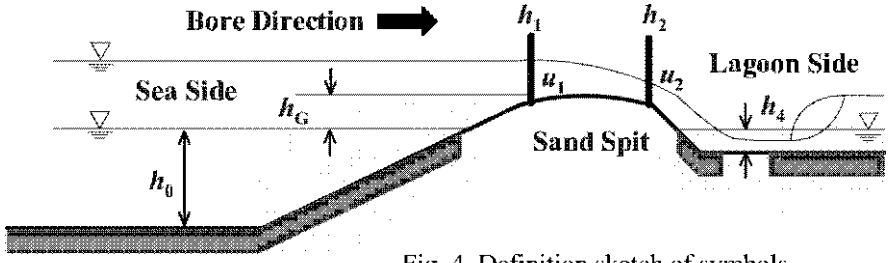

Fig. 4. Definition sketch of symbols.

Table 1. Experimental conditions.

h_U (cm)	11～21
h_0 (cm)	6.67
h_4 (cm)	1.0
h_G (cm)	1.5
S	1/26
L (cm)	10, 30, 50
(%)	0, 0.5, 1.0, 1.5
Pattern	Staggered, Grid
Leaves	h_{tr}=1.5cm, =0.7

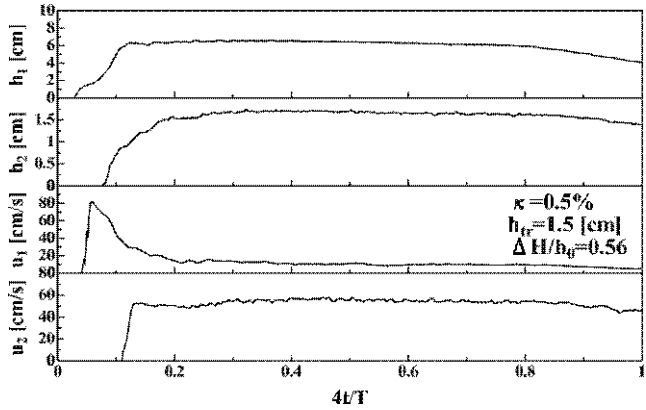

Fig. 5. Time history of experimental data.

3 Fluid force on vegetation

3.1 EQUIVALENT DIAMETER

When calculating drag force, it is necessary
perpendicular to inundation flow. It is difficult to evaluate vegetation projection area, however, because the structures of vegetation consisting of trunk, branch, and leaves

are extremely compact and difficult to simulate. Therefore, in order to simply estimate the vegetation projection area, vegetations are replaced with cylinders.

In this case, the volume of vegetation under water surface is replaced with an equivalent volume of cylinder, and the vegetation projection area is replaced with an equivalent cylinder projection area. The relationship between the diameters of the vegetation and the equivalent cylinder is given in Eq. (2).

$$\frac{\pi d'^2}{4} h \quad (1-\lambda)\cdot b_w^2 \cdot (h - h_{tr}) \quad \frac{\pi}{4} d^2 h_{tr} \tag{2}$$

where d is the equivalent diameter, h is the inundation depth, b_w is the width of foliage and h_{tr} is the height of trunk from the ground surface to the bottom of foliage. In this equation, the volume of vegetation is reflected but the vegetation projection area is not precisely accounted for. Therefore, further development on this equation is being considered.

3.2 FLUID FORCE

In this study, the concept of oscillation of floating structure (Takayama et al., 1980) is applied to the shaking of tree foliage. It is necessary, however, to modify the existing method of oscillation of floating structure in order to apply it to the vegetation foliage. The wave making resistance force F_W is proportional to both current velocity u and object velocity u_{ob} as follows:

$$F_W \quad \theta(u + u_{ob}) \tag{3}$$

where is the linear wave making resistance coefficient.

In this experiment, the current velocity u was five times higher than the object velocity u_{ob} which is measured using video camera (30 frame/s), and therefore, it was decided to neglect u_{ob} in this study.

The linear wave making resistance force resulting from the oscillation is dependent on the surface area of the movement direction. Therefore, by representing the surface area with the equivalent diameter and the inundation depth, Eq. (3) could be written as follows:

$$F_W \quad \frac{\pi}{2} \rho \theta' d' h u \tag{4}$$

where θ is linear wave making resistance coefficient for vegetation, which is different from the conventional linear wave making resistance coefficient.

The factors affecting wave making phenomena are considered to be the ratio of the stiffness of the trunk to that of the branch of vegetation, the distribution of leaves, and the deformation of branches and leaves (i.e., the change in projection area) due to the current. In order to facilitate the evaluation in the present study, however, these factors

were combined into one factor: θ. It should be also noted that the vegetation model in the experiment had one type only and the void ratio of the foliage was very small compared to real trees. Tbe fluid force on the vegetation is evaluated using Morrison's Equation (Morrison et al., 1950) for rigid cylinders assuming F_w with a uniform distribution along the depth.

The fluid force dF in an infinite depth dy can be represented as Eq. (5),

$$dF = \frac{1}{2}\rho C_D d' u|u|dy + \frac{\pi}{4}\rho C_M d'^2 \frac{\partial u}{\partial t}dy + \frac{\pi}{2}\rho\theta' d' u dy \tag{5}$$

where C_D is drag coefficient, C_M is mass or inertia coefficient.

Assuming that fluid force is distributed equally on the vegetation model cylinders in the control volume, Eq. (6) can be obtained.

$$\Sigma dF = \frac{1}{2}\rho N C_D d' u|u|dy + \frac{\pi}{4}\rho N C_M d'^2 \frac{\partial u}{\partial t}dy + \frac{\pi}{2}\rho N\theta' d' u\, dy \tag{6}$$

where N is the number of vegetation model cylinders in the control volume.

If Eq. (6) integrated over the depth is applied to the equation of motion in shallow water theory, Eq. (7) can be obtained.

$$\frac{\partial q}{\partial t} + \frac{\partial}{\partial x}\left(\frac{q^2}{h}\right) + gh\frac{\partial h}{\partial x} + \frac{gn_0^2}{h^{7/3}}q|q| + \frac{1}{2}N_U d' h C_D \frac{q|q|}{h^2} + \frac{\pi}{4}N_U d'^2 C'_M\left(\frac{\partial q}{\partial t} + \frac{q}{h}\frac{\partial q}{\partial x}\right) + \frac{\pi}{2}N_U\theta' q d' \tag{7}$$

where q ($=hu$) is tbe discharge flux per unit width, N_U is the number of vegetations per unit area, $C_M = C_M - 1$, n_0 is Manning's roughness coefficient at $\kappa = 0\%$.

3.3 METHOD OF ANALYSIS

The equation used for analysis is Eq. (7), where the unknowns are the three coefficients: C_D, C_M and θ. As in the conventional analysis method (Noji et al., 1993), the change of these coefficients is assumed to be very small for an infinite period of time. The hydraulic values u and h are measured from the experiment, and are defined by Eqs. (8) and (9).

$$u(t) = \frac{1}{2}\{u_1(t) + u_2(t)\} \tag{8}$$

$$h(t) = \frac{1}{2}\{h_1(t) + h_2(t)\} \tag{9}$$

Simultaneous equations of the unknown coefficients are written for each time interval Δt. By solving these equations, the time histories of each coefficient can be obtained. In the present study, the infinite time interval is set at $\Delta t = 0.01$ s.

When each fluid force in the right hand side of Eq. (7) is arranged as shown in Eqs. (8) and (9), the determinant of the simultaneous equations at a time t can be written as follows:

$$F(t) \quad C_D \hat{F}_D(t) \quad C'_M \hat{F}_M(t) \quad \theta' \hat{F}_W(t) \tag{10}$$

where,

$$F(t) = \frac{\partial q}{\partial t} \quad \frac{\partial}{\partial x}\left(\frac{q^2}{h}\right) \quad gh\frac{\partial h}{\partial x} \quad \frac{gn_0^2}{h^{7/3}}|q|q$$

$$C_D \cdot \hat{F}_D(t) = -\frac{1}{2} N_U d' h C_D \frac{q}{h}\left|\frac{q}{h}\right|$$

$$C'_M \cdot \hat{F}_M(t) = -\frac{\pi}{4} N_U d'^2 C'_M \left(\frac{\partial q}{\partial t} \quad \frac{q}{h}\frac{\partial q}{\partial x}\right)$$

$$\theta' \cdot \hat{F}_W(t) = -\frac{\pi}{2} N_U \theta' q d'$$

$\bar{t}$ is the time at which an evaluation is made. Rearranging the above equations into Eqs. (11) and (12), each coefficient can be obtained from Eq. (13).

$$\{F(\bar{t})\} = \{F(t - \Delta t) \quad F(t) \quad F(t + \Delta t)\}^T \tag{11}$$

$$[B(\bar{t})] \begin{bmatrix} \hat{F}_D(t-\Delta t) & \hat{F}_M(t-\Delta t) & \hat{F}_W(t-\Delta t) \\ \hat{F}_D(t) & \hat{F}_M(t) & \hat{F}_W(t) \\ \hat{F}_D(t+\Delta t) & \hat{F}_M(t+\Delta t) & \hat{F}_W(t+\Delta t) \end{bmatrix} \tag{12}$$

$$\{C_D \quad C'_M \quad \theta'\}^T_{\bar{t}} \quad \frac{1}{|B(\bar{t})|}[B(\bar{t})]^{-1} \cdot \{F(\bar{t})\} \tag{13}$$

4 Discussions

4.1 DRAG COEFFICIENT

Figure 6 shows the relationship between the drag coefficient C_D and $\Delta H/h_0$. The drag Coefficient is the time average value of the quasi-steady stage of tsunami flow. The increase of $\Delta H/h_0$ was accompanied by a small decrease in C_D. This is consistent with the relationship between C_D and Reynolds number on a single pile because the increase of $\Delta H/h_0$ means that of Reynolds number, and therefore the relationship of C_D and $\Delta H/h_0$ is in agreement with the conventional knowledge.

Coefficient C_D decreases as κ increases. This seems to be attributed to the relationship between the vegetation interval and the restoring distance of the wake. The value of C_D ranges between 0.9-1.5.

4.2 MASS COEFFICIENT

The relationship between the mass coefficient and $\Delta H/h_0$ is shown in Figure 7. C_M ($=1+C_M$) is the time average value in the early stage of the tsunami flow.

C_M shows a tendency to decrease when $\Delta H/h_0$ increases, in a similar manner to C_D. In the case of an independent pillar, the decrease of C_M with the increase of the ratio of depth to diameter h/d has already been confirmed by many previous experimental works (for example, Tsuchiya et al., 1974). In the present experiment, the equivalent diameter is about 1 to 7 times the trunk diameter. If the equivalent diameter is considered constant for every κ, and h/d is represented by $\Delta H/h_0$, then the decrease of C_M with the increase in $\Delta H/h_0$ matches the conventional results.

C_M decreases as κ increases. This is considered to be due to the relationship between the restoring distance of the wake and the vegetation interval. The vegetation of the front row disperses the inertia force, and therefore the inertia force on the following rows is reduced. The value of C_M ranges between 1.5-2.5.

4.3 WAVE MAKING RESISTANCE FORCE COEFFICIENT

Figure 8 shows the relationship between the linear wave making resistance coefficient and $\Delta H/h_0$. θ represents the time average value of the quasi-steady stage of tsunami flows. θ shows a tendency to increase with the increase in $\Delta H/h_0$ until the vegetation is completely submerged. After that the value of θ becomes fixed as θ cannot be applied to completely submerged objects. θ shows a tendency to decrease as κ increases. This is attributed to the very narrow interval between the trees in the experiment of κ=1.0-1.5 %, and therefore the vegetation behaved as one unit which restrains the shaking movement. θ ranges in the experiment from 0.02 to 0.07.

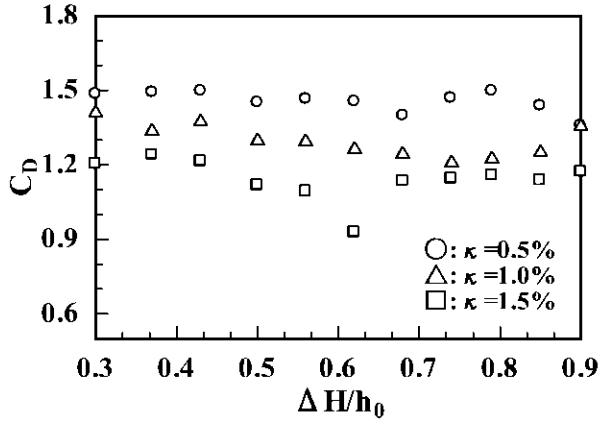

Fig. 6. Relationship between C_D and $\Delta H/h_0$.

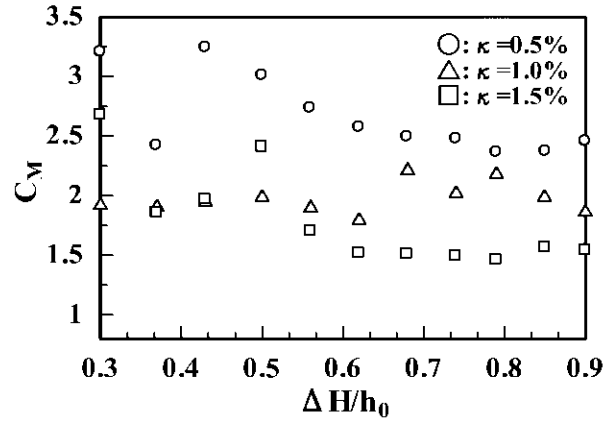

Fig. 7. Relationship between C_M and $\Delta H/h_0$.

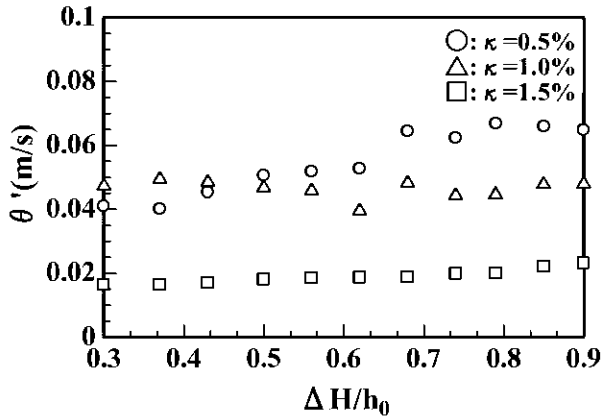

Fig. 8. Relationship between θ and $\Delta H/h_0$.

4.4 RATIOS OF THE FLUID FORCES ON VEGETATION

4.4.1 *Fluid force without linear wave making resistance force*

The drag force F_D and the drag force without wave making resistance force F_{DWW} are shown in Figure 9 for the case of $\Delta H/h_0 = 0.62$ and $\kappa = 1.0$ %. F_{Dmax} is the maximum drag force in this case. It is noted that the value of C_D is 1.53 for F_{DWW} and 1.26 for F_D. F_{DWW} is about 20 % larger than F_D, and F_W is slightly less than 20 % of F_{Dmax}. The above ratios apply only to the steady state and change after that as can be seen in the figure. This is because the oscillation velocity of the vegetation is replaced with the current velocity (refer to Eq. (4)). However, for the evaluation of the fluid force on the vegetation, the important phases are the early stage and the quasi-steady stage of

inundated flow, and thus the above ratios can be applied. After these stages, a method adopted more reasonable velocity in oscillation speed should be used.

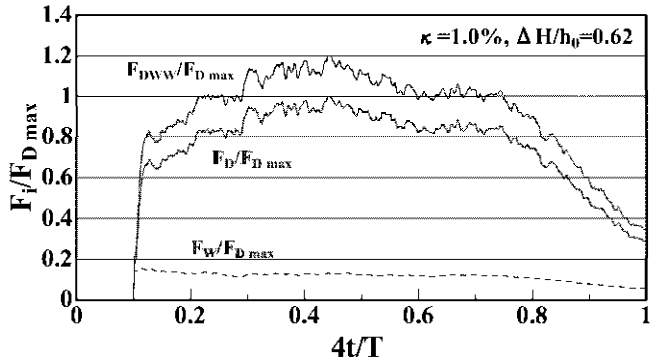

Fig. 9. Time histories of F_D and F_{DWW}.

4.4.2 *Variation of each fluid force with time*

Variation of each fluid force with time is shown in Figures 10 (a), (b) and (c) for the cases of $\Delta H/h_0 = 0.62$, $\kappa = 0.5$, 1.0, and 1.5 % respectively. The time history of each fluid force is slightly different. However, as the previous results (for example, Matsutomi and Ohmukai, 1999), the main fluid force is F_D, and the inertia force F_M reaches its maximum value at the front of inundated flow. And although it might exceed the value of F_{Dmax} in some instance depending on κ, F_M is in average about 40-50 % of F_{Dmax}. On the other hands, F_W decreases with the increase of κ. The reason is that the vegetation interval becomes narrower as κ increases, and as a result the shaking of foliage is restrained causing F_W to decrease.

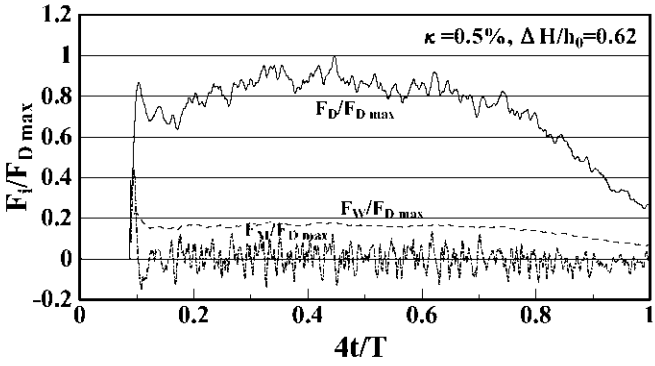

(a) κ=0.5%

Fig. 10. Variation of each fluid force with time.

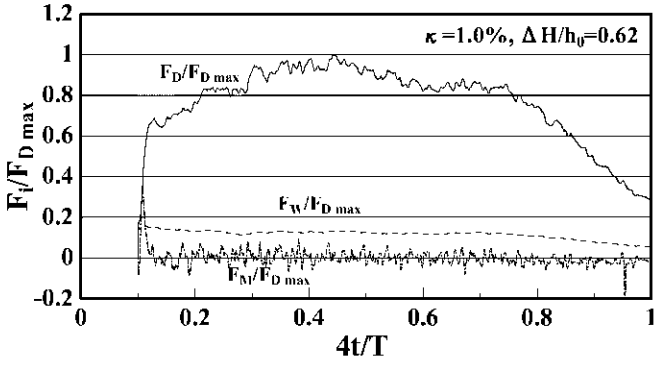

(b) κ=1.0%

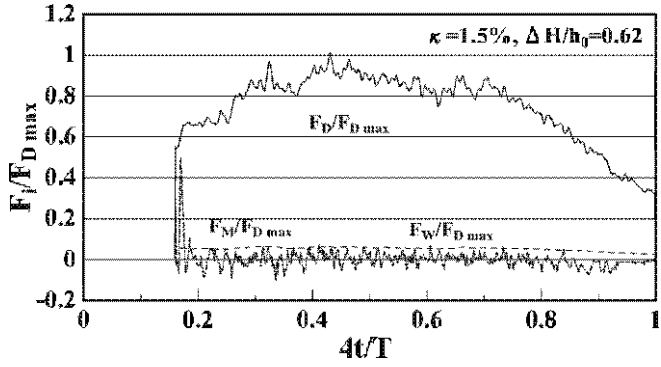

(c) κ=1.5%

Fig. 10. (cont'd) Variation of each fluid force with time.

5 Conclusions

1) The inertia force F_M reaches 50 % of the maximum drag force F_{Dmax} at the early stage, and after that the drag force F_D and the linear wave making resistance force F_W become dominant.
2) The ratio of F_D to F_{Dmax} is about 0.2. Therefore F_W cannot be ignored.
3) The drag coefficient C_D is 0.9-1.5, the mass coefficient C_M is 1.5-2.5, the linear wave making resistance coefficient θ is 0.02-0.07.
4) C_D and C_M change with the same tendency as those of a group of piles in an open channel flow.
5) C_D and C_M decrease as κ increases.

References

Matsutomi, H., Y. Kawata, N. Shuto, Y. Tsuji, K. Fujima, F. Imamura, M. Matsuyama, T. Takahashi, N. Maki and S. S. Han: Flow Strength on Land and Damage of the 1998 Papua New Guinea Tsunami, Advances in Natural and Technological Hazards Research, Vol.18, Kluwer Academic Publishers, pp.179-195, 2001.

Shuto, N.: Effectiveness and limit of tsunami control forests, Proceedings of Coastal Engineering, JSCE, Vol.32, pp465-469, 1985. (in Japanese)

Stoker, J. J: The formation of breakers and bores, Communications on Pure and Applied Mathematics, Vol. 1, pp. 1-87.1948.

Takayama, T., T. Nagai, O. Kikuchi and K. Moroishi: Motions and Mooring Forces of a Rectangular Floating Body in Wave (1st report), REPORT OF P.H.R.I, pp71-103, 1980. (in Japanese)

Morison, J. R, M. P. O'Brien, J. W. Johnson and S. A. Schaaf : The force exerted by surface waves on piles, Petroleum Transaction, AIME, Vol. 189, pp.149-154.1950.

Noji, M., F. Imamura and N. Shuto: Numerical simulation of movement of larger rocks transported by tsunamis, Proceedings of Coastal Engineering, JSCE, Vol.40, pp176-180, 1993. (in Japanese)

Tsuchiya, Y. and M. Yamaguchi: Total wave force on a vertical circular cylindrical pile, Proceedings of the Japan society of civil engineers, pp.11-21, 1974. (in Japanese)

Matsutomi, H. and T. O hmukai: Laboratory Experiments on fluid force of tsunami flooded flows, Proceedings of Coastal Engineering, JSCE, Vol.46, pp336-340, 1999. (in Japanese)

HYDRO-ACOUSTIC MONITORING ON THE KAMCHATKA SHELF: A POSSIBILITY OF EARLY LOCATION OF OCEANIC EARTHQUAKE AND LOCAL TSUNAMI WARNING

E. V. SASOROVA[1], B. W. LEVIN[1], V. E. MOROZOV[1] AND I. N. DIDENKULOV[2]

[1] *Shirshov Institute of Oceanology, Russian Academy of Sciences, 36 Nakhimovsky prosp. Moscow, 117851, Russia*
[2] *Institute of Applied Physics RAS, Nizhny Novgorod, Russia*

Local tsunami warning remains a difficult task. A possible way to solve this problem is to process acoustic signals, which appear in the water at the critical stage of a submarine earthquake preparation. An earthqua
zone is characterized by increasing micro-crack density. This process generates acoustic signals (AS) with frequencies in the range 10-100 Hz. The AS are decaying fast in the solid rocks but in the ocean these signals propagate far due to weak attenuation of the signal in incompressible water. We analyzed the observation data obtained by high-quality hydro-acoustic receiving array of hydrophones at the Kamchatka Pacific shelf and the local Kamchatka earthquake catalog data. Two types of acoustic signals were detected: the micro-earthquakes (MEQ) and the seismic rumble, which appears just before the main shock. The duration of MEQs was about 3-4 seconds, and their frequency was in the range 40-75 Hz. It was shown that the MEQ sources had shallow focuses, while the earthquake focus may locate significantly deeper. It was revealed that acoustic signals of MEQ occurred before oceanic EQ with M>4 with advancing about 10 - 100 minutes. The results of the study show that the monitoring of hydro-acoustic signals in the ocean may be used for the early location of oceanic EQ preparation zone and for improvement of the local tsunami warning system.

1 Introduction

Local tsunami warning remains a difficult task. Local tsunamis are generated in the ocean at a distance not exceeding 100 km from the coastline, and their propagation time from the source to the coast is less than 1 hour. This makes tsunamis extremely dangerous. The locations of tsunamigenic EQ epicenters (EQ with magnitudes M_S > 6.0) near the Kamchatka Peninsula over a period of 50 years (from 1950 to 2000) are presented in Figure 1.

The data were obtained from the Expert Tsunami Database for the Pacific Ocean (ETDB/PAC) collected and supported by the Novosibirsk Tsunami Laboratory of the

K. Satake (ed.), Tsunamis: Case Studies and Recent Developments, 305-317.

ICMMG SB RAS (ETDB/PAC, 2003). All EQ epicenters, which are marked by solid circles with different diameters (depending on the EQ magnitude), are located in the near-shore zone (less than 70 km offshore). Solid black line in Figure 1 is the oceanic tectonic plate boundary.

The information on these EQs (dates, coordinates, depth, magnitude and maximum run-up) is presented in Table 1. The rightmost column shows minimum distance to the coastline (letters C/L are used for the EQs that occurred just under the coastline). Mean offshore distance for all listed events is slightly less than 18 km. The bottom part of the table contains rough estimates of tsunami propagation velocity and tsunami travel time for the mean distance. It is impossible to prepare the warning message both theoretically and practically for near-shore seismic events. The situation is similar for the Pacific coast of the Kuril Islands.

Propagation times of the seismic signals, acoustic signals and tsunami waves for the local events are shown in Figure 2. Vertical axis corresponds to time, and the zero point corresponds to the origin time of the seismic events; the negative part of the time axis is related to the time interval before the earthquake (at critical stage of the EQ preparation). The horizontal axis corresponds to the distance between the EQ epicenter and the observation point. Thus, according to rough estimates, tsunami waves would propagate a distance of 30 km in 300 seconds (a distance of 50 km would be passed in 500 s). It is clear that the preparation of tsunami warning messages based either on tide-gauges or seismic information is impractical. A possible way to solve this problem is to detect the signals preceding the main shock for near-shore EQs, i.e. to get the indications of the EQ preparation in the critical stage.

Table 1. The tsunamigenic EQs near Kamchatka Pacific coast line (1950-2000, M>6.0).

Date	Lat	Lon	Depth	Ms	Hmax	Dist.
			km		m.	km.
04.11.52	52.75	159.5	30	8.2	20	43
17.03.53	50	156.4	70	6.2	3	43
04.05.59	53.4	159.6	30	7.7	2	C/L
10.01.61	50.02	156.2	68	7.1		32
22.11.69	57.73	163.6	8	7.3	15	17
15.12.71	56.02	163.2	26	7.8	0.47	5
28.02.73	50.48	156.6	60	7.5	1.5	20
17.08.83	55.79	161.3	93	6.7	0.02	C/L
28.12.84	56.21	163.4	19	7	0.02	1
08.06.93	51.2	157.8	60	7.2	0.5	29
13.11.93	51.94	158.6	35	7	0.1	25
05.12.97	54.83	162	34	7.7	1.5	C/L
The mean distance between the EQ epicenter and coastal line is 17.92 km. The mean ocean depth in epicenter zone is 160 m The mean travel time is 7.5 min C/L denotes coastal line						

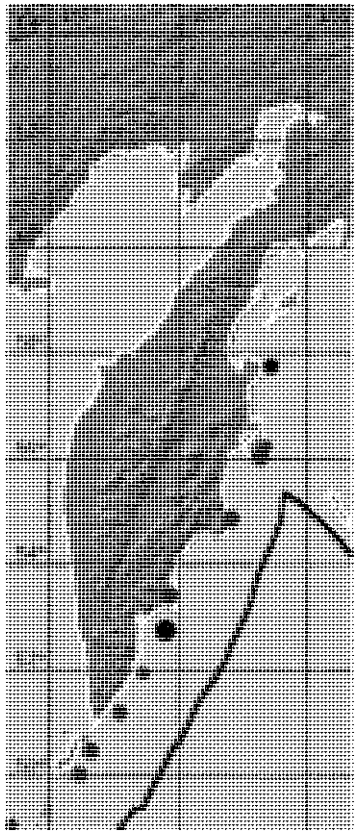

Fig. 1. Tsunamis caused by earthquakes near the Kamchatka Pacific coastline (years 1950-2000, M > 6.0). Thick solid line is the ocean trench line; solid circles are the epicenters of the earthquakes.

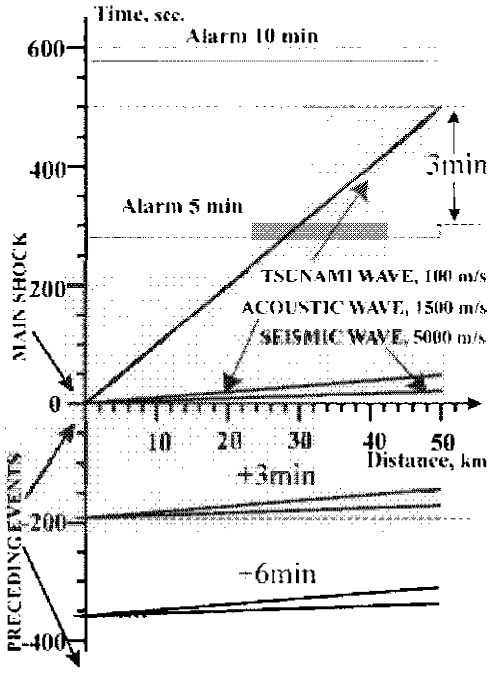

Fig. 2. Sketch of wave propagation from the submarine seismic source.

2 Hydro-acoustic data

Recently, we had an opportunity to analyze the signals recorded by an array of the "Agam" type (developed in the "Morphyzpribor" Institute, St. Petersburg, Russia), located near the eastern coast of Kamchatka Peninsula in the Pacific Ocean. The array was deployed in the near bottom water layer; its size was 100 m × 17 m (Demianovich, 1998; Karlik, 2002). Several hundreds of hydrophones were grouped in separate blocks (channels, clusters) that allowed us to detect the direction to the source from the time lags of signal arrivals to different channels.

In the first stage, we had a possibility to analyze the data of the 1998-1999 "ATOC" International program (Acoustic Thermometry of the Oceanic Climate). This allowed us to detect and study the acoustic signals from the oceanic EQ preparation zone. The data contained 162 digital records obtained during the period from July 12, 1998 to March 21, 1999. The length of each hydro-acoustic record (HAR) is 1323.73 s (slightly greater than 22 min). Every day there were up to 6 scheduled records (performed at 2:54:20, 6:54:20, 10:54:20, 14:54:20, 18:54:20, and 22:54:20 GMT). However, on some days there were no records and on other days there were less than six sessions. The sampling rate was 300 per second; the instrumental band-pass filter isolated the frequency range from 40 to 110 Hz. The records were made in different seasons, daytime and weather conditions; therefore we could examine the acoustic background. During the experiment there were 14 working channels of the array. The total observational period was 276 days, and the total length of records was 3564 minutes or 2.475 days. During this observational period, 3058 seismic events occurred in the Kamchatka area (48°-60° N, 151°-173° E) according to the Regional Kamchatka Earthquake Catalog. The main goal of our study was the comparison of seismic and hydro-acoustic signals (HAS) and detection of the sources of the acoustic signals.

In the second stage, we analyzed reconstructed archive analog data, which were transformed to the digital form. The length of the continuous records was approximately 24 hours.

3 Analysis of hydro-acoustic signals and Kamchatka Regional Earthquake Catalog

We used the Kamchatka Regional Earthquake Catalog (Kamchatka REQC) for a comparative analysis and prepared the diagram for daily acoustic observation sessions (examples are shown in Figures 3a, 3b, and 3c for October 20, 24 and 28, 1998, respectively). Horizontal axis corresponds to time (in hours), the vertical axis corresponds to the EQ energetic class. Solid vertical lines with arrows at the top denote EQs, rectangles show the sessions, during which hydro-acoustic observations (records) were made.

We found one case of complete time coincidence between the seismic event that started in the source at 03:15:46 and the HAS record (record of 20.10.1998, first session continued from 02:54:20 till 03:16:24, Figure 3a). The EQ arrival time on the HARs coincided with the very end of the session. According to the Regional Catalog, the energy class of the EQ was K = 10.3, the depth was 119 km, the horizontal distance from the epicenter to the receiving array was 50.4 km, and the distance from the hypocenter was 129.23 km. Relation between an energy class K and magnitude M is expressed by simple equation $K = 1.5\,M + 4.6$.

There were also a few events, when EQs occurred soon after the end of the record. In all these cases, we found series of clear records of signals generated from the sources located in the near epicenter zones, which arrived before the main shock.

We identified two types of signals preceding the main shock. The first type is the MEQ. Acoustic signals were generated in the near-epicenter zone. MEQs have very sharp amplitude variations within the first 1-2 seconds (20 times greater than the amplitude of the background noise), its frequency range was 40-75 Hz and duration was approximately 3-4 sec. Table 2 presents the data for 9 MEQs, detected during the first recording session of 20.10.98. Initially, the frequency of the high-amplitude part of the signal is 60-75 Hz, later the amplitude and frequency decrease (frequency decreases down to 40-50 Hz).

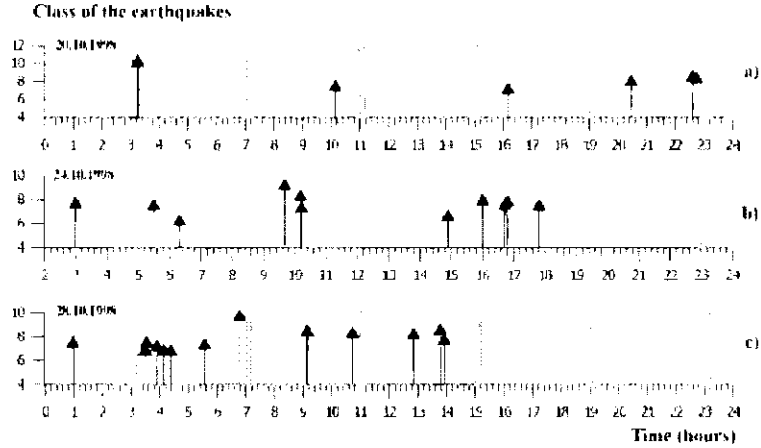

Fig. 3. The Regional Catalog and timetable of the digital records on the time axis: Fragments for October 20 (a), October 24 (b), and October 28 (c), 1998.

Table 2. MEQs and the seismic rumble time sequence in the hydro-acoustic record (on October 1998, the first observation session from 02:54:20 up to 03:16:24). MEQs and the seismic rumble parameters.

Time sequence of events	Arrival time (h:min:sec)	Estimation tS-tP, sec	Source depth estimation for MEQ (under the ocean bottom), m	Signal frequency Hz	Signal source size estimation, m
Beginning of the session	02:54:20	-	-	-	-
MEQ 1	03:03:39	0.083	191(207)	65	0,59
MEQ 2	03:05:47	0.093	214(232)	59	0,71
MEQ 3	03:07:35	0.103	237(258)	61	0,67
MEQ 4	03:09:01	0.143	329(358)	58	0,74
MEQ 5	03:10:03	0.07	161(175)	73	0,47
MEQ 6	03:11:6	0.08	184(200)	75	0,44
MEQ 7	03:13:12	0.08	184(200)	55	0,83
MEQ 8	03:14:24	0.057	131(143)	62	0,65
MEQ 9	03:15:46	0.087	200(218)	71.5	0,49
Rumble arrival	03:16:05	-	-	43	1,34
End of the session	03:16:24	-	-	-	-

The second type of detected acoustic signals is high-frequency acoustic rumble (30-40 Hz) with amplitudes 4 times greater than the background level. The rumble appears just before the EQ (see Table 2) and it merges with the seismic signal from the main shock.

The estimated values of the destruction zone size for every MEQ, calculated from the signal frequency with maximum amplitude are given in Table 2. Figure 4a shows a spectrogram of the HAS record on October 20,1998 (first session from 02:54:20 to 03:16:24). Figure 4b is the original digital record for the case, when the HAR and the EQ coincided. In the spectrogram, the intensity of the black color at each point shows the energy of the respective frequency at the given time moment. There are several sections where the MEQs, preceding the main shock, are clearly seen. Nine of such sections are shown in Figures 4a and 4b. The high-frequency rumble distinguished at the end of the record (Figure 4b) is also shown as a separated section in Figure 5f.

Figure 5 shows five fragments of the same record for the first channel. These fragments with equal length (1000 samples approximately 3.3 sec long) contain MEQs (5a, 5b, 5c, 5d, 5e), and high-frequency rumble (5f), which appeared just before the main shock.

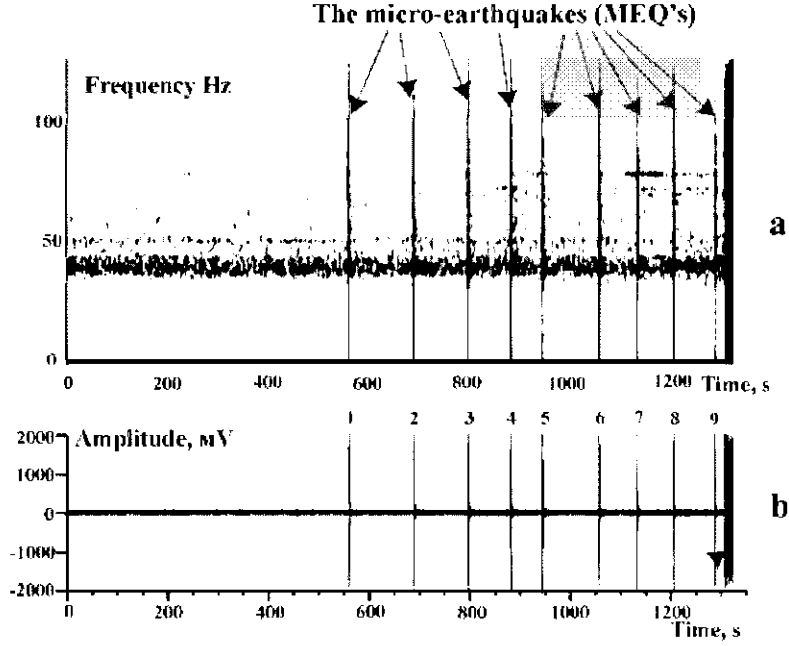

Fig. 4. Coincidence of the hydro-acoustic observation session (on October 20 1998 from 02:54:20 up to 03:16:24) and earthquake (October 20 1998, origin time 03:15:46, Coordinates: 52.5060 N, 158.0690 E; H–119km, M–4.6 (K–10.3)). Spectrogram of the HAR is shown in Figure 6a, and HAR is shown in Figure 6b.

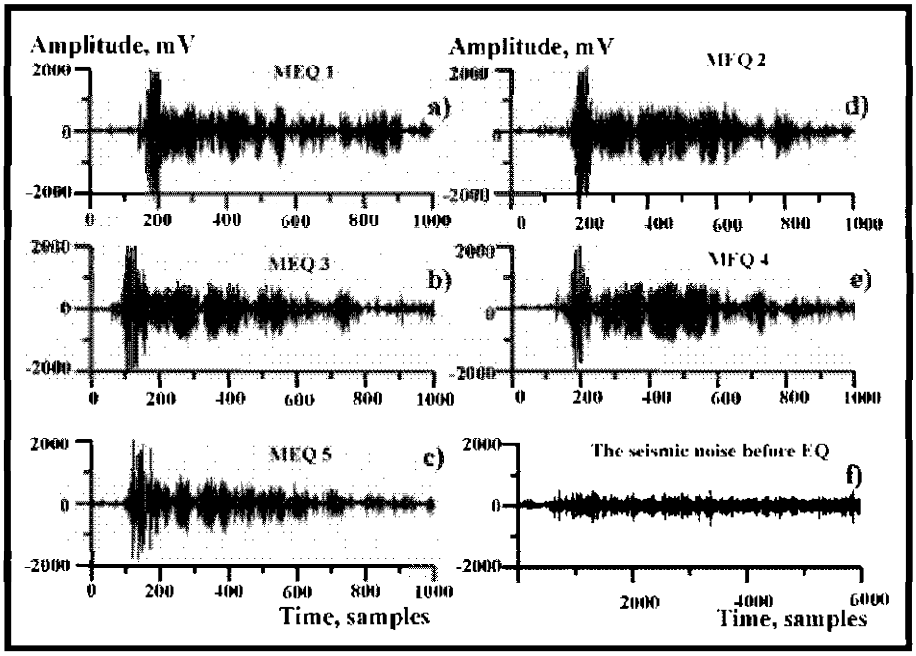

Fig. 5. Fragments of HAR from the first channel (observation session on October 20, 1998 from 02:54:20 up to 03:16:24): five MEQs and seismic rumble were detected. Horizontal axis of each fragment corresponds to time (samples), vertical axis corresponds to amplitude (mV). Duration of every fragment is approximately 3.3 s.

All of the 14 channels of the array have reliably recorded all MEQs. The character of the signal from the same MEQ at different channels was almost identical. Only the arrival times to the channels were different that allowed us to identify the direction towards the signal source (Morozov, 2002). The MEQs extracted from the record of October 20, 1998 and the epicenter of the main shock were located in the same direction in the line of the horizontal axis of the array.

Only compression waves propagate in water. At the water/bottom boundary, transverse waves propagating in solid medium convert into compression waves in water. The difference in the arrival times of these waves to the receiving array enables us to estimate the distance between the MEQ focus and the bottom area, where these waves are radiated into the water (in the water all waves propagate with equal velocity). Table 2 shows that the difference in the arrival times between the P-wave and transformed S-waves is about 0.1 sec. Thus, we can conclude that the MEQs did not occur in the near hypocenter zone, but they happened in the near-bottom zone. This table presents estimated distances between the source of each MEQ (the event of October 20, 1998) and the ocean bottom.

The farther EQ epicenter is located from the array, the more significant character of the HAS change. In these cases seismic signals will arrive at the water-bottom boundary with significant decay in the solid medium. Acoustic signals at the solid-liquid boundary will be generated on the whole denoted area. These signals will propagate in water almost whitout attenuaton and then after superposition will be registered by acoustic receivers. Thus MEQs on HAR will not be so sharp as shown in Figure 5, tbey will have trapezoidal shapes.

In those cases when the EQ started several tens of minutes after the end of the observation session it was possible to detect from hydro-acoustic records only the MEQs preceding the main shock. On February 5, 1999, we had six observation sessions. Eight EQs occurred on this day, but none of them happened between the second and third observation sessions (time period from 07:16:24 to 11:54:20). Spectrograms for all sessions of this day are shown in Figure 6a. The seismic events from the Kamchatka Regional Earthquake Catalog and the digital records superposed on the same time axis as rectangles are shown in Figure 6b. The MEQs are clearly seen in all spectrograms except for the record that started on 6:54:20 A.M. After the termination of this session, no EQs occurred for more than four hours. The analysis of other records, preceding EQs, gives us similar results. The MEQs were usually distinguished in the hydro-acoustic records, if the time interval between the record termination and the EQ start did not exceed three hours.

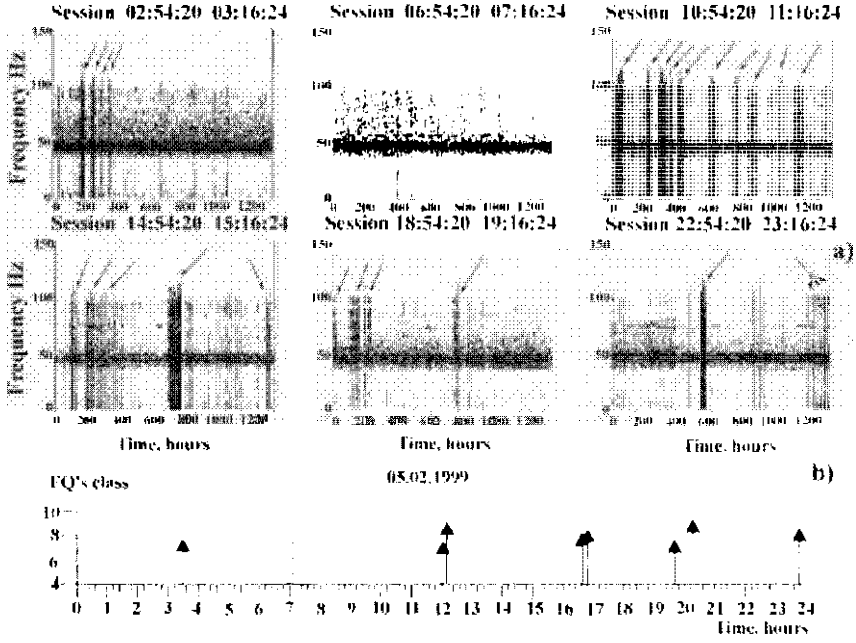

Fig. 6. Six spectrograms for six observation sessions (a) and the local catalog fragment and observation sessions on the time axis (b); February 05, 1999.

Now let us consider the results of processing the records of the second type of hydro-acoustic data. The records are reconstructed from the archive analog data transformed to the digital form. The length of the continuous records was approximately 24 h (computer memory requirements for operation with such data are approximately 4 Gb). The Pacific coast of the Kamchatka Peninsula is a very active seismic region. About ten EQs on average per day occur in this region. Thus, the study of such long continuous records is very informative. Figure 7 shows six EQs that took place from May 12, 1988 to May 13, 1988 (24 hours) near the pacific coast of Kamchatka. They coincided in time with the HAR. The information on these EQs is presented in Table 3. The epicenter of each EQ marks by circle and digit, which corresponds to the EQ number in Table 3. Black circles mark the epicenters of the EQs that were preceded by the series of MEQs detected from HAR. All these EQs occurred under the sea bottom and the signals generated by MEQs didn't decay completely before their arrival to the water/bottom boundary. After this the signals propagated in water over sufficiently long distance (up to 450 km) practically without attenuation.

The epicenters of the EQs marked by white circles were located under the Kamchatka Peninsula far from the sea. We failed to find the signals generated by MEQs from HAR of these EQs. Probably, we could do it if we used the digital records of the ground-based seismic station.

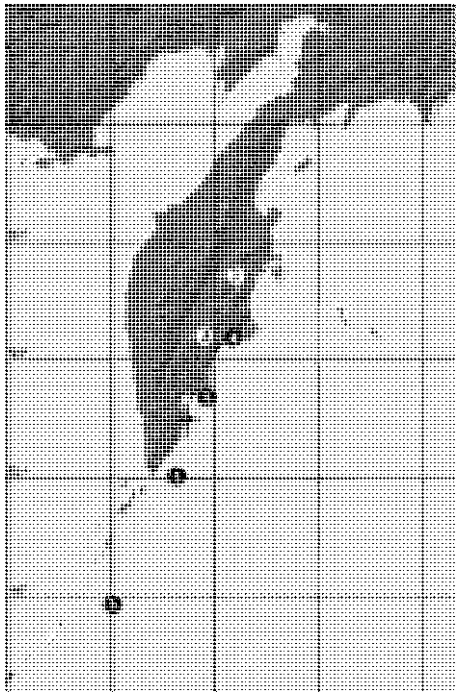

Fig. 7. The EQs on Kamchatka region from May 12 1988 to May 13 1988 (24 hours), which corresponded in time to series of HARs. Black circle - the epicenter of the EQ, which was preceded by series of MEQs.

Table 3. Six EQs from May 12, 1988 to May 13, 1988 (24 hours) near the Pacific coast of Kamchatka.

	Date	H	Min.	Sec.	Lat.	Long	Dep. km	Mb	Source
1	1988 05 12	14	11	57.1	50.96	158.07	40	4.5	KREQC*
2	1988 05 12	15	7	5.3	56.16	161.06	133	4.0	KREQC
3	1988 05 12	15	13	41.6	54.49	159.46	157	4.0	KREQC
4	1988 05 13	3	20	41.6	54.63	161.04	89	4.5	KREQC
5	1988 05 13	9	0	28.4	52.96	159.94	44	4.3	KREQC
6	1988 05 13	5	44	10.2	47.69	155.08	33	4.8	NEIC

* KREQC- Kamchatka Regional Earthquake Catalog

A few seismic stations, belonging to the Kamchatka Regional Seismic Network, are located at the southeastern Kamchatka coast near the epicenter area of the EQ of October 20, 1998. We selected 3 stations, which are the nearest to the epicenter: GRL station is located in the area of Gorely Volcano, RUS is located in Russkaya Bay, and PET is located in Petropavlovsk-Kamchatski. These stations (Figure 8) transmit all regular seismic observations by radio channel to the central station where these data are digitized (with sampling frequency of 128 samples per second at the receiver). The records are stored in archives. We analyzed records from all three stations, which started at 00-00 GMT on October 20, 1998. A certain increase in the seismic activity occurred during a few minutes before the EQ but it was impossible to detect reliable micro-events. The most likely explanation is that the high-frequency seismic signals associated with respective MEQs decay in solid medium and become apparent only in water.

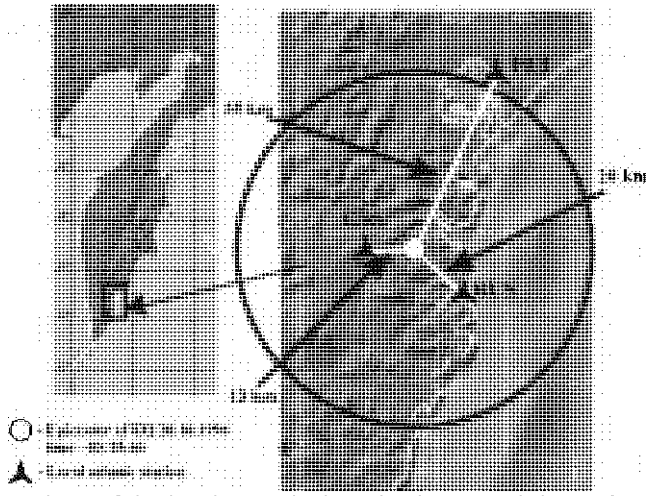

Fig. 8. Three stations of the local Kamchatka seismic network located not far from the epicenter for the event October 20, 1998 at 03:15:46.

4 Discussion

The obtained results are corresponding to some well-known physical approaches.

An increase of the mechanical stress in the Earth's crust, the process of the micro-crack appearance, and partial destruction of solid rocks lead to the acoustic waves generation. The periods of these waves depend on the source size, which are relatively small in comparison with the EQ destruction zone.

An attenuation of the plane sound wave in the medium follows the law: $I(x) = I_0 \cdot \exp(-\beta x)$, where β is coefficient of attenuation, I_0 is wave energy in the source, and $I(x)$ is wave energy at distance x from the source. The sound decay in water at the frequencies up to 1000 Hz is proportional to squared frequency ($\beta \sim f^2$). Sound attenuation in sediments and in hard rocks is proportional to the sound frequency ($\beta \sim f$) (Clay and Medwin, 1977; Sheriff and Geldart, 1995). An acoustic signal (at a frequency of 100 Hz) decays completely: in a rock layer over a distance of 20 km, in the sediments over a distance of 2-3 km, and in a sand layer less than over one kilometer. The acoustic signal attenuation coefficient (α) at a frequency of 100 Hz in water is 100 times smaller than in a hard rock and 10000 times smaller than in sediments.

It is well known that seismic observations by sea-bottom stations give a significantly larger number of recorded EQs than surface stations (Soloviev et al, 1989a, 1989b; Smith et al, 2003). Seismic signals from weak EQs decay completely in sedimentary layers, and are practically not recorded by the surface stations.

Some laboratory experimental studies were dedicated specifically to analyze the acoustic signals, which appear before sample destruction. The signals generated by micro-destructions have small amplitude, significantly high frequency and decay very fast in the rock sample body.

The EQ preparation zones are specified by increase of the micro-crack density and the crack system evolution (crack sizes grow progressively, and their amount decreases). Such zones are named "dilatant" zones, and they are characterized by increased value of the shear and tension stress. It was shown (Alekseev et al, 2001) that two specifically dilatant zones occurred in the EQ preparation stage (Figure 9). The first one is located around the source and the second one represents the near-surface dilatant zone, whose size may be up to 200 km.

The processes of the micro-crack generation take place in the near-surface dilatant zones. In this case, the seismic and acoustic signals radiated from near bottom zone may reach the ocean floor. Then signals propagate in the water practically without attenuation; hence hydro-acoustic sensors can detect them. Our observations confirm the possibility of the EQ preparation zone location by hydro-acoustic receivers.

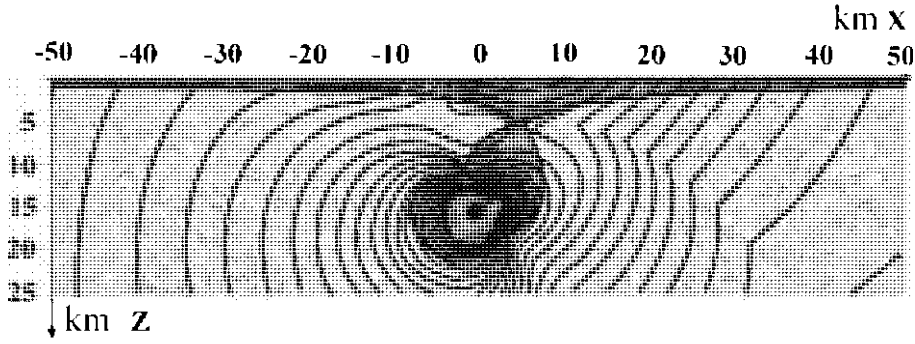

Fig. 9. Two dilatant zones, which occurred in the earthquake preparation stage. The first one located around the focus and the second one is the near surface with size up to 200 km. (Alekseev et al, 2001).

5 Conclusions

1. We analyzed the data from a hydro-acoustic array located near the sea bottom that recorded the acoustic signals radiated from the EQ preparation zone. Joint analysis of digital HARs and the Kamchatka REQC enabled us to select hydro acoustic records, which coincided in time with seismic events or preceded them. We detected two types of acoustic signals preceding the main shock: MEQs whose epicenters were located in the same area as the epicenter of the future EQ and the seismic rumble. The rumble appears just before the EQ start and continues up to the main shock. The EQs were also recorded by hydro-acoustic array.

2. The MEQ focuses were located in the crust near the water/bottom boundary (according to our estimates from 100 to 400 m below the water/bottom boundary). The MEQ duration is from 3 to 20 seconds; the frequency in the first stage of the MEQs is from 3 to 75 Hz. Initially, the amplitude maximum stage of hydro-acoustic signal corresponds to the frequency maximum stage, later the frequency and amplitude decrease. The amplitude in the first stage of the MEQs is several times greater than the acoustic background.

3. At present, the MEQs are not recording by the ground-based seismic stations (the local network). The signals decay practically completely in the hard rock and sediments.

4. The MEQs preceded the EQs (up to three hours) and they occurred in the near-surface dilatant zone. Thus, these signals didn't decay in the course of propagation to the hydro-acoustic receiver. An accurate study of acoustic phenomena using underwater hydro-acoustic array may help us to solve the warning problem of local tsunami.

Acknowledgements.

The research was supported by the RFBR grant No 01-05-64162 and by the Program of Leading Scientific Schools (grant NS-2104.2003.5).

References

Alekseev A.S., Belonosov A.S., Petrenko V.E., 2001, A concept of multidisciplinary earthquake prediction based on an integral precursor. Problems in Lithosphere Dynamics and Seismisity, Coll. sci. proc., Computational Seismology, Iss 32, Moscow, GEOS, pp.81-97 (in Russian).

Clay C.S., and Medwin H., 1977: Acoustical oceanography, New York, J. Wiley, 576 p.

Demianovich V. V., 1998: How "Agam" was created. In: From the History of Russian Hydro Acoustics, Sankt-Petersburg, pp.295-315 (in Russian).

ETDB/PAC (2003) Expert Tsunami Database for the Pacific, Version 4.9 of December 31, 2003, CD-ROM, Tsunami Laboratory, ICMMG SD RAS, Novosibirsk, Russia (http://tsun.ssec.ru/htdbpac).

Kamchatka REQC Kamchatka Regional Earthquake Catalog, ОМСП Geophysical servise of RAS, Petropavlovsk-Kamchatsky, Russia (http://data.emsd.iks.ru).

Karlik Ya. S., 2002: Hydroacoustic antenna: A powerful tool to forecast tsunamigenic earthquakes, In: Proc. Intern.Workshop: Local Tsunami warning and mitigation, Petropavlovsk-Kamchatski, Russia, 68-70.

Morozov V. E., 2002: High-frequency hydro-acoustic signals (40-110 Hz), foregoing the earthquakes, on the Pacific shelf of the Kamchatka Peninsula, In: Proc. Intern. Workshop: Local Tsunami warning and mitigation, Petropavlovsk-Kamchatski, Russia, 99-106.

Sheriff R. E., and Geldart L. P.: 1995, Exploration Seismology. 2nd edition, Cambridge Univ. Press, 592 p.

Smith D. K., Escartin Jav, Cannat M., Tolstoy M., Fox C.G., Bohnenstiehl D.R., Bazin S., 2003: Spatial and temporal distribution of seismicity along the northern Mid-Atlantic Ridge (15 35N), Journal of Geophysical Research, 108, B3, 2167, doi:10.1029/2002JB001964

Soloviev S. L., Ferry M., Kuzin I. P., and Kovachev S. A., 1989a: Seismicity of the Earth crust in the southeastern part of the Tyrrhenian Sea (results of joint bottom and surface seismic observations), Dokl. RAS, 305, 6, 1339-1343 (in Russian).

Soloviev S. L., Kovachev S. A., Kuzin I. P., and Tassos S., 1989b, Seismicity of the Earth crust in the southern part of the Aegean Sea (results of bottom seismic observations). Dokl. RAS, 305, 6, 1085-1089 (in Russian).

ELECTROMAGNETIC TSUNAMI MONITORING: THEORY AND RECOMMENDATIONS

O. NOVIK[1], Y. RUZHIN[1] AND S. ERSHOV[2]

[1] *Inst. Terrestrial Magnetism, Ionosphere and Radio Wave Propagation of Russian Acad. Sci., 117246, POB 51, Moscow, Russia. E-mail: onovik@online.ru*
[2] *Keldysh Inst. Appl. Mathematics of Russian Acad. Sci., 125047, Moscow, Russia*

We formulated a nonlinear mathematical model of seismo-hydro-electromagentic field interaction (in presence of gravity) and calculated generation and propagation of seismic disturbances of these fields in a lithosphere-hydrosphere-atmosphere zone including the basin of a marginal sea (2D schematization of the central part of the Sea of Japan). Amplitude of the computed magnetic signals (300 pT at the ocean-atmosphere interface, 10 sec after a model seismic excitation in the upper mantle), their main frequency (0.25 Hz), delay of the seismic wave with regard to the magnetic signal (20 sec at the shore), and parameters of the tsunami wave of a small amplitude are of orders observed. So, to discover a seismic activation in ocean lithosphere and a tsunami wave far from a shore, the magnetic recordings at the sea surface and above (buoys, balloons, magnetometers, and satellite instrumentation) should be combined with seismic, magnetic and temperature recordings at the sea bottom.

1 Introduction

Electromagnetic (EM) signals of seismic activation of ocean lithosphere have been detected several times, in particular by ground-based magnetometers in Pacific regions (Belov *et al.*, 1974; Hayakawa and Fujinawa (Editors), 1994; Iyemori *et al.*, 1996; Ruzhin and Depueva (1996); Johnston and Parrot (Editors),1998; Hayakawa and Molchanov (Editors), 2002; Hayakawa (Editor), 2003).

This paper aims to calculate EM signals on a sea bottom, sea surface, and in atmosphere accompanying a tsunami process beginning from a seismic excitation in lithosphere beneath a sea floor, up to the stage of a hydrodynamic long wave of a small amplitude far from a shore.

As a physical mechanism of transformation of a seismic process under a sea floor into a tsunami wave and EM signals we consider elasto-hydro-EM interaction in the lithosphere-hydrosphere-atmosphere medium, caused by a disturbance of the stationary (in presence of gravity) configuration of the elastic field at a focal depth in lithosphere under the sea bottom (a seismic excitation).

K. Satake (ed.), Tsunamis: Case Studies and Recent Developments, 319-340.

Based on the theory of magneto-thermo-elasticity (in lithosphere) and on the magneto-hydrodynamic theory (the nonlinear shallow water theory is used) (Maugin, 1988; Landau and Lifshits, 1986), we formulate a nonlinear system of partial differential equations, together with the contact and boundary conditions, and calculate generation and propagation of seismo-EM signals in the basin of a marginal sea including the transfer of seismic and EM energy from the upper mantle to hydrosphere and EM emission into atmosphere up to ionosphere domain D.

According to physical theories described above we are trying to clarify connection between EM signal characteristics (amplitudes, spectra, delay with regard to the beginning of a seismic excitation) at different levels of a seismically active media available for measurements, on the one hand, and characteristics of deep seismic excitations in ocean lithosphere and tsunami waves, on the other hand. Numerical investigations are needed to estimate the possibilities of the EM tsunami monitoring, to determine parameters of receivers, and to interpret signals.

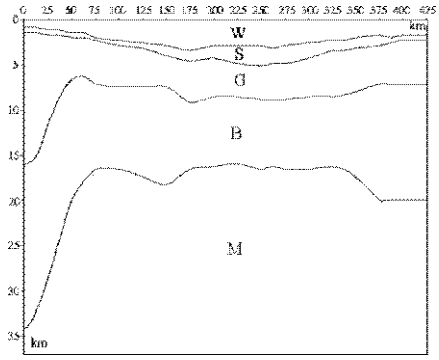

Fig. 1. The sea (W, water) and the geological structure of the lithosphere part of the medium: S – sediments, G – granites, B – basalts, M – the upper mantle, depths under the sea level (0) and horizontal co-ordinates are in km. The cross-section end-points are: (43.2^0 N, 132^0 E) and (39.7^0 N, 133.7^0 E).

2 Characteristics of the model medium and its seismic excitation

We consider a 2D problem of seismic generation and propagation of elastic, hydrodynamic, electromagnetic (EM) and temperature (generated by dissipation in rocks) field disturbances in a domain including: a vertical cross-section of the central part of the Sea of Japan down to the upper mantle at the depth of 37 km below the sea level, the sea, and the atmosphere up to the lower boundary of the ionosphere domain D at the height $L_D = 70$ km.

The cross-section runs from the Bay of Peter the Great throughout the Pervenets Rise, the Yamato Basin, and ends at the North Yamato Rise. The co-ordinates $\boldsymbol{x} = (x_1, x_2)$ are chosen so that x_1 is directed *downwards* with $x_1 = 0$ at the sea surface, and x_2 is directed horizontally, $0 \le x_2 \le L_2 = 425$ km. In figures and captures notations (x,y) are used

instead of (x_1, x_2). Sea water, the sedimentary, granite, basaltic, and upper mantle layers are denoted by W, S, G, B, and M respectively (Figure 1, Table 1)).

Table 1. Physical parameters of the medium: the values (in SI units) of density ρ, elastic wave velocities v_p and v_s, electric and thermal conductivities σ_e and κ, and densities of heat sources q are shown.

	ρ, kg/m^3	v_p, m/s	v_s, m/s	σ_e, S/m	κ, W/(m×K)	q, μW/m^3
W	1000	—	—	3.5	—	—
S	2500	5000	3000	0.005	1.3	1.2
G	2700	5800	3200	0.001	2.5	0.9
B	2900	6300	4000	0.005	2.1	0.4
M	3300	7200	4800	0.020	3.2	0.4

Heat capacity is $c_V = 660$ [J/(kg×K)] everywhere and magnetic permeability is

$$\mu_e = \mu_0 = 4\pi\times10^{-7} \text{ (SI units)}.$$

To model the seismic excitation, due to a seismic wave arriving (from a deeper source) at the lower external boundary $x_1 = L_1 = 37$ km, we use the vector $\boldsymbol{u}_0 = (u_{01},u_{02})$ as a non-stationary boundary condition for elastic displacements $u_1(t, x_1, x_2)$ and $u_2(t, x_1, x_2)$:

$$u_1(t, L_1, x_2) = u_{01}, \qquad u_2(t, L_1, x_2) = u_{02}$$

where

$$\begin{aligned} u_{01} &= a_1 \times te^{-bt-\alpha(x_2-x_{20})^2}\cos(\omega t)\cos\frac{2\pi x_2}{d}, \\ u_{02} &= a_2 \times te^{-bt-\alpha(x_2-x_{20})^2}\sin(\omega t)\sin\frac{2\pi x_2}{d} \end{aligned} \qquad (2.1)$$

Here: $a_1 = 7$ cm, $a_2 = 3.5$ cm, $b = 1/3$ sec^{-1}, $\alpha = 5\times10^{-11}$ m^{-2}, $0 < t < T$, $\omega = 5/3$ rad/sec, $x_{20} = L_2/2 = 212.5$ km, $d = 150$ km, $T = 20$ sec.

The duration of this model seismic excitation (varied in different simulations) is several seconds, the amplitude is about 5 cm, main frequency is about several hertz (Figure 2, the spectrum of u_{02} is the same), and the excitation decays with time and far from the centre of the domain. Other initial and external boundary conditions are described in next section along with field and contact (i.e. at an internal boundary) equations. Surely, these conditions are necessary (and sufficient, together with (2.1)) for a well-posed initial boundary value problem of seismo-hydro-EM interaction in a domain of the lithosphere-hydrosphere-atmosphere system (below), but (2.1) describes the energy supply to the system and influence of this condition on main numerical results (the seismic signals characteristics in the central part of the domain) occurred to be stronger as compared with influence of the initial and other external boundary conditions (as a result of plenty of runs with variable but reasonable values of parameters including changes of these conditions). Hence the external boundary conditions at the lower boundary (at a focal depth in the upper mantle under the ocean

bottom) of the domain considered are included in this section (devoted to the main data) and are mentioned in the next one.

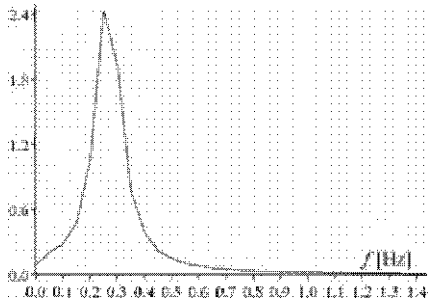

Fig. 2. Power spectrum of vertical seismic elastic displacements (2.1) in the upper mantle at depth 37 km and horizontal co-ordinate $y = 212.5$ km. Spectrum of horizontal component is twice smaller in amplitude.

3 Equations of seismo-hydro-electromagnetic interaction

Based on the assumptions described in the previous section, the magnetic field may be described in the 2D case by a scalar equation. Let us consider the magnetic field equation for a conductive moving medium (a seismically disturbed lithosphere domain and a sea above it, conductivity of the atmosphere above the sea is neglected) and low frequency processes, i.e. without displacement currents:

$$\frac{\partial \boldsymbol{B}}{\partial t} + \nabla \times (\sigma_e^{-1} \nabla \times \boldsymbol{H}) - \nabla \times (\boldsymbol{w} \times \nabla \times \boldsymbol{B}) = 0$$

where: $\boldsymbol{B} = \mu_e \boldsymbol{H}$ is magnetic induction, $\boldsymbol{H} = (H_1, H_2, 0)$ is magnetic field intensity, $\boldsymbol{w}$ is the velocity. For the 2D case, i.e. for this vector magnetic diffusion equation may be written in the form of a system of the 2D scalar magnetic diffusion equations:

$$\frac{\partial B_1}{\partial t} + \frac{\partial}{\partial x_2}\left(\sigma_e^{-1} \cdot \left(\frac{\partial H_2}{\partial x_1} - \frac{\partial H_1}{\partial x_2}\right)\right) - \frac{\partial}{\partial x_2}(w_1 B_2 - w_2 B_1) = 0$$

$$\frac{\partial B_2}{\partial t} - \frac{\partial}{\partial x_1}\left(\sigma_e^{-1} \cdot \left(\frac{\partial H_2}{\partial x_1} - \frac{\partial H_1}{\partial x_2}\right)\right) + \frac{\partial}{\partial x_1}(w_1 B_2 - w_2 B_1) = 0$$

Since magnetic permeability μ_e is spatially uniform these equations may be replaced with the equation for the scalar magnetic potential $A(t, x_1, x_2)$:

$$\mu_0 \frac{\partial A}{\partial t} - \frac{1}{\sigma_e} \Delta A + \mu_0 \cdot \left(w_1 \frac{\partial A}{\partial x_1} + w_2 \frac{\partial A}{\partial x_2}\right) = 0$$

Indeed, the magnetic intensity components H_1 and H_2 being determined as the spatial derivatives of A (A is rather a quasi-potential because of ⋯, but we omit the prefix):

$$H_1 \equiv -\frac{\partial A}{\partial x_2}, \quad H_2 \equiv \frac{\partial A}{\partial x_1}$$

obey the system of the 2D magnetic diffusion equations (above) with $\mu_e = \text{const}$.

Let us consider the function A as a sum:

$$A = A_0 + A'$$

where A_0 is the stationary magnetic potential (before the seismic excitation) and A' is its seismic disturbance, i.e. seismo-magnetic potential.

The components H_{10} and H_{20} of the stationary geomagnetic field $\boldsymbol{H}_0$, $\boldsymbol{H}_0 = (H_{10}, H_{20})$, $H_{10} = -\partial A_0/\partial x_2$, $H_{20} = \partial A_0/\partial x_1$, are supposed to be uniform:

$$H_{10} = \text{const}, \; H_{20} = \text{const}, \; \Delta A_0 = \partial H_{20}/\partial x_1 - \partial H_{10}/\partial x_2 = 0$$

Therefore the above equation for A may be replaced with the following equation for the scalar seismo-magnetic potential A':

$$\mu_0 \frac{\partial A'}{\partial t} - \sigma_e^{-1} \Delta A' + \mu_0 \cdot (w_1 \frac{\partial A'}{\partial x_1} + w_2 \frac{\partial A'}{\partial x_2} + w_1 H_{20} - w_2 H_{10}) = 0$$

The seismic disturbance (H_1', H_2') of the magnetic field intensity is determined by A': $H_1' = -\partial A'/\partial x_2$, $H_2' = \partial A'/\partial x_1$. Below, we use notations A, H_1, H_2, and B_1, B_2 for seismic disturbances of the magnetic potential, magnetic field intensity and induction.

Now we are going over to the system (3.1) of equations of seismo-EM interaction in the lithosphere part D_{lit} of the considered domain of the lithosphere–hydrosphere-atmosphere system. We shall use the following notations: λ and μ are parameters of Lame, $\boldsymbol{u}(t,\boldsymbol{x}) = (u_1, u_2)$ is the elastic displacement at point $\boldsymbol{x}$ at time t; g_1 is the acceleration of gravity and $g_2 = 0$; $\beta = (2\mu+3\lambda)\alpha_\theta$ where α_0 is the coefficient of thermal expansion, $\alpha_\theta = 5 \times 10^{-6}\,\text{K}^{-1}$; $\boldsymbol{v} = (v_1, v_2)$ is the velocity $\partial \boldsymbol{u}/\partial t$ of elastic displacements; and $\vartheta(t,\boldsymbol{x}) - \Theta(t,\boldsymbol{x}) - \vartheta_0$ is the deviation of temperature Θ from its initial value ϑ_0 existed at $t = 0$. Evolution of fields in the lithosphere part D_{lit} of the medium according to the assumptions above and principles of the theory of elasticity, electrodynamics of slowly moving media and irreversible thermodynamics, i.e. the magneto-thermo-elasticity theory (Maugin, 1988) obeys

$$\begin{aligned}
\rho \frac{\partial^2 u_i}{\partial t^2} &= \frac{\partial}{\partial x_k}\left(\mu\left(\frac{\partial u_i}{\partial x_k} + \frac{\partial u_k}{\partial x_i}\right)\right) + \frac{\partial}{\partial x_i}\left(\lambda \frac{\partial u_k}{\partial x_k}\right) - \frac{\partial(\beta\vartheta)}{\partial x_i} + \rho g_i, \quad i = 1,2 \\
\frac{\partial A}{\partial t} &= \frac{1}{\mu_0 \sigma_e} \Delta A - v_k \frac{\partial A}{\partial x_k} + v_2 H_{10} - v_1 H_{20} \qquad (3.1) \\
\rho c_V \frac{\partial \vartheta}{\partial t} &= \operatorname{div}(\kappa \cdot \operatorname{grad}\vartheta) - \beta\vartheta_0 \operatorname{div} \boldsymbol{v} + \frac{1}{\sigma_e}(\Delta A)^2 + q
\end{aligned}$$

Here and below there is summation over repeated subscripts which take at 1 and 2.

At the sea bottom the normal component v_n of elastic velocity $\boldsymbol{v}$ equals the normal component w_n of the water velocity $\boldsymbol{w} = (w_1, w_2)$:

$$(\boldsymbol{v}\cdot\boldsymbol{n}) = (\boldsymbol{w}\cdot\boldsymbol{n}) \qquad (3.2)$$

where $\boldsymbol{n}$ and $\boldsymbol{\tau}$ (see (3.3)) are the local normal and tangent to the sea bottom (directed inward the water). Then, the normal component of force f_n acting from the sediment

layer equals the water pressure p at this point, while the tangent component of this force f_τ vanishes because we neglect shear stresses in water:

$$f_n = \sigma_{ij} n_i n_j = p, \quad f_\tau = \sigma_{ij} \tau_i n_j = 0, \tag{3.3}$$

where the Hooke's relation is used

$$\sigma_{ij} \equiv \mu\left(\frac{\partial u_i}{\partial x_j} + \frac{\partial u_j}{\partial x_i}\right) + \delta_{ij}\lambda \frac{\partial u_k}{\partial x_k}. \tag{3.4}$$

We describe the water dynamics in the framework of the "shallow water" theory (e.g., Landau and Lifshits, 1986) which operates horizontal velocity w_2 and elevation of sea surface $\eta(t,x_2)$:

$$\begin{gathered} \frac{\partial}{\partial t}(\eta + h_u) + \frac{\partial}{\partial x_2}((\eta + h) w_2) = 0, \\ \frac{\partial w_2}{\partial t} + w_2 \frac{\partial w_2}{\partial x_2} + g \frac{\partial \eta}{\partial x_2} = 0 \end{gathered} \tag{3.5}$$

The sea bottom is a moving line $x_1 = h(t, x_2) = h_0(x_2) + h_u(t,x_2)$ where $h_0(x_2)$ is the stationary profile and $h_u(t,x_2)$ is its perturbation due to elastic deformations caused by seismic excitation (2.1) in the upper mantle.

Now we'll consider the seismo-hydro-EM interaction in the ocean-atmosphere system. The potential A in the water obeys the equation

$$\frac{\partial A}{\partial t} = \frac{1}{\mu_0 \sigma_e} \Delta A - w_k \frac{\partial A}{\partial x_k} + w_2 H_{10} - w_1 H_{20}. \tag{3.6}$$

The vertical component w_1 of the hydrodynamic velocity is calculated from w_2 and elastic velocity using equations (3.2), (3.5) and continuity condition

$$\frac{\partial w_1}{\partial x_1} + \frac{\partial w_2}{\partial x_2} = 0 \tag{3.7}$$

Electric conductivity is assumed to be continuous across the sea bottom (i.e. a thin transition layer is used in computations, see Section 6.3).

The equation for A above the sea (where $x_1 < 0$) and the conjugation conditions at the sea surface $x_1 = 0$ are:

$$\begin{gathered} \Delta A = 0 \quad \text{for } x_1 < 0, \quad 0 < x_2 < L_2, \quad t > 0; \\ A\Big|_{x_1=+0} = A\Big|_{x_1=-0}, \quad \frac{\partial A}{\partial x_1}\Big|_{x_1=+0} = \frac{\partial A}{\partial x_1}\Big|_{x_1=-0} \end{gathered} \tag{3.8}$$

The *initial conditions* were chosen so that before the moment $t = 0$ the system was at rest, thus the water velocities and elevation of sea surface is 0; elastic displacements equal stationary configuration under the gravity force; initial magnetic field is uniform in space: $H_{10} = 30$, $H_{20} = 35$ [A/m]. For all fields, the normal derivative vanishes at the

left ($x_2 = 0$) and right ($x_2 = L_2$) boundaries. The remaining "outer" boundary conditions are (see (2.1) and the commentaries in previous section):

$$\partial A / \partial x_1\big|_{x_1=-L_D} = \partial A / \partial x_1\big|_{x_1=L_1} = 0,$$
$$\vartheta\big|_{x_1=h_0(x_2)} = 0, \quad \partial\vartheta / \partial x_1\big|_{x_1=L_1} = 0, \tag{3.9}$$
$$\boldsymbol{u}\big|_{x_1=L_1} = \boldsymbol{u}_0(t, x_2)$$

Our simulation algorithms allow to compute evolution of fields under a wide class of initial and boundary conditions, including volume seismic excitation instead of a boundary excitation. We have varied the parameters of the excitation and other conditions at the outer boundaries $x_1 = L_1$, $x_1 = -L_D$ and $x_2 = 0$, $x_2 = L_2$ as well as characteristics of the medium (geophysical and petrophysical restrictions are taken into account), but the main features of evolution of model seismic perturbations of fields, especially the relation between seismic excitations in the earth depth and EM signals at the sea surface and above, remained the same.

This approach to modelling of seismo-hydro-EM processes (*seismo-hydro-electromagnetics*) is further development of the authors works (Novik, 1995; Novik *et al.*, 1998; Ershov *et al.*, 2001; Novik *et al.*, 2001), which are the first ones devoted to this subject, as far as we know. A detailed physical and mathematical background was expounded in (Novik and Ershov, 2001). Other approaches to seismo-electromagnetics and bibliography may be found in (Belov *et al.*, 1974; Hayakawa (Editor), 2003; Hayakawa and Fujinawa, (Editors), 1994; Hayakawa and Molchanov (Editors), 2002; Johnston and Parrot (Editors), 1998; Iyemori *et al.*, 1996).

4 Early measurable signals of a seismic excitation of geological structures beneath a sea floor

According to the model (2.1), (3.1)–(3.9), the lithosphere EM signal (i.e. a diffusive seismic disturbance of the EM field) arises at the bottom of the upper mantle layer M (Figure 1) and reaches the depth $x_1 = 25$ km by the moment $t = 1$ sec with amplitude about 20 pT.

In the crust layers B, G, and S, which have lower electric conductivity (as compared to that of M, see Table 1), the propagation of the EM signal accelerates and its horizontal magnetic component B_2 [pT] reaches the sea bottom, i.e. the top of the sedimentary layer S which may be regarded as the lower level available (without a sea bottom drilling) for observation.

This first measurable signal of seismic excitation under the ocean floor is represented by oscillations with the frequency of the order of 0.1 Hz (Figure 3). The amplitude of oscillations of the horizontal magnetic induction component B_2 is about 10 pT at the moment $t = 2.5$ sec after the beginning of the seismic excitation (2.1), see Figures 3 and

4. At the moment $t = 3.5$ sec the seismo-magnetic (i.e. caused by seismic excitation) field amplitude is of the order of 30 pT at the sea bottom. These signals may be regarded as the first measurable (and protected by sea water from ionosphere EM disturbances) magnetic signals of a seismic excitation in the earth depth under the sea.

The propagation of the lithosphere EM signal then significantly decelerates due to high electric conductivity (3.5 S/m) of the sea water: in the interval $3.5 \le t < 5.25$ sec, i.e. before the seismic wave arrival at the sea bottom, the front of the seismic magnetic disturbance replicates the configuration of the sea bottom surface and looks "*frozen*".

The elastic P-wave arrives at the surface of the sea bottom at the point with the horizontal co-ordinate $x_2 = 175$ km at the moment $t_p = 5.25$ sec (Figure 5). One can see the increase of the amplitude of the oscillations of the seismo-magnetic field components up to 40 pT at this moment and the change of the dependence of the sea bottom seismic signals on horizontal co-ordinate. In Figure 6, propagation of the magnetic and elastic (P and S) signals is shown along the sea bottom surface at the moment $t = 6$ sec.

Let us note that in the course of the seismo-hydro-EM process under consideration, the magnetic field oscillation amplitude increases up to 240 pT for the vertical component B_1 and up to 200 pT for B_2 at the sea bottom during 7 sec after the beginning of the seismic excitation (Figure 3).

The computed amplitude of the temperature disturbance (accompanying the seismic and EM wave propagation in the lithosphere part of the model medium, see (3.1)) is of order of a few mK at the top of the sedimentary layer (see Section 6.2).

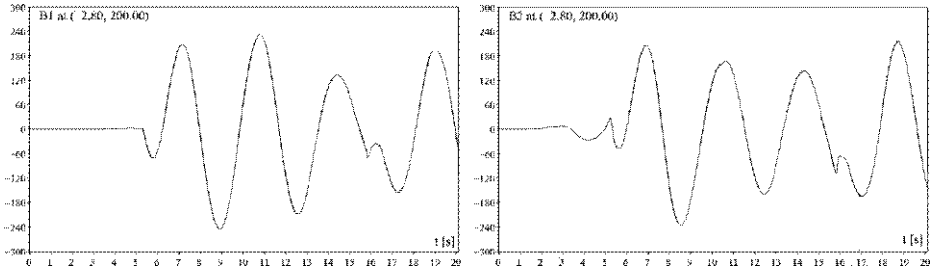

Fig. 3. Measurable (about 50 pT) oscillations of the horizontal component B_2 of magnetic induction at the sea bottom's point with $x = 2.8$ km, $y = 200$ km begins at the moment $t = 3.5$ sec after the beginning of the seismic excitation (2.1) at the moment $t = 0$ sec. The beginning of oscillations of the vertical component B_1 delays with regard to B_2.

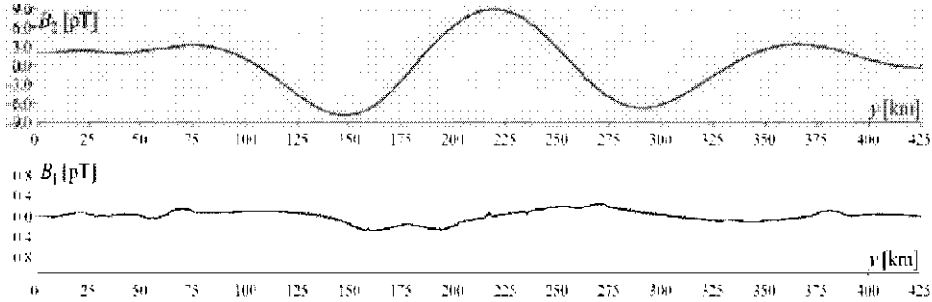

Fig. 4. Profiles along the sea bottom of the horizontal B_2 and vertical B_1 components of magnetic induction at the moment $t = 2.5$ sec. Electric field E and elastic displacements u_1 (vertical) and u_2 (horizontal) at the sea bottom are still indistinguishable from zero and thus not plotted. So all measurable signals delay with regard to B_2.

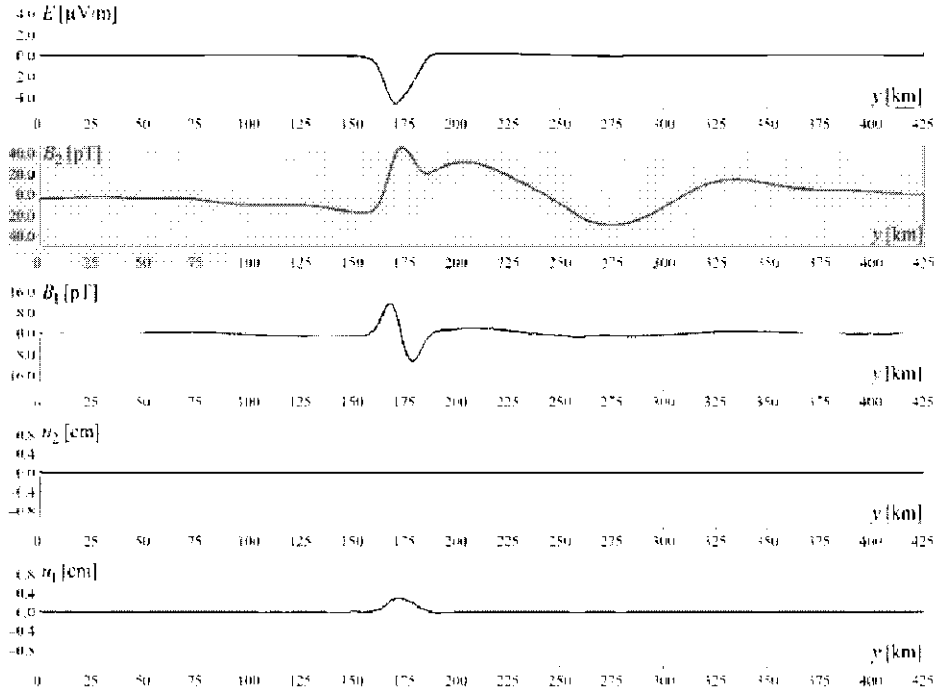

Fig. 5. Changes (cf. Figure 4) of the sea bottom's signal profiles after the seismic P wave (u_1, the lower panel) arrival at the sea bottom at time $t = 5.25$ sec. Electric signal (the horizontal component E of the electric field intensity, the upper panel) appears.

5 Seismo-EM signals at the sea surface and in atmosphere

According to our computations, slightly after the moment $t_p = 5.25$ sec of the seismic wave shock into the sea bottom (i.e. the arrival of the P wave at the sea bottom surface) the seismo-hydrodynamic velocity field $\boldsymbol{w} = (w_1, w_2)$, caused by seismic deformations of the sea bottom, is localised in a narrow water column, say $Q_s(t)$, whose base is a spreading spot where the seismic wave front is interacting with the sea bottom. So the EM field is generated in $Q_s(t)$, in presence of the geomagnetic field, and emitted from the top of $Q_s(t)$ (at the sea surface) into atmosphere. Details of the computed seismo-hydro-EM process of transformation of a seismic excitation under a sea bottom into EM signals at the sea surface and above (as well as a qualitative physical explanation without computations of particularities of the process on the base of the model (3.1)–(3.9)) may be found in the authors' works referenced in Section 3 (see Section 6.5).

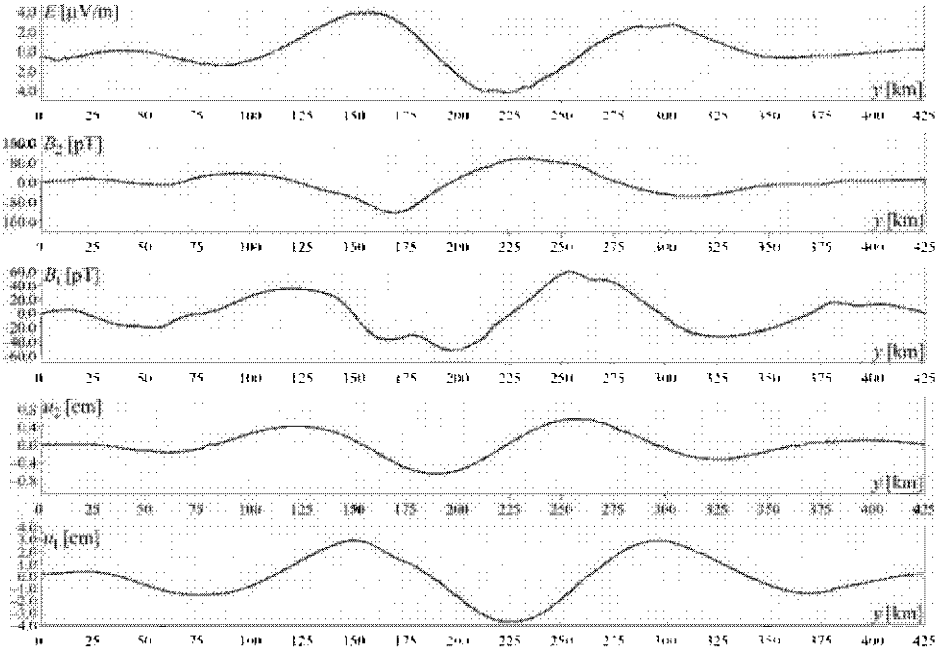

Fig. 6. The profiles of seismic signals along the sea bottom at the moment $t = 6$ sec after the beginning of the seismic excitation in the upper mantle under the sea bottom (cf. Figures 4 to 6).

Here we are going over to the computed seismic EM signals at the sea surface. The dependence of the electric intensity E, the horizontal B_2 and vertical B_1 magnetic induction components on the horizontal co-ordinate along the undisturbed sea surface is shown in Figure 7 at the moment $t = 6$ sec after beginning of the seismic excitation (2.1) in the upper mantle under the sea bottom.

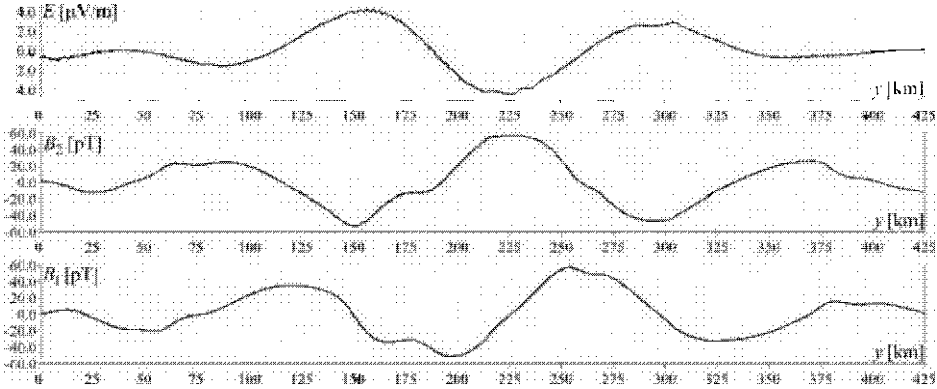

Fig. 7. Electric E and magnetic (B_1 and B_2 are the vertical and horizontal components) seismic signals at the sea surface at the moment $t = 6$ sec. The horizontal magnetic component at the sea surface is about a half of the horizontal component at the sea bottom (cf. Figures 6 and 7).

One can see that a magnetic signal of the order of a few tens of pT may be observed at the sea surface at the distance of the order of a hundred of km from the point ($x_2 = 175$ km, Figure 5) of the seismic P wave's initial contact with the sea bottom. Figure 8 shows that the seismic magnetic signal at the sea surface increases considerably during 10 sec after the beginning of a seismic activation of the upper mantle under the sea bottom, e.g. up to 240 pT for the vertical component B_1 of magnetic induction at the point with the horizontal co-ordinate 200 km. The spectrum of this magnetic signal at the sea surface is similar to the spectrum of the seismic excitation under the ocean floor (see Figures 2 and 9). At the height of 10 km in atmosphere above this nearly central point of the area of water concerned, the computed vertical component of the seismic disturbance of magnetic induction B_1 is up to 160 pT at the moment $t = 11$ sec and the horizontal component B_2 is up 80 pT in this point at the moment $t = 9$ sec.

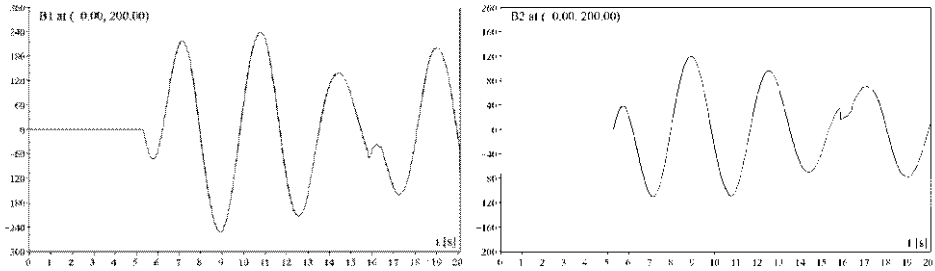

Fig. 8. The vertical (B_1, the left panel) and horizontal B_2 seismic magnetic signal components at the sea surface ($x = 0$), the horizontal co-ordinate $y = 200$ km.

Attenuation of seismo-magnetic signals at this height above the sea (up to 80 and 60 pT for B_1 and B_2 respectively) is shown in Figure 10 at the distance of 100 km from the central point. The energy spectrum with the main frequency of the order of a few tenths of Hz (see Figures 2 and 9) inherited from the seismic excitation is a characteristic feature of these EM signals above the sea (as well as for heights near the lower boundary of the ionosphere domain D, the computed signal amplitude being of the order of a few tens of pT).

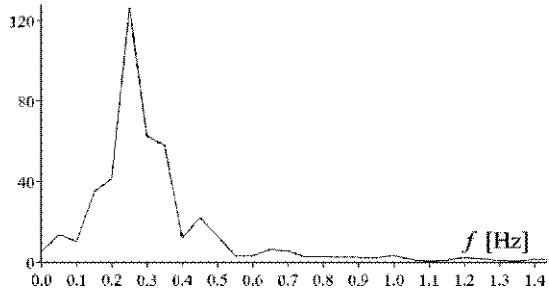

Fig. 9. Power spectrum of disturbances of vertical component B_1 of magnetic induction at the sea surface ($x = 0$, the horizontal co-ordinate is 200 km). It resembles spectrum of seismic excitation in the upper mantle, see Figure 2. The spectrum of the horizontal component is similar.

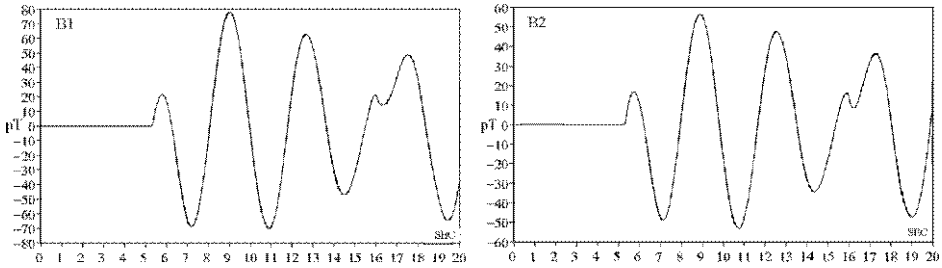

Fig. 10. The seismic magnetic signal components B_1 (vertical) and B_2 at the height of 10 km at the point with the horizontal co-ordinate 100 km, i.e. 100 km from the west shore.

The above Figures represent the dependence of the seismic EM signals on the time or on the horizontal co-ordinate only. The spatial structure of the field of the horizontal component B_2 of the seismic disturbance of the magnetic field is shown in Figure 11 at the moment $t = 10$ sec (see the right boundary of the Figure). This figure presents the part of the model medium including the lithosphere zone up to the depth of 37 km and the atmosphere up to the height of 20 km. The surface of the sea bottom is seen distinctively (see Section 6.5). Maximal absolute values of the magnetic perturbation (1700 pT) are achieved in the lithosphere (see the right boundary of Figure 11). The seismo-hydro-magnetic signal (let us remember it is a magnetic signal resulting from seismo-hydro-EM interaction in the lithosphere-hydrosphere-atmosphere model medium) above the sea is considerably non-homogeneous in the horizontal co-ordinate

and its peaks (contrary to EM signals from ionosphere) correspond to the structure of the seismic magnetic field under the sea bottom. In its turn, this magnetic field is spatially modulated by the seismic P wave, i.e. the period of the magnetic component B_2 along the vertical axis equals to the P wave's length whereas the main period of B_2 (about 100 km, Figure 11) along the horizontal axis, as well as the horizontal period of the computed P wave's field, equals to the main period of the seismic excitation, see (2.1).

A more detailed numerical investigation of the spatial modulation of a low frequency diffusive magnetic field by a seismic wave may be found in the authors' works referenced in Section 3. Let us note, the pictures including fields of different physical nature (Figure 11 is a panel of one of these pictures) and illustrating the sequential stages of evolution of the spatial structure of the interacting seismic, hydrodynamic, EM and temperature fields and the transformation of a seismic excitation under the ocean bottom into measurable EM signals at different levels of the lithosphere–hydrosphere–atmosphere system available for measurements, may be found in these works as well, especially in (Novik and Ershov, 2001).

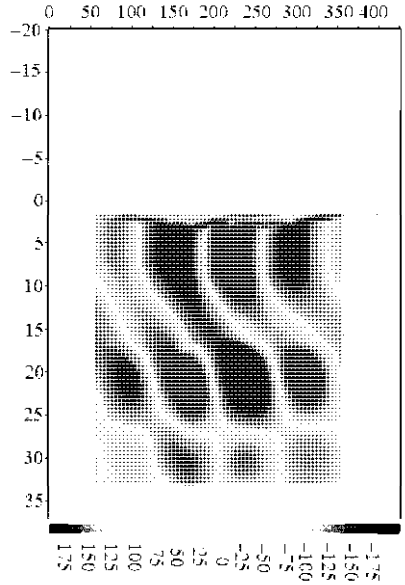

Fig. 11. Spatial structure of the horizontal component B_2 of the seismic disturbance of the magnetic field at the moment $t = 10$ sec shown in the vertical cross section of the domain. Field amplitude is grey-scale coded (see legend below, in [pT]). Axes labels are in kilometers.

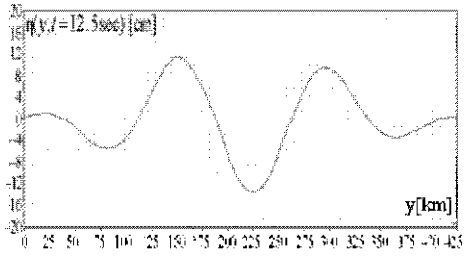

Fig. 12. Long seismic hydrodynamic wave of small amplitude: η [cm] is elevation of the sea surface, the distance from the west shore (Figure 1) is in km.

In this paper devoted to applications of the theory of EM accompanying of the initial stage of a tsunami (only a few numerical fragments were shown to demonstrate characteristics of expected signals), a hydrodynamic wave caused by seismic deformation of the sea bottom should be presented. One can see from Figure 12 that the computed hydrodynamic long (150 km) wave amplitude far from the seashore is less than 15 cm. But the accompanying EM signal (precursor) is propagating above the sea with the light velocity. So, EM observations are needed to discover tsuuami wave far from a shore (together with other methods, see Section 7 as well) and, may be, prior to a pressure gauge at the sea bottom, because this sensor is not active before the hydrodynamic wave arrival. Let us note, even a few seconds are of importance to turn out some technological processes.

6 Discussion

6.1 WEAK SEISMIC EXCITATIONS

The word tsunami has been used in this paper to denote a hydrodynamic wave generated by a rather moderate seismic excitation, namely elastic displacements (2.1), in the ocean lithosphere. We apply here a widespread terminology: hydrodynamic waves caused by a change of a steady state of geological structures of a sea bottom (including elastic seismic excitations as well as displacements of a large parts of the Earth's crust under the sea) belong to the tsunami type. Let us note: a) tsunamis of seismic origination are typical for the Pacific regions (where the Sea of Japan is a marginal sea) because of their high seismicity; b) weak (e.g. elastic) seismic excitations and corresponding EM signals may occur before strong motions as precursory phenomena. Besides, from physical and computational points of view, elastic seismic excitations and corresponding weak EM and hydrodynamic disturbances are simplest ones to begin modeling of seismo-hydro-EM interaction in the lithosphere-hydrosphere-atmosphere system and to obtain threshold characteristics of monitoring devices.

6.2 SIMPLIFICATION OF THE MODEL

According to the principles of magneto-thermo-elasticity and magneto-hydrodynamics used in model (3.1)-(3.9), electromagnetic (EM) forces must be included in the equations of motion. Taking account of variety of characteristics of seismic media and their excitations, we have developed algorithms for models with EM forces (including mathematical investigations of the algorithms). Comparing results of numerical calculations with EM forces and without them we have found that these results are

similar and, therefore, the EM forces may be omitted. We applied several other simplifications formulated in Sections 2 and 3.

Though our aim is to formulate the simplest adequate model, we believe it is hardly possible to simplify model (3.1)-(3.9) considerably from the physical point of view. For instance, weak seismo-temperature signals (of the order of 1 mK to 1 K, quartz thermo resistors had been used by geophysicists) occurred to be effective for the prognosis of the place and magnitude of an earthquake. Probably, it is true for a seaquake as well and recordings of temperature disturbances in sea bottom sediments must be applied. Therefore, it is not reasonable to ignore temperature field in model (3.1)-(3.9). Let us note, in other runs (with acceptable characteristics of the medium and its seismic excitation) we have obtained seismic temperature disturbances with the amplitude up to 20 mK. Possibly, the thermal stresses' term in equations of motion may be omitted without considerable (say, of the order of 10 pT taking account of high precision magnetometers) change of computed magnetic signal depending on the velocity field. Plenty of direct comparisons (by different reasonable input data, just like in the case of EM forces) of calculations with the thermal stresses' term and without it are needed to clarify this question which is not of importance because the neglect of this term does not reduce the time of computations considerably whereas the possible error can not be estimated simply with an acceptable accuracy.

As far as geometry of the cross-section is concerned, it is impossible to apply 1D schematization for tectonically active lithosphere domains of subduction zones with their specific relief of layers' boundaries (Figure 1). Indeed, due to these particularities, the front of a seismic wave is being deformed as compared with the 1D case of plain layers' boundaries. Therefore, the seismo-hydrodynamic interaction at the sea bottom and the fields generated by this interaction (e.g. the hydrodynamic field in the sea and EM field at the sea surface and in atmosphere) are rather different for the 1D and 2D cases, as well as quantitative characteristics of seismic signals (e.g. the time of arrival at the shore) So, the 1D approach must be checked by the 2D one with mathematically investigated algorithms (our case).

6.3 ALGORITHM AND TESTS

In the lithosphere part D_{lit} of the model medium, i.e. for the modelling of seismo-EM interaction, we applied: 1) the Galerkin approximation (e.g. Novik, 1995); 2) the explicit finite difference approximation of the hyperbolic equations of motion combined with the implicit approximation (the alternating direction method) of the parabolic equations of heat transfer and scalar magnetic potential (Novik and Ershov, 2001). We obtained the proper numerical results by both methods, but the speed of the second one occurred to be higher by the same accuracy (below) and an acceptable volume of the memory. Hence the second method was used to calculate seismo-hydro-EM interaction

in the lithosphere part of the lithosphere-hydrosphere-atmosphere domain according to model (3.1) – (3.9). The hydrodynamic shallow water equations were rewritten in terms of the Riemannian invariants (e.g. Richtmyer, 1978) and directions of the characteristic lines were taken into account by the net approximation of the equations for the invariants and formulation of boundary conditions. The co-ordinates and, correspondingly, the differential operators of field equations and boundary conditions, were transformed to get straight line as the lithosphere-hydrosphere boundary and to avoid a net approximation of the differential elasto-hydrodynamic contact conditions at a curvilinear boundary.

The same problem arises by the net approximation of the differential operators of the contact conditions at the boundaries of the lithosphere layers because of their active relief typical for seismic lithosphere zones. The space co-ordinate transformation allowing to get straight lines as the layers' boundaries for all layers simultaneously is possible but it is not reasonable from the computational point of view. As a well-known computational method for a piecewise homogenous medium D_{lit} we have applied thin transition layers between main ones determined by Figure 1 and Table 1. If these auxiliary layers are thin enough (as compared with the size of D_{lit} at whole) and physical parameters' values change continuously in these layers then dependence of the computed fields upon thickness of auxiliary layers (and upon the auxiliary medium parameters' values introduced in these layers) is negligible and the field values are practically the same (with an arbitrary accuracy) as by field contact conditions at the boundaries of the main layers. Let us note, that it is a formulation (adopted for our case) of the theorem about stability of the solution of an initial boundary value problem against small (in the sense of an integral norm for D_{lit}) variations of coefficients of differential equations. We should emphasize that though thin transition layers exist between approximately homogenous main layers in real geological structures, we have not proper data about them for the case of the Sea of Japan and the thin layers described above were introduced as a computational method only. Hence, these layers may not be included in the principal cross-section (Figure 1). On the other hand, there were from 2 to 10 nodes along the vertical net line in the auxiliary layers, therefore, the thickness was of the order of a few hundreds of meters in different runs (see the net parameters below). So the auxiliary transition layers can not be imaged by the vertical scale of Figure 1. We checked that computed field values are independent (with the accuracy of 10%) of thickness of the auxiliary transition layers. The dependence of the physical parameters of the medium upon the vertical co-ordinate was supposed to be linear in transition layers (let us remember that any other continuous dependence is acceptable and influence of this choice on computed fields is negligible if the transition layers are thin enough and it is just our case). At the same time, at the sea surface we used contact condition (3.8) of continuity of the scalar potential and its derivative because this surface is almost plain (contrary to the boundaries of the lithosphere layers, Figure 1)

due to the small amplitude (Figure 12) of the hydrodynamic long wave, as compared with the height (70 km) of the upper boundary of the atmosphere domain.

Magnetic permeability is supposed to be independent of spatial co-ordinates (see Section 2). Therefore magnetic field components must be continuous everywhere in the model medium including the lithosphere layers' contacts, sea bottom and sea surface. This condition, as one of the tests for the algorithm and program, was checked for the computed horizontal magnetic field component considered as the function of the vertical co-ordinate for a few fixed horizontal co-ordinates and moments of time, including ones after the seismic P wave shock into the sea bottom. In particular, we considered the sub-domain near the sea bottom where the electric conductivity changes rapidly from small values in the sedimentary layer to large ones in seawater (Table 1). Discontinues of the magnetic field components are absent there, as well as at the sea surface and other contacts.

The non-linear system of the net seismo-hydrodynamic contact conditions and hydrodynamic equations (in terms of the Riemannian invariants) was solved by iterations with controlled accuracy. To check this method, we constructed the method based on the system of integral equations deduced (using the Green function of the simplest heat transfer equation) from the shallow water equations with the 'vanishing viscosity' (Rihtmyer, 1978). The evolution of a solitary hydrodynamic wave was described by two methods and the coincidence occurred to be satisfactory between these methods as well as with the well-known formula $(gh)^{1/2}$ for the velocity of the wave, where h is the depth of the water. Besides, steepness of the wave front was increasing in the course of moving to the shore.

Numerical results were stable against change of mesh resolution. The difference between simulations with spatial mesh resolution 500×500 by the time step of 0.005 sec and 2000×2000 by the time step of 0.001 sec was within 10%. Therefore accuracy of computations is not less than the accuracy (about 20%) of geophysical and petrophysical data.

6.4 OTHER COMPUTATIONS

In this paper, we considered seismic signals of different physical nature caused by a weak seismic excitation in the upper mantle under the sea and only one (because of lack of pages) typical run was described including the mathematical model, input data and characteristics of the signals. In runs on the basis of the model (2.1), (3.1)-(3.9) but with more strong elastic seismic excitations (we mean increase of the amplitude and duration of excitations without non-elastic deformations) of the same medium, we have found that the signal amplitude increases, approximately in proportion to the excitation's amplitude, up to a few nT at the sea bottom and above. This proportionality was obtained as a computational result and may be derived from the equations of the model

in the case of weak (i.e. elastic) excitations. In its turn, the factor of proportionality and, therefore, computed EM signals, is grater by several fold for some values of the excitation's parameters different from values used in (2.1) (e.g. by $a_1 = 7$ cm, $a_2 = 0$ (the vertical polarization of the excitation), $b = 1/24$ sec^{-1}, $\alpha = 5\times10^{-11}$ m^{-2}, $\omega = 4$ rad/sec, $x_{20} = 212.5$ km, $d = 42.5$ km, $T = 100$ sec). Surely, the general problem of resonances in the considered seismo-hydro-EM oscillatory system may not be considered there. Also our preliminary computations with the modified model (shallow water equations were replaced by acoustic equations, i.e. the incompressibility supposition was not used) show considerable amplification of computed seismic EM signals in the sea near the bottom, as compared with the case of Section 4. Let us note, non-elastic deformations (typical for tsunamigenic earthquakes) and corresponding EM signals (these signals are stronger than ones generated by elastic seismic excitations considered above) may be described by another modification of the model of Section 3.

6.5 COMMENTS ON FIGURE 11.

In Figure 11, one can see considerable attenuation of the seismic disturbance of the horizontal component of the magnetic field in the sea as compared with its values under the bottom. This attenuation of the horizontal magnetic component is connected with the structure of the seismo-hydrodynamic velocity field $\boldsymbol{w} = (w_1, w_2)$ slightly after the moment $t_p = 5.25$ sec of the seismic P wave shock into the sea bottom, see Section 5. Namely, $\boldsymbol{w} = 0$ outside of the narrow water column $Q_s(t)$, where $w_2 = 0$ (the tangent acceleration may not be transferred into the sea trough the bottom, see (3.3)), and the vertical velocity component w_1 is independent of the vertical co-ordinate x_1 due to the incompressibility condition (3.7), $t \approx t_p$, $t > t_p$. So, in equation (3.6) for the scalar magnetic potential A in the sea, the only coefficient depending on co-ordinates is $w_1 = w_1(t,x_2)$, $t \approx t_p$, $t > t_p$. Let us suppose for a time, we consider equation (3.6) in a whole plane instead of the sea. Then the solution A, which is zero for $t = t_p$ (induction is absent in the sea before the seismic P wave shock into the bottom) and vanishes for $x_2 \to \infty$, is independent of the vertical co-ordinate: $A = A(t,x_2)$, as well as $w_1(t,x_2)$. Let us consider now an internal sub-domain, say D_{int}, in the sea with some positive distance $r(D_{int})$ between the boundary of D_{int} and boundary of the sea, i.e. the sea bottom and surface. EM signals are propagating (diffusing in accordance with equation (3.6)) in seawater rather slowly because of its high electric conductivity. Therefore, some definite time, say $\tau(D_{int})$, is needed for arising considerable EM disturbances in D_{int} because of signals propagating from the boundary of the sea. In other words, the influence of the sea boundaries is negligible in D_{int} if the time $t - t_p$ after the seismic P wave shock into the sea bottom is small enough: $t - t_p < \tau(D_{int})$. So, the structure of the scalar magnetic potential A in D_{int} is approximately the same as in the case of the whole plane, i.e. $A = A(t,x_2)$, during a short time after the seismic P wave shock. Hence, if the time after the

seismic P wave shock into the sea bottom is short enough, then the seismic disturbance $B_2 = -\mu_e \partial A/\partial x_1$ of the horizontal component of magnetic induction is negligible (as compared with its values under the sea) in the sea depth; let us remember, D_{int} is an arbitrary internal sub-domain in the sea. According to our computations, the domain of negligible values of the seismic disturbance B_2 of the horizontal component of magnetic induction in the sea is disappearing in course of the seismic energy transfer from the lithosphere, developing of the seismo-hydrodynamic flow and propagation of seismic EM disturbances. An intermediate stage of this process is shown in Figure 11. Other particularities of the seismo-hydro-EM process at whole and their more formal explanations may be found in (Novik *et al.*,2001; Ershov *et al.*, 2001; Novik and Ershov, 2001).

7 Recommendations and conclusion

According to the mathematical model (2.1), (3.1)-(3.9), the ULF seismo-EM signals at the sea bottom, sea surface and above do provide information about seismic excitations beneath the sea bottom and can be used to discover development of a tsunami process before (by EM measurements at the sea bottom) or during a small amplitude phase of a hydrodynamic wave. The computed EM, temperature, and hydrodynamic wave amplitudes, frequencies, the delay of the computed seismic wave with regard to the EM signal, and the delay of the latter with regard to the beginning of a seismic excitation beneath the sea bottom are of orders observed (Belov *et al.*, 1974; Iyemori *et al.*, 1996; Johnston and Parrot (Editors), 1998; Hayakawa and Molchanov (Editors), 2002; Hayakawa (Editor), 2003).

So, ULF seismo-EM signals at the sea bottom, surface and atmosphere should be measured for a monitoring of seismic excitations beneath a sea bottom and tsunamis. Based on these results the authors develop the project of the Lithosphere-Ocean-Atmosphere Multilevel Observatory (LOAMLO) including a bottom station, a moored ocean surface buoy, and an observation stratosphere balloon.

The bottom station will be equipped with: a broadband seismometer and magnetometer (in particular, to investigate polarization of the first seismic magnetic signal at the bottom); a thermometer on the base of a quartz thermo-resistor; an inclinometer (to observe seismic and non-seismic motions of the station in bottom sediments); a magnetotelluric block for investigation of dynamics of conductivity beneath the sea floor; and a gravimeter.

The buoy and balloon complexes will record the meteorological and oceanographic parameters' variations including changes of reflection (optics and radio frequencies) from a sea surface caused by a tsunami wave propagation. The long cables of the balloon and moored buoy will be used as receiving antennas and for measurements,

including the gradient ones, with multidisciplinary sensors at different points (i.e. heights above the Ocean and depth in it) of these cables.

The project includes geophysical investigations at the sea bottom with controlled sources as well as the sounding of the ionosphere (including radio tomography) from the board of the balloon. The balloon and buoy complexes will transmit data to a shore station over satellite link.

The frequency ranges and sensitivity thresholds of all of the sensors of the LOAMLO will be adopted to the characteristics of expected signals according to the numerical research above. Also the computational methods of seismo-hydro-electromagnetics and statistical analysis of the recorded multidimensional (because of different physical nature of signals and different heights of observation points) time series will be used for a prognostic interpretation.

We believe that the multidisciplinary multilevel measurements are needed for understanding physics of seismo-hydro-EM and temperature interaction in the lithosphere-hydrosphere-atmosphere system, in particular penetration of disturbances of different nature from the atmosphere and sea surface into the sea depth, including origination and specific characteristics of noises (pressure, EM, temperature, currents) at the sea bottom. For instance, the multilevel recordings will provide a stable noise (ionosphere, atmosphere, hard sea, industry) and event detection because of attenuation and delay of EM disturbances (e.g. ionosphere Pc pulsations) in seawater along a path to the receiver of the sea bottom station. Besides, we suppose, a temperature disturbance at the sea bottom or at the top of sediments (boreholes) caused by an internal hydrodynamic wave arrival is negligible as compared with a temperature disturbance caused by a seismic wave (up to 20 mK in our runs, see Section 6.2). Probably, changes of electric conductivity under the sea bottom (geo-electric methods are included in this project, see above) caused by an internal hydrodynamic wave are negligible as compared with changes caused by a seismogenic deformation process. We believe temperature and electric conductivity changes are not the only signs which may be used by the LOAMLO to read seismic signals trough high level noises (typical for many seafloor regions), e.g. spectral and correlation characteristics of the recorded multidimensional time series, the ratio of the signal components and others.

The theory and recommendations above may be developed to understand in more detail physics and quantitative characteristics of multidisciplinary interaction processes in tectonically active parts of the lithosphere-hydrosphere-atmosphere system and above, e.g. transfer of energy of seismic origination above the Ocean. The problems and hypothesis mentioned above may be considered as parts of the scientific program of the LOAMLO which should not be a monitoring system only.

The forecasting of geophysical processes is developing rapidly, especially due to increasing interest to global changes, and a few references are given there from an

ocean of possible ones (Heinson, 2000; Pinardi and Woods, 2002; Romanowicz *et al.* (Editors), 2001; Rona *et al.*, 2002; Shapiro *et al.*, 1998; Webb, 1998).

Acknowledgements

We are grateful to Prof. M.J.S. Johnston, Dr. Yu. A. Kopytenko, Dr. T.V. Kusnetzova, Dr. K. Satake, Dr. V.S. Shneyer, Prof. V.V. Sochelnikov, Academician V.N. Strahov, Prof. B.S. Svetov for encouraging interest to our work and useful discussions. Thanks are expressed to Dr. D.G. Repin and Dr. K. I. Sigova for the data on the Sea of Japan geological structures and to unknown reviewers for remarks we used to improve the paper.

References

Belov, S.B., Migunov, N.I., and Sobolev, G.A., 1974. Magnetic effect of the Strong Earthquakes at Kamchatka. *Magnetism and Aeronomy*, *14*, pp. 380-382 (in Russian).

Ershov, S., Mikhaylovskaya, I., and Novik, O., 2001. Electromagnetic signals of seismic excitation of geological structures beneath a sea bottom. *Phys. and Chem. of the Earth, 26*, No. 10-12, pp. 761-768.

Hayakawa (Editor), 2003. *Atmospheric and Ionospheric Electromagnetic Phenomena associated with Earthquakes*. Terra Scientific Publishing Company (TERRAPUB), Tokyo.

Hayakawa, M. and Fujinawa,Y. (Editors), 1994. *Electromagnetic Phenomena Related to Earthquake Prediction*. Terra Scientific Publishing Company (TERRAPUB), Tokyo.

Hayakawa, M. and Molchanov, O. (Editors), 2002. *Seismo-Electromagnetics*. Terra Scientific Publishing Company (TERRAPUB), Tokyo.

Heinson, G., Constable, S., and White, A., 2000. Episodic melt transport at a mid-ocean ridge inferred from magnetotelluric sounding. *Geophys. Research Letters, 27*, pp. 2317-2320.

Johnston, M.J.S and Parrot, M. (Editors), 1998. *Phys. Earth Planet. Inter.*(Special Issue),*105*, Nos. 3-4.

Iyemori T. *et al.*, 1996. Co-seismic geomagnetic variations observed at the 1995 Hyogoken-Nanbu earthquake. *J. Geomag. Geoelectr., 48*, pp.1059-1070.

Landau, L.D. and Lifshits, E.M., 1986. *Course of Theoretical Physics*, Vol. VI. *Fluid Mechanics*. Academic Press.

Maugin, G..A., 1988. *Continuum Mechanics of Electromagnetic Solids*. North-Holland, Amsterdam.

Novik, O.B., 1995. The Galerkin method for a three-dimensional nonlinear system of magnetothermoelasticity equations. *Transactions (Doklady) of the Russian Academy of Sci., 335A*, No 3, pp.15-21.(Translated from Russian: *Doklady Rossiyskoy Akademii Nauk*, 1994, *334*, pp. 100-102).

Novik, O.B. and Ershov, S.V., 2001. *Electromagnetic and temperature signals from the Earth's depth* (Scientific Monographs of Federal Program of Integration of High Education and Fundamental Science, Moscow, in Russian).

Novik, O.B., Ershov, S.V., and Mikhaylovskaya, I.B. 2001. Electromagnetic signals in atmosphere caused by dynamic processes in ocean lithosphere, in *Proceedings of the 15th European Space Agency Symposium on Rocket and Balloon Programs and Related Research*, Biarritz, France, 28-31 May 2001, pp. 369-373.

Novik, O.B., Ershov, S.V., and Mikhaylovskaya, I.B., 1998. Mathematical Problems of Seismological Monitoring of Geothermal Areas. *Proceedings of XXIII Workshop on Geothermal Reservoir Engineering, Stanford University, January* 26-28, 1998, pp.461-467.

Pinardi, N. and Woods, J., 2002. *Ocean Forecasting*. Springer.

Richtmyer, R.D., 1978. Principles of advanced mathematical physics, Vol. 1. (Springer-Verlag, New-York, Heidelberg, Berlin).

Romanowicz, B., Suyehiro, K., and Kawakatsu, H. (Editors), 2001. *Long-Term Observations in the Oceans.* Workshop Report, January 21-27, 2001, Japan.

Rona P.A., Bemis, K.G., Silver, D., and Jones, C.D., 2002. Acoustic imagine, visualization, and quantification of buoyant hydrothermal plumes in the Ocean, *Marine Geophysical Researches, 23,* No 2, pp. 147-168.

Ruzhin, Yu. Ya. and Depueva, A.K., 1996. Seismoprecursors in space as plasma and wave anomalies, *Journal of Atmospheric Electricity, 16*, No 3, pp. 271-288.

Shapiro, N. M., Singh, S.K., and Pacheco, J., 1998. A fast and simple diagnostic method for identifying tsunamigenic earthquakes, *Geophysical Research Letters, 25,* No 20, pp. 3911-3914.

Webb, S. C., 1998. Broadband seismology and noise under the Ocean, *Reviews of Geophysics, 36*, No 1, pp. 105-142.

SUBJECT INDEX

(Papers included the terms are generally indexed only once)

Advances in Natural and Technological Hazards Research

Series Editor: Prof. Dr. Mohammed I. El-Sabh, *Département d'Océanographie, Université du Québec à Rimouski, 310 Allée des Ursulines, Rimouski, Québec, Canada G5L 3A1*

Publications

1. S. Tinti (ed.): *Tsunamis in the World.* Fifteenth International Tsunami Symposium (1991). 1993 ISBN 0-7923-2316-5
2. J. Nemec, J.M. Nigg and F. Siccardi (eds.): *Prediction and Perception of Natural Hazards.* Symposium Perugia, Italy (1990). 1993 ISBN 0-7923-2355-6
3. M.I. El-Sabh, T.S. Murty, S. Venkatesh, F. Siccardi and K. Andah (eds.): *Recent Studies in Geophysical Hazards.* 1994 ISBN 0-7923-2972-4
4. Y. Tsuchiya and N. Shuto (eds.): *Tsunami: Progress in Prediction, Disaster Prevention and Warning.* 1995 ISBN 0-7923-3483-3
5. A. Carrara and F. Guzzetti (eds.): *Geographical Information Systems in Assessing Natural Hazards.* 1995 ISBN 0-7923-3502-3
6. V. Schenk (ed.): *Earthquake Hazard and Risk.* 1996 ISBN 0-7923-4008-6
7. M.I. El-Sabh, S. Venkatesh, H. Denis and T.S. Murty (eds.): *Land-based and Marine Hazards.* Scientific and Management Issues. 1996 ISBN 0-7923-4064-7
8. J.M. Gutteling and O. Wiegman: *Exploring Risk Communication.* 1996 ISBN 0-7923-4065-5
9. G. Hebenstreit (ed.): *Perspectives on Tsunami Hazard Reduction.* Observations, Theory and Planning. 1997 ISBN 0-7923-4811-7
10. C. Emdad Haque: *Hazards in a Fickle Environment: Bangladesh.* 1998 ISBN 0-7923-4869-9
11. F. Wenzel, D. Lungu and O. Novak (eds.): *Vrancea Earthquakes: Tectonics, Hazard and Risk Mitigation.* 1999 ISBN 0-7923-5283-1
12. S. Balassanian, A. Cisternas and M. Melkumyan (eds.): *Earthquake Hazard and Seismic Risk Reduction.* 2000 ISBN 0-7923-6390-6
13. S.L. Soloviev, O.N. Solovieva, C.N. Go, K.S. Sim and N.A. Shchetnikov: *Tsunamis in the Mediterranean Sea 2000 B.C. – 2000 A.D.* 2000 ISBN 0-7923-6548-8
14. J.V. Vogt and F. Somma (eds.): *Drought and Drought Mitigation in Europe.* 2000 ISBN 0-7923-6589-5

15. M. Oya: *Applied Geomorphology for Mitigation of Natural Hazards.* 2001 ISBN 0-7923-6719-7
16. E. Coles, D. Smith and S. Tombs (eds.): *Risk Management and Society.* 2001 ISBN 0-7923-6899-1
17. T. Glade, P. Albini and F. Francés: *The Use of Historical Data in Natural Hazard Assessments.* 2001 ISBN 0-7923-7154-2
18. G.T. Hebenstreit (ed.): *Tsunami Research at the End of a Critical Decade.* 2001 ISBN 1-4020-0203-3
19. J. Locat and J. Mienert (eds.): *Submarine Mass Movements and Their Consequences.* 1st International Symposium. 2003 ISBN 1-4020-1244-6
20. K.F. O'Loughlin and J.F. Lander: *Caribbean Tsunamis.* A 500-Year History from 1498-1998. 2003 ISBN 1-4020-1717-0
21. J.P. Stoltman, J. Lidstone and L.M. DeChano (eds.): *International Perspectives on Natural Disasters: Occurrence, Mitigation, and Consequences.* 2004 ISBN 1-4020-2850-4
22. L.C. Botterill and D.A. Wilhite (eds.): *From Disaster Response to Risk Management.* Australia's National Drought Policy. 2005 ISBN 1-4020-3123-8
23. K. Satake (ed.): *Tsunamis.* Case Studies and Recent Developments. 2005 ISBN 1-4020-3326-5